Transactions of the ASME

Journal of Engineering for Power

Published Quarterly by The American Society of Mechanical Engineers
VOLUME 104 • NUMBER 3 • JULY 1982

Journal of Engineering for Power (ISSN 0022-0825) is edited and published quarterly at the offices of The American Society of Mechanical Engineers, United Engineering Center, 345 E. 47th St., New York, N. Y. 10017. ASME-TWX No. 710-581-5267, New York. Second Class postage paid at New York, N.Y., and at additional mailing offices.

CHANGES OF ADDRESS must be received at Society headquarters seven weeks before they are to be effective. Please send old label and new address.

PRICES: To members, $30.00, annually; to nonmembers, $60.00. Single copies, $20.00 each. Add $5.00 for postage to countries outside the United States and Canada.

INDEXED by the Engineering Index, Inc.

TECHNICAL PAPERS

525 **A Study of the Modal Truncation Error in the Component Mode Analysis of a Dual-Rotor System** (81-GT-144)
D. F. Li and E. J. Gunter

533 **Fractional-Frequency Rotor Motion Due to Nonsymmetric Clearance Effects** (81-GT-145)
D. W. Childs

542 **Short Duration Measurements of Heat-Transfer Rate to a Gas Turbine Rotor Blade** (81-GT-146)
H. Consigny and B. E. Richards

552 **Component Mode Synthesis of Large Rotor Systems** (81-GT-147)
D. F. Li and E. J. Gunter

561 **Turbulence Characteristics in the Annulus-Wall Boundary Layer and Wake Mixing Region of a Compressor Rotor Exit** (81-GT-148)
B. Lakshiminarayana and R. Davino

571 **Analysis and Asymptotic Solutions of Compressible Turbulent Corner Flow** (81-GT-149)
A. G. Mikhail and K. N. Ghia

580 **Equivalent Performance Testing of Multisection Compressors** (81-GT-150)
M. A. Strite and N. A. Samurin

586 **Engine Dynamic Analysis With General Nonlinear Finite-Element Codes, Part 1: Overall Approach and Development of Bearing Damper Element** (81-GT-151)
M. L. Adams, J. Padovan, and D. G. Fertis

594 **Ceramic to Metal Attachment Using Low Modulus BRUNSBOND Pad** (81-GT-160)
R. P. Tolokan, J. C. Nablo, and J. B. Brady

601 **Fabrication of Injection Molded Sintered Alpha SiC Turbine Components** (81-GT-161)
R. S. Storm, R. W. Ohnsorg, and F. J. Frechette

607 **Water-Cooled Gas Turbine Monometallic Nozzle Fabrication and Testing** (81-GT-162)
P. W. Schilke and C. L. DeGeorge

617 **The Effect of Bending-Torsion Coupling on Fan and Compressor Blade Flutter** (81-GT-163)
O. O. Bendiksen and P. P. Friedman

624 **Nuclear Blast Response of Airbreathing Propulsion Systems: Laboratory Measurements With an Operational J-85-5 Turbojet Engine** (81-GT-164)
M. G. Dunn and J. M. Rafferty

633 **The Influence of Blade Number Ratio and Blade Row Spacing on Axial-Flow Compressor Stator Blade Dynamic Load and Stage Sound Pressure Level** (81-GT-165)
H. E. Gallus, H. Grollius, and J. Lambertz

642 **Application of Lifting Line Theory to Streamsurface Theory in Subsonic Flow** (81-GT-166)
P. T. Chang

650 **An Inverse Time Marching Method for the Definition of Cascade Geometry** (81-GT-167)
G. Meauzé

657 **A Method for the Calculation of the Wall Layers Inside the Passage of a Compressor Cascade With and Without Tip Clearance** (81-GT-168)
A. Comte, G. Ohayon, and K. D. Papailiou

668 **Solution of Plane Cascade Flow Using Improved Surface Singularity Methods** (81-GT-169)
E. R. McFarland

675 **Supersonic Stall Flutter of High-Speed Fans** (81-GT-184)
J. J. Adamczyk, W. Stevans and R. Jutras

683 **The Influence of Unsteady Rotor Response on a Distorted Flow Field** (81-GT-185)
R. E. Henderson and I. C. Shen

692 **Effect of Time-Dependent Flight Loads on Turbofan Engine Performance Deterioration** (81-GT-203)
B. L. Lewis, A. Jay, and E. G. Stakolich

698 **Boundary Layer Development on Turbine Airfoil Suction Surfaces** (81-GT-204)
O. P. Sharma, R. A. Wells, R. H. Schlinker, and D. A. Bailey

(Contents continued on p. 532)

(Contents Continued)

707 **Mechanical Design of a High-Efficiency 7.5-MW (10,000-hp) Gas Turbine** (81-GT-210)
J. P. Van Buijtenen and W. M. Farrell

715 **Theoretical Study of Flow Instabilities and Inlet Distortions in Axial Compressors** (81-GT-211)
P. Ferrand and J. Chauvin

ANNOUNCEMENTS

560 **Change of address form for subscribers**

570 **Mandatory excess-page charges**

722 **Errata**

D. F. Li[1]

E. J. Gunter

Professor.

Mechanical and Aerospace,
Engineering Department,
University of Virginia,
Charlottesville, Va. 22901

A Study of the Modal Truncation Error in the Component Mode Analysis of a Dual-Rotor System

In the component mode synthesis method, the equation of motion in the generalized coordinates is built upon the undamped eigenvalue data of the component structures. Error is inevitable when truncated modes are used. In this paper, two model truncation schemes were evaluated with regard to the critical speed, stability, and unbalance response of a two-spool gas turbine engine. The numbers of modes required to yield acceptable accuracy in these cases were determined. Guidelines for modal truncation were derived from these results.

Introduction

One of the major considerations in a truncated model analysis is determining the modes to be retained for accuracy and yet maintaining computational efficiency. Some amount of error is always introduced in the use of a number of modes less than the number of degrees of freedom presented in the system. The resulting modal representation will be somewhat "stiffer" than it actually is because the higher modes are omitted. However, despite this slight disadvantage, the modal method continues to play an important role in the analysis of large dynamic systems because of the substantial saving in computation time associated with the resultant reduction in the problem size.

The modal method has been applied to the analysis of linear and nonlinear rotor systems. Childs performed transient rotor dynamic analyses using undamped normal modes in [1-4]. Dennis, et al. presented a transient solution of an aircraft engine in [5]. Gunter, et al. illustrated and evaluated the accuracy of the planar mode approach in single shaft flexible rotor with bowed shaft and skewed disk effects [6]. Transient motions of a flexible rotor in fluid film bearings were simulated by Choy [7]. Lund [8] used the damped modal coordinates to calculate the unbalance response and the transient motion of a multi-mass rotor caused by a shock loading. In [9] the effects of bearing mass and prescribed base motion was computed by Pilkey et al. using damped modes.

The present paper focuses on the component mode synthesis method using undamped modes. This procedure is used extensively in the aerospace industry for the calculation of the undamped natural frequencies of large air-frame structures (Hurty [10] and Craig et al. [11]) and was applied to multi-component flexible rotor systems by Childs [4] and Li [13,17]. In this method, a large structure is first partitioned into a number of substructures. The modal information for each individual substructure is then derived either analytically or from vibration tests [12]. "Reconstruction" of the original structure is performed in the modal coordinates using only a few modes from each substructure.

In this paper, an aircraft gas turbine engine consisting of two coaxially mounted rotors is used as a vehicle for the comparison of the component mode synthesis method to an accurate method using transfer matrices [13-15]. Efforts are directed to the evaluation of two proposed mode selection criteria [16] and the determination of the number of lower modes that ought to be retained. The accuracy of the component mode method in this application is examined with regard to linear dynamics in the critical speeds, stability, and forced unbalance response.

Description of the Gas Turbine Rotor System

Figure 1 represents a schematic drawing of the two-spool gas turbine engine used in this analysis. The engine consists of two coaxial rotors. The inner core rotor called the power turbine is supported by two main bearings. There are two intermediate differential bearings, Front Differential Bearing (FDB) and Aft Differential Bearing (ADB), connecting the power turbine to a gas generator rotor. The gas generator rotor consists of a two-stage turbine driving an axial compressor. It is supported by four rolling element bearings.

The computer model in Fig. 2 has a total of 38 nodes (lumped masses) - 22 nodes in the power turbine rotor and 16 nodes in the gas generator rotor. Each node has two translational degrees of freedom and two rotational degrees of freedom. Thus, this engine has a total of 152 degrees of freedom.

Gas Turbine Undamped Component Modes

A component mode analysis requires the undamped eigenvalues and the orthonormal mode shapes of each sub-

[1] Now at the General Motors Research Laboratories, Mechanical Research Department, Warren, Michigan 48090.

Contributed by the Gas Turbine Division and presented at the International Gas Turbine Conference and Products Show, Houston, Texas, March 9-12, 1981, of THE AMERICAN SOCIETY OF MECHANICAL ENGINEERS. Manuscript received at ASME Headquarters, December 15, 1980. Paper No. 81-GT-144.

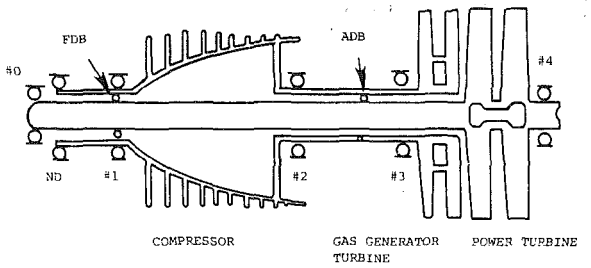

Fig. 1 Two-spool aircraft turbine engine with eight bearings

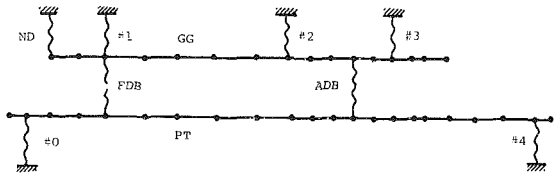

Fig. 2 Two-spool aircraft turbine engine lumped parameter computer model (*PT*-power turbine rotor, *GG*-gas generator rotor)

system to be known. In this case, the engine is considered to be consisting of two subsystems—the gas generator rotor and the power turbine rotor. The modes of the rotors were obtained independently of each other by omitting the intermediate bearings. The effects of disk gyroscopic are excluded by applying zero rotor speed in this calculation.

The method of transfer matrices was used to obtain all undamped normal modes of the gas generator rotor and the power turbine rotor below (1,833 Hz) 110,000 r/min. Below this speed (about 6 times the top operating speed of the rotors), there are a total of five modes in the gas generator rotor and nine modes in the power turbine rotor. The first 5 in each rotor are presented in Figs. 3 and 4.

The mode shapes $[\phi]$ are to be arranged in the following fashion.[2]

$$[\phi_1] = \begin{bmatrix} [\phi_G] & [0] \\ [0] & [\phi_G] \end{bmatrix}; [\phi_2] = \begin{bmatrix} [\phi_p] & [0] \\ [0] & [\phi_P] \end{bmatrix} \quad (1)$$

The accuracy of the undamped mode shapes are evaluated with a test of their orthogonality weighted by the mass matrix. In such a test of product of the matrices $[\phi_i]^T [M] [\phi_i]$, $i = 1,2$, is computed and the off-diagonal elements of the resultant matrix (which should be equal to zero) are compared to the diagonal elements. For the normal modes calculated, the ratio of the off-diagonal to the diagonal elements is in the order of 10^{-10}. With transfer matrices, each mode requires about 1.8 s of computer time to evaluate.

Gas Turbine Engine Mode Selection

Selection of the component modes from each subsystem to be used in the synthesis of the engine is made according to one of the following criteria.

1 The first criterion is based on a comparison of the subsystem undamped natural frequencies to an upper frequency limit. Only the component modes that are below this limit are retained, those that are above are discarded. In a rotating machine, this upper limit is usually set at several times the maximum rotor speed.

2 The second criterion proposed by Tolani in [16] is based on the strain energy of the subsystems. In this case, an upper limit on the strain energy is set and only the component modes that have strain energy below this value are considered. For each subsystem component mode having the mode shape $\{\phi_i\}$, the strain energy (PE) is calculated from the system stiffness matrix by

$$PE = \frac{1}{2} \{\phi_i\}^T [K] \{\phi_i\} \quad (2)$$

the mode shape $\{\phi_i\}$ is normalized such that the sum of the absolute values of the elements in $\{\phi_i\}$ is equal to one.

[2] Subscripts 1 and 2 refer to subsystem 1 and subsystem 2. $[\phi_G]$ and $[\phi_p]$ represent the planar component modes in the gas generator and the power turbine, respectively.

Table 1 represents the selections of the component modes for the truncated modal problem based on these two criteria. For example, with a problem size of 12 (i.e., taking six component modes in each lateral direction), the modes selected on the basis of frequency include all that are below 500 Hz. This frequency is about 1.5 times the maximum rotor speed. While based on strain energy, a limiting energy of 508 J is imposed. With the strain energy criterion, the tendency is towards selecting more power turbine modes and fewer gas generator modes because the power turbine is more flexible. Note that after the problem size reaches 24, the schemes become identical to each other.

To evaluate the mode selection schemes, the undamped critical speeds of the gas turbine engine are compared for the various reduced problems. Of particular interest in this investigation is the comparison in the suitability of the criteria for this application with regard to solution accuracy.

Here, both rotors are assumed to rotate in the same direction with the gas generator operating at 15,000 r/min and the power turbine operating at 20,000 r/min. The inter-shaft bearings are added to the modal equation in the generalized coordinates [13]. The percentage errors in the system eigenvalues or the engine critical speeds due to modal truncation are established by a comparison to an accurate solution of the full size problem.

Figures 5-6 show the errors of the first four forward engine modes and the first four backward engine modes for the two modal selection schemes. In general, the component mode method predicts the engine modes to be higher in frequency than they actually are. As more component modes are used, the magnitude of the error decreases monotonically. With the exception of the third forward, the first backward, and the fourth backward engine modes, the mode selection scheme based on frequency appears to yield better results than the selection scheme based on strain energy. This is particularly true with the second forward and the second backward engine modes.

When all 28 component modes are used, the largest error of only 1 percent is observed (in the third forward engine mode). The smallest error is 0.01 percent with the second forward mode of the engine.

If only the engine critical speeds below the top speed of the rotors (20,000 r/min) are considered, the upper frequency limit for the modal selection necessary to meet a certain error tolerance may be established. This information is tabulated in Table 2.

Gas Turbine Lateral Critical Speeds

There are two possible modes of operation in a two-spool rotor system: one is that both rotors corotate simultaneously in the same direction, the other is that the rotors counter-rotate with respect to each other. In this analysis, only the case of corotation is considered. The gas generator and the power turbine are assumed to be operating at 15,000 r/min and 20,000 r/min, respectively. With the transfer matrix method, the first five forward and the first five backward engine critical speeds are calculated (the backward modes are obtained by specifying negative rotor speeds in the computer

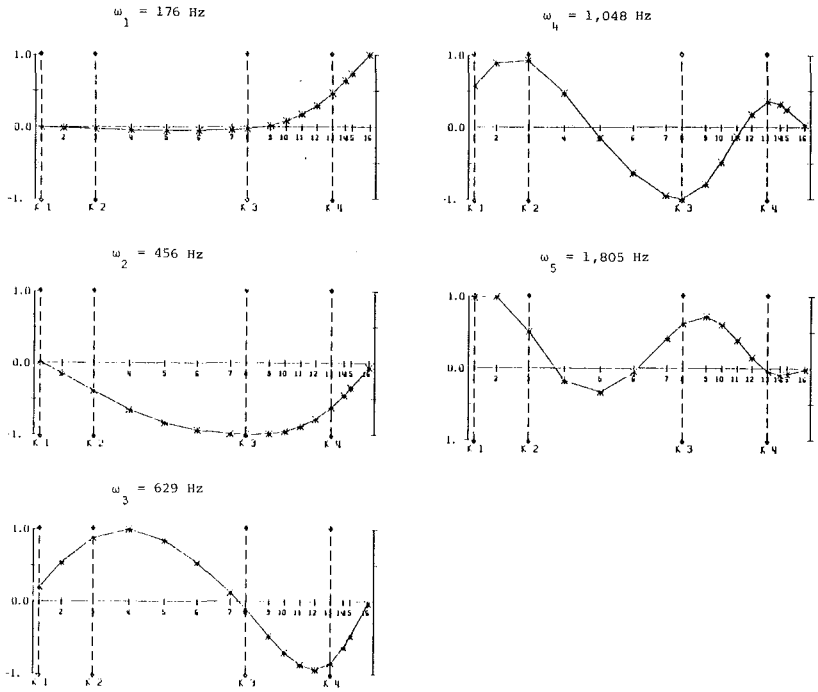

Fig. 3 Gas generator rotor undamped component mode 1 to mode 5. $K1 = 1.75 \times 10^8$ N/m; $K2 = 1.75 \times 10^8$ N/m; $K3 = 0.88 \times 10^8$ N/m; $K4 = 0.70 \times 10^8$ N/m.

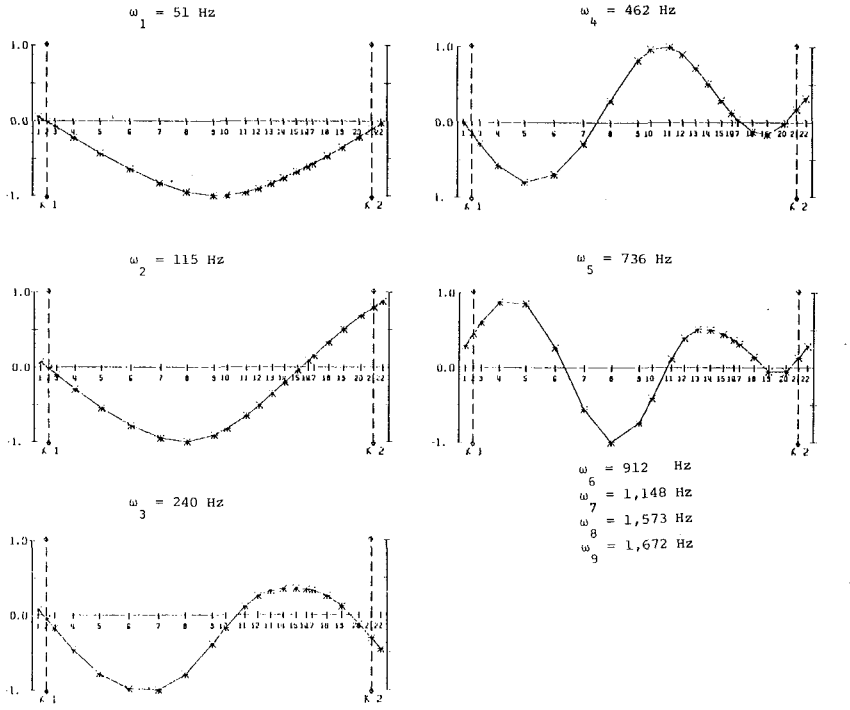

Fig. 4 Power turbine rotor undamped component mode 1 to mode 5. $K1 = 0.88 \times 10^8$ N/m; $K2 = 1.05 \times 10^7$ N/m

program). This result, calculated to an error of less than 1.0×10^{-5} percent, is used to assess the accuracy of a truncated component mode analysis for the following reduced problems using: (*a*) two gas generator modes and four power turbine modes, (*b*) three gas generator modes and six power turbine modes, (*c*) five gas generator modes and nine power turbine modes. The component modes have been selected according to the frequency criterion described previously. The critical speeds are calculated with a stability program assuming zero damping. The result of this investigation is tabulated in Table 3. Good accuracy of the modal method is obtained. Errors less than 1 percent are achieved with the largest problem size. Reasonably accurate results are also obtained for the problem size of 18 with the use of three gas generator modes and six

Table 1 Gas turbine engine mode selection schemes

REDUCED PROBLEM DIMENSION	MODE SELECTION BASED ON FREQUENCY		MODE SELECTION BASED ON STRAIN ENERGY	
	GAS GENERATOR MODES RETAINED	POWER TURBINE MODES RETAINED	GAS GENERATOR MODES RETAINED	POWER TURBINE MODES RETAINED
8	1	3	0	4
10	2	3	0	5
12	2	4	1	5
14	3	4	2	5
16	3	5	2	6
18	3	6	2	7
20	4	6	2	8
22	4	7	3	8
24	4	8	4	8
26	4	9	4	9
28	5	9	5	9

Table 2 Modal truncation cut-off frequency versus percentage error in the undamped modes (* modes retained in each lateral plane)

UPPER FREQUENCY LIMIT BELOW WHICH MODES ARE RETAINED (MULTIPLES OF TOP ROTOR SPEED)	GAS GENERATOR MODES * RETAINED	POWER TURBINE MODES * RETAINED	ERROR IN THE UNDAMPED MODES BELOW TOP ROTOR SPEED
1.5	2	4	< 20%
2.5	3	5	< 6%
4	4	6	< 3%
5	4	8	< 1.5%
6	5	9	< 1%

power turbine modes. In this case, the third forward mode has the largest error of 3.29 percent.

The computer time requirement for the calculation of the undamped critical speeds using transfer matrices is about 3.8 s for each mode computed. A direct comparison of the computational efficiency of the two methods based on the result in this section was not possible because the eigenvalues calculated with the method of component modes were generated from a stability computer program using complex arithmetic. Furthermore, an eigenvalue extraction scheme based on similarity transformations was used such that all existing eigenvalues including both forward and backward modes are computed simultaneously. For example, with a problem size of 18, 18 conjugate pairs of roots with zero real parts are produced in 77 s. In contrast, the transfer matrix computer program calculates only the modes required by iterating on the frequency determinant in real arithmetic. If a similar procedure is employed in the modal calculation, it is anticipated that the computer time requirement of the component mode method will be comparable to, if not less than that of the transfer matrix method.

The mode shapes of the first, second, and the third forward modes obtained with component modes and transfer matrices are presented in Figs. 7-9. For the first and second modes, very little error due to modal truncation is observed. When a reduced modal problem consisting of only six component modes per lateral plane is used, some inaccuracy is indicated in the third forward mode shapes. The percentage error in this mode is 20 percent according to data in Table 3.

Gas Turbine Lateral Stability

In the stability analysis, two fluid film components are added to the system. The No. 3 gas generator bearing is replaced by a squeeze film damper assumed to have a stiffness of 2.15×10^7 N/m (123,000 lb/in.) and a damping of 1.7×10^4 N-s/m (100 lb-sec/in.). In comparison to the original stiffness of 7.0×10^7 N/m (400,000 lb/in.) used in the component normal mode evaluation, this modification

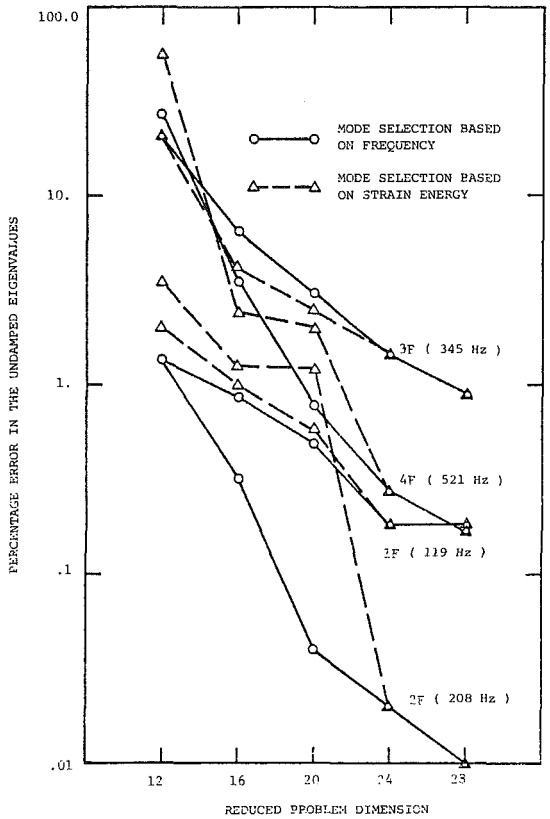

Fig. 5 Percentage error in the gas turbine undamped forward modes due to modal truncation

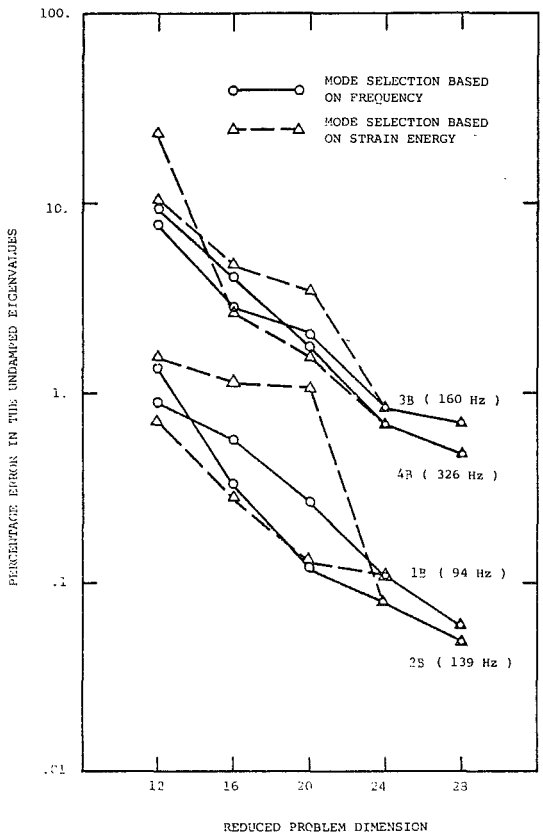

Fig. 6 Percentage error in the gas turbine undamped backward modes due to modal truncation

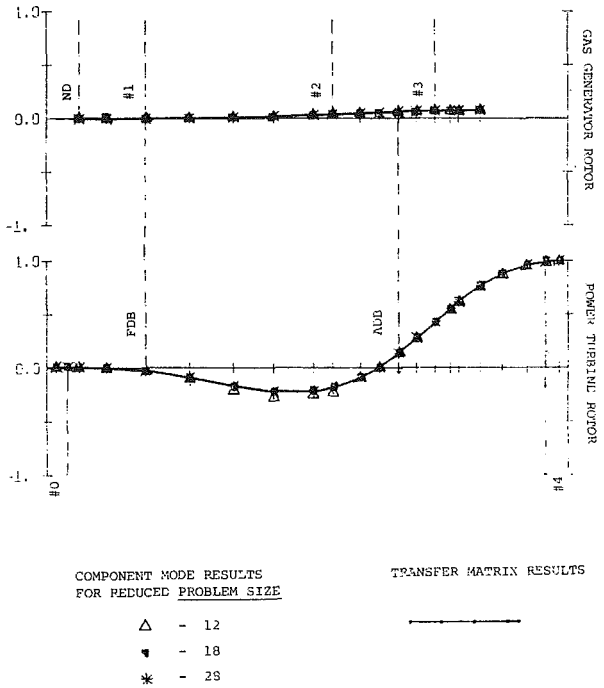

Fig. 7 Gas turbine engine critical speed mode shape error due to component mode truncation—first system forward mode (119 Hz)

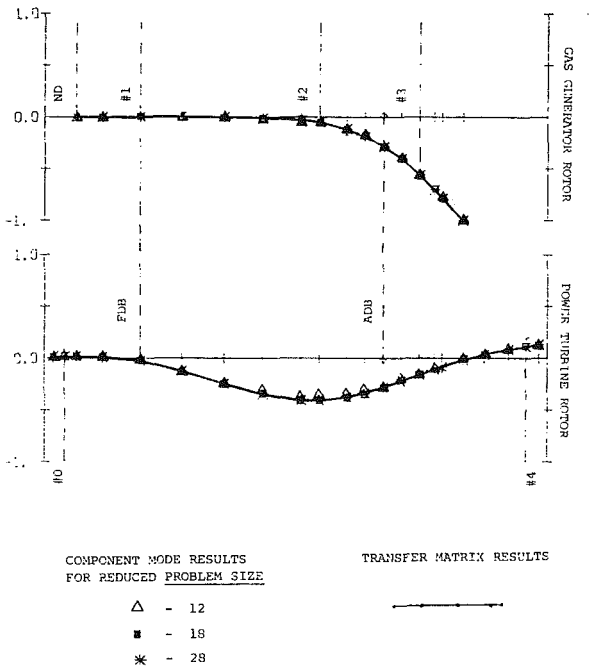

Fig. 8 Gas turbine engine critical speed mode shape error due to component mode truncation—second system forward mode (208 Hz)

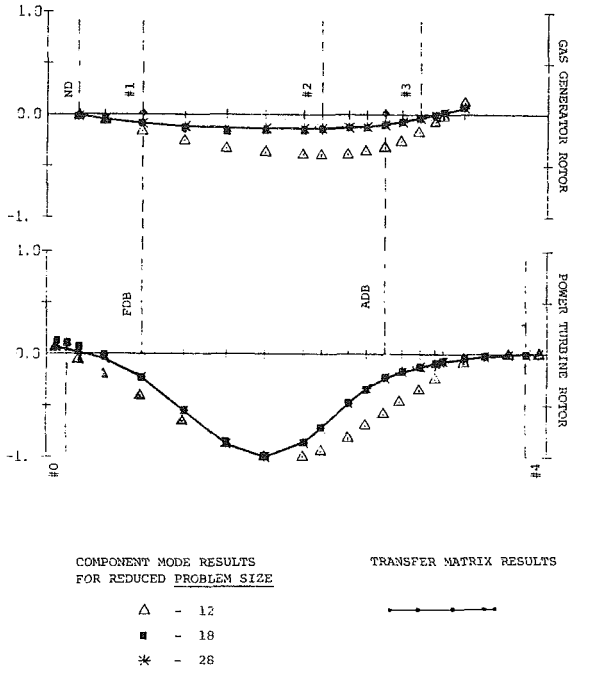

Fig. 9 Gas turbine engine critical speed mode shape error due to component mode truncation—third system forward mode (345 Hz)

Table 3 Error in the gas turbine critical speeds using truncated component modes. (*Problem size is the dimension of the second order modal equation.)

UNDAMPED MODE	TYPE	CRITICAL SPEED, r/min (Hz)	% ERROR FOR THE REDUCED*PROBLEM SIZE		
			12	18	28
1st Mode	Forward	7,115.7 (119)	1.38	0.52	0.18
2nd Mode	Forward	12,471.0 (208)	1.31	0.32	0.01
3rd Mode	forward	20,677.7 (345)	20.17	3.29	0.89
4th Mode	Forward	31,283.1 (521)	26.88	1.38	0.17
5th Mode	Forward	35,403.9 (590)	23.44	2.43	1.22
1st Mode	Backward	5,656.4 (95)	0.90	0.28	0.06
2nd Mode	Backward	8,311.7 (139)	1.38	0.30	0.05
3rd Mode	Backward	9,596.3 (160)	7.86	2.04	0.70
4th Mode	Backward	19,528.6 (326)	9.67	2.42	0.48
5th Mode	Backward	27,563.9 (460)	28.22	1.43	0.39
Computer Time Required to Calculate the Component Modes			11 s	16 s	25 s
Computer Time Required to Calculate all Eigenvalues Using a Transformation Method			35 s	77 s	179 s

requires a negative stiffness of 4.85×10^7 N/m (277,000 lb/in.) to be applied at the No. 3 bearing location in the modal synthesis process. In addition, an inter-shaft fluid-film bearing is incorporated near the aft differential bearing. The bearing is 38 mm long, 66 mm in diameter and has a radial clearance of 0.25 mm. Turborotor speeds are taken to be 15,000 r/min for the gas generator and 17,000 r/min for the power turbine rotating in the same direction. The dynamic coefficients are computed according to the short bearing theory. A bearing eccentricity ratio of 0.3 is assumed. The function of the fluid-film bearings is to provide some of the damping required to relieve the high loading experienced by the aft differential bearing when the rotor is operated near a power turbine mode. In this calculation, all the rolling element bearings are taken to have damping of 350 N-s/m (2 lb-sec/in.) each.

The complex eigenvalues of the damped system are computed with an error of less than 0.01 percent by the transfer matrix method. This result forms the basis for evaluating the accuracy of the component mode approach. For the purpose of comparison, all engine modes below 51.7 Hz (31,000 r/min), including four forward modes and five backward modes, are considered. With the use of transfer matrices, each complex root requries about 3.9 s to compute.

Table 4 shows the truncation error for the three different

Table 4 Error in the gas turbine engine stability using truncated component modes. (*Problem size is the dimension of the second order modal equation.)

DAMPED MODE	DAMPING EXPONANT, 1/s	DAMPED FREQUENCY, r/min (Hz)	% ERROR IN THE DAMPING EXPONENT FOR THE REDUCED PROBLEM SIZE *			% ERROR IN THE DAMPED FREQUENCY FOR THE REDUCED PROBLEM SIZE*		
			12	18	28	12	18	28
1st Forward	-19.85	6,978.3 (116)	-43.1	-1.64	-1.55	2.00	0.39	0.19
2nd Forward	-155.2	8,926.0 (149)	-13.3	-3.17	-0.94	8.33	1.74	0.23
3rd Forward	-14.48	20,758.1 (346)	216.	13.1	-0.61	18.01	3.16	0.85
4th Forward	-52.71	30,257.3 (504)	416.	5.17	1.29	31.19	1.42	0.29
1st Backward	-9.71	5,924.8 (99)	-5.60	-2.16	-0.47	0.45	0.12	0.02
2nd Backward	-87.03	6,167.7 (103)	-14.5	-2.94	-1.32	1.46	0.44	0.35
3rd Backward	-1.91	10,093.8 (168)	79.6	53.8	13.94	8.51	2.01	0.70
4th Backward	-136.2	18,674.5 (311)	-15.6	-1.91	0.00	8.38	2.01	0.25
5th Backward	-194.0	25,970.1 (433)	-91.2	-7.21	-3.08	25.60	2.18	0.57
Computer Time Required to Calculate the Undamped Component Modes						11 s	16 s	25 s
Computer Time Required to Calculate All Eignevalues Using a Transformation Method						32 s	66 s	177 s

problem sizes using component modes. The component mode selection scheme is the same as those for the critical speed analysis in the last section. A common feature of the modal result is that the resonant frequencies of the damped engine system have a positive error. This means that these frequencies are always overestimated due to modal truncation. In contrast, tendency of the error in the damping exponent does not seem to show any definite pattern.

The amount of error in the damped frequency of the reduced modal problems is of the same order of magnitude as that in the undamped critical speeds computed previously. For a problem size of 28, in which 14 component modes in each lateral plane are used, the largest error in the frequencies is only 0.85 percent. But when the problem size is reduced to 18, the amount of error increases. In this case, the largest error of about 3 percent is observed in the third forward mode. A further decrease in the accuracy is indicated for the problem size of 12. If only the damped modes that are below 334 Hz (20,000 r/min) are considered, an error of up to 18 percent can be seen.

The real part of the eigenvalues is shown to have considerably larger error than the damped frequency. Even when all of the 28 undamped planar modes are employed, an error as high as 14 percent in the exponent of the third backward mode is obtained. For the same problem size, the largest inaccuracy in the forward modes is 1.6 percent. With a reduction of the problem size to 18, the largest overall error is 54 percent and the largest forward mode error is 13 percent. Unacceptable error is produced in the damped exponents for the problem size of 12. This general inaccuracy of the real part of the complex eigenvalues is also reported by Gunter, et al. in [6].

It should be noted that all four backward modes appear to be less stable than the forward modes. Since the majority of the damping comes from the No. 3 gas generator squeeze film damper bearing, it is reasoned that the result reflects a lower efficiency of the squeeze-film damper bearing in the backward modes.

Gas Turbine Lateral Unbalance Response

The forced response of the gas turbine engine due to mass unbalance in the power turbine rotor is computed with the same bearing configurations as those described in the last section. For this analysis, two unbalances of 35 g.cm each are assumed to be present at the mid-span of the power turbine rotor and at the second stage turbine 180 deg out of phase from each other. The gas generator is taken to be balanced and operating at 15,000 r/min.

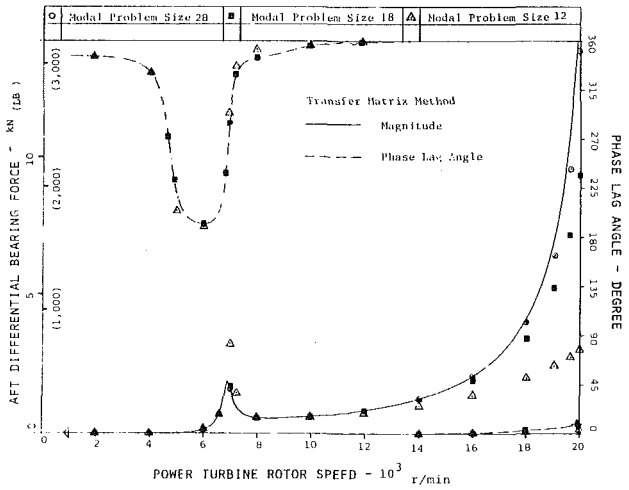

Fig. 10 Component mode truncation error in the aft differential bearing force due to coupled power turbine unbalance

The dynamic coefficients of the bearings, including those of the squeeze film damper and the intershaft journal bearing, are considered to be constant with speed. Again, the unbalance response problem is solved first with the transfer matrix method, then with component modes using a truncated number of modes.

Because mass unbalance in a rotor generates circular forces that rotate in the same direction as the rotor spin vector, only the forward modes are excited. According to Table 4, the first three damped forward modes of the engine occur at 116 Hz (6,978 r/min), 149 Hz (8,926 r/min), and 346 Hz (20,758 r/min). Therefore, within the speed range of 1,000 r/min to 20,000 r/min the rotors have to operate through the first two modes and below, but close to the third mode of the system.

In general, there are two predominant factors that determine whether the response amplitudes and the bearing forces will be higher or lower than the actual value due to modal truncation. The first factor depends on the error introduced in the damping available for each mode due to the omission of some of the higher component modes. As it is concluded in the last section, the tendency of the error in this respect does not have a definite pattern. If the error tends towards producing less damping, a response of lesser amplitude will be computed. The reverse will be true if the error tends toward producing more damping in a particular mode. The second factor is determined by the shift of the damped resonant frequency towards a higher value due to the loss of system

flexibility. Consequently, the amplitude of vibration computed by a modal method will be lower on the low-speed side but higher on the high-speed side of the actual response peak.

The steady-state forces transmitted to the outer raceway of the differential bearing are presented in Fig. 10. Due to the large damping coefficient assumed at the No. 3 gas generator bearing, the second mode, which shows predominant gas generator motion in the mode shape, has been completely damped out. The magnitude of the bearing forces shows a peak of about 1.8 kN at the first critical speed and starts to build up rather rapidly as the power turbine rotor is operated toward the third system mode. A bearing force higher than 14 kN is indicated at rotor speeds above 19,000 r/min.

The symbols in Fig. 10 represent the bearing forces calculated by the component mode method using the reduced problem sizes of 12, 18, and 28. With the problem size of 12, (two gas generator modes and four power turbine modes used) the force magnitude at the first critical speed is almost 70 percent higher than the correct value. This appears to be in correlation with the damped eigenvalue result which indicates an error of 43 percent less damping available to this mode for the same reduced problem size. As the rotor is operated near the third mode at about 20,000 r/min, a large error in the bearing force as much as 400 percent is indicated. The observation of a lower response amplitude and more gentle response slope associated with this mode is consistent with the eigenvalue error in the damping exponent of 216 percent as shown in Table 4. This combines with the shift towards a higher resonant frequency producing the observed result.

Excellent correlation between the transfer matrix method and the modal method for the problem size of 18 and 28 is indicated for bearing force in the first mode. When the rotor operates in the vicinity of the third mode, good accuracy can still be seen with the larger problem size of 28; however, about 40 percent error can be seen at 20,000 r/min with the problem size of 18.

Figure 11 shows the rotor response at the second stage turbine of the gas generator rotor. It is seen that the rotor has rather high amplitudes when it is operated near the first and third critical engine speeds (power turbine modes). Again, the amplitude at the second engine mode (gas generator mode) is almost damped out by the large amount of damping at the No. 3 gas generator bearing. According to the mode shapes in the power turbine modes (Figs. 7 and 9), the gas generator bearing location has very little motion. Therefore, damping applied to the gas generator at this location does not effectively reduce the vibration amplitude in these modes. Very large error is indicated with the problem size of 12, particularly near the first mode and the third mode. The shift of the second mode towards a higher frequency is clearly seen. When the problem size is increased to 18, the error is reduced to a more reasonable level. Good accuracy is again obtained with the problem size of 28 in which five gas generator modes and nine power turbine modes are included. The modal method appears to yield more accurate results in the phase angles than in the vibration amplitudes in this unbalance response analysis.

The computer time required in the calculation of the above results using the modal approach is 0.45 s for a problem size of 12, 0.67 s for a problem size of 18, and 1.47 s for a problem size of 28. These figures represent one steady-state response computation, excluding computer time taken to calculate the components modes. In comparison, the transfer matrix method requires 0.87 s per calculation.

Conclusions

Based on the results in this analysis, the selection of component modes according to an upper frequency limit is recommended. Furthermore, all component modes that have

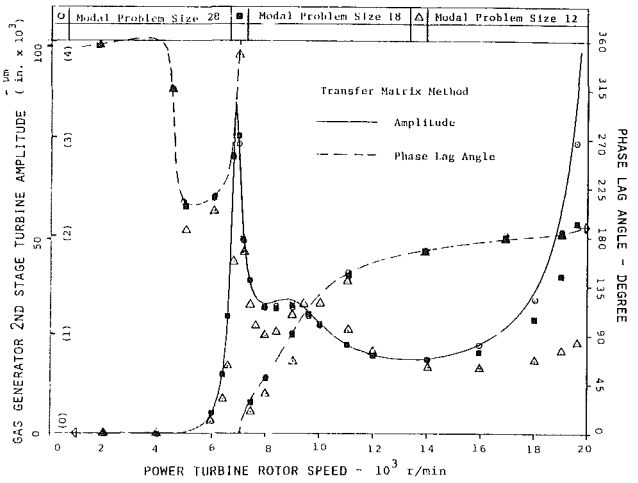

Fig. 11 Component mode trunction error in the gas generator response amplitude due to coupled power turbine unbalance

frequencies below 4 to 5 times the top rotor speed must be included in a critical speed analysis to give sufficient accuracy. Component mode synthesis is a fast and economical method for the calculating the undamped modes in a large rotor system.

Stability analysis using component modes must be performed with extreme caution. Accuracy in the damping exponent can only be obtained when all modes that lie below at least six times the highest rotor speed are retained in the calculation

For the computation of the steady-state unbalance response near the lower modes and up to the second mode in the operating speed range, the component mode method is more economical than the transfer matrix method both in computation time and accuracy. However, for higher mode computation, the transfer matrix method is superior.

Due to modal truncation, the resonant frequencies are always overestimated. But because the tendency of the error in the damping (relating to the real part of the eigenvalue) does not show any definite pattern, the unbalance response peaks may either be higher or lower than the actual values. It is shown that the damping exponents of the eigenvalues and the unbalance peak response always exhibit the largest error.

Because the modal method still provides the only efficient way to perform transient analysis of complex rotor systems, precaution must be taken in the interpretation of computer-simulated transient solutions using truncated modes. When the quantitative result is of interest, the analyst must ascertain that enough number of modes is included. An accurate solution is reached only when no significant change in the result can be achieved by the addition of more component modes.

Acknowledgments

This work is supported in part by the following research grants.

NASA - NAS8-31951-5
NASA Lewis - NSG-3177
ARMY - DAG 29-77-C-009

References

1 Childs, D. W., "A Rotor-Fixed Modal Simulation Model for Flexible Rotating Equipment," ASME *Journal of Engineering for Industry*, Vol. 96, No. 2, 1974, pp. 359–669.

2 Childs, D. W., "Two Jeffcott-Based Modal Simulation Models for Flexible Rotating Equipment," ASME *Journal of Engineering for Industry*, Vol. 97, No. 3, 1975, pp. 1000–1014.

3 Childs, D. W., "A Modal Transient Rotor Dynamic Model for Dual-Rotor Jet Engine Systems," ASME *Journal of Engineering for Industry*, Vol. 98, No. 3, 1976, pp. 876–882.

4 Childs, D. W., "The Space Shuttle Main Engine High-Pressure Fuel Turbopump Rotor - Dynamic Instability Problem," ASME JOURNAL OF ENGINEERING FOR POWER, Vol. 100, No. 1, 1978, pp. 48–57.

5 Dennis, A. J., Erikson, R. H., and Seitelman, L. H., "Transient Response Analysis of Damped Rotor Systems by the Normal Mode Method," ASME Paper No. 75-GT-58, Gas Turbine Conference, Houston, Texas, Mar. 1975.

6 Gunter, E. J., Choy, K. C., and Allaire, P. E., "Modal Analysis of Truborotors Using Planar Modes - Theory," *Journal of the Franklin Institute*, Vol. 305, No. 4, pp. 221–243.

7 Choy, K. C., Gunter, E. J., Allaire, P. E., "Fast Fourier Transform Analysis of Rotor-Bearing Systems," *Topics in Fluid Film Bearing and Rotor Bearing System Design and Optimization*, presented at the ASME Design Engineering Conference and Shows, Illinois, Apr. 1978.

8 Lund, J. W., "Modal Response of a Flexible Rotor in Fluid Film Bearings," ASME *Journal of Engineering for Industry*, Vol. 96, No. 2, 1974, pp. 525–532.

9 Pilkey, W. D., Strenkowski, J. S., and Chang, P. Y., "Transient Response of a Rotor in Damped Bearings," ASME Paper No. 77-DET-21, presented at the Design Engineering Technical Conference, Chicago, Illinois, Sept. 26-30, 1977.

10 Hurty, W. C., "Dynamic Analysis of Structural Systems Using Component Modes," *AIAA Journal*, Vol. 3, No. 4, 1965, pp. 678–685.

11 Craig, R. R., and Bampton, M. C. C., "Coupling of Substructures for Dynamics Analysis," *AIAA Journal*, Vol. 6, No. 7, July 1968, pp. 1313–1319.

12 Klosterman, A. L., *On the Experimental Determination and Use of Modal Representations of Dynamics Characteristics*, Ph.D. dissertation, University of Cincinnati, 1971.

13 Li, D. F., *Dynamics Analysis of Complex Multi-Level Flexible Rotor Systems*, Ph.D. dissertation, University of Virginia, Aug. 1978.

14 Prohl, M. Z., "A General Method for Calculating Critical Speeds of Flexible Rotors," ASME *Journal of Applied Mechanics*, Vol. 67, 1945, Vol. 12, p. A-142.

15 Pestel, E. C., Leckie, F. A., *Matrix Methods in Elastomechanics*, McGraw-Hill, 1963.

16 Tolani, S. K., and Rocke, R. D., "Modal Truncationof Substructures Used in Free Vibration Analysis," ASME *Journal of Engineering for Industry*, Vol. 98, No. 3, 1976, pp. 827–834.

17 Li, D. F., and Gunter, E. J., "Component Mode Synthesis of Large Rotor Systems," to be presented at the Gas Turbine Conference and Product Show, Houston, Texas, Mar. 9-12, 1981.

Fractional-Frequency Rotor Motion Due to Nonsymmetric Clearance Effects

D. W. Childs
Mechanical Engineering Department,
Texas A&M University,
College Station,
Texas 77843

Analysis based on the Jeffcott model is presented to explain 1/2 speed and 1/3 speed whirling motion occurring in rotors which are subject to periodic normal-loose or normal-tight radial stiffness variations. The normal-loose stiffness variation results due to bearing-clearance effects, while normal-tight stiffness variations result from rubbing over a portion of a rotor's orbit. The results demonstrate that 1/2 speed subharmonic motion can be explained as either a linear parametric-excitation phenomenon or as a stable nonlinear subharmonic motion. The 1/3 speed motion is shown to be possible due to the radial stiffness nonlinearity. A linear parametric-excitation analysis demonstrates that during a normal-tight rubbing condition, Coulumb damping significantly widens the potential range of unstable speeds.

Introduction

Bently [1] has proposed and demonstrated experimentally that large subsynchronous rotor motion can result from the following types of nonsymmetric clearance effects:

(*a*) The rotor's synchronous motion causes a rubbing condition with a stationary surface over a portion of the rotor's orbit. Contact with the stationary surface causes a periodic increase in the rotor's stiffness yielding what Bently calls a "normal-tight" condition. A jammed or off-centered seal generally provides the physical mechanism for this condition.

(*b*) A "normal-loose" rotor-stiffness condition is also possible if the rotor's radial stiffness is reduced over a fraction of its synchronous orbit. The possible loss of radial stiffness is an abnormal circumstance in units supported by hydrodynamic bearings, which can result from excessive bearing clearances or inadequate vertical bearing restraints. However, in rotors supported by rolling element bearings, a small radial clearance is normally provided to allow axial shaft motion. This clearance, in combination with a fixed direction side load, provides the continuing possibility for a normal-loose condition.

Subsynchronous motion resulting from either of these conditions is an exact fraction of running speed, at predominantly 1/2 of running speed in field experience but occasionally 1/3 or 1/4 of running speed. The subsynchronous motion is most easily excited when the rotor running speed is a corresponding multiple of the rotor's critical speed, i.e., 1/2 speed motion is the general result of running speeds which are approximately twice the first rotor critical speed. In contrast to rotor instabilities due to hydrodynamic bearings, this motion tends to be exactly 1/2 running speed rather than slightly less than 1/2 running speed. Stated differently, motion due to nonsymmetric clearance effects is a fractional-frequency phenomenon, while the frequency of unstable motion due to hydrodynamic bearings is at the rotor critical speed, which depends less directly on running speed. Motion from either source may be large and potentially damaging.

Bently interprets his experimental findings in terms of analytical results for both linear parametric excitation phenomena, modeled by the Mathieu equation [2], and nonlinear subharmonic motion modeled by Duffing's equation [2], but presents neither models for formal analysis to support his very insightful conclusions. In another published work dealing with nonsymmetric-clearance effects, Ehrich and O'Connor [3] have employed nonlinear simulations to explain 1/2 frequency field data, and Ehrich [4] has employed nonlinear analysis and simulations to explain sum-and-difference frequency phenomena. Both of the rotor units examined by Ehrich were supported by ball-bearings.

The author [5] carried out an analysis, based on the Jeffcott model, which provides a linear parametric-excitation explanation for the 1/2 speed fractional-frequency response results obtained by Bently for the loose-tight rub condition. Predictably, this analysis provides no explanation for the 1/3 speed response and other characteristically nonlinear phenomena. The present work remedies this deficiency by presenting both linear and nonlinear analyses for the normal-loose condition, and a new parametric excitation analysis for the normal-tight condition with Coulomb rub.

Contributed by the Gas Turbine Division and presented at the International Gas Turbine Conference and Products Show, Houston, Texas, March 9-12, 1981, of THE AMERICAN SOCIETY OF MECHANICAL ENGINEERS. Manuscript received at ASME Headquarters December 15, 1980. Paper No. 81-GT-145.

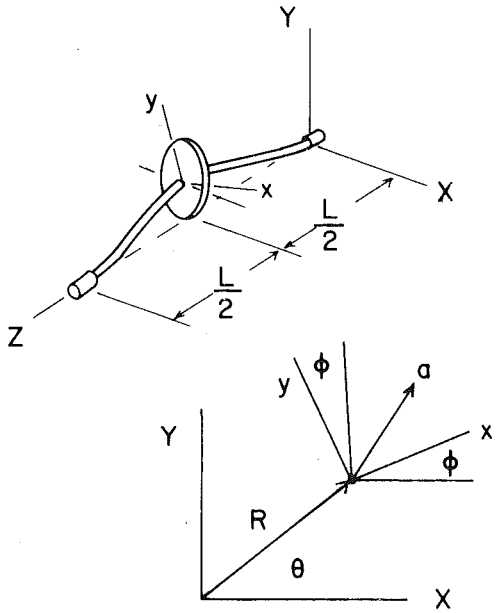

Fig. 1 The Jeffcott Model

The Physical Model

The Jeffcott model [6] of Fig. 1 is employed for the present analysis, and has the following constant-running-speed equations of motion

$$m\ddot{R}_X + c\dot{R}_X + kR_X = ma\omega^2 \cos\phi$$

$$m\ddot{R}_Y + c\dot{R}_Y + kR_Y = ma\omega^2 \sin\phi - W$$

where ω is the disk angular velocity, and $\phi = \phi_0 + \omega t$ defines the rotor-disk rotation with respect to the inertial $X - Y - Z$ axes. For convenience, the imbalance vector **a** is assumed to be in alignment with the rotor-fixed x axis. The stiffness k represents the combined, circumferentially-symmetric stiffness of the rotor's shaft and bearings. Dividing these equations by m yields the form

$$\ddot{R}_X + 2\zeta_0\lambda_0\dot{R}_X + \lambda_0^2 R_X = a\omega^2 \cos\phi$$

$$\ddot{R}_Y + 2\zeta_0\lambda_0\dot{R}_Y + \lambda_0^2 R_Y = a\omega^2 \sin\phi - z \tag{1}$$

The solution may be stated

$$R_X = A\cos(\phi + \psi)$$

$$R_Y = A\sin(\phi + \psi) - D \tag{2}$$

where $D = k/W$ is the static rotor deflections due to gravity, and

$$A = a\omega^2/\{(\lambda_0^2 - \omega^2)^2 + 4\zeta_0^2\lambda^2\omega^2\}^{1/2}$$

$$\psi = \tan^{-1}\{-2\zeta_0\lambda_0\omega/(\lambda_0^2 - \omega^2)\} \tag{3}$$

Normal-Loose Radial Stiffness Model

Figure 2 illustrates the solution to equation (3), and may be used to explain the discontinuous radial-stiffness model used in the present analysis. The assumption is made that the rotor's *radial* shaft-bearing stiffness is reduced for $R_Y > 0$. More specifically, the nominal stiffness value holds when the solution amplitude A is less than the static deflection amplitude D; however, when $A > D$ the stiffness becomes $k(1 - \epsilon)$. Figure 3 illustrates the dependence of the Y component of radial spring force upon R_Y, and demonstrates again that the stiffness discontinuity has no influence on the solution providing $A \leq D$; or equivalently $R_Y \leq 0$.

The differential equations of motion including the stiffness variation are

Nomenclature

a = imbalance vector magnitude (L)
b = transient solution amplitude defined in equations (18) and (23), (L)
c = linear damping coefficient, (FT/L)
$d = \tilde{q}\lambda/2$ = defined by equation (38), (T^{-1})
$f(t), \tilde{f}(t)$ = Fourier series defined in equations (10) and (32)
g = acceleration of gravity (LT^{-2})
h = change in natural frequency defined by equation (15), (T^{-2})
k = rotor-bearing radial stiffness (F/L)
m = rotor mass (M)
$p = \Delta/2\lambda$ = fractional change in excitation frequency about $\omega = 2\lambda$
$q, \tilde{q} = \frac{\epsilon\beta}{\pi}, \frac{\epsilon\tilde{\beta}}{\pi}$ = defined in equations (11) and (34)
$x_0, y_0; x_1 y_1$ = perturbation variables defined in equation (15), (L)
A = synchronous solution amplitude defined by equation (3), (L)
B, C = parameters to define a displaced clearance circle as defined in equation (25), (L)
$D = k/W$ = static deflection amplitude due to rotor weight, (L)
E = minimum clearance defined by equation (28), (L)
$H(\theta)$ = clearance function defined by equation (25), (L)
R_X, R_y = components of the rotor displacement vector **R**, (L)
R = magnitude of **R**, (L)
$U(\ )$ = unit step function
W = rotor weight, (F)
$\frac{\beta}{\pi}, \frac{\hat{\beta}}{\pi}, \frac{\bar{\beta}}{\pi}, \frac{\tilde{\beta}}{\pi}$ = fraction of fundamental period $2\pi/\lambda$ during which radial stiffness is either increased or decreased
ϵ = fractional loss or increase in radial rotor stiffness due to nonlinearity
ψ = steady-state synchronous solution phase angle defined in equation (3)
$\lambda_0 = \sqrt{k/m}$ = base rotor natural frequency, (T^{-1})
λ = rotor natural frequency resulting from loose or tight nonlinearity, (T^{-1})
$\zeta_0 = c/2\sqrt{mk}$ = base rotor damping factor
$\zeta = \zeta_0/\xi$ = rotor damping factor including clearance effects
ϕ = rotor rotation angle illustrated in Fig. 1
ω = rotor rotational speed, (T^{-1})
σ = complex root defined in equation (39), (T^{-1})
Δ = perturbation about $\omega = 2\lambda$ excitation frequency, (T^{-1})
μ = Coulomb damping factor
θ = polar coordinate illustrated in Fig. 1

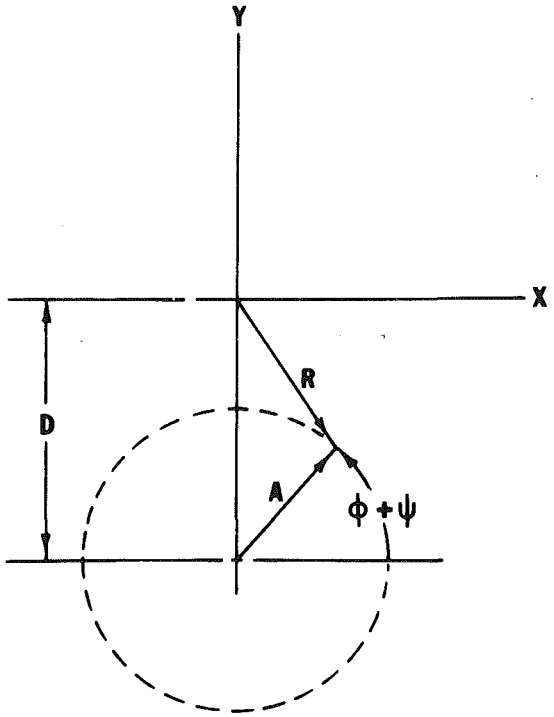

Fig. 2 Steady-state solution for the Jeffcott Model with gravity

$$\ddot{R}_X + 2\zeta_0\lambda_0\dot{R}_X + \lambda_0^2[1-\epsilon U(R_Y)]R_X = a\omega^2\cos\phi$$

$$\ddot{R}_Y + 2\zeta_0\lambda_0\dot{R}_Y + \lambda_0^2[1-\epsilon U(R_Y)]R_Y = a\omega^2\sin\phi - g \tag{4}$$

where $U(R_Y)$ is the unit step function defined by

$$U(R_Y) = 0 \quad ; \quad R_Y \le 0$$

$$U(R_Y) = 1 \quad ; \quad R_Y > 0$$

Normal-Loose Parametric-Excitation Analysis

The parameter ϵ in equation (4) lies in the range $0 \le \epsilon \le 1$, with $\epsilon = 1$ corresponding to a complete loss of radial stiffness. In the present analysis, we assume that ϵ is small in comparison to unity, and examine the following perburbation solution

$$R_X = D(1+\epsilon)\cos(\phi+\psi) + x_1$$

$$R_Y = D(1+\epsilon)\sin(\phi+\psi) - D + y_1 \tag{5}$$

where x_1 and y_1 are assumed to be small compared to D. Observe that the amplitude of the synchronous portion of this solution is slightly larger than the static amplitude D; hence the synchronous orbit periodically traverses the region of reduced radial stiffness. The present analysis seeks to determine the influence of this periodic stiffness variation on the perturbation variables x_1, y_1.

Substituting equation (5) into equation (4) and discarding second order terms in ϵ yields the perturbation differential equations

$$\ddot{x}_1 + 2\zeta_0\lambda_0\dot{x}_1 + \lambda_0^2 x_1[1-\epsilon U(R_Y)] = \epsilon g\cos(\phi+\psi)\,U(R_Y)$$

$$\ddot{y}_1 + 2\zeta_0\lambda_0\dot{y}_1 + \lambda_0^2 y_1[1-\epsilon U(R_Y)] = -\epsilon g[1-\sin(\phi+\psi)]U(R_Y) \tag{6}$$

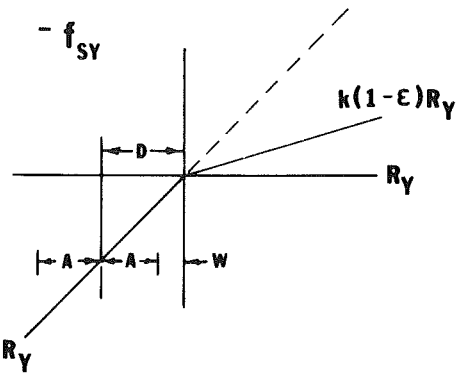

Fig. 3 The Y component of radial spring force as a function of R_Y

We assume that the system is lightly damped, and operating well above its critical speed; hence, $\psi \simeq -\pi$. For convenience, the initial rotation angle is chosen[1] to be $\phi_0 = -\pi/2$. Hence the differential equations become

$$\ddot{x}_1 + 2\zeta_0\lambda_0\dot{x}_1 + \lambda_0^2 x_1[1-\epsilon U(R_Y)] = -\epsilon g\sin\omega t\,U(R_Y)$$

$$\ddot{y}_1 + 2\zeta_0\lambda_0\dot{y}_1 + \lambda_0^2 y_1[1-\epsilon U(R_Y)] = -\epsilon g(1-\cos\omega t)\,U(R_Y) \tag{7}$$

As noted above, the present analysis seeks to determine the influence on the perturbation variables x_1, y_1 of a periodic stiffness variation due to synchronous motion. Further, we have assumed that y_1 is small compared to D. Hence the following additional assumption is made

$$U(R_Y) \simeq U(R_{Y0})$$

where R_{Y0} is the base synchronous solution

$$R_{Y0} = D(1+\epsilon)\cos\omega t - D \tag{8}$$

The functions R_{Y0} and $U(R_{Y0})$ are both illustrated in Fig. 4. The function R_{Y0} is positive over the rotation angle 2β, and yields $U(R_{Y0}) = 1$ over this interval. The angle β is related to ϵ by

$$\cos\beta = 1/(1+\epsilon)$$

and for small β is defined by

$$\beta \simeq \left(\frac{2\epsilon}{1+\epsilon}\right)^{1/2} = (2\epsilon)^{1/2}(1-\epsilon+\epsilon^2+\ldots \tag{9}$$

The Fourier series definition for $U(R_{Y0})$ is

$$U(R_{Y0}) = \frac{\pi}{\beta}[1+f(t)] \tag{10}$$

$$f(t) = 2\sum_{j=1}^{\infty} c_j\cos j\omega t \quad ; \quad c_j = \frac{\sin j\beta}{j\beta}$$

The functions $(1-\cos\omega t)\,U(R_{Y0})$ and $\sin\omega t\,U(R_{Y0})$ in equation (7) yield Fourier series on the order of $(\beta/\pi)^3$ and are assumed to represent a negligible direct excitation of the perturbation equations. In any case, it is the homogeneous portion of equation (7) which is of interest. The homogeneous equations for x_1 and y_1 in equation (7) are equivalent, and the equation for y_1 may be stated as

[1] This is equivalent to the choice of the initial time.

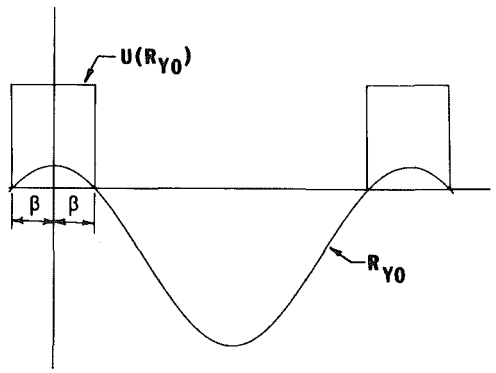

Fig. 4 The function R_{Yo} from equation (8) and the associated function $U(R_{Y0})$

$$\ddot{y}_1 + 2\zeta_0\lambda_0\dot{y}_1 + \lambda_0^2[(1-q) - qf(t)]y_1 = 0 \quad ; \quad q = \frac{\epsilon\beta}{\pi} \tag{11}$$

The looseness model yields both a reduction in the apparent natural frequency and a harmonic oscillation in the coefficient of y_1. The equation may be restated as a Hill equation [2] of the form

$$y_1'' + 2\zeta\left(\frac{\lambda}{\omega}\right)y_1' + \left(\frac{\lambda}{\omega}\right)^2\left[1 - 2q\sum_{j=1}^{\infty} c_j \cos j\tau\right]y_1\ 0$$

where the prime denotes differentiation with respect to the dimensionless time variable, $\tau = \omega t$, and

$$\lambda^2 = \lambda_0^2(1-q) \quad ; \quad \zeta\lambda = \zeta_0\lambda_0$$

The *stability* requirements for this equation are [2]

$$\left[\left(\frac{\lambda}{\omega}\right)^2 - \left(\frac{j}{2}\right)^2\right]^2 + 2\left[\left(\frac{\lambda}{\omega}\right)^2 + \left(\frac{j}{2}\right)^2\right]\zeta^2\left(\frac{\lambda}{\omega}\right)^2 + \zeta^4\left(\frac{\lambda}{\omega}\right)^4 \geq q^2 c_j^2\left(\frac{\lambda}{\omega}\right)^4, j = 1, 2, \ldots \tag{12}$$

In general, this inequality yields the possibility of an instability at the running speeds

$$\omega = 0, 2\lambda, \lambda, \frac{2\lambda}{3}, \ldots \frac{2\lambda}{m}$$

Our interest here is with the $\omega = 2\lambda$ parametric excitation frequency, since the experimental data cited and provided by Bently demonstrate a half-frequency whirl associated with normal/loose bearing characteristics. For small β, the *unstable* speed range about $\omega = 2\lambda$ is defined from the $j = 1$ condition of (12) by

$$\left[\left(\frac{\omega}{2\lambda}\right)^2 - 1 + \zeta^2\right]^2 \leq q^2 - 4\zeta^2\left(\frac{\omega}{2\lambda}\right)^2$$

For zero damping this reduces to

$$1 - q \leq \left(\frac{\omega}{2\lambda}\right)^2 \leq 1 + q,$$

while for $\omega = 2\lambda$, and small q, the peak damping required for stability is

$$\zeta(\omega = 2\lambda) \cong q/2 \tag{13}$$

Figure 5 illustrates the stability curves in terms of q and the new parameter p, defined by

$$\frac{\omega}{2\lambda} = 1 + p \tag{14}$$

where p represents the fractional change in running speed

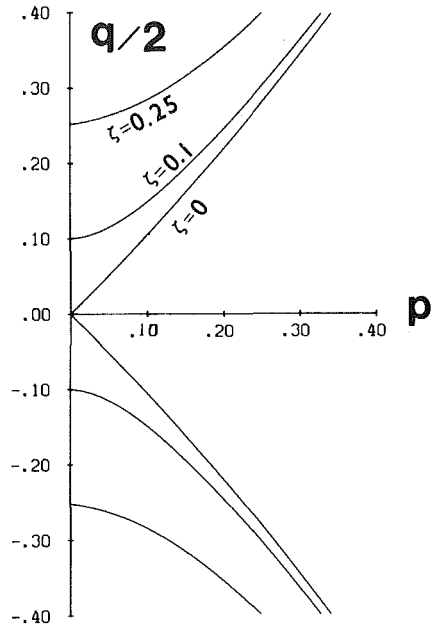

Fig. 5 Stability curves for normal-loose ($q > 0$) and normal-tight ($q < 0$) parametric excitation

about $\omega = 2\lambda$. Our normal-loose model has been predicated upon a positive value for ϵ as illustrated in the top-half q plane, where motion is stable below the stability curves. The lower half plane, corresponding to negative ϵ values, defines a normal-tight stiffness condition. The parameter q is proportional to both ϵ, the increase/decrease in radial stiffness parameter, and β/π the fraction of the rotor's whirl orbit for which an increase/decrease in radial stiffness results. Hence increases in either ϵ or β/π broaden the range of unstable speeds centered about $\omega = 2\lambda$.

Normal-Loose Nonlinear Analysis

The analysis of the preceding section provides a linear parametric-excitation explanation for the 1/2 frequency whirl motion cited and experimentally produced by Bently, but fails to explain his 1/3 frequency motion. The following nonlinear analysis provides an explanation for the 1/3 frequency motion and an alternative explanation for the 1/2 frequency motion.

Following conventional nonlinear analysis procedures [2], the following perturbation solution is assumed for equation (4).

$$R_X = x_0 + \epsilon x_1 \quad , \quad R_Y = y_0 + \epsilon y_1 \tag{15}$$

$$\lambda^2 = \lambda_0^2 - \epsilon h$$

Substitution from this equation yields the following perturbation differential equations

$$\epsilon^0: \quad \ddot{x}_0 + \lambda^2 x_0 = a\omega^2\cos\phi \tag{16}$$

$$\ddot{y}_0 + \lambda^2 y_0 = a\omega^2\sin\phi - g$$

$$\epsilon^1: \quad \ddot{x}_1 + \lambda^2 x_1 = -h\,x_0 + \lambda^2 U(R_y)x_0 \tag{17}$$

$$\ddot{y}_1 + \lambda^2 y_1 = -h\,y_0 + \lambda^2 U(R_y)y_0$$

where, for our present purposes, damping has been dropped.

The half-frequency subharmonic solution will be in-

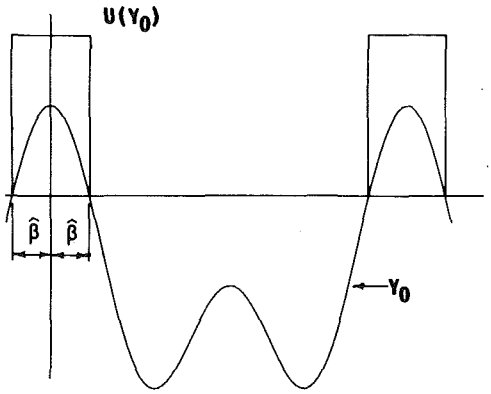

Fig. 6 The function y_0 from equation (18) and the associated function $U(y_0)$

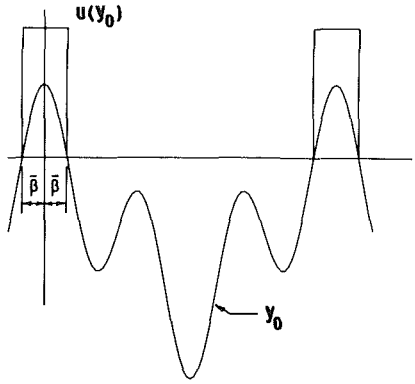

Fig. 7 The function y_0 from equation (23) and the associated function $U(y_0)$

vestigated first, and we accordingly set $\omega = 2\lambda$, and for convenience, choose $\phi_0 = -\pi/2$ to obtain the following ϵ^0 differential equations

$$\ddot{x}_0 + \lambda^2 x_0 = 4a\lambda^2 \sin 2\lambda t$$

$$\ddot{y}_0 + \lambda^2 y_0 = -4a\lambda^2 \cos 2\lambda t - g$$

The particular solution for y_0 is

$$y_{op} = A\cos 2\lambda t - D \quad ; \quad A = \frac{4a}{3}$$

As noted earlier, if $A \leq D$, the solution is not influenced by the radial stiffness discontinuity. If $A = D(1 + \epsilon)$ is slightly larger than D, the synchronous motion itself provides a periodic activation of the nonlinearity, and leads to the parametric excitation situation of the preceding section. To investigate the possibility of subharmonic motion, we consider a complete solution for y_0 of the form

$$y_0 = b\cos\lambda t + A\cos 2\lambda t - D$$

The additional term of this solution would decay exponentially in a linear damped system. In the present nonlinear system, it may reinforce itself and be sustained in a steady-state condition.

To consider this possibility, we assume $U(R_y) \simeq U(y_0)$. The nonlinearity is activated by the motion providing $(b + A - D) > 0$, and is always activated if $A > D$. For convenience, we assume[2] that $A = D$, i.e.,

$$y_0 = b\cos\lambda t + D(\cos 2\lambda t - 1) \tag{18}$$

With this solution, any finite amplitude transient solution amplitude $b > 0$ will periodically activate the nonlinearity at the fundamental frequency λ. The functions y_0 and $U(y_0)$ are illustrated in Fig. 6. The assumed solution yields a periodic variation in radial stiffness at the frequency λ over a $\hat{\beta}/\pi$ fraction of the $2\pi/\lambda$ period. The angle $\hat{\beta}$ is defined by

$$b\cos\hat{\beta} + D\cos 2\hat{\beta} = D \tag{19}$$

The function $Y_0 U_{y_0}$ may be expanded in the Fourier series

$$Y_0 U(y_0) = \frac{a_0}{2} + \sum_{i=1}^{\infty} a_i \cos i\lambda t \quad ; \quad a_i = \frac{2\lambda}{\pi}\int_0^{\hat{\beta}} y_0 \cos i\lambda t\, dt$$

Substituting this result, together with y_0 from equation (18), into equation (17) yields

$$\ddot{y}_1 + \lambda^2 y_1 = \left(Dh + \frac{a_0\lambda^2}{2}\right) + \cos\lambda t(-bh + a_1\lambda^2)$$

$$+ \cos 2\lambda t(-Dh + a_2\lambda^2) + a_3\lambda^2 \cos 3\lambda t + \ldots$$

[2] This solution corresponds to the initial conditions $y_0 = b, \dot{y}_0 = 0$.

The constant term on the right indicates that the normal-loose radial stiffness model causes the average rotor position to be above the static deflection position $R_y = -D$. The secular term on the right is removed by requiring

$$h = a_1\lambda^2/b = \hat{Q}\lambda^2 \tag{20}$$

where

$$\hat{Q} = \frac{1}{\pi}\left[1 + \frac{\sin 2\hat{\beta}}{2} + \frac{D}{3b}(\sin 3\hat{\beta} - 3\sin\hat{\beta})\right]$$

For small $\hat{\beta}$ and (b/D), one obtains from this result and equation (19).

$$\hat{Q} \simeq \frac{1}{\pi}\left(1 + \frac{7\hat{\beta}}{3}\right) \quad ; \quad \hat{\beta} \simeq \frac{1}{2}\left(\frac{2b}{D}\right)^{1/2} \tag{21}$$

Hence, h is always positive and is well-behaved for reasonable values of b/D. Substituting from equation (20) into equation (15) yields the frequency relationship

$$\lambda^2 = \lambda_0^2/(1 + \epsilon\hat{Q}) \tag{22}$$

This result indicates that a 1/2 frequency subharmonic solution can be generated for a range of running speeds at or below the value $\omega = 2\lambda_0$, depending upon the ratios (b/D) and ϵ.

In a comparable analysis [2] of Duffing's equation or similar nonlinear differential equations, the stability of the nonlinear solution provided by equation (18) is investigated by examining a perturbation about the assumed solution of the form $R_y = y_0 + \epsilon u$. However this is not possible for the differential equations (4) because the functions $\lambda_0^2[1 - \epsilon U(R_Y)]R_X$, $\lambda_0^2[1 - \epsilon U(R_Y)]R_Y$ have discontinuous derivatives with respect to the coordinates R_X, R_Y. The close resemblance between the solution of equation (18) and Bently's experimental results provides the strongest evidence for the stability of the subharmonic solution.

The 1/3 running-speed solution is investigated by setting $\omega = 3\lambda$ in equation (16) to obtain

$$\ddot{x}_0 + \lambda^2 x_0 = 9a\lambda^2 \sin 3\lambda t$$

$$\ddot{y}_0 + \lambda^2 y_0 = -9a\lambda^2 \cos 3\lambda t - g,$$

where once again $\phi_0 = \pi/2$. The assumed solution for y_0 is

$$y_0 = b\cos\lambda t + D(\cos 3\lambda t - 1) \quad ; \quad D = \frac{9a}{8} \tag{23}$$

As illustrated in Fig. 7, this function is positive for $\bar{\beta}/\pi$ of the fundamental period where $\bar{\beta}$ is defined by

$$b\cos\bar{\beta} + D\cos 3\bar{\beta} = D$$

The remaining analysis for the 1/3 frequency motion is the same as that employed for the 1/2 frequency motion, with $\bar{\beta}$

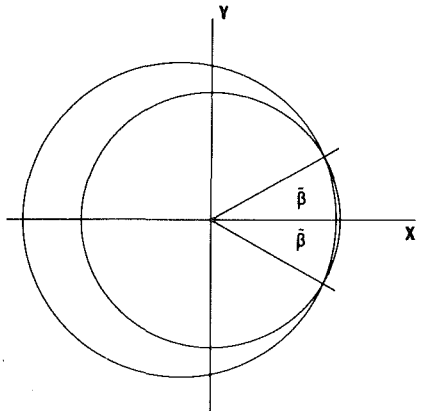

Fig. 8 Radial clearance function for normal-tight interference

replacing $\hat{\beta}$. However, the small $\hat{\beta}$ and (b/D) solutions of equation (21) now reduce to

$$\bar{Q} \simeq \frac{1}{\pi}\left(1+\frac{19}{27}\bar{\beta}\right) \quad ; \quad \bar{\beta}=\frac{1}{3}\left(\frac{2b}{D}\right)^{1/2} \tag{24}$$

This result demonstrates that $\bar{\beta}$ is smaller than $\hat{\beta}$ for the same b/D ratio, and the corresponding frequency reduction is also smaller.

Normal-Tight Rubbing with Coulomb Damping

The preceding analysis for the normal-loose motion is mathematically equivalent to a normal-tight condition if Coulomb damping is neglected. Simply changing the sign of ϵ in equation (4) yields an increase in stiffness rather than a loss of stiffness. However, the following analysis will demonstrate that the presence of Coulomb damping during rubbing can cause markedly different results between the normal-loose and normal-tight conditions.

As illustrated in Fig. 8, the radial clearance function between the shaft equilibrium position and its stator at a specified axial location is assumed to be of the form

$$H(\theta)=B-C\cos\theta \tag{25}$$

Hence the clearance varies from a minimum of $B - C$ on the right to $B + C$ on the left, and the shaft is in contact with the stator if $R \geq H$. For an assumed forward precessional motion, the equations of motion are

$$\begin{aligned}\ddot{R}_X &+ 2\zeta_0\lambda_0\dot{R}_X+\lambda_0^2R_x[1+\epsilon U(R-H)]=a\omega^2\cos\phi\\ &-\mu\lambda_0^2(1+\epsilon)(R-H)\frac{R_Y}{R}U(R-H)\\ \ddot{R}_Y &+ 2\zeta_0\lambda_0\dot{R}_Y+\lambda_0^2R_Y[1+\epsilon U(R-H)]=a\omega^2\sin\phi\\ &+\mu\lambda_0^2(1+\epsilon)(R-H)\frac{R_X}{R}U(R-H)\end{aligned} \tag{26}$$

where μ is the Coulomb damping factor. These equations state that rubbing causes the radial stiffness to increase from k to $k(1 + \epsilon)$, and also yields a *tangential* Coulomb damping force.

The normal-loose model in the preceding portion of this discussion permitted a planar analysis. However, the Coulomb damping term in equation (26) couples the motion in the $X-Z$ and $Y-Z$ plane. A parametric excitation analysis continues to be feasible for these equations, and is demonstrated in the following section. A nonlinear perturbation analysis to examine subharmonic motion was begun, but requires an analysis of the second-order perturbation equations which was not attempted.

The parametric-excitation analysis which follows differs from the earlier analysis by the author [5] in the use of a more reasonable interference model, and Cartesian rather than polar coordinate kinematics. This coordinate selection yields somewhat different perturbation equations and final results.

Normal-Tight Parametric-Excitation Analysis

A perturbation about the synchronous solution of the form

$$\begin{aligned}R_X &= E(1+\epsilon)\cos(\phi+\psi)+x_1\\ R_Y &= E(1+\epsilon)\sin(\phi+\psi)+y_1\end{aligned} \tag{27}$$

where x_1 and y_1 are assumed to be small compared to the minimum clearance

$$E=B-C \tag{28}$$

is assumed. Substituting this solution into equation (25), and discarding second and higher order terms in ϵ yields the perturbation equations

$$\begin{aligned}\ddot{x}_1 &+ 2\zeta_0\lambda_0\dot{x}_1+\lambda_0^2[1+\epsilon U(R-H)]x_1\\ &= -\epsilon\lambda_0^2E[\cos(\phi+\psi)-\mu\sin(\phi+\psi)]U(R-H)\\ &-\epsilon\mu\lambda_0^2y_1\,U(R-H)\\ \ddot{y}_1 &+ 2\zeta_0\lambda_0\dot{y}_1+\lambda_0^2[1+\epsilon U(R-H)]y_1\\ &= -\epsilon\lambda_0^2E[\sin(\phi+\psi)+\mu\cos(\phi+\psi)]U(R-H)\\ &+\epsilon\mu\lambda_0^2x_1\,U(R-H)\end{aligned}$$

We continue to assume that ω is substantially greater than the natural frequency λ_0; hence $\psi \simeq -\pi$, and choose $\phi_0 = \pi$ which yields

$$\begin{aligned}\ddot{x}_1 &+ 2\zeta_0\lambda_0\dot{x}_1+\lambda_0^2[1+\epsilon U(R-H)]x_1\\ &= -\epsilon\lambda_0^2[\cos\omega t-\mu\sin\omega t]U(R-H)\\ &-\epsilon\mu\lambda_0^2y_1\,U(R-H)\\ \ddot{y}_1 &+ 2\zeta_0\lambda_0\dot{y}_1+\lambda_0^2[1+\epsilon U(R-H)]y_1\\ &= -\epsilon\lambda_0^2[\sin\omega t+\mu\cos\omega t]U(R-H)\\ &+\epsilon\mu\lambda_0^2x_1\,U(R-H)\end{aligned}$$

Assuming that x_1 and y_1 are small compared to E, the solution of equation (27) causes R to exceed H for ωt in the interval $[-\tilde{\beta},\tilde{\beta}]$, with $\tilde{\beta}$ defined by the relationship

$$\begin{aligned}E(1+\epsilon) &= B-C\cos\tilde{\beta}\\ \text{or}\\ \epsilon(B-C) &= C(1-\cos\tilde{\beta})\end{aligned} \tag{30}$$

Hence, the function $U(R-H)$ may be expanded in the Fourier series

$$U(R-H)=\frac{\tilde{\beta}}{\pi}[1+\tilde{f}(t)] \tag{31}$$

where

$$\tilde{f}(t)=2\sum_{j=1}^{\infty}c_j\cos j\omega t \quad ; \quad c_j=\frac{\sin j\tilde{\beta}}{j\tilde{\beta}} \tag{32}$$

The terms $\cos\omega t\,U(R-H)$, $\sin\omega t\,U(R-H)$ on the right hand

side of equation (29) may be expanded in comparable series; however, we are concerned here with the homogeneous solutions for these coupled time-varying equations. The definition provided by equation (31) for $U(R-H)$ yields the following homogeneous equations

$$\ddot{x}_1 + 2\zeta\lambda\dot{x}_1 + \lambda^2[1+\tilde{q}\tilde{f}(t)]x_1 - \tilde{q}\,\mu\lambda^2[1+\tilde{f}(t)]y_1 = 0$$

$$\ddot{y}_1 + 2\zeta\lambda\dot{y}_1 + \lambda^2[1+\tilde{q}\tilde{f}(t)]y_1 + \tilde{q}\,\mu\lambda^2[1+\tilde{f}(t)]x_1 = 0 \tag{33}$$

where second order terms in ϵ have been dropped, and

$$\lambda^2 = \lambda_0^2(1+\tilde{q}) \quad , \quad \zeta\lambda = \zeta_0\lambda_0 \quad , \quad \tilde{q} = \frac{\epsilon\tilde{\beta}}{\pi} \tag{34}$$

Equation (34) demonstrates that rubbing contact increases the rotor's natural frequency.

The stability of these coupled time-varying equations will be examined by a method due to Struble [7] and Hsu [8]. The first step in this procedure is the determination of potential parametric excitation frequencies. To this end, the following perturbation solution

$$x = a_1\cos\lambda t + b_1\sin\lambda t + \tilde{q}u$$

$$y = a_2\cos\lambda t + b_2\sin\lambda t + \tilde{q}v$$

is substituted into the first of equation (33). Neglecting damping, the result may be stated

$$\ddot{u}+\lambda^2 u = -\lambda^2(a_1\cos\lambda t + b_1\sin\lambda t)\tilde{f}(t)$$
$$+\mu\lambda^2(a_1\cos\lambda t + b_2\sin\lambda t)(1+\tilde{f}(t)) \tag{35}$$

where second and higher-order terms in $\tilde{q}$ have been discarded. An inspection of this equation shows the potential parametric excitation frequencies to be

$$\omega_j = 0, 2\lambda, \lambda, \frac{2\lambda}{3}, \ldots \frac{2\lambda}{j},$$

since if ω is equal to any of these values, terms will result on the right-hand side of the form $C\cos\lambda t$ or $C\sin\lambda t$, and the solution for u will diverge. The $\omega = 2\lambda$ parametric-excitation-frequency possibility is of interest, since it agrees with Bently's experimental results. This potential parametric excitation frequency term results from the $c_1\cos\omega t$ term of the $\tilde{f}(t)$ series in equation (32).

Establishment of the unstable speed range about the running speed $\omega = 2\lambda$ is mananged by (a) assuming a solution of the form

$$x_1 = a_1(t)\cos\lambda t + b_1(t)\sin\lambda t$$

$$y_1 = a_2(t)\cos\lambda t + b_2(t)\sin\lambda t \tag{36}$$

where the coefficients a_1, b_1, a_2, b_2 are assumed to be slowing varying, (b) setting $\omega = 2\lambda + \Delta$ where Δ is small, and (c) retaining only the first term in the series definition for $\tilde{f}(t)$. This term, $c_1\cos\omega t$, is responsible for the $\omega = 2\lambda$ parametric excitation, and for small β, $c_1 \simeq 1$. The resulting equations are

$$-2\lambda\dot{a}_1\sin\lambda t + 2\dot{b}_1\lambda\cos\lambda t$$
$$+2\zeta\lambda(\dot{a}_1\cos\lambda t + \dot{b}_1\sin\lambda t - \lambda a_1\sin\lambda t + \lambda b_1\cos\lambda t)$$
$$+2q\lambda^2(a_1\cos\lambda t + b_1\sin\lambda t)\cos(2\lambda+\Delta)t$$
$$-\mu q\lambda^2(a_2\cos\lambda t + b_2\sin\lambda t)$$
$$-2\mu q\lambda^2(a_2\cos\lambda t + b_2\sin\lambda t)\cos(2\lambda+\Delta)t \tag{37}$$
$$-2\lambda\dot{a}_2\sin\lambda t + 2\lambda\dot{b}_2\lambda\cos 2\lambda t$$
$$+2\zeta\lambda(\dot{a}_2\cos\lambda t + \dot{b}_2\sin\lambda t - \lambda a_2\sin\lambda t + \lambda b_2\cos\lambda t)$$
$$+2q\lambda^2(a_2\cos\lambda t + b_2\sin\lambda t)\cos(2\lambda+\Delta)t$$
$$+\mu q\lambda^2(a_1\cos\lambda t + b_1\sin\lambda t)$$
$$+2\mu q\lambda^2(a_1\cos\lambda t + b_1\sin\lambda t)\cos(2\lambda+\Delta)t$$

where second derivatives of the slowly-varying coefficients a_1, b_1, a_2, b_2 have been dropped. The differential equation for a_1 is obtained by multiplying the first of these equations by $\sin\lambda t$, and integrating over the interval $[0, 2\pi/\lambda]$, treating a_1, b_1, a_2, b_2 and $\sin\Delta t$, $\cos\Delta t$ as slowly-varying parameters. Similar procedures are employed for the remaining variables to obtain the following system of equations

$$\dot{a}_1 - \lambda(\dot{b}_1 - \lambda a_1) + \frac{\tilde{q}\lambda}{2}(a_1\sin\Delta t + b_1\cos\Delta t) = 0$$
$$+\mu\frac{\tilde{q}}{2}\lambda(b_2 - a_2\sin\Delta t - b_2\cos\Delta t)$$
$$\dot{b}_1 + \zeta(\dot{a}_1 + \lambda b_1) + \frac{\tilde{q}\lambda}{2}(a_1\cos\Delta t - b_1\sin\Delta t) = 0$$
$$-\mu\frac{\tilde{q}}{2}\lambda(a_2 + a_2\cos\Delta t - b_2\sin\Delta t)$$
$$\dot{a}_2 - \zeta(\dot{b}_2 - \lambda a_2) + \frac{\tilde{q}\lambda}{2}(a_2\sin\Delta t + b_2\cos\Delta t) = 0$$
$$-\mu\frac{\tilde{q}}{2}\lambda(b_1 - a_1\sin\Delta t + b_1\cos\Delta t)$$
$$\dot{b}_2 - \zeta(\dot{a}_2 + \lambda b_2) + \frac{\tilde{q}\lambda}{2}(a_2\cos\Delta t - b_2\sin\Delta t) = 0$$
$$+\mu\frac{\tilde{q}}{2}\lambda(a_1 + a_1\cos\Delta t - b_1\sin\Delta t)$$

Substituting the change of variables

$$X_1 = a_1 + jb_1 \quad , \quad Y_1 = a_1 - jb_1$$

$$X_2 = a_2 + jb_2 \quad , \quad Y_2 = a_2 - jb_2$$

yields the complex differential equations

$$\dot{X}_1(1+j\zeta) + \zeta\lambda X_1 + j\,dY_1e^{-j\Delta t} - j\,d\mu(X_2 + Y_2e^{-j\Delta t}) = 0$$
$$\dot{Y}_1(1-j\zeta) + \zeta\lambda Y_1 - j\,dX_1e^{j\Delta t} + j\,d\mu(Y_2 + X_2e^{j\Delta t}) = 0$$
$$\dot{X}_2(1+j\zeta) + \zeta\lambda X_2 + j\,dY_2e^{-j\Delta t} + j\,d\mu(X_1 + Y_1e^{-j\Delta t}) = 0$$
$$\dot{Y}_2(1-j\zeta) + \zeta\lambda Y_2 - j\,dX_2e^{j\Delta t} - j\,d\mu(Y_1 + X_1e^{j\Delta t}) = 0$$

where

$$d = \frac{\tilde{q}\lambda}{2} \tag{38}$$

Substituting the assumed solutions

$$X_1 = X_{10}e^{(\sigma - j\frac{\Delta}{2})t} \quad , \quad Y_1 = Y_{10}e^{(\sigma + j\frac{\Delta}{2})t}$$

$$X_2 = X_{20}e^{(\sigma - j\frac{\Delta}{2})t} \quad , \quad Y_2 = Y_{20}e^{(\sigma + j\frac{\Delta}{2})t}$$

yields

$$\begin{bmatrix} B+\zeta\lambda & jd & -j\mu d & -j\mu d \\ -jd & \bar{B}+\zeta\lambda & j\mu d & j\mu d \\ j\mu d & j\mu d & B+\zeta\lambda & jd \\ -j\mu d & -j\mu d & -jd & \bar{B}+\zeta\lambda \end{bmatrix} \begin{Bmatrix} X_{10} \\ Y_{10} \\ X_{20} \\ Y_{20} \end{Bmatrix} = 0 \quad (39)$$

where

$$B = \left(\sigma - j\frac{\Delta}{2}\right)(1+j\zeta) \quad (40)$$

and is its conjugate. Expansion of the determinant in equation (39) yields the characteristic equation

$$(A-d^2)^2 = -4\mu d^2\left[d-\left(\zeta\sigma-\frac{\Delta}{2}\right)\right]^2 \quad (41)$$

where

$$A = |B|^2 + \zeta\lambda(B+\bar{B}) + y^2\lambda^2 \quad (42)$$

Equation (41) has the following two solutions

$$A = d^2 \pm j\,2\mu d\left(d-\zeta\sigma+\frac{\Delta}{2}\right)$$

The positive and negative choices yield

$$\left[\frac{\sigma}{\lambda}(1+\zeta^2)+\zeta\left(1+j\frac{\mu\tilde{q}}{2}\right)\right]^2 = E_1 + jD_1 = (E_1^2+D_1^2)e^{j\gamma}$$

$$\left[\frac{\sigma}{\lambda}(1+\zeta^2)+\zeta\left(1-j\frac{\mu\tilde{q}}{2}\right)\right]^2 = E_1 - jD_1 = (E_1^2+D_1^2)e^{-j\gamma}$$

where

$$E_1 = \frac{\tilde{q}^2}{4}[1+\zeta^2(1-\mu^2)] - [p(1+\zeta^2)+\zeta^2]^2$$

$$D_1 = \mu\tilde{q}\left[\left(p+\frac{\tilde{q}}{2}\right)(1+\zeta^2)+\zeta^2\right], p = \Delta/2 \quad (43)$$

Solving these equations for σ/λ yields

$$\frac{\sigma}{\lambda}(1+\zeta^2) = -\zeta\left(1+j\frac{\mu\tilde{q}}{2}\right) \pm (E_1^2+D_1^2)^{1/4} e^{j\frac{\gamma}{2}}$$

$$\frac{\sigma}{\lambda}(1+\zeta^2) = -\zeta\left(1-j\frac{\mu\tilde{q}}{2}\right) \pm (E_1^2+D_1^2)^{1/4} e^{-j\frac{\gamma}{2}}$$

For stability, the real part of σ must be nonnegative; hence, either of these equations yields the following stability requirement.

$$\zeta \geq (E_1^2+D_1^2)^{1/4}\cos\frac{\gamma}{2},$$

which can be stated

$$4\zeta^4 - 4\zeta^2 E_1 \geq D_1^2$$

Substitution from equation (43) yields

$$p^2(1+\zeta^2)\left(\zeta^2-\mu^2\frac{\tilde{q}^2}{4}\right)+2p\left\{\zeta^4-\mu^2\frac{\tilde{q}^2}{4}\left[\frac{\tilde{q}}{2}(1+\zeta^2)+\zeta^2\right]\right\}$$

$$-\left\{\zeta^2\left(\frac{\tilde{q}^2}{4}-\zeta^2\right)+\mu^2\frac{\tilde{q}^3}{8}\left[\frac{\tilde{q}}{2}(1+\zeta^2)+2\zeta^2\right]\right\} \geq 0 \quad (44)$$

or alternatively

$$\zeta^4(1+p)^2+\zeta^2\left(p+\frac{\tilde{q}}{2}\right)\left[\left(p-\frac{\tilde{q}}{2}\right)-\mu\frac{\tilde{q}^2}{4}\left(p+\frac{\tilde{q}}{2}+2\right)\right]$$

$$-\mu^2\frac{\tilde{q}^2}{4}\left(p+\frac{\tilde{q}}{2}\right)^2 \geq 0 \quad (45)$$

External damping is required to satisfy this condition for any finite $\mu > 0$. The maximum required damping is anticipated at $\omega = 2\lambda$ or $p = 0$, which reduces condition (45) to

$$\zeta^4 - \zeta^2\frac{\tilde{q}^2}{4}\left[1+\mu\frac{\tilde{q}}{2}(2+\frac{\tilde{q}}{2})\right] - \mu^2\left(\frac{\tilde{q}}{2}\right)^4 \geq 0$$

For small $\tilde{q}$, the required damping is

$$\zeta(p=0) \simeq \left(1+\mu\frac{\tilde{q}}{2}\right)\frac{\tilde{q}}{2} \quad (46)$$

which, for $\mu = 0$, agrees with the earlier result of equation (13). For large p, the limiting value of damping required for stability is defined from equation (44) to be

$$\zeta(p\to\infty) = \mu\frac{q}{2} \quad (47)$$

Figure 9 illustrates the amount of damping required for stability as a function of p for selected values of μ and q. Motion is stable above the stability boundaries, and unstable below them. The figure confirms the results of equations (46) and (47). Specifically, the maximum required damping at $p = 0$ is not appreciably influenced by Coulomb damping. However, damping is required over a much broader speed range to suppress an instability due to partial rubbing.

Discussion of Results

The models, and accompanying analysis presented here for normal-loose and normal-tight radial stiffness conditions in rotors, basically confirm the parametric-excitation and nonlinear mechanisms proposed by Bently as explanations for fractional frequency whirl. Bently's findings with respect to 1/2 frequency whirl were as follows:

(*a*) For normal-loose conditions, the excitation frequency (running speed) must be twice or somewhat lower than the rotor critical speed.

(*b*) For normal-tight conditions, the excitation frequency must be twice or about anything higher than twice the critical speed.

The nonlinear results of equation (22) explain these shifts upwards/downwards of the base rotor critical speed with running speed as a result of the discontinuous radial stiffness model. This result basically agrees with Bently's view of the normal-tight conditions, viz., that an increase in effective rotor stiffness accounts for the persistence of 1/2 speed whirl motion with increasing speed. However, the preceding analysis indicates that the persistence of this motion may be equally the result of Coulomb damping.

One aspect of these results which should be considered carefully is the magnitude of damping required to suppress fractional frequency motion resulting from nonsymmetric clearance effects. The values of $q = \epsilon(\beta/\pi)$, 0.1 and 0.25, used in Fig. 9 are comparatively modest since the relative-stiffness parameter ϵ can range up to unity for normal-loose

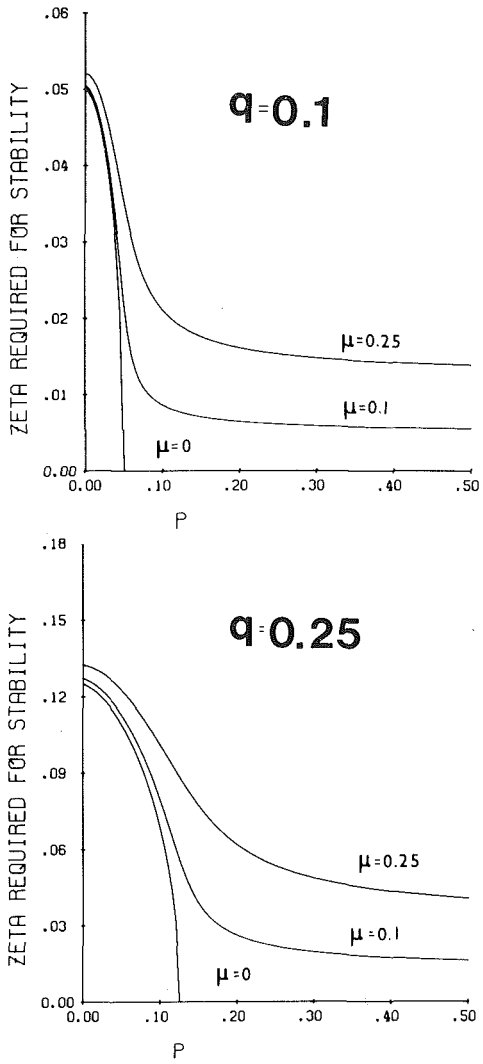

Fig. 9 Damping required for stability as a function of *p*

conditions, and achieve much larger values for normal-tight conditions. Moreover, rotors operating at twice their first critical speed are very likely to be lightly damped, and not have a first mode damping factor on the order of 5 or 10 percent of critical. Hence, as Bently emphasizes, fractional-frequency whirl due to nonsymmetric clearance effects represents a very serious source of large and potentially damping vibration levels.

As noted in the introduction to this paper, radial-bearing clearances in roller-element rotors present a continuing possibility of normal-loose radial-stiffness conditions, depending on the relative amplitudes of the static deflection D and synchronous amplitude A of Fig. 2. Specifically, if the rotor imbalance is large enough to drive the rotor orbit through the "dead-band" region of the radial stiffness function, 1/2 frequency whirl motion is likely to result over substantial speed ranges, irrespective of the unit's "classical" linear stability. Since the occurrence of this motion depends both on the state of rotor balance and the tolerance stack-up defining bearing clearances, a considerable unit-to-unit variation in vibration characteristics of ball-bearing units is likely.

Acknowledgments

The research herein was supported in part under NASA Contract NAS8-3123 supported by Marshall Space Flight Center, technical monitor Dr. Stephen Winder. A significant portion of this work was completed while the author was a visiting faculty member at the Danish Technical University. The quiet and productive environment provided by my hosts at this university is gratefully acknowledged.

References

1 Bently, D., "Forced Subrotative Speed Dynamic Action of Rotating Machinery," ASME Paper 74-PET-16, Petroleum Mechanical Engineering Conference, Dallas, Texas, Sept. 1979.

2 Hayashi, C., *Nonlinear Oscillations in Physical Systems,* McGraw-Hill, New York, 1964.

3 Ehrich, F. F., and O'Connor, J. J. "Stator Whirl with Rotors in Bearing Clearances," ASME *Journal of Engineering for Industry,* Aug. 1967, pp. 381–390.

4 Ehrich, F. F., "Subharmonic Vibrations of Rotors in Bearing Clearance," ASME Paper 66-MD-1, Design Engineering Conference and Show, Chicago, Ill., May 9–12, 1966.

5 Childs, D. W., "Rub-Induced Parametric Excitation in Rotors," ASME Paper No. 78-WA/DE-14, Presented at 1978 ASME Winter Annual Meeting, Accepted for publication, ASME *Journal of Mechanical Design.*

6 Jeffcott, N. N., "Lateral Vibrations of Loaded Shafts in the Neighbourhood of a Whirling Speed — The Effect of Want of Balance," *Phil. Mag.,* Vol. 37, 1919, pp. 304–314.

7 Struble, R. A., *Nonlinear Differential Equations,* McGraw-Hill, Inc., New York, 1962.

8 Hsu, C. S., "Further Results on Parametric Excitation of a Dynamic System," ASME *Journal of Applied Mechanics,* 1965, p. 373.

H. Consigny

Research Engineer.
ONERA, Av. de la division Leclerc,
92320 Chatillon-sous-Bagneut, France

B. E. Richards

Professor, now Head,
Department of Aeronautics
and Fluid Mechanics,
The University, Glasgow,
G12 8QQ

Von Karman Institute for
Fluid Dynamics,
72, Chaussee de Waterloo,
B-1640, Rhode-Saint-Genese,
Belgium

Short Duration Measurements of Heat-Transfer Rate to a Gas Turbine Rotor Blade

The paper describes the results of an experimental study of the effect of Mach number, Reynolds number, inlet flow angle, and free-stream turbulence level on heat transfer rate to a gas turbine rotor blade. The measurements were made in the VKI short-duration isentropic light piston tunnel using thin film heat transfer gages painted on a machinable ceramic blade of 80 mm chord and 100 mm height. The tests were performed for three cascade inlet Mach numbers: 0.62, 0.92, 1.15; inlet unit Reynolds number was varied from 0.3 × 10^7 m^{-1} to 1.2 × 10^7 m^{-1}; the inlet flow angle from 30 to 45 deg (for an inlet blade angle of 30 deg); the turbulence level from 0.8 percent to approximately 5 percent. The effect of changing these parameters on boundary layer transition and separation, on leading edge and average heat transfer to the blade was examined. For typical situations, experimental blade heat distributions were compared with boundary layer predictions using a two-equation closure model.

Introduction

The accurate knowledge of heat transfer distribution on various engine components such as end walls or blades is of primary importance to improving the efficiency of aircraft gas turbines. Documentation in this area is noticeably scarce and there is very little reliable experimental information to be found that could be used to verify or develop available calculation techniques. This dearth of experiments results from the difficulty in generating good heat transfer data obtained under conditions which closely simulate the turbine environment, the important variables being Mach and Reynolds numbers, wall-to-recovery temperature ratio, and turbulence level.

The isentropic light piston tunnel, used for these experiments, proved to be very well-adapted for heat transfer measurements on simplified geometric configurations [1]. The object of the present work is to demonstrate that the more complex situation of the flow through a transonic rotor cascade can also be treated. Typical comparison with a sophisticated boundary layer code will reveal the usefulness of experimental studies of this nature.

Experimental Apparatus

Test Facility. The test facility used for this investigation is the VKI isentropic light piston tunnel CT2. This short duration wind tunnel operates on a principle of isentropic compression of the test gas by a light-weight piston driven by compressed air until the desired total pressure and hence temperature are obtained. The flow through the test section is initiated by a fast operating shutter valve, triggered by the output of a fast response pressure transducer measuring the total pressure ahead of the piston. The principle of the facility is described by Jones, et al. [2]; justification and advantages of using such a wind tunnel is given by Richards [3]. During a test, (typically 100 ms), flow temperature from 400 K to 600 K to 600 K and reservoir pressure up to 5 atmosphere can be achieved. For this study, the ideal stagnation temperature was kept constant and equal to 430 K (giving a wall-to-recovery temperature ratio of approximately 0.70), this relatively low value facilitating turbulence measurements. Departures from the isentropic process have been investigated, and real flow temperature carefully measured using the fine wire technique [4], to be taken into account in data reduction.

The Reynolds number of the incoming flow was varied by changing the total pressure, and the cascade outlet Mach number was set by adjusting the pressure in the exit dump tank. The CT2 facility is a cascade tunnel based on a 5 m long, 1 m diameter tube (Fig. 1(*a*)) and the maximum test section dimensions are 100 mm (blade height) × 240 mm [5].

Model. All tests reported herein were carried out on the same rotor blade section. The cascade geometry illustrated in Fig. 1(*b*) is as follows:

Chord length	=	80 mm
Blade height	=	100 mm
Stagger angle	=	−38.5 deg
Space to chord ratio	=	0.670
Arcsin (throat/space)	=	21.0 deg
Inlet blade angle	=	30 deg
Design inlet flow angle	=	30 deg (referred to axial direction)

Contributed by the Gas Turbine Division and presented at the International Gas Turbine Conference and Products Show, Houston, Texas, March 9–12, 1981 of THE AMERICAN SOCIETY OF MECHANICAL ENGINEERS. Manuscript received at ASME Headquarters December 15, 1980. Paper No. 81-GT-146.

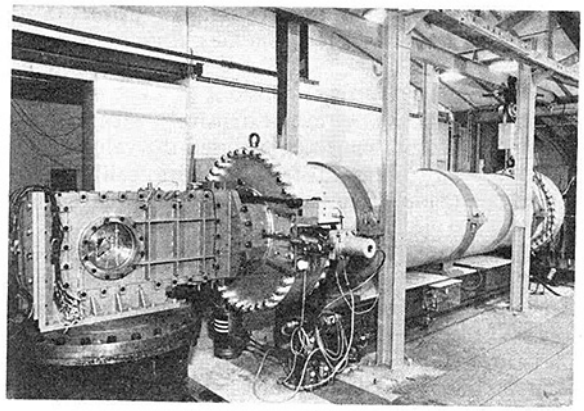

(a) CT2 Hot cascade facility

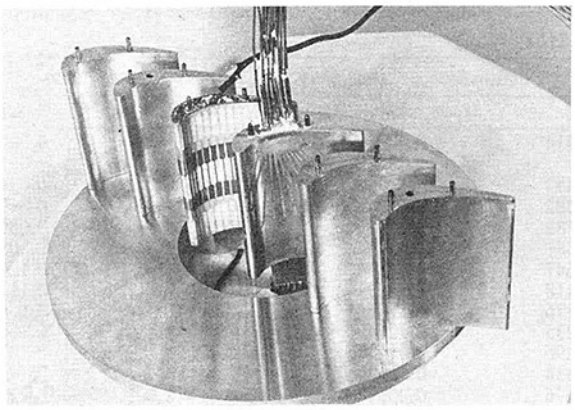

(c) Cascade mounted

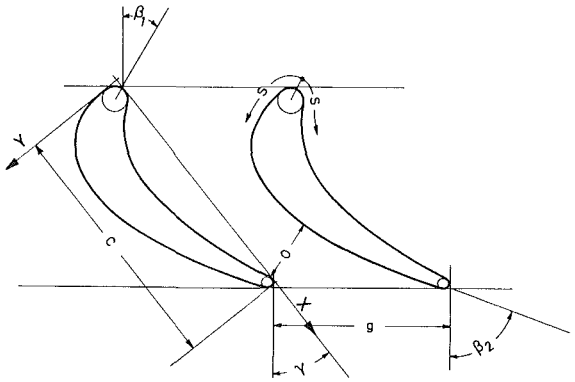

(b) Cascade geometry

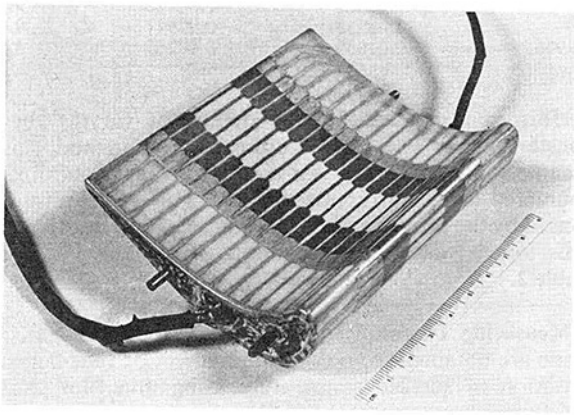

(d) Details of instrumented blade

Fig. 1 Wind tunnel and models

Design outlet flow angle = −69.5 deg
Leading edge diameter = 6.25 mm
Trailing edge diameter = 3.0 mm
Blade coordinates are given in Table 1.

The cascade which consisted of 1 ceramic and 5 aluminum airfoils, is shown in Fig. 1(*c*).

Blade surface pressure measurements were obtained with a row of 31 static pressure taps located at mid-span on one aluminum blade (17 for suction side, 12 for pressure side, 2 for leading and trailing edges). The inlet Mach number is determined one chord upstream. The outlet Mach number is measured and cascade periodicity adjusted using 17 wall pressure taps located one chord downstream (in flow direction) in a parallel direction to the blade trailing edges. Heat transfer data were obtained with 40 thin film gages distributed over the ceramic blade surface. Important features concerning gage manufacturing and measurement techniques are given below.

Turbulence Generation. The external turbulence in this study was generated by a grid of parallel horizontal bars, 3 mm diameter, 9 mm apart giving a solidity of 0.33. With such a grid, different turbulence intensities may be obtained by placing it at different streamwise positions upstream of the cascade. The turbulence level, defined here as $\sqrt{\overline{u'^2}}/U$ has been measured using a VKI manufactured constant temperature anemometer; the evaluation of total temperature fluctuation (which finally turned out to be negligible) was

Nomenclature

c = chord length
c = specific heat of ceramic
h = blade height
k = thermal conductivity of ceramic
K = pressure gradient parameter
M = Mach number
Nu_D = Nusselt number based on leading edge diameter
Nu_m = blade mean Nusselt number
Q_w = wall heat transfer
Re_C = Reynolds number based on chord length
Re_D = Reynolds number based on leading edge diameter
s = curvilinear distance from stagnation point
T = temperature
Tu_∞ = turbulence level at cascade inlet
β = flow angle
ρ = density of ceramic

Subscripts

aw = adiabatic wall
is = isentropic
0 = total condition
w = wall
1 = upstream
2 = downstream

Table 1 Co-ordinates of blade profile axes as indicated in Fig. 1(*b*)

Suction Side		Pressure Side	
x/c	*y/c*	*x/c*	*y/c*
0.01414	0.02059	0.01414	0.02059
0.0	0.08588	0.05059	0.0
0.00353	0.13294	0.09412	0.02682
0.01882	0.18588	0.12941	0.06871
0.05882	0.25035	0.15294	0.08976
0.10588	0.28741	0.17647	0.10506
0.17647	0.31824	0.20588	0.12035
0.24118	0.33271	0.25882	0.14129
0.31176	0.33458	0.32941	0.15647
0.38235	0.32647	0.40	0.16012
0.45296	0.31	0.47059	0.15565
0.52353	0.28647	0.54118	0.14447
0.61176	0.25094	0.61176	0.12941
0.71765	0.20024	0.68235	0.11094
0.82353	0.14318	0.75294	0.08918
0.92941	0.07965	0.82353	0.06412
0.96471	0.05647	0.89412	0.03576
0.98824	0.04059	0.94118	0.01518
1.0	0.02118	0.97941	0.00
0.99765	0.01059	0.99765	0.01059

performed using the classical method of varying the wire constant ratio. The main features of the method, and the assumption appropriate for the particular conditions encountered here, are discussed in [4]. The total pressure loss caused by the presence of the grid measured to be 3.5 percent. This loss is taken into account in the values indicated in Table 2.

Measuring Techniques. Local rates of heat transfer to the blade are obtained from the measurement of time-dependent variation of surface temperature using thin film platinum resistance thermometer gages deposited onto the blade surface. This transient technique has been fully described in [6]. The blade was machined from Corning "Macor" machinable ceramic using conventional tools, its surface well polished and the thin film gages brush painted ('Hanovia Liquid Bright Platinum 05-X') and fired. Several coats were generally needed to achieve a resistance value compatible with the measurement chain (typically 100 Ω). The sensor active part is approximately 1 mm wide and 15 mm long. At each end, wider strips are painted (having negligible resistance) in order to permit the slightly protruding electrical leads (silver conducting painting) to be far from the central part of the blade. Figure 1(*d*) illustrates the details of the instrumented airfoil.

The temperature coefficient of these thermometers was found by calibration to 200° C in a temperature controlled oil-bath. Analog networks are used to extract a signal proportional to heat transfer from the output of the resistance thermometers.

The value of the thermal constant $(\rho ck)^{0.5}$ which is well known for quartz has not been extensively measured for the ceramic. For the present tests, we used the value of 0.210 J cm^{-2} $K^{-1}S^{-1/2}$ obtained from relative calibration with identical quartz models in flat plate [4] and impingement flow situations.

Since reference [1], great improvement was provided in data treatment and reduction using the 12-bit resolution on-line medium-speed data acquisition system designed and built by the VKI Electronics Department. On 16 available channels, 10 are used for heat transfer, five for static and total pressures, one for shutter valve displacement transducer signal. Since sufficient spatial resolution is generally achieved with only 30 gauges, three tests are necessary to complete each configuration ($M_{2_{is}}$, β_1, Tu_∞). Sampling rate was set to 2 k Hz/channel for heat transfer measurements, and 25 k Hz/channel for turbulence measurements. Fast calibration, data reduction, and files management procedures are performed using a set of several interactive programs especially developed for a DIGITAL PDP 11/34 mini-computer. Floppy disks are used for data archiving. Using this system, accuracy and repeatability proved to be very satisfactory, and experimental uncertainty on heat transfer results is estimated to be less than ± 5 percent.

Test Program and Test Conditions. The tests were made for outlet Mach numbers $M_{2_{is}}$ of 0.62, 0.92, 1.15; however, the main effort was devoted to the transonic regime for which the blade had been designed. Values of cascade inlet angle studied were β_1 = 30, 35, 40, and 45 deg; heat transfer distributions for β_1 = 35 and 40 deg are not presented here although the corresponding data are taken into account in Fig. 6. The test conditions are summarized in Table 2.

Experimental Results

Pressure Measurements. Figure 2 shows the results of the blade Mach number distribution for the different conditions, compared with two classic predictions currently used at VKI. For the subcritical regime, the code is based on an extension of a singularities method to compressible flow [7], and, in the transonic case, on the solution of Euler's equations by a pseudo-unsteady method [8].

On the suction surface, agreement is generally satisfactory, but on the pressure side, some discrepancies are observed. These are caused by the two following experimental difficulties. First of all, the Mach number is deduced from the value of the total to static pressure ratio, a method rather

Table 2 Test conditions and symbol significance

TEST CASE	M_1	$M_{2_{is}}$	β_1	P_o Real ($X10^{-5}$ Pa)	T_o Real (K)	T_w (K)	$(Re_c)_1$ ($X10^{-5}$)
A	0.24	0.62	30°	1.275	419	296	3.385
B	0.278	1.15	30°	2.070	419	294	6,315
C1	0.278	0.92	30°	0.774	420	294	2.349
C2	-"-	-"-	-"-	1,571	419	295	4.790
C3	-"-	-"-	-"-	2,364	418	292	7,231
C4	-"-	-"-	-"-	3,071	417	294	9.421
D2	0.350	0.92	45°	1.535	416	290	5.820
D3	-"-	-"-	-"-	2.348	417	290	8.867

Tu_∞ = .8% (No Grid)	Tu_∞ = 3%	Tu_∞ = 3.8%	Tu_∞ = 5.2%

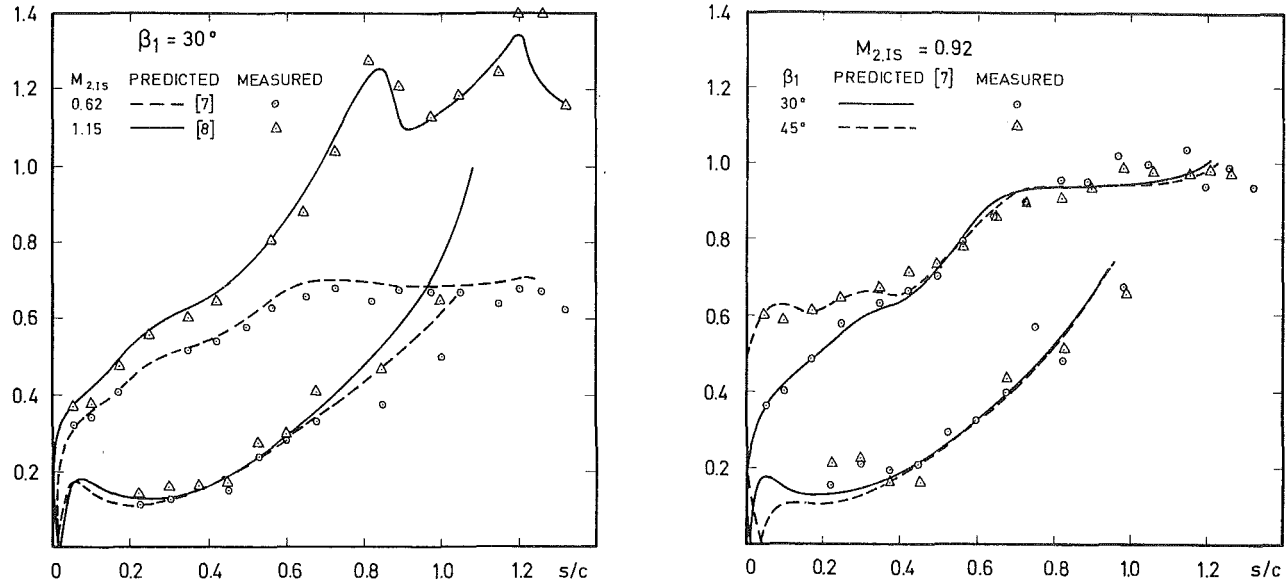

(a) Inlet flow angle = 30 deg (b) Exit Mach number = 0.92

Fig. 2 Blade Mach number distribution

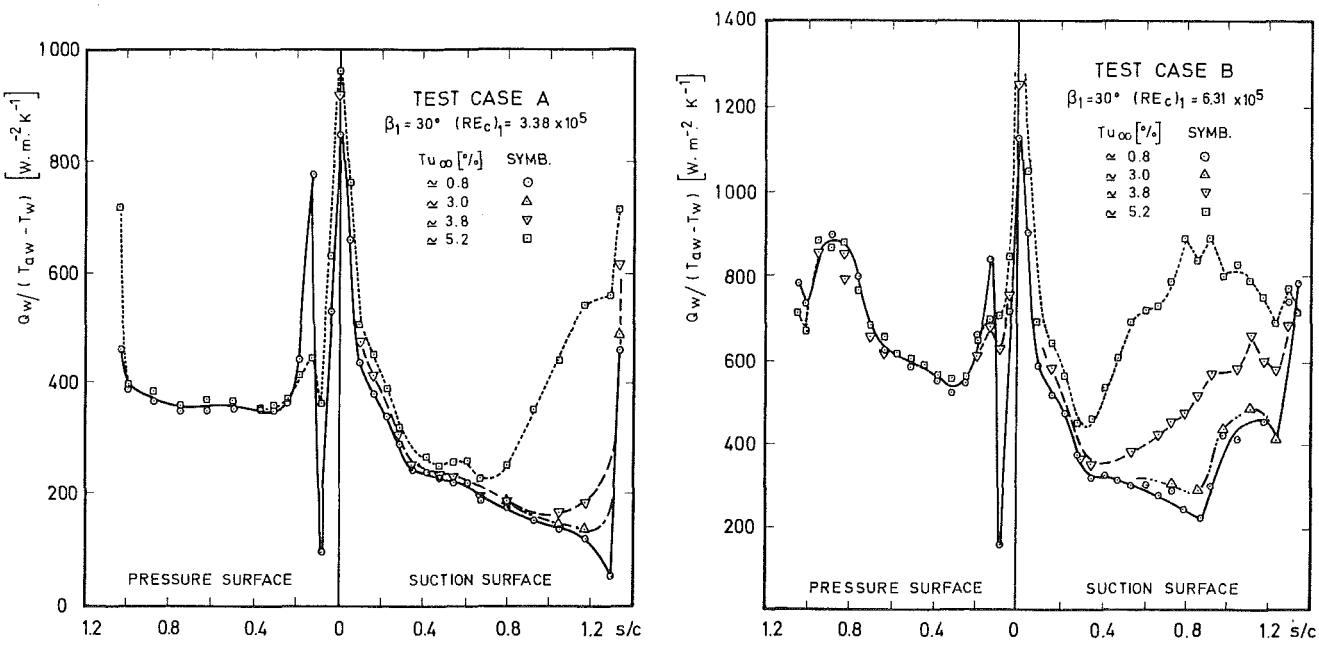

(a) Test case A (b) Test case B

Fig. 3 Influence of Mach number on heat transfer distribution

inappropriate for low Mach number situations. This region could be obtained more accurately from a velocity measurement with a differential transducer used to measure the difference between total and static pressure as for incompressible flows. But, because of the relatively high pressure levels and short running time, one must be careful about the response time being the same on both sides of the transducer. Furthermore, the thinness of the trailing edge necessitated the use of smaller diameter tubes on the pressure side than on the suction side. Bending the tubes in this confined space may have caused either crimping or leaks which explain the scatter in the data.

Heat Transfer Results. The heat transfer results are presented as heat transfer coefficient $Qw/(T_{aw}-T_w)$ versus reduced distance from the leading edge. Because the boundary layer state is uncertain until after the data reduction is completed, the recovery wall temperature T_{aw} has been systematically calculated using the value 0.89 for the recovery factor r, as if the boundary layer were turbulent everywhere

on the airfoil. In the laminar regions, the Mach number is generally small so that T_{aw} is very close to T_0, whichever value of r is taken. The order of error incurred is illustrated by the fact that even at M = 1, it would not exceed 2 percent.

a) Typical result. Before examining the influence of changing conditions on the heat transfer distribution the main features of the flowfield will be discussed using Fig. 3 (the symbol significance is given in Table 2).

After having reached very high values in the region of the leading edge, the heat transfer level falls quite rapidly on either side of the blades: this behavior corresponds to laminar heating. This level of heating is slightly but significantly (taking into account uncertainties) increased by increasing free-stream turbulence but the effect is less important than at the stagnation point. Similar results were obtained for constant-pressure and accelerating laminar boundary layers developing on a flat plate [4].

For the case $M_{2is} = 0.62$, the rapid increase of heat transfer coefficient, near $s/c = 0.7 - 0.8$ and only for $Tu_\infty \simeq 5.2$ percent, denotes the onset of transition. For smaller values of Tu_∞, heat transfer continues to diminish, but in the region close to the trailing edge, transition occurs for $Tu_\infty \simeq 3.8$ percent while for $Tu_\infty \simeq 0.8$ percent the boundary layer appears to separate. These uncertain trends may be attributed to viscous phenomena particularly important on this part of the blade.

On the pressure side, immediately downstream of the leading edge, the important deceleration causes laminar separation for a short distance resulting in an extremely low heat transfer level followed by the expected high heating rate due to the reattaching turbulent boundary layer.

The influence of free-stream turbulence on the magnitude of this heat transfer jump is illustrated by the near disappearance of the laminar bubble at $Tu_\infty = 5.2$ percent. It can also be seen that the heat transfer in the turbulent boundary layer developing downstream of reattachment is not affected by a change in turbulence level.

In the trailing edge zone, generally high heating rates are found sometimes close to values seen near the leading edge. This has important implications since the region is the most difficult to cool, unless trailing edge bleed is allowable. This high heating is thought to be caused by localized high speed flows associated with the finite size of the trailing edge. The effect of turbulence appears to be generally small when the boundary layer on each side of the blade is turbulent. When the flow on the suction surface near the trailing edge is becoming increasingly turbulent with increase in turbulence level, the heat transfer rate at the extremity increases markedly accordingly. The importance of heating in this region and the dependence of its value on the state of the boundary layer on either side of the blade deserves an independent study of the sort carried out on base pressure measurements [9] on an enlarged model.

For supersonic outlet Mach number (Fig. 3(*b*)) at the lowest two turbulence levels shock induced transition is observed on the suction side (at $s/c \simeq 0.85$). The shock wave, however, influences little the local heat transfer distribution for the high turbulence level cases when a turbulent boundary layer exists at that positiion. Apart from these two latter observations it is difficult to separate both the Mach number and Reynolds number effects from these results.

b) Influence of Reynolds Number. The measurements obtained for different inlet Reynolds number and turbulence levels but keeping the outlet Mach number and inlet cascade angle to their design values (see Table 2) are shown in Figs. 4(*a*) to 4(*d*). A number of interesting features can be seen from these plots. On the suction surface it can be seen that the flow changes from all laminar for the low Re cases to nearly completely transitional and turbulent for the high Re cases. Transition advances with increasing Reynolds number and turbulence level, and the transition region roughly has the same length as the laminar region. Increase in heating with decrease in turbulence can result in the early stages of the turbulent boundary due to low Reynolds number effects (see Fig. 4(*d*)). On the pressure surface a small separation bubble occurs in all cases with reattachment to turbulent flows. At the lowest Reynolds number, heat transfer decreases with distance, a different trend from higher Reynolds number cases, probably indicative of relaminarization in this region of strong favorable pressure gradient, as expected of a region (near $s/c \simeq 0.4$) where the pressure gradient parameter $K = (\mu/\rho u^2)du/dx$ is 15×10^{-6} considerably greater than the usually accepted value of 2×10^{-6} above which laminarization has been found to occur. For this case the heating never decreases below twice the expected predicted two-dimensional value, which indicates that complete laminarization is not achieved and possibly the flow is dominated by three-dimensional flow of the streamwise vortex type expected on concave surfaces. The recovery from flow separation may also have an influence on the heat transfer level.

c) Influence of cascade inlet angle. The effect of increasing the cascade inlet angle from 30 to 45 deg has quite an obvious consequence on Mach number evolution around the leading edge, (Fig. 2). In particular the positive pressure gradient on the pressure side is suppressed and, consequently, the laminar separation bubble disappears (Fig. 5).

For test case D3 (Fig. (*b*)), and $Tu_\infty \simeq 0.8$ percent, the laminar boundary layer developing on a short distance after the leading edge is followed by a rapid transition. At the higher turbulence level it is no longer easy to distinguish the laminar region.

For the low Reynolds number case (Fig. 5(*a*)), the experimental results reveal (on the pressure side) a very interesting combination of the effects of high turbulence intensity and strong acceleration on the boundary layer, leading to a set of well-defined experimental heat transfer curves.

Leading Edge Heat Transfer and Blade Average Nusselt Number. Figure 6 shows the blade leading edge heat transfer results, presented in the usual form (i.e. Nusselt number versus Reynolds number, both based on the leading edge diameter) together with classical correlations which all refer to the case of a circular cylinder in cross-flow and for the incompressible regime (10) to (14).

The figure indicates that data correlate well and also that the measured effect of turbulence on heat transfer level is very similar in magnitude to that seen in the correlations. However, the fact that the experiment lies approximately 20 percent below prediction indicate that the experiments probably represent an average over a finite but small area in the leading edge zone, in which there exists a very sharp gradient of pressure and heat transfer. This fact is confirmed by the negligible influence of inlet angle and by the Dyban and Kurosh correlation [13] dealing with the average value over the stagnation region for an angular distance of ± 60 deg.

A brief summary of existing airfoil mean heat transfer data (for further details see [16]) is presented in Fig. 7, together with data obtained from the present results. The important scatter observed is undoubtedly caused by the different experimental methods used by each investigator but also by the various types of blade sections tested. In this domain, it would be illusory to expect a unique correlation for each value of Tu_∞ but the excellent testing conditions which can be achieved with the present facility will certainly contribute to clarify the situation, and in the future, the blade loading would probably be a fundamental parameter to take into account. Never-

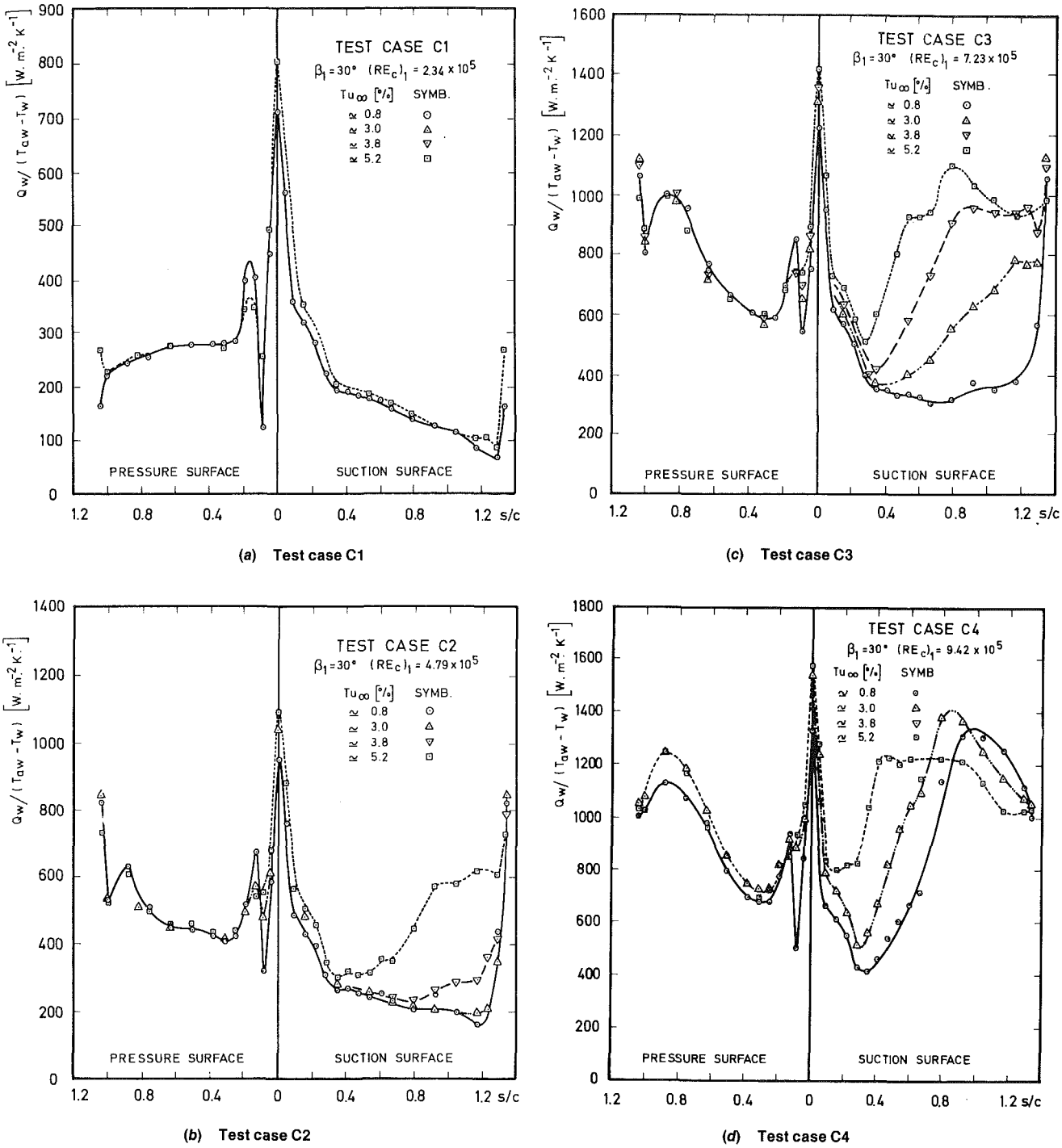

Fig. 4 Influence of Reynolds number on heat transfer distribution

theless, one can see that the present data are in good agreement with the recent measurements of Turner [16] and Dumuren [17].

Comparison with Predictions

Description of Boundary Layer Code. The experimental blade heat transfer distributions were compared with the results of boundary layer calculations using a two-equation closure model, i.e., for the turbulent kinetic energy k, and for the dissipation ϵ. The basic equations, the values of modeling constants, as well as the low Reynolds number corrections which were used, are identical to those recommended by Jones and Launder [18]. The turbulent heat flux is modeled via constant turbulent Prandtl number, the usual value of 0.90 being taken.

The edge boundary conditions for k and ϵ are known from the solution of the transport equations for these two quantities in their free-stream limiting form, and from the initial values which are easily evaluated from the turbulence decay measured behind the grid.

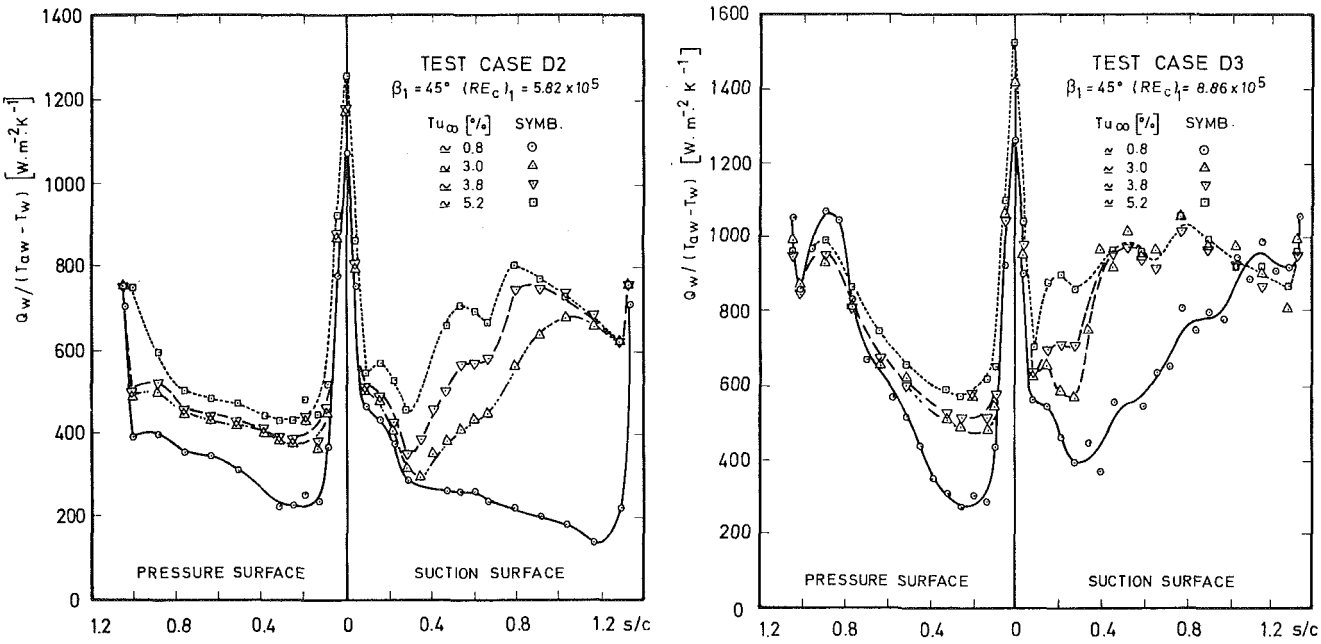

(a) Test case D2 *(b) Test case D3*

Fig. 5 Influence of inlet blade angle on heat transfer distribution

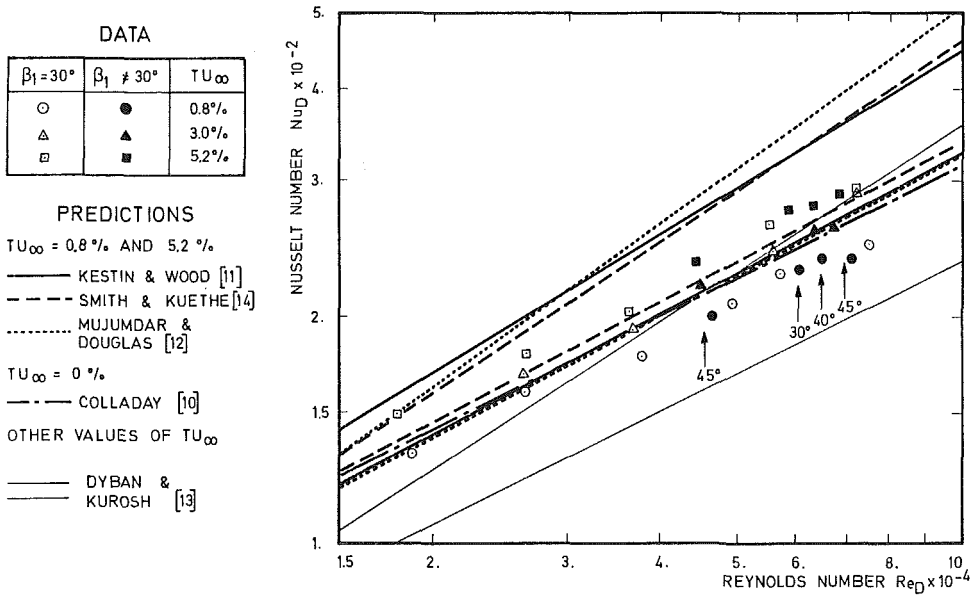

Fig. 6 Influence of turbulence on leading edge heat transfer

For the laminar case the initial velocity profile is given by the solution of the Falkner-Skan equation, and for temperature the equivalent equation [19]. For the turbulent regime, the velocity profile is estimated using the very flexible method of Whitfield [20]; furthermore, the temperature profile is deduced using the Crocco relation [19]. The k profile is obtained using the mixing length hypothesis and assuming proportionality between shear stress and kinetic energy. The ϵ profile is deduced using the equation relating turbulent viscosity, kinetic energy and dissipation profiles which are used in the present modeling [18].

The solution of the four equations is based on a numerical procedure similar to the well-known method of Patankar and Spalding [21]. Ninety points are used across the boundary layer and a complete calculation, as presented in Fig. 8, typically requires 200 s computation time on a CDC 6600 machine.

Typical Result. It has been noticed by various investigators (for example in [22]) that the k-ϵ model, for reasons difficult to understand, could reasonably predict the evolution of most important quantities during transition at least in the case of an incompressible constant pressure boundary layer developing on a flat plate. The present set of data is most useful towards examining this interesting feature in a more realistic situation.

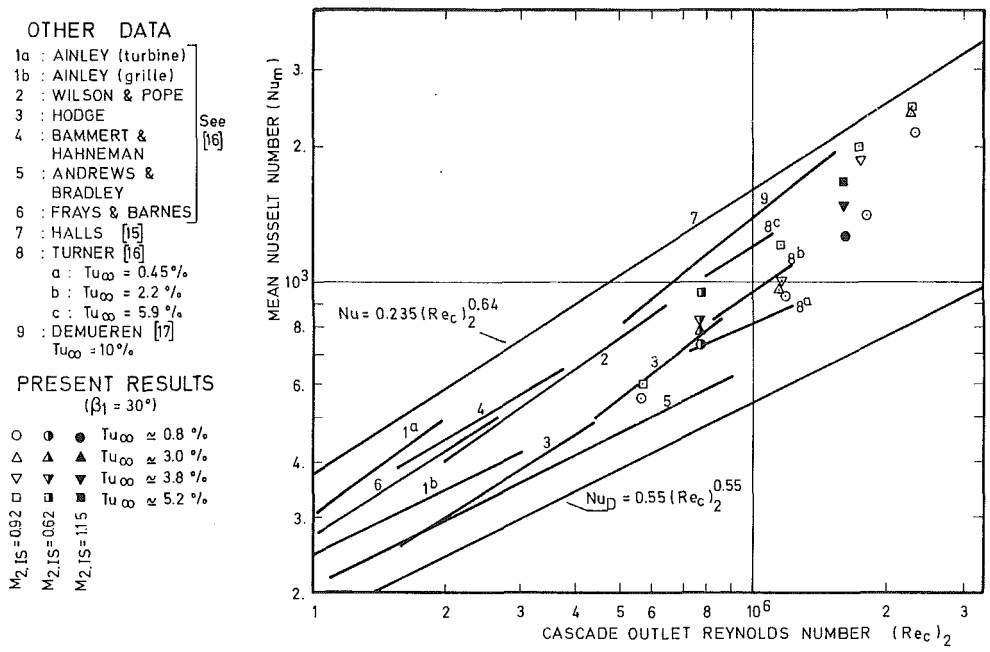

Fig. 7 Influence of turbulence on blade mean Nusselt number

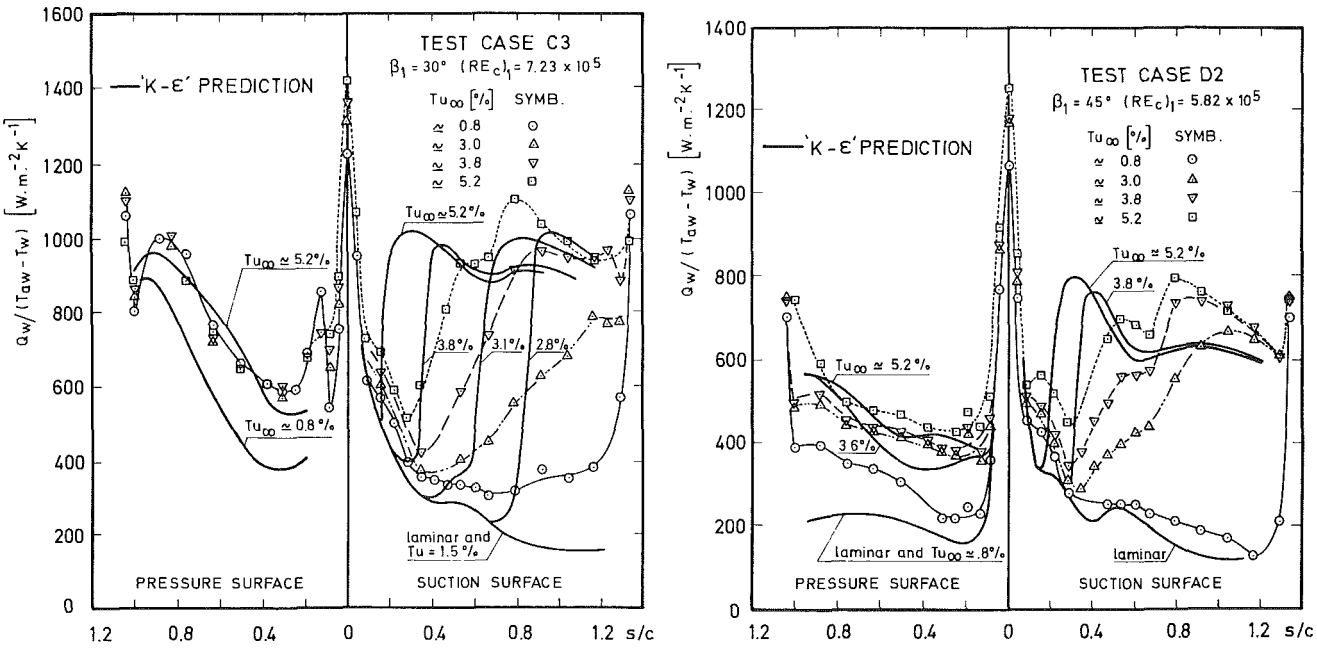

(a) Test case C3 (b) Test case D2

Fig. 8 Typical result of *K-ε* two equation model prediction

Some typical results are presented in Fig. 8. In this case, calculations were performed with the theoretical Mach number distribution, the approach taken by a designer. Considering first the suction side, some discrepancies are observed.

The computed laminar heat transfer is not affected by the change in the free-stream turbulence.

The figure also shows that the beginning of transition is not well located, and in some cases, not predicted at all. This disagreement would be taken in the light that in the calculation, turbulence intensity is taken as $\sqrt{(u'^2+\overline{v'^2}+\overline{w'^2})/3U^2}$ $3V$ where from experiments we deduced it as $\sqrt{\overline{u'^2}/U^2}$. Departures from isotropy can lead to important differences between definitions.

The most important feature is that the evolution of the Stanton number during transition is far from being satisfactorily reproduced by the calculation. In particular, pressure gradient effects seem to be ignored after the process is initiated, causing quasi-instantaneous predicted transition

even in highly accelerating regions. In Fig. 8(*a*), predictions for $Tu_\infty \simeq 3.1$ and 2.8 percent with experiments for $Tu_\infty \simeq 3$ percent give a good illustration of the situation.

In the case of a flat plate boundary layer subjected to a strong favorable pressure gradient, similar and even more characteristic results have been obtained [23], indicating that the model is not adapted to deal with this particular complex situation, which is mainly influenced by intermittency phenomena not catered for in the present modeling.

Nevertheless, the well-known ability of the k-ϵ model to predict highly nonequilibrium situations, or relaminarizing flows, makes it a very useful tool. Great benefit would be obtained by the introduction of higher empiricism for the treatment of the transitional region, however.

In Fig. 8(*b*), on the pressure side, the prediction is shown to compare more favorably with the experiment, although the conditions are undoubtedly more complicated remembering the inevitable interaction between free-stream turbulence and three-dimensional effects expected to occur on concave surfaces.

In the case of a turbulent boundary layer developing downstream of a reattachment point, (Fig. 8(*a*)) the result of any boundary layer prediction seems to be compromised because of the lack of information concerning the profile shapes necessary to start the calculation. In the present case, the calculation started at $s/c = 0.20$ with a realistic velocity profile (computed after [20], for a form factor of 3) leads, in the case of $Tu_\infty \simeq 0.8$ percent, to an underestimation of more than 30 percent of the heat transfer level but to a satisfactory result in the case of $Tu_\infty \simeq 5.2$ percent although the experiment demonstrates only negligible influence of Tu_∞.

Conclusions

The paper presents detailed heat transfer measurements made on a gas turbine rotor blade under differing conditions of Mach number, Reynolds number, inlet flow angle, and flow turbulence level. These were made under the well-controlled conditions obtained in the short duration flow of a piston tunnel, and hence are considered particularly useful towards validating or developing predictive techniques for designers of turbine cooling systems. The most noteworthy observations are: start of transition advances with increase in Reynolds number and turbulence level; stagnation point, laminar and transitional heating are increased by turbulence but turbulent heating is unaffected; in regions of high favorable pressure gradient, the heating rate reflects initiation of laminarization; high heating is found at the trailing edge of finite thickness; transition can be initiated by the presence of shocks in transonic flow; separation bubbles easily recognized on the suction surface disappear with increased inlet flow angle. The tests illuminated several areas of uncertainty in flow behavior, such a separated boundary layers, trailing edge flow, shock boundary layer interaction, which deserve closer experimental examination.

A sophisticated boundary layer calculation using a second order closure model was compared with typical measurements. The results were found to be encouraging although some fundamental discrepancies were observed. In particular, the calculation coped poorly with the variation of heat transfer in the transition region and in the prediction of the turbulent boundary layer downstream of the separation bubbles. It is suggested that empirical modeling of intermittency could improve the predictions.

Acknowledgments

The authors are indebted to Prof. C.H. Sieverding for advice concerning the cascade aspects of this study and to Prof. W. Kollmann for many helpful discussions relating to the theoretical aspect.

References

1 Consigny, H., Richards, B.E., and Ville, J.P., "Short Duration Measurements of Heating to Cooled Gas Turbine Surfaces," ASME Paper No. 78-GT-22, Apr. 1978.

2 Jones, T.V., Schultz, D.L., and Hendley, A.D., "On the Flow in an Isentropic Free Piston Tunnel," ARC R & M 3731, Jan. 1973.

3 Richards, B.E., "Isentropic Light Piston Facilities for Simulation of Hot Flows Through Turbines," VKI LS 78 *Advanced testing techniques in turbomachines* Apr., 1975.

4 Consigny, H., Chan, C.K., and Richards, B.E., "The Effect of Pressure Gradient and External Turbulence on Heat Transfer to a Cold Flat Plate," VKI TN 128, Feb. 1979.

5 Richards, B.E., "A Review of Heat Transfer Work in the VKI Hot Cascade Tunnel," AGARD Specialists meeting on *Testing and measurement techniques in heat transfer and combustion,* Brussels, AGARD CP 281, May, 1980.

6 Schultz, D.L., and Jones, T.V., "Heat Transfer Measurements in Short Duration Hypersonic Facilities," AGARDograph 165, 1973.

7 Van Den Braembussche, R., "Calcul de l'ecoulement soussonique Dans les Grilles d'aubes avec variation de la hauteur," VKI CR 1979-24, May, 1979.

8 Couston, M., "Methode de calcul de l'ecoulement inter-aube pseudo-tridimensionnel en regime transonique," Ph.D. VKI-Brussels University, Sept., 1976.

9 Sieverding, C.H., Stanislas, M., and Snoek, J., "The Base Pressure Problem in Transonic Turbine Cascades," ASME Paper 79-GT-120, March, 1979.

10 Colladay, R.S., "Turbine cooling," NASA SP 290, 1975.

11 Kestin, J., and Wood, R.T., "The Influence of Turbulence on Mass Transfer from Cylinders," ASME *Journal of Heat Transfer,* Nov. 1971.

12 Mujumdar, A.S., and Douglas, W.J.M., " Some Effects of Turbulence and Wake Induced Periodicity on Heat Transfer from Cylinders," 20th Canadian Chemical Engineering Conference, Sarnia, Ontario, Canada, Oct. 1970.

13 Dyban, E.P., and Kurosh, V.D., "Heat Transfer at the Leading Edge of a Turbine Blade," *Heat transfer - Soviet research,* Vol. 2, No. 1, Jan. 1970.

14 Smith, M.C., and Kuethe, A.M., "Effects of Turbulence on Laminar Skin Friction and Heat Transfer," *The Physics of Fluids,* Vol. 9, No. 12, Dec. 1966, p. 2337.

15 Halls, G.A., "Air Cooling of Turbine Blades and Vanes AGARDograph 120, *Supersonic Turbojet Propulsion Systems and Components,* Ed. J. Chauvin, 1967.

16 Turner, A.B., "Local Heat Transfer Meaurements on a Gas Turbine Blade," *Journal Mechanical Engineering Science,* Vol. 13, No. 1, 1971.

17 Demuren, H.O., "Aerodynamic Performance and Heat Transfer Characteristics of High Pressure Ratio Transonic Turbines," Ph.D., Massachusett Institute of Technology, 1976.

18 Jones, W.P., and Launder, B.E., "The Prediction of Laminarization with a Two-Equation Model of Turbulence," *International Journal of Heat and Mass Transfer,* Vol. 15, 1972, pp. 301–314.

19 Schlichting, H., "*Boundary Layer Theory*", 4th edition, McGraw-Hill, 1968.

20 Whitfield, D.L., "Analytical Description of the Complete Two-Dimensional Turbulent Boundary Layer Velocity Profile," AEDC Report No. TR 77-79, March, 1979.

21 Patankar, S.V., and Spalding, D.B., *Heat and Mass Transfer in Boundary Layers,* Intertext, London, 1970.

22 Arnal, D., Juillen, J.C., and Michel, R., "Analyse experimentale et calcul de l'apparition et du developpement de la transition de la conche limite," Paper No. 13, AGARD-CP-224, *Laminar Turbulent Transition,* 1977.

23 Consigny, H., "Etude experimentale et theorique des echanges thermiques convectifs a la surface des aubes de turbines," Ph.D., VKI - Brussels University, 1980.

even in highly accelerating regions. In Fig. 8(*a*), predictions for $Tu_\infty \simeq 3.1$ and 2.8 percent with experiments for $Tu_\infty \simeq 3$ percent give a good illustration of the situation.

In the case of a flat plate boundary layer subjected to a strong favorable pressure gradient, similar and even more characteristic results have been obtained [23], indicating that the model is not adapted to deal with this particular complex situation, which is mainly influenced by intermittency phenomena not catered for in the present modeling.

Nevertheless, the well-known ability of the k-ϵ model to predict highly nonequilibrium situations, or relaminarizing flows, makes it a very useful tool. Great benefit would be obtained by the introduction of higher empiricism for the treatment of the transitional region, however.

In Fig. 8(*b*), on the pressure side, the prediction is shown to compare more favorably with the experiment, although the conditions are undoubtedly more complicated remembering the inevitable interaction between free-stream turbulence and three-dimensional effects expected to occur on concave surfaces.

In the case of a turbulent boundary layer developing downstream of a reattachment point, (Fig. 8(*a*)) the result of any boundary layer prediction seems to be compromised because of the lack of information concerning the profile shapes necessary to start the calculation. In the present case, the calculation started at $s/c = 0.20$ with a realistic velocity profile (computed after [20], for a form factor of 3) leads, in the case of $Tu_\infty \simeq 0.8$ percent, to an underestimation of more than 30 percent of the heat transfer level but to a satisfactory result in the case of $Tu_\infty \simeq 5.2$ percent although the experiment demonstrates only negligible influence of Tu_∞.

Conclusions

The paper presents detailed heat transfer measurements made on a gas turbine rotor blade under differing conditions of Mach number, Reynolds number, inlet flow angle, and flow turbulence level. These were made under the well-controlled conditions obtained in the short duration flow of a piston tunnel, and hence are considered particularly useful towards validating or developing predictive techniques for designers of turbine cooling systems. The most noteworthy observations are: start of transition advances with increase in Reynolds number and turbulence level; stagnation point, laminar and transitional heating are increased by turbulence but turbulent heating is unaffected; in regions of high favorable pressure gradient, the heating rate reflects initiation of laminarization; high heating is found at the trailing edge of finite thickness; transition can be initiated by the presence of shocks in transonic flow; separation bubbles easily recognized on the suction surface disappear with increased inlet flow angle. The tests illuminated several areas of uncertainty in flow behavior, such a separated boundary layers, trailing edge flow, shock boundary layer interaction, which deserve closer experimental examination.

A sophisticated boundary layer calculation using a second order closure model was compared with typical measurements. The results were found to be encouraging although some fundamental discrepancies were observed. In particular, the calculation coped poorly with the variation of heat transfer in the transition region and in the prediction of the turbulent boundary layer downstream of the separation bubbles. It is suggested that empirical modeling of intermittency could improve the predictions.

Acknowledgments

The authors are indebted to Prof. C.H. Sieverding for advice concerning the cascade aspects of this study and to Prof. W. Kollmann for many helpful discussions relating to the theoretical aspect.

References

1 Consigny, H., Richards, B.E., and Ville, J.P., "Short Duration Measurements of Heating to Cooled Gas Turbine Surfaces," ASME Paper No. 78-GT-22, Apr. 1978.

2 Jones, T.V., Schultz, D.L., and Hendley, A.D., "On the Flow in an Isentropic Free Piston Tunnel," ARC R & M 3731, Jan. 1973.

3 Richards, B.E., "Isentropic Light Piston Facilities for Simulation of Hot Flows Through Turbines," VKI LS 78 *Advanced testing techniques in turbomachines* Apr., 1975.

4 Consigny, H., Chan, C.K., and Richards, B.E., "The Effect of Pressure Gradient and External Turbulence on Heat Transfer to a Cold Flat Plate," VKI TN 128, Feb. 1979.

5 Richards, B.E., "A Review of Heat Transfer Work in the VKI Hot Cascade Tunnel," AGARD Specialists meeting on *Testing and measurement techniques in heat transfer and combustion,* Brussels, AGARD CP 281, May, 1980.

6 Schultz, D.L., and Jones, T.V., "Heat Transfer Measurements in Short Duration Hypersonic Facilities," AGARDograph 165, 1973.

7 Van Den Braembussche, R., "Calcul de l'ecoulement soussonique Dans les Grilles d'aubes avec variation de la hauteur," VKI CR 1979-24, May, 1979.

8 Couston, M., "Methode de calcul de l'ecoulement inter-aube pseudo-tridimensionnel en regime transonique," Ph.D. VKI-Brussels University, Sept., 1976.

9 Sieverding, C.H., Stanislas, M., and Snoek, J., "The Base Pressure Problem in Transonic Turbine Cascades," ASME Paper 79-GT-120, March, 1979.

10 Colladay, R.S., "Turbine cooling," NASA SP 290, 1975.

11 Kestin, J., and Wood, R.T., "The Influence of Turbulence on Mass Transfer from Cylinders," ASME *Journal of Heat Transfer,* Nov. 1971.

12 Mujumdar, A.S., and Douglas, W.J.M., " Some Effects of Turbulence and Wake Induced Periodicity on Heat Transfer from Cylinders," 20th Canadian Chemical Engineering Conference, Sarnia, Ontario, Canada, Oct. 1970.

13 Dyban, E.P., and Kurosh, V.D., "Heat Transfer at the Leading Edge of a Turbine Blade," *Heat transfer - Soviet research,* Vol. 2, No. 1, Jan. 1970.

14 Smith, M.C., and Kuethe, A.M., "Effects of Turbulence on Laminar Skin Friction and Heat Transfer," *The Physics of Fluids,* Vol. 9, No. 12, Dec. 1966, p. 2337.

15 Halls, G.A., "Air Cooling of Turbine Blades and Vanes AGARDograph 120, *Supersonic Turbojet Propulsion Systems and Components,* Ed. J. Chauvin, 1967.

16 Turner, A.B., "Local Heat Transfer Meaurements on a Gas Turbine Blade," *Journal Mechanical Engineering Science,* Vol. 13, No. 1, 1971.

17 Demuren, H.O., "Aerodynamic Performance and Heat Transfer Characteristics of High Pressure Ratio Transonic Turbines," Ph.D., Massachusett Institute of Technology, 1976.

18 Jones, W.P., and Launder, B.E., "The Prediction of Laminarization with a Two-Equation Model of Turbulence," *International Journal of Heat and Mass Transfer,* Vol. 15, 1972, pp. 301-314.

19 Schlichting, H., "*Boundary Layer Theory*", 4th edition, McGraw-Hill, 1968.

20 Whitfield, D.L., "Analytical Description of the Complete Two-Dimensional Turbulent Boundary Layer Velocity Profile," AEDC Report No. TR 77-79, March, 1979.

21 Patankar, S.V., and Spalding, D.B., *Heat and Mass Transfer in Boundary Layers,* Intertext, London, 1970.

22 Arnal, D., Juillen, J.C., and Michel, R., "Analyse experimentale et calcul de l'apparition et du developpement de la transition de la conche limite," Paper No. 13, AGARD-CP-224, *Laminar Turbulent Transition,* 1977.

23 Consigny, H., "Etude experimentale et theorique des echanges thermiques convectifs a la surface des aubes de turbines," Ph.D., VKI - Brussels University, 1980.

DISCUSSION

Ronald M.C. So[1] and Russell E. Sheer[1]

Dr. Consigny and Professor Richards are to be commended for a fine piece of work on turbine blade heat transfer. The results, so clearly and convincingly presented, no doubt will contribute to the understanding of this very complicated phenomenon.

Of the many effects examined, the free-stream turbulence effect on blade heat transfer is most valuable to heat transfer

[1]Corporate Research and Development Center, General Electric Company, Schenectady, NY.

designers. It points to the fact that this important effect has to be considered in any heat transfer design analysis. Otherwise, the surface heat flux on the suction side of the blade will be grossly underestimated. In view of the push for higher turbine efficiency, and hence, higher inlet gas temperature to the turbine, this underestimation of surface heat flux could severely affect the durability and life of the blades. Since the turbulence level of the inlet gas stream in a turbine is usually of the magnitude of ~ 15 percent or greater, it would be interesting to see if the suction side surface heat flux would be further affected when the free-stream turbulence level is increased from 5.2 to about 15 percent. Perhaps Dr. Consigny and Professor Richards would care to speculate on this behavior.

The Reynolds number effect on transition is most convincingly presented in Figs. 4(*a-d*). However, in addition to this and the free-stream turbulence effect discussed by Dr. Consigny and Professor Richards, the effect of blade geometry (surface curvature) is also important. Surface curvature effect on turbulent flow is well documented [24, 25]. With the right convex curvature, turbulence in the boundary layer could be "turned off" [26]. Hence, one would expect that increasing the convex curvature on the suction surface could delay transition for flows with the same Reynolds number. Evidence in support of this argument can be found in the measurements obtained by Liepmann [27].

Liepmann's data are used to develop a transition criterion that takes into account such effects as pressure gradient, surface curvature and roughness, Mach number and free-stream turbulence. The criterion is then used to determine an intermittency factor which is used to modify the eddy viscosity. Thus formulated, transitional flow with a finite transition region, the length of which depends on the influences of the various effects, is calculated rather than a point transition as shown in the calculations of this paper. The calculations are in good agreement with some heat transfer measurements on turbine blade cascade obtained recently at General Electric Company. These data are quite similar to those shown in Figs. 4($a-d$), and they are obtained at a temperature ratio, $T_w/T_0 = 0.4$, which is more representative of actual turbine conditions. Both the data and the calculations will be submitted for publication.

Dr. Consigny and Professor Richards's conclusion that empirical modeling of intermittency is required to improve the surface heat flux prediction is borne out by our calculation. It will be interesting to see if the proposed transition criterion can also correctly predict the data presented in Figs. 3-5. Finally, it should be pointed out that, in order to correctly calculate the heat transfer on the pressure side, the ability to predict and calculate across a separation bubble is essential in any turbine blade heat transfer boundary-layer calculation. An effort is presently underway in General Electric to develop just such a technique.

Additional References

24 So, R.M.C., and Mellor, G.L., "An Experimental Investigation of Turbulent Boundary Layers Along Curved Surfaces," NASA CR-1940, 1972.

25 Bradshaw, P., "Effects of Streamline Curvature on Turbulent Flow," AGARDograph No. 169, 1973.

26 So, R.M.C. and Mellor, G.L., "Experiment on Convex Curvature Effects in Turbulent Boundary Layers," *Journal of Fluid Mechanics,* Vol. 60, 1973, pp. 43-62.

27 Liepmann, H.W., "Investigations on Laminar Boundary Layer Stability and Transition on Curved Boundaries," NACA war time Report W-107, 1943.

AUTHOR'S CLOSURE

We are appreciative of the time and effort Dr. So and Dr. Sheer spent preparing their discussion of our paper.

The remarks brought out are quite relevant and we agree that there remain several problems to be studied in this particular field from both the fundamental and applied point of view.

Particularly, the simulation of more realistic free-stream turbulence characteristics (intensity and scale) would be of interest for the designer. The use of "active turbulence grids" (like rotating or vibrating grids, [28] or like "jet grids" [29]) instead of the more classical device used in the present study would make it possible to generate high-turbulence intensities, to change continuously the turbulence level and the turbulence scale, and also to simulate upstream blades wakes.

We are also aware that the study of the effects of parameters – like surface roughness and longitudinal curvature – would also be of great help to the industry. The influence of the latter parameter has been qualitatively investigated in [23] by comparing the results presented in this paper and those obtained in the case where a flat plate boundary layer is strongly accelerated. As mentioned by Dr. So and Dr. Sheer, it has been observed that convex curvature significantly delays boundary layer transition. This result demonstrates that this important parameter must be incorporated in any transition criterion dealing with turbomachinery applications.

Additional References

28 Kiock, R., "Influence of the Degree of Turbulence on the Aerodynamic Coefficients of Cascades," AGARDograph 164, part 1-4, 1972.

29 Gad-El-Hak, M., and Corrsin, S., "Measurements of the Nearly Isotropic Turbulence Behind a Uniform Jet Grid," *Journal of Fluid Mechanics*, Vol. 62, No. 1, 1974, pp. 115-143.

Component Mode Synthesis of Large Rotor Systems

D. F. Li[1]

E. J. Gunter
Mechanical and Aerospace Engineering Department, University of Virginia, Charlottesville, Va. 22901

A scheme is presented for calculating the vibrations of large multi-component flexible rotor systems based on the component mode synthesis method. It is shown that, by a modal expansion of the elastic interconnecting elements, the system modal equation can be conveniently constructed from the undamped eigen representations of the component subsystems. The capability of the component mode method is demonstrated in two examples: a transient simulation of a two-spool gas turbine engine equipped with a squeeze-film damper; and an unbalance response analysis of the Space Shuttle Main Engine oxygen turbopump in which the dynamics of the rotor and the housing are both considered.

Introduction

When the total number of degrees of freedom of a dynamic system is too large for even modern digital computers to handle economically, analysts resort to the modal method in which the system is represented by its free vibration modes. The advantage of using a modal representation consisting of a few low frequency modes is that the associated problem size can be reduced, leading to a subsequent saving in computer time [1-12]. The modal method has been a popular tool in solving difficult problems involving single and double spool rotors. Childs [1-2, 4-5] performed transient rotor-dynamic analyses with undamped normal modes. Choy [6, 8] and Gunter, et al. [7] evaluated the accuracy of the modal method in single-shaft linear rotor analysis including bowed shaft and skewed disk effects. Transient analyses of dual-rotor aircraft engines were attempted by Dennis, et al. [3] and Childs [4]. In both papers, the transient orbits of the rotors due to suddenly applied unbalance were computed with the undamped normal modes of the linearized system. In [4], rotor viscous destabilizing internal damping was accounted for by judiciously applying anti-symmetric, cross-coupled stiffness factors to the modal equations. In all these analyses, the system modal equation was based on normal modes calculated from the full equation of motion of the complete system.

A more advanced form of the normal mode method is offered in the use of component modes [9-11]. In this scheme, a dynamic structure is partitioned into a number of smaller substructures. Each substructure modal character is individually derived, through analytical means or actual vibration testing [12]. The total structure is then constructed from a reduced number of component modes from each substructure. This procedure, besides having the benefit of representing thousands of degrees of freedom by only a handful of normal modes, also allows one to build a sound analytical model because each substructure can be conveniently checked for accuracy before assembly. Furthermore, equation size that the computer has to handle at one time can be further reduced, and the type of interface between the substrucures can be altered without having to recalculate a new set of modal coordinates. Component mode synthesis is used extensively in the aerospace industry for the calculation of the undamped natural frequencies of large airframe structures. Hurty [9] and Craig, et al. [10] are among the earlier investigators. A summary on component mode analysis was presented by Hou [11]. Experimental extraction of undamped modes and the use of a "building block" approach were investigated by Klosterman [12]. In most applications, the substructures are required to share common degrees of freedom at the interconnections of the substructures. Therefore, a set of constraint equations is necessary to determine a reduced modal equation of motion. In rotor systems, a similar but different problem is usually encountered. Interface between substructures consists of bearings, seals, and flexible supports that are themselves elastic. When there is no common degree of freedom being shared by the substructures, flexible connections can be introduced simply as generalized damping, stiffness, and forces into the modal equations. This procedure is exemplified in the analysis of a linear rotor-casing system using undamped modes [5]. Childs started with two sets of casing modes in the two asymmetric planes. Together with the rotor free-free modes, the undamped modes of the rotor-casing system (i.e. the free vibration modes of the total system) were obtained using component mode synthesis. The system modes were then used to develop the system modal equations with the added damping. The total number of generalized coordinates is equal to the number of undamped component modes originally used.

In this paper, a systematic approach to establish the modal equation of motion from component modes is presented. Here, it is built directly from the component modes of the

[1] Now at the General Motors Research Laboratories, Mechanical Research Department, Warren, Michigan 48090.

Contributed by the Gas Turbine Division and presented at the International Gas Turbine Conference and Products Show, Houston, Texas, March 9-12, 1981 of THE AMERICAN SOCIETY OF MECHANICAL ENGINEERS. Manuscript received at ASME Headquarters December 15, 1980. Paper No. 81-GT-147.

substructures; therefore, the extra step involved in computing the system undamped mode (as it is done in [5]) is eliminated. The scheme is completely general and not limited to any fixed system configuration.

Theory

A component mode analysis starts with dividing the system into a number of substructures or subsystems. There is generally no constraint on how large a portion of the total system that each subsystem represents. For example, a subsystem may include all possible degrees of freedom in a rotor shaft. Alternatively, the same rotor may also be represented by three subsystems: one for the coordinates in the two lateral planes, one for torsion, and one for axial vibration. The undamped orthonormal mode shapes and eigenvalues of each subsystem are obtained by omitting all interconnecting elements and damping. (The associated eigenvalue problem may be solved by the transfer matrix method for all rotors and beam-like structures. More complicated structures may be treated by the finite element method.)

For a subsystem consisting of a linearly elastic nonrotating structure, the stiffness matrix is always symmetrical. The eigenvalue problem is

$$[M_x]\{\ddot{x}\} + [\tilde{K}_s]\{x\} = \{0\} \tag{1}$$

and the orthogonality may be expressed as

$$[\phi]^T[M_x][\phi] = [\underline{I}] \tag{2}$$

$$[\phi]^T[\tilde{K}_s][\phi] = [\underline{\omega_s}^2] \tag{3}$$

And for a subsystem consisting of a rotor, the stiffness matrix is generally asymmetrical due to internal friction and asymmetric bearing stiffness. The usual approach is to separate it into a symmetric part and an asymmetric part [5-7]. Only the symmetric stiffness part is used in the evaluation of the undamped component modes. The asymmetric part is added to the modal equations at a later stage. Following this approach, one has the choice of either the free-free rotor modes, containing the shaft stiffness alone, or the rotor-bearing modes, containing both the shaft stiffness and the principal bearing stiffnesses. In the first case, the eigenvalue problem for the free-free rotor modes has the same form as in equations (1) to (3). In the second case, identical modal characteristics are used in both lateral planes to minimize the amount of computations. Hence, the mean bearing stiffness in the lateral directions is considered; the eigenvalue problem becomes:

$$[M_x]\{\ddot{x}\} + \left[[K_s] + \frac{[\underline{K_{xx}}] + [\underline{K_{yy}}]}{2}\right]\{x\} = \{0\} \tag{4}$$

with the orthogonality,

$$[\phi]^T[M_x][\phi] = [\underline{I}] \tag{5}$$

$$[\phi]^T[K_s][\phi] + \frac{[\phi]^T[[\underline{K_{xx}}] + [\underline{K_{yy}}]][\phi]}{2} = [\underline{\omega_p}^2] \tag{6}$$

The modal transformation for the rotor in the lateral planes is therefore given by,

Nomenclature

e = viscous damping coefficient (T)
e_u = unbalance eccentricity
J_p, J_T = polar moment and transverse moment of inertia of a disk (ML^2)
Re[ ] = real part of the complex quantity in [ ]
X, Y, x, y = lateral displacements (L)
$\dot{x}, \dot{y}$ = velocities in x and y directions (L/T)
$\ddot{x}, \ddot{y}$ = accelerations in x and y directions (L/T^2)
Z, z = axial displacement (L)
α, β = phase angle of unbalance in lateral and rotational coordinates
ϵ = dry friction loss angle
θ = rotating coordinate with vector in the Y direction
ϕ = rotating coordinate with vector in the $-X$ direction
τ = disk skew angle
ζ_s = viscous modal damping ratio
ψ = torsional coordinate with vector in the Z-direction
ω = frequency of harmonic vibration (1/T)
Ω = rotor spin speed (1/T)
$\dot{\Omega}$ = rotor acceleration ($1/T^2$)

Matrices

$[C]$ = system damping matrix
$[C_{xx}], [C_{yy}], [C_{x\theta}]$ . . . etc = bearing damping matrices
$[c]$ = modal damping matrix
$[c]^{(ij)}$ = modal damping due to interconnections
$[\underline{J_t}], [\underline{J_p}]$ = transverse and polar moment of inertia
$[I]$ = unity matrix
$[K_{xx}], [K_{yy}], [K_{x\theta}]$, . . . etc = bearing stiffness matrices
$[\tilde{K}_s]$ = symmetric stiffness matrix
$[k]$ = modal stiffness matrix
$[k]^{(ij)}$ = modal stiffness due to interconnection
$[M]$ = system mass matrix
$[m]$ = modal mass matrix
$[0]$ = zero matrix
$\{q^{(i)}\}$ = generalized coordinates in subsystem i
$\{q\}, \{\dot{q}\}, \{\ddot{q}\}$ = generalized displacement, velocity, and acceleration vectors
$[\phi]$ = orthonormal eigenvector matrix
$[\underline{\omega_s^2}]$ = undamped eigenvalue diagonal matrix for rotor free-free modes or structural modes
$[\underline{\omega_p^2}]$ = undamped eigenvalue diagonal matrix for rotor modes including bearing stiffness
$[\underline{\ }]$ = indicates diagonal matrix
$[\ ]^T$ = transpose of matrix [ ].
$\Delta[\ ], \Delta\{\ \}$ = small increment in matrix [ ] and { }

$$\begin{Bmatrix} \{x\} \\ \{y\} \end{Bmatrix} = \begin{bmatrix} [\phi] & [0] \\ [0] & [\phi] \end{bmatrix} \begin{Bmatrix} \{q_x\} \\ \{q_y\} \end{Bmatrix} \tag{7}$$

The shaft flexural stiffness is now implicit in the mode shape and conveniently expressed by the eigenvalues. Axial and torsional vibrations of the shaft that are not coupled to the lateral shaft motion may be treated by equations (1) to (3) and added to equation (7) in the generalized coordinates.

Assembly of Modal Equation. A global model equation consisting of w subsystems is shown below.

$$\begin{bmatrix} [I] & [0] & . & . & . \\ [0] & [I] & . & . & . \\ . & . & . & . & . \\ . & . & . & [I] & [0] \\ . & . & . & [0] & [I] \end{bmatrix} \begin{Bmatrix} \{\ddot{q}^{(1)}\} \\ \{\ddot{q}^{(2)}\} \\ . \\ \{\ddot{q}^{(w-1)}\} \\ \{\ddot{q}^{(w)}\} \end{Bmatrix}$$

$$+ \begin{bmatrix} [c]^{(11)} & [c]^{(12)} & . & . & . \\ [c]^{(21)} & [c]^{(22)} & . & . & . \\ . & . & . & . & . \\ . & . & . & [c]^{(w-1,w-1)} & [c]^{(w-1,w)} \\ . & . & . & [c]^{(w,w-1)} & [c]^{(w,w)} \end{bmatrix} \begin{Bmatrix} \{\dot{q}^{(1)}\} \\ \{\dot{q}^{(2)}\} \\ . \\ \{\dot{q}^{(w-1)}\} \\ \{\dot{q}^{(w)}\} \end{Bmatrix}$$

$$+ \begin{bmatrix} [k]^{(11)} & [k]^{(12)} & . & . \\ [k]^{(21)} & [k]^{(22)} & . & . \\ . & . & . & . \\ . & . & . & . \\ . & . & [k]^{(w-1,w-1)} & [k]^{(w-1,w)} \\ . & . & [k]^{(w,w-1)} & [k]^{(w,w)} \end{bmatrix} \begin{Bmatrix} \{q^{(1)}\} \\ \{q^{(2)}\} \\ . \\ . \\ \{q^{(w-1)}\} \\ \{q^{(w)}\} \end{Bmatrix} = \begin{Bmatrix} \{f^{(1)}\} \\ \{f^{(2)}\} \\ . \\ . \\ \{f^{(w-1)}\} \\ \{f^{(w)}\} \end{Bmatrix} \tag{8}$$

The above equation has been partitioned into submatrices. Each of the diagonal submatrices is square and has the dimension equal to the number of normal modes employed in the corresponding subsystem. The off-diagonal matrices represent the coupling of the subsystems due to the interconnecting elements. The stiffness and damping submatrices in equation (8) can be expressed as the summations of two terms:

$$[k]^{(ij)} = \delta_{ij}[\omega^2]^{(ii)} + [\bar{k}]^{(ij)} \tag{9}$$

$$[c]^{(ij)} = \delta_{ij}[d]^{(ii)} + [\bar{c}\,]^{(ij)} \tag{10}$$

where

$$\delta_{ij} = \begin{cases} 0\ , & i \neq j \\ 1\ , & i = j \end{cases} \tag{11}$$

The first matrix on the right hand side of equations (9-10) for a nonrotating flexible structure is determined by the subsystem eigenvalues (equations (3, 6)) and the associated structural modal damping,

$$[\omega^2]^{(ii)} = [\underline{\omega_s}^2]^{(ii)} \tag{12}$$

$$[d]^{(ii)} = [2\underline{\zeta_s}\omega_s]^{(ii)\,2} \tag{13}$$

and for a flexible rotor (treated as a subsystem containing both lateral planes),

$$[\omega^2]^{(ii)} = \begin{bmatrix} a[\omega_A{}^2] & b[\omega_A{}^2] \\ -b[\omega_A{}^2] & a[\omega_A{}^2] \end{bmatrix} + \begin{bmatrix} [\omega_B{}^2] & [0] \\ [0] & [\omega_B{}^2] \end{bmatrix} \tag{14}$$

$$[d]^{(ii)} = e \begin{bmatrix} [\omega_A{}^2] & [0] \\ [0] & [\omega_A{}^2] \end{bmatrix} \tag{15}$$

where

$$a = \frac{1}{\sqrt{1+\epsilon^2}} \tag{16}$$

$$b = a\epsilon + e\Omega \tag{17}$$

The effects of internal friction are represented in the above equations by the dry friction loss angle ϵ and the viscous friction coefficient e (see Appendix). When the free-free shaft modes are used, $[\omega_A{}^2]$ and $[\omega_B{}^2]$ in equations (14-15) are defined by

$$[\omega_A{}^2] = [\underline{\omega_s}^2] \text{ (in equation (3))} \tag{18}$$

$$[\omega_B{}^2] = [0] \tag{19}$$

Otherwise, when the bearing stiffness is included in the normal modes (as in equation (4)), they become:

$$[\omega_A{}^2] = [\underline{\omega_p}^2] - [\omega_B{}^2] \tag{20}$$

$$[\omega_B{}^2] = \frac{[\phi]^T[[K_{xx}] + [K_{yy}]][\phi]}{2} \tag{21}$$

The linearly elastic elements omitted in the undamped mode calculation contribute to the coupling matrices $[k]^{(ij)}$ and $[c]^{(ij)}$ in the second term of equations (9-10). Typically, these elements consist of the bearing stiffness and damping, gyroscopic moments, and rotor acceleration. To aid in forming $[k]^{(ij)}$ and $[c]^{(ij)}$, it is advantageous to assign a number to

[2] The viscous damping ratio $\underline{\zeta_s}$ for each mode is related to the viscous damping coefficient by $\underline{\zeta_s} = e\,\omega_s/2$.

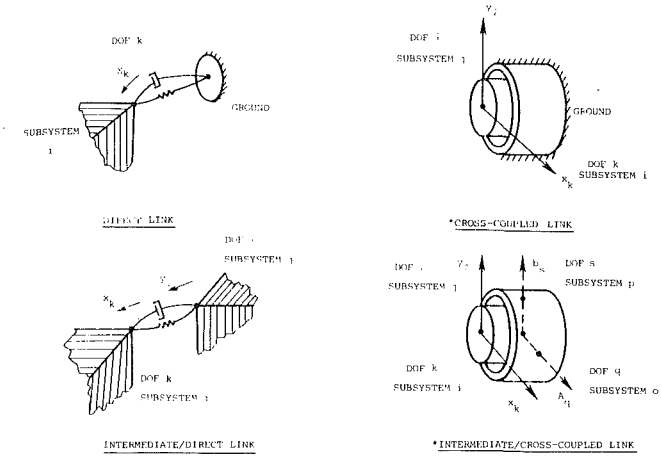

Fig. 1 Linearly elastic connection types in component mode synthesis (* Figures show $i=j$ and $o=p$)

every DOF (degree of freedom) in each subsystem. Modal expansion matrices are used to establish the equivalence of the elastic elements in the modal coordinates. A linear element connecting the k^{th} degree of freedom in subsystem i and the ℓ^{th} degree of freedom in subsystem j has the following modal expansion.

$$[\Gamma]_{\substack{k\ell \\ m\times n}}^{(ij)} = \{\phi_{k1}{}^{(i)}\, \phi_{k2}{}^{(i)} \ldots \ldots \phi_{km}{}^{(i)}\}^T \{\phi_{\ell 1}{}^{(j)}\, \phi_{\ell 2}{}^{(j)} \ldots \ldots \phi_{\ell n}{}^{(j)}\} \tag{22}$$

where

$\phi_{rs}{}^{(f)}$ = deflection at the r^{th} degree of freedom in the s^{th} mode of subsystem f

m,n = number of modes used in the subsystem i and subsystem j respectively.

All linearly elastic elements may be generalized into four distinct linking types (or combinations of these types) as illustrated in Fig. 1. Each link consists of a stiffness coefficient K and a damping coefficient C.

Direct Link. This link represents a linear element connecting the k^{th} DOF in the i^{th} subsystem to the stationary ground. The contributions in the modal stiffness and damping are:

$$\underset{m\times m}{\Delta[\bar{k}]}^{(ii)} = K[\Gamma]_{kk}^{ii} \tag{23}$$

$$\underset{m\times m}{\Delta[\bar{c}\,]}^{(ii)} = C[\Gamma]_{kk}^{ii} \tag{24}$$

Cross-Coupled Link. In this link, a coupling force is induced at the k^{th} DOF in the i^{th} subsystem by the motion at the ℓ^{th} DOF in the j^{th} subsystem. This type of link can be found in dynamic components involving a fluid (e.g. fluid-film bearing). The modal contribution consists of:

$$\underset{m\times n}{\Delta[\bar{k}]}^{(ij)} = K[\Gamma]_{k\ell}^{ij} \tag{25}$$

$$\underset{m\times n}{\Delta[\bar{c}\,]}^{(ij)} = C[\Gamma]_{k\ell}^{ij} \tag{26}$$

Intermediate/Direct Link. This link consists of an elastic element interconnected between the k^{th} DOF in the i^{th} subsystem and the ℓ^{th} DOF in the j^{th} subsystem. The contribution to model stiffness is:

$$\underset{m\times m}{\Delta[\bar{k}]}^{(ii)} = K[\Gamma]_{kk}^{ii} \tag{27}$$

$$\underset{n\times n}{\Delta[\bar{k}]}^{(jj)} = K[\Gamma]_{\ell\ell}^{jj} \tag{28}$$

$$\underset{m\times n}{\Delta[\bar{k}]}^{(ij)} = -K[\Gamma]_{k\ell}^{ij} \tag{29}$$

$$\underset{n\times m}{\Delta[\bar{k}]}^{(ji)} = -K[\Gamma]_{\ell k}^{ji} = \left[\Delta[\bar{k}]^{(ij)}\right]^T \tag{30}$$

The contribution to modal damping is computed by replacing $[k]$ by $[c]$ and K by C in the above expressions.

Intermediate/Cross-Coupled Link. In this link, equal and opposite forces are developed at the ℓ^{th} DOF in the j^{th} subsystem and the s^{th} DOF in the p^{th} subsystem due to the coupling effect of the relative motion between the k^{th} DOF in the i^{th} subsystem and the q^{th} DOF in the o^{th} subsystem. It is equivalent to a cross-coupled link connecting two pairs of DOFs. An example of this is the cross-coupled dynamic coefficient of a journal bearing installed intermediately between two concentric rotating shafts. The stiffness K contributes to:

$$\underset{n\times m}{\Delta[\bar{k}]}^{(ji)} = K[\Gamma]_{\ell k}^{ji} \tag{31}$$

$$\underset{u\times t}{\Delta[\bar{k}]}^{(po)} = K[\Gamma]_{sq}^{po} \tag{32}$$

$$\underset{n\times t}{\Delta[\bar{k}]}^{(jo)} = -K[\Gamma]_{\ell q}^{jo} \tag{33}$$

$$\underset{u\times m}{\Delta[\bar{k}]}^{(pi)} = -K[\Gamma]_{sk}^{pi} \tag{34}$$

Again, similar expressions are applicable for computing the contribution due to damping by replacing K with C in the above equations.

The total effect due to linear linking elements is the sum of all the individual contributions. (For example, a fluid-film bearing mounted in a rigid housing is representable by two direct links, and two cross-coupled links between the shaft and the ground.)

The gyroscopic forces associated with a rotor represent additional modal contributions. This is dealt with in a similar manner using modal expansion. For each pair of angle DOFs, k^{th} DOF in subsystem i and ℓ^{th} DOF in subsystem j, that has polar moment of inertia along the rotor axis,

$$\underset{m\times n}{\Delta[k]}^{(ij)} = \frac{\dot{\Omega} J_P}{2}\,[\Gamma]_{k\ell}^{ij} \tag{35}$$

$$\underset{n\times m}{\Delta[k]}^{(ji)} = \frac{-\dot{\Omega} J_p}{2}\,[\Gamma]_{\ell k}^{ji} = -\left[\Delta[k]^{(ij)}\right]^T \tag{36}$$

$$\underset{m\times n}{\Delta[c]}^{(ij)} = \Omega J_p\,[\Gamma]_{k\ell}^{ij} \tag{37}$$

$$\underset{n\times m}{\Delta[c]}^{(ji)} = -\Omega J_p\,[\Gamma]_{\ell k}^{ji} = -\left[\Delta[c]^{(ij)}\right]^T \tag{38}$$

Normally, the cross-coupling is between the θ DOF and ϕ DOF (see Appendix) in the same subsystem such that $i = j$. (An exception is when vibrations in the x-z and y-z planes are treated as separate subsystems.)

Finally, summing up all the foregoing modal contributions, the second term of the modal stiffness matrix in equation (9) for $i, j = 1$ to w is:

$$[k]^{(ij)} = \sum_{\substack{\text{over all}\\ \text{elastic}\\ \text{links}}}^{\text{sum}} \Delta[\bar{k}]^{(ij)} + \sum_{\substack{\text{over all}\\ \text{gyroscopic}\\ \text{links}}}^{\text{sum}} \Delta[\bar{k}]^{(ij)} \tag{39}$$

The corresponding damping matrix in equation (10) is obtained by replacing $[\bar{k}]^{(ij)}$ by $[\bar{c}\,]^{(ij)}$ in the above equation.

Modal forces are related to the actual forces acting at the nodes according to the mode shapes. For a forcing function F existing at the k^{th} DOF in the i^{th} subsystem, the resulting modal forces are

$$\underset{m\times 1}{\Delta\{f^{(i)}\}} = \{\phi_{k1}{}^{(i)}\, \phi_{k2}{}^{(i)} \ldots \phi_{km}{}^{(i)}\}^T F \tag{40}$$

This expression is used to expand concentrated forces due to unbalance, disk skew, or nonlinear forces at any of the nodal degrees of freedom. The real displacement at the k^{th} DOF in the i^{th} subsystem at any given time is:

$$x_k^{(i)} = \{\phi_{k1}^{(i)}\ \phi_{k2}^{(i)} \ldots \phi_{km}^{(i)}\}\ \{q^{(i)}\} \tag{41}$$

Hence, it is shown that the governing equation of a complex rotor system may be expressed in the generalized coordinates by adding up the contributions of all the linearly flexible links to the basic uncoupled modal equation. Once the governing equation is established, critical speeds, stability, forced or transient responses may be solved in the modal coordinates. The final results can be transformed back into real coordinates by equation (41). Note that in nonlinear transient analyses, it is usually necessary to transform back and forth between the real and the modal coordinates during computation of the nonlinear forces.

Applications

The theory is applied to two high-speed turbomachines; (1) a two-spool aircraft gas turbine engine, (2) Space Shuttle Main Engine liquid oxygen turbopump (SSME HPOTP).

Two-Spool Aircraft Engine

Figure 2 represents a computer model of the two-spool gas turbine engine. The engine consists of an inner core rotor called the power turbine, which is supported by two main bearings located at the shaft extremities. There are two intermediate differential bearings (FDB and ADB) connecting the power turbine to the gas generator rotor. The gas generator is supported principally by four bearings. In this engine design, a squeeze-film damper bearing is incorporated at the No. 3 bearing location to reduce turbine vibration amplitudes and bearing forces.

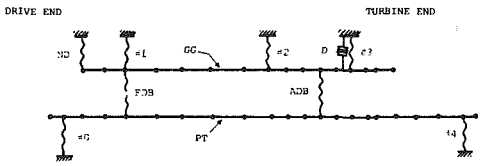

Fig. 2 Two-spool aircraft turbine engine lumped parameter computer model (*PT* - power turbine rotor, *GG* - gas generator rotor, *FDB* - front differential bearing, *ADB* - aft differential bearing, *D* - damper bearing)

The model, which has a total of 38 nodes and 152 degrees of freedom, is considered as being composed of two subsystems; namely, the gas generator rotor, and the power turbine rotor. The component modes of the rotors are obtained independently of each other by omitting the effects of disk gyroscopics, the squeeze-film damper, and the two intershaft bearings. To keep the computer time requirement within reasonable limits, a total of 12 component modes containing two gas generator component modes and four power turbine component modes in each lateral plane are used. This includes all undamped component modes that are below 500 Hz (30,000 cycles per minute (CPM)).

The first part of this application is to compute the transient response of the gas turbine due to a suddenly applied unbalance in the power turbine rotor under steady-speed operation. The gas generator is taken to be balanced and operating at 1571 rad/s (15,000 r/min). The power turbine is operating steadily at 1780 rad/s (17,000 r/min) with zero vibration level when an unbalance distribution is imposed. This particular unbalance consists of 25 g cm each at the second stage turbine and at the rotor mid-span at π rad (180 deg) apart from each other. In this case, the system is assumed to be linear. Figure 3 shows the orbits observed at the second stage gas generator turbine for the first 10 and the last 15 cycles in a total of 40 cycles of simulation. Although the steady-state orbit is not yet completely developed after 40 cycles, the magnitude and the phase angle of the vibration are quite established. A comparison of this result with an independent steady-state response calculation has indicated excellent correlation. The maximum response amplitude observed during the initial transient motion is about two times the size of the steady-state orbit.

Due to the use of an improperly designed damper, a nonlinear "jump" was observed in the gas generator vibration during engine tests. A study is presented here in which the jump phenomena is simulated. The squeeze-film damper has a length of 11 mm, a diameter of 129 mm, and a radial clearance of 0.1 mm. A retainer spring of 2.15×10^7 N/m is used to center the outer raceway of the rolling element bearing inside the damper. The diaphragm which supports the squeeze-film damper bearing is taken to be rigid. The bearing force is calculated with the short bearing theory in the simulation. The power turbine rotor is assumed to be

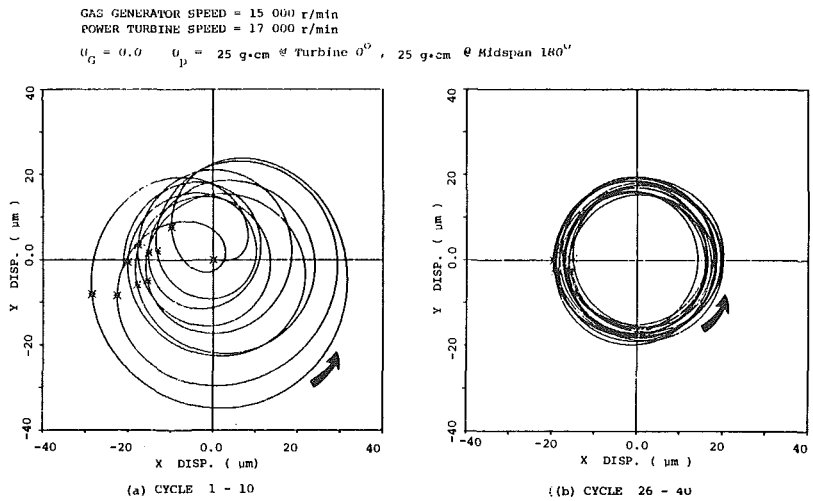

Fig. 3 Linear transient orbits of the gas generator second stage turbine due to coupled power turbine unbalance (– direction of rotor precession)

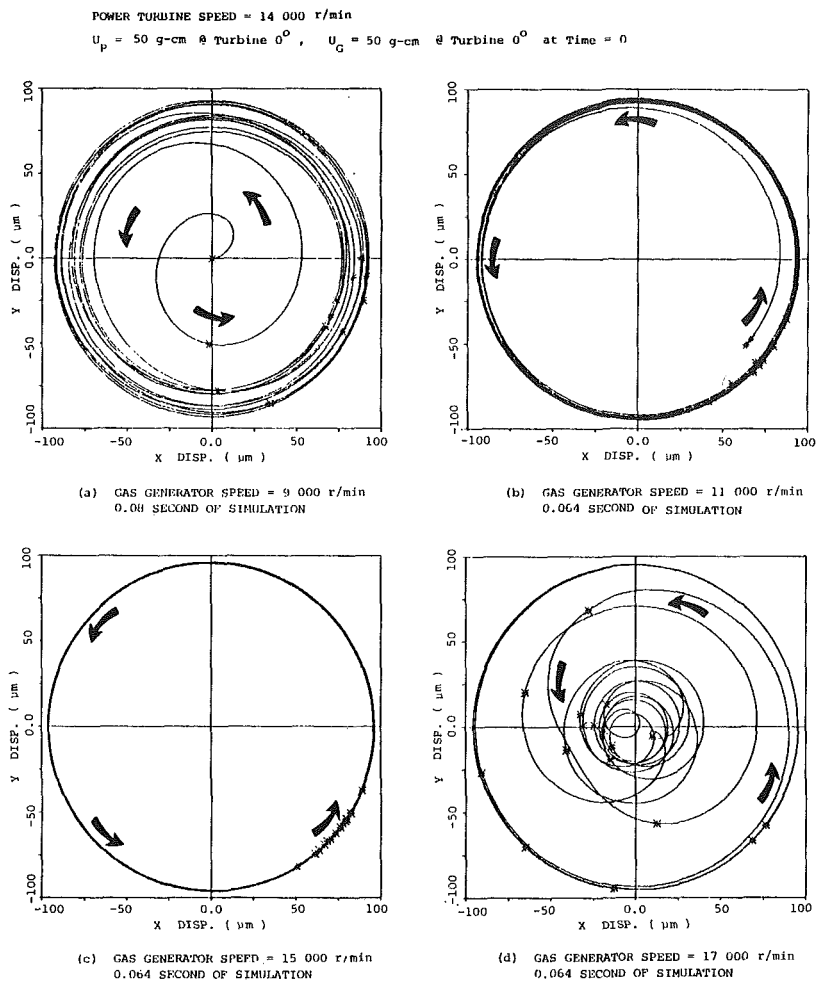

Fig. 4 Nonlinear transient rotor orbits at squeeze film damper bearing showing nonlinear jump (→ direction of rotor precession)

operating at 1466 rad/s (14,000 r/min) with an unbalance of 50 g cm at the turbine end. The gas generator rotor has 50 g cm of unbalance at the second stage turbine.

The gas generator rotor speed is increased from 943 rad/s (9000 r/min) in steps of 209 rad/s (2000 r/min) until the jump phenomena occurs. At 943 rad/s (9000 r/min), the transient motion is started initially at zero displacement and velocity. For each speed, the nonlinear transient is calculated for about 10 gas generator rotor revolutions. The starting conditions at rotor speeds other than the initial speed of 943 rad/s (9000 r/min) are taken to be equal to the final displacement and velocity computed at the end of the simulation cycles for the previous gas generator speed.

Figure 4 represents the transient orbits of the gas generator rotor at the damper location as the gas generator is brought up in speed until the jump phenomena occur. The initial transient rotor motion at 943 rad/s (9000 r/min) is shown in Fig. 4(*a*). The orbits are calculated for about 11 gas generator rotor revolutions after it is released with zero velocity from the bearing center. The timing mark is synchronized with the unbalance vector in the gas generator and is shown as an asterisk at the end of each gas generator rotor revolution. Because the rotors are operating at different speeds, the unbalance forces have two frequency components. Therefore, a response pattern repeating itself for every revolution is not observed even when the system has reached steady-state operation.

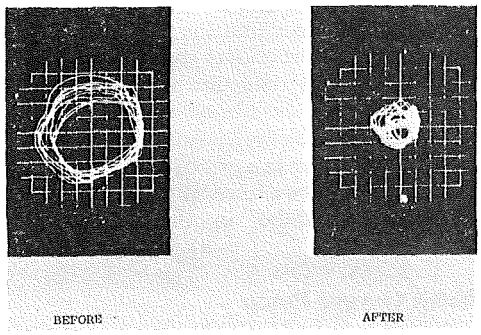

Fig. 5 Experimental gas turbine engine casing vibration orbits before and after nonlinear jump phenomena [13]

Figure 4(*b*) shows the nonlinear rotor motion at the damper location at 1152 rad/s (11,000 r/min). Limiting orbits of large amplitude are formed very rapidly in less than one gas generator revolution. The damper is seen to be operating at eccentricities in excess of 0.9 of the radial clearance. A fluctuation of the phase lag angle about 45 deg persists throughout the simulation at this speed. At 1571 rad/s (15,000 r/min), a case of an extremely overloaded damper is observed in Fig. 4(*c*). The rotor appears to orbit in a large circle with an eccentricity ratio of about 0.95.

Finally, Fig 4(*d*) illustrates the nonlinear jump phenomena

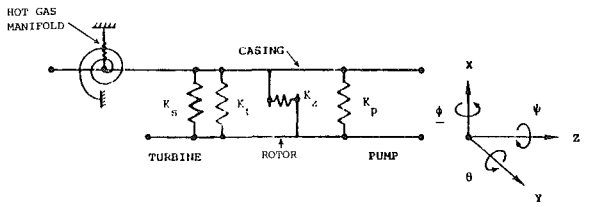

Fig. 6 Space Shuttle Main Engine oxygen pump computer simulation lumped parameter model (K_p · pump bearing, K_z · balance piston, K_t · turbine bearing, K_s · turbine seals)

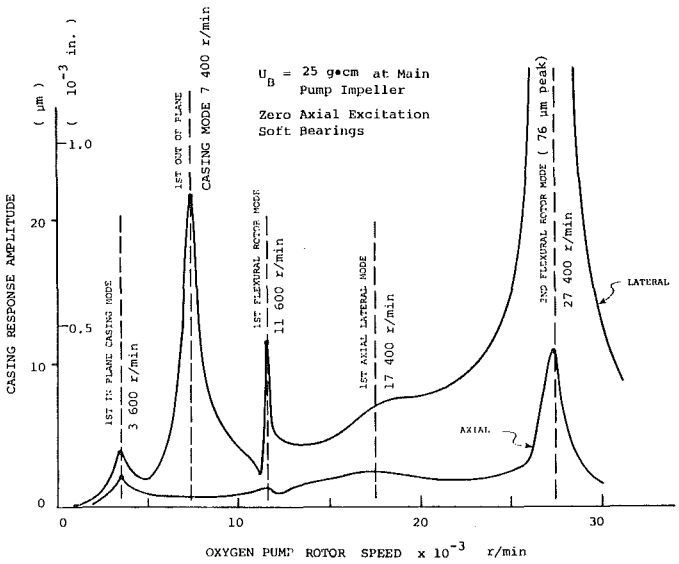

Fig. 7 Lateral and axial steady-state response amplitudes at casing preburner pump end due to main pump impeller unbalance

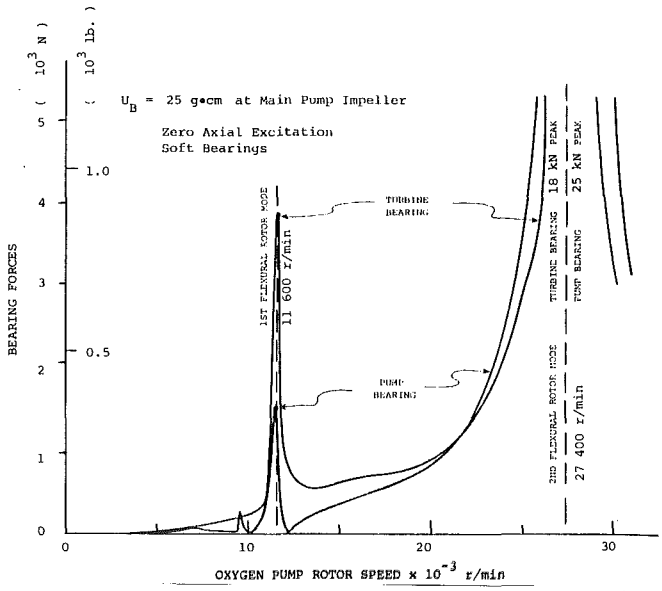

Fig. 8 Bearing forces in the x-direction due to main pump impeller unbalance

at the gas generator speed of 9780 rad/s (17,000 r/min). It is seen that the rotor orbit is reduced to about a quarter of its initial size within five revolutions. The jump in the amplitude is accompanied by a shift of the timing mark to align approximately with the negative x-axis. This phase angle change is important as it indicates that the gas-generator rotor has rapidly passed through the critical speed of the gas-generator mode due to the sudden reduction in the effective damper stiffness which resulted from a smaller orbit size.

Figure 5 represents the experimentally measured vibration orbits of the engine casing in a test run taken before and after the jump occurs. The appearance of these orbits seems to be similar to those obtained in the transient computer simulation.

Space Shuttle Oxygen Pump

In this application, the linear steady-state unbalance response of the space shuttle oxygen pump is computed. Figure 6 shows a computer model of the oxygen pump assembly. It consists of a single rotating shaft mounted in two pairs of flexibly supported rolling element bearings inside a flexible casing. Due to the flexibility in the hot gas manifold, which serves as the only major casing support, a number of rotor/casing resonsant modes are created.

During the development of the oxygen pump, accelerometers were placed on the pump casing to monitor the radial and axial vibration levels. Due to the limited space available inside the test pump, no proximity probes were installed to measure the rotor motions directly. The lack of a measurement of the rotor shaft amplitudes has made it extremely difficult to determine whether a pump failure occuring at about 2618 rad/s (25,000 r/min) was caused by a resonant mode of the rotor or a resonant mode introduced by the flexibly mounted casing. It was intended that the unbalance response analysis would aid in the identification of this failure mode.

The pump is considered to be composed of two subsystems – the casing and the turbopump rotor. Each node in the casing structure is taken to have six degrees of freedom. The casing modes with the hot gas manifold are calculated individually in the x-θ-z lateral axial and the y-$\phi\Psi$ lateral torsional planes. A total of four modes in each plane are included. The frequency of the lowest mode in each plane has been verified by experimental data. The rotor modes are computed using free-free boundary conditions. The highest of the eight modes used at 5672 Hz (340,300 CPM) is more than ten times the full power speed of the turbopump.

In the rotor-flexural mode calculation, the axial and torsional motions are not considered. The axial rotor coordinate is accounted for in the modal analysis by the addition of a rigid body rotor axial mode. Each node in the rotor, therefore, has five degrees of freedom.

In this system, a total of 289 degrees of freedom is represented by 25 generalized coordinates. Five percent modal damping, based on test data, is applied to each of the casing modes. The balance piston has a stiffness of 36.7 ω^2 N/m (0.21 ω^2 lb/in.) and is taken to provide 10 percent of the critical damping in the axial direction. It is assumed that each pair of bearings produces 7.0×10^5 N/m to 1.57×10^6 N/m (0.4×10^6 lb/in. to 0.9×10^6 lb/in.) of stiffness (depending on the rotor speed), and 876 N•s/m (5 lb•s/in) of damping. An unbalance of 25 g cm is placed at the main pump impeller.

Figure 7 represents the calculated casing vibration at the pump end. The vibration modes have been identified in a critical speed calculation according to the proportion of strain energy in the rotor and the pump casing. It can be seen that the highest response amplitude is predicted at the second rotor mode of about 2870 rad/s (27,400 r/min). Axial vibration in this mode is due to the coupling of the axial and lateral forces at the hot gas manifold. The axial-lateral mode at 1822 rad/s (17,400 r/min) does not appear to be particularly sensitive to this unbalance.

The computed forces transmitted to the bearings are presented in Fig. 8. A serious threat to the safety of the pump

is uncovered at the second rotor critical speed where the magnitudes of the forces increase to as high as 25 kN (5600 lb.). Vibrations due to casing flexibility, although readily detected on the casing, do not generate much forces at the bearings.

The result in this analysis indicates that the second rotor mode is a potential danger to the operation of the oxygen pump and could have been responsible for the vibration problem encountered in the test pump. Further testings are now underway to examine this possibility.

Summary and Conclusions

A procedure was developed for the dynamic analysis of large flexible rotor systems with the component mode method. This procedure does not restrict the form of the rotor model. Yet it keeps the size of the governing equation manageable. Because a large system can be divided into a number of much simpler subsystems, the representative component modes can be easily and accurately computed. If desired, these modal informations may be verified by experimental testing.

A two-spool aircraft gas turbine engine equipped with a squeeze film damper bearing and the Space Shuttle Main Engine oxygen turbopump were used to illustrate the capability and versatility of the component mode method. In particular, a transient vibration simulation of the aircraft engine and an unbalance response analysis of the turbopump were presented. The results in both applications were generated by a master computer program. This program has been successfully employed for analyzing the stability, the synchronous response, and the transient response of generally connected multi-component systems.

Acknowledgments

This work is supported in part by the following grants.

NASA - NAS8-31951-5
NASA Lewis - NSG-3177
ARMY - DAG 29-77-C-009

Gratitude is extended to L. E. Barrett of the University of Virginia for providing the damper bearing data and to A. O. DeHart of the General Motors Research Laboratories for reviewing the manuscript.

References

1 Childs, D. W., "A Rotor-Fixed Modal Simulation Model for Flexible Rotating Equipment," ASME *Journal of Engineering for Industry*, Vol. 96, No. 2, 1974, pp. 359-669.

2 Childs, D. W., "Two Jeffcott-Based Modal Simulation Models for Flexible Rotating Equipment," ASME *Journal of Engineering for Industry*, Vol. 97, No. 3, 1975, pp. 1000-1014.

3 Dennis, A. J., Erikson, R. H., and Seitelman, L. H., "Transient Response Analysis of Damped Rotor Systems by the Normal Mode Method," ASME Paper No. 75-GT-58, Gas Turbine Conference, Houston, Texas, March 1975.

4 Childs, D. W., "A Modal Transient Rotor Dynamic Model for Dual-Rotor Jet Engine Systems," ASME *Journal of Engineering for Industry*, Vol. 98, No. 3, 1976, pp. 876-882.

5 Childs, D. W., "The Space Shuttle Main Engine High-Pressure Fuel Turbopump Rotor - Dynamic Instability Problem," ASME JOURNAL OF ENGINEERING FOR POWER, Vol. 100, No. 1, 1978, pp. 48-57.

6 Choy, K. C., *Dynamic Analysis of Flexible Rotor-Bearing Systems Using a Modal Approach*, Ph.D. thesis, University of Virginia, 1977.

7 Gunter, E. J., Choy, K. C., and Allaire, P. E., "Modal Analysis of Turborotors Using Planar Modes - Theory," *Journal of Franklin Institute*, Vol. 305, No. 4, pp. 221-243.

8 Choy, K. C., Gunter, E. J., and Allaire, P. E., "Fast Fourier Transform Analysis of Rotor-Bearing Systems," *Topics in Fluid Film Bearing and Rotor Bearing System Design and Optimization*, presented at the ASME Design Engineering Conference and Shows, Illinois, Apr. 1978.

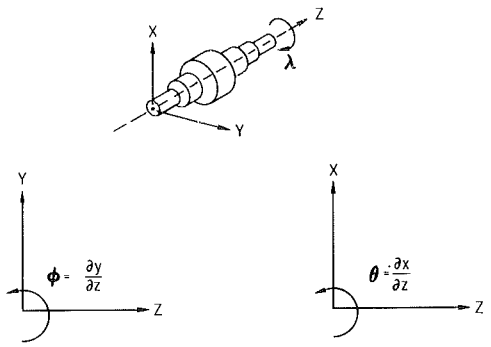

Fig. 9 Rotor coordinates

9 Hurty, W. C., "Dynamic Analysis of Structural Systems Using Component Modes," *AIAA Journal*, Vol. 3, No. 4, Apr. 1965, pp. 678-685.

10 Craig, R. R., and Bampton, M. C. C., "Coupling of Substructures for Dynamic Analysis," *AIAA Journal*, Vol 6, No. 7, July 1968, pp. 1313-1319.

11 Hou, Shou-nien, "Review of Modal Synthesis Techniques and a New Approach," *Shock and Vibration Bulletin 40*, Pt. 4, 1969, pp. 25-39.

12 Klosterman, A. L., *On the Experimental Determination and Use of Modal Representations of Dynamic Characteristics*, Ph.D. dissertation, University of Cincinnati, 1971.

13 Gunter, E. J., Barrett, L. E., and Allaire, P. E., "Design of Nonlinear Squeeze-Film Dampers for Aircraft Engines," ASME *Journal of Lubrication Technology*, Vol. 99, No. 1, 1977, pp. 57-64.

14 D. F. Li, *Dynamic Analysis of Complex Multi-Level Flexible Rotor Systems*, Ph.D. dissertation, University of Virginia, 1978.

APPENDIX

The equation of motion for a rotor [14] is stated without derivation here. The coordinate system for this rotor is shown in Fig. 9. Axial and torsional motion in the z direction are excluded. The effect of internal friction has been added to the governing equation from [7-8]. Forces due to unbalance, disk skew, and rotor acceleration are included in this formulation.

$$\begin{bmatrix} [M_x] & [0] \\ [0] & [M_y] \end{bmatrix} \begin{Bmatrix} \{\ddot{x}\} \\ \{\ddot{y}\} \end{Bmatrix} + \begin{bmatrix} [C_{xx}] & [C_{xy}] \\ [C_{yx}] & [C_{yy}] \end{bmatrix} \begin{Bmatrix} \{\dot{x}\} \\ \{\dot{y}\} \end{Bmatrix} + \begin{bmatrix} [K_{xx}] & [K_{xy}] \\ [K_{yx}] & [K_{yy}] \end{bmatrix} \begin{Bmatrix} \{x\} \\ \{x\} \end{Bmatrix} = \begin{Bmatrix} \{F_x\} \\ \{F_y\} \end{Bmatrix} \tag{42}$$

where

$$[M_x] = [M_y] = \begin{bmatrix} [\underline{M}] & [0] \\ [0] & [\underline{J_T}] \end{bmatrix} \tag{43}$$

$$[C_{xx}] = \begin{bmatrix} [C_{\underline{xx}}] & [C_{\underline{x\theta}}] \\ [C_{\underline{\theta x}}] & [C_{\underline{\theta\theta}}] \end{bmatrix} + e[\tilde{K}_s] \tag{44}$$

$$[C_{yy}] = \begin{bmatrix} [C_{\underline{yy}}] & [C_{\underline{y\phi}}] \\ [C_{\underline{\phi y}}] & [C_{\underline{\phi\phi}}] \end{bmatrix} + e[\tilde{K}_s] \tag{45}$$

$$[C_{xy}] = \begin{bmatrix} [C_{\underline{xy}}] & [C_{\underline{x\phi}}] \\ [C_{\underline{\theta y}}] & [C_{\underline{\theta\phi}}] \end{bmatrix} + \Omega \begin{bmatrix} [0] & [0] \\ [0] & [J_P] \end{bmatrix} \tag{46}$$

$$[C_{yx}] = \begin{bmatrix} [C_{\underline{yx}}] & [C_{\underline{y\theta}}] \\ [C_{\underline{\phi x}}] & [C_{\underline{\phi\theta}}] \end{bmatrix} - \Omega \begin{bmatrix} [0] & [0] \\ [0] & [J_P] \end{bmatrix} \tag{47}$$

$$[K_{xx}] = \begin{bmatrix} [K_{\underline{xx}}] & [K_{\underline{x\theta}}] \\ [K_{\underline{\theta x}}] & [K_{\underline{\theta\theta}}] \end{bmatrix} + \frac{1}{\sqrt{1+\epsilon^2}} [\tilde{K}_s] \tag{48}$$

$$[K_{yy}] = \begin{bmatrix} [K_{\underline{yy}}] & [K_{\underline{y\phi}}] \\ [K_{\underline{\phi y}}] & [K_{\underline{\phi\phi}}] \end{bmatrix} + \frac{1}{\sqrt{1+\epsilon^2}} [\tilde{K}_s] \tag{49}$$

$$[K_{xy}] = \begin{bmatrix} [K_{\underline{xy}}] & [K_{\underline{x\phi}}] \\ [K_{\underline{\theta y}}] & [K_{\underline{\theta\phi}}] \end{bmatrix} + \left(\frac{\epsilon}{\sqrt{1+\epsilon^2}} + e\Omega \right) [\tilde{K}_s] + \frac{\dot{\Omega}}{2} \begin{bmatrix} [0] & [0] \\ [0] & [J_{\underline{P}}] \end{bmatrix} \tag{50}$$

$$[K_{yx}] = \begin{bmatrix} [K_{\underline{yx}}] & [K_{\underline{y\theta}}] \\ [K_{\underline{\phi x}}] & [K_{\underline{\phi\theta}}] \end{bmatrix} - \left(\frac{\epsilon}{\sqrt{1+\epsilon^2}} + e\Omega \right) [\tilde{K}_s] - \frac{\dot{\Omega}}{2} \begin{bmatrix} [0] & [0] \\ [0] & [J_{\underline{P}}] \end{bmatrix} \tag{51}$$

$$\{F_x\} = \begin{Bmatrix} \{\mathrm{Me}_u[\Omega^2\cos(\lambda+\alpha) + \dot{\Omega}\sin(\lambda+\alpha)]\} \\ \{\tau(J_P - J_T)[\Omega^2\cos(\lambda+\beta) + \dot{\Omega}\sin(\lambda+\beta)]\} \end{Bmatrix} \tag{52}$$

$$\{F_y\} = \begin{Bmatrix} \{\mathrm{Me}_u[\Omega^2\sin(\lambda+\alpha) - \dot{\Omega}\cos(\lambda+\alpha)]\} \\ \{\tau(J_P - J_T)[\Omega^2\sin(\lambda+\beta) - \dot{\Omega}\cos(\lambda+\beta)]\} \end{Bmatrix} \tag{53}$$

$$\{X\} = \begin{Bmatrix} \{x\} \\ \{\theta\} \end{Bmatrix}; \quad \{y\} = \begin{Bmatrix} \{y\} \\ \{\phi\} \end{Bmatrix} \tag{54}$$

The size of this equation is four times the number of nodes in the rotor model.

Turbulence Characteristics in the Annulus-Wall Boundary Layer and Wake Mixing Region of a Compressor Rotor Exit[2]

R. Davino[1]

B. Lakshminarayana

Director of Computational Fluid Dynamics Studies and Professor of Aerospace Engineering.

Department of Aerospace Engineering, The Pennsylvania State University, University Park, Pa. 16802

The flow at the exit of a turbomachinery rotor near the annulus wall is three-dimensional with a varying degree of turbulence and nonisotropic characteristics. The characteristics of the turbulence vary considerably with radial and axial location, blade loading, Reynolds number, free-stream turbulence, and the rotor blade geometry. This paper is concerned with the turbulence properties near the annulus wall region of a moderately loaded compressor blade. The variation of the streamwise, normal, and radial intensities as well as the stresses across the wake, its profile and decay characteristics, were determined with a tri-axial hot-wire probe in the stationary frame of reference. The turbulence characteristics in the annulus-wall region of the rotor exit were found to be highly complex due to the interaction of the blade wake and the annulus wall.

Introduction

The mean velocity defect and the turbulent velocity fluctuations in a rotor wake contribute to the overall noise production, aerodynamic losses, and vibration characteristics of turbomachinery. The study of the turbulence structure downstream of a rotor blade row is important since it introduces unsteadiness and affects the boundary layer behavior in the succeeding blade row. Recent investigations have revealed that the turbulent property of the annulus-wall boundary layer and of the rotor boundary layer and wake contribute significantly to unsteady blade forces, performance deterioration, and noise generated in turbomachines. Therefore, a thorough knowledge of the turbulence quantities in the compressor rotor wake in the end-wall region is crucial to improved design, reduced losses, and improved efficiency and performance of turbomachinery.

The rotor wake and the annulus wall boundary layer is not only influenced by the annulus and hub wall and the upstream flow condition, but is also controlled by such parameters as blade spacing, solidity, hub-tip ratio, blade loading, and Coriolis and centrifugal forces induced by curvature and rotation. The effect of all these is to make the flow highly three-dimensional, which introduces many complications in the experimental and theoretical investigations of the rotor wake and end-wall flow [1].

The general structure of the rotor wake was studied by Raj and Lakshminarayana [2], Reynolds et al. [3], and Ravindranath [4]. These data were taken from lightly and moderately loaded axial flow fans outside the end-wall region. The annulus- and hub-wall boundary layers affect the development and decay of the rotor wake near the wall regions. The nature of the mean velocities and turbulence quantities of the wake are considerably affected.

This paper reports some results of a comprehensive investigation of the wake near the annulus wall of such a moderately loaded compressor rotor conducted at the Turbomachinery Laboratory of The Pennsylvania State University. The immediate objective of the program is to include a thorough investigation of the flow ahead of, within, and downstream of the rotor [1]. In the present paper one aspect of the study will be discussed: a detailed study of the structure and decay characteristics of turbulence in the annulus-wall boundary layer and wake mixing region of the rotor exit. Available literature on the structure of turbulence in this region is very limited and no data are available for this region in particular. The main objective of this investigation is to provide a study of the structure of turbulence in this region.

Experimental Equipment and Procedure

The measurements reported in this investigation were performed using the axial-flow compressor facility located in the Turbomachinery Laboratory of The Pennsylvania State University. The measurements were acquired employing a stationary three-sensor hot-wire probe located behind the rotor blade row. These measurements yielded information on the three components of mean velocity, turbulence intensity, and Reynolds stress, and various characteristics of the flow in the rotor exit annulus-wall region.

[1] Presently, Aeroacoustics Engineer, Aircraft Engine Group, General Electric Company, Evendale, Ohio.

[2] This is a companion paper to reference [1]. Mean flow properties are presented in [1]; the current paper deals with the corresponding turbulence properties.

Contributed by the Gas Turbine Division and presented at the International Gas Turbine Conference and Products Show, Houston, Texas, March 9-12, 1981, of THE AMERICAN SOCIETY OF MECHANICAL ENGINEERS. Manuscript received at ASME Headquarters, December 15, 1980. Paper No. 81-GT-148.

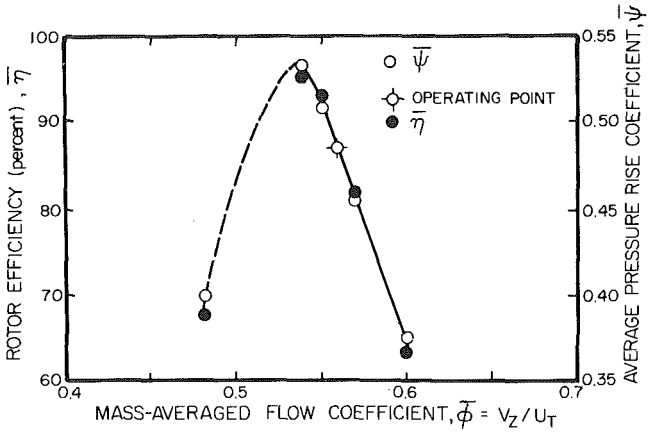

Fig. 1 Operating characteristics of the rotor

The Axial-Flow Compressor Facility. The axial-flow compressor facility used in this investigation is described in reference [5]. The general description of the stage is given by Smith [6]. Pressure rise and efficiency characteristics of the rotor as well as the operating point are shown in Fig. 1. The hub/annulus-wall diameter ratio of the facility is 0.5, with the diameter of the annulus wall equal to 0.932 m. The inlet guide vane which consists of 43 blades is followed by the rotor of 21 blades. The rotor is driven by a 37.29 kW variable speed motor through a belt and pulley system. The speed of the rotor can be continuously varied from 175 to 1695 rpm with accurate and precise control and can be held constant to ±1 rpm. The rotating rotor hub is followed by a stator with 25 blades. Downstream of the stator is located a Joy axial-flow fan with variable blade setting for the variation of pressure rise and mass flow. The facility is terminated downstream by an aerodynamically designed throttle which provides additional control of the stage operating characteristics. Table 1 lists some of the relevant data concerning the facility specifications and operating conditions.

Probe, Instrumentation, and Data Transmission System. A tri-axial hot-wire probe, similar to that used in references [3] and [4], was employed for all measurements reported in this paper. The probe sensors were built of tungsten wire and had a length to diameter ratio of 300 and each sensor had a resistance of approximately 4.1 ohms. The probe calibration was performed employing a low turbulence open-jet calibration facility. The resulting calibration was corrected for yaw and pitch angle sensitivity, temperature variation, and aging of the sensor.

The stationary probe measurement technique employed was developed by Lakshminarayana and Poncet [7] and has been continuously improved to increase the accuracy. The latest technique and the computer program is given by Hah [8]. The sensors were connected to three DISA 55M10 constant-temperature anemometer units. The signals of these anemometers were channeled to an integral digital voltmeter to obtain the overall mean voltage of the anemometer output. The fluctuating a.c. signals were amplified and recorded with a SAVRE IV FM signal recorder/reproducer at a tape speed of 15 i.p.s. The center frequency of recording was 43 kHz and the frequency of the signals could vary from 0 to 10 kHz. A specific position behind the rotor was identified by referring to a pusle generator which was installed on the compressor axis. This pulse generator provided one sharp pulse for each revolution of the rotor row. Each of the rotor passage-flows could be identified with the pulse signal. An ensemble average was obtained for the specific passage-flow of interest. All three instantaneous anemometer output signals and the pulse signal were displayed on a Tektronix type RM 561A storage oscilloscope.

Due to the high rotational speed of the rotor (1066 rpm) and number of rotor blades (21), one survey of a blade passage requires very little time (0.0027 s). This gives an impractically high sampling speed; therefore, the analog signal was digitized at 1/16 real time. The H.P. 7900 A.D.C. unit was used for this analog-to-digital conversion. The digitizing was performed at a tape reproduction speed of 15/16 i.p.s. This was based on the number of points required to represent

Nomenclature

c = blade chord length
L = blade span
$L.E.$ = blade leading edge
PS = pressure side of rotor blade wake
R = radius ratio (r/r_{tip})
r = local radius, radial direction, radial location of the probe
S = blade spacing
SS = suction side of the blade wake
(s,n,r) = end-wall flow coordinate system (streamwise, normal, and radial coordinate directions)—Fig. 1
$T.E.$ = blade trailing edge
U_{tip} = peripheral speed of the rotor blade
W = flow relative velocity (Fig. 1)
w' = fluctuating component of relative velocity
Ye = tangential distance at the exit of the blade passage
Z = axial distance from the rotor blade trailing edge normalized by the rotor blade chord
z = axial coordinate direction corresponding to the axis of the compressor
α = air outlet angle at mid-passage (Fig. 1)
ρ = fluid density
τ_s, τ_n, τ_r = normalized turbulence intensities in the streamwise, normal, and radial directions, respectively $[\sqrt{\overline{(w_s'^2)}}/W_s$, $\sqrt{\overline{(w_n'^2)}}/W_s$, $\sqrt{\overline{(w_r'^2)}}/W_s)$
τ_{sn}, τ_{nr} = stress correlations given by $\overline{w_s' w_n'}/W_s^2$, $\overline{w_n' w_r'}/W_s^2$, respectively
Ω = rotational speed of the rotor blade
$\bar{\psi}$ = mass averaged pressure rise coefficient (normalized by $\rho U_{tip}^2/2$)
$\bar{\eta}$ = rotor efficiency = $\bar{\psi}/\bar{\psi}_{Euler}$

Subscripts

max = maximum value
0 = free-stream value
(s,n,r) = values in the streamwise, normal, and radial coordinate directions, respectively
(z,θ,r) = values in the axial, tangential, and radial coordinate directions, respectively

Superscripts

— = average value
′ = fluctuating quantity

Table 1 Axial-flow compressor facility specifications, operating conditions, and measurement stations

Particular	Facility Specifications
Number of blades	43-IGV, 21-Rotor, 25-Stator
Outer diameter of rotor	0.929 m
Hub/tip ratio	0.5
Blade element	See Ref. [6]
Tip clearance (average)	0.254 cm at $Z = 0.750$ 0.2870 cm at $Z = 0.979$
Rotor drive power	37.29 kW
Auxiliary fan	Series 1,000 Joy Airvane Fan #0 to #16 blade setting, fan diameter = 0.9652 m
Fan drive power	37.29 kW
Particular	**Operating Conditions**
Inlet static pressure	-5.321 cm of H_2O
Inlet velocity	29.04 m/s
Flow coefficient	0.56
Rotor speed	1066 rpm
Average pressure rise coefficient (midradius)	0.4864
Blade chord and spacing at the tip	15.41 cm, 14.12 cm
Stagger angle	45 deg
Measurement stations	$Z = 0.021, 0.042, 0.125, 0.458$ $R = 0.891$ (22), 0.918 (16), 0.945 (11) 0.959 (8), 0.973 (5.4), 0.98 (4) 0.986 (2.8) (Numbers in parentheses represent percent span from the blade tip)

adequately the passage-flow. The digitized hot-wire signal was converted to a corresponding instantaneous cooling velocity. The instantaneous flow velocity was obtained from the cooling velocities of the three sensors using hot-wire equations. The various mean and turbulent flow characteristics in the rotor frame of reference were obtained statistically with these instantaneous velocities. A detailed discussion of the data processing procedure and the error analysis is given by Reynolds and Lakshminarayana [9].

Experimental Results, Interpretation, and Correlation

The data processing procedure described above provided sufficient information to derive the three components of mean velocity and the six components of turbulence stress (including normal stress). These quantities were derived in the (s,n,r) coordinate system shown in Fig. 2(*a*). The orientation of this coordinate system, as well as the flow angle α and the meridional angle β, with respect to the compressor coordinate system (z,θ,r) is indicated. The (s,n,r) coordinate system follows the projection of the flow at the mid-passage in the radial plane for the various axial measurement locations. The reported measurements consist of tangential surveys across the rotor blade passage at various axial and radial locations. The measurement was taken at axial (Z) locations of 0.021, 0.042, 0.125, 0.458, at each of the radial locations $R = 0.891$, 0.918, 0.945, 0.959, 0.973, 0.980, and 0.986. The axial distance from the blade trailing edge and the radial distance from the compressor axis are normalized by the blade chord and radius of the blade tip, respectively.

Figure 2(*b*) shows the variation of the exit flow angle α at various radial and axial locations. The effect of the annulus-wall boundary layer is seen near the blade tip. Figure 2(*b*) also specifies the orientation of the (s,n,r) coordinate system with respect to the (z,θ,r) coordinate system.

Turbulence Intensity Profiles. Tangential variation of the three turbulent intensity components (see Fig. 1) at various radial and axial locations are shown in Figs. 3 through 14. Due to the data acquisition and reduction technique, these measurements are presented as a continuous profile. The various components of turbulence intensity are normalized by the local mean velocity, since the turbulence is dependent upon the local flow conditions. The tangential distance across the rotor passage is normalized by the blade spacing. The pressure and suction sides of the blade wake are indicated with a tangential distance of $Y_e = 0.00$ indicating the wake center, and a tangential distance of $Y_e = 0.5$ indicating the mid-distance between successive wakes.

Streamwise Turbulence Intensity. The streamwise tur-

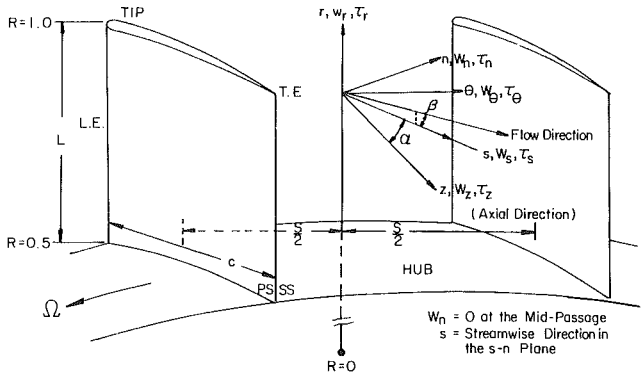

Fig. 2(*a*) Definition of streamwise (*s,n,r*) coordinate system

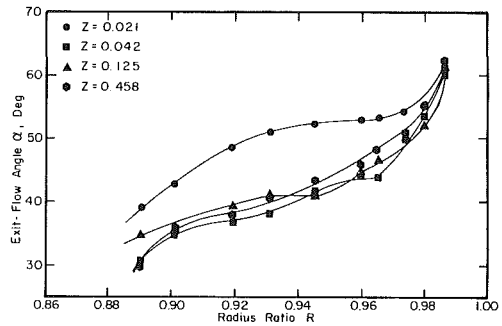

Fig. 2(*b*) Variation of the rotor blade exit-flow angle in the *s-n* plane

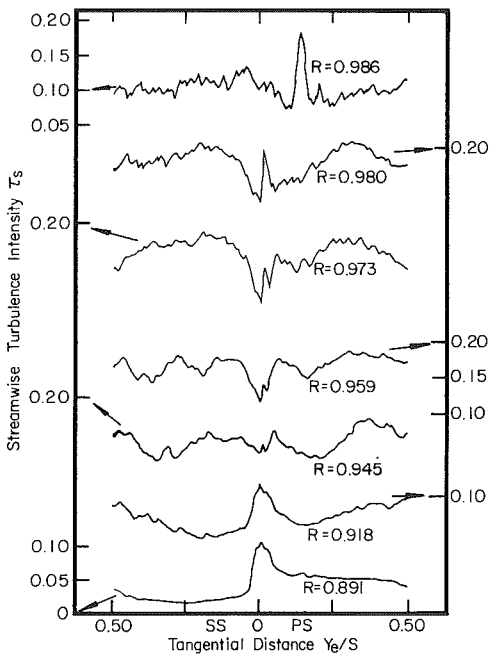

Fig. 3 Streamwise turbulence intensity profiles, $Z = 0.021$

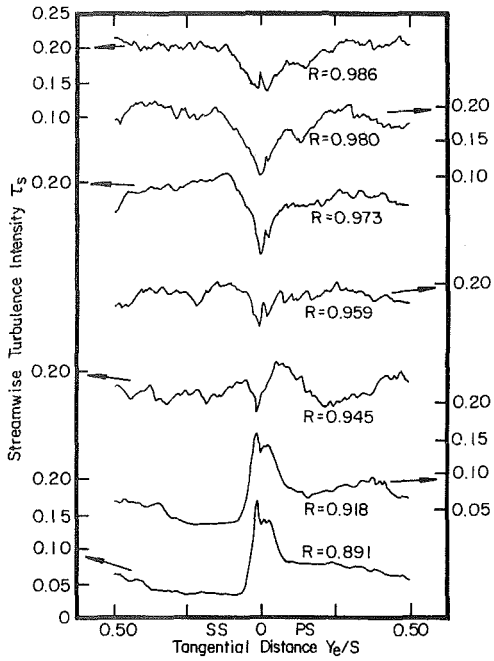

Fig. 4 Streamwise turbulence intensity profiles, Z = 0.042

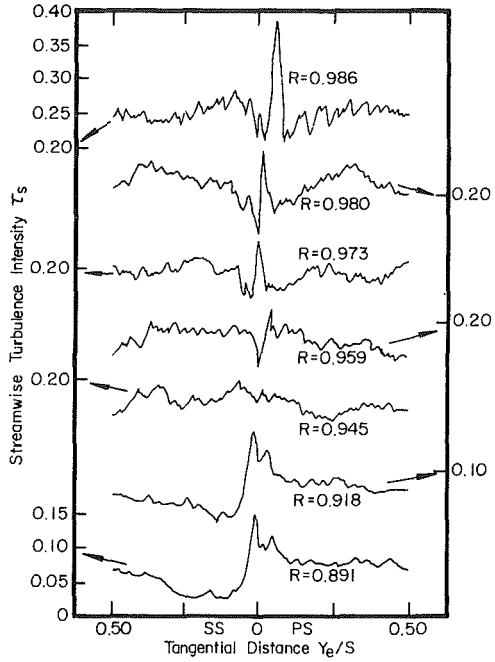

Fig. 5 Streamwise turbulence intensity profiles, Z = 0.125

bulence intensity profiles in the annulus-wall boundary layer and wake mixing region are presented in Figs. 3 through 6. These profiles indicate very high values of streamwise turbulence intensity at the tangential location of the blade wake and an increase in free-stream turbulence intensity as the annulus wall is approached. At higher radial locations, above $R = 0.945$, the level of streamwise turbulence intensity in the free-stream is amplified to a level observed in the interference region of the blade passage-flow. This region, within the blade passage, is induced by the complex interaction of the blade boundary layers, the annulus-wall boundary layer, the tip leakage flow, the secondary flow and the scraping vortex. This phenomenon is discussed in detail in reference [1]. The redistribution of turbulence intensity is also observed at lower radial locations and for other components of turbulence intensity.

The influence of the annulus-wall is not readily observed below the radial location of $R = 0.945$. In this region the streamwise turbulence intensity profiles show typical trends. The profiles are asymmetrical but tend to become symmetrical far downstream. This trend is also observed in the profiles of the other components of turbulence intensity. The asymmetry in the profiles results from the differential growth of turbulence on the suction- and pressure-surface of the rotor blade. Figures 4 and 5 show a dip in the profile at the centerline of the wake. This dip occurs because the turbulence intensity is zero on the blade surface and the maximum value of intensity will occur slightly away from the blade surfaces. Higher intensities on the pressure side, where the gradients in velocity are higher, and lower intensities on the suction side are evident from these figures. The magnitude of the turbulence intensity in the wake decreases with axial distance.

The streamwise turbulence intensity profiles at radial locations above $R = 0.945$ are also plotted in Figs. 3 through 6. These profiles depict the complex turbulence structure in the annulus-wall region. The effect of the interaction of the secondary flow, tip leakage flow, and the blade wake is observed in these plots. The turbulence intensity is substantially higher across the entire passage at higher radial locations. A free-stream value of 5 percent at $R = 0.891$ has increased to 20 percent at $R = 0.986$ for $Z = 0.042$. Im-

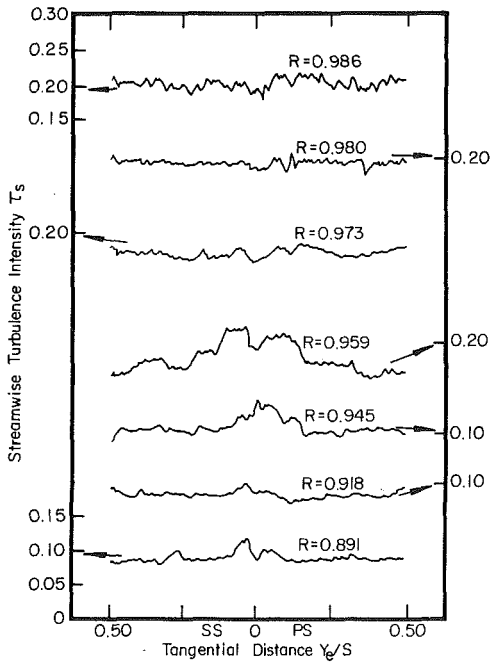

Fig. 6 Streamwise turbulence intensity profiles, Z = 0.458

mediately behind the blade, $Z = 0.021$, the free-stream turbulence intensity is about 10 percent. This indicates that there is intense mixing in these regions. Area of high turbulence tend to spread out and mix with the free-stream as the flow develops. At these higher radial locations, the higher turbulence intensity within the wake is still evident and is magnified due to the complex flow interactions. The presence of the annulus-wall and the associated flow mixing causes the streamwise turbulence intensity to increase in both the rotor blade wake and the free-stream.

Some of the peculiar behavior of the end-wall flow is evident from these figures. The region $R = 0.891$ to $R =$

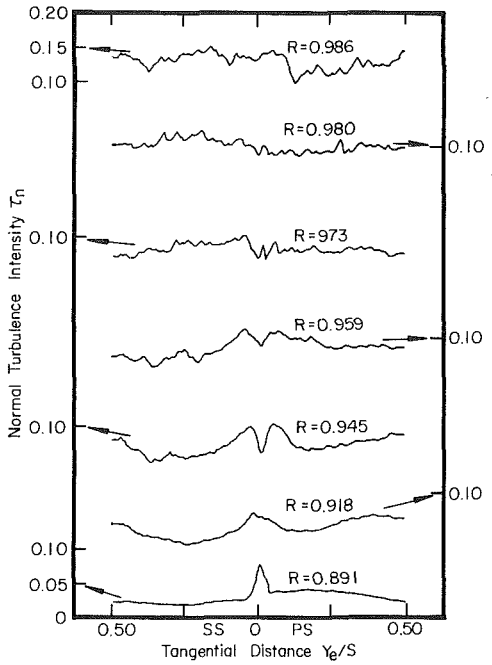

Fig. 7 Normal turbulence intensity profiles, $Z = 0.021$

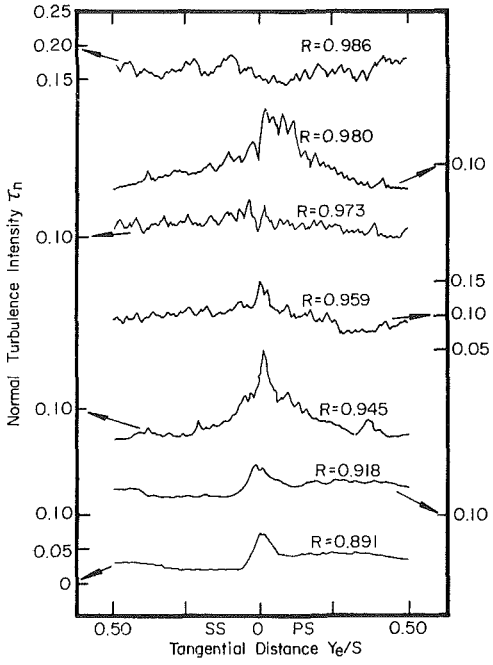

Fig. 9 Normal turbulence intensity profiles, $Z = 0.125$

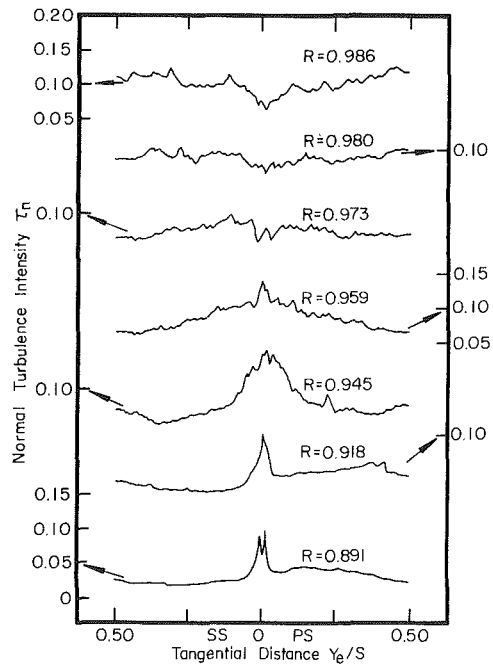

Fig. 8 Normal turbulence intensity profiles, $Z = 0.042$

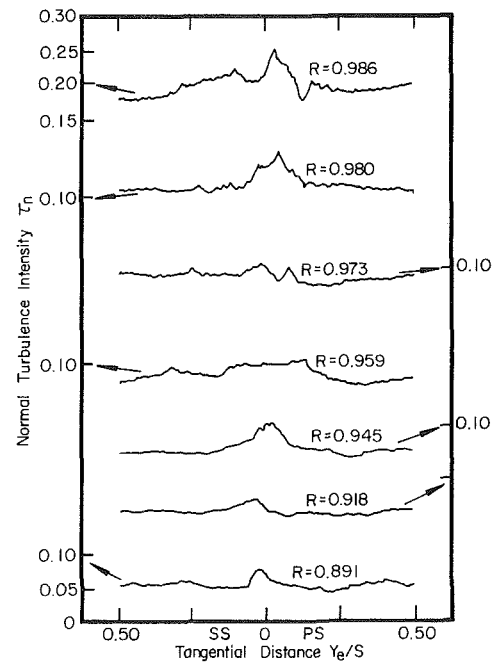

Fig. 10 Normal turbulence intensity profiles, $Z = 0.458$

0.945 is dominated by the wake effects. The peak intensities decrease continuously with distance downstream. The intensities beyond $R = 0.945$ show a complex trend. At $Z = 0.021$, $R > 0.945$, the wake width on both sides is very thick [1] and this is reflected in Figs. 3 through 6. The peak intensities occur on the pressure side, with a dip in the center and reasonably high intensities across the entire passage. Because of the large wake thickness (resulting from a thick boundary layer) the hot wire sensor was able to pick up low intensities in the middle of the wake. Between $Z = 0.021$ and 0.042 (compare Figs. 3 and 4), the peak intensities disappear leaving only the dip in intensities near the wake center caused by the surface layers. The peak intensities reappear again at $Z = 0.125$. The authors speculate that this may have been caused by the roll-up of the leakage flow jet with the mainstream. The mixing of the leakage flow with the main flow and resulting vortex formation may have caused higher intensities in this region. These intensities decay very rapidly between $Z = 0.125$ and 0.458. At the last measuring station ($Z = 0.458$), the wake is diffused completely with consequent uniform intensities around 20 percent in this region.

Normal Turbulence Intensity. Figures 7 through 10 display the tangential variation of the normal turbulence intensity profiles observed in the blade wake and the annulus-wall boundary layer mixing region. These profiles show high

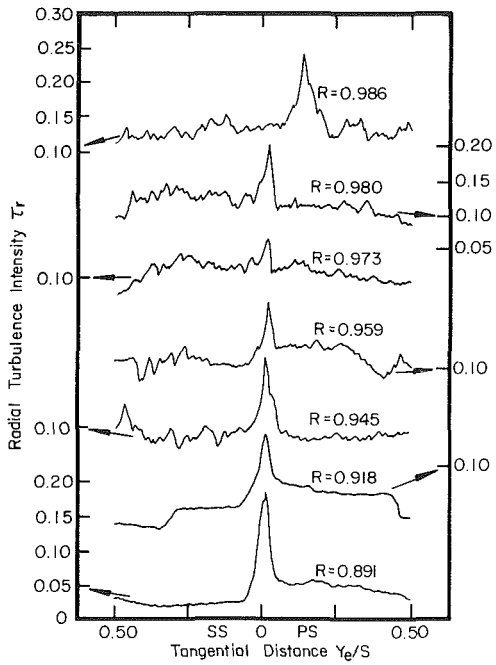

Fig. 11 Radial turbulence intensity profiles, $Z = 0.021$

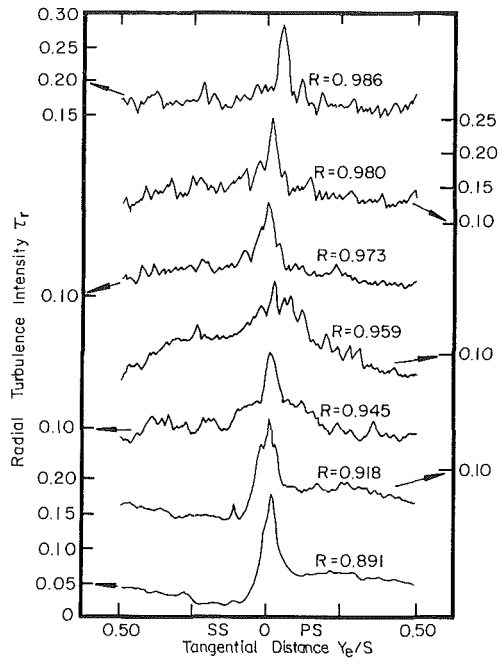

Fig. 13 Radial turbulence intensity profiles, $Z = 0.125$

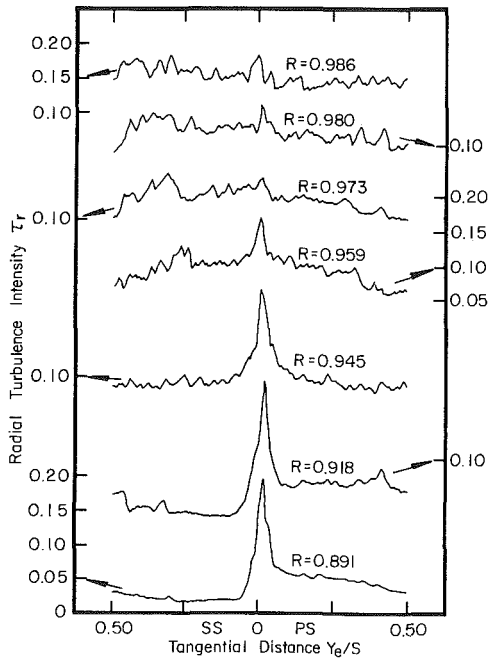

Fig. 12 Radial turbulence intensity profiles, $Z = 0.042$

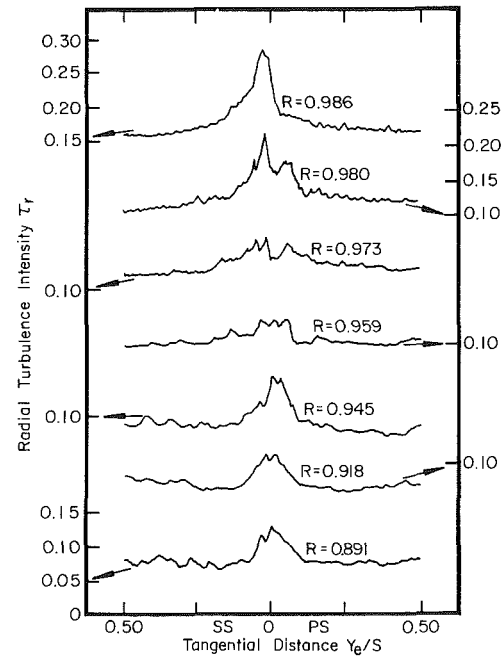

Fig. 14 Radial turbulence intensity profiles, $Z = 0.458$

values of turbulence at the tangential location of the blade wake and at radial locations near the blade tip. Below the radial location of $R = 0.945$, the freestream turbulence level is about 4 percent with the wake turbulence level reaching 10 percent of the local mean velocity. Above $R = 0.945$ the complex turbulence structure in the annulus-wall region is apparent. The effect of flow interactions is to increase the overall level of turbulence in this region. At $Z = 0.125$ the free-stream turbulence level has increased from 4 percent at $R = 0.891$ to 17 percent at $R = 0.986$. This increase is not as high immediately behind the blade where the free-stream intensity level is 13 percent at $R = 0.986$. This again indicates that the flow requires a small axial distance after exiting the blade row to induce maximum flow mixing. This region of flow mixing increases the turbulence level of the free-stream and rotor wake flow.

A comparison between the streamwise and normal turbulence intensity levels at the lower radial locations shows that these components of intensity are approximately equal in the free-stream. This indicates isotropic flow in this region. However, this is not true for the higher radial locations where the complex flow interactions are observed.

In general, the normal intensities follow the same trend as streamwise intensities, with lower values at most locations. Far downstream ($Z = 0.458$), the normal intensities are generally higher than the streamwise component.

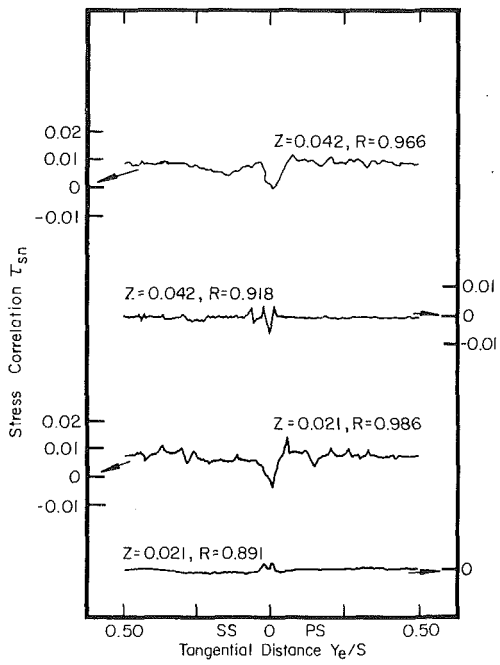

Fig. 15 Stress component τ_{sn}; $Z = 0.021, 0.042$

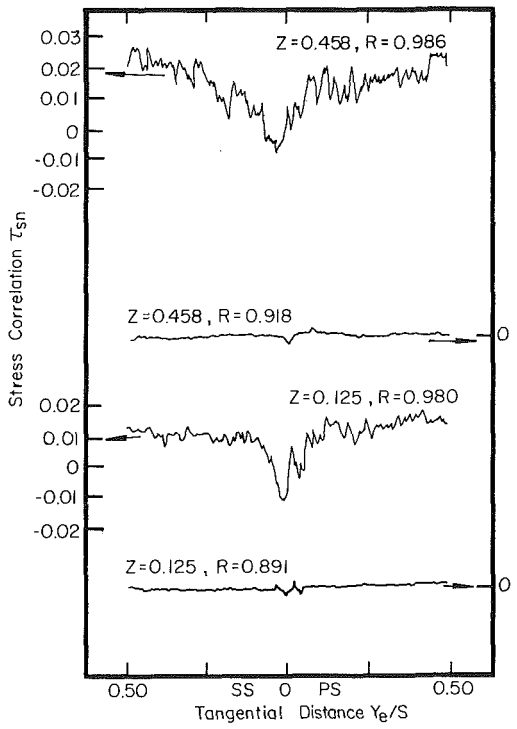

Fig. 16 Stress component τ_{sn}; $Z = 0.125, 0.458$

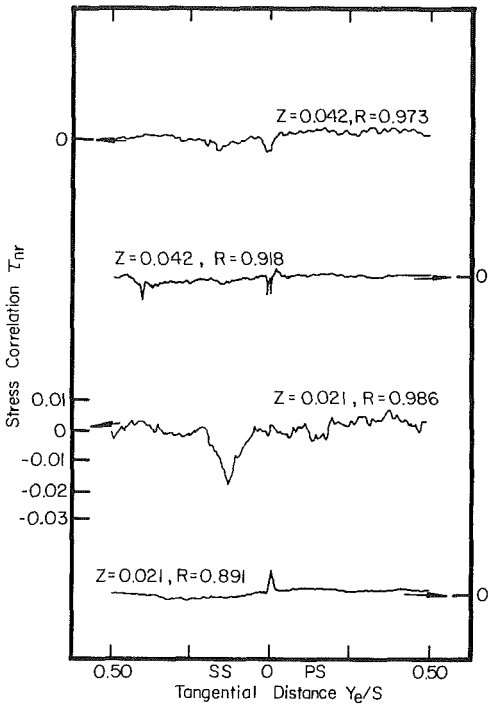

Fig. 17 Stress component τ_{nr}; $Z = 0.021, 0.042$

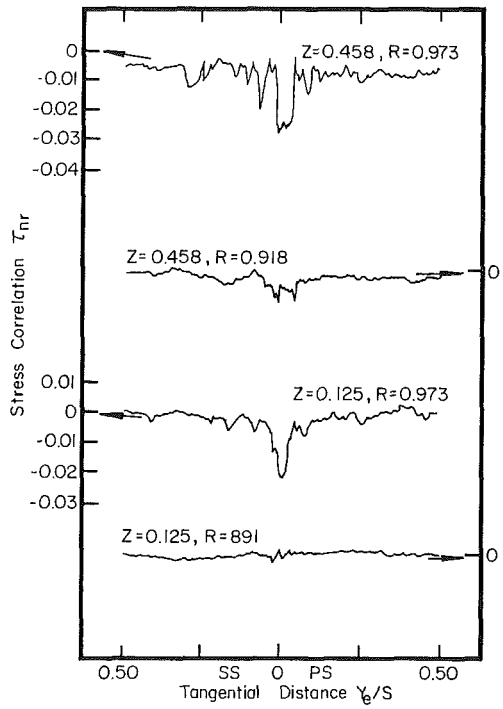

Fig. 18 Stress component τ_{nr}; $Z = 0.125, 0.458$

Radial Turbulence Intensity. Radial turbulence intensity profiles of the flow near the annulus-wall are presented in Figs. 11 through 14. The radial intensities below the radial location of $R = 0.945$ show predominately the wake structure. These intensities are larger than the streamwise and normal components in magnitude and reach values of 20 percent of the local mean velocity at the wake center. The free-stream level of turbulence is approximately 3 percent, with high values ocurring on the pressure side of the wake. The existence of the large radial component of intensity at the wake location reflects the character of the rotor blade boundary layers under the influence of rotation. The existence of these large radial components of intensity also demonstrates the three-dimensional nature of the rotor wake.

At radial locations above $R = 0.945$, the flow is subjected to complex interactions resulting from the annulus-wall boundary layer, the rotor wake, the tip leakage flow, and the secondary flow. The result of this flow interaction is to increase the overall radial turbulence intensity. The free-stream value of turbulence increases from 3 percent at the lower radial locations to 16 percent at the radial location of R = 0.986. However, this level occurs at $Z = 0.042$ and slowly

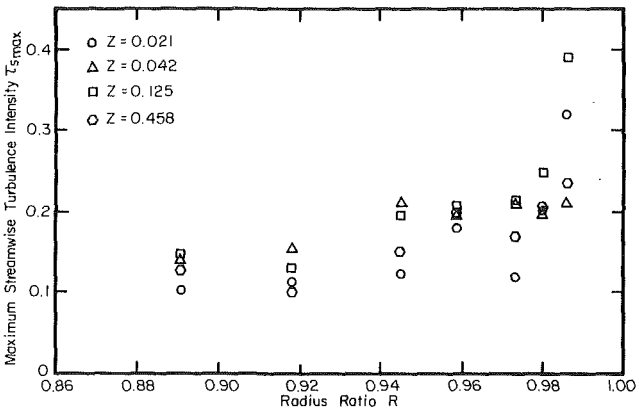

Fig. 19 Radial and axial variation of the maximum streamwise turbulence intensity

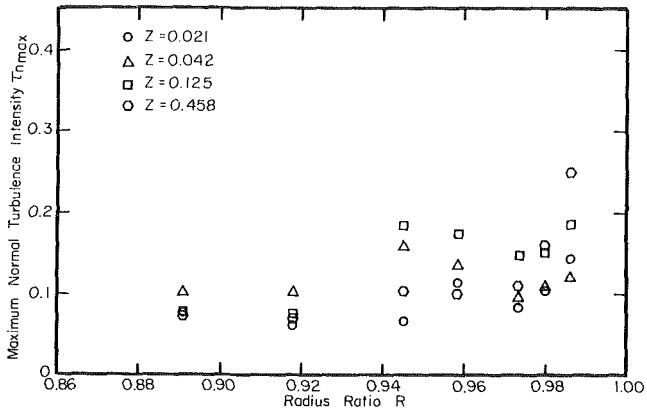

Fig. 20 Radial and axial variation of the maximum normal turbulence intensity

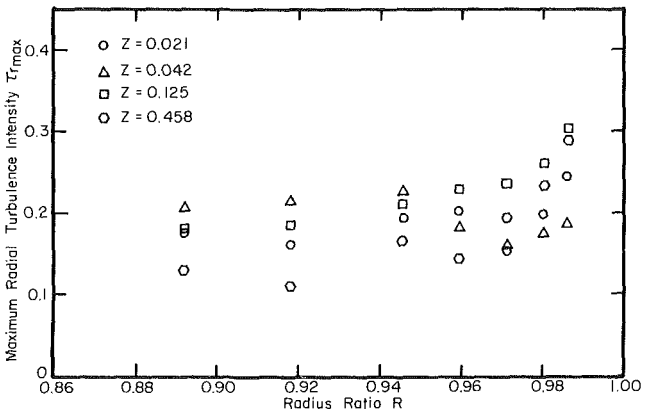

Fig. 21 Radial and axial variation of the maximum radial turbulence intensity

decreases with axial distance. At $Z = 0.021$ and the same radial location, the radial turbulence intensity is only 12 percent of the local mean velocity. This increase and then decrease in radial turbulence intensity indicates that the development of the flow mixing region initially grows stronger before it begins to decay. A similar trend is observed in the wake at radial locations near $R = 0.959$. This suggests the presence of a trailing vortex which initially grows in strength before decaying. This phenomenon has been reported by Ravindranath and Lakshminarayana [10]. The decay of the radial intensity in the wake seems to be slower than the streamwise intensity.

Turbulent Shear Stress Profiles. Figures 15 through 18 show the tangential distribution of the two turbulence shear stress correlations (see Fig. 1) derived from the three-sensor hot-wire measurements described earlier. The stress correlations are normalized by the local streamwise velocity and the tangential distance behind the rotor is normalized by the blade spacing.

The turbulent stresses in the rotor exit-flow are very small in the free-stream and increase in magnitude near the wake center. At this location they reach their maximum value. This type of trend is brought about by gradients of the mean velocity and turbulence intensity. The variation of the streamwise stress τ_{sn} shows the expected reversal of stress at the wake center. This reversal of stress is induced by opposite gradients of streamwise mean velocity about the wake center. The profiles are also asymmetrical about the wake center. The location of the zero stress correlation does not occur where $\partial W/\partial n$ is zero. This characteristic has also been reported by Raj and Lakshminarayana [2] and Hah [8]. The profiles show a decay of the stress correlation τ_{sn} with axial distance; however, the stress correlation increases with radial distance. The interaction of the two shear layers, the annulus-wall boundary layer, and the rotor wake, produces large amounts of flow mixing which results in an increase of the stress correlations.

The radial stress τ_{nr} also exhibits an asymmetric profile about the wake center. At the lower radial locations the radial velocities are smaller than the streamwise velocities, which give τ_{nr} to be less than τ_{sn}. This trend is not fully realized by the data presented. At some low radial locations the stress components are equal in magnitude and in other instances it is seen that τ_{nr} is greater than τ_{sn}. This observation indicates the effect of rotation on the stresses. Lakshminarayana and Reynolds [11] have argued, on the basis of the Reynolds stress equation in the rotating coordinate system, that the effect of rotation is to attenuate the stress component τ_{nr}. As the blade tip is approached, the situation becomes more complicated due to the viscous interactions associated with the annulus wall. The magnitude of the stress correlation τ_{nr} increases rapidly. The effect of the interaction of the annulus-wall boundary layer with the rotor wake, the tip leakage vortex, and the secondary flow is to amplify this stress component. The viscous interaction of the flow field in this region compliments the effect of rotation.

The stress components near the annulus-wall show an increase inside the wake with axial distance. The exact nature of this increase is difficult to determine. However, due to the experimental set-up, the smoothness of the annulus-wall varied with axial distance. The increase in the stress correlations might reflect an interaction between the exit-flow and the surface of the annulus-wall. It should also be noted that the stress correlations presented in Figs. 15 through 18 are subject to spatial errors which are inherent in a three-sensor hot-wire probe. An estimate of the scales of the flow and the expected order of error is given in reference [1]. However, the contribution to stress from eddies larger than the distance between the probe sensors was measured accurately.

Maxmimum Turbulence Intensity in the Wake. The variation of the maximum streamwise, normal, and radial maximum turbulence intensities in the wake is shown plotted in Figs. 19, 20, and 21. It is seen that the intensities are higher in the trailing-edge region, increasing towards the blade tip, and that the decay rate of the turbulence intensity is higher as the blade tip is approached.

Lakshiminarayana and Reynolds [11] have given qualitative analysis of the effects of rotation on turbulence. They have shown that the turbulence structure of a rotating blade is different compared to a stationary blade. The radial

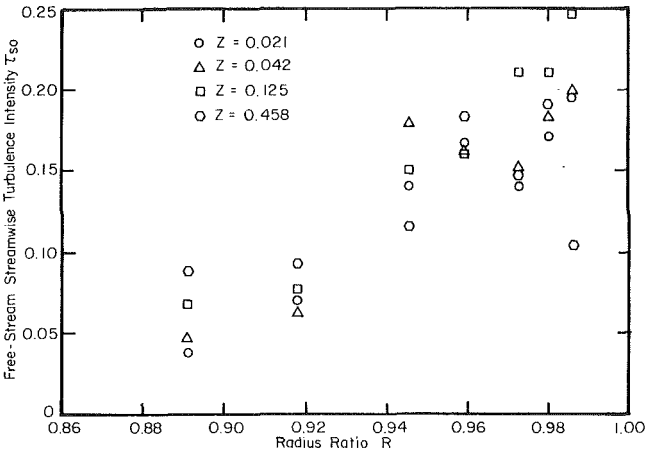

Fig. 22 Radial and axial variation of the free-stream streamwise turbulence intensity

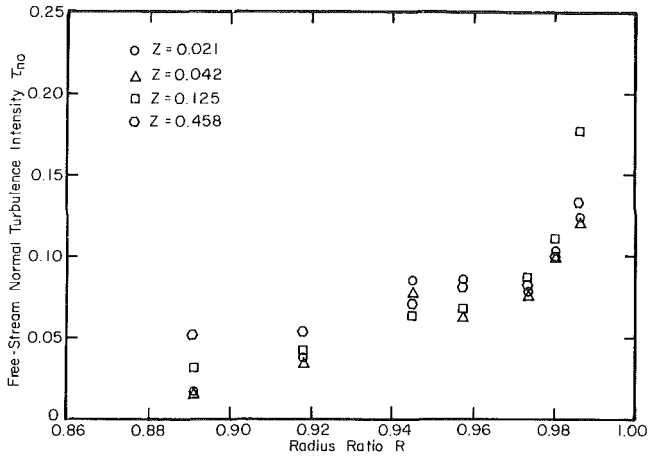

Fig. 23 Radial and axial variation of the free-stream normal turbulence intensity

turbulence intensities are likely to be higher than the streamwise and normal components. The present data confirm their analysis at radial locations below $R = 0.945$. For the radius $R = 0.891$, the maximum radial component is 0.209 while the streamwise and normal components are 0.141 and 0.102, respectively. These data also partially confirm the analysis of Raj and Lumley [12] who have shown that if the gradient of the radial component of mean velocity across the wake is larger than the angular velocity of the machine, then

$$\tau_r > \tau_n > \tau_s.$$

At radial locations above $R = 0.945$, the viscous effects of the annulus-wall boundary layer, the secondary flow, and the tip leakage flow induce higher turbulence intensities. At $R = 0.986$ the maximum streamwise intensities are higher than radial intensities. At $R = 0.980$, both the streamwise and radial components of turbulence intensity reach values of 30 percent of the free-stream velocity. This indicates the severe flow mixing which occurs in the radial and streamwise directions as the wake is adjusting to the mainstream viscous flow.

The turbulence intensities near the tip decay much more rapidly than the corresponding value away from the tip.

Free-Stream Turbulence Intensity. Variations of the free-stream streamwise, normal, and radial turbulence intensities are shown plotted in Figs. 22, 23, and 24, respectively. Near the blade tip, where the wake structure encompasses the entire blade passage, the free-stream location was taken to be at $Y_e/S = 0.5$. The free-stream turbulence structure does affect the rotor wake characteristics and losses in a compressor stage. It is useful to designers in evaluating the inlet flow conditions to a subsequent stage. It is interesting to note the turbulence amplification through the rotor blade row in the annulus-wall region. The effect of the blade force acting on the fluid is the probable cause of this amplification at the lower radial locations. Here a 2 percent free-stream streamwise and normal turbulence intensity increases to approximately 4 percent behind the blade row. The radial turbulence intensity is seen to increase to values near 5 percent of the free-stream velocity. This clearly indicates the effect of centrifugal and coriolis forces on the radial turbulence intensity.

As the annulus-wall is approached, all components of intensity experience a substantial increase. At $R = 0.986$ the streamwise turbulence intensity has increased to 20 percent while the normal and radial components of intensity approach a value of 15 percent of the mean velocity. These high values of intensity indicate the interactions of the wake, leakage

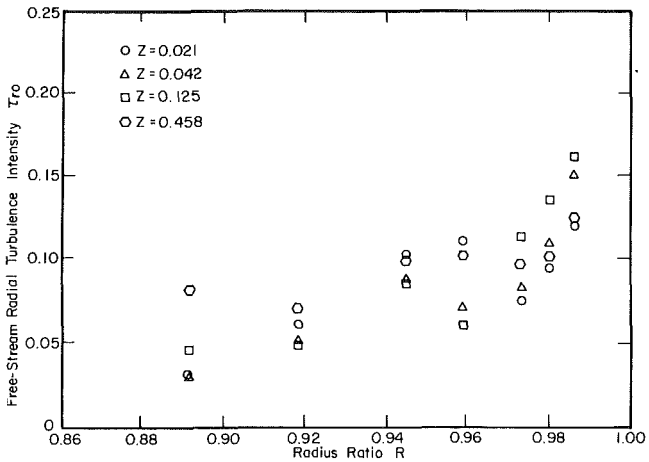

Fig. 24 Radial and axial variation of the free-stream radial turbulence intensity

flow, annulus-wall boundary layer, and the secondary flow. The highest levels of intensity for all components occur at approximately 12 percent of the blade chord downstream of the blade trailing edge. This indicates that the interference region of these flows occurs with maximum strength at a distance behind the blade. This distance is required by the wake and tip leakage flow to become fully developed.

As these figures show, in a multi-stage machine there is a spanwise and axial gradient in turbulence intensity. This gradient alters the flow distribution into a succeeding blade row which results in a spanwise and axial gradient in noise generation and propagation as well as stagnation pressure loss.

Conclusions

1 The turbulence structure of the rotor exit-flow is asymmetric behind the rotor blade and tends toward symmetry with axial distance. Near the blade tips, complex flow interactions result in an increase in turbulence intensity. This increase is most pronounced for the radial component. The turbulence intensities do not decay until a location 4 percent of the blade chord downstream. The flow mixing region initially increases in turbulence level before it begins to decay.

2 The effect of the blade force acting on the fluid causes an amplification of the turbulence level in the free-stream behind the rotor at radial locations above 20 percent of the blade span from the blade tip. As the tip is approached, the free-

stream turbulence level increases due to the flow mixing with the annulus-wall boundary layer.

3 The locations of high turbulence stresses are concentrated in the high turbulence intensity areas of the mixing region near the blade tip. The effect of rotation is to attenuate the streamwise-stress component and amplify the radial-stress component.

4 The radial intensities are generally higher in the wake-dominated region and the streamwise intensities are generally higher at other locations. This resutls from the effects of rotation on turbulence.

5 The turbulence intensities decay more rapidly in the end-wall region due to intense mixing.

6 The free-stream turbulence, outside the wake, is nearly isotropic.

7 The maximum intensities in the wake increase rapidly towards the annulus wall, reaching a value as high as 40 percent at some locations.

8 The radial and streamwise component of stresses are about the same order of magnitude, a consequence of the rotation effects.

9 Most of the turbulence intensity components decay to nearly freestream values within half-a-chord downstream of the trailing edge.

10 The mixing effects of leakage flow cause higher streamwise turbulent intensities at about 10 percent of the chord downstream from the trailing edge.

Acknowledgments

This work was supported by the National Aeronautics and Space Administration through Contract No. NSG 3212, with P. M. Sockol as the Project Monitor. The authors wish to acknowledge G. Kane and J. Rishell for their aid in experimental set-up and instrumentation.

References

1 Davino. R., and Lakshminarayana, B., "Characteristics of Mean Velocity in the Annular Wall Region at the Exit of Turbomachinery Rotor Passage," AIAA Paper No. 81—0068 (to be published in *AIAA Journal*, 1982).

2 Raj, R., and Lakshminarayana, B., "Three-Dimensional Characteristics of Turbulent Wakes Behind Axial Flow Turbomachinery," ASME J. ENGINEERING FOR POWER, Vol. 98, Apr. 1976, pp. 218–228.

3 Reynolds, B., Lakshminarayana, B., and Ravindranath, A., "Characteristics of the Near-Wake of a Compressor or Fan Rotor Blade," *AIAA Journal*, Vol. 17, No. 9, Sept. 1979, pp. 959–967.

4 Ravindranath, A., "Three-Dimensional Mean and Turbulence Characteristics of the Near Wake of a Compressor Rotor-Blade," M.S. thesis, Department of Aerospace Engineering, The Pennsylvania State University, 1979.

5 Lakshminarayana, B., "An Axial Flow Research Compressor Facility Designed for Flow Measurement in Rotor Passages," *Proc. ASME Symp. on Measurement Methods in Rotating Components of Turbomachinery*, pp. 31–42, New Orleans, 1980, ASME *Journal of Fluids Engineering*, Vol. 102, No. 4, Dec. 1980, pp. 402–411.

6 Smith, L. H., "Three-Dimensional Flow in an Axial Flow Turbomachinery," QADC, Technical Report 55-348, Vol. 2, Johns Hopkins University, 1956.

7 Lakshminarayana, B., and Poncet, A., "A Method of Measuring Three Dimensional Wakes in Turbomachinery," ASME *Journal of Fluids Engineering*, Vol. 96, No. 2, June 1974, pp. 87–91.

8 Hah, C., "A Numerical and Experimental Study of the Turbulent Wakes of Turbomachinery Rotor Blades, Isolated Airfoils, and a Cascade of Airfoils," Ph.D. thesis, Department of Aerospace Engineering, The Pennsylvania State University, 1980.

9 Reynolds, B., and Lakshminarayana, B., "Characteristics of Fully Loaded Fan Rotor Blade Wakes," NASA-CR-3188, Oct. 1979.

10 Ravindranath, A., and Lakshminarayana, B., "Structure and Decay Characteristics of Turbulence in the Near- and Far-Wake of a Moderately Loaded Compressor Rotor Blade," ASME JOURNAL OF ENGINEERING FOR POWER, Vol. 103, No. 1, Jan. 1981, pp. 131–140.

11 Lakshminarayana, B., and Reynolds, B., "Turbulence Characteristics in the Near-Wake of a Compressor Rotor Blade," *AIAA Journal*, Vol. 18, No. 11, Nov. 1980, pp. 1354–1362.

12 Raj, R., and Lumley, J. L., "A Theoretical Investigation on the Structure of Fan Wakes," ASME *Journal of Fluids Engineering*, Vol. 100, 1978, pp. 113–119.

Analysis and Asymptotic Solutions of Compressible Turbulent Corner Flow[1]

A.G. Mikhail[2]
Research Associate.
Mem. ASME

K.N. Ghia
Professor.
Mem. ASME

Department of Aerospace Engineering
and Applied Mechanics,
University of Cincinnati,
Cincinnati, Ohio 45221

The turbulent compressible flow along an unbounded 90 deg axial corner has been analyzed. The limiting equations for the far-field boundary, simulating a two-dimensional boundary layer with crossflow, have been obtained appropriately. This latter set of equations have been solved using a semi-implicit second-order accurate numerical marching scheme. The turbulent stresses have been modeled first using a Cebeci-Smith type two-layer algebraic model in which isotropy is assumed. The turbulence stresses were also modeled using a modified form of the Gessner-Emery anisotropic model. Results have been presented for a range of Mach numbers between 0 and 2.0 with adiabatic as well as heat transfer boundary conditions at the corner walls. Effect of suction and injection have also been included. The anisotropy in the turbulence modeling showed insignificant effect on the flow field at far-field boundary, but it is believed to be essential in the inner corner region. The analysis presented recovers all previously available results for the simplified cases of this corner configuration.

Introduction

The high-speed flow for corner configurations which occur in important aerodynamic applications such as wing-body junctions wind tunnel walls, aircraft inlets, turbomachine blade-hub junctions, etc., are characterized by various interaction phenomena. One of the important interaction phenomena is the one associated with the lateral displacement effect due to displacement-thickness interactions. For laminar incompressible as well as compressible flows, Rubin, Ghia and their coworkers [1–6] analyzed the fundamental corner configuration in detail. The fundamental 90 deg-corner configuration [7] as well as more complex configurations with one or more contoured surfaces [8, 9] have been analyzed using the full three-dimensional Navier-Stokes equations or their parabolized approximate forms.

Klinksiek [10] analyzed the incompressible turbulent 90 deg axial corner flow using a semi-implicit numerical technique. Algebraic turbulence modeling was used for the Reynolds stresses. The streamwise velocity compared satisfactorily with experimental data but no information was given about the cross-flow velocities. Shafir and Rubin [11] studied the asymptotic turbulent incompressible corner flow and provided a solution for the turbulent boundary layer near a corner. The streamwise momentum equation was formulated in terms of a stream function in such a manner that, for laminar flow, the equations reduce to the familiar nonsimilar form of the boundary-layer equation. On the other hand, for high-speed flows, Shang et al. [12] have provided Navier-Stokes solutions for the flow along an axial corner formed by the intersection of two wedges. To date, to the authors' best knowledge, asymptotic turbulent compressible corner flow solutions have not been determined.

The present study is carried out with the objective of analyzing turbulent flow along an axial corner and, more importantly, for studying the effects of compressibility and turbulence on shock-free asymptotic corner flow in the presence of viscous interactions, namely, the lateral displacement thickness interactions. The turbulence is modeled using the three-dimensional, two-layer eddy viscosity model of the form used by Cebeci [13]. Numerical solutions are obtained for a range of Mach numbers and wall-temperature boundary conditions. For some supersonic cases, the effect of suction and injection at the walls is also studied.

Analysis

The axial 90-deg corner flow geometry is depicted in Fig. 1. Due to the displacement-thickness interaction, the flow field of interest is inherently three-dimensional in nature. The oncoming flow upstream of the corner is laminar. As the flow progresses along the corner, boundary layers build up on the solid surfaces and the flow becomes turbulent downstream after experiencing transition. The analysis needed for formulating the mathematical model for this flow configuration is comprised of two steps, namely, the derivation of the corner-layer equations in terms of the Reynolds stresses, followed by modeling the Reynolds stresses using the appropriate turbulence model.

[1] This research was supported by the Air Force Office of Scientific Research under Contract No. F49620-78-C-0041 and AFOSR Grant No. 80-0160. The authors are thankful to Professor Urmila Ghia of the University of Cincinnati for her many useful suggestions and discussions throughout the course of this study.

[2] Present address: Kaman Avidyne, Burlington, Mass.

Contributed by the Gas Turbine Division and presented at the International Gas Turbine Conference and Products Show, Houston, Texas, March 9-12, 1981, of THE AMERICAN SOCIETY OF MECHANICAL ENGINEERS. Manuscript received at ASME Headquarters, December 15, 1980. Paper No. 81-GT-149.

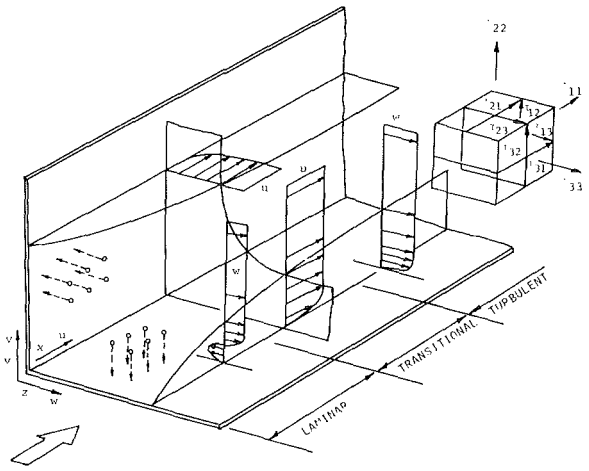

Fig. 1 Corner-flow geometry and nomenclature

The Governing Equations. The governing equations for the turbulent corner-layer flow are derived in a manner analogous to the analysis for laminar flow [6, 14] except for the fact that, in the present case, the starting equations are the time-averaged Navier-Stokes equations. The subsequent steps in the analysis are based on the method of singular perturbations and matched asymptotic expansions. Only the viscous interactions between the boundary layers on the two intersecting walls are considered in the analysis. Furthermore, it is assumed that the supersonic flow field is shock free. Thus, the lowest-order corner layer equations are obtained in the following form.

Continuity Equation

$$(\rho u)_x + \rho(v_Y + w_Z) + v\rho_Y + w\rho_Z = 0 \tag{1a}$$

x-*Momentum Equation*

$$\rho u u_x + \rho v u_Y + \rho w u_Z = (\mu u_Y)_Y + (\mu u_Z)_Z + (\tau_{t_{12}})_Y + (\tau_{t_{13}})_Z \tag{1b}$$

Y-*Momentum Equation*

$$\rho u v_x + \rho v v_Y + \rho w v_Z = -p_Y + [2\mu v_Y + \lambda(u_x + v_Y + w_Z)]_Y + [\mu(v_z + w_Y)]_Z + (\mu u_Y)_x + (\tau_{t_{22}})_Y + (\tau_{t_{23}})_Z + (\tau_{t_{12}})_x \tag{1c}$$

z-Momentum Equation

$$\rho u w_x + \rho v w_Y + \rho w w_Z = -p_Z + [2\mu w_Z + \lambda(u_x + v_Y + w_Z)]_Z + [\mu(w_Y + v_Z)]_Y + (\mu u_Z)_x + (\tau_{t_{33}})_Z + (\tau_{t_{23}})_Y + (\tau_{t_{13}})_x \tag{1d}$$

Energy Equation

$$\rho u T_x + \rho v T_Y + \rho w T_Z = \frac{1}{\mathrm{Pr}}[(\mu T_Y)_Y + (\mu T_Z)_Z] + (\gamma-1)M_\infty^2[\mu(u_Y)^2 + \mu(u_Z)^2] + \frac{1}{\mathrm{Pr}_t}[(\rho\epsilon_{22}T_Y)_Y + (\rho\epsilon_{33}T_Z)_Z] + (\gamma-1)\mathrm{M}_\infty^2[\tau_{t_{12}}u_Y + \tau_{t_{13}}u_Z] \tag{1e}$$

The auxiliary equations required to close this set of equations, namely, the equation of state and Sutherland's viscosity law, will be given later in this section together with an appropriate model for turbulence.

In the above set of nondimensional equations (1), (x, Y, Z) are the independent coordinates such that $Y = y\sqrt{\mathrm{Re}}$ and $Z = z\sqrt{\mathrm{Re}}$, u is the streamwise velocity component while v and w are the cross-plane velocity components along the Y and Z directions, respectively. Further, ρ, T, M_∞ and μ are the density, temperature, free-stream Mach number, and viscosity, and the subscript t denotes turbulence quantities. The symbol ϵ_{ii} represents the appropriate eddy viscosity, while the eddy conductivity $K_{t_{ii}}$ is expressed in terms of the turbulent Prandtl number Pr_t and ϵ_{ii}, since $K_{t_{ii}} = \epsilon_{ii}/\mathrm{Pr}_t$. Most of the dependent variables are nondimensionalized as in [14]. The turbulent stresses introduced here are nondimensionalized like the pressure p, that is, with $\rho_\infty U_\infty^2$. All velocities, including the fluctuating velocities, are nondimensionalized by the free-stream velocity U_∞. Further, the turbulent heat conduction flux is nondimensionalized with $\rho_\infty U_\infty C_p T_\infty$. The anisotropy in the turbulent heat conductivity coefficient $K_{t_{ii}}$ is made possible through the eddy viscosity coefficient ϵ_{ii}.

The governing equations are now recast in terms of a new set of dependent variables, such that the form of the new equations is similar to the corresponding laminar flow equations. Since the turbulent corner flow possesses no self-similar solution as x increases, the similarity coordinates (η, ζ) used earlier in [3, 6] for the laminar corner flow are no longer very advantageous. Moreover, their use also does not lead to the desired form of the asymptotic equations for large ζ. Hence, the coordinates used in this study are defined simply as $\eta \triangleq Y$ and $\zeta \triangleq Z$ for convenience. Similar reasoning led to the use of the cross-flow velocity functions ϕ and ψ defined as $\phi \triangleq -v$, $\psi \triangleq -w$. Finally, the vorticity θ is defined as $\theta \triangleq v_Z - w_Y \triangleq \eta - \phi_\zeta$ and the function Λ as $\Lambda \triangleq -v_Y - w_Z \triangleq \phi_\eta + \psi_\zeta$. The barred variables used in [14] are not essential since the present variables ϕ, ψ and θ are now bounded quantities and are directly suitable for use in the present analysis.

The new streamwise independent coordinate ξ is defined simply as x. Thus, the final form of the turbulent corner-layer equations, in terms of the new independent and dependent variables, is given as follows.

Continuity Equation

$$\rho\Lambda + \phi\,\rho_\eta + \psi\,\rho_\zeta = (\rho u)_\xi \tag{2a}$$

Streamwise Momentum Equation

$$\mu(u_{\eta\eta} + u_{\zeta\zeta}) + u_\eta(\rho\phi + \mu_\eta) + u_\zeta(\rho\psi + \eta_\zeta) + (\tau_{t_{12}})_\eta + (\tau_{t_{13}})_\zeta = \rho u u_\xi \tag{2b}$$

Equation for ϕ

$$\phi_{\eta\eta} + \phi_{\zeta\zeta} + \theta_\zeta - \Lambda_\eta = 0 \tag{2c}$$

Equation for ψ

$$\psi_{\eta\eta} + \psi_{\zeta\zeta} - \theta_\eta - \Lambda_\zeta = 0 \tag{2d}$$

Streamwise Vorticity Equation

$$(\mu\theta)_{\eta\eta} + (\mu\theta)_{\zeta\zeta} + \rho\phi\,\theta_\eta + \rho\psi\,\theta_\zeta + \rho\theta(\phi_\eta + \psi_\zeta) - \phi[\rho_\zeta\phi_\eta - \rho_\eta\psi_\eta] - \psi[\rho_\zeta\phi_\zeta - \rho_\eta\psi_\zeta] + 4(\mu_\eta\phi_{\eta\zeta} - \mu_\zeta\psi_{\zeta\eta}) + 2\mu_{\zeta\zeta}(\psi_\zeta - \phi_\eta) + 2(\mu_{\eta\eta}\phi_\zeta - \mu_{\zeta\zeta}\psi_\eta) + (\tau_{t_{22}} - \tau_{t_{33}})_{\zeta\eta} + (\tau_{t_{13}})_{\zeta\zeta} - (\tau_{t_{23}})_{\eta\eta} + [(\tau_{t_{12}})_\zeta - (\tau_{t_{13}})_\eta]_\xi = \rho u\,\theta_\xi - (\rho u)_\zeta\phi_\xi + (\rho u)_\eta\psi_\xi - (\mu_\zeta u_\eta - \mu_\eta u_\zeta)_\xi \tag{2e}$$

Energy Equation

$$\frac{\mu}{\mathrm{Pr}}(T_{\eta\eta} + T_{\zeta\zeta}) + \left(\rho\phi + \frac{\mu_\eta}{\mathrm{Pr}}\right)T_\eta + \left(\rho\psi + \frac{\mu_\zeta}{\mathrm{Pr}}\right)T_\zeta + (\gamma-1)\mathrm{M}_\infty^2[\mu u_\eta^2 + \mu u_\zeta^2] + \frac{\rho}{\mathrm{Pr}_t}(\epsilon_{22}T_{\eta\eta} + \epsilon_{33}T_{\zeta\zeta}) + \frac{1}{\mathrm{Pr}_t}[T_\eta(\rho\epsilon_{22})_\eta + T_\zeta(\rho\epsilon_{33})_\zeta] + (\gamma-1)\mathrm{M}_\infty^2(\tau_{t_{12}}u_\eta\tau_{t_{13}}u_\zeta) = \rho u\,T_\xi \tag{2f}$$

The underscored terms represent the additional terms associated with the turbulence in the flow. The above equations have been written in a form such that terms containing derivatives with respect to ξ appear only on the right-hand sides. Equation (2*c*) is derived from the definitions of θ and Λ by appropriately differentiating and eliminating ψ. Similarly, equation (2*d*) is derived by appropriately differentiating the definitions of θ and Λ and eliminating ϕ. This provides second-order elliptic equations for ϕ and ψ which are better suited for implicit numerical solution techniques. Equation (2*e*) is obtained by appropriately differentiating and combining equations (1*c*) and (1*d*) to eliminate the transverse pressure gradients p_y and p_z.

Asymptotic Equations for Far-Field Boundary. For the present unbounded corner configuration, the asymptotic equations for the far-field boundary are obtained by taking the limit of equations (2*a*–2*f*) as $\zeta \to \infty$ such that all derivatives with respect to ζ vanish. This approach leads to a consistent set of the lowest-order equations, which have the displacement interaction effect in them. These equations are given as follows:

Continuity Equation

$$\rho\Lambda + \phi\ \rho_\eta = (\rho u)_\xi \tag{3a}$$

Streamwise Momentum Equation

$$\mu\ u_{\eta\eta} + u_\eta\,(\rho\phi\mu_\eta) + (\tau_{t_{12}})_\eta = \rho u u_\xi \tag{3b}$$

Equation for ϕ

$$\phi_{\eta\eta} + \frac{1}{\rho}\,\rho_\eta\phi_\eta + \left(\frac{1}{\rho}\,\rho_{\eta\eta} - \frac{1}{\rho^2}\,\rho_\eta^2\right)\phi = \left[\frac{1}{\rho}\,(\rho u)_\xi\right]_\eta \tag{3c}$$

Equation for ψ

$$\psi_{\eta\eta} - \theta_\eta = 0 \tag{3d}$$

Streamwise Vorticity Equation

$$\mu\theta_{\eta\eta} + (\rho\phi + 2\mu_\eta)\,\theta_\eta + (\rho\phi_\eta\mu_{\eta\eta})\,\theta + \phi\ \rho_\eta\psi_\eta - (\tau_{t_{23}})_{\eta\eta} = \rho\ u\ \theta_\xi + (\rho u)_\eta\psi_\xi \tag{3e}$$

Energy Equation

$$\frac{\mu}{\mathrm{Pr}}\,T_{\eta\eta} + \left(\rho\phi + \frac{1}{\mathrm{Pr}}\,\mu_\eta\right)T_\eta + (\gamma-1)\mathrm{M}_\infty^2\mu u_\eta^2 + \frac{\rho\epsilon_{22}}{\mathrm{Pr}_t}\,T_{\eta\eta} + \frac{1}{\mathrm{Pr}_t}\,(\rho\epsilon_{22})_\eta T_\eta + (\gamma-1)M_\infty^2\,(\tau_{t_{12}}\,u_\eta) = \rho u\ T_\xi \tag{3f}$$

Equation 3(*a*) and the limiting form of equation (2*c*) are combined to yield equation (3*c*). This eliminates Λ and, hence, eliminates the explicit need for equation (3*a*) in the solution of the problem.

The turbulent stress term $[(\tau_{t_{13}})_\eta]_\xi$ appearing in equation (2*e*) drops out in the limiting process. This is because, as $\zeta \to \infty$, $u_\zeta \to 0$ and w_ξ is of lower order than the remaining terms in this equation. Also, as can be seen from the set of equations (3), there are three turbulent stresses present, namely, $\tau_{t_{12}}$ and $\tau_{t_{23}}$ appearing explicitly in this set of equations (3) and the stress $\tau_{t_{22}}$ appearing implicitly through the eddy viscosity ϵ_{22} present in the limiting form of the energy equation.

The auxiliary equations needed are the following:

Equation of State

$$p = \rho T(1/\gamma\mathrm{M}_\infty^2) \tag{3g}$$

Sutherland's Viscosity Law

$$\mu = T^{3/2}[(1+S_1)/(T+S_1)] \tag{3h}$$

Here, γ is the ratio of specific heats and S_1 is a parameter that depends on the freestream temperature T_∞ and is taken as 0.38. The turbulence modeling required for closing the equation set (3) is discussed later in this section.

The corner-flow configuration of Fig. 1 possesses symmetry along the bisector $\eta = \zeta$. This symmetry property is used to help in reducing the region of interest to only the triangular region bounded by the bisector $\eta = \zeta$, the far-field boundary as $\zeta \to \infty$ and the wall $\eta = 0$. Before prescribing the boundary conditions for the equation set (3), the suction/injection that are to be implemented at the walls are considered next. Thus, for the lower triangular half of the corner region, the boundary condition on the wall $\eta = 0$ needs only to be discussed.

Mass Transfer at the Corner Wall $\eta = 0$. Small suction or injection $[v_w = 0\,(1/\sqrt{\mathrm{Re}})]$ at the wall $\eta = 0$ can be adequately treated by appropriately modifying the boundary condition for the transverse velocity v_w at $\eta = 0$. For cases with large mass transfer, the present corner-layer analysis is not quite valid. Earlier while studying laminar corner flow, Mikhail [14] had arrived at suitable forms of the transverse velocity at the wall. Because of the prevailing streamwise similarity in the laminar flow, only certain prescribed forms as shown by Mikhail [14] were found admissible for v_w. However, for the present turbulent flow, there is no assumption of similarity in the streamwise direction and, hence, there is no restriction on the form of suction or injection at the wall. The following forms of transverse velocity v_w were considered suitable:

Streamwise uniform injection/suction

$$v_w = \pm K_0\,\frac{1}{\sqrt{\mathrm{Re}}} \tag{4a}$$

Streamwise decreasing injection/suction

$$v_w = \pm K_1\,\frac{1}{\sqrt{2\xi}}\,\frac{1}{\sqrt{\mathrm{Re}}} \tag{4b}$$

Streamwise increasing injection/suction

$$v_w = \pm K_2\sqrt{2\xi}\,\frac{1}{\sqrt{\mathrm{Re}}} \tag{4c}$$

The constants appearing in equations (4) were chosen as $K_0 = 0.05$, $K_1 = 0.2$ and $K_2 = 0.002$.

Boundary Conditions for the Asymptotic Equations. In this study, only the asymptotic corner-layer equations (3) are solved presently. Hence, the appropriate boundary conditions are presented only for the set of equations (3).

At the plate surface, i.e., at $\eta = 0$ and $\xi > 0$:

$$u = 0, \phi = -v_w, w = 0, \theta = \psi_\eta, T = T_w \text{ or } T_\eta = \text{const.} \tag{5a}$$

At the symmetry line, i.e., at $\eta \to \infty$ and $\xi > 0$:

$$u = 1, \phi_\eta = 0, \psi = \phi, \theta = 0, T = 1. \tag{5b}$$

The initial condition for this initial-boundary-value problem was taken to be a uniform flow with zero vorticity and constant temperature. To complete the formulation of this problem, the turbulent stresses need to be modeled appropriately and, as such, the turbulence modeling used is discussed next.

Algebraic Two-Layer Turbulence Model of Cebeci-Smith Type. Shang et al. [12] used the Cebeci-Smith type [15] algebraic model to successfully study the turbulent flow along a corner formed by two intersecting wedges. Cebeci [13] has given the extended form of the Cebeci-Smith model for three-dimensional boundary-layer flow. This model is used in the present analysis and a brief description of the model is given here in the physical plane in order to facilitate better understanding of it. The turbulent stresses $\tau_{t_{12}}$ and $\tau_{t_{23}}$ for the asymptotic corner layer flow can be expressed as:

$$\tau_{t_{12}} = \frac{\rho}{\mathrm{Re}}\,\epsilon\,u_y \text{ and } \tau_{t_{23}} = \frac{\rho}{\mathrm{Re}}\,\epsilon\,w_y \tag{6a}$$

where ϵ denotes the isotropic eddy viscosity and is given as

$$\epsilon = \begin{cases} [0.4y(1-e^{-B})]^2 \mid u_y + C_1 w_y \mid \Gamma_{tr} \text{ for } 0 \le y \le y_0, \\ 0.0168(u_e + C_1 w_e)^{1/2} \delta_e \Gamma_{tr} \text{ for } y_0 < y. \end{cases} \quad (6b)$$

Here, y_0 is the location where the expressions for the inner and outer layers are matched. The expression for eddy viscosity in the outer region is then appropriately modified by an intermittency factor γ defined as, $\gamma = [1 + 5.5\ (y/\delta_{2D})^6]^{-1}$ where δ_{2D} is the two-dimensional laminar boundary layer thickness. The various other quantities appearing in equation (6*b*) are defined as follows

$$B = \frac{y}{A} = \frac{y\, u_\tau}{26\upsilon}, u_\tau = \left(\frac{\upsilon_w}{\mathrm{Re}}\right)^{1/2} [u_y^2 + C_1 w_y^2]_{y=0}^{1/4},$$

$$C1 = \begin{cases} 0 \text{ for 2-D} \\ 1 \text{ for 3-D} \end{cases}$$

$$\delta = \int_0^\infty \frac{1}{q_e} [q_e - (u^2 + C_1 w^2)^{1/2}] dy, q_e = [u_e^2 + C_1 w_e^2]^{1/2}. \quad (6c)$$

The transition intermittency factor, Γ_{tr}, is taken as

$$\Gamma_{tr} = 1 - \exp\left[-\frac{G}{u_e}(x - x_{tr})^2\right]$$

with

$$G = \frac{3}{C_2^2} \frac{u_e^3}{\upsilon^2} (\mathrm{Re}_{tr})^{-1.34} \text{ and } C_2 = 60 + 4.86\ \mathrm{M}_e^{1.92}. \quad (6d)$$

In equation (6*d*), Re_{tr} is the Reynolds number where transition is assumed to begin and is taken to be 5×10^5. The value of x_{tr} at the onset of transition is equal to 20.

Modification of Turbulence Model for Mass Transfer. Bushnell, et al. (see [15]) have shown that the algebraic two-layer turbulence model is valid for configurations with mass transfer through the walls if the Van Dreist's damping factor A^+, taken to be equal to 26 in equation (6*c*), is adjusted properly. After some numerical experimentation, the following expression suggested by Cebeci et al. [15] was used in the present study

$$A^+ = 26\ e^{-5.9\, \upsilon_w / \sqrt{\tau_w/\rho}} \quad (7)$$

Modified Form of Gessner and Emery's Turbulence Model

Bradshaw [16] has discussed the interaction of two shear layers for a complex axial corner configuration and pointed out the difficulties in obtaining an accurate turbulence model for this flow. Morel and Torda [17] have provided an analysis and demonstrated the applicability of Bradshaw's interaction hypothesis to two-dimensional free-shear flows. In the present study, the anisotropic turbulence model of Gessner and co-workers [18, 19] for the 90 deg bounded corner formed in a square duct is modified for use with the unbounded corner shown in Fig. 1, to appropriately include the effect of interacting shear layers. The anisotropic turbulence model of Gessner and co-workers [18, 19] for the 90 deg bounded corner formed in a square duct is modified for use with the unbounded corner shown in Fig. 1. The modification is required partly because, for the square duct, the cross-plane turbulent stress $\tau_{t_{23}}$ vanishes at the mid-plane of the duct cross-section due to symmetry. In the present problems, this mid-plane of the square duct is to be replaced by the far-field boundary where the basic flow is still quasi-three-dimensional. For example, the shear stress $\tau_{t_{23}}$ is represented in the following modified form:

$$\tau_{t_{23}} = -\rho\, \overline{v'w'} = \rho\left[\left(\frac{2F_{12} + \alpha_1 - 2}{\alpha_2}\right) \ell_p^2 (-C_3)\right] u_y w_y \quad (8)$$

where $\alpha_1 = 1.2$, $\alpha_2 = 0.25$ and F_{12} is an algebraic function of α_1 and α_2, and C_3 is given as

$$C_3 = \alpha_2 / [2F_{12} + \alpha_1 - 2]. \quad (9)$$

An appropriate expression for the mixing length ℓ_p appearing in equation (8) for the present corner configuration has been given by Shang and Hankey [12] as

$$\ell_p' = \frac{2K' yz}{(y + z + \sqrt{y^2 + z^2})}. \quad (10a)$$

This expression is based on Buleev's formula and reduces to its two-dimensional form

$$\ell_p' = K' y \quad (10b)$$

when $z >> y$. The value used for K' is 0.45 instead 0.4. This deviation in the value of K' is compatible with a modified form of the damping factor [20] used here, namely,

$$\ell_p = \ell_p' \left\{1 - \exp\left[-\frac{y u_\tau}{A^+ \upsilon}\left(1 - \frac{y}{\delta_{2D}}\right)^r\right]\right\} \quad (11)$$

Gessner and Po [19] suggested the value of r to be 2, based on the analysis of Launder, et al. [20] for the best fit. Gessner and Emery [21] used the value of A^+ to be 29.0 instead of 26.0 for a better fit with the data. Near the wall, at the far-field boundary, $z \to \infty$, the mixing length degenerates to the form given by equation (10*b*). However, this is not the case in the outer region, i.e., as $y \to \infty$, at the far field boundary. The form of ℓ_p' given by equation (10*a*) will increase indefinitely with the increase in y. This expression for ℓ_p' must be multiplied by a suitable expression of the intermittency factor to give an appropriate value of ℓ_p to be used in equation (8). Thus,

$$\ell_p = \ell_p' \sqrt{\gamma} \quad (12a)$$

where

$$\gamma = [1 + 5.5(y/\delta_{2D})^6]^{-1}. \quad (12b)$$

For $y/\delta_{2D} > 0.2$, equation (12*b*) aided in giving an appropriate mixing length ℓ_p to be used in equation (8). A similar analysis was used to represent the other stresses in the anisotropic turbulence model for the present flow field; presentation of those details is avoided here in the interest of brevity.

Numerical Analysis

Transformations. In order to satisfactorily resolve the wall region for turbulent flow, a geometric progression was used for the normal step size such that the ratio of lengths of any two adjacent intervals is constant, that is, $\Delta\eta_i = K\, \Delta\eta_{i-1}$ with $K = 1.24$. With the use of 51 grid points in the normal direction and the smallest $\Delta\eta = 0.007$ at the wall, this led to placing the last point at $\eta = 1370$. This nonuniform grid distribution was transformed to a uniform grid using a numerical transformation between η and N such that the uniform grid points are located between $N = 0$ and $N = 1$. The $\eta - N$ transformation derivatives, $N_\eta = 1/\eta_N$ and $N_{\eta\eta} = -\eta_{NN}/\eta_N^3$, were computed numerically. The use of this transformation is significant since it helps in maintaining second-order accuracy with respect to $\Delta\eta$ while facilitating the computer coding since only uniform increments are then used.

On the Numerical Method. The discretization of the problem is based on the use of two semi-implicit marching

methods of uniform second-order accuracy. The derivatives in the η-direction are approximated using second-order accurate central differences. In the first of the two methods, second-order accuracy is also maintained in the streamwise marching direction by using the Crank-Nicolson implicit scheme. The second of the two methods which has been proven equally efficient but slightly more stable, uses second-order accurate three-point backward differences for the streamwise derivatives. The iterations generally required because of nonlinearities are avoided by appropriately quasilinearizing the nonlinear terms in the equations. Two or three iterations at a given station were still needed because of coupling and the criterion for advancing to the next station was that $\Delta C_{fw} \leq 5 \times 10^{-6}$. The Crank-Nicolson scheme for the simple heat conduction equation $u_x = u_{YY}$ is known to be unconditionally stable. Since the nature of the asymptotic equations (3) is parabolic, a von Neumann stability analysis was also conducted for the simple linear heat-conduction equation, using a three-point backward difference formula. In this Fourier stability analysis, the general error term was taken as $\psi(x)\ e^{j\beta y}$. Substituting this in the heat-conduction equation leads to the following equation for the amplification factor ξ:

$$\xi^2\left[3+8\lambda\sin^2\beta\frac{\Delta y}{2}\right]-4\xi+1-0 \tag{13}$$

that is

$$\xi_{1,2}=\frac{2\pm\sqrt{1-8\lambda\sin^2\beta\,\Delta y}}{2+(1+8\lambda\sin^2\beta\,\Delta y)} \tag{14a,b}$$

which implies $|\xi_{1,2}| \leq 1$. In equations (14), $\lambda = \Delta x/\Delta y^2$, β is the wave number and $j = \sqrt{-1}$.

Sequence of Calculations. The numerical procedure is similar to that of Mikhail and Ghia [6]. Briefly, it can be stated as follows. The temperature T is determined from the energy equation and then the auxiliary equations are solved to update ρ and μ and also the eddy viscosity is calculated. Next, the streamwise momentum equation is solved, followed by the equation for ϕ. Finally, the streamwise vorticity equation for θ and the equation for ψ for the cross-flow velocity are solved simultaneously in order to implicitly treat the wall boundary condition on the vorticity. The entire cycle is repeated at a given station to meet the convergence criterion based on the local skin friction. Thereafter, the calculations proceed to the next station.

Results and Discussion

Validation of the Results. The asymptotic set of equations (3) is solved using the numerical method developed in this study. No special treatment is provided for the leading-edge singularity; hence, the results in the close proximity of the leading edge of the corner geometry must be used with caution. The laminar self-similar results were recovered as the solution progressed in the downstream direction. Gradual transition was then initiated to approach the turbulent flow.

To assess the analysis and the corresponding computer program, results were first obtained for the corresponding adiabatic incompressible flow. This configuration was chosen because Shafir and Rubin [11] have provided numerical results for it. The results of this comparative study are shown by curves 1 and 3 in Fig. 2. A maximum deviation of 15 percent is observed with the present analysis showing higher skin-friction values than those of Shafir and Rubin [11]. This discrepancy led to a further comparative study of a still degenerate case, namely, the flow past a flat plate. For this latter case, experimental data of Weighardt [22] are available and so also is the corresponding analytical result given in reference [15]. Both of these results are also depicted in Fig. 2.

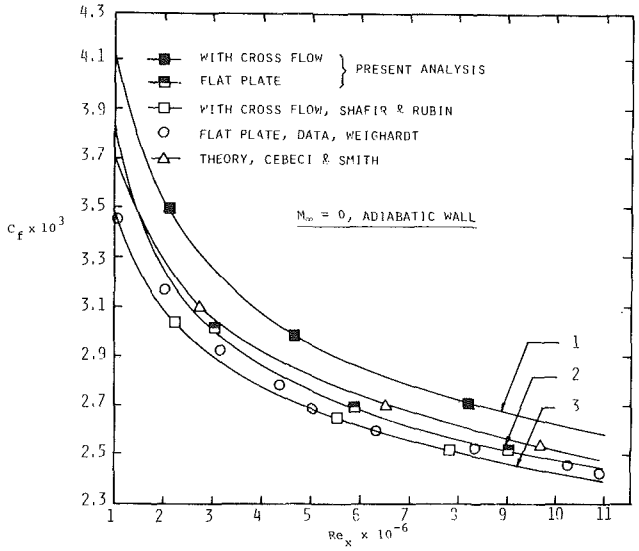

Fig. 2 Comparative study of streamwise variation in skin-friction coefficient

To complete this comparison, it was essential to obtain results of the present computations without cross-flow. As seen in Fig. 2, the present analysis agrees very favorably with these data. A close examination of the set of equations (3) and, in particular, the streamwise momentum equation (3*b*), reveals that the streamwise component of velocity even at infinity is coupled with the cross-flow equations through the turbulent eddy viscosity ϵ which depends on the normal gradient of the cross-flow velocity w_y as given in equation (6*b*). Thus, it is felt that a slightly higher skin-friction coefficient is possible for this quasi-three-dimensional asymptotic flow.

Further, a study of the step size in the η direction was conducted for the same configuration. The present calculations were repeated using a grid identically the same as that used in reference [11], namely, 140 grid points in the normal direction. The results of this study for the streamwise velocity u, and the cross-flow velocity w, are presented in Fig. 3. These show a maximum deviation of about five percent for the cross-flow velocity component in the laminar flow region, further verifying the accuracy of the results obtained in the present study with only 51 grid points in the normal direction. Thus, to conclude, it is believed that the deviation in the results may be due to the following factors. Shafir and Rubin [11] used a first-order accurate marching scheme. In the transition region, the streamwise step size is twice as large in their study and, further, in the turbulent region that follows, their step-size is twenty times larger than that used in the present study. Finally, due to the nonuniform grid, second-order accuracy in the normal direction may not have been maintained in their study.

The results for this incompressible configuration were also studied using the modified form of the anisotropic turbulence model of Gessner and Emery [19]. The skin-friction coefficient obtained using the two different turbulence models are presented in Fig. 4. The conformity between these two sets of results led to the conclusion that the effect of anisotropy is not significant in a study of the asymptotic corner flow. It also further justifies the use of the simple two-layer algebraic turbulence model for this study.

Effect of Compressibility. For supersonic flow, results are obtained for several configurations and are discussed next. The streamwise velocity u and the cross-flow velocity w are shown in Fig. 5 for three streamwise locations. The u-velocity profile is laminar at $Re_x = 5 \times 10^5$ and goes through tran-

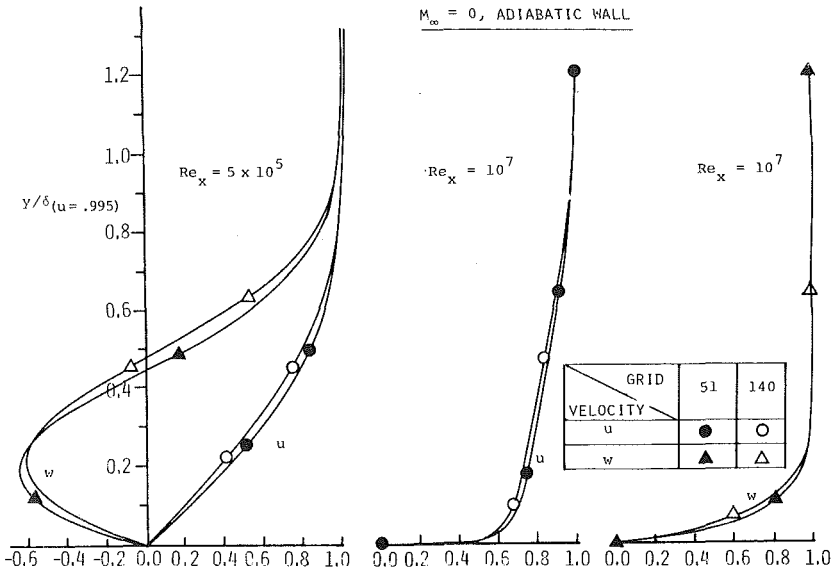

Fig. 3 Effect of normal step size on velocities

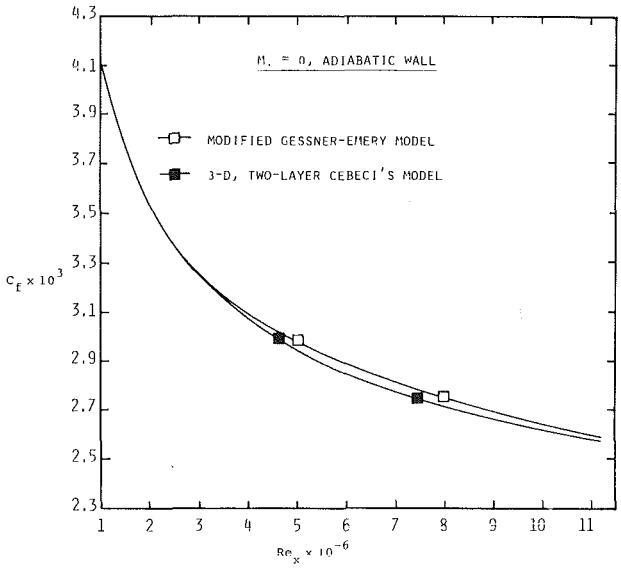

Fig. 4 Comparative study of isotropic and anisotropic turbulence models

sition to approach the fully turbulent profile at $Re_x = 10^7$. The reversal in the cross-flow velocity, as seen in Fig. 5, disappears as the laminar flow goes through a transition to turbulent flow. The streamwise variations of skin-friction and heat transfer coefficients are depicted in Fig. 6. As seen in this figure plotted on a log-log scale, the present results show that the asymptotic equations including cross-flow lead to the same values for these quantities as for the corresponding two-dimensional flow. On the scale used in this figure for C_f, the present solutions including cross-flow show no significant deviation from the results for two-dimensional flow. The streamwise variation of the heat-transfer coefficient has a trend very similar to that of the skin-friction coefficient. Finally, the effect of Mach number on the skin-friction coefficient is presented in Fig. 7. The skin-friction coefficient decreases with the increase in Mach number as well as with the increase in streamwise distance due to the growth in the boundary layer. Also shown in this figure are the variations in the skin-friction coefficient computed for two configurations using available analytical expressions (see Cebeci, et al. [15]).

Effect of Mass Transfer. The effect of suction or injection at the corner wall, $\eta = 0$, is studied and solutions are obtained for various wall boundary conditions for the case with free stream Mach number $M_\infty = 2.0$, and wall temperature, $T_w = 1.08$. Figure 8 shows the variations in the streamwise as well as the cross-flow velocities due to suction and injection at the wall for both laminar as well as turbulent flows. Uniform suction and injection are incorporated here. Their effect on the streamwise velocity is minimal for laminar as well as turbulent flows. On the other hand, the same is not true for the cross-flow. For laminar flow, suction at the wall increases the swirling motion at the far-field such that the maximum value of the reversed cross-flow velocity increases by approximately 60 percent over the corresponding no mass-transfer case. Injection has the opposite effect of suppressing the swirling motion and, consequently, it decreases the maximum value of the reversed cross-flow velocity by approximately 55 percent from the corresponding no mass-transfer value. In the turbulent region, even for the cross-flow velocity itself, the effect of mass transfer is relatively very minimal, with injection showing a slightly larger effect compared to suction. Also, the effect is confined to a small region near the wall $\eta = 0$.

Finally, the effect of mass transfer is studied on the skin-friction coefficient, using the supersonic flow configuration with $M_\infty = 2.0$ and $T_w = 1.08$ (Fig. 9). The first of two forms used here for the mass transfer provide streamwise decreasing injection and suction at the wall $\eta = 0$, with $K_1 = +0.2$ and $K_1 = -0.2$. In the laminar flow region, suction increases the wall friction, whereas injection has the opposite effect. For the corresponding turbulent flow, the reduced amount of suction or injection present at these far downstream locations has a very minimal effect on C_f, with the trend in variation of C_f being similar to that of laminar flow. The behavior of the skin-friction coefficient is somewhat irregular near the leading edge region due to the presence of the singularity which has not been given any special treatment. When uniform suction and injection are applied with $K_0 = 0.05$ and $K_0 = -0.05$, initially up to $Re_x = 2 \times 10^4$, the effect of mass transfer on the flow is minimum but the effect gradually increases as the laminar flow progresses. Thereafter, this effect reduces gradually in the turbulent flow regime. For this case also, suction increases the C_f whereas injection decreases it.

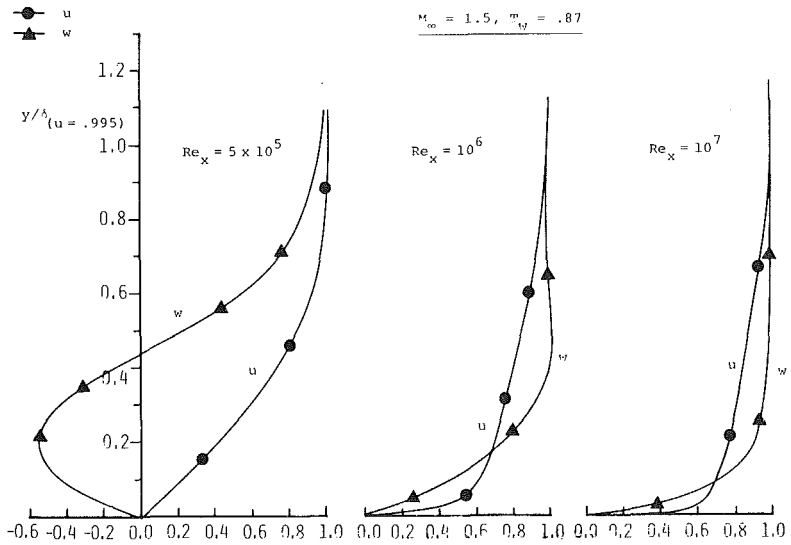

Fig. 5 Streamwise variation of velocity profiles

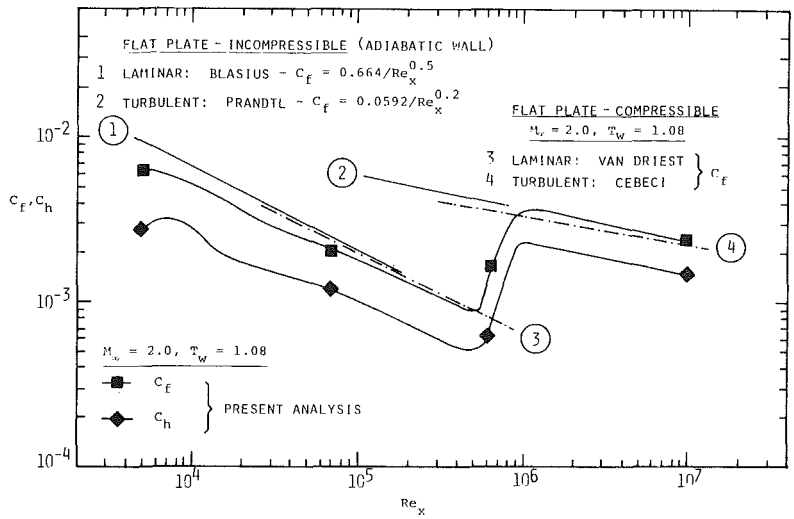

Fig. 6 Streamwise variation of skin-friction and heat-transfer coefficients

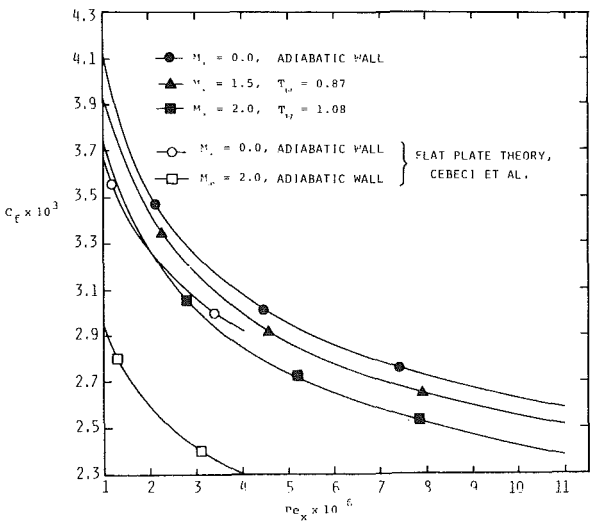

Fig. 7 Effect on Mach number and wall temperature on skin friction coefficient

Conclusion

The 90 deg axial corner flow is analyzed using a velocity-vorticity formulation to study the effect of compressibility and turbulence. The governing equations for the quasi-three-dimensional flow at the far-field boundary are obtained as the limiting equations as $Z \rightarrow \infty$, starting with the general corner-layer equations presented in this study. These asymptotic equations are solved using a semi-implicit, second-order accurate marching scheme. The turbulence is modeled by a two-layer algebraic model which uses an isotropic-eddy viscosity. In order to study the effect of anisotropy, Gessner and Emery's algebraic model is modified, to suit the present geometry to represent the turbulent stresses appropriately. This latter model is essential if the solutions are obtained for the entire corner region, rather than for the asymptotic corner region alone.

The asymptotic incompressible corner-flow results are presented to validate the analysis. Typical results are presented for a couple of Mach numbers and wall temperatures depicting the effect of compressibility on the asymptotic turbulent corner flow. The computations were performed on the AMDAHL 470/V6 computer and required

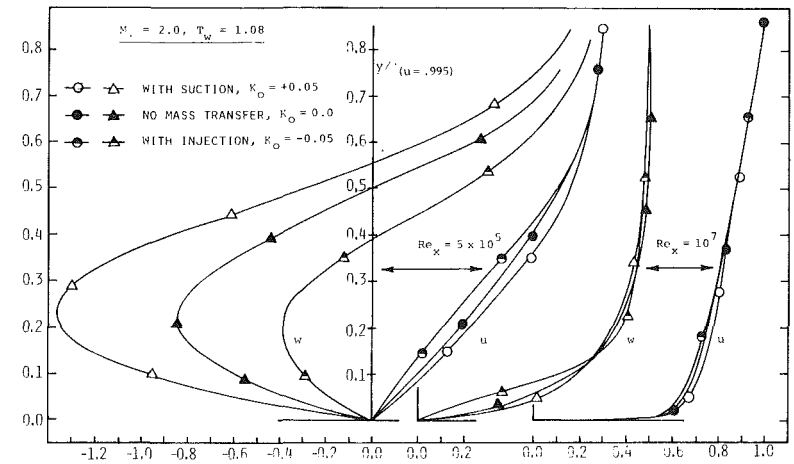

Fig. 8 Effect of mass transfer on the laminar and turbulent velocity profiles

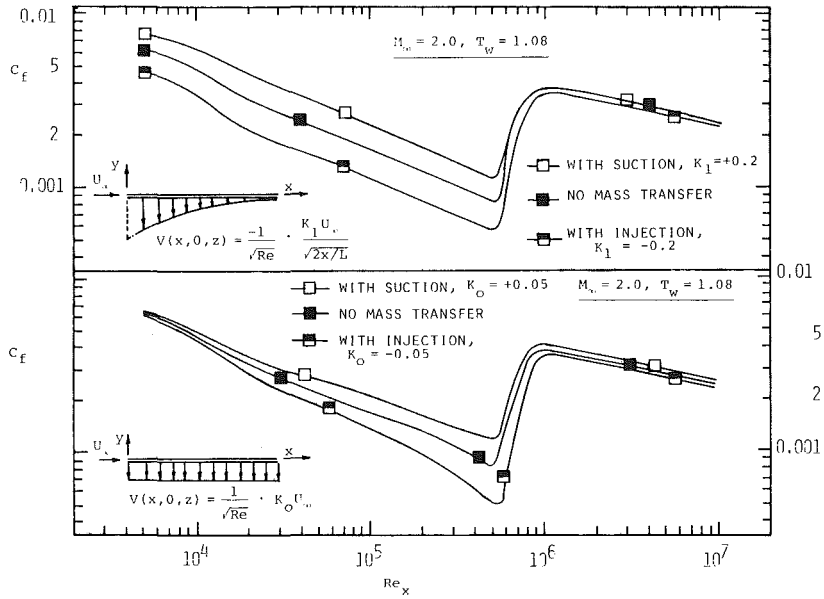

Fig. 9 Effect of mass transfer on skin-friction coefficient

2.5 min of CPU time for the flow to achieve $Re_x = 10^7$. Quantitative results for the streamwise variation in skin-friction and heat-transfer coefficients are made available for this configuration for the first time. The effect of mass transfer shows a larger influence on the flow field in the laminar region as compared to the turbulent region. Suction at the wall increases the swirling motion whereas injection dampens this behavior. Finally, the anisotropy in the turbulence modeling of this flow does not have an appreciable effect on this asymptotic corner flow field. The present asymptotic solutions for turbulent compressible flow at the far-field boundary provide the necessary boundary condition for the complete corner-flow study. After a closer examination of the modified Gessner-Emery turbulence model, a study of general corner-layer flow is planned.

References

1 Rubin, S. G., "Incompressible Flow Along a Corner," *Journal of Fluid Mechanics*, Vol. 26, Part 1, Jan. 1966, pp. 97–110.

2 Rubin, S. G., and Grossman, B., "Viscous Flow Along a Corner: Numerical Solution of the Corner Layer Equation," *Quarterly Journal of Applied Mathematics*, Vol. 29, No. 2, July 1971, pp. 169–186.

3 Ghia, K. N., "Streamwise Flow Along an Unbounded Corner," *AIAA Journal*, Vol. 13, No. 7, July 1975, pp. 202–207.

4 Ghia, K. N., and Davis, R. T., "A Study of Compressible Potential and Asymptotic Viscous Flows for Corner Region," *AIAA Journal*, Vol. 12, No. 3, Mar. 1974, pp. 355–359.

5 Weinberg, B., and Rubin, S. G., "Compressible Corner Flow," *Journal of Fluid Mechanics*, Vol. 56, Dec. 1972, pp. 753–774.

6 Mikhail, A. G., and Ghia, K. N., "Viscous Compressible Flow in the Boundary Region of an Axial Corner," *AIAA Journal*, Vol. 16, Sept. 1978, pp. 931–939; also AIAA Paper No. 77-685.

7 Li, C. P., "A Numerical Study of the Axial Corner Flow," AIAA Paper No. 78-1146.

8 Shang, J. S., and Hankey, W. L., "Numerical Solution of the Navier-Stokes Equations for a Three-Dimensional Corner," *AIAA Journal*, Vol. 15, 1977, pp. 1575–1582.

9 Hung, C. M., and MacCormack, R. W., "Numerical Solution of Supersonic Laminar Flow Over a Three-Dimensional Compression Corner," AIAA Paper No. 77-694.

10 Klinksiek, D. T., "An Implicit Numerical Solution for the Laminar and Turbulent Flow of an Incompressible Fluid Along the Axis of a 90 deg Corner," Ph.D. dissertation, Aug. 1972, Virginia Polytechnic Institute and State University.

11 Shafir, M., and Rubin, S. G., "The Turbulent Boundary Layer Near a Corner," ASME *Journal of Applied Mechanics*, Vol. 43, No. 4, Dec. 1976, pp. 567–570.

12 Shang, J. S., Hankey, W. L., and Petty, J. S., "Three-Dimensional Supersonic Interacting Turbulent Flow Along a Corner," *AIAA Journal*, Vol. 17, No. 7, July 1979, pp. 706–713.

13 Cebeci, T., "Calculation of Three-Dimensional Boundary Layers: II. Three-Dimensional Flows in Cartesian Coordinates," *AIAA Journal*, Vol. 13, No. 8, Aug. 1976, pp. 1056–1064.

14 Mikhail, A. G., "Analysis and Numerical Solution of General Com-

pressible Viscous Flow Along a 90 deg Axial Corner," Ph.D. dissertation, August 1976, University of Cincinnati.

15 Cebeci, T., and Smith, A. M. O., "*Analysis of Turbulent Boundary Layers*," Academic Press, 1974.

16 Bradshaw, P., "Review - Complex Turbulent Flows," ASME *Journal of Fluids Engineering*, Vol. 97, No. 2, June 1975, pp. 146–154.

17 Morel, T., and Torda, T. P., "Calculation of Free Turbulent Mixing by the Interaction Approach," *AIAA Journal*, Vol. 12, No. 4, Apr. 1974, pp. 533–540.

18 Gessner, F. B., and Emery, A. F., "A Reynolds Stress Model for Turbulent Corner Flows - Part I: Development of the Model," ASME *Journal of Fluids Engineering*, Vol. 98, No. 2, June 1976, pp. 261–268.

19 Gessner, F. B., and Po, J. K., "A Reynolds Stress Model for Turbulent Corner Flows - Part II: Comparisons Between Theory and Experiment," ASME *Journal of Fluids Engineering*, Vol. 98, No. 2, June 1976, pp. 269–276.

20 Launder, B. E., and Priddin, C. H., "A Comparison of Some Proposals for the Mixing Length Near a Wall," *International Journal of Heat and Mass Transfer*, Vol. 16, No. 3, Mar. 1972, pp. 700–702.

21 Gessner, F. B., and Emery, A. F., "A Length-Scale Model for Developing Turbulent Flow in a Rectangular Duct," ASME *Journal of Fluids Engineering*, Vol. 99, No. 2, June 1977, pp. 347–357.

22 Wieghardt, K., "Proceedings - Computation of Turbulent Boundary Layers - 1968," AFOSR-IFP-Stanford Conference, eds., D. E. Coles and E. A. Hirst.

M. A. Strite
Supervisor,
Test Engineering.

N. A. Samurin
Manager,
Turbomachinery Development.

Elliott Co., a division of Carrier Corp.,
Subsidiary of United Technologies Corp.,
Jeannette, Pa., 15642

Equivalent Performance Testing of Multisection Compressors

Equivalent performance testing of multisection compressors has largely been ignored by the various test codes. Existing code methods have been modified and adapted for testing multisection compressors by the manufacturers and users. The performance testing of two types of multisection units—the externally cooled and the sideload compressor—are discussed here. Each compressor type has had specific test difficulties that require identification and resolution. Prior to the start of testing, an overview of the problems, along with some solutions, is presented.

Introduction

Testing of multisection compressors is complex, even in the manufacturer's shop. Actual field conditions cannot be duplicated in the shop; however, they can be effectively simulated, using modified code methods. Better instrumentation can be more economically applied, flows can be more easily varied, and test gases with known compositions and properties are available for the shop test. Test gases and operating conditions have to be selected to give equivalent performance of the units, compatible with the manufacturer's test facilities. Modification of the existing codes is required due to the uniqueness of the compressor designs and aerodynamic and thermodynamic effects between adjacent stages.

This paper will not attempt to discuss each particular item in detail, but it will provide some insight into their testing difficulties.

Cooled Compressors

The cooled compressor has an inlet and a discharge for each section, with at least two sections on a common shaft in a single casing; each section may have several stages. Typically, a cooler or heat exchanger is located between sections. Cooled compressors are used to reduce process horsepower or when the maximum temperature is limited by process or safety reasons. Usually no mixing of gas streams occurs between sections. Gas composition and/or mass flow may vary significantly between sections.

The test methods of a two-section machine adapt readily to three or more sections. Cooled compressors are less complex than sideload compressors, and their tests are simpler to conduct. However, the initial selection of a test configuration is more difficult for cooled compressors because of the many possible piping arrangements.

Two section cooled compressors may be loop tested with one or two coolers; (See Figs. 1 and 2, respectively). Air is a suitable test gas for some cooled compressors. Air tests may be run with open inlets and discharges or with a cooler. As the figures indicate, air test piping is analogous to the closed loop configuration with one less cooler. The following discussion applies to both air and closed loop tests, except where noted.

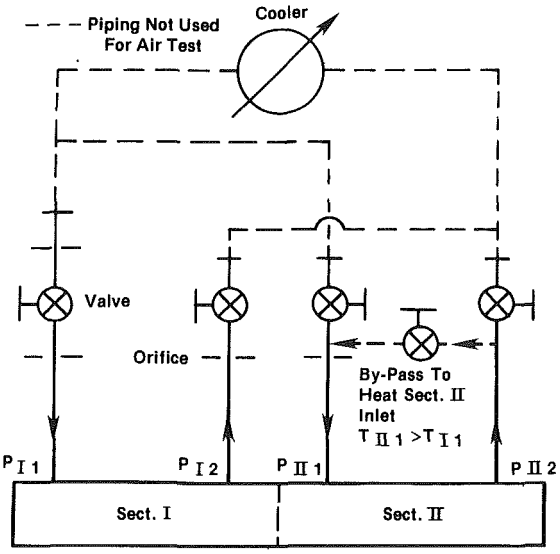

Fig. 1 Test loop for closed loop test of cooled compressor, using one cooler. The analogous loop for air is indicated by dashed lines. Location of the orifices should be noted.

Two basic casing designs are used for cooled compressors. Figure 3(*a*) shows the unidirectional design, and Fig. 3(*b*), the back-to-back design. Each casing design has potential test problems that can be minimized by the test setup.

In the unidirectional cooled compressor, heat transfer and leakage occur at the common wall between sections (Fig. 4). The effects of heat transfer or leakage on each section's performance are difficult to measure accurately. These are usually calculated by the manufacturer prior to test and used in the correction of test data to design conditions. Both the

Contributed by the Gas Turbine Division of THE AMERICAN SOCIETY OF MECHANICAL ENGINEERS and presented at the Gas Turbine Conference and Products Show, March 9-12, 1981, Houston, Texas. Manuscript received at ASME Headquarters December 16, 1980. Paper No. 81-GT-150.

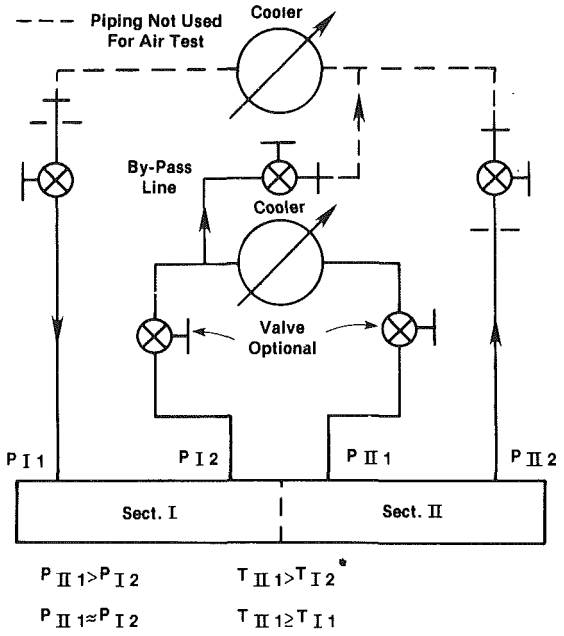

Fig. 2 Test loop for closed loop test of cooled compressor, using two coolers

heat transfer and leakage can be minimized by the test setup, so that the unidirectional cooled compressor can often be tested by code methods, without any additional calculations or measurements. Heat transfer and leakage effects may be more significant for certain designs.

Heat transfer decreases the flange temperature of the first section discharge and increases the internal temperature (over the flange reading) of the second section inlet temperature. Since an increase in the internal temperature increases the externally measured section temperature rise, the net effect is energy generated in one section is measured in another section; heat transfer can cause erroneous test results unless the effects are similar for design and test. Heat-transfer effects are distorted if the ratio of flows for the two sections are not the same for both test and design or if the temperature differential between sections is grossly different between design and test.

Leakage of hot gas from the first section also increases the second section internal temperature and the externally measured section temperature rise. However, since the flow leaks from one section to the other without recirculation through an impeller, the compressor shaft horsepower is not increased by the leakage. (The temperature rise occurs between the inlet and the first impeller; the mass flow through the section is unchanged by the leakage.) Leakage effects are minimized by keeping the pressure drop between sections small.

Leakage and heat-transfer effects are minimized by using a cooler between the first and second sections for test. Heat transfer is partially controlled by the test gas selection.

The two-cooler closed loop system is easier to control and operate than the single cooler system. However, it requires a second cooler which may not be available in the test facility. The benefits of the second cooler in the unidirectional cooled compressor test are lost if the second section inlet must be throttled due to power or pressure limitations.

A single cooler loop test may be satisfactorily used for many unidirectional cooled compressors. The choice of the number of coolers used for performance testing a cooled compressor must be made by the manufacturer. A poor performance test setup will result in erroneously high horsepower, so the penalty is also on the manufacturer.

In the back-to-back design, Fig. 5, gas leakage from the high-pressure section into the low-pressure section is the major problem. The leakage flow passes from the second

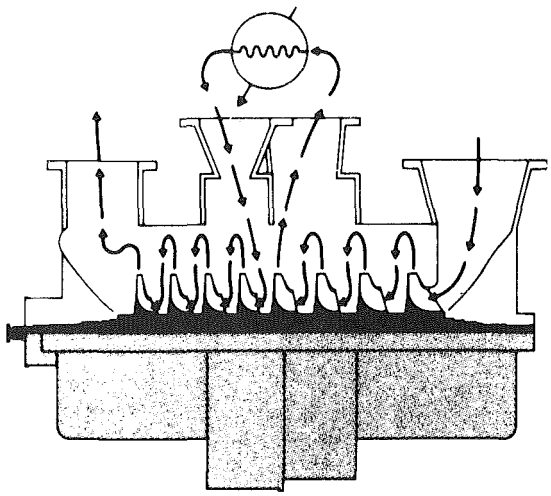

Fig. 3(*a*) Unidirectional cooled compressor

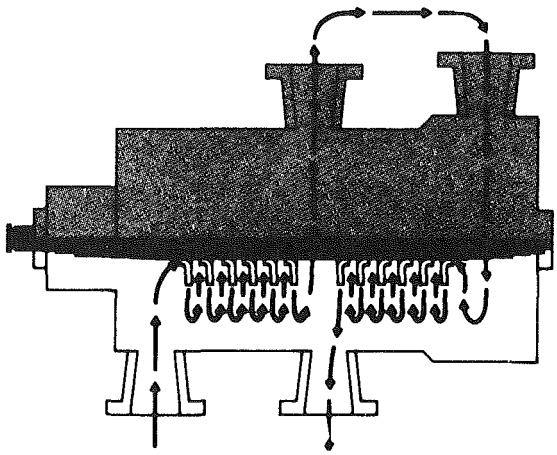

Fig. 3(*b*) Back-to-back cooled compressor

Fig. 3 Examples of cooled compressor designs.

Nomenclature

P = pressure
T = temperature
W = mass flow rate
ΔH = heat transfer
$>$ = greater than
$<$ = less than
$\approx$ = approximately equal

Subscripts

A = mass flow rate of first section
B = mass flow rate into second section
Int = parameter measured internal to casing
F = parameter measured in loop piping (at the flange) of casing
I = first section
II = second section
1 = parameter at inlet of section
2 = parameter at discharge of section
L = leakage flow

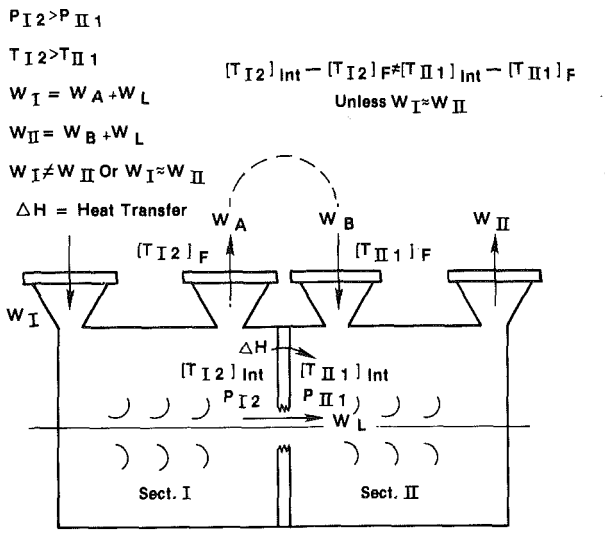

Fig. 4 Common wall between sections of a unidirectional cooled compressor. Heat transfer H and leakage W_L occur at this wall.

section discharge to the first section discharge and then recirculates through the second section. In most cases, the leakage cannot be measured on test; it must therefore be calculated by the manufacturer and its effects included in the evaluation of the test results. Since the leakage may not be similar for test and design, it must be evaluated carefully for either loop design. A single-cooler loop may be satisfactory for a back-to-back cooled compressor.

As a general rule on cooled compressors, flow errors are eliminated by measuring at the main inlet and the main discharge. On all compressor performance tests, the manufacturer must consider the effects of balance piston leakage and seal buffer flows; if the effects are not similar for test and design, special corrections must be made on the test data. These items tend to be more critical for cooled compressors than for other compressor designs.

In the process intercooler, certain process gas constituents may be knocked out, resulting in a varying gas composition from section to section. However, the same gas composition must be used throughout a test loop, so the knockout process cannot be duplicated. Different gas compositions may result in different sectional test speeds—the lower mole weight section requires a lower test speed for volume ratio equivalence if test inlet temperatures are the same for all sections. A common test speed may be obtained by increasing the test inlet temperature of the section with the lower design mole weight. In extreme cases, the test inlet temperature of the low mole weight section—usually the second section—may be increased enough so that no cooling is required between the first and second sections; the two sections are connected by a U-shaped pipe that contains both inlet and discharge pressure and temperature probes.

The test mass flow rates may not be equal for the two sections of a cooled compressor. Unequal mass flows are handled automatically by the single cooler loop (Fig. 1) while a bypass around the second section is needed for the two cooler loop (Fig. 2). On the other hand, the single cooler loop requires a bypass from a discharge to an inlet if test inlet temperatures of both sections are not identical.

In some instances, separate test conditions must be specified for each section. One compressor section may have to be ignored while test data are taken on the other section.

Vendor facilities may not permit loop testing of high-capacity, low-volume ratio compressors. Piping and cooler losses may be excessive. Many of these compressors can be tested on air. A test that does not meet all code equivalency limits can still verify the compressor head and flow range.

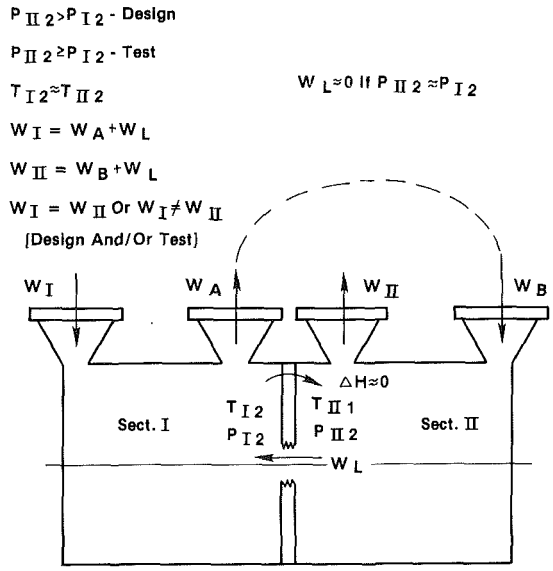

Fig. 5 Path of leakage flow for back-to-back cooled compressor

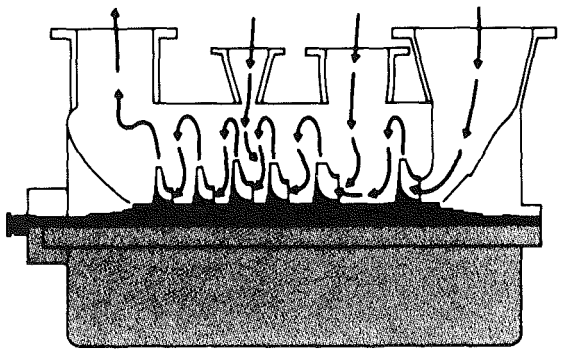

Fig. 6 Example of compressor with two sideloads

Sideload Compressors

General. The sideload compressor may have one to four inlets and one or more discharges: the maximum number of inlets and discharges is usually five (See Fig. 6). Incoming flows, at points other than the main inlet, are called sideloads; outgoing flows, except at the main discharge, are called extractions. A sideload nozzle marks the discharge of one section and the inlet of the next.

Sections of a sideload compressor should not be thought of as separate compressors, especially when designing an equivalency test. At a sideload, flow enters from outside the compressor and mixes with flow from the preceding section: the combined flow enters the next impeller. Actual measurements show that pressure losses occur during the mixing process; these losses can be minimized, but not eliminated, through careful aerodynamic design which keeps the mixing streams at equal velocities. Due to the mixing losses, the actual polytropic head of the compressor is slightly lower than the sum of the heads of the individual sections. Extractions are assumed to have no effect on internal velocities.

The basic problem of testing this unit configuration, unlike the cooled compressor, is that instrumentation in the loop piping will not accurately evaluate the performance of a section. Code-prescribed external instrumentation is used for flow readings, for all data at the main inlet and main discharge, and for sideload temperatures. Actual performance is dependent upon the mixed properties of state

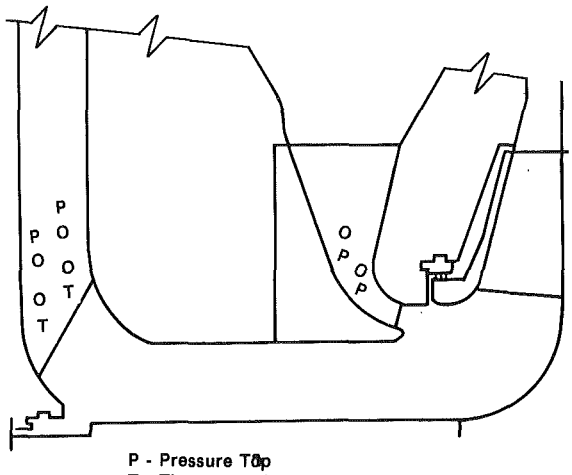

Fig. 7 Internal instrumentation used for performance testing a sideload compressor. Instrumentation is normally installed in the vanes closest to the casing splitline. Four pressure and temperature probes are installed at each station.

entering each section and, thus, is not directly available from flange readings alone. Internal instrumentation is required.

The pressures and temperatures discharging from a section before mixing with a side stream can only be measured in internal flow passages. Figure 7 shows typical internal instrumentation. Compressor hardware differs from manufacturer to manufacturer; what is successful for one design may not work well, if at all, for another. With the rapid advancements in technology, new methods of instrumentation will be available in the future. The present test codes do not specify internal instrumentation, and, in future code revisions, care should be taken so as not to make inflexible specifications.

Establishing Test Conditions. The additional data accumulated from testing a multisection compressor automatically make it more complicated than testing a single-section compressor. It is in the best interest of both the manufacturer and the user to simplify testing as much as possible. One effective means of simplifying the test is to gather data at one test speed. To do this, some compromise of code recommendations may have to be made, but this will not affect the integrity of the test.

The basic equations for establishing test speed are the same as those used for a single section compressor. They must, of course, be applied to each section individually, the inlet pressure of each section is equal to the discharge pressure of the preceding section. The inlet temperature of a section following a sideload is computed from the discharge temperature and flow of the preceding section, combined with the side stream temperature and mass flow rate. The process of determining the inlet temperature and the mass flow rate that gives the design Q/N is iterative. At an extraction, the discharge pressure and temperature of one section are the inlet conditions of the next; the inlet flow is equal to the primary flow stream less the extraction flow stream.

When the individual test speed of each section gives 100 percent volume ratio matching, the resulting test speeds will be different for each section. Test codes allow some variations on Mach number and volume ratio, such as

Volume Ratio, percent of Design 95-105
Mach Number, percent of Design 95-105

For M greater than 0.8

Mach numbers are normally high in compressors with sideloads and the highest value in the machine is at the first stage. Since Mach number and choke flow are related, the Mach number ratio is the most critical for the first section. Reduced Mach number limits of 98 to 102 percent allow some flexibility in the test setup but ensure closer correlation to field conditions. The speed that meets this criteria normally sets the speed for the test.

It may be impossible to select test conditions of a sideload compressor such that all sections meet Mach number and volume ratio criteria at a single speed. The purpose of a performance test is to check critical parameters. As stated above, Mach number is usually the most critical in the first section—and least important in the last section. The last stage of a compressor discharges into a volute rather than a return channel; the efficiency of a volute is less sensitive to changes in flow caused by discrepancies in volume ratio than is a return channel. Volume ratio and Mach number limits can be allowed to drop to as low as 90 percent in the last section without affecting the integrity of the performance test.

Once the test has started, the data should be examined concurrent with unit operation to determine if choke, surge or curve shape indicate the need for test speed to be adjusted for one or more sections. Additional data taken at another test speed may be needed to resolve serious performance questions. In most instances, however, a single-speed test satisfies all requirements.

The number of coolers used for testing sideload compressors is optional, but the decision has to be left to the manufacturer. Most compressors of this type can be tested with a single cooler. The single cooler provides flows at nearly constant inlet temperatures and valves provide different pressure levels for each section. The single cooler loop can be used to conduct a single speed test that meets most code requirements, including the surging of individual sections.

Selection of Test Gas. Selection of the test gas requires careful analysis. The gases commonly used for testing this type of compressor are refrigerants 11, 12, and 22. When a refrigerant is used, it is normally in a gaseous state throughout the test loop piping, but it may liquify in the static instrument lines, which, under static conditions, cool to ambient temperature. The result is erroneous pressure readings. Means of avoiding this problem are available, and should be recognized when setting up the test to avoid questionable data and a poor test.

Some sideload compressors will require test inlet pressures of 5-10 psia to avoid instrumentation problems at the discharge; an adverse effect of the subatmospheric inlet pressure is that any piping leaks will contaminate the test gas. Proper safety precautions should be observed. Purities of 95 percent or better can usually be maintained. Lower gas purity will adversely affect volume ratio and the validity of the test could be in question. Additionally, varying purity may change properties for the actual gas mixture gives a more accurate measure of the performance and is recommended; with the heavy mole weight refrigerants used as test gases, 1 percent air gives approximately 1 percent error in both head and efficiency if properties for the pure refrigerant are used. Real gas properties will not eliminate all of the effects of varying purity.

Test Setups. Figure 8 is a schematic of the single-cooler test loop for a compressor with two sideloads and an extraction. Inlet pressures are regulated by valves. Flow measurements are made for each section; the number of flow measuring stations is one less than the number of inlets and discharges. Since the first section tends to have the most limited flow range and also the smallest mass flow of any section, the flow of the first section should be a direct measurement and not a function of the other flow measurements. Inlet orifices located upstream of control valves avoid critical flow in the

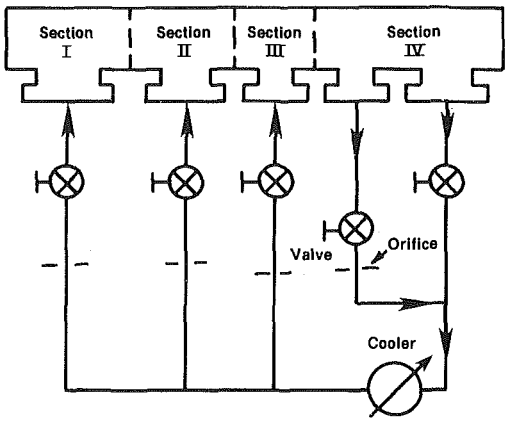

Fig. 8 Test loop for compressor with two sideloads and one extraction, using single cooler

orifice. (Note: If a sideload is located downstream of an extraction, either a second cooler or special piping is required.)

The piping for compressors with several inlets and discharges is complex. Code requirements for straight runs of pipe may have to be compromised to set up the test in the manufacturer's shop. The test facility may not have room for the straight runs of large diameter pipes or for certain nozzle orientations.

Small sideloads or extractions can be blanked off without affecting the integrity of the test. Internal instrumentation is used for measuring both pressures and temperatures and, thus, performance.

Conducting the Performance Test. Test operating conditions for a sideload compressor must be maintained with far less variation than for a straight-through or cooled compressor. The effects of small changes may be magnified and distorted going through the sections of the compressor.

Stabilization time is the time required for the system to reach equilibrium. Stabilization is a function of many things - curve shape, unit size (associated with the mass of material), internal leakage, test loop configuration, heat transfer, etc. Internal pressures and temperatures are more affected by stabilization than are external measurements. Probes at some internal locations may exhibit considerable scatter which settles out with time: the time may be as short as 15 min or as long as 2 hr, depending on the test system.

Stabilization can affect curve shape, especially when the head rise to surge is small. Allowing for adequate stabilization time will result in a more accurate test of the head curve shape and efficiency. Data scatter indicates insufficient time is being allowed.

Experience indicates that a 2 percent variation allowed by the code on inlet pressure is excessive and can prevent some systems from stabilizing. The variation is less serious if it represents scatter in the individual probes at a given reading instead of the difference between two sets of readings.

Holding a constant pressure for prolonged periods is difficult. Three sets of date readings in 15-20 min provides sufficient accuracy. The five or more readings required by many test codes is unnecessary. If stability of a point is in question, the point should be retaken. Prolonged data taking at a given flow tends to become a test of the system instead of a test of the compressor.

The mixing of flows at a sideload makes the performance of one section somewhat dependent on other sections in the sideload compressor. Compressors of this type should, therefore, be tested as near to constant turndown as possible. Constant turndown means that the volume flows of all sections are at the same percentage of their respective design flows. If the system does not permit a strict constant turndown (say with 10 percent or less variation in flows), the data should be taken so that the points for all sections are in the same order flow-wise; a high flow point of one section should not be the low flow point of another.

If possible, each section should be surged independently. In some test systems, two sections are tied together too closely to permit surging of each independently. Surging of a compressor with sideloads on a closed loop is disappointing to the observer who expects a loud "bang." The changes in noise may be detectable only adjacent to the pipe. Manometers and gages may or may not react at the same time. Some surges are accompanied by increased mechanical vibration; these surges are peculiar to one section. More sophisticated methods of detecting surge, such as transducers, are available.

The surging of sections of a sideload compressor may occur at flows much lower than predicted; the head curve may droop as flows are reduced below the prediction level. No attempt will be made here to define surge. However, it appears that some surges "measured" on closed loop performance tests are artificial and cannot be reproduced in the field. The predicted surge flow may be more reliable than the test value; manufacturers are not expected to be overly conservative in these predictions.

Internal pressures and temperatures recorded at sideloads and extractions may give erratic readings that do not respond to more stabilization time and do not appear defective based on electrical checks. The probes may be in better agreement with others at the same station on certain flow points. The conclusion is that the erratic probes are measuring correctly! They are reading true pressures or temperatures that reflect the effects of nonuniform mixing at the sideloads—nothing is done to more uniformly mix the flows, since it would require extra power.

If the variations in readings at a given station are significant, extra probes may resolve the problem—or they may emphasize the scatter! Comparison of test data to predictions may be useful, especially for scatter in temperature data. Since the temperature rise of the overall unit can be measured accurately, it may be necessary to adjust internal temperature data on this basis if considerable scatter exists. Variations in internal pressures are less severe; a manufacturer who is familiar with test data on similar compressors knows if flange or other internal data is a satisfactory backup.

Due to internal mixing, the evaluation of the test data is very complicated. A high degree of sophistication and technology are required to establish reliable test data. Interpretation of the data and prediction of the compressor's performance at design conditions also require care and experience.

Space does not permit a detailed discussion of the mixing phenomena. Conservation of mass, momentum, and enthalpy must be observed. Velocities in external piping are usually low—in the range of 100 FPS. Internal mixing may be done in high-velocity regions—with velocities of several hundred feet per second—or low-velocity regions, depending upon the compressor design. Mixing of fluid streams should be done at static pressures, since the difference between static and total conditions may be significant. High internal velocities and a local jetting effect can produce internal total pressures that are higher than the flange readings.

Conclusion

The purchaser must have an understanding of the limitations and capabilities of the manufacturer. Such an understanding can easily be arrived at in a pre-test negotiation

meeting. The equipment manufacturer must be careful to point out the specific test limitations and the deviation from expected traditional results within the framework of the existing test codes. Any shop equivalent test of a sideload compressor is normally going to involve compromise due to the uniqueness of the unit and the capabilities of the manufacturer. Interpretation of data and methods of data reduction should all be resolved prior to testing. Such methods should be carefully reviewed by the purchaser to insure his understanding of the methods. The accuracy of these tests, the data scatter which can easily occur depending upon test techniques, and many other variables which cannot be predicted prior to test, all have to be carefully considered. It is the vendor's responsibility to minimize misunderstandings that may be encountered during the test.

More guidance in the testing of multi-section machines is needed from test codes. The subject may be too extensive to cover easily in the standard code, but it should not be ignored.

Acknowledgments

The authors are indebted to Elliott Company, a Division of Carrier Corporation, subsidiary of United Technologies Corporation, for permission to publish this paper, and to the many individuals within the company who encouraged the writing of the paper.

Engine Dynamic Analysis With General Nonlinear Finite-Element Codes, Part 1: Overall Approach and Development of Bearing Damper Element

M. L. Adams

Associate Professor of Mechanical Engineering.

J. Padovan

Professor of Mechanical Engineering.

D. G. Fertis

Professor of Civil Engineering.

University of Akron, Akron, Ohio 44325

There is currently a considerable interest and level of activity in developing computational schemes to predict general engine dynamic behavior. The general feeling among researchers working on engine vibration problems is that various modes of operation, such as blade-loss events, require a high level of analysis sophistication to realistically model the engine. Proper account of system nonlinearities (particularly at the bearings, dampers and rubs) appears to be necessary if analytical predictions are to be realistic. The approach described in this paper seeks to make use of already proven general finite-element nonlinear time-transient computer codes which are available on the open market. The work specifically described in this paper covers the first phase of a three-phase NASA-Lewis-sponsored research grant on engine dynamic simulation with available finite element codes. The first phase was concentrated on the development of a bearing-damper element computer software package suitable for "plug-in" to available finite element codes.

Introduction and Background

Present-day jet engine configurations have evolved to a substantial degree through a trial-and-error process involving extensive testing. There are many fundamental dynamic phenomena which take place within these engines for which basic description and understanding have yet to be generated. Nonetheless, they work well. Modern aircraft engines are typical of current high-technology products in which the recently acquired computing capabilities of today are being used to better understand and improve what is already designed, built and operating.

A better understanding of the basic dynamic characteristics of existing and new engine configurations is a prerequisite for producing acceptable engine efficiencies on advanced configurations (i.e., smaller rotor/stator running clearances). Also, a better definition of engine dynamic response would more than likely provide valuable information and insights leading to reduced maintenance and overhaul costs on existing configurations. Furthermore, application of advanced engine dynamic simulation methods could potentially provide a considerable cost reduction in the development of new engine configurations by eliminating some of the trial-and-error process done with engine hardware development.

The emergence of advanced finite element codes, such as NASTRAN, NONSAP, MARC, ADINA, ANSYS and ABAQUS and related algorithmic advances, have placed comprehensive engine system dynamic analyses within reasonable reach. What remains to be done is to develop new component element software to properly model engine rotor/stator interactive components, such as the squeeze-film damper, within the algorithmic logic of already proven finite element codes. This is the major mission of this work.

For good reasons, aircraft gas turbine engines use rolling element bearings exclusively. This design philosophy has, until recent years, deprived engines of the beneficial damping inherent in many other types of rotating machinery where fluid-film journal bearings are used. The implementation of squeeze-film dampers in recent engine designs has now provided engine designers with an effective means of vibration energy dissipation. The net result is that engines with squeeze-film dampers are less sensitive to residual rotor imbalance and better able to control vibration and transmitted force levels resulting from various excitation sources within the engine.

The field of rotor dynamics has evolved to its present state primarily through the solution to problems in classes of machinery older than aircraft engines. In most other types of rotating machinery (e.g., steam turbines, centrifugal pumps and compressors, fans, generators, motors, etc.) the rotor can

Contributed by the Gas Turbine Division and presented at the International Gas Turbine Conference and Products Show, Houston, Texas, March 9–12, 1981 of THE AMERICAN SOCIETY OF MECHANICAL ENGINEERS. Manuscript received at ASME Headquarters December 15, 1980. Paper No. 81-GT-151.

be adequately modeled as an Euler or Timoshenko beam [1]. In addition, the support structure holding each bearing can often be adequately modeled as a separate mass-damping-stiffness path to ground (i.e., to the inertial frame). Also, for most purposes, bearing dynamic properties are characterized as stiffness and damping elements, linearized for small vibration amplitudes about some static equilibrium state. With few exceptions (e.g., Hibner [2]), it is this level of sophistication that has been utilized for the most part is rotor-dynamics analyses of aircraft engines.

Present day aircraft engines are structurally far more complex than most other types of rotating machinery. The multi-shaft configuration, plus the fact that the shafts are thin rotating shells, creates unique but significant complicating differences between aircraft engines and other machinery. Also, the stator structural support at each rotor bearing represents anything but a separate mass-damper-stiffness path to an inertial frame. In fact, setting the inertial frame for the engine is not a simple matter when the full range of in-service maneuvers is realized. Dynamic paths between different bearings exist not only through the rotor but through several other paths within the nonrotating engine structure, i.e., a "multi-level," multi-branch" system. As many as eight significant "levels" have been identified.

The feasibility of nonlinear dynamic analyses of multi-bearing flexible rotors has been recently demonstrated on non-aircraft applications [3]. There are highly nonlinear dynamic effects in aircraft engines, particularly under large excitation forces, such as blade or disk failures, hard landings, and foreign matter ingestion events.

Clearly, the field of aircraft engine dynamics is presently in a position where there is both a need for substantial advances and feasible means available by which such advances can be accomplished.

Time-Transient Nonlinear Dynamic Analyses

In recent years it has become evident that an important class of engine dynamic phenomena can not be studied without accounting for the highly nonlinear forces produced at bearings/dampers, labyrinths and other close-running rotor/stator clearances under large amplitude vibrations. In such cases, linear theory typically predicts vibration amplitudes larger than the actual running clearances. Furthermore, important vibratory phenomena, such as subharmonic resonance and motion limit cycles, are "filtered" out of the problem with a linear model, giving grossly erroneous predictions, qualitatively as well as quantitatively [3].

With few exceptions, nonlinear dynamics problems must be solved numerically as time-transient responses, whether the sought answer is a steady-state periodic motion or is strictly a transient phenomenon. The problem, is mathematically categorized as an initial value problem in which the displacements and velocities of the complete system must all be specified at the beginning of the transient. From that point forward in time, the equations of motion are numerically integrated (known as "marching") as far in time as one wishes to study the system motions and forces. If the system is dynamically stable, the transient motion dies out yielding the steady state response which in a system with a periodic force excitation will be a periodic motion. In a stable system with no time-varying force excitation, the transient will die out as the system comes to rest at one of its stable static equilibrium positions. If the system is unstable, the transient does not die out but continues to grow in time unless or until some nonlinear mechanism in the system limits the motion to what is frequently called a "limit cycle" [3].

In order to study the general dynamical characteristics of aircraft engines, nonlinear dynamics computational schemes

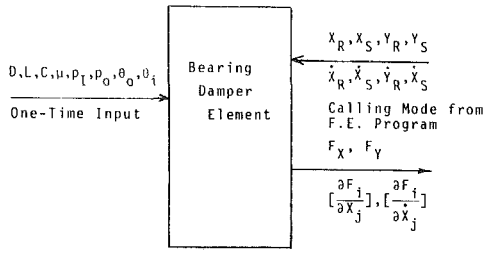

Fig. 1 Input/output of damper pilot code

are required. The approach taken is to develop software packages to model engine components which are not typically found on dynamical structures and therefore are not already built into existing nonlinear finite element structural dynamics computer codes. The initial effort has concentrated on developing such a software package for squeeze-film bearing dampers.

Overall Approach-Interactive Elements

Considering the typical engine structural complexities, an improved computational approach is necessary if a proper transient/steady-state model is to be developed for gas turbine engines. In this approach, it appears that the finite element method is one of the attractive modeling techniques for such problems. Its inherent capabilities include features essential to modern engines: 1) automatically handles multi-branch, multi-level structures in a more direct and efficient manner than flexibilities approaches, 2) well-suited to handle nonlinearities associated with structural kinematic and kinetic effects [4], 3) easily accommodates various types of boundary and constraint conditions, and 4) easily accommodates material nonisotropy and nonlinearity [4,5]. A body of established and proven algorithms are available which can handle these various important effects [4,6] as well as geometric complexities (e.g., beam, plate, 2-D and 3-D elements [7].

The required features which are presently not available with general purpose finite-element codes are provisions to handle rotor/stator interactive forces originating from squeeze-film dampers, seals and rub/impact events. Presented herein are the results of an effort to develop a squeeze-film damper computer software package which can be "plugged" into existing finite element codes. This work is detailed in the following section of this paper.

Squeeze-Film Damper Element

The bearing damper element is essentially an interactive element to represent squeeze film dampers. Its purpose is to bridge the "gap" between structural elements which are separated in the actual engine by a squeeze film damper. In its simplest version, it has an input/output setup as shown in Fig. 1. A source listing of this code is given in reference [8].

The rotor/stator interactive force generated in a bearing squeeze film damper is modeled using an adaptation of the classical Reynolds lubrication equation for incompressible laminar isoviscous films.

$$\frac{\partial}{\partial x}\left(\frac{h^3}{\mu}\frac{\partial p}{\partial x}\right)+\frac{\partial}{\partial z}\left(\frac{h^3}{\mu}\frac{\partial p}{\partial z}\right)=6\frac{\partial}{\partial x}(hU)+12\frac{dh}{dt} \qquad (1)$$

where

z = axial coordinate
x = circumferential coordinate = $r\theta$
h = local film thickness

$\frac{dh}{dt}$ = instantaneous local rate of change in h

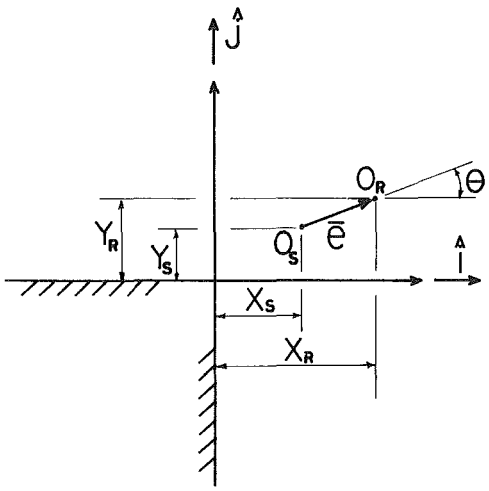

Fig. 2 Inertial coordinates

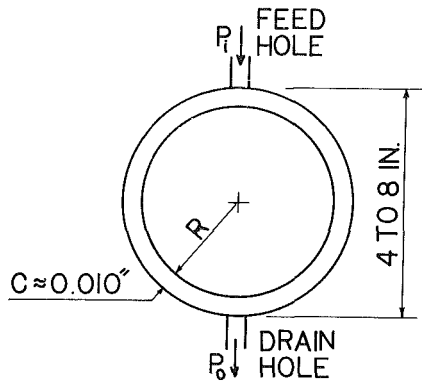

Fig. 3 A typical aircraft engine damper configuration

U = sliding velocity = $R\omega$, typically zero in a damper
C = radial clearance of damper annulus.

The relationship between system inertial coordinates and damper parameters comes through the expression for h, $\partial h/\partial x$ and dh/dt. Referring to Fig. 2, these relationships are summarized as follows:

$$\bar{e} = (X_R - X_S)\hat{i} + (Y_R - Y_S)\hat{j} \tag{2}$$

$$\dot{\bar{e}} = (\dot{X}_R - \dot{X}_S)\hat{i} + (\dot{Y}_R - \dot{Y}_S)\hat{j} \tag{3}$$

then

$$h = C - \bar{e}\cdot\hat{n} = C - (X_R - X_S)\cos\theta - (Y_R - Y_S)\sin\theta \tag{4}$$

$$\frac{\partial h}{\partial x} = \frac{1}{R}\frac{\partial h}{\partial \theta} = \frac{1}{R}[(X_R - X_S]\sin\theta - (Y_R - Y_S)\cos\theta] \tag{5}$$

and

$$\frac{dh}{dt} = -(\dot{X}_R - \dot{X}_S)\cos\theta - (\dot{Y}_R - \dot{Y}_S)\sin\theta \tag{6}$$

Typical configurations of dampers which are currently being employed in engines have done away with centering springs common in older designs. Design simplicity as well as centering-spring fatigue life are apparently the major reasons. Also, in the majority of cases, damper end seals are used because this keeps damper throughflow sufficiently low to be compatible with the overall engine lub system of pre-damper configurations. However, the disadvantage of having end seals is that a "large" damper clearance of typically 10 mils is required in order for the squeeze-film action to effectively dissipate vibration energy. From other considerations, a smaller damper clearance would be desireable (e.g., blade tip clearances). Without end seals, the optimum damper clearance is considerably smaller. Engines with higher oil flow capacity and no damper end seals are probably the trend on future designs.

Two typical configurations are shown in Figs. 3 and 4. The end seal configuration in Figs. 3 and 4(*a*) essentially divides the lubricant annulus into two pressure domains whereas that in Fig. 4(*b*) is a one-domain problem. In both cases, the "long-bearing" solution is appropriate. Conversely, without end seals a "short-bearing" type of solution is appropriate. Both solutions are options in the software package developed in this work.

For the "long-bearing" solution, $\partial p/\partial z << \partial p/\partial x$, and the following ordinary differential equation (two-point boundary value problem) is obtained from equation (1), (for $U = 0$).

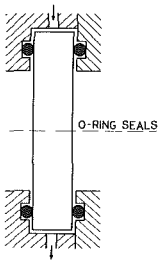

Fig. 4(*a*) Configuration frequently used in military applications

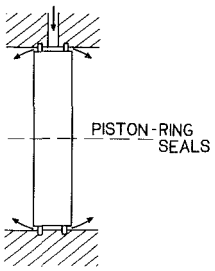

Fig. 4(*b*) Configuration frequently used in commercial applications

$$\frac{d}{dx}\left(\frac{h^3}{\mu}\frac{dp}{dx}\right) = 12\frac{dh}{dt} \tag{7}$$

For configurations with no end seals, an improved adaptation of the short-bearing approach is used by implementing the parabolic assumption of O'Donoghue [9]. The following approximation is made.

$$p(\theta,z) = p(\theta,0)\left(1 - \frac{4z^2}{L^2}\right) \tag{8}$$

This assumes an axially symmetric axial pressure distribution at every circumferential location, and results in the following pressure field equation.

$$\frac{1}{\mu}\frac{\partial}{\partial x}\left(h^3\frac{\partial p}{\partial x}\right) = 12\frac{dh}{dt} + 8\frac{p(\theta,0)h^3}{L^2} \tag{9}$$

This is actually a first-order Fourier approximation using the parabola as the single approximative function.

A convergent approximation to the full two-dimensional Reynolds equation can be obtained, as an extension of the foregoing approach by O'Donoghue [9]. The number of Fourier terms is increased to N, resulting in N simultaneous ordinary differential equations.

$$p(\theta,z) = p_1(\theta,0)\cos\frac{\pi z}{L} + p_2(\theta,0)\cos\frac{3\pi z}{L} + \ldots$$

$$+ p_N(\theta,0)\cos\frac{(2N-1)\pi z}{L} \tag{10}$$

Substitution into the general 2-D Reynolds equation (1), followed by LHS:RHS segregation by arguments yields N ordinary differential equations, one for each $p_i(\theta,0)$, [9].

Method of Solution

Although there are computationally fast closed-form solutions available such as given in [10,11], they do not retain sufficient generality to handle the specified pressure boundaries at supply and drain ports (Figs. 3,4,5) of typical configurations. Also, they are not amenable to structural deflections of the damper elements. For these reasons, the following approach has been used. Although somewhat computationally slower than closed-form solutions, it is nonetheless computationally quite efficient, and retains the generality deemed necessary. The solution method given below is used for all three formulations (i.e., equations (7) through (10). It is described below as implemented for the long-bearing formulation.

Based on a 3-point central difference, the following long-bearing equation yields equation (11).

$$h^3\frac{d^2p}{dx^2} + 3h^2\frac{dh}{dx}\frac{dp}{dx} = 12\mu\frac{dh}{dt}$$

$$\left(\frac{dp}{dx}\right)_i \cong \frac{P_{i+1}-P_{i-1}}{2\Delta x}$$

$$\left(\frac{d^2p}{dx^2}\right)_i \cong \frac{P_{i+1}-2P_i+P_{i-1}}{\Delta x^2}$$

$$h_i^3\left(\frac{P_{i+1}-2P_i+P_{i-1}}{\Delta x^2}\right) + 3h_i^2\frac{dh_i}{dx}\left(\frac{P_{i+1}-P_{i-1}}{2\Delta x}\right) = 12\mu\frac{dh_i}{dt} \tag{11}$$

Rearranging (11) produces

$$\underbrace{P_{i+1}\left[\frac{h_i^3}{\Delta x^2} + \frac{3h_i^2}{2\Delta x}\frac{dh_i}{dx}\right]}_{D_j} + \underbrace{P_i\left[-\frac{2h_i^3}{\Delta x^2}\right]}_{C_j} + \underbrace{P_{i-1}\left[\frac{h_i^3}{\Delta x^2} - \frac{3h_i^2}{2\Delta x}\frac{dh_i}{dx}\right]}_{E_j} = \underbrace{12\mu\frac{dh_i}{dt}}_{R_j}$$

which is condensed to the following form.

$$C_jP_j + E_jP_{j-1} + D_jP_{j+1} = R_j \tag{12}$$

Employing the recursion relationship,

$$P_{j-1} = A_jP_j + B_j \tag{13}$$

equation (12) can be expressed in terms of only two adjacent grid points as follows

$$C_jP_j + E_j(A_jP_j + B_j) + D_jP_{j+1} = R_j \tag{14}$$

or

$$P_j(C_j + E_jA_j) + E_jB_j + D_jP_{j+1} = R_j \tag{15}$$

Therefore,

$$P_j = \left(\frac{-D_j}{C_j + E_jA_j}\right)P_{j+1} + \frac{R_j - E_jB_j}{C_j + E_jA_j} \tag{16}$$

which when compared to equation (13), yields the following recursion relationships:

$$A_{j+1} = -\frac{D_j}{C_j + E_jA_j} \tag{17}$$

$$B_{j+1} = \frac{R_j - E_jB_j}{C_j + E_jA_j} \tag{18}$$

From the upstream boundary condition for each domain, the $\{A\}$ and $\{B\}$ vectors are determined by starting with $A_2 = 0$, $B_2 = P_1$ (called the forward sweep).

The downstream boundary condition is inserted at the beginning of the backward sweep as follows.

$$\begin{aligned} P_{M-1} &= A_MP_M + B_M \\ P_{M-2} &= A_{M-1}P_{M-1} + B_{M-1} \\ &\vdots \quad\quad \vdots \\ P_2 &= A_3P_3 + B_3 \end{aligned} \tag{19}$$

Film rupture is handled by the following substitution. If $P_j < P_{\text{vapor}}$, set $P_j = P_{\text{vapor}}$ before computing P_{j-1}. This is equivalent to the condition $\partial p/\partial x = 0$ at the film-rupture, full-film boundary. In the case of the 2-D convergent approach indicated by equation (10), this point-by-point test is made on the local summation.

$$P(\theta_j,z) = \sum_{k=1}^{N} P_k(\theta_j,z).$$

The method of solution, although not closed-form, is noniterative and is a 1-D adaptation of the 2-D finite difference method of Castelli and Shapiro [12]. While it does entail a one-dimensional, finite-difference scheme, it requires only a very small amount of CPU time and is therefore ideally suited to time transient rotor dynamics analyses. It has major advantages over the purely closed-form approximations, e.g., [10,11], as noted earlier. These major advantages are immediate account of specified-pressure boundary conditions at feed and drain holes of a damper. Also, the finite difference approach easily permits account of static as well as dynamic deflections which alter the oil film gap geometry from ideal rigid circular shapes.

Force and Force Gradients. Forces components on rotor are computed by numerical integration of the instantaneous film pressure distribution, as is standard.

$$\begin{aligned} F_X &= -\int_{A^p}\cos\theta dA = -LR\int_{\theta_1}^{\theta_2} p(\theta)\cos\theta d\theta \\ F_Y &= -\int_{A^p}\sin\theta dA = -LR\int_{\theta_1}^{\theta_2} p(\theta)\sin\theta d\theta \end{aligned} \tag{20}$$

Stator force components are equal but opposite the rotor force components.

Force gradients (i.e., instantaneous tangent stiffness and damping) components are obtained by local "small" perturbations, as is standard.

$$[C_{ij}]_{2\times 2} = \left[-\frac{\partial F_j}{\partial \dot{X}_j}\right];\ [K_{ij}]_{2\times 2} = \left[-\frac{\partial F_i}{\partial x_j}\right] \tag{21}$$

where

$$\frac{\partial F_i}{\partial \dot{X}_j} \cong \frac{\Delta F_i}{\Delta \dot{X}_j};\ \frac{\partial F_i}{\partial X_j} \cong \frac{\Delta F_i}{\Delta X_j} \tag{22}$$

Numerical differentiation is performed with small $\Delta\dot{X}_j$ and ΔX_j increments about instantaneous conditions. This provides continuous updating of $\{F_j\}$, $[C_{ij}]$ and $[K_{ij}]$.

Application of Damper Element

For purposes of checking out the damper element coded and to demonstrate its use, two types of computations were made. First, a parametric study of damper pressure

distributions was made for a variety of specified circular orbits, for both long-bearing and short-bearing solutions. Second, a four-degree-of-freedom rotor-damper-stator model was investigated under conditions of small rotor unbalance through large rotor unbalance. These results are summarized below.

For the parametric study on pressure distribution, the following damper annulus parameters were used:

Diameter, $D = 6$ in.
Length, $L = 1.25$ in.
Radial clearance, $C = 0.010$ in.
Lubricant viscosity, $\mu = 1 \times 10^{-6}$ reyns
Angle between inlet oil port and drain port, $(\theta_i - \theta_0) = 180$ deg
Inlet oil port pressure, $P_i = 55$ psia
Drain port pressure, $p_0 = 15$ psia

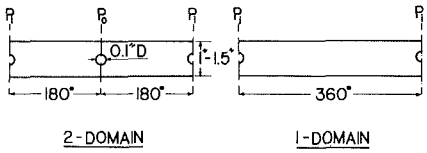

Fig. 5 Unwrapped squeeze-film pressure solution domains for configurations shown in Fig. 4

Lubricant vapor pressure, $p_v = 1.5$ psia
Orbit angular velocity, $\Omega = 3600$ cpm (377. rad/sec)

The above damper parameters are typical for modern gas turbine aircraft engines. A parametric study was made postulating the outer ring of the damper fixed and the inner ring having a constant-radius constant-velocity concentric orbit. Eccentricity ratios (i.e., orbit radius/radial clearance) from 0.05 to 0.95 were computed, both for the long-bearing and short-bearing solutions.

Circumferential center-line pressures were plotted as a function of circumferential position and time, for one period of prescribed motion. The results for the long-bearing solution are shown in Fig. 6, and for the short-bearing solution in Fig. 7. The difference between long-bearing and short-bearing solution is quite large when compared with the same radial clearance. One therefore sees why dampers with no end seals require smaller clearances to work properly than dampers with end seals.

A simple "driver" code was written (see listing [8]) which uses the damper-element code in the same manner as a general application with large finite element codes. The "driver" code is based on a four-degree-of-freedom system, i.e., planar motion of the inner and outer damper elements. This then simulates a single-mass rotor connected to a single-mass stator via the damper element. The system analyzed is shown in Fig. 8. The model is coded to simulate arbitrary rotating

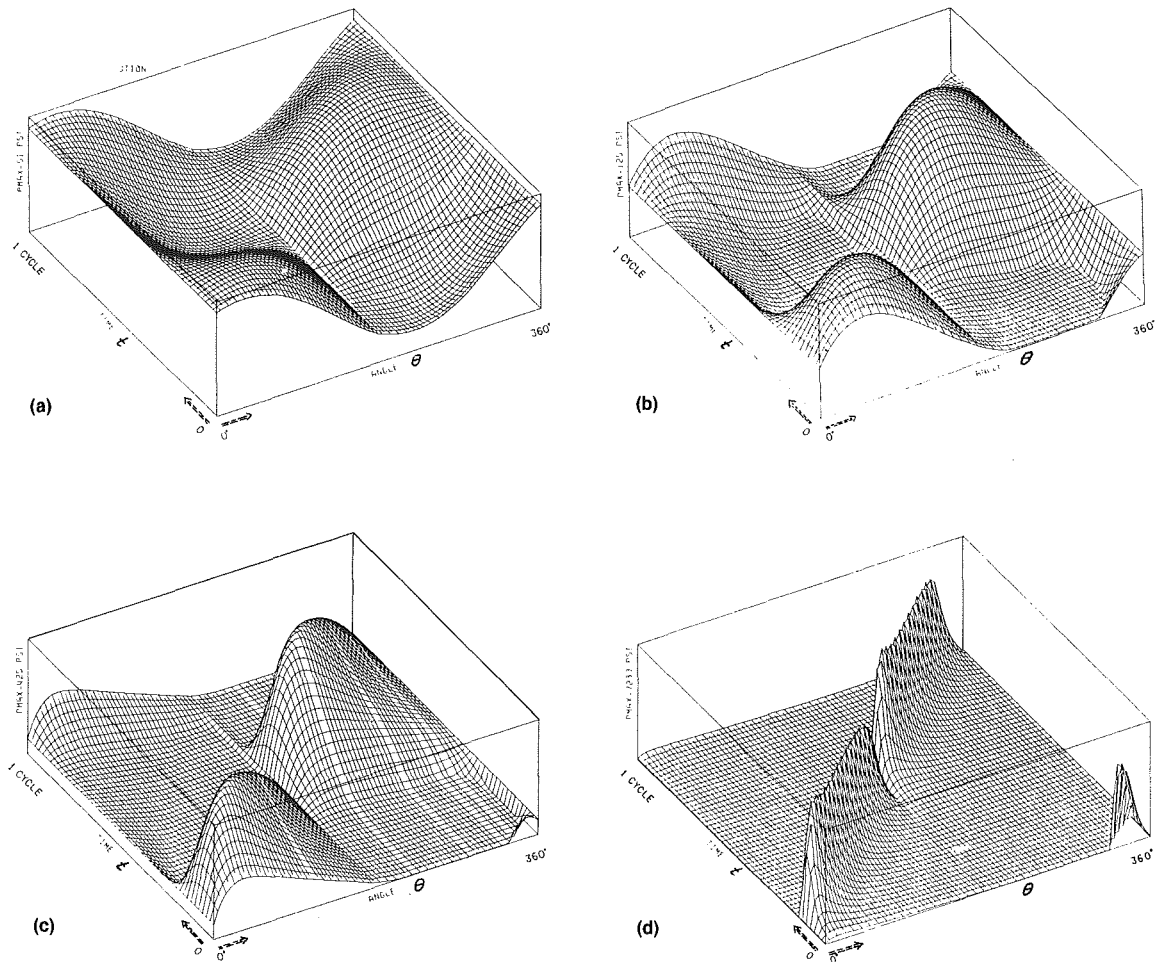

Fig. 6 Pressure distribution in circumferential direction and time of one cycle of circular orbit (long-bearing solution) (a) $e/c = 0.05$, (b) $e/c = 0.20$, (c) $e/c = 0.60$, (d) $e/c = 0.95$

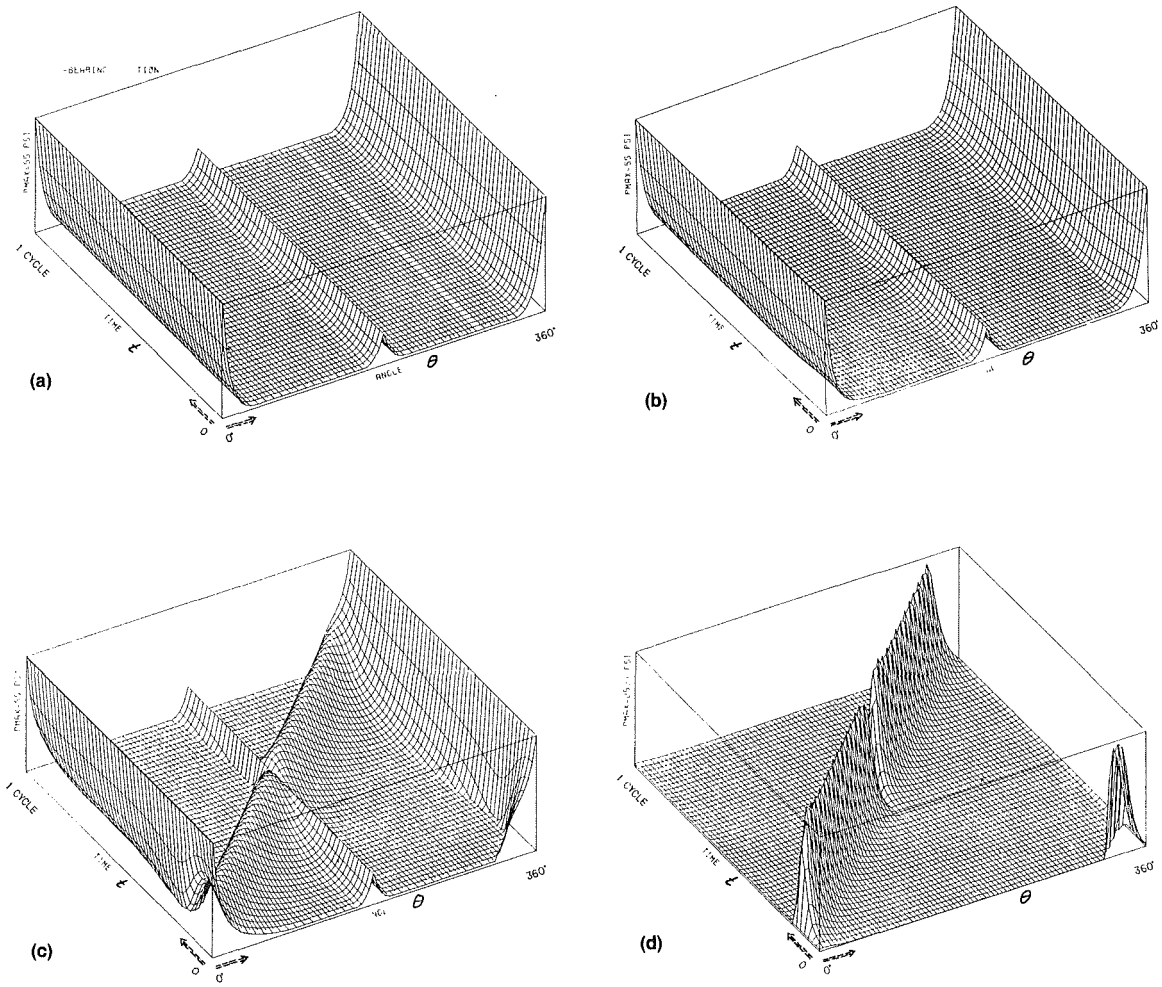

Fig. 7 Pressure distribution in circumferential direction and time of one cycle of circular orbit (short-bearing solution), (*a*) $e/c = 0.05$, (*b*) $e/c = 0.20$, (*c*) $e/c = 0.6$, (*d*) $e/c = 0.95$

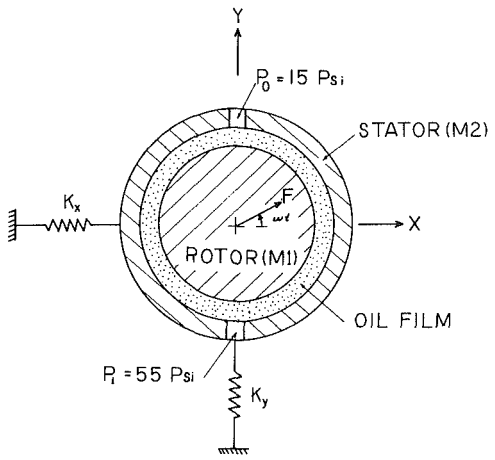

Fig. 8 Simple 2-mass, 4-degree-of-freedom test case (same damper parameters as on page 5)

and/or static radial loads. Aside from demonstration purposes, this four-degree-of-freedom model has been devised to check against the same type of system when executed with the damper element implanted into the general purpose nonlinear finite element code ADINA.

Note from Fig. 8 that the high-pressure port (i.e., feed port) is located on the bottom of the damper so as to assist "lift-off". Since centering springs are not typically used, they have been excluded in this example. Lift-off therefore requires some amount of vibration to overcome the dead-weight load. Rotating unbalance loads of 100, 200, 300, 500, and 1000 lbs were run with $\Omega = 150$ rad/s. Orbital plots were made showing rotor and stator total motion on one plot and rotor-relative-to-stator motion on a second plot. The plotted results are shown in Figs. 9 through 13.

For a 100 lb rotating load (Fig. 9) the motions shown are for a 20 cycle transient from time = 0. The rotor and stator each show close to the same motion, and their relative motion is small, with the rotor barely "lifting off". The relative orbit is essentially oscillatory. However, when the rotating load is increased to 200 lbs, (Fig. 10), the relative orbital motion shows the beginnings of orbital motion, i.e., a "cresent moon" shape as measured by numerous investigators. Further increase in magnitude of the rotating load to 300 lbs (Fig. 11) shows a well-defined steady-state total motion as well as relative motion. Note that with a 300 lbs rotating load, the relative (rotor-to-stator) orbit is still small in comparison to the radial damper clearance and confined to the region of the bottom of the damper. However, an increase of rotating load magnitude to 500 lbs causes a considerable change to the relative orbit (Fig. 12). Notice now that the relative motion of the rotor with respect to the stator fills a major portion of the

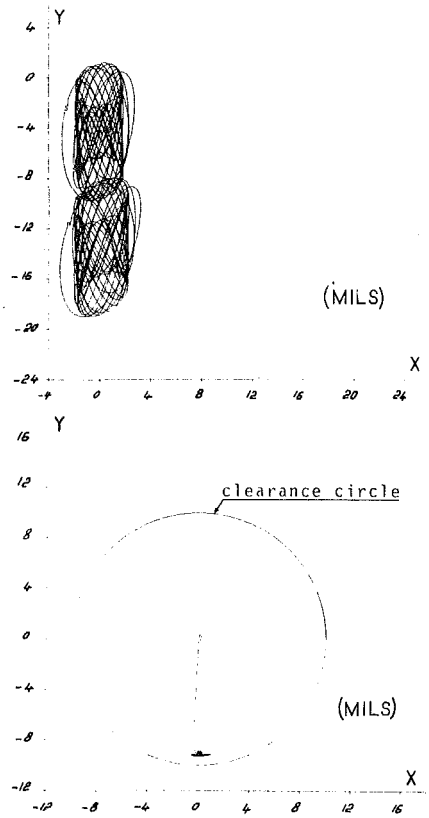

Fig. 9 Nonlinear dynamic transient of simple 4 DOE system (see Fig. 8) $|F|$ = 100 lbs, ω = 150 rad/s, M1 = M2 = 500 lbs, $Kx = Ky = 116{,}000$ lbs/in.

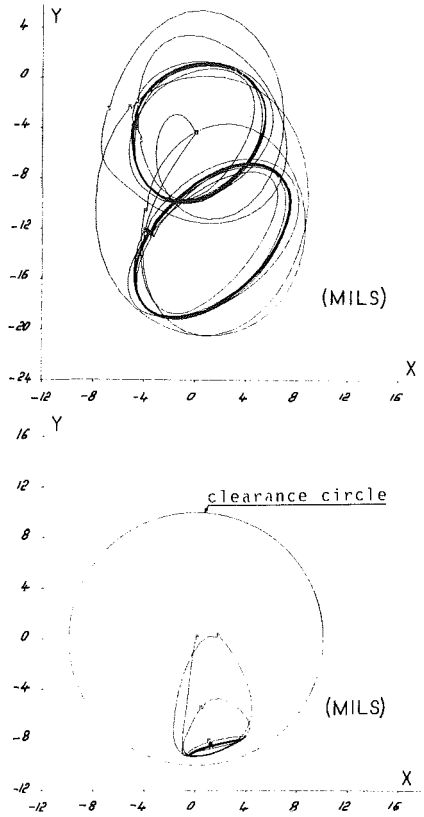

Fig. 11 Nonlinear dynamic transient of simple 4 DOE system (see Fig. 8) $|F|$ = 300 lbs, ω = 150 rad/sec, M1 = M2 = 500 lbs, $Kx = Ky = 116{,}000$ lbs/in.

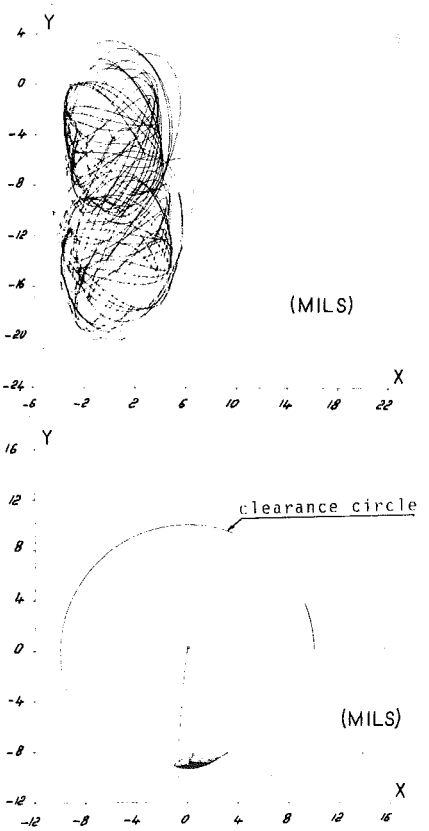

Fig. 10 Nonlinear dynamic transient of simple 4 DOE system (see Fig. 8) $|F|$ = 200 lbs, ω = 150 rad/s, M1 = M2 = 500 lbs, $Kx = Ky = 116{,}000$ lbs/in

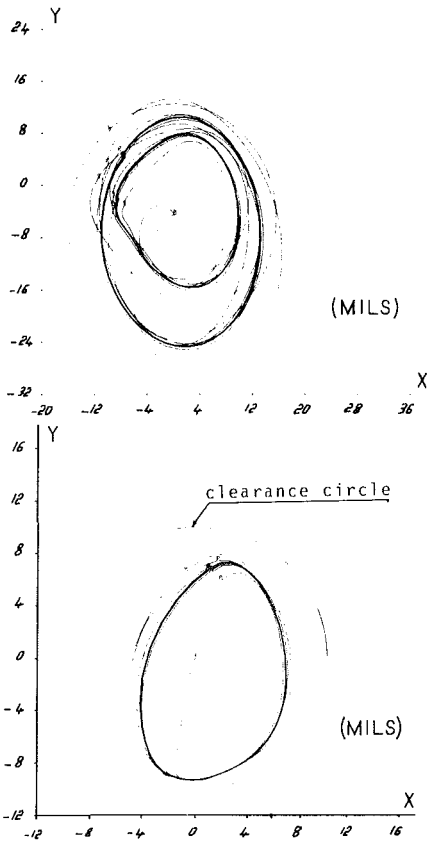

Fig. 12 Nonlinear dynamic transient of simple 4 DOE system (see Fig. 8) $|F|$ = 500 lbs, ω = 150 rad/s, M1 = M2 = 500 lbs, $Kx = Ky = 116{,}000$ lbs/in.

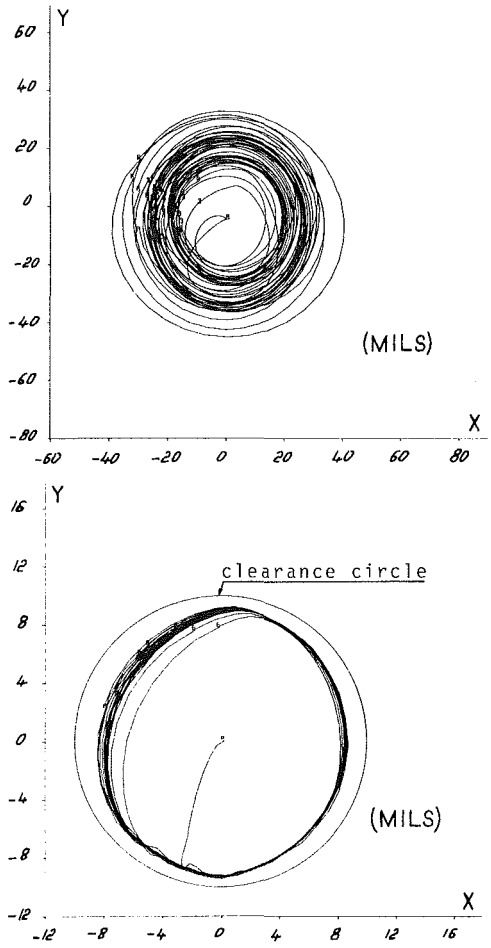

Fig. 13 Nonlinear dynamic transient of simple 4 DOE system (see Fig. 8) $|F|$ = 1000 lbs, ω = 150 rad/s, M1 = M2 = 500 lbs, $Kx = Ky = 116{,}000$ lbs/in.

clearance circle. Further increase of rotating load magnitude to 1000 lbs (Fig. 13) simply causes the steady-state relative orbit to expand and fill even more of the damper clearance circle.

Summary

This paper summarizes the work completed on the first-year effort of a three-year project. A detailed scope of work for the remaining two-year effort is given in reference [8]. The work completed and presented in this paper has produced (*i*) an overall solution strategy to the general engine dynamics problem, (*ii*) a clear definition of where present efforts should be concentrated to utilize available and proven FE codes, and (*iii*) a squeeze-film damper software package ready for implant into available FE codes.

Acknowledgment

The work reported in this paper was sponsored by NASA Lewis Research Center under NASA Grant NSG-3283. The NASA coordinator on this grant was Dr. C. C. Chamis, whose suggestions and encouragement are greatly appreciated.

References

1 Fertis, D. G., "Dynamics and Vibrations of Structures," Wiley, New York, 1973.

2 Hibner, D. H., "Dynamic Response of Viscous-Damped Multi-Shaft Jet Engines," *AIAA Journal of Aircraft*, Vol. 12, 1975, pp. 305-312.

3 Adams, M. L., "Nonlinear Dynamics of Flexible Multi-Bearing Rotors," *Journal of Sound and Vibration*, Vol. 71, No. 1, 1980, pp. 129-144.

4 Belytschko, T., "Nonlinear Analyses-Descriptions and Numerical Stability," *Computer Programs in Shock and Vibration*, ed., W. Pilkey and B. Pilkey, Shock and Vibration Information Center, Washington, D.C., 1975, pp. 537.

5 Zienkiewicz, O. D., "The Finite Element Method," McGraw Hill, London, 1977.

6 Felippa, C. A., and Park, K. C., "Direct Time Integration Methods in Nonlinear Structural Dynamics," presented at FENOMECH, University of Stuttgart, 1978.

7 *Structural Mechanics Computer Programs*, edited by Pilkey, W., Saczalski, K. and Schaeffer, H., University Press of Virginia, Charlottsville, 1975.

8 Adams, M. L., Padovan, J., and Fertis, D. G., "Finite Elements for Rotor/Stator Interactive Forces in General Engine Dynamic Simulation, Part 1: Development of Bearing Damper Element," (to appear as NASA Report on Grant NSG-3283).

9 O'Donoghue, J. P., Koch, P. R., and Hooke, C. J., "Approximate Short Bearing Analysis and Experimental Results Obtained Using Plastic Bearing Liners," *Proc. Institute of Mechanical Engineers*, Vol. 194, 1969, pp. 190-196.

10 Rhode, S. M., and Li, D. F., "A Generalized Short Bearing Theory," ASME *Journal of Lubrication Technology*, Vol. 102, No. 3, 1980, pp. 278-282.

11 Barrett, L. E., Allaire, P. E., and Gunter, E. J., "A Finite Length Bearing Correction Factor for Short Bearing Theory," ASME *Journal of Lubrication Technology*, Vol. 102, No. 3, 1980, pp. 283-290.

12 Castelli, V., and Shapiro, W., "Improved Method for Numerical Solutions of the General Incompressible Fluid Film Lubrication Problem," ASME *Journal of Lubrication Technology*, Vol. 89, No. 2, 1967, pp. 211-218.

R. P. Tolokan

Manager, Applications Engineering.

J. C. Nablo

Product Engineer.

J. B. Brady

Product Development Engineer.

Brunswick Corporation,
Technetics Division,
DeLand, Fla. 32730

Ceramic to Metal Attachment Using Low Modulus BRUNSBOND® Pad

BRUNSBOND® Pad is a low modulus sintered fiber metal material developed for attaching high temperature ceramic coatings to metal substrates. The fiber metal pad acts as a compliant strain absorbing interlayer to accomodate the differences in thermal expansivity and operating temperature between the ceramic and metal substrate. Ceramic coatings, 0.060 - 0.125 in. thick, remain intact on metal substrates through severe multiple cycle thermal excursions. The fiber metal pad is comparable in insulating value to the ceramic coating. Applications include ceramic thermal barrier coatings for high temperature gas turbine engine seals and combustors, MHD electrodes, and internal combustion engine insulators.

Introduction

Ceramic thermal barrier coatings are used extensively to protect metal substrates exposed to high temperature, erosive and corrosive environments. These coatings are very beneficial for insulation and corrosion protection but are severely limited in application by problems of maintaining attachment to the metal substrate. Ceramic to metal joints are impaired by the significant difference in coefficients of thermal expansion between ceramic and metal. This expansivity difference imposes substantial stress at the ceramic-metal bondline during thermal cycling which leads to fracture and failure by spalling of the ceramic coating. Adherence of ceramic coatings has been improved through the development of intermediate bond coats. Nevertheless, ceramic coatings are generally limited to thicknesses of 0.010 - 0.040 in. (0.25-1.0mm) to maintain coating adherence in a thermally stressed environment. Limiting thermal excursions and matching ceramics to low expansivity alloys is useful but does not provide an adequate solution to the attachment problem for high temperature ceramic-metal systems cycled through a wide temperature range. One method for improving ceramic attachment is to introduce an intermediate, expansivity compensating layer between metal and ceramic which can absorb the stress generated during thermal cycling. A sintered, oxidation resistant structure of metal fibers was developed to provide a compliant, low modulus structure which can absorb the bondline stresses between ceramic and metal. This intermediate compliant fiber metal pad allows the ceramic-metal composite to withstand severe thermal shock without delamination of the ceramic coating.

Brunswick Corporation manufactures metal fibers and sintered fiber metal products in its DeLand, Florida plant. Fiber metal products are made from randomly oriented fibers which are sintered for strength. A wide range of properties can be obtained by controlling product fiber diameter, porosity (or density), and sintering conditions. Fiber metal products include FELTMETAL® abradable seals and acoustic media, filters, wicks, gaskets, and other products.

Development of products for ceramic-metal attachment has its origins in the use of nickel-chromium alloy fiber metal abradable seals in the compressor sections of gas turbine engines. These products are useful to 1100°F (600°C) for long term operation. To achieve higher temperature operating capability, the iron-nickel-chromium-aluminum BRUNSLLOY® abradable seal products were developed for turbine seal applications to 1700°F (925°C). For even higher operating temperatures, metal systems are approaching their operating limit and ceramic systems are being evaluated for temperatures greater than 2200°F. The fiber metal low modulus ceramic attachment concept was developed as an interlayer between ceramic and metal for ceramic seal applications. The fiber metal layer allows the ceramic seal to withstand the cyclic thermal stresses of the gas turbine engine without delamination.

The Attachment Concept

Use of an intermediate layer between the ceramic and metal substrate has been investigated by others as a means of improving ceramic attachment. Low expansivity alloy intermediates are used for lower temperature applications. The graded alpha technique is also used wherein layers of material between the ceramic and metal substrate are graded in expansivity from a high expansivity layer on the metal side to a low expansivity layer on the ceramic side. By controlling the thermal and mechanical properties of each layer, the ceramic to metal attachment can be maintained. While the graded expansivity approach is useful, it is a complex manufacturing procedure requiring good control of intermediate layer application.

Ceramic attachment can be approached by introducing a

Contributed by the Division of The American Society of Mechanical Engineers and presented at the International Gas Turbine Conference, Houston, Texas, March 8-12, 1981. Manuscript received by the Gas Turbine Division, December 18, 1980. Paper No. 81-GT-60.

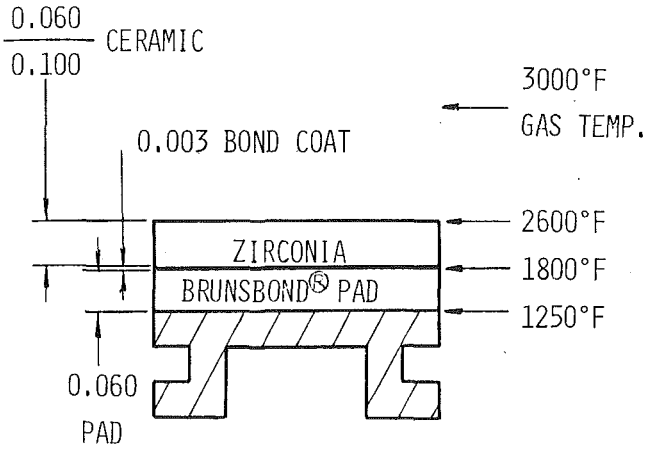

Fig. 1 High temperature ceramic seal cross section

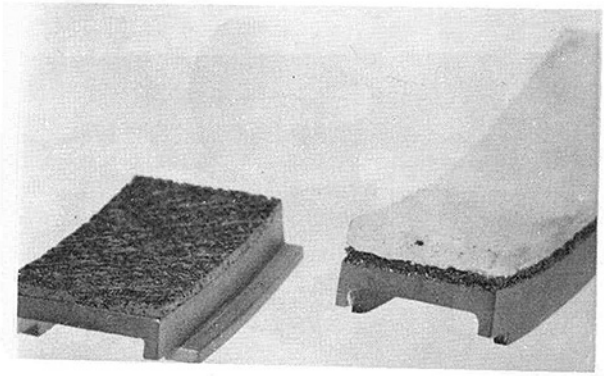

Fig. 2 Test hardware showing BRUNSBOND® Pad - zirconia ceramic and pad on metal backings

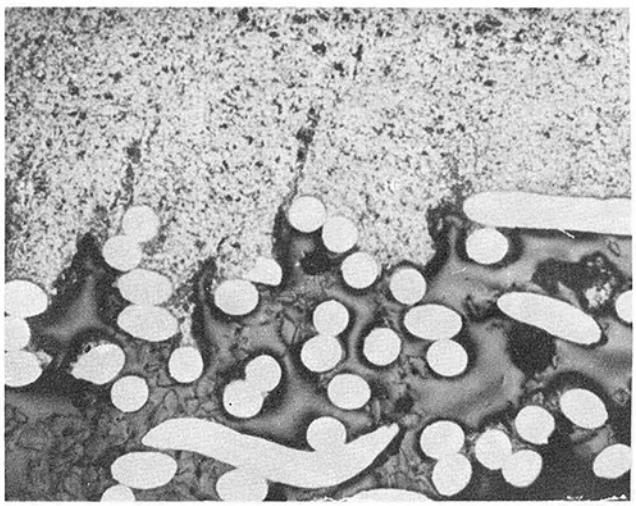

Fig. 3 Cross section of the ceramic to pad interface (25X)

low modulus compliant strain isolator intermediate between the ceramic and metal. This strain isolator will elastically absorb the stresses generated during thermal cycling by the mismatch in the coefficients of thermal expansivity of the ceramic and metal and by the difference in temperature of the ceramic and metal components. Fiber metal materials are uniquely suited as a strain absorbing layer due to the inherent properties of these structures. Fiber metal structures are composed of randomly arrayed fibers which are sintered together to produce a fiber network of continuous porosity. These materials can be treated as a three dimensional grid whose mechanical and thermal properties are a fraction of the properties of the solid alloy from which the product is made. Properties vary and are controlled by product density (percent by volume of solid metal). The higher the product density, the closer fiber metal product properties will approach the properties of the solid alloy.

BRUNSBOND® Pad is the designation chosen for fiber metal products used for ceramic attachment. Fiber metal materials are low modulus products with an elastic modulus lower than either the metal substrate or the ceramic. Thus, the fiber metal layer takes up the strain induced by the expansivity mismatch and reduces the stress transmitted to the ceramic. The fiber metal interlayer also absorbs the distortion induced initially as the very hot ceramic expands rapidly relative to the cooler metal backing. Fiber metal density is chosen to achieve a balance between product compliance and strength. Products also have a high elastic range and will allow up to 2 percent elongation to failure. The BRUNSBOND® Pad approach provides a relatively simple, single intermediate layer method for attaching ceramics to a metal substrate. The fiber metal pad is brazed to the metal substrate. Usually, the ceramic is applied by plasma spraying. The pad is first coated with a suitable bondcoat (0.003 in. or 0.076mm thick) to improve ceramic adherence, followed by ceramic spraying. The plasma sprayed ceramic penetrates the surface porosity of the fiber metal pad to form mechanical and chemical bonding between the ceramic and pad. Presintered ceramics can also be applied to the pad by metallizing the ceramic and direct brazing.

The ceramic attachment concept is illustrated in Fig. 1 for a high temperature turbine seal application. At operating temperature a substantial temperature drop is achieved through the ceramic and pad. The compliant BRUNSBOND® Pad interlayer allows a relatively thick ceramic coating to be used for insulation without delaminating. The fiber metal pad in itself is a good insulator because of its porosity. The pad is equivalent or better as an insulator than the high density ceramic coating. The insulating value of the pad improves the thermal barrier effect of the ceramic-pad system and allows large temperature drops to be taken across both the ceramic and BRUNSBOND® Pad.

Figure 2 shows two views of a ceramic attachment test piece using a strain absorbing fiber metal pad. The part on the left shows the BRUNSBOND® Pad as brazed to the metal backing. The part on the right shows backing, pad and plasma sprayed zirconium oxide ceramic coating.

A cross section of the ceramic-pad interface is shown in Fig. 3 while the pad-metal backing interface is shown in Fig. 4. Note the good penetration of both ceramic and braze alloy into the pad. The porous nature of the pad surface is illustrated in Fig. 5.

BRUNSBOND® Pad products can be made from different alloys to obtain required properties. The alloy most used is Hoskins 875 (FeCrAl) which was chosen for its good long term oxidation resistance to 1800°F (1000°C). Nickel has also been used for MHD electrodes for improved electrical conductivity. 347SS is used for lower temperature applications. The fiber metal pad is formable as illustrated in Fig. 6.

Attachment Product Properties

Product Description. The BRUNSBOND® Pad compliant layer consists of a mat of randomly oriented fibers, diffusion bonded (sintered) together at high temperatures. The mat can be formed to very low densities, approaching 10 percent of the theoretical density of the base alloy. The upper limit of density is approximately 70 percent but as compliant layers, 30 - 60 percent is a more practical limit. Product area densities (weight per unit area) ranging from 0.20 to 5.5 lb/ft^2 (0.10-2.7 gr/cm^2) have been produced for widely varying ap-

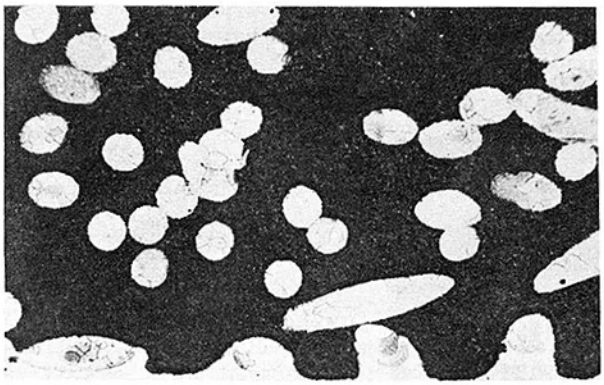

Fig. 4 Cross section of the braze bondline between BRUNSBOND® Pad and metal backing (25X)

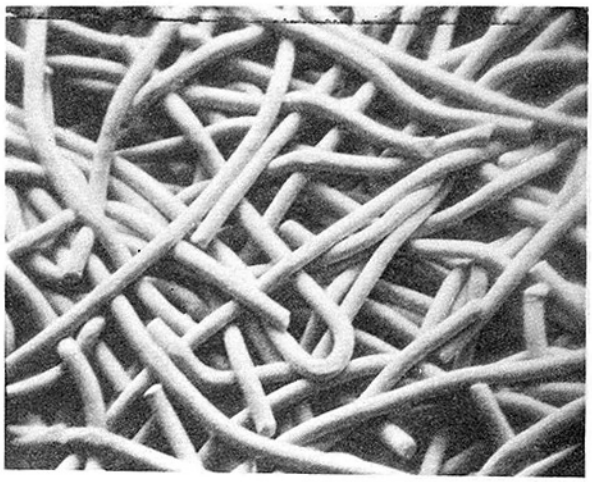

Fig. 5 SEM macrograph of a Hoskins 875 BRUNSBOND® Pad surface (10X)

plications. Any alloy that is sufficiently ductile to be drawn into fine wire and is sinterable can be processed into BRUNSBOND® Pad. Commonly used alloys are nickel, stainless steel and alloy 875[1]. Alloy 875 is a solid solution alloy of FE - 22.5 percent CR-5.5 percent AL composition, consisting of a ferrite matrix with chrome and titanium carbides. Compositional stability of the alloys is maintained even during high temperature sintering. Alloy selection is based primarily on the anticipated operating temperature of the product with nickel and stainless steel used for the low temperature ranges and Alloy 875 for the high temperature range. Fiber diameter, while not a factor in most mechanical properties, does have a strong effect on oxidation resistance. Large fibers have lower specific surface areas and as a result, possess better oxidation/corrosion resistance.

Product density is the single most important variable in the design of the compliant layer because it determines mechanical strength (UTS, yield strength, modulus) and thermal conductivity. In the majority of current BRUNSBOND® Pad applications, the density is in the 35 - 45 percent range (2.8 - 3.6 gm/cc). Product percent density is defined as the ratio of the apparent density of the fiber metal product to the density of the solid alloy from which the fibers are produced times 100. As a rule of thumb, increasing the density of a product 7 points will aproximately double the ultimate tensile strength.

[1] Hoskins Alloy 875, Hoskins Mfg. Co., Detroit, Mich.

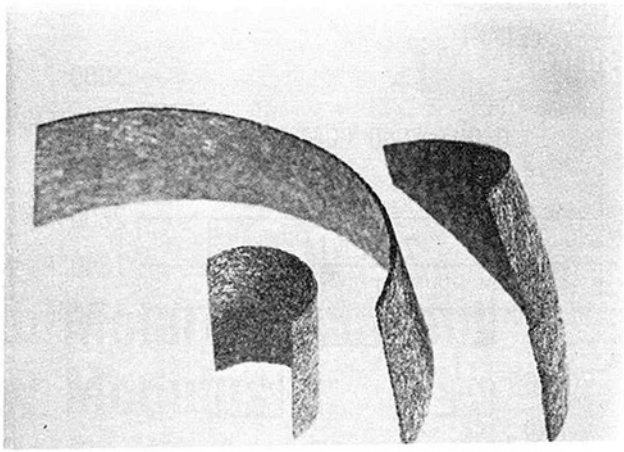

Fig. 6 As formed configurations of BRUNSBOND® Pad

An important property of all fiber metal structures, and specifically BRUNSBOND® Pad, is the anisotropic nature of product mechanical and thermal properties. Because many more fibers are aligned parallel to the *X-Y* plane (plane of the sheet) than parallel to the *Z* plane (thickness direction), the mechanical strength and thermal conductivity of the product are much higher in the *X-Y* plane. For most BRUNSBOND® Pad products, the *Z* plane ultimate tensile strength (flatwise UTS) is about 15 - 35 percent of the *X-Y* strength. This physical anisotropy must be considered when designing for BRUNSBOND® Pad applications.

Mechanical Properties. Basic mechanical properties testing to determine the short term tensile and compressive stress/strain characteristics for H-875 BRUNSBOND® Pad, 35 percent dense at 0.100 in. thick (0.25 cm), has been performed at room and elevated temperatures. From these tests, stress/strain relationships, ultimate tensile and 0.2% offset yield strengths as well as modulus of elasticity, have been derived. Properties testing was carried out using Instron universal testers, equipped with various load cells and a high temperature resistance type tube furnace for elevated temperature tests. Specially constructed Inconel 625 jaws were used for all high temperature tests. Because of its anisotropic nature, the pad was tensile tested in both the *X-Y* (4.0 in. gage length - 10.2 cm) and *Z* planes (0.100 in. or 0.25 cm gage length) at room temperatures and 1500°F (816°C). Crosshead movement was used to determine sample strain in all tensile tests.

Compressive stress/strain properties of the pad are different than tensile properties because the compressive forces tend to increase the sample density, thereby increasing its load bearing capacity. Single layer, 0.100 in. thick (0.25 cm) one quarter square in., (1.5 cm^2) samples were tested in a specially built test rig equipped with a high temperature furnace. Because compressive sample strains in the *Z* plane were so small, an accurate extensometer, mounted outside the hot zone, was used to measure sample strain.

Results of the properties testing are summarized in Table 1. The low elastic modulus of the fiber metal pad is evident with a room temperature tensile modulus of 1.2 million psi and a room temperature compressive modulus of 120,000 psi. The anisotropic properties of the fiber metal product are also shown in Table 1. Both strength and modulus are significantly greater in the *X-Y* plane (or plane of the sheet) than in the *Z* plane (or thickness direction). *Z* plane strength is seen to be 20 percent of the *XY* plane values. The thermal conductivity of fiber metal products is also lowest through the product thickness making the product a good insulator. This direc-

Table 1 Mechanical properties of 35 percent Density Hoskins 875 BRUNSBOND® Pad - 0.100 in. thick

PROPERTY & TEST PLANE		TEST TEMP. (°F) 70	1500
ULTIMATE STRENGTH (PSI)			
Tensile	X-Y Plane	4850	1000
	Z Plane	1000	750
Shear		2200	590
0.2% OFFSET YIELD STRENGTH (PSI)			
Tensile	X-Y Plane	4600	850
	Z Plane	850	690
Shear		1950	550
Compressive	Z Plane	3300	520
STRAIN AT UTS (%)			
Tensile	X-Y Plane	1.0	5.6
	Z Plane	7.5	11.0
Shear		13.5	14.0
MODULUS OF ELASTICITY (PSI X 10^3)			
Tensile	X-Y Plane	1150	260
	Z Plane	25.0	9.0
Shear		21.0	13.0
Compressive	Z Plane	120	26.0
Flexure		1200	-

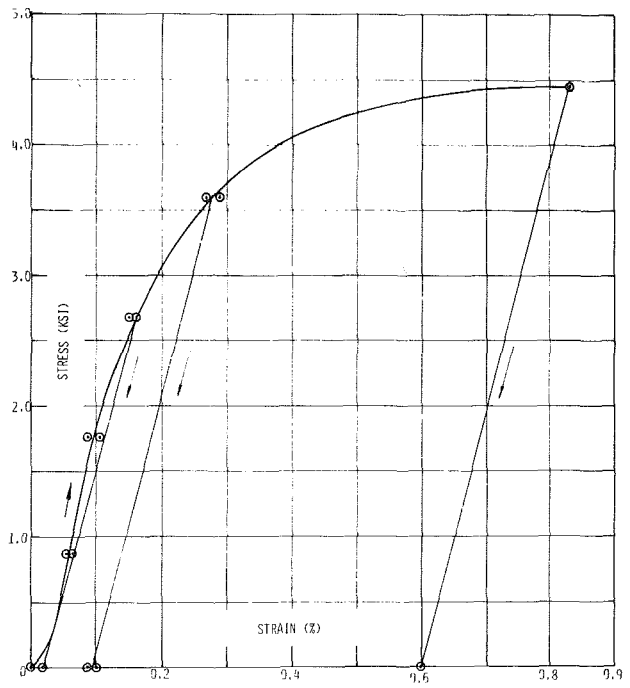

Fig. 7 X-Y tensile stress/strain @ room temperature for 35 percent dense H-875 BRUNSBOND® Pad

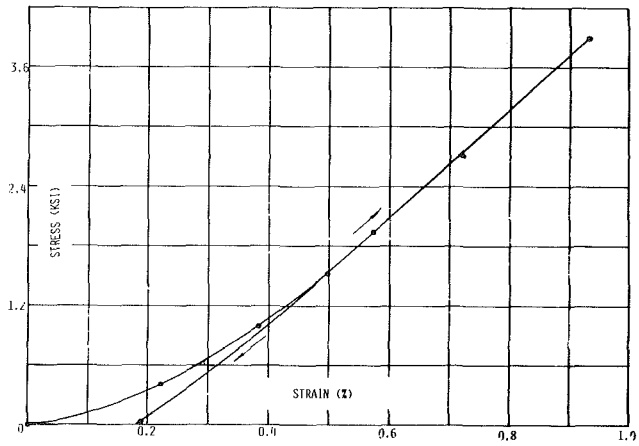

Fig. 8 "Z" compressive stress/strain @ room temperature for H-875 BRUNSBOND® Pad

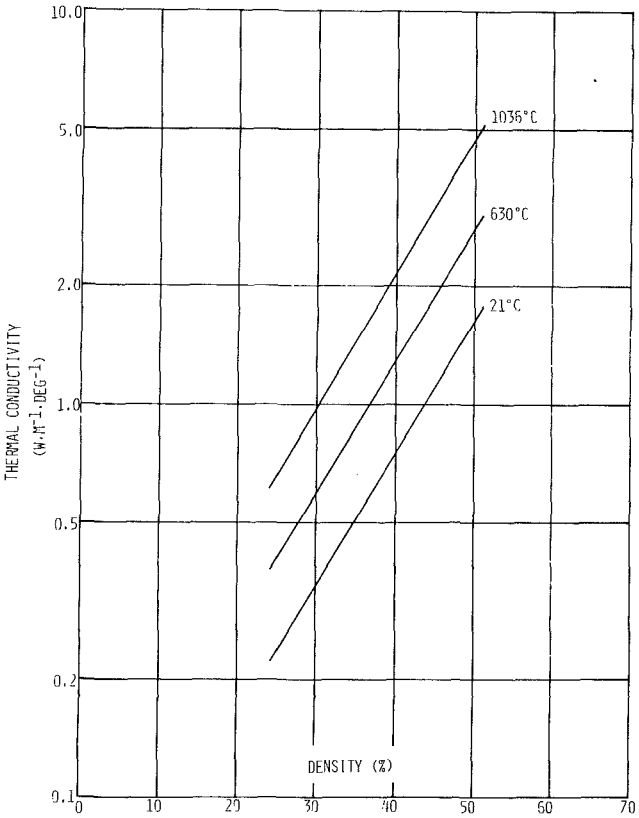

Fig. 9 Thermal conductivity versus density for H-875 BRUNSBOND® Pad

tionality of properties can be used to advantage and must be considered in component design.

Increasing product test temperature to 1500°F (816°C) reduces tensile strength and modulus to about 20 percent for *X-Y* properties and 60 percent for *Z* plane properties. *Z* plane properties are lower at room temperature but change less in going to high temperature. This effect could be caused by fiber reorientation and strengthening in *Z* plane elongation at elevated temperatures. At room temperature, fibers apparently fail at bond sites without significant reorientation or elongation. The effect of high temperature on fiber metal properties is proportional to the temperature effect on the solid alloy from which the fibers are made. Thus, if the effect of temperature on alloy properties is known, the high temperature properties of fiber metal made from that alloy can be predicted.

Yield strength and tensile strength in both fiber metal planes are nearly equal indicating a brittle type failure. In tension and compression, fiber metal products show no discontinuity as the applied load is increased and the proportional limit is not obvious. In compression, fiber metal products have no ultimate strength as such because the product does not fail; it will continue to compress and increase in resistance to compression as it densifies until essentially a solid compact results.

Figure 7 shows a typical tensile stress/strain curve for 35 percent dense H-875 BRUNSBOND® Pad at room tem-

perature in the X-Y plane. Testing was performed by successive load/unload cycles with sample measurements taken at each step. The curve shows the amount of permanent set taken by the sample during each cycle. Slight permanent set was noted above 2500 psi, (17.2 MPa) while considerable set occurred above 3500 psi (24.1 MPa).

A plot of compressive stress/strain is presented in Fig. 8 for H-875 pad. Note that the sample did not exhibit a distinct yield point up to the maximum stress of 4000 psi (27.6 MPa). Permanent deformation during the testing totaled 0.18 percent which corresponds to an elastic recovery of 82 percent. Elastic recovery, of course, is greatly reduced at elevated temperatures.

Thermal Conductivity. BRUNSBOND® Pad, like other low density fiber products, is a good thermal insulator. The product is influenced more by the air filling its pores than by its metal fiber skeleton. In fact, H-875 BRUNSBOND® Pad at 35 percent density is as good an insulator as many plasma sprayed ceramic thermal barrier coatings such as yttria stabilized zirconia. It is a better insulator than many dense presintered ceramics like alumina. The advantage of good insulation in ceramic attachment applications is that less cooling air is needed on the solid metal side of the composite and lower grade materials may be substituted. The pad is self insulating and under high heat flux conditions, proper design is required to prevent pad overheating at the pad-ceramic interface.

Figure 9 shows the thermal conductivity for H-875 BRUNSBOND® Pad at three temperatures over the 25 to 50 percent density range. This plot represents an extrapolation of thermal conductivity measurements of 35 and 41 percent dense pad tested over the range of temperatures.. The measurements were made by an independent lab using the guarded hot plate method. The conductivity of 35 percent dense pad at room temperature was measured to be 0.5 W-m^{-1} - deg^{-1} or about 2.7 percent of the solid alloy. This measurement is made through the thickness (Z plane) of the material. From Fig. 9, the significant effect of product density on through thickness thermal conductivity is apparent. Product density is an important factor in controlling product thermal conductivity as well as mechanical properties. Product strength and thermal conductivity are increased significantly as product density is increased.

Oxidation Life. Most ceramic attachment applications place the compliant layer in a relatively hostile environment in terms of temperature, stress, and corrosive elements. For these reasons, it is imperative that the pad have excellent oxidation/corrosion resistance. Alloy 875 was selected for high temperature applications because of its excellent oxidation life at temperatures up to 2100°F (1150°C) in air. With its high aluminum content (5 - 6 W/o), Alloy 875 forms a protective layer of aluminum oxide (Al_2O_3) during high temperature exposure to air. This oxide film is very stable and limits the diffusion of oxygen to the interior of the fibers. Silicon in the alloy helps to promote oxide layer adherence during severe thermal shock.

Samples of sintered pad and unsintered wire (all 5.6 mil fiber dia 0.14mm) were oxidized at 1900 and 2100°F (1040 and 1150°C) in air in zircon boats. Accurate weighings were made at selected intervals to determine weight gain. Results were plotted and extrapolated to 10,000 hours. Fig. 10 shows oxidation life (in still air) versus temperature, for a maximum weight gain of 7 percent. A 40 percent reduction of ultimate tensile strength normally occurs after oxidation to this level.

In using the ceramic-pad system, it is necessary to shield or protect the edges of ceramic-pad components. Edge protection prevents hot gases from flowing around the ceramic surface and overheating and rapidly oxidizing the strain isolator pad.

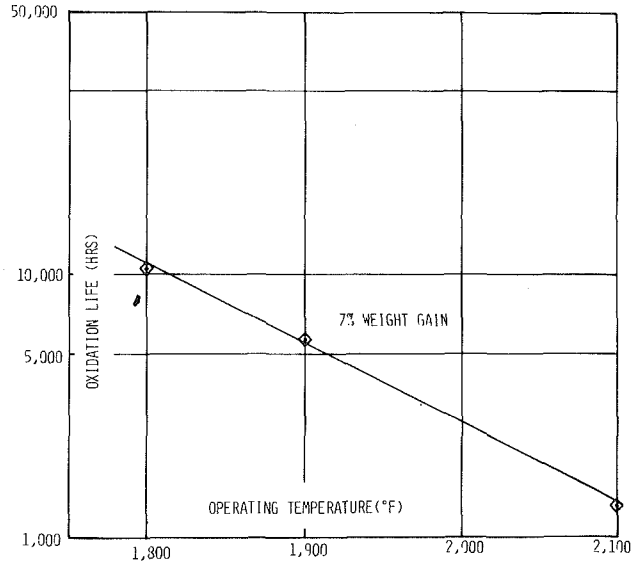

Fig. 10 Oxidation life versus operating temperature for H-875 BRUNSBOND® Pad - 7 percent limiting weight gain

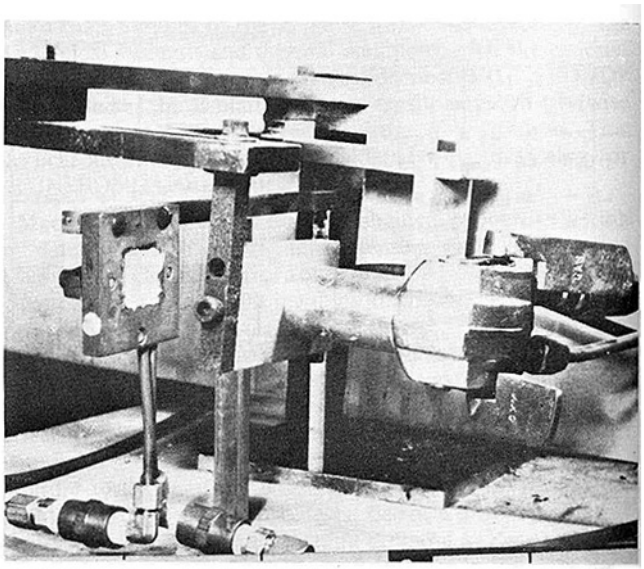

Fig. 11 Thermal shock rig showing front of sample in heating position

Pad to Substrate Attachment. The compliant layer must be attached to the solid metal substrate in such a way as to provide a thermally and mechanically stable base for the ceramic top coat. This attachment is normally provided by brazing with an alloy that is compatible with both pad and substrate and is chemically stable at the maximum operating temperature of the bondline. Properly brazed, the bond strength will always exceed the pad flatwise or shear strength at all points.

For high temperature applications, the nickel base braze alloys, such as AMS 4777 and AMS 4782, have been fully developed for attaching Alloy 875 BRUNSBOND® Pad to nickel, iron or cobalt base superalloy components. For lower temperatures, copper or silver base alloys have been used. The brazing process consists of pad preparation, fixturing, and heat treating. The pad is formed by various methods to fit the shape of the component and is assembled to the substrate with braze alloy on the surface to be brazed. Mechanical fixturing is applied to the assembly and tightened to a pre-set pressure. This assembly is then furnace brazed, usually in vacuum or

dry hydrogen. After brazing, the part is inspected and cleaned by grit blasting prior to application of the ceramic top coat. A nondestructive method for testing braze bond integrity is currently under investigation.

Thermal Shock Testing

Thermal shock testing of plasma sprayed ceramic thermal barriers applied to metal substrates using an intermediate BRUNSBOND® Pad attachment has been performed both in house and in several external test programs [1,2,7]. Results of thermal shock testing have shown that a well designed ceramic-pad-metal substrate can withstand as many as one thousand thermal shock cycles without delamination of the ceramic. A typical test rig is shown in Figure 11. The ceramic face of the sample is heated to temperatures of 2600 - 3000°F (1240 - 1650°C) while the backside of the metal substrate is maintained at 900 - 1000°F (500°C) by air cooling. After a typical 3 minutes at temperature, the heat source is removed and the sample is air cooled for 1 minute dropping the temperature of the ceramic face to below 1000°F (540°C). Testing to 1000 cycles was chosen as a useful indicator of ceramic life. After 1000 cycles, the ceramic-pad system shows pitting and microcracking of the ceramic surface to relieve stresses. Ceramic surface microcracks close up as the ceramic is heated. The ceramic remains intact attached to the pad and metal substrate without impairment of its insulating capability. Thermal shock testing is being used to evaluate and improve ceramic-pad design. Ceramic-pad systems are also currently being tested in a variety of engine applications.

Applications

The usefulness of the BRUNSBOND® Pad ceramic attachment concept is in thermal barriers which are subjected to high temperatures and large thermal excursions. The fiber metal pad absorbs much of the strain caused by the thermal expansivity mismatch and minimizes the stress on the ceramic at the ceramic-pad interface.

One application is for attachment of zirconia ceramic abradable seals for the first turbine stage of advanced gas turbine engines [7]. An insulating ceramic seal system is required to withstand turbine inlet temperatures up to 3100°F which will occur as turbines operate at higher temperatures for improved efficiency. Ceramic seal systems can take the high temperatures and provide insulation to contain the heat in the turbine and minimize heat transfer to the metallic case. Substantial development progress has been made over the past two years in producing abradable, thermal shock resistant ceramic coatings for engine seal applications. A typical ceramic seal ring consists of individual 30 percent arc segments which together form a ring. The seal consists of a cobalt or nickel base alloy backing shoe to which a 35 percent density Hoskins 875 BRUNSBOND® Pad is brazed. After applying a NiCrAlY bond coat about 0.003 in. (0.0076cm) thick, an yttria stabilized zirconia is plasma sprayed onto the pad 0.060 – 0.100 in. (0.15 - 0.25 cm) thick to form the ceramic seal. A ceramic seal schematic is shown in Fig. 2. Ceramic-pad thermal barriers are also suitable for other turbine components such as vane endwalls.

Attached plasma sprayed ceramics are also being used as thermal barriers for gas turbine engine combustors. As combustion temperatures are raised for greater thermal efficiency, metallic combustors even with a thin ceramic coating suffer significantly reduced operating life. Using the ceramic-pad thermal barrier approach dropped the outside temperature of the combustor 500°F (280°C) in a typical application to greatly extend combustor life. Optimization of combustor thermal barrier designs should also allow cost reduction through use of less oxidation resistant burner alloys. The ceramic-BRUNSBOND® Pad insulating system offers substantial benefits as a thermal barrier liner and should see increasing application in combustors.

Another application for ceramic attachment is in electrodes for MHD reactors. A set of electrodes was prepared jointly with the Advanced Energy Systems Division of Westinghouse Electric Corp. for testing in the U-02 channel on the joint US-USSR nonslagging gas fired MHD program. Electrodes consisted of electrically conductive nickel fiber metal pads brazed to a water cooled copper base. A presintered conductive lanthanum chromite ceramic was brazed to the pad surface. Test results [5] indicated that the nickel fiber metal pad performed satisfactorily in terms of attachment, thermal and electrical conductivity. The U-02 channel was operated at temperature for 132 hours during the test, with 107 hours at full MHD conditions.

Yet another potential use of the ceramic-pad concept is in combustion chamber insulation for diesel and internal combustion engines. Combustion chamber insulation allows combustion temperatures to be raised and combustion thermal efficiences to be improved. Improved combustion chamber insulation translates into less heat removal through the engine and more heat energy converted into useful work. Development work on ceramic-pad combustion insulators is currently ongoing at several companies.

The aforementioned applications are areas of active current development for ceramic-BRUNSBOND® Pad systems. It is expected that other thermal barrier applications will emerge where the need for good insulation and thermal cycle stability are essential. Ceramic thermal barriers for chemical processing, including synfuels, is a long term possibility.

Conclusions

A compliant fiber metal interlayer is useful for attaching ceramic overlay coatings to metal substrates in high temperature, thermally cycled environments. The low modulus fiber metal product, designated BRUNSBOND® Pad, absorbs the strain between the metal and the ceramic caused by differences in the thermal expansivity and by the thermal gradients. The strain absorbing pad reduces the stress applied to the ceramic at the pad-ceramic interface allowing the ceramic to remain in place intact through multiple thermal cycles. A typical BRUNSBOND® Pad is composed of sintered 0.0056 in. (0.014 cm) diameter Hoskins 875 wire at .062-.125 in. thick (0.16 - 0.32 cm) and 35 percent density (65 percent porosity). The product exhibits strength, compliance, oxidation resistance and good insulating properties comparable to that of the ceramic itself. Product characteristics can be tailored to specific applications by varying parameters such as percent density, fiber diameter, alloy and thickness.

A typical ceramic-pad system is fabricated by brazing the BRUNSBOND® Pad to the metal substrate. A NiCrAlY bond coat followed by an yttria stabilized zirconia ceramic is then applied by plasma spraying.

Applications being developed include thermal barriers for high temperature ceramic seal and turbine components of gas turbine engines, electrodes for MHD generator channels, combustor liners for gas turbine and burner applications and combustion chamber liners for diesel and internal combustion engines. Key requirements of each of these applications are high temperature capability, good insulating properties and durability under conditions of multiple thermal cycles.

References

1 Bill, R.C., Allen, G.P. and Wisander, D.W., "Composite Wall Concept for High Temperature Turbine Shrouds - Survey of Low Modulus Strain Isolator Materials," NASA TM-81443, AVRADCOM TR-80-C-7, Mar. 1980

2 Erickson, A.R., Nablo, J.C., and Panzera, C., "Bonding Ceramic

Materials to Metallic Substrates for High Temperature Low Weight Applications," ASME 78-WA/GT-16, Sept. 1978

3 Kennedy, F.E., and Bill, R.C., "Thermal Stress Analysis of Ceramic Gas-Path Seal Components for Aircraft Turbines," NASA TP-1437, Apr. 1979

4 Madsen, P., and Runsnak, R.M., "Oxidation Resistant Porous Materials for Transpiration Cooled Vanes," NASA Contract NAS3-10477, May 1972

5 Sadler, J.W., "Joint US-USSR Test of the U.S. MHD Electrode System in the U-02 Facility - Phase III," Westinghouse Electric Corp. DOE Contract EX-76-C-01-2248, June 1979

6 Shiembob, L.T., Stewart, O.L., and Bill, R.C., "Development of Sprayed Ceramic Seal Systems for Turbine Gas Path Sealing," ASME 78-WA/GT-7, January 1979, NASA TM-79022

7 Wallace, M.J., "Turbine Ceramic Seal Systems," ASME Gas Turbine Conference, Mar. 1979

R. S. Storm

R. W. Ohnsorg

F. J. Frechette
The Carborundum Company,
A Kennecott Company,
Niagara Falls, N.Y. 14302

Fabrication of Injection Molded Sintered Alpha SiC Turbine Components

Fabrication of a sintered alpha Silicon Carbide turbine blade by injection molding is described. An extensive process variation matrix was carried out to define the optimum fabrication conditions. Variation of molding parameters had a significant impact on yield. Turbine blades were produced in a reasonable yield which met a rigid quality and dimensional specification. Application of injection molding technology to more complex components such as integral rotors is also described.

Introduction

Sintered alpha SiC is being considered for use in a variety of turbine engine applications. The high temperature capability of this material offers the potential of increased turbine efficiencies associated with higher operating temperatures. The fabrication techniques currently available for sintered alpha SiC (SASC) offer net shape or near net shape component production. Furthermore, there are no critical raw material supply problems for Silicon Carbide (which is manufactured by the Acheson process utilizing carbon and sand), as opposed to an uncertain future for super alloy components containing Cobalt and Chromium.

Carborundum has been working with the Detroit Diesel Allison Division of General Motors for several years on turbine engine programs which are sponsored by the Department of Energy and administered through the NASA-Lewis Research Laboratory. The development of an injection molded turbine blade for the "Ceramic Applications in Turbine Engines" (CATE) program will be described. This has lead to component development on a second DOE program, the Automotive Gas Turbine (AGT) with Carborundum acting as a subcontractor to both Detroit Diesel Allison and Garrett Turbine Engine Co. Fabrication of several of these components will be discussed.

Material

The physical properties of sintered alpha Silicon Carbide fabricated by injection molding are shown in Table 1. Material strength is essentially constant from room temperature up to 1500°C (2732°F) [1]. Sintered alpha Silicon Carbide is extremely resistant to oxidation at temperatures up to 1400°C (2552°F) [2]. Short term maximum exposure temperatures of 1750°C (3182°F) in air have been demonstrated [3].

Table 1 Properties of Injection Molded Sintered Alpha SiC

Property	Units	RT	1000°C
Hardness	Kg/mm^2	2800	
Density	gm/cc	3.10-3.18	
Young's modulus	Mpsi(MPa)	58.9(4.06)	54.9 (378)
Shear modulus	Mpsi(MPa)	25.8(178)	24.5 (169)
Poisson ratio	–	0.142	.118
Flexural strength (4pt, 1/8 × ¼ × 2 in bar, 1.5 in. outer span, 0.5 in. inner span)	psi(MPa)	61,500(424)	57,500*(396)
Weibull modulus (2 parameter, 30 samples)	–	5.8	6.0*
Fracture toughness $ksi_{in}^{1/2}$ (double tortion and SENB)	($MPa\ m^{1/2}$)	4.2 (4.6)	5.8 (6.4)

* 1200°C (2192°F)

The results of cyclic exposure testing at 1200°C (2192°F) for Refel®, reaction sintered Silicon Carbide, reaction bonded Silicon Nitride (ACC RBSN 101) and sintered alpha Silicon Carbide (cold pressed) have recently been reported [4]. Test bars were placed in a rotating fixture and exposed to temperatures alternating between ambient and 1200°C. After 2100 hours, the Refel® reaction sintered Silicon Carbide exhibited a definite downward trend, while the reaction bonded Si_3N_4 (RBSN) had a slight downward trend. The sintered alpha SiC strengths were essentially constant, or perhaps slightly higher for 3500 hours. Only the RBSN and SASC were selected for 1370°C (2500°F) testing. The RBSN displayed a clearly downward trend and testing was stopped at 2100 hours. The SASC strengths when tested at room temperature were constant up to the test limit of 3500 hours (with the exception of an anomolous test at 2100 hours which was not reproducible in subsequent retesting). The 1200°C (2192°F) strengths dropped from 350 Mpa (51KSI) after 3,500 hours at 1370°C to 225 MPa (33KSI).

Blade Fabrication

Injection molding of sintered alpha SiC components has

Contributed by the Gas Turbine Division of THE AMERICAN SOCIETY OF MECHANICAL ENGINEERS and presented at the International Gas Turbine Conference, Houston, Texas, March 8-12, 1981. Manuscript received at ASME Headquarters, December 18, 1980. Paper No. 81-GT-161.

Table 2 Process variations for sets 1-9 of injection molded blades/bars

Set:	1	2	3	4	5	6	7	8	9
Temp. zone 3	T_1	T_1	T_1	T_2	T_2	T_2	T_3	T_3	T_3
Temp. zone 2	T_2	T_2	T_2	T_3	T_3	T_3	T_4	T_4	T_4
Temp. zone 1	T_3	T_3	T_3	T_4	T_4	T_4	T_5	T_5	T_5
Temp. nozzle	T_6	T_6	T_6	T_7	T_7	T_7	T_8	T_8	T_8
Temp. mold	T_9	T_{10}	T_{11}	T_{11}	T_{10}	T_9	T_9	T_{10}	T_{11}
Injection pressure	P_1	P_1	P_1	P_1	P_1	P_1	P_1	P_1	P_1
Gate	G_1	G_1	G_1	G_1	G_1	G_1	G_1	G_1	G_1
Machine	NB	NB	NB	NB	NB	NB	NB	NB	NB
Yield of good blades after molding	13	13	13	13	10	11	15	12	11
Yield of good bars after molding	14	7	15	15	0	9	13	9	15

been under development at Carborundum for several years [5], and was selected as the processing technique to fabricate the first stage rotor blade for the CATE (truck turbine) program. This process was hoped to provide net shape fabrication capability with the exception of limited grinding to be carried out on the attachment platform and blade tip areas.

The process developed at Carborundum involves preparing a blend of thermoplastic resins and plasticizers with alpha SiC powder. This blend can then be formed into complex shapes using conventional plastic forming equipment. After molding, the parts are baked using an accurately controlled heat-up rate to remove the organics. During sintering, the parts undergo a linear shrinkage of approximately 18 percent producing a strong, single phase Silicon Carbide body with a density in excess of 95 percent of the theoretical value (3.21 gm/cc). One of the goals of this program was to establish the degree to which this shrinkage could be controlled, especially with regard to minimizing distortion. Detroit Diesel Allison established the airfoil dimensional specification which they employed for metal turbine blades as a program goal. This was a tolerance band of ± 0.002 in. (.005 cm) over the entire surface of the airfoil. In addition, there were rigorous NDE specifications (fluorescent penetrant and X-ray) which were established.

The initial stages of the DDA-Carborundum program utilized a prototype blade design which enabled Carborundum to carry out initial process development while a final blade design was being optimized by DDA. An injection molding tool was built and parts were successfully fabricated, i.e. blades were obtained which were free of major flaws or defects, and distortion was kept to a minimum.

Based on the accomplishments in this initial phase, a new injection molding tool was constructed using a revised, optimized design which was fully analyzed by DDA to calculate thermal and mechanical stress distributions. This tool was a two cavity mold: the turbine blade and an accompanying test bar. The two cavities were fed by a U-shaped runner and since the cavities were of differing dimensions, the system was not balanced; i.e. one cavity would fill while the other was only partially filled during injection.

An initial set of turbine blades was fabricated using a trial and error technique to produce parts which had an optimum appearance based on the elimination of cracks and flow lines. Two types of injection molding gate were employed: a conventional circular end gate, and a fan gate which spreads the material flow out 90° before the plastic is injected into the blade cavity. Parts were supplied to DDA after baking and sintering. Their dimensional analysis indicated that the standard gate provided blades of greater uniformity. The parameters used for processing these blades were then used as a starting point for establishing a process variation matrix. The variables which were thought to be significant in controlling part quality and variability were defined and a systematic variation established. The sintered parts would then be evaluated using NDE techniques (microscopic visual examination at 8-40X, fluorescent penetrant and X-ray), as well as dimensionally to establish the conditions that resulted in the maximum yield of acceptable parts.

The parameters which were judged to be of maximum importance for this study were melt temperature in the injection molding barrel, temperature of the nozzle, temperature of the mold, injection pressure, gate geometry and type of injection molding machine. These variables had been seen to produce the greatest degree of change in part quality based on Carborundum's previous experience in molding and sintering. Conversely, injection speed, injection time, holding pressure, holding time, and cooling time were judged to be less critical and were held constant throughout this study.

An initial set of nine experiments was defined to select the optimum temperatures for molding. The variations carried out are shown in Table 2. Zones 1-3 refer to the sections of the injection molding barrel, zone 3 being the feed end and zone 1 the nozzle end. Sets 1,2,3 employed the same barrel and nozzle temperatures while the mold temperature was varied. Sets 4,5,6 then used a new set of barrel and nozzle temperatures while carrying out the same variation in mold temperature that was used for sets 1-3. This pattern was repeated in sets 7,8,9 with new barrel and nozzle temperatures and the same mold temperature variation. Injection pressure was held constant. The gate configuration used was the standard circular gate. Molding was carried out on a 175 ton New Britian reciprocating screw type injection molding machine. Fifteen blade/bars pairs were molded for each set.

The molded blades were examined visually using 8-40X magnification. Yield of acceptable blades varied from 67 percent for set 5 to 100 percent for set 7. The yield of bars passing visual inspection ranged from 0 percent for set 5 to 100 percent for sets 3,4, and 9.

The next step was then to define the optimum injection pressure. The conditions for sets 3 and 4 were used as a center point, about which pressure was varied as shown in Table III.

Set 11 was thus a repeat of set 3, and set 14 a repeat of set 4. It can be observed from the yield data in Tables 2 and 3 that the conditions which appear to optimize the yield of good blades do not necessarily coincide with those for good bars. This is the consequence of using an unbalanced runner system and illustrates the potential for misinterpretation in using the test bar as a measure of blade quality or strength.

Although earlier dimensional analysis at DDA indicated the preference for the standard gate, three sets of parts were run using the fan gate to ensure the preliminary observations were correct. The conditions for sets 11, 14, and 15 were thus repeated using a fan gate as shown in Table 4.

Finally, the type of injection molding machine was considered.

The first 18 sets were molded on a reciprocating screw injection molding machine. The high shear action of the screw provides most of the heat required to melt the thermoplastic

Table 3 Process variations for sets 10-15 injection molded blades/bars

Set:	10	11	12	13	14	15
Temp. zone 3	T_1	T_1	T_1	T_2	T_2	T_2
Temp. zone 2	T_2	T_2	T_2	T_3	T_3	T_3
Temp. zone 1	T_3	T_3	T_3	T_4	T_4	T_4
Temp. nozzle	T_6	T_6	T_6	T_7	T_7	T_7
Temp. mold	T_{11}	T_{11}	T_{11}	T_{11}	T_{11}	T_{11}
Injection pressure	P_2	P_1	P_3	P_3	P_1	P_2
Gate	G_1	G_1	G_1	G_1	G_1	G_1
Machine	NB	NB	NB	NB	NB	NB
Yielding of good blades after molding	7	15	15	11	12	12
Yield of good bars after molding	15	15	3	4	13	14

Table 4 Process variations for sets 16-18 of injection molded blades/bars

SET:	16	17	18
Temp. zone 3	T_1	T_2	T_2
Temp. zone 2	T_2	T_3	T_3
Temp. zone 1	T_3	T_4	T_4
Temp. nozzle	T_6	T_7	T_7
Temp. mold	T_{11}	T_{11}	T_{11}
Injection pressure	P_1	P_1	P_1
Gate	G_2	G_2	G_2
Machine	NB	NB	NB
Yield of good blades after molding	14	9	13
Yield of good bars after molding	13	13	11

The blades and bars that passed a visual examination were x-rayed after the molding study was completed. Parts that had no detectable defects were then baked and subjected to another visual examination (8-40X). The NDE yield summary on blades and bars is summarized in Table 6.

Table 6 Yield of acceptable parts after molding and baking

Set	Molded visual	Molded X-Ray	Baked Visual	Molded Visual	Molded X-Ray	Baked visual
1	13	13	4	14	14	14
2	13	13	9	7	7	7
3	13	12	11	15	15	14
4	13	12	12	15	8	6
5	10	8	8	0	0	0
6	11	8	7	9	1	1
7	15	10	5	13	4	4
8	12	9	7	9	5	5
9	11	8	8	15	10	10
10	7	5	5	15	7	7
11	15	15	15	15	12	11
12	15	15	15	3	2	2
13	11	11	11	4	4	4
14	12	11	11	13	9	8
15	12	7	6	14	9	9
16	14	13	13	13	12	12
17	9	5	4	13	9	9.
18	13	9	8	11	9	9
19	10	2	1	4	2	2
20	6	3	3	11	5	4
21	13	7	6	12	6	5
22	11	8	5	12	11	11
23	12	9	1	14	10	10
24	13	13	9	15	11	9
25	12	11	9	13	10	8
26	13	11	0	14	12	9

binder. Another type of machine commonly used in ceramics processing is a plunger type machine. External heaters provide the energy to melt the thermoplastics which are forced out of the barrel by the forward travel of a plunger.

For the balance of this study, parts were molded on a Tempcraft 160 ton plunger machine at Carborundum. Earlier development work on a variety of molded parts provided the baseline conditions for molding on this machine, which were slightly different than those established as the baseline on the reciprocating screw machine. A series of 8 sets was molded as shown in Table 5. The first two sets (19,20) were run with the same barrel and nozzle temperatures. However, based on the observations on the first 18 sets, the mold temperature was held constant, while the injection pressure was varied. The barrel and nozzle temperature were then varied for set 21. These three groups were all molded with the fan gate. The gate geometry was then switched back to the standard configuration for the last four sets for which a temperature-pressure variation was carried out.

In general the plunger machine results in lower yields of acceptable blades. Considering the first 18 sets (reciprocating screw machine) there is significant variability in part yield: acceptable blade yields ranged from 27 to 100 percent, and bars ranged from 0 to 93 percent. However, since the objective of this program was to make good blades rather than test bars, subsequent evaluation of conditions was based exclusively on blade quality.

Seven of these 18 sets had a reasonable yield of blades through the bake state:

Set #	Acceptable number through bake
3	11
4	12
11	15
12	15
13	11
14	11
16	13

Table 5 Process variations for sets 19-26 of injection molded blades/bars

SET:	19	20	21	22	23	23	25	26
Temp. zone 3	T_1	T_1	T_2	T_2	T_2	T_2	T_1	T_1
Temp. zone 2	T_2	T_2	T_3	T_3	T_3	T_3	T_2	T_2
Temp. zone 1	T_3	T_3	T_4	T_4	T_4	T_4	T_3	T_3
Temp. nozzle	T_3	T_3	T_4	T_4	T_4	T_4	T_3	T_4
Temp. mold	T_{10}	T_{10}	T_{10}	T_{10}	T_{10}	T_{10}	T_{10}	T_{10}
Injection Pressure	P_4	P_5	P_5	P_5	P_4	P_6	P_4	P_6
Gate	G_2	G_2	G_2	G_1	G_1	G_1	G_1	G_1
Machine	T	T	T	T	T	T	T	T
Yield of good blades after molding	10	6	13	11	12	13	12	13
Yield of good bars after molding	4	11	12	12	14	15	13	14

Table 7 Yield after acceptable parts after NDE

Set	Blades: Visual baked	Blades: Visual sintered	Blades: Zyglo sintered	Blades: X-Ray sintered	Overall acceptable sintered
3	11	9	6	8	6
4	11	7	6	8	4
12	15	13	11	10	1
13	11	9	9	9	8
16	13	7	5	11	4

Table 8 Dimensional and overall process yield

Group	Yield contour	Max. deviation	Yield attack angle	Max. deviation	Overall acceptable parts
3	8/10	+.035in	5/10	1.0°	3
4	8/9	+.004in	4/9	2.0°	1
12	13/14	+.012in	3/14	2.0°	1
13	11/11	–	9/11	1.3°	8
16	12/13	+.008in	5/11	1.5°	0

The first 6 were all molded with the standard circular gate while set 16 had the fan gate. Of these 6, two, were a duplication of conditions: Set 11 was a repeat of set 3, and 14 a repeat of 4. The molding conditions for groups 3, 4, 11, 17, while not identical, were reasonably similar, providing an apparent "window" for some variation in machine conditions.

All the blades that passed inspection after bake were sintered (a sintered blade is shown in Fig. 1). Since it was anticipated that additional blades would be rejected in the basis of the stringent NDE and dimensional requirements, only these seven sets with a reasonable yield were subjected to a full NDE examination. The yields of acceptable parts passing the NDE examination after sintering are shown in Table 7 for five of the groups.

(Since sets 11 and 14 were a duplication of sets 3 and 4, it was decided to try a variation in sintering conditions. However these parts were all lost in furnacing). Of the remaining groups, yields ranged from 27 to 60 percent. The blades that were sintered without any gross defects were then sent to DDA for dimensional analysis, the results of which are presented in Table 8, along with an overall process yield.

Clearly, the blades molded with the fan gate were not acceptable: overall yield of acceptable blades was zero. Set 13 on the other hand produced 8 out of 15 blades that passed all NDE and dimensional requirements. This is a 53 percent yield of good parts.

A large run of injection molded blades is anticipated using the conditions defined for set 13,

and will be reported on at a later time. In addition, development work has been carried out at Carborundum on other components such as turbocharger rotors using a new reciprocating screw injection molding machine which is microprocessor controlled. This work has indicated that significantly higher yields are obtained when the microprocessor is used to control the reproducibility of machine settings. A limited matrix of processing conditions for the turbine blade using this machine is also planned for the near future.

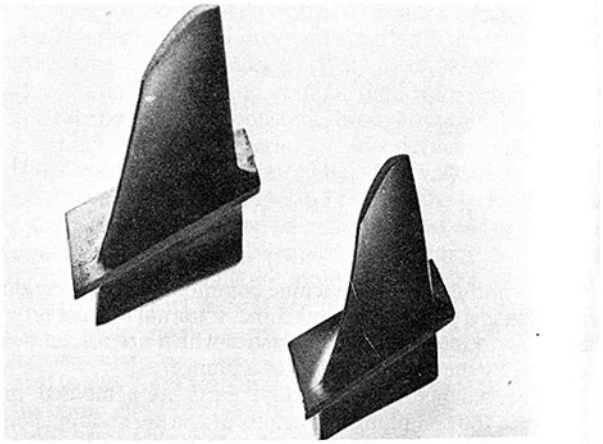

Fig. 1 Injection molded SASC turbine blade

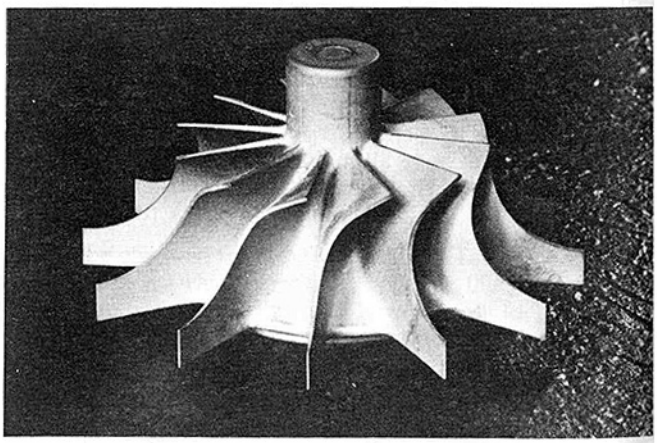

Fig. 2 Injection molded, sintered alpha SiC turbine rotor

Other Turbine Components

The injection molding of turbine components at Carborundum for Detroit Diesel Allison programs has progressed beyond the relatively small, thin cross section components such as the turbine blades. Recently the first crack free sintered alpha SiC turbine rotors for the DDA-AGT program were fabricated by injection molding (Fig. 2). Processing was very similar to that described for the blades. The part was a one piece molding which was baked and sintered with minor

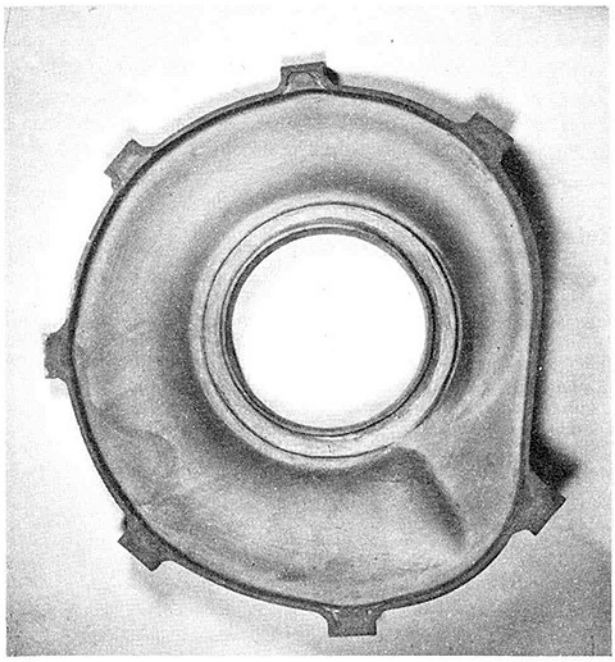

Fig. 3 Slip cast sintered alpha SiC turbine scroll backplate

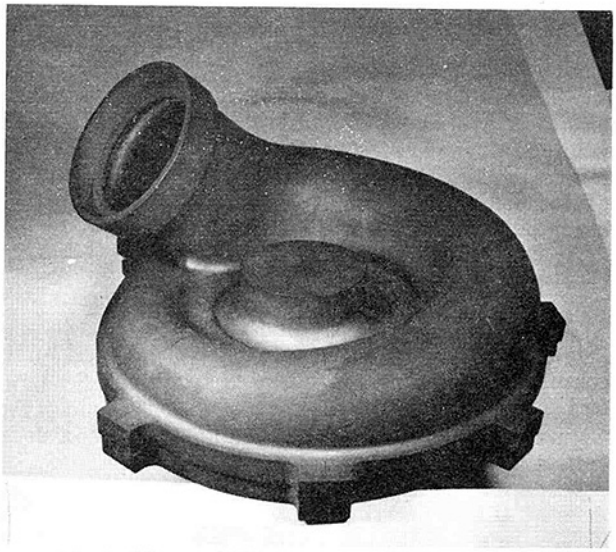

Fig. 4 Slip cast SASC turbine scroll front and backplate

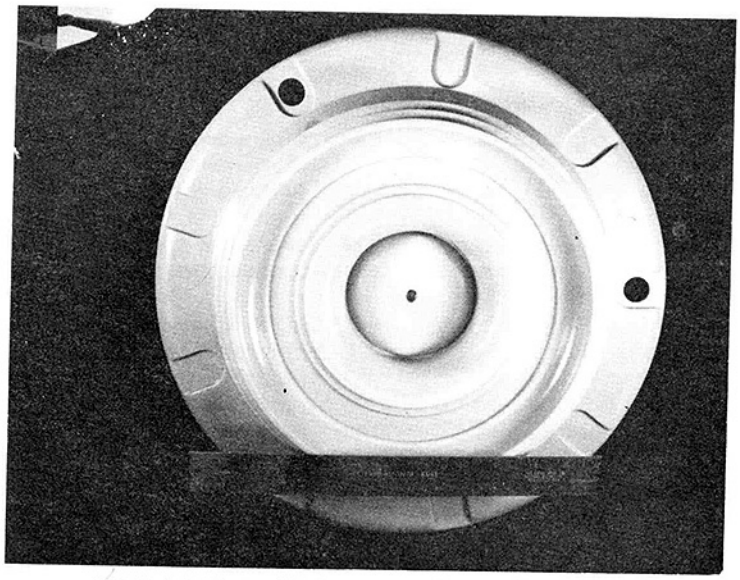

Fig. 5 Injection molded wax replica, turbine shroud

deviations from those described earlier. The hub of this rotor as molded has a maximum thickness of approximately 3 in. with an outer diameter at the blade tips of 5.25 in. These rotors will be spin tested within the coming months.

Injection molding is also being considered for larger components which traditionally have been fabricated by slip casting. An injection molding tool has been built for this component which has a maximum diameter of 14 inches, and initial molding trials will be started shortly. The entire scroll assembly is shown in Fig. 4). While this component was also slip cast, it is anticipated that this scroll will also be attempted in the future by injection molding.

A large component from the Garrett Turbine Engine Company program is also being attempted by injection molding. Figure 5 shows a wax pattern for the turbine shroud which was formed in the completed injection molding die. Maximum wall thickness is 1.25 in and diameter is over 16 inches. The sintered part will be 13.6 in. in dia and will weigh approximately 10 lb.

Conclusions

Using optimized molding conditions, turbine components such as turbine blades can be fabricated in reasonable yields to exacting specifications for net shape or near net shape configurations. Molding and processing conditions must be carefully controlled to obtain those yields. Technological improvements such as the use of microprocessor controlled injection molded equipment should facilitate the degree to which those conditions can be duplicated and thus will have a significant impact on improving the yields further. Injection molding technology has progressed to the point where more complex components such as turbine rotors with relatively thick cross-sections appear feasible today. Furthermore, large thin - wall static components which were previously fabricated

only by slip casting are also being addressed by injection molding. This is of particular significance if these turbine components are to be of commercial utility. Slip casting appears too labor intensive to produce automotive production quantities of parts at reasonable costs. While the price of an injection molding die is relatively high, the tooling cost per part for high volume production is reasonable, especially when the labor savings for processing are considered.

Acknowledgments

Funding for the turbine programs was provided by the Department of Energy and managed by the NASA-Lewis Research Center. The Detroit Diesel Allison Ceramics Applications in Turbine Engines Program is funded under Contract DN3-17 and the DDA-AGT under DEN3-168. The Garrett Turbine Engine Co. AGT program is funded under Contract DEN3-167. The authors wish to acknowledge the cooperation of Mr. John Wertz of Detroit Diesel Allison for his assistance in coordinating the turbine blade activity.

References

1 Larson, D.C., "Property Screening and Evaluation of Ceramic Turbine Engine Materials," Technical Report AFML-TR-79-4188, 1979.

2 "*Proceedings of International Symposium on Factors in Densification and Sintering of Oxide And Non Oxide Ceramics,*" p. 412, S. Somiya and S. Saito Editors, Published by Association for Science Documents Information, 1978.

3 Internal Carborundum Document.

4 Presented by D. Carruthers, Automotive Propulsion System/Contractors Coordination Meeting, April 14-18, 1980. Dearborn, Mich.

5 Smoak, R. H., and Storm, R. S., "Iterative Development of Injection Molded Sintered Alpha SiC Turbine Material," ASME Publication #79-GT-77, 1979.

Water-Cooled Gas Turbine Monometallic Nozzle Fabrication and Testing

P. W. Schilke

C. L. DeGeorge

General Electric Co.,
Schenectady, N.Y. 12345

This paper describes the fabrication and testing of the second-stage monometallic water-cooled nozzles for the Department of Energy funded High-Temperature Turbine Technology (HTTT) program. The materials and processes development work required to fabricate these nozzles has been reported in an earlier paper. The fabrication of these nozzles—including investment casting, Shaped Tube Electrolytic Machining (STEM), Electrode discharge Machining (EDM), conventional machining, and brazing—is described. The testing of these nozzles in a static hot-gas path development test stand is also described, and the results of this testing are discussed in terms of the overall component design goals.

Introduction

The General Electric Company began working toward the design and construction of a water-cooled gas turbine in the early 1960's. In 1967 the first laboratory water-cooled turbine was tested successfully. Since 1974 the Electric Power Research Institute (EPRI) has funded preliminary design and development work necessary to define and resolve potential problems. In May 1976 the United States Energy Research and Development Administration (ERDA) awarded a High-Temperature Turbine Technology (HTTT) Phase I contract to General Electric to conduct a preliminary design study aimed at utilizing a water-cooled turbine in a combined-cycle plant. The resultant design was based on a gas turbine firing temperature (gas temperature entering the first-stage buckets) of 2600 °F (1427 °C), combusting a coal-derived low-Btu gas or coal-derived liquid fuel and had a growth capability to 3000 °F (1694 °C) firing temperature.

At the conclusion of the Phase I contract, the United States Department of Energy (DOE) awarded an HTTT Phase II contract to the General Electric Gas Turbine Division directed toward component design and technology testing in critical areas of water-cooled gas turbine technology. This effort was directed principally at the hot-gas path components and included the fabrication and testing of critical water-cooled components.

This paper describes the fabrication and testing of one of these critical components, the second-stage water-cooled monometallic nozzle. An earlier paper [1] described the component design goals, materials selection, and the materials and processes development required to fabricate this component. Further information, regarding the combined-cycle gas turbine design and the definition of the program, has also been previously reported [2–7].

Contributed by the Gas Turbine Division of THE AMERICAN SOCIETY OF MECHANICAL ENGINEERS and presented at the Gas Turbine Conference & Products Show, Houston, Texas, March 8-12, 1981. Manuscript received at ASME Headquarters, December, 18, 1980. Paper No. 81-GT-162.

Second-Stage Nozzle Fabrication

Fabrication Objectives. To maintain metal temperatures below 1000 °F (538 °C), a full-flow closed loop, pressurized water-cooling circuit has been designed for the second-stage nozzles. The water is pressurized to 1250 lb/in.^{2} (8.618 MPa) and flows through over 125 cooling holes drilled into the nozzles. These holes are arranged in a combination series/parallel circuit which causes water to flow through each endwall and through the airfoil in a double pass. Design analysis has determined that the wall thickness (distance between the cooling holes and the nozzles' gas path surface) must be closely controlled to minimize thermal strains in the nozzles. Therefore, primary fabrication objectives included the following:

- Achieving tight casting design tolerances
- Precision locating of cooling holes in the castings [1]

Investment Casting and Hot Isostatic Pressing. Using the split mold investment casting process [1] two groups of eight castings each were cast by TRW, Inc. The castings were poured as single nozzles with the trailing edge in the up position. The gating used to feed the castings is shown in Fig. 1. A short mold preheat time was found to eliminate casting hot spots (and hence eliminate shrinkage) which would normally occur around the core trailing edge. By using a short preheat time, the core preheat temperature is held below the mold temperature. Therefore, solidification proceeded away from the core and towards the mold.

After the castings were poured and the gates rough cut-off, the core was removed by grit blasting. This blasting procedure prevented molten caustic, the normal core removal material, from entering and contaminating any surface-connected shrink cavities which were present in the casting, and thereby allowed closure of these cavities by welding and subsequent hot isostatic pressing (HIP). Each casting was then visually inspected for indications of surface shrinkage. Any indications found were marked and weld-repaired using 718 filler alloy.

Hot isostatic pressing (HIP) of the castings was conducted

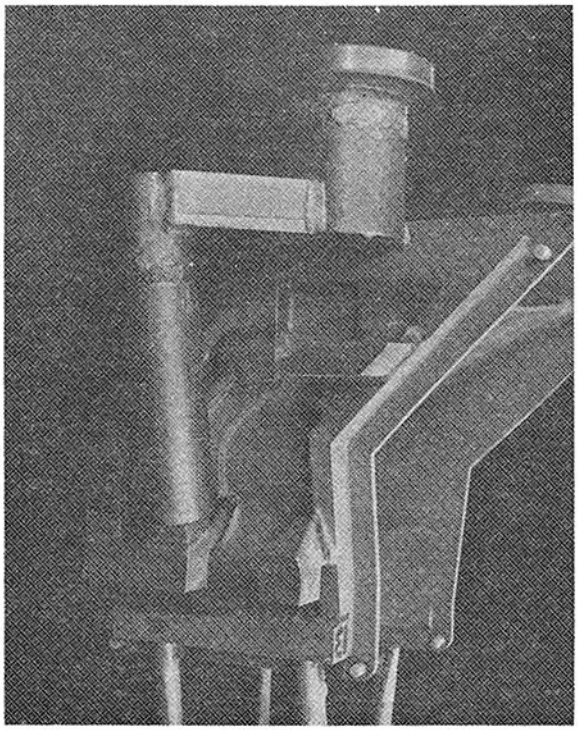

Fig. 1 Gating arrangement used by TRW, Inc. for the second-stage nozzle castings

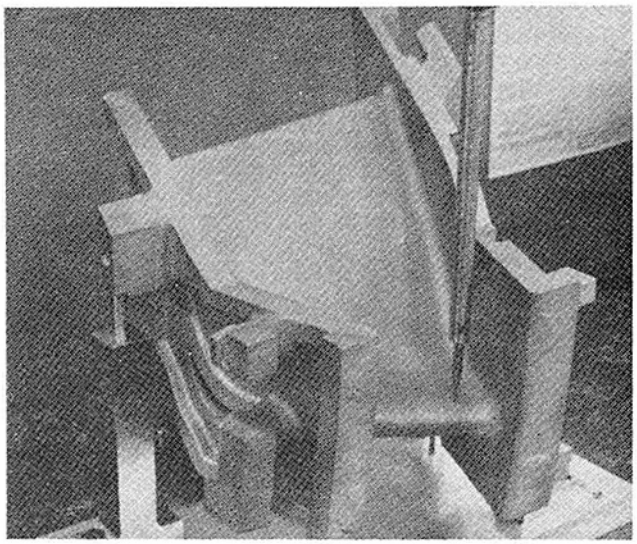

Fig. 2 Second-stage nozzle being measued by a three-axis coordinate measuring device

by Industrial Materials Technology, Inc, at 2175 °F ± 20 °F (1191 °C ± 11 °C), 15 ksi (103 MPa), for 4 hours. This cycle was used because it had demonstrated the capability to completely eliminate Laves phase present in large cast alloy 718 section sizes, and thereby increase strength [8]. After HIP, the casting gate stubs were removed by Electrode Discharge Machining (EDM), and a six-point nest (a series of points which define the coordinate axes locations) was machined into each casting using a fixture which balanced the airfoil for best fit.

X-ray inspection of the castings was conducted using conventional and single-wall airfoil exposures to enhance sensitivity and pinpoint defects. These X-rays revealed a few internal inclusions in some castings. All inclusions greater

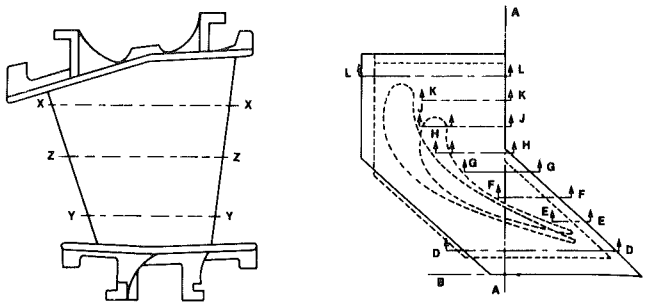

Fig. 3 Second-stage nozzle dimensional measurements

than 0.030 in. (0.76 mm) in diameter were ground out and weld-repaired using 718 filler alloy. It was necessary to remove these inclusions to prevent dwells from occurring during the Shaped Tube Eelectrolytic Machining (STEM) process used for creating the cooling passages. The source of these inclusions was determined to be pieces of mold material from the gating and risers which fed metal into the split nozzle molds. Subsequent fluorescent penetrant inspection revealed a number of small ceramic inclusions and gas holes on the casting surfaces. These were also repaired.

Dimensional and Tensile Test Results. Examination of the trailing edges of these castings revealed a bow of approximately 0.015-0.020 in. (0.38-0.51 mm). This slight bow was removed by straightening in a hydraulic press. The castings were then placed in a fixture and examined for dimensional variances using a three-axis coordinate measuring device (Fig. 2). The locations of the dimensional measurements that were taken on the airfoil and endwall gas path surfaces are shown in Fig. 3.

The results of these measurements showed good airfoil contours, generally within the ± 0.006 in. (± 0.152 mm) contour tolerance. The endwall dimensional data showed a variance up to 0.010 in. (0.254 mm) out of the design tolerance band of ± 0.005 in. (± 0.127 mm). These results were considered excellent in view of the newness of the casting process and tooling.

After casting, HIP, and dimensional check of the second-stage nozzles, one was selected for destructive evaluation. This nozzle was aged at 1325 °F (718 °C) for eight hours, furnace cooled to 1150 °F (621 °C) and held at 1150 °F (621 °C) for eight hours. Twelve tensile specimens were then machined from this nozzle: half from the endwalls and half from the airfoil. Equal numbers of each were then tensile tested at ambient and 1000 °F (538 °C). The results, shown in Table 1, fully meet the part design goals. The chemical composition of the second-stage nozzle master heat is presented in Table 2.

Machining. The machining of these castings can be divided into four major elements:

- Machining of the nozzle manifold covers and plugs
- Conventional machining of nozzle endwalls and hooks
- Electrode Discharge Machining (EDM) of nozzle manifold pockets and seal slots
- Shaped Tube Electrolytic Machining (STEM) of nozzle water-cooling passages

The manifold covers and plugs were machined by the Corry Manufacturing Company, and all the machining performed on the nozzles was conducted by Johnson Mold and Manufacturing. Each of these major machining elements is discussed below.

Manifold Covers and Plugs. The closed-loop water-cooling circuit to cool the second-stage nozzle was installed by drilling

Table 1 Tensile test results of specimens machined from a second-stage nozzle

Specimen	Test Temp. [°F (°C)]	Ultimate (ksi)	0.2% Yield (ksi)	Elon. (%)	R.A. (%)
1*	70 (22)	157	131	27	35
3*	70 (22)	156	133	20	29
5*	70 (22)	160	140	17	29
7	70 (22)	155	140	13	26
9	70 (22)	166	141	24	20
11	70 (22)	160	141	23	23
Average	70 (22)	159	141	20	27
2*	1000 (538)	126	115	18	37
4*	1000 (538)	126	124	10	33
6*	1000 (538)	126	110	18	32
8	1000 (538)	131	123	15	29
10	1000 (538)	129	118	19	29
12	1000 (538)	132	118	13	25
Average	1000 (538)	128	119	16	31

*Removed from endwall location, all others removed from airfoil location.
Conversion factor: ksi = 1.45×10^{-1} MPa

Table 2 Chemical Composition of the second-stage nozzle master heat

Element	Weight (%)	Element	Weight (%)
C	0.056	Ti	1.07
S	0.0038	Al	0.66
Si	0.10	Co	0.52
Mn	0.05	Cu	0.06
Cr	18.48	Cb	4.82
Mo	2.89	Ta	0.07
Fe	17.69	Ni	Balance

the required holes and manifold pockets in the nozzle. Therefore, each hole's entrance and/or exit and manifold pocket had to be plugged to form the closed-loop circuit. The plugs and manifold covers were machined from alloy 718 wrought and bar stock. The plugs and manifold covers required for a single nozzle are shown in Fig. 4.

The airfoil-shaped covers were cold formed on hard dies to achieve the cylindrical and conical shapes required to fit the nozzle. After forming, the final contours were cut on a wire EDM machine programmed with the data coordinate points which defined the final part contours. Multiple blanks (up to six at once) were cut in a single wire EDM run. The other flat covers were also cut using wire EDM, and the cylindrical plugs were centerless ground.

Conventional Machining. The final group of eight nozzles was conventionally machined (predominantly by end milling) on the endwall edges and on the nozzle hooks or lugs. This machining was very similar to that required for standard gas turbine nozzles. The conventional machining established most of the starting surfaces for the subsequent manifold pocket and hole drilling operations. Correct alignment with respect to the airfoil was obtained by use of holding fixtures which picked up on the original six-point nest machined into the casting.

EDM Manifold Pockets and Slots. Machining of the water collection manifold pockets and the seal slots was performed on the first group of eight castings by EDM using a series of graphite electrodes for each shape machined. There are three linear endwall manifold pockets in each nozzle, two on the leading edge face and one on the trailing edge face. There are four airfoil-shaped manifold pockets per nozzle, a leading edge and trailing edge pocket on both inner and outer endwalls. The leading edge face pockets can be seen in Fig. 5, and the airfoil-shaped pockets in the outer endwall can be seen in

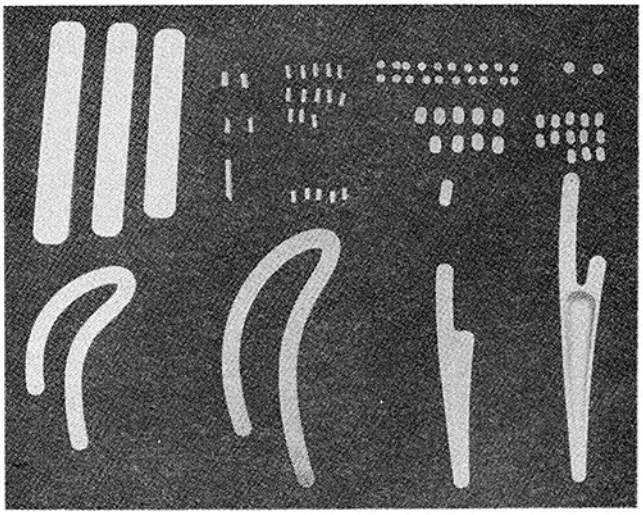

Fig. 4 Second-stage nozzle manifold covers and plugs required for a single nozzle

Fig. 6. After these pockets were EDM'ed recesses around each pocket were also machined such that the covers would fit flush with the surrounding surfaces.

The seal slots, which contain seals to prevent air leakage between the nozzles' adjacent endwalls, were also EDM'ed into the nozzles. Both inner and outer endwall seal slots were installed with one electrode to maintain proper seal slot orientation and spacing on the nozzles.

STEM Drilling of Cooling Passages. The majority of the cooling passages in the second-stage nozzle [as described previously [1]] were installed by STEM drilling. Specialized tooling for this part was developed by Johnson Mold and Manufacturing and GE to maintain close control over wall thicknesses. This tooling located the part in critical areas to ensure maximum control of wall thicknesses. The selection of these critical areas was based on the nozzle's geometry and the planned cooling hole locations. Multiple holes were drilled in a single setup where possible, as can be seen in Fig. 7.

At the completion of the hole-drilling operations, the nozzles were both visually examined and X-rayed to ensure proper hole intersections and placements. Figure 8 is an X-ray exposure of one of the nozzles. In this exposure most of the airfoil and endwall cooling holes can be observed. All holes

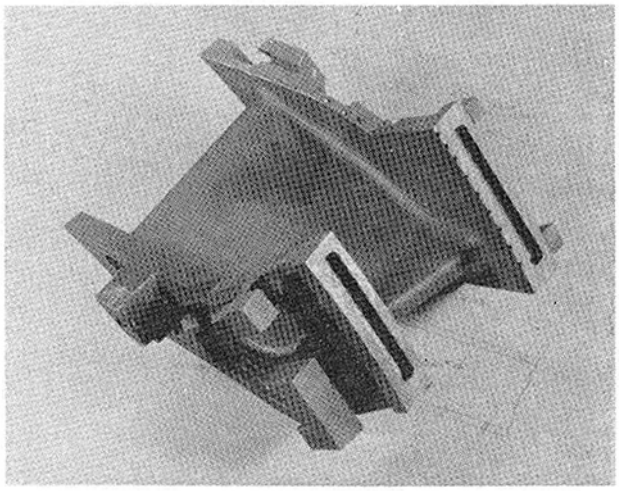

Fig. 5 Second-stage nozzle leading edge face pockets

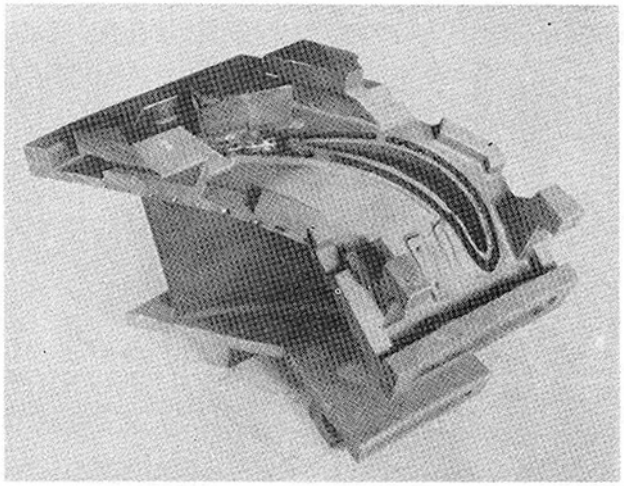

Fig. 6 Second-stage nozzle airfoil-shaped pockets in the outer end-wall

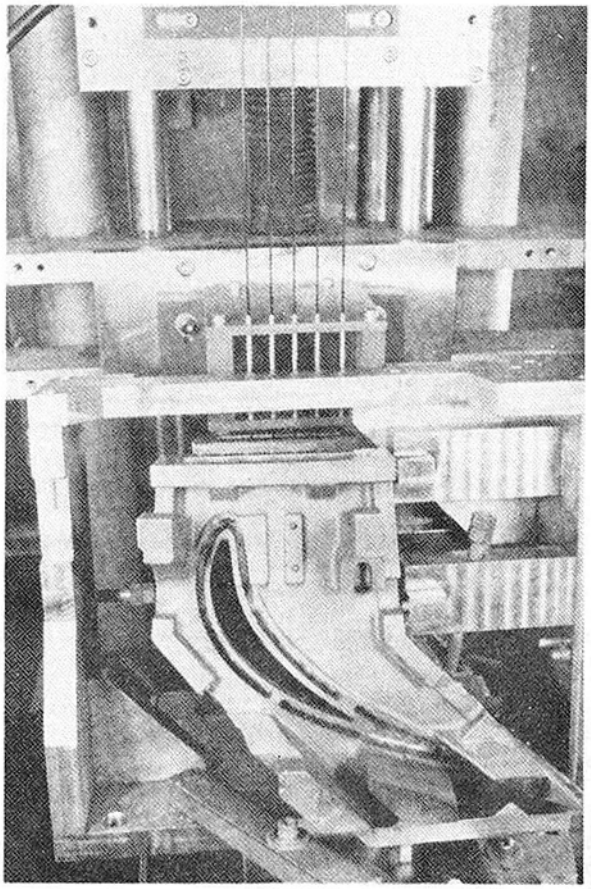

Fig. 7 Second-stage nozzle STEM drilling setup for drilling five holes simultaneously

were verified and all intersections were determined to be within the acceptable design ranges, by airflow checking.

Brazing. Two manifold cover test specimens were vacuum brazed by Aerobraze Corp. with AMS-4786 (Palniro 7) Au, Ni, Pd alloy to verify the selected braze material and joint configurations, prior to brazing the nozzles. After brazing, these specimens were tested for 6000 cycles from 0 to 1500 lb/in.^{2} (10.3 MPa) at 500 °F (260 °C). No leakage or plastic deformation of the samples was observed, and subsequent metallographic examination showed good braze joints.

The same brazing procedure and techniques were then applied by Aerobraze to a partially machined nozzle to verify the brazing procedure on the actual nozzle geometry and to enable a hydrostatic leak check to be conducted. Visual examination of this nozzle after brazing revealed a lack of braze fillet and leakage where large gaps were present between the airfoil contoured manifold covers and manifold pocket recesses (Fig. 9). Additional brazing development work was then performed to define a method for brazing the wide gaps present in the nozzle assemblies.

This work resulted in the application of a multistep progressively lower temperature vacuum brazing procedure to the nozzles. The first step utilized AMS-4786 (Palniro 4) Au, Ni, Pd to braze the instrumentation quills together at 2175 °F

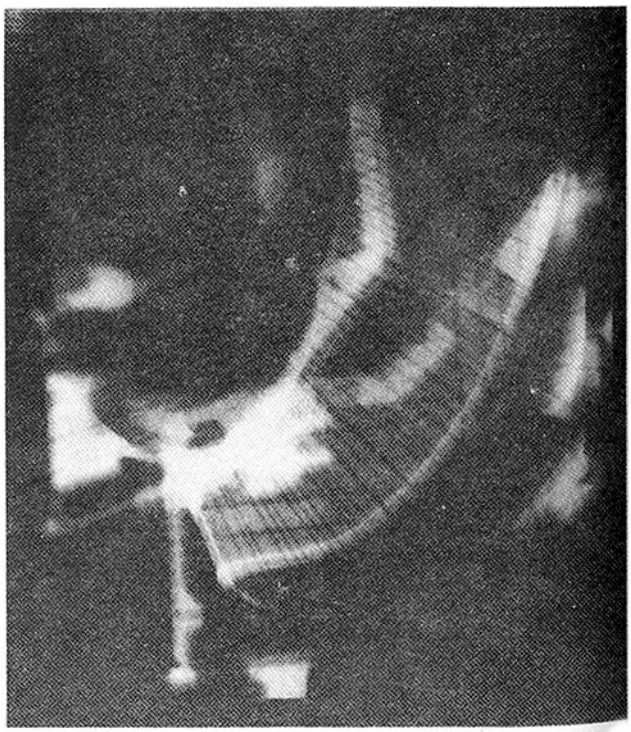

Fig. 8 X-ray exposure of STEM-drilled second-stage nozzle

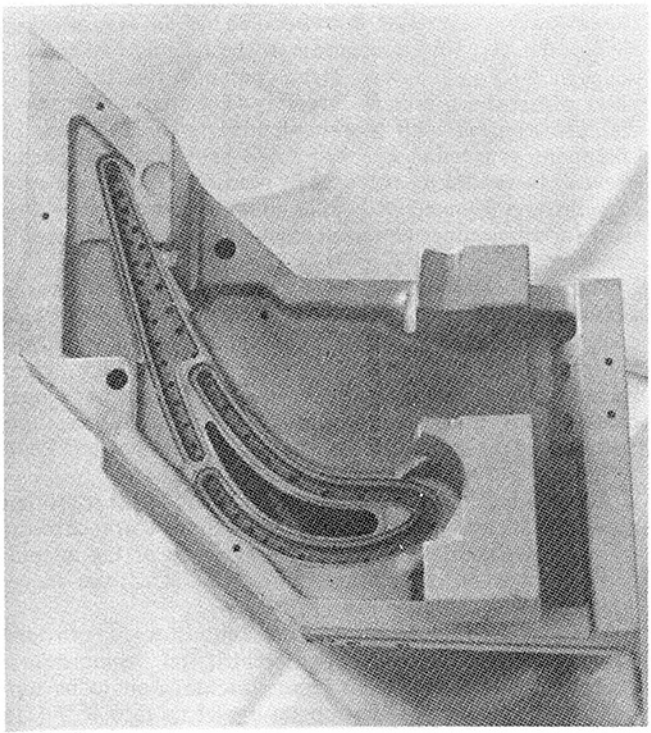

Fig. 9 Second-stage nozzle inner endwall airfoil-contoured manifold pocket and recess

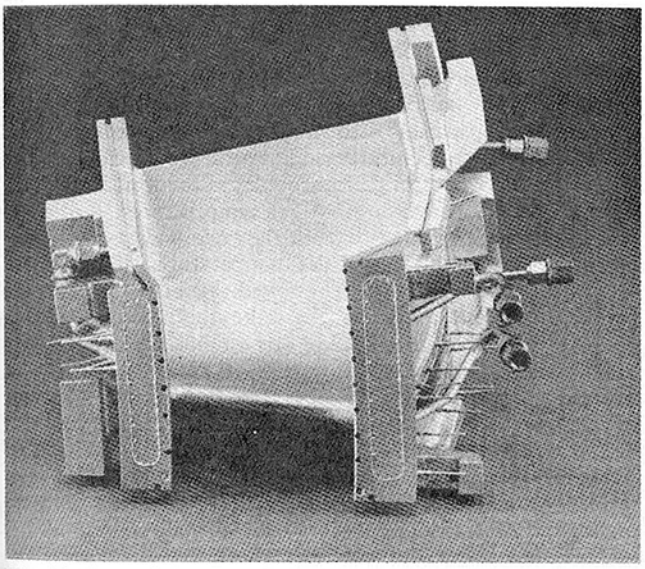

Fig. 10 Second-stage nozzle braze assembly as viewed from the leading edge

(1191 °C). The second step utilized AMS-4784 (Palniro 1) Au, Ni, Pd to braze all the manifold covers and plugs except those on the inner endwall at 2065 °F (1129 °C). The third step utilized AMS-4786 (Palniro 7) to braze the remaining covers and plugs on the inner endwall at 1950 °F (1066 °C).

During prebraze assembly, any gaps found to be excessive were filled with a NiCr powder prior to the application of the braze alloy. Also, during each brazing step the nozzles' airfoil contoured manifold covers were placed in an "up" position to be brazed. The use of these techniques resulted in high-quality vacuum braze joints on the nozzles (Fig. 10 and Fig. 11).

Hydrostatic leak checks were performed on all the nozzles after brazing at 1500 lb/in.^{2} (10.3 MPa). All braze joints were found to be leak-tight.

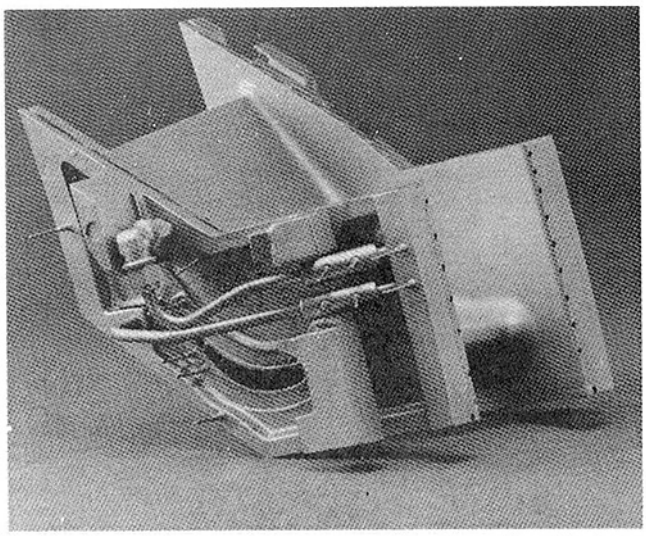

Fig. 11 Second-stage nozzle braze assembly as viewed from the inner endwall side

Table 3 Summary of airfoil ultrasonic wall thickness results (percentage of airfoil readings falling within design goals and within two broader wall thickness ranges)

Casting Number	Wall thickness range [mils(mm)] 40(1.0)min 86(2.2)max*	30(0.76)min 96(2.4)max	20(0.51)min 106(2.7)max
23 (Backup)	90%	95%	98%
22 Prime Suct. Slave	83	95	100
21 (Backup Suct. Slave)	68	89	98†
18 Prime Press. Slave	67	93	100
17 Prime	91	99	99†
16 Prime	87	97	99†

*Design tolerances
†No holes less than 20 mils (0.51 mm) min. wall thickness

Ultrasonic Wall Thickness Measurements. Ten predetermined section lines were laid out on each of the nozzles to check the cooling holes' wall thicknesses. Using a 20 MHz, 0.125 in. (3.2 mm) diameter buffer rod transducer and Tektronix model 7603 oscilloscope, time measurements were made on each hole along the section lines.

The signal transit time between the gas path surface and the cooling passage was minimized by peaking out the amplitude of the reflected signal and recording the indicated time in microseconds for each hole. Holes which were either difficult to read or were outside design goals were measured twice. The signal transit times were multiplied by the average velocity (determined on a calibration piece of cast alloy 718 of known thickness) and the resulting wall thickness readings were tabulated in mils.

The results generally show good conformance to the wall thickness design goals. These results are very encouraging since these parts were the first parts of this type ever made using completely new tooling.

An overall summary of the airfoil wall thickness results is presented in Table 3. This table shows (as a percent of total airfoil measurements taken on each casting) the number of airfoil readings which fell within the design goals and two broader wall thickness ranges. The two castings with the best airfoil wall thickness readings were selected as prime test nozzles, with the remaining nozzles to be used as spares. These prime nozzles were judged to be fully acceptable for

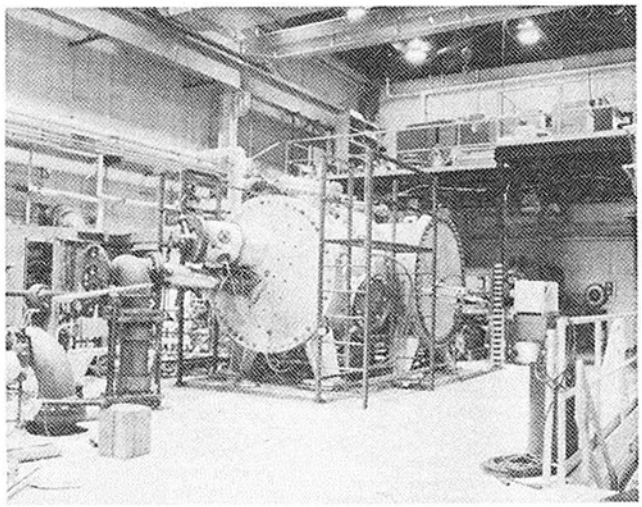

Fig. 12 Test stand for HTTT component

testing in the Hot-Gas Path Development Test Stand (HGPDTS).

Second-Stage Nozzle Testing

Test Objectives and Plan. The primary purpose of the second-stage nozzle test program was to verify the nozzles' design in a simulated gas turbine environment (hot-gas path cascade test apparatus) and to compare the nozzles' performance with the design predictions. To accomplish this a test plan was formulated which subjected the nozzles to the design point operating conditions and to variations in the hot-gas stream and nozzles' cooling water flow rates and temperatures. The nozzles' cooling water and metal temperatures were monitored and compared with design predictions for each of these test points.

Design analysis has indicated that the life-limiting factor for a water-cooled monometallic nozzle is low-cycle fatigue (LCF) due to machine startup and shutdown thermal cycles. Therefore, the test plan also included enough cyclic nozzle testing to demonstrate that sufficient LCF life was present in the nozzles for successful testing in a protoytpe water-cooled gas turbine. A summary of the test plan which was used for this second-stage nozzle testing is given below.

Part 1. An unfired hot-air nozzle and test facility checkout was made to ensure that all nozzle and test stand systems and instrumentation were functioning properly.

Part 2. A fired nozzle and test facility checkout was made, during which the design operating points were approached by gradually increasing heat flux and decreasing nozzle cooling water temperature. During this phase of testing, the nozzles' cooling water and hot-gas stream temperatures and flows were also varied individually.

Part 3. Cyclic testing of the nozzles followed a cycle which simulated a startup, maximum power, and shutdown sequence.

Test Facility. Testing of the HTTT second-stage nozzle was conducted in the General Electric Gas Turbine Development Laboratory in Schenectady, NY. As part of General Electric's HTTT effort, a new test stand was designed and built for testing water-cooled turbine hot-gas path hardware. The test stand is shown in Fig. 12.

The nozzle was tested as a four-vane, three-throat assembly (Fig. 13). The nozzle assembly was mounted on a water-cooled heat shield. Hot gases, exiting the nozzle, passed through an opening in the heat shield into the water-quench chamber of the test stand. Water-cooled baffles were attached to the first and fourth segments at the leading and trailing edges of the nozzle airfoil. These contained the flow of hot gases within the four-vane assembly. The four nozzles were clamped together with a spring-loaded yoke. This type of compliant connection between single-vane nozzle segments prevents thermal stresses caused by rigid-frame effects present in multivane segments. A similar compliant approach will be used for connecting the nozzle segments in the water-cooled turbine.

The combustion gas generator used for the test was a standard General Electric MS7000E industrial turbine combustor. The combustor was coupled to an MS7000E transition piece. The transition piece was cooled by compressor discharge air flowing over its outer surface. A plenum chamber surrounded the transition piece to provide the same cooling airflow conditions as would be seen in an MS7000E turbine.

An adapter, bolted to the downstream end of the transition piece, was used to narrow the flow path to the entrance of the second-stage nozzle assembly. The majority of the adapter was impingement cooled, except for its downstream flange which had film cooling holes.

The air mass flow supplied to the combustor was provided by two large electric-driven centrifugal compressors. Preheaters allowed the compressor discharge air to be supplied to the combustor at temperatures of up to 600 °F (316 °C).

The nozzle instrumentation consisted of thermocouples and pressure taps inserted into the water passages and manifolds. Thermocouples were also attached to the metal surface of the nozzles away from the gas path. Gas path surface temperatures on the suction side of the airfoils were measured by scanning these surfaces with an infrared pyrometer.

A five-by-five matrix of rake thermocouples located in the adapter, just upstream of the nozzle, was used to determine the average gas temperature and temperature profile entering the nozzle. Five control thermocouples in the transition piece were also used to measure hot-gas temperatures. Radiation corrections were applied to both the rake and control thermocouples to obtain actual gas temperatures. The control thermocouples were then calibrated against the average temperature determined by the rake thermocouples. Gas temperature during fired testing was established by reference to the control thermocouples.

Total and static pressure probes were present in the hot-gas stream ahead of the nozzle. A static pressure probe was also placed downstream of the nozzles. Cooling water flow entering each nozzle segment was measured with a turbine flow meter. Water exiting the segments was measured with an orifice and ΔP transducer calibrated against its corresponding turbine flow meter. Loss of coolant flow from any of the nozzle segments could be determined by comparing inlet and outlet flows. The difference in flow between the nozzle inlet and outlet was continuously monitored throughout the test as an indicator of nozzle cracking or other damage.

Instrumentation output from the nozzle and support hardware was recorded by a computer which organized the data into displays and calculated nozzle performance as the test proceeded. The computer was also capable of tripping the test system by an instantaneous shutoff of the fuel supply to the combustor if it detected an unsafe condition. Trips were set for low coolant flow and pressure, high coolant temperature, excessive loss of coolant, and excessive combustion gas temperatures.

Test Program. Flow testing of the nozzle high-pressure cooling water system, gas path air leakage testing, and hot-air flow testing were accomplished during Part 1 of the test program.

Table 4 Test combinations of inlet temperatures, flow rates, and pressures

Temp [°F (°C)]	Inlet pressure (lb/in.^{2})	Flow (lb/s)			
		Vane 1	Vane 2	Vane 3	Vane 4
99 (37)	454	0.31	0.44	0.44	0.32
202 (94)	459	0.33	0.47	0.46	0.33
305 (152)	462	0.34	0.48	0.48	0.35
93 (34)	456	0.44	0.62	0.62	0.45
205 (96)	461	0.46	0.64	0.64	0.46
321 (161)	458	0.49	0.66	0.67	0.49
299 (148)	458	0.48	0.66	0.66	0.47
301 (149)	461	0.62	0.77	0.78	0.63
298 (148)	1263	0.49	0.65	0.65	0.48

Conversion factors: lb/in.^{2} = 1.45 × 10^{-4} Pa
lb/s = 2.20 kg/s

Table 5 Test point parameters for steady-state testing

Gas Temperature [°F (°C)]	Gas Mass Flow Rate (lb/s)	Inlet Water Temperature [°F (°C)]	Heat Input Per Segment (Btu/s)	Time Point (hours)
1200 (649)	8.5	290 (143)	21	0.5
1500 (816)	15.0	242 (117)	47	1.5
1800 (982)	20.0	172 (78)	77	2.0
2082 (1139)	23.8	152 (67)	102	1.0
2082 (1139)*	24.0	223 (106)	100	4.0

*Design point
Conversion factors: lb/s = 2.20 kg/s
Btu/s = 9.48 × 10^{-4} J/s

The cooling water flow test was conducted to establish the following:

- Determine if the flow distribution to the nozzles and water-cooled baffles was satisfactory
- Investigate the pressure distribution within the nozzle cooling circuit
- Establish the effect of water flow rate and water temperature on the total pressure drop across the nozzle cooling circuit
- Ensure that the water temperature thermocouples were functional
- Calibrate the orifices and ΔP transducers measuring the flow exiting the nozzles
- Make a final inspection for leaks in the nozzles' high-pressure water circuits.

The combinations of inlet temperatures, flow rates, and pressures that were run during that testing are shown in Table 4.

All of the water temperature thermocouples were scanned at each of the inlet water temperatures to verify their accuracy. The rate of cooling water loss due to leaks in the high-pressure water system was measured at the 1250 lb/in.^{2} (8.618 MPa) design pressure.

The use of film cooling holes on the downstream end of the adapter and the nature of the seal between adapter and the nozzle entrance caused the leakage of a certain amount of compressor discharge air into the gas path, downstream of the thermocouple rakes. In order to obtain an accurate measurement of the gas temperature entering the nozzle, the amount of this leakage had to be determined for each test point. This was accomplished by devising a test to find the effective flow area of the leaks. The test was conducted by sealing off the entrance to the transition piece and leaving the nozzle exit open to atmospheric pressure. The pressure in the combustion chamber was set at several different values, and the air mass flow rate out of the stand was measured for each pressure ratio. The rake temperatures could then be corrected based on the percentage leakage of compressor discharge air. This was done by a simple mixture calculation of combustor exit air and compressor discharge air.

The heat flux experienced bv the nozzles during fired testing is dependent upon the aerodynamic conditions in the nozzle gas path. A hot-air flow test was run to ensure that the aerodynamic design of the nozzle was correct. Several pressure ratios were set across the nozzle with a constant upstream total pressure. The air mass flow was measured for each pressure ratio. The flow function was plotted versus pressure ratio and compared to the predicted curve. The effective area of the nozzle throat was also determined.

Steady-state testing at both design and off-design fired operating points was conducted during Part 2 of the nozzle test program. A series of test points, that increased heat flux in relatively equal steps, were set by simultaneously increasing firing temperature and air mass flow rate while decreasing cooling water temperature. Instrumentation data scans were taken and evaluated at each point before moving on to the next point. Steady-state operation at the conditions corresponding to a 2600 °F (1427 °C) firing temperature [average gas temperature = 2082 °F (1139 °C)] was maintained for four hours to ensure that no thermal instabilities were developing. The test point parameter used in this portion of the test are shown in Table 5.

After accumulating four hours at the 2082 °F (1139 °C) design point, parameter variation testing was conducted. This portion of the test was designed to evaluate the nozzles' sensitivity to individual changes in the test parameters. The parameters that were varied were cooling water temperature and flow rate, hot-gas temperature, and hot-gas flow rate. The test points that were run during parameter variation testing are given in Table 6. Complete data scans of the instrumentation were taken at each steady-state test point.

Infrared pyrometer scans of the airfoil suction surface were made for each point during Part 2 of the test. The scans were circumferential traverses of nozzles 1, 2, and 3 looking upstream. A scan was made at the pitch radius of the nozzles for all of the off-design points. At the 2082 °F (1139 °C) design

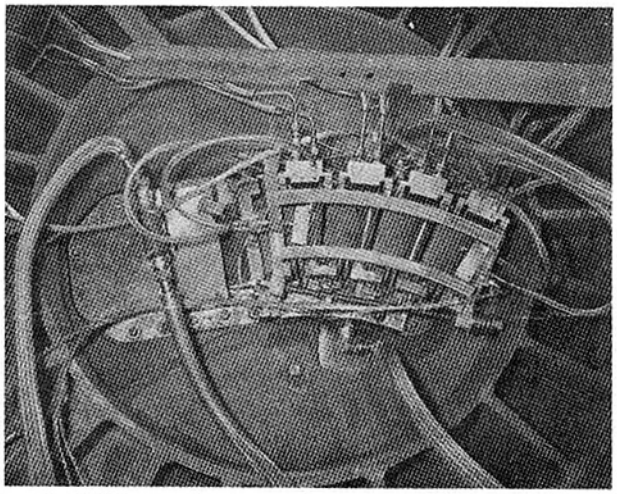

Fig. 13 HTTT second-stage nozzle test assembly mounted in test stand

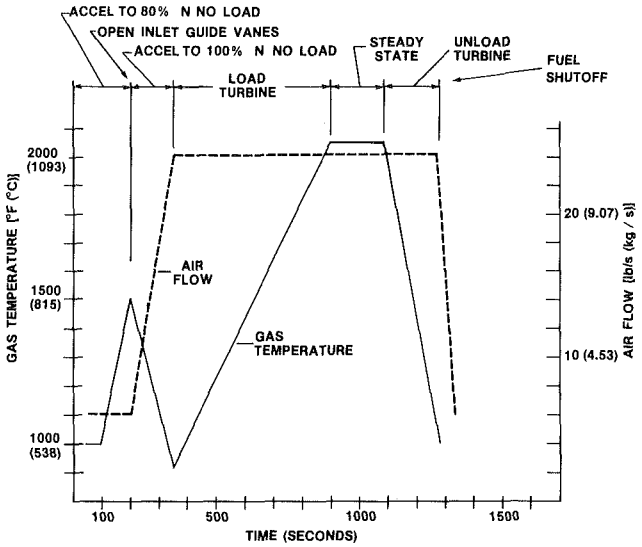

Fig. 14 Simulated turbine startup-shutdown cycle for HTTT second-stage nozzle testing

Table 6 Test points for parameter variation testing

Gas Temp [°F (°C)]	Gas Mass Flow Rate (lb/s)	Water Temperature [°F (°C)]	Water Flow Rate (lb/s)
2082 (1139)	24.2	153 (67)	0.63
2082 (1139)	24.2	173 (78)	0.63
2082 (1139)	24.2	199 (93)	0.63
2082 (1139)	24.2	223 (106)	0.63
2082 (1139)	24.2	223 (106)	0.55
2082 (1139)	24.2	223 (106)	0.48
1701 (927)	24.3	223 (106)	0.63
1904 (1040)	24.3	223 (106)	0.63
2082 (1139)	21.2	223 (106)	0.63
2082 (1139)	18.2	223 (106)	0.63
2082 (1139)	15.0	223 (106)	0.63

Conversion factor: lb/s = 2.20 kg/s

point, six scans were made covering the entire gas path height. This allowed the determination of the radial height. This This allowed the determination of the radial surface temperature gradient on the airfoil surface.

The simulated turbine startup-shutdown cycle used in Part 3 of the test program is shown in Fig. 14. All the major events in the actual startup-shutdown sequence are represented in this cycle. Each cycle included three minutes steady state at the 2082 °C (1139 °C) design point conditions. Forty-seven repetitions of this cycle were accumulated. This brought the total time at this design point to over eight hours. Excursions from startup to design point to shutdown in Part 2 of the test and inadvertent trips from design point brought the total number of cycles to 52.

During the cyclic portion of the test, all instrumentation readings were recorded on magnetic tape at 35 second intervals. The infrared pyrometer was also used to measure the nozzles' response to the transient. This was achieved by focusing the pyrometer on a single point on the suction side of the airfoil during the entire cycle. This allowed surface temperature to be plotted as a function of time. Different points on the nozzle were chosen for each cycle. In order to determine the temperature gradient in the nozzle during the transient, readings from metal temperature thermocouples in the core were recorded on a strip chart recorder. The rate of change of the core metal temperatures was compared to the rate of change of the gas path surface temperature as measured by the pyrometer.

Test Results

Part 1—Unfired Testing. The results of the cooling water flow test indicated that sufficient flow was being supplied to all passages in the nozzle cooling circuit. The total measured pressure drop across the nozzle cooling circuit was 123 lb/in.^{2} (0.848 MPa) at the design flow rate of 0.625 lb/s (0.283 kg/s) and average cooling water temperature of 300 °F (149 °C). This compared to a calculated pressure drop of 117 lb/in.^{2} (0.807 MPa). The measured system leakage rate was 1.2 liters/hr, primarily due to fitting leakage.

The total effective flow area of air leaks downstream of the thermocouple rakes was demonstrated to be approximately 2 in.^{2} (1.29×10^{-3} m^2) by the seal leakage test. At the 2082 °F (1139 °C) design point, compressor discharge air was supplied at 600 °F (316 °C) and 67 lb/in.^{2} (0.462 MPa). The gas path static pressure was 60 lb/in.^{2} (0.414 MPa). This resulted in a 1.6 lb/s (0.726 kg/s) leakage rate and a 110 °F (43 °C) downward correction being applied to the average gas temperature entering the nozzle.

The effective throat area of the nozzle test assembly determined by the hot-air flow test was 29.36 in.^{2} (0.0189 m^2). The geometric throat area had previously been measured to be 31.98 in.^{2} (0.0206 m^2). This resulted in a flow coefficient of 0.92 for this test assembly. The experimental plot of flow function versus pressure ratio closely followed the predicted curve.

Part 2—Steady-State Fired Testing. Data for the 2082 °F (1139 °C) design point are presented below and compared to predicted values. The data presented include cooling water temperature rise across the entire nozzle and individual portions of the circuit, pyrometer measurements of metal temperatures on the suction surface of the pitch airfoil section, and metal temperatures in the nozzle core and on the nongas-path surface of the outer endwall. The measured metal temperatures, changes in water temperature, and the corresponding predicted values are presented in Table 7. The locations of the thermocouples and the infrared pyrometer measurement locations are shown in Fig. 15 and Fig. 16.

The measured temperatures correlate well with the temperatures predicted by analysis. The largest discrepancy occurs with the infrared pyrometer measurements of airfoil suction surface temperatures forward of the trailing edge. This test was the first utilization of this infrared pyrometer to measure gas path surface temperatures through a hot-gas stream, and several sources of instrument error were possible and are being investigated.

Table 7 Measured metal temperatures, water temperatures, and predicted values

Location	Measured temperature [°F (°C)]	Calculated temperature [°F (°C)]
Airfoil suction surface —pyrometer measurement		
Trailing edge (TE)	700 (371)	680 (360)
2 in. fwd of TE	690 (366)	815 (435)
Core		
TC 37	462 (239)	507 (264)
TC 38	444 (229)	455 (235)
TC 39	477 (247)	469 (243)
TC 40	585 (307)	524 (273)
TC 41	555 (291)	567 (297)
Outer endwall		
TC 32	586 (308)	602 (317)
TC 34	537 (281)	459 (237)
TC 35	405 (207)	376 (191)
TC 36	407 (208)	376 (191)
Cooling water ΔT		
Outer endwall—aft	19 (11)	11 (6)
Vane TE	51 (28)	66 (37)
Inner endwall	15 (8)	18 (10)
Vane leading edge	42 (23)	34 (19)
Outer endwall—fwd	20 (11)	15 (8)
Entire nozzle	147 (82)	144 (80)

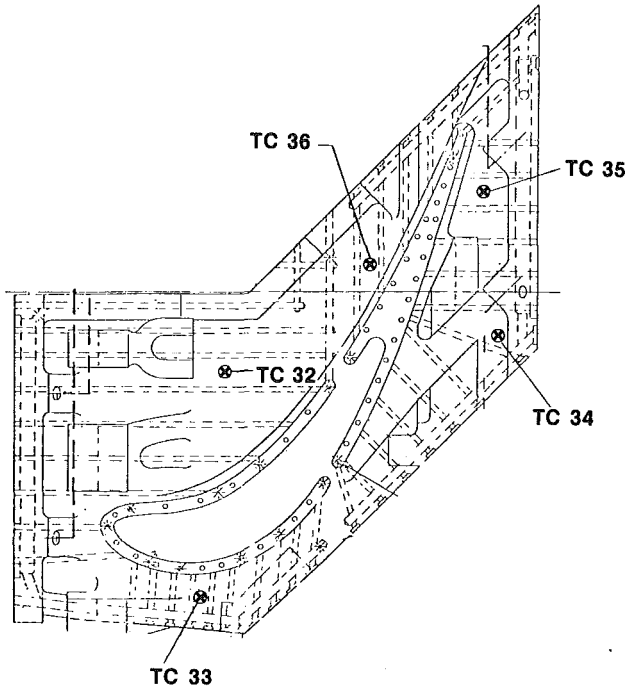

Fig. 15 Outer endwall thermocouple locations

Part 3—Cyclic Testing. The cyclic portion of the test was of particular interest since in current production, air-cooled nozzle fatigue life is a function of how the part responds to a transient. Figure 17 shows the temperature response of the pitchline airfoil trailing edge to the simulated startup-shutdown sequence of Fig. 14. This response was typical for the other points on the airfoil surface that were observed during the cyclic portion of the test program. Portions of the response profile showed no change in temperature because the airfoil surface temperature was below the measurable threshold of the pyrometer.

The important feature of the nozzle response was that neither the gas path surface temperature nor the core surface temperature lagged the gas temperature during the cycle. This implies that the temperature gradient and resulting thermal stress reach a maximum at steady state rather than during the transient. Therefore a water-cooled turbine may be able to tolerate a more rapid startup sequence than an air-cooled turbine and might also be far less affected by trips.

Post Test Inspection. After each part of the testing program, a close visual examination of the second-stage nozzles was made. The inspection after the hot-air testing, Part 1, showed no discernable change in the appearance of the nozzles. Obvious visual changes did occur after the Part 2 and Part 3 portions of the testing.

Examination after the Part 2 (steady-state) and Part 3 (cyclic) testing of the nozzles showed surface areas which were discolored in between the cooling passages of the nozzles. These markings clearly showed the pattern of cooling passages inside the nozzles (Fig. 18). It is believed these areas were discolored as a result of a very slight oxidation of the hot surfaces in between the water cooling passages. Since the fuel used in this testing was propane, no deposits would be expected. No indications of cracking, overheating, or other distress were observed during these inspections. In addition, a total water system leakage test at 1250 lb/in.^{2} (8.618 MPa) showed no change compared to the measurement taken at the start of the testing. The nozzles appeared to be in excellent condition after the testing with no discernable indications of distress.

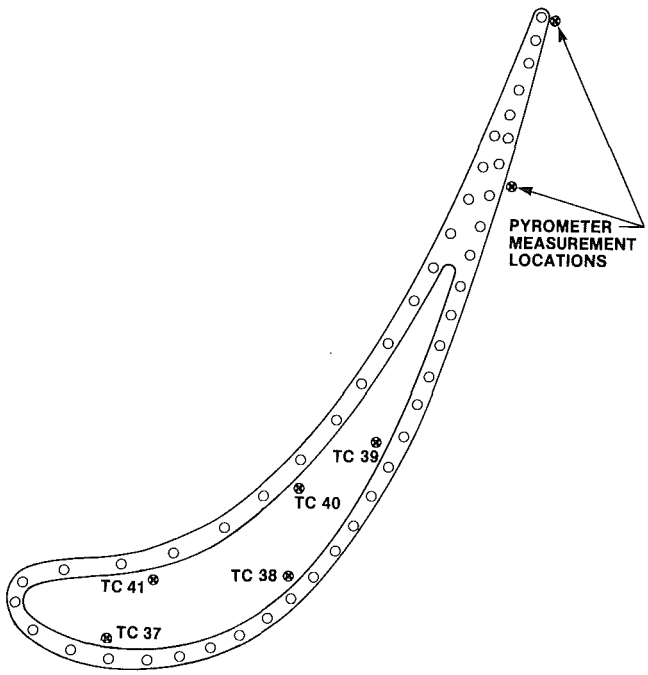

Fig. 16 Airfoil and core temperature measurement locations

Summary

The HTTT water-cooled second-stage nozzle fabrication and testing were successfully conducted, and these results have demonstrated that the technology is ready for additional testing and incorporation into a prototype water-cooled turbine. The materials fabrication techniques and the design predictions were verified by this testing and will form the

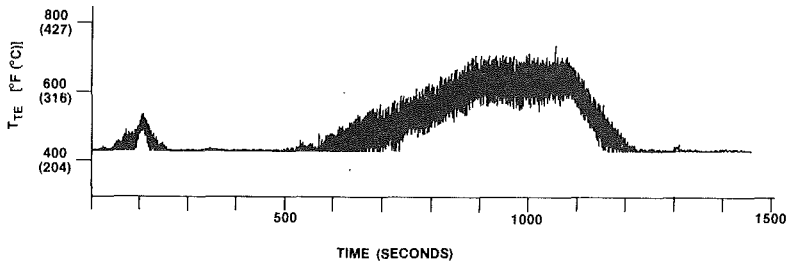

Fig. 17 Trailing edge temperature response to simulated startup-shutdown cycle

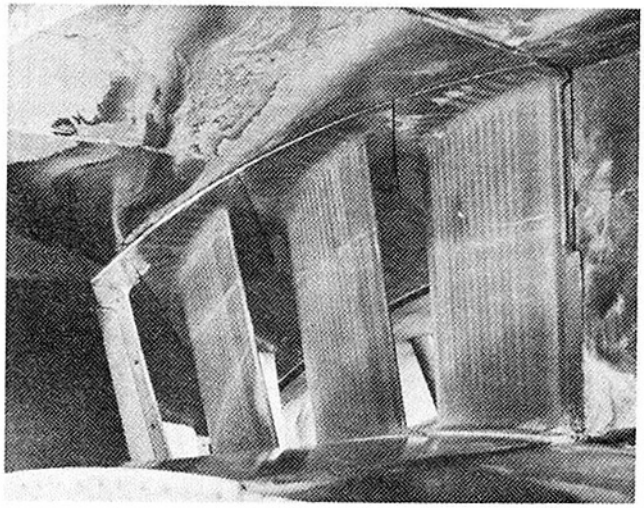

Fig. 18 Second-stage nozzles after completion of testing

basis for continued design of water-cooled monometallic gas turbine components for a prototype turbine.

Acknowledgments

The authors would like to acknowledge W.S. Blazek of TRW; D. Marville of Johnson Mold and Manufacturing; J. Lombardo of Aerobraze; and W. Schilling, K. Zeman, D. Geiling, L. Willmott, T. Smith, and J. Roncevich of the General Electric Company for their conscientious efforts and guidance on this program. The United States Department of Energy is recognized for sponsoring the HTTT Phase II program.

References

1 Schilke, P., et al., "Water-Cooled Gas Turbine Monometallic Nozzle Development," ASME Paper No. 80-GT-97, Mar. 1980.

2 Caruvana, A., et al., "Evaulation of a Water-Cooled Gas Turbine Combined Cycle Plant," ASME Paper No. 78-GT-77, Apr. 1978.

3 Caruvana, A., et al., "System Status of the Water-Cooled Gas Turbine for the High Temperature Turbine Technology Program," ASME Paper No. 79-GT-39, Apr. 1979.

4 Horner, M.W., et al., "Development of a Water-Cooled Gas Turbine," ASME Paper No. 78-GT-72, Apr. 1978.

5 Horner, M.W., et al., "Water-Cooled Gas Turbine Technology Development," ASME Paper No. 79-GT-72, Mar. 1979.

6 Kydd, P.H., and Day, W.H., "An Ultra High Temperature Turbine for Maximum Performance and Fuels Flexibility," ASME Paper No. 75-GT-77, Mar. 1975.

7 Sims, C.T., "High Temperature Gas Turbine Engine Component Materials Testing Program, Task 1, Fireside I.," Final Report, FE-1765-44, July 1978.

8 Bouse, G.K., and Schilke, P.W., "Process Optimization of Cast Alloy 718 for Water-Cooled Gas Turbine Application," *Proceedings of the Fourth International Conference in Superalloys,* Seven Springs, Pa., Sept. 1980.

The Effect of Bending-Torsion Coupling on Fan and Compressor Blade Flutter

O.O. Bendiksen
Assistant Professor,
Department of Aerospace Engineering,
University of Southern California,
Los Angeles, Calif. 90007

P.P. Friedmann
Professor,
Mechanics and Structures Department,
University of California,
Los Angeles, Calif. 90024

A study of the effects of bending-torsion interaction of the flutter boundaries of turbomachinery blading is presented. The blades are modeled as equivalent sections, and the equations of motion allow for the general case of structural, inertial and aerodynamic coupling, in the presence of structural damping. Two different speed regimes are investigated: incompressible flow, and supersonic flow with a subsonic leading edge locus. Flutter boundaries are presented for cascade design parameters representative of current technology fan rotors. These results illustrate that bending-torsion interaction has a pronounced effect on the flutter boundaries for both speed regimes, although the mode frequencies show no appreciable tendency to coalesce as flutter is approached. Several cases of bending branch instability were observed, without incorporating the effects of finite mean lift or strong shocks in the analysis.

Introduction

It has been recognized for some time that turbomachinery and isolated wing flutter differ in several ways. Some of the differences are obvious: the interference from adjacent blades in a stage, plus rotational effects, introduce complications into the aerodynamic analysis not found in the fixed wing case. The dynamic mode shapes of shrouded fan rotors tend to be more complicated than those of an isolated wing. As a result, most of the results from fixed-wing aeroelasticity are not directly applicable to the turbomachinery field. A more subtle difference is introduced through fabrication differences; the solid titanium or steel construction typical of fan and compressor blades results in mass ratios (μ) much higher than those of representative fixed-wing constructions. It was recognized by early researchers such as Pearson [1], Schnittger [2] and Whitehead [3] that this higher mass ratio would make the flutter frequency virtually independent of the relative air velocity. This prediction is in good agreement with experimental data. It might appear plausible to expect that the vibratory mode shapes shold also remain relatively unaffected by the aerodynamic loads, an assumption which is in wide use among turbomachinery aeroelasticians [4-6]. Unfortunately, experimental data on flutter mode shapes are scarce and not quantitative enough to be conclusive on this point, although progress is being made in this direction [7].

If both the frequency and the mode shape assumptions are correct, the aeroelastic analysis simplifies considerably. Instead of solving a complex eigenvalue problem to obtain the flutter boundaries, they can be obtained through a single-degree-of-freedom (SDOF) energy analysis based on the natural mode shapes and frequencies of the rotor. This is essentially the approach proposed by Carta [4] and developed further at Pratt & Whitney Aircraft [5,6]. Recent research, however, indicates that the problem is very sensitive to the flutter mode shape, and ignoring the effects of the unsteady aerodynamic loads on the mode shape can lead to errors in the predicted flutter boundary [8,9].

The purpose of this paper is to examine the effects of bending-torsion interaction on the flutter boundaries of fan and compressor blades. It will be shown that this interaction affects the flutter boundaries significantly, but results in little or no tendency for the bending- and torsion-branch frequencies to coalesce as flutter is approached. Although some data from earlier work by the authors is used [8,9], the emphasis in this paper is on illustrating the practical consequences of the results in the design and flutter prediction of fan and compressor rotors.

Structural Model

The rotor is modeled as an infinite two-dimensional cascade of identical airfoils in a uniform upstream flow, as shown in Fig. 1. The blades are modeled as equivalent sections, Fig. 2, where the bending stiffness and torsional rigidity are modeled by springs of stiffnesses K_h and K_α, respectively. Geometric and inertial properties of the blades are represented by their respective values at the three-quarters station of blade span. The blades are considered to have two degrees of freedom: bending displacement h normal to the chord, and torsional displacement α about the elastic axis (EA). It will be assumed that all airfoils execute identical simple harmonic motion with a constant phase angle σ between adjacent blades. The phase angle σ is restricted to the N_b discrete values $\sigma = 2\pi n/N_b$;

Contributed by the Gas Turbine Division of THE AMERICAN SOCIETY OF MECHANICAL ENGINEERS and presented at the International Gas Turbine Conference and Products Show, Houston, Texas, March 9-12, 1981. Manuscript received at ASME Headquarters, December 18, 1980. Paper No. 81-GT-163.

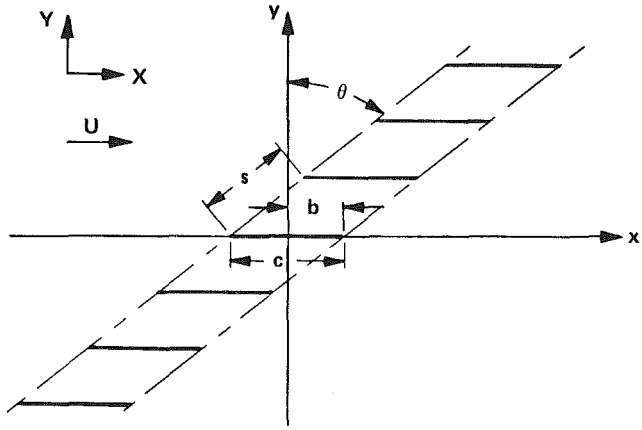

Fig. 1 Cascade geometry

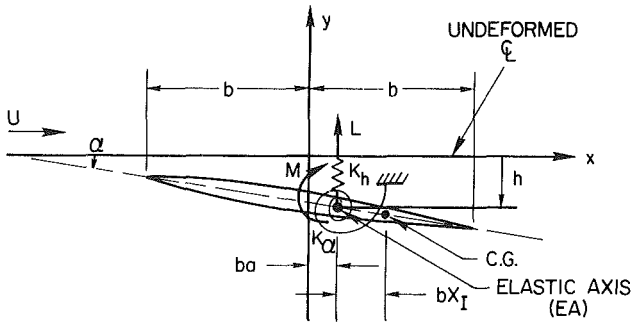

EQUIVALENT SECTION AT 75% SPAN

Fig. 2 Blade geometry and structural model

$n = 0, 1, 2, \ldots, N_b - 1$, in accordance with Lane's [10] analysis of the permissible flutter mode shapes of a tuned rotor.

It should be mentioned that the mode shape assumption is not as restrictive as it might appear. As long as the vibration amplitudes are sufficiently small for linear analysis to hold, Fourier analysis can be used to obtain the most general mode shape, where both amplitude and interblade phase vary from blade to blade, by superimposing elementary constant amplitude, constant σ solutions. A simple example of this is the superposition of forward and backward traveling waves to produce the standing waves typical of the natural modes of vibration of a bladed disk.

The coupled bending-torsion equations of motion can be written in matrix form as [8]

$$[M]\{\ddot{q}\} + [K_d]\{q\} = \{F\} \tag{1}$$

where the mass matrix $[M]$, stiffness matrix $[K_d]$, generalized coordinates $\{q\}$ and force $\{F\}$ are given by

$$[M] = \begin{bmatrix} m & S_\alpha \\ S_\alpha & I_\alpha \end{bmatrix}; [K_d] = \begin{bmatrix} (1+ig_B)m\omega_B^2 & 0 \\ 0 & (1+ig_T)I_\alpha\omega_T^2 \end{bmatrix} \tag{2a}$$

$$\{q\} = \begin{Bmatrix} h \\ \alpha \end{Bmatrix}; \{F\} = \begin{Bmatrix} -L \\ M \end{Bmatrix} \tag{2b}$$

Nomenclature

a = location of elastic axis, nondimensionalized (Fig. 1)
b = semichord
c = $2b$ = chord
$C_{M\alpha}^R, C_{M\alpha}^I$ = real and imaginary parts of moment coefficient due to torsion
g = structural damping
g_B, g_T = structural damping in bending and torsion, respectively
h = bending deflection (Fig. 2)
$\bar{h}$ = h/b
I = $mr_\alpha^2 b^2$ = mass moment of inertia per unit span about axis $x = ba$
k = $\omega b/U$ = reduced frequency
$\bar{k}$ = $kM/(M^2-1)$
K_h, K_α = blade bending and torsional stiffness, respectively
L = lift, positive up, per unit span
m = mass per unit span of blade
M = moment about axis $x = ba$, positive clockwise, per unit span; also Mach number
N = rotor speed, rpm
N_b = number of blades in rotor
$\tilde{p}$ = $p/\omega_T = \tilde{p}_R + i\tilde{\omega}$ = nondimensionalized exponent $[\tilde{p}_0(\tilde{x})^R]$; $[\tilde{p}_0(\tilde{x})^I]$ = real and imaginary parts of pressure jump amplitude across zeroth blade, nondimensionalized with respect to $\rho_0 U^2$
r_α = radius of gyration, nondimensionalized with respect to semichord
s = blade spacing (Fig. 1)
$\bar{s}_2$ = $(s/b)\cos\theta$
S_α = mbx_1 = static mass moment per unit span about axis $x = ba$, positive when center of gravity (CG) is aft
t = time
T_0 = total temperature (°R) at engine intake
U = freestream velocity relative to blades
U_F = flutter speed
x_I = nondimensionalized CG - EA offset positive when CG is aft (Fig. 2)
α = torsional deflection, positive clockwise
δ = logarithmic decrement (damping)
θ = stagger angle; also $T_0/519°\text{R}$
λ = comples eigenvalue
μ = $m/\pi\rho_0 b^2$ = mass ratio of blade
ρ_0 = air density
σ = interblade phase angle
ϕ = phase by which torsion lags bending
ω = frequency in rad/s
$\tilde{\omega}$ = ω/ω_T = nondimensionalized freqency
ω_B, ω_T = uncoupled frequencies in bending and torsion, respectively
$\{\bullet\}$ = differentiation with respect to time
$(\ )_0$ = complex amplitude of harmonic variable

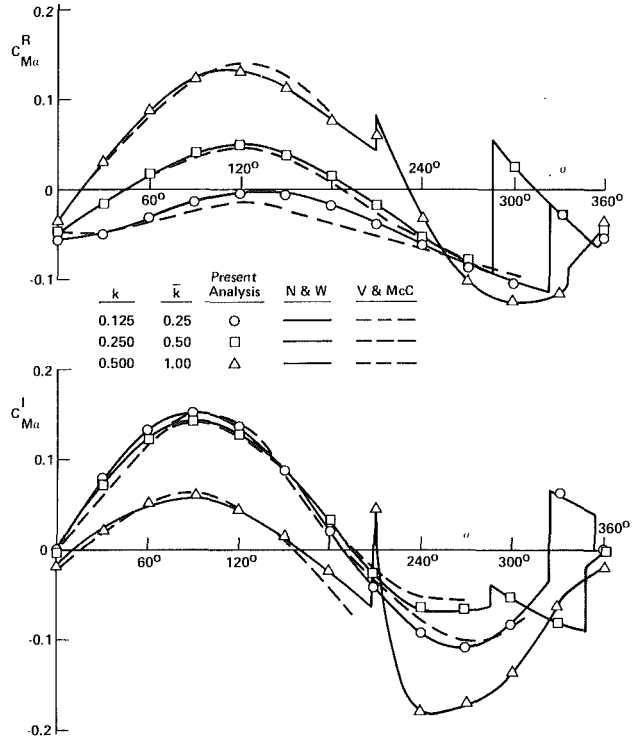

Fig. 3 Comparison of moment coefficient due to torsional oscillations with results of Nagashima and Whitehead (N&W) [14], and Verdon and McCune (V&McC) [12] (Cascade *B*, $a = 0$)

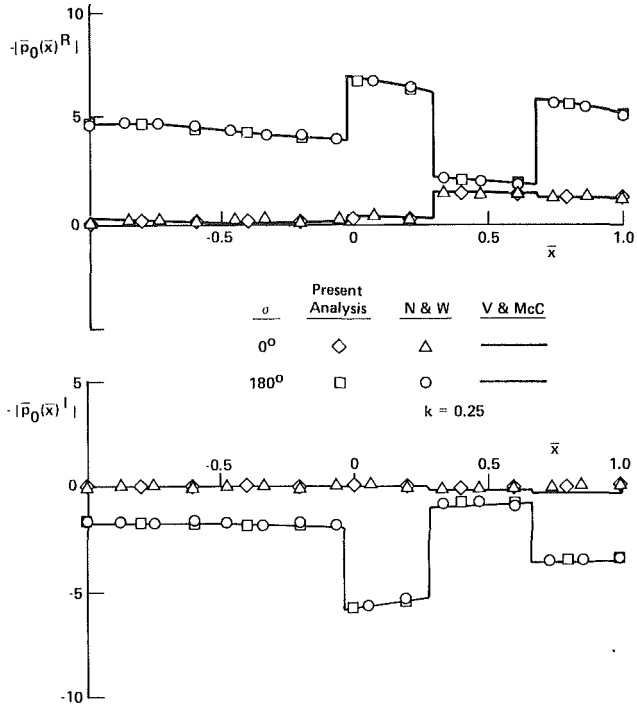

Fig. 4 Comparison of pressure jump amplitude due to torsional oscillations with results of Nagashima and Whitehead [14], and Verdon and McCune [12] (Cascade *B*, $a = 0$)

The structural damping coefficients g_B and g_T are related to the logarithmic decrement α by $\alpha \cong \pi g$, for small g.

With the assumption that the blades execute simple harmonic motion, $\{q\} = \{q_0\} \exp(i\omega t)$, the unsteady aerodynamic forces can be written in terms of nondimensional coefficients A_{ij} as follows:

$$L = L_0 e^{i\omega t} = -\pi\rho_0 b^3 \omega^2 [A_{11}(h/b) + A_{12}\alpha] \quad (3)$$

$$M = M_0 e^{i\omega t} = \pi\rho_0 b^4 \omega^2 [A_{21}(h/b) + A_{22}\alpha] \quad (4)$$

When equations (3) and (4) are substituted into equation (1), it is shown in reference [8] that the following nondimensional eigenvalue problem is obtained

$$[D]\{\bar{q}\} = \lambda\{\bar{q}\} \quad (5)$$

where $\lambda = 1/\bar{\omega}^2$. The matrix $[D]$ is given by[1]

$$[D] = \frac{1}{\mu}\begin{bmatrix} \dfrac{\mu + A_{11}}{\gamma_\omega^2(1+ig_B)} & \dfrac{\mu x_I + A_{12}}{\gamma_\omega^2(1+ig_B)} \\ \dfrac{\mu x_I + A_{21}}{r_\alpha^2(1+ig_T)} & \dfrac{\mu r_\alpha^2 + A_{22}}{r_\alpha^2(1+ig_T)} \end{bmatrix} \quad (6)$$

The CG-EA offset x_I is used to model the combined inertial and structural coupling strength between bending and torsion. Additional comments on the physical significance and limitations of this model can be found in reference [8].

Unsteady Aerodynamics

Two speeds regimes were investigated: incompressible flow, and supersonic flow with a subsonic leading edge locus. The unsteady aerodynamic loads for the incompressible case were evaluated using Whitehead's [3] solution. A computer program has been written to evaluate the force and moment coefficients for given values of θ, s/c, k, and σ, and to calculate the aerodynamic matrix [A] required for the flutter analysis. Details of this calculation can be found in reference [11].

For the supersonic case, the unsteady loads were calculated by the method established by Bendiksen [11], and also discussed in reference [9]. Numerical results show good agreement with those published by Verdon and McCune [12], Verdon [13], Nagashima and Whitehead [14], and Adamczyk and Goldstein [15]. An illustration of this is shown in Figs. 3 and 4, where results for Verdon's cascade B are compared with computations by Nagashima and Whitehead, and Verdon and McCune. The agreement between the present solution and that of Nagashima and Whitehead is excellent, and the agreement with Verdon and McCune's solution is good, except for $k = 0.125$. The reason for the difference for $k = 0.125$, which remains in Verdon's later improved solution [13], is not known.

Both the incompressible and the supersonic cascade theories used in this study are based on two-dimensional, first-order, linearized small disturbance theory. Because the governing equations and boundary conditions in such a theory are linearized about the unperturbed uniform flow, the effects due to thickness, camber and mean angle of attack may be evaluated separately and superimposed, provided these are small. In this case, it is well established [16] that these additional effects only appear in the steady problem, i.e. the eigenvalue problem governing the flutter boundaries remains unchanged. This is the justification for treating the blades as flat plates at zero incidence. If thickness, camber or mean incidence are not small, there can be significant coupling between the steady and unsteady flow perturbations, as shown in the work of Atassi and Akai [17].

It should be mentioned, though, that the supersonic cascade might be more sensitive to thickness and profile parameters in general, because of the strong effect the cross-sectional blade shape has on the location, generation, and reflection of shock waves. Nevertheless, results reported by Snyder and Com-

[1] The expression for $[D]$ in reference [8] contains a misprint.

Table 1 Cascade Design Parameters

Parameter	Cascade A	Cascade B	Cascade C
Stagger θ	59.5°	63.4°	60°
Spacing $\bar{s}_2$	0.8	0.6	1.0
Mach No. M	1.3454	1.2806	0

merford [5] indicate that for practical blade shapes, this effect is probably small. They tested two different blade profiles in a supersonic cascade tunnel: an uncambered, symmetrical *J*-blade with a 5 percent thickness to chord ratio, and a precompression blade with a 4 percent thickness to chord ratio. The *J*-blade had a normal shock at the blade passage entrance, followed by subsonic flow in the passage; the precompression blade had a weak shock system at the entrance and in the blade passage. Despite these large qualitative differences in the flow, the flutter boundaries were found to differ only by approximately 5 percent.

Method of Solution for the Aeroelastic Eigenvalue Problem

The flutter boundaries are obtained by solving a complex eigenvalue problem, equation (5), analogous to the fixed wing case. The harmonic time dependence exp ($i\omega t$) is temporarily replaced by a general time dependence exp(pt), where the exponent p is assumed complex, and the eigenvalue problem is solved directly. From the two complex eigenvalues λ_1 and λ_2, two values for p are obtained through the relation.

$$p = (i\sqrt{\lambda})\omega_T \tag{7}$$

or, in nondimensional form

$$\bar{p} = p/\omega_T = \bar{p}_R + i\bar{\omega} \tag{8}$$

Flutter occurs when $\bar{p}_R > 0$

An independent check of the flutter boundary calculations can be obtained by considering the energy exchange between the rotor (cascade) and the surrounding flow [8]. Excellent agreement was obtained for all cases checked.

If the flutter mode shape can be assumed known *a priori*, Carta's energy method [4] will yield the same flutter boundaries as obtained by the solution of the eigenvalue problem. It has been found that, the assumption that the flutter mode shape will coincide with a natural mode of the rotor, is unreliable, particularly for reduced frequencies in the practical range $k < 0.5$, although the error decreases with increasing coupling strength x_I.

Flutter Boundaries

Numerical results will be presented for three different cascade configuration. The design parameters, summarized in Table 1, have been chosen in the practical range of current technology fan rotor design. Cascades A and B are identical to Verdon's [12, 13] cascades A and B, and were used in all calculations for supersonic flow; cascade C was used for all calculations for incompressible flow. In all cases, a titanium rotor with 40 blades and a mass ratio of $\mu = 200$ was assumed.

Incompressible Flow. Figure 5 illustrates the typical behavior of the frequency and damping in bending and in torsion as flutter is approached, for cascade C in incompressible flow. In this example, it is the torsional branch which becomes unstable. Note the insensitivity of the modal frequencies to the relative air velocity; there is no significant tendency toward frequency coalescence. In fact, the flutter frequency is within 0.6 percent of the natural frequency of the torsional branch in vacuum. If this instability were encountered experimentally, it would almost certainly be identified as "pure torsional flutter," unless accurate mode

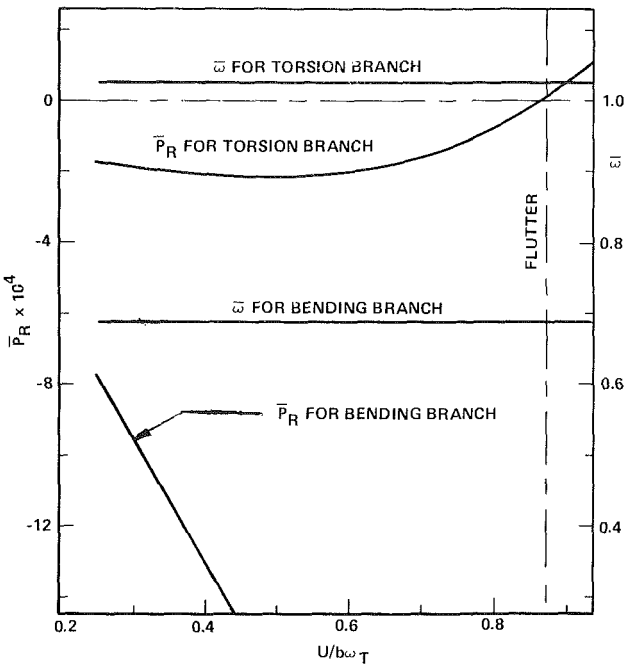

Fig. 5 Frequency and damping in bending and torsion versus airspeed for cascade C in incompressible flow ($a = 0, r_\alpha^2 = 1/3, g_B = g_T = 0, \omega_B/\omega_T = 0.7, x_I = 0.1$)

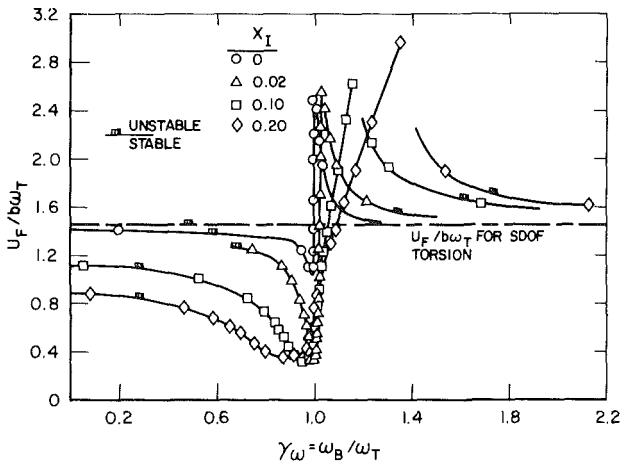

Fig. 6 Coupled bending-torsion flutter boundaries for cascade C in incompressible flow (*EA* at midchord, $a = 0, r_\alpha^2 = 1/3, g_B = g_T = 0$)

shape measurements were also obtained. The actual flutter mode has a bending/torsion displacement ratio $\bar{h}_0/\alpha_0$ of 0.179, i.e. it contains a significant bending component.

That bending/torsion coupling can have significant effects on the flutter boundaries is clearly shown in Fig. 6. The flutter boundaries are plotted as nondimensionalized flutter speed $U_F/b\omega_T$ versus frequency ratio $\gamma_\omega = \omega_B/\omega T$, for various values of coupling strength x_I. Recall that x_I, which is the nondimensionalized offset between the elastic axis and the cross-sectional center of mass of the blade, is used to model the combined inertial and structural coupling strength in this study. In addition, the modes are coupled aerodynamically through the off-diagonal terms A_{12} and A_{21} of the aerodynamic matrix. Additional results presented in reference [8] indicate that there are pronounced differences between the SDOF and the coupled flutter boundaries for the 1/4-chord and 3/4-chord elastic axis locations as well, and that these differences persist in the presence of structural damping.

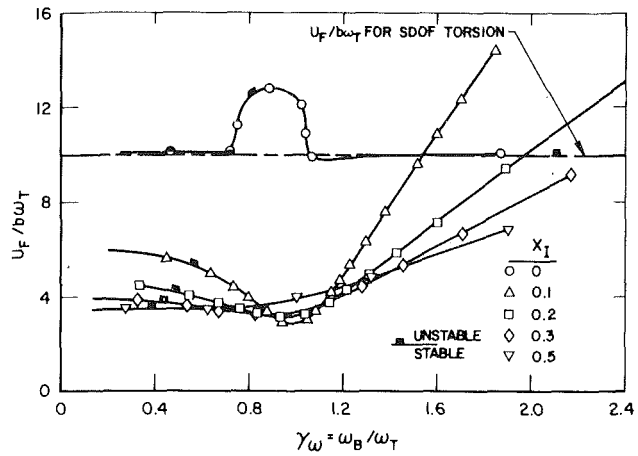

Fig. 7 Effect of strong structural damping on flutter boundaries for cascade C in incompressible flow (EA at 1/4-chord, $a = -0.5$, $r_\alpha^2 = .5833$, $g_B = g_T = 0.02$)

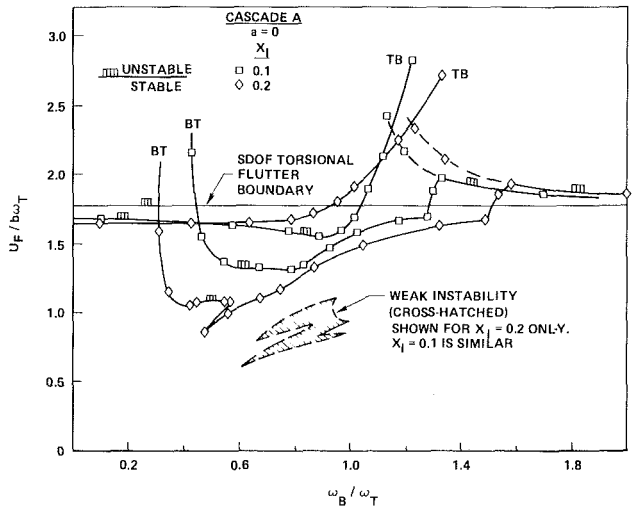

Fig. 8 Coupled bending-torsion flutter boundaries for cascade A in supersonic flow ($a = 0$, $r_\alpha^2 = 1/3$, $g_B = g_T = 0$)

Figure 7 is a good illustration of this, for the case of the elastic axis at 1/4-chord and strong structural damping.

Supersonic Flow. Results illustrating the effect of bending-torsion interaction on the flutter boundaries for Verdon's cascade A and B are presented in Figs. 8-12. Because both the bending and the torsional branches exhibit instability over a wide range of frequency ratios, care must be exercised in labeling the branches. It must be kept in mind that the mode shape $\bar{h}_0/\alpha_0$ for a given branch changes as a function of frequency ratio. Therefore, the label BT for "bending-torsion" is used to indicate that bending dominates for low frequency ratio and torsion dominates for high frequency ratios. Conversely, the label TB for "torsion-bending" indicates that the reverse is true: torsion dominates for low frequency ratios and bending dominates for high frequency ratios. Typical values of the interblade phase angle σ at flutter are also shown in Figs. 9 and 12. It can be seen that the TB branches have relative low values of σ, whereas the BT branches have relatively high values of σ.

There are two interesting differences between the incompressible and the supersonic cascade flutter boundaries. The first is in the behavior of the BT branch, which in the supersonic case shows a marked tendency to become critical for frequency ratios ω_B/ω_T as low as 0.2-0.3. In the incompressible case, the BT branch usually becomes critical only for $\omega_B/\omega_T > 1$, except for negative values of coupling x_I. The second noticable difference appears in the form of bubble- and cavity-like regions of weak instability, and finger-like regions of weak stability. These are due to the presence of multiple "humps," i.e. local maxima and minima, in the damping versus relative airspeed plot of the BT mode, as illustrated in Fig. 10. The corresponding behavior of the bending (BT) and torsion (TB) branches and the phase angle ϕ between bending and torsion for each branch, are shown in Fig. 11. Since the coupling (x_I) is strong in this example, the mode shapes and phase angles are relatively unaffected by increasing airspeed U/bw_T, although there is a small change in the bending branch immediately before and after it becomes unstable. Note, however, that for $(U/b\omega_T) > 2$, i.e. $k_T < 0.5$, the effect of the airloads on the torsional branch become significant and cannot be ignored.

By introducing small amounts of structural damping, the

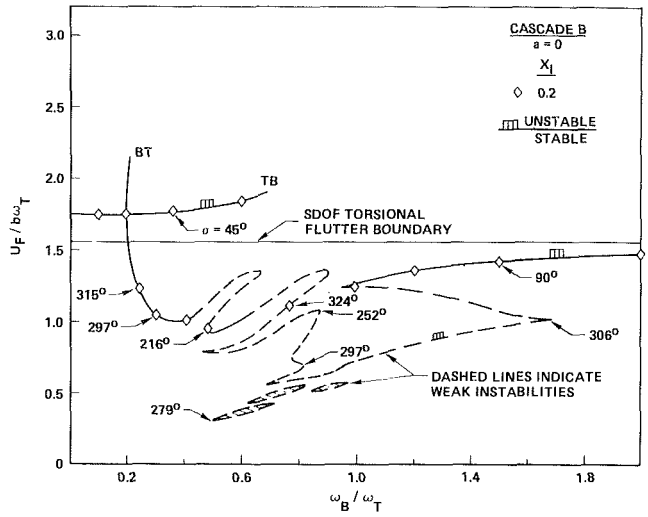

Fig. 9 Coupled bending-torsion flutter boundaries for cascade B in supersonic flow ($a = 0$, $r_\alpha^2 = 1/3$, $g_B = g_T = 0$)

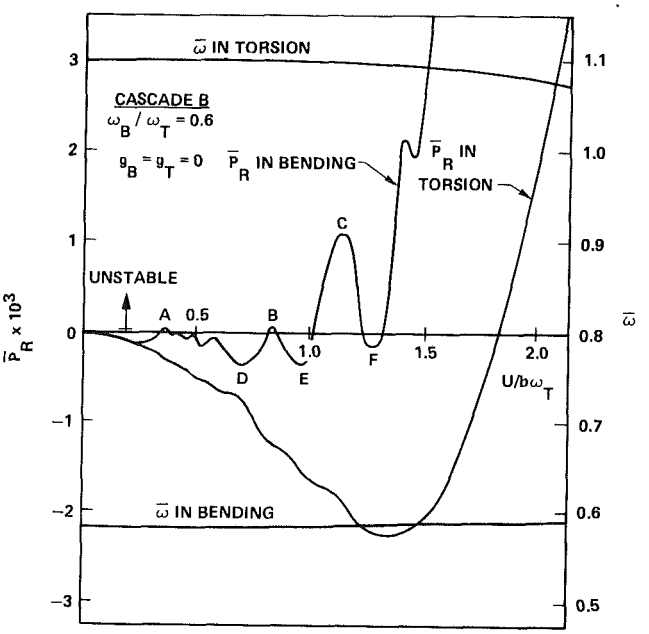

Fig. 10 Frequency and damping versus relative airspeed for cascade B in supersonic flow ($a = 0$, $r_\alpha^2 = 1/3$, $\omega_B/\omega_T = 0.6$, $g_B = g_T = 0$)

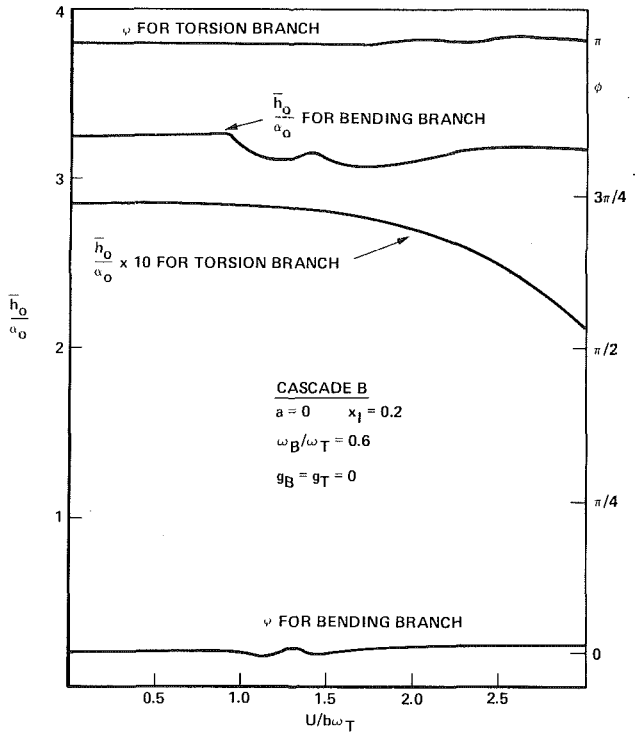

Fig. 11 Amplitude ratio $\bar{h}_0/\alpha_0$ and phase angle ϕ between bending and torsional displacements for the bending and torsional branches, corresponding to Fig. 10

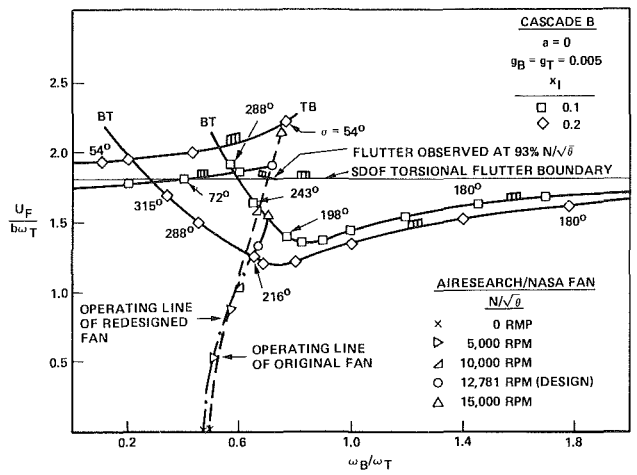

Fig. 12 Effect of structural damping on flutter boundaries of cascade B ($a = 0$, $r_\alpha^2 = 1/3$, $g_B = g_T = 0.005$), and operating lines of AiResearch/NASA fan [24, 25]

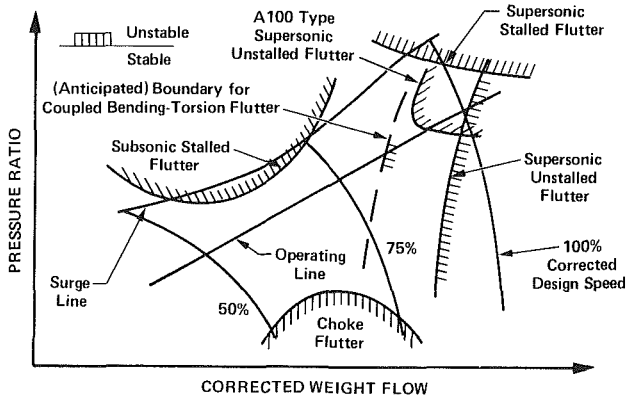

Fig. 13 Compressor map showing typical flutter boundaries

regions of weak instability can be eliminated. The finger-like regions of weak stability observed in Fig. 9 also disappear, leaving the flutter boundaries reasonably smooth, as shown in Fig. 12. Note that for the regions of weak stability, the introduction of structural damping can actually be destabilizing. It should be mentioned that similar weak instabilities are also known to occur in rotary-wing aeroelasticity [18].

Some Design Implications

Realizing the difficulties in extrapolating cascade predictions to 3-dimensional rotors, one can understand the reluctance of designers to rely too heavily on cascade calculations alone. Strictly speaking, there is no theoretical foundation for such an extrapolation, and its validity can only be established through carefully conducted experiments. Published flutter data on full-scale fan and compressor rotors are scarce and incomplete from a quantitative standpoint, often because some or all of this data is considered proprietory. Another problem is that the instrumentation is seldom sufficient to obtain all the parameters required. This is particularly true for flutter mode shape measurements; in fact, recent data [19, 20] suggests that mistuning effects may have to be considered, thus adding to the instrumentation requirements.

A qualitative sketch of the various flutter regimes which may be encountered in a fan or compressor rotor is shown in Fig. 13. The two distinctly different boundaries for supersonic unstalled flutter indicate that the exact shape of this boundary is a function of the design of the rotor, and that generalizations should be cautioned against. It should also be realized that experimentally obtained flutter boundaries plotted in this manner can be functions of many variables: reduced frequency, relative Mach number, finite incidence effects, separation and stall effects, and so on. For potential flow situations, one might expect the flutter boundaries to follow a line of constant corrected speed, $N/\sqrt{\theta}$, since the relative Mach number is approximately constant along such a line. From Fig. 13 one concludes that this is not the case, at least for supersonic unstalled flutter; there appears to be definite effect due to the blade loading.

A word of caution is appropriate at this point. Because the unsteady airloads also depend on the reduced frequency k, they are also functions of the *absolute* relative airspeed U and hence N. This means that the flutter boundaries plotted on a compressor map as in Fig. 13 *cannot be unique*, and both absolute speed and temperature effects remain in the data. Halliwell has discussed these effects in a recent paper [21], and has presented test data correlations with corrected speed, air temperature, and air density. The destabilizing effect of increasing the air density ρ_0 has been documented in several earlier tests [5, 6, 22], although some very recent data on choke flutter obtained by Jutras, et al. [23] do not exhibit this trend. This density effect is often explained by noting that the work done by the air on the cascade is proportional to ρ_0; therefore, increasing ρ_0 will increase the work input to the rotor and, if positive, require a higher level of structural damping to check the instability. Accordingly, in the absence of structural damping, the density should have no effect on the flutter boundaries [5].

Although the preceding explanation is reasonable, it is incomplete. First of all, from equation (5) it is clear that the density ρ_0 only enters the eigenvalue problem through the mass ratio μ in the matrix $[D]$, equation (6). One should therefore speak of the effect of mass ratio, which is a relative

density, and not of density per se. But more important is the conclusion that, according to equations (5) and (6), this effect clearly remains even in the absence of structural damping.

In Fig. 12 data from an AiResearch/NASA research fan [24,25] have been superimposed on the flutter boundaries for cascade B. This fan, which was not developed for flutter testing, encountered flutter around 93 percent $N/\sqrt{\theta}$ during initial testing, with subsequent failure of the mid-span shrouds from high cycle fatigue. The blade was successfully redesigned by increasing its thickness and changing the shroud geometry. This raised the torsional frequency by approximately 45 percent, and moved a given corrected speed point toward lower values of $U/b\omega_T$, as can be seen from Fig. 12. The observed flutter point occurred remarkably close to both the SDOF torsional flutter boundary, as well as to the torsional and bending branches for a coupling strength x_I slightly below 0.10. One should be cautioned against attaching too much significance to this agreement, however, since the AiResearch/NASA fan at 75 percent of blade span is only qualitatively similar to cascade B; its Mach wave reflection pattern is similar, but its geometry and relative Mach number are slightly different.

Finally, two additional predictions which are of interest to the designer should be mentioned. The first has to do with the possibility of encountering bending flutter, which in the supersonic case is a real possibility for EA locations around midchord and frequency ratios in the practical range $0.3 < \omega_B/\omega_T < 0.8$. This is clearly demonstrated in Figs. 8, 9, and 12. Since the bending branch frequency has been found extremely insensitive to relative airspeed, e.g. Figs. 5 and 11, the flutter frequency would be very close to the natural frequency of the bending mode in vacuum. If encountered during flutter testing, this type of instability would probably therefore be classified as "bending flutter." It is interesting to note that this is predicted to be a low k, high σ type flutter, characteristics which it has in common with the shock-induced bending flutter predicted by the theory of Goldstein et al. [26].

The second prediction deals with the effect of the location of the elastic axis. Although the SDOF torsional flutter boundaries predicted by Whitehead's theory for incompressible flow are very sensitive to the EA location, coupling between bending and torsion was found to reduce this sensitivity dramatically [8]. For the supersonic cascades considered here and in references [9, 11], the SDOF torsional flutter boundaries are less sensitive to the EA location, and only cascade A displays a distinct minimum of the flutter speed, at approximately 73 percent of chord. For cascade B the worst axis location from a SDOF torsional flutter standpoint is actually forward of midchord, at around 27 percent of chord.

Conclusions

The following conclusions can be drawn:

1. Coupling between the bending and torsional degrees of freedom changes the flutter boundaries of a typical fan or compressor rotor significantly. This is true both in incompressible and in supersonic relative flow.

2. There is no appreciable tendency for the bending and torsional frequencies to coalesce as flutter is approached, except at very low reduced frequencies. This makes it impossible to assess the degree of modal coupling from the observed flutter frequency alone.

3. Both the torsional and the bending branch exhibit instabilities in the practical range of design parameters and coupling strength.

4. The bending branch instability in supersonic flow is characterized by low reduced frequency and high interblade phase angle. It often manifests itself as a hump mode, generating both bubble-like regions of weak instability as well as finger-like regions of weak stability. Both were found to disappear when structural damping of the order of 1.5 percent of critical was introduced.

5. Structural damping has a pronounced beneficial effect on the flutter boundaries, except in regions of weak stability, where damping often is destabilizing.

References

1 Pearson, H., "The Aerodynamics of Compressor Blade Vibration," Fourth Anglo-American Aeronautical Conference, London, 15th-17th September, 1953, pp. 127–162.

2 Schnittger, J.R., "Flutter Problems in Gas Turbines," in *Design and Performance of Gas Turbine Powerplants*, ed. by W.R. Hawthorne and W.T. Olson, Princeton University Press, Princeton, N.J., 1960, pp. 425–459.

3 Whitehead, D.S., "Force and Moment Coefficient for Vibrating Aerofoils in Cascade," Great Britain A.R.C. R&M 3254, 1960.

4 Carta, F.O., "Coupled Blade-Disk-Shroud Flutter Instabilities in Turbojet Engine Rotors," ASME *Journal of Engineering for Power*, Vol. 89, No. 3, July 1967, pp. 419–427.

5 Snyder, L.E., and Commerford, G.L., "Supersonic Unstalled Flutter in Fan Rotors; Analytical and Experimental Results," ASME *Journal of Engineering for Power*, Vol. 96, No. 4, Oct. 1974, pp. 379–386.

6 Mikolajczak, A.A., Arnoldi, R.A., Snyder, L.E., and Stargardter, H., "Advances in Fan and Compressor Blade Flutter Analysis and Predictions," *Journal of Aircraft*, Vol. 12, No. 4, Apr. 1975, pp. 325–332.

7 Stargardter, H., "Optical Determination of Rotating Fan Blade Deflections," ASME Paper No. 76-GT-78, Mar. 1976.

8 Bendiksen, O., and Friedmann, P., "Coupled Bending Torsion Flutter in Cascades," *AIAA Journal*, Vol. 18, No. 2, Feb. 1980, pp. 194–201.

9 Bendiksen, O., and Friedmann, P., "Coupled Bending-Torsion Flutter in a Supersonic Cascade," AIAA Paper No. 80-0701 presented at the AIAA/ASME/ASCE/AHS 21st Structures, Structural Dynamics, and Materials Conference, Seattle, Washington, May 12-14, 1980.

10 Lane, F., "System Mode Shapes in the Flutter of Compressor Blade Rows," *Journal of the Aeronautical Sciences*, Vol. 23, No. 1, Jan. 1956, pp. 54–66.

11 Bendiksen, O., "Coupled Bending-Torsion Flutter in Cascades with Applications to Fan and Compressor Blades," Ph.D. dissertation, Mechanics and Structures Department, University of California, Los Angeles, Mar. 1980.

12 Verdon, J.M., and J.E. McCune, "Unsteady Supersonic Cascade in Subsonic Axial Flow," Vol. 13, No. 2, Feb. 1975, pp. 193–201.

13 Verdon, J.M., "Further Developments in the Aerodynamic Analysis of Unsteady Supersonic Cascades, Parts 1 and 2," *Journal of Engineering for Power*, Vol. 99, Oct. 1977, pp. 509–525.

14 Nagashima, T., and Whitehead, D.S., "Linearized Supersonic Unsteady Flow in Cascades," Great Britain A.R.C. R&M 3811, 1978.

15 Adamczyk, J.J., and Goldstein, M.E., "Unsteady Flow in a Supersonic Cascade with Subsonic Leading-Edge Locus," *AIAA Journal*, Vol. 16, No. 12, Dec. 1978, pp. 1248–1254.

16 Fung, Y.C., *An Introduction to the Theory of Aeroelasticity*, Dover Publications, Inc., New York, N.Y., 1969, p. 395.

17 Atassi, H., and Akai, T.J., "Aerodynamic and Aeroelastic Characteristics of Oscillating Loaded Cascades at Low Mach Number, Part I: Pressure Distribution, Force and Moments," ASME Paper No. 79-GT-111, Mar. 1979.

18 Friedmann, P., "Recent Developments in Rotary-Wing Aeroelasticity," *Journal of Aircraft*, Vol. 14, Nov. 1977, pp. 1027–1041.

19 Nieberding, W.C., and J.L. Pollack, "Optical Detection of Blade Flutter," ASME Paper No. 77-GT-66, Mar. 1977.

20 Hockley, B.S., Ford, R.A., and Foord, C.A., "Measurement of Fan Vibration Using Double Pulse Holography," ASME Paper No. 78-GT-111, Apr. 1978.

21 Halliwell, D.G., "Effect of Intake Conditions on Supersonic Unstalled Flutter in Turbofan Engines," *Journal of Aircraft*, Vol. 17, No. 5, May 1980, pp. 300–304.

22 Jeffers, II, J.D., and Meece, Jr., C.E., "F100 Fan Stall Flutter Problem Review and Solution," *Journal of Aircraft*, Vol. 12, Apr. 1975, pp. 350–357.

23 Jutras, R.R., Stallone, M.J., and Bankhead, H.R., "Experimental Investigation of Flutter in Mid-Stage Compressor Designs," AIAA Paper No. 80-0786 presented at the AIAA/ASME/ASCE/AHS 21st Structures, Structural Dynamics, and Materials Conference, Seattle, Washington, May 12-14, 1980.

24 Wright, L.C., Vitale, N.G., Ware, T.C., and Erwin, J.R., "High-Tip-Speed, Low-Loading Transonic Fan Stage, Part I," NASA CR-121095, Apr. 1973.

25 Ware, T.C., Kobayashi, R.J., and Jackson, R.J., "High-Tip-Speed, Low-Loading Transonic Fan Stage, Part 3," NASA CR-121263, Feb. 1974.

26 Goldstein, M.E., Braum, W. and Adamczyk, J.J., "Unsteady Flow in a Supersonic Cascade with Strong In-Passage Shocks," *Journal of Fluid Mechanics*, Vol. 83, Part 3, Nov. 1977, pp. 569–604.

Nuclear Blast Response of Airbreathing Propulsion Systems: Laboratory Measurements With an Operational J-85-5 Turbojet Engine

M. G. Dunn

Aerodynamic Research Department,
Calspan Advanced Technology Center,
Buffalo, N.Y. 14225

J. M. Rafferty

Headquarters,
Defense Nuclear Agency

This paper describes an experimental technique that has been developed for the performance of controlled laboratory measurements of the nuclear blast response of airbreathing propulsion systems. The experiments utilize an available G.E. J-85-5 turbojet engine located in the test section of the Calspan Ludwieg-tube facility. Significant modifications, described herein, were made to this facility in order to adapt it to the desired configuration. The J-85 engine had previously been used at Calspan for other purposes and thus came equipped with eight pressure transducers at four axial locations along the compressor section. These transducers have a frequency response on the order of 40 KHz. Pressure histories obtained at several circumferential and axial locations along the compressor are presented for blast-wave equivalent overpressures up to 17.2 kPa (2.5 psi) at corrected engine speeds on the order of 94 percent of maximum speed.

Introduction

Propulsion-system blast tolerance, including the relative importance of inlet flow distortion and internal blast-wave propagation, is governed by many factors. The engine type is of obvious importance; for example, turbojets, turbofans or ramjets, will repsond differently to any given blast environment. For any particular engine type, the detailed internal gas-dynamic response will depend generally on the internal engine configuration, (the number and type of compressor and turbine stages, or combustor type), the engine operating point (stage pressure and stall-margin ratios, nozzle pressure ratio, turbine inlet temperature, and fuel/air ratio) and the engine control system (measurement parameters or response characteristics). The inlet type (internal, external, or mixed compression; high or low length-to-diameter ratio; and boundary-layer bleed and bypass provisions) can modify blast waves entering the engine from the front by changing the blast strength and introducing distortion. Finally, the local blast strength and orientation with respect to the propulsion system will strongly affect the transient internal engine pressures and temperatures that result.

A nuclear blast wave has associated with it a nearly step-function pressure and temperature pulse to which an operating engine may be subjected. The blast response of the propulsion system is recognized as an important consideration that must be treated in studies of systems utilizing airbreathig propulsion. Because this is a relatively new aspect of nuclear blast response, it is one for which only limited experimental and theoretical work has been done.

The only other similar laboratory measurement program that we are aware of is the one reported [1-3] by the Canadian group[1] at the Defence Research Establishment, Suffield. The purpose of the Canadian experiments was to test the general response of the Orenda 8 engine in contrast to the purpose of the present program which was to develop a technology that could provide the detailed data necessary to predict the general behavior of airbreathing propulsion systems.

In the remainder of this paper, the facility modifications will be discussed, followed by a discussion of experimental results.

Experimental Facility and Modifications

The basic Ludwieg-tube facility (sketched in Fig. 1), around which this technology program has been developed, was previously in existence at Calspan. The existing facility consisted of a supply tube (the driver gas supply) of 1.10-meters (3.5-ft) diameter by 18.3-meters (60-ft) long and the test section (in which the J-85 engine was located) which is 2.44-meters (8-ft) diameter by 18.3-meters (60-ft) long. The driver pressure limitation on the supply tube is 1379 kPa (200 psia) which, as will be shown later, is almost a factor of ten greater than necessary to achieve the maximum allowable overpressure for the J-85 engine. The experiments reported here required supply-tube pressures less than 172.4 kPa (25 psig). In order to convert the existing facility to one that could

Contributed by the Gas Turbine Division of THE AMERICAN SOCIETY OF MECHANICAL ENGINEERS and presented at the International Gas Turbine Conference, Houston, Texas, March 8-12, 1981. Manuscript received at ASME Headquarters, December 18, 1980. Paper No. 81-GT-164.

[1] In the early stages of the Calspan program (July, 1978) the DRES people were visited to discuss the detailed results of their previous experiments

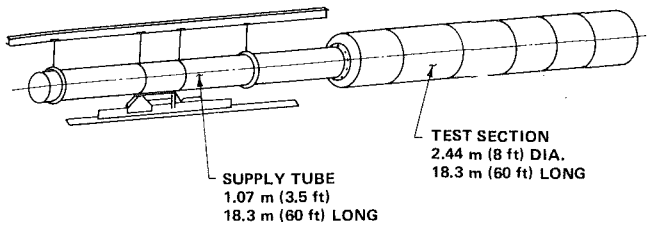

Fig. 1 Ludwieg-tube facility

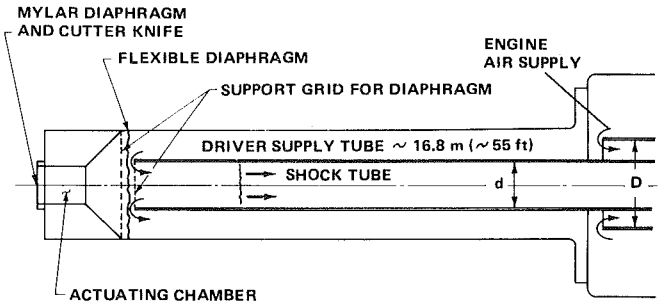

Fig. 2 Sketch of system

be used to study the blast response of airbreathing propulsion systems, several modifications were necessary.

An important restriction on the generation of shock waves that would eventually be directed into the engine is that the flow environment be free of foreign particles. It was thus necessary to modify the facility as shown in Fig. 2 so as to incorporate a driver technique [1-3] consisting of an actuating chamber and a flexible diaphragm in order to drive the appropriate shock waves. A photograph of the actuating chamber and the flexible diaphragm (neoprene) is shown in Fig. 3. This chamber is initially pressurized to a static pressure of 13.8 to 34.5 kPa (2 to 5 psi) in excess of the Ludwieg-tube driver supply tube in order to seal the flexible diaphragm against the shock-tube flange and support grid. The sketch shown in Fig. 2 illustrates that two additional tubes, in addition to the actuating chamber, were added to the facility in order to perform the desired experiments. The shock wave is initiated in the small diameter tube by rapid removal of the flexible diaphragm from the tube entrance. This is accomplished by venting the actuating chamber to the outside away from the engine by rupturing a mylar diaphragm using an air-operated knife. A shock wave is then formed in the 0.25-meter (0.83-ft) diameter tube (d) and progresses on to the larger diameter tube (D) where it weakens and eventually is directed into the operating engine. For steady-state operation of the engine prior to initiation of a shock wave, the engine draws its supply air through the annulus bounded by the two tubes of diameters d and D as shown in Fig. 4. For the experiments to be described in this paper, the engine was operated with an ASME bellmouth into which the shock wave is directed as illustrated in Fig. 4. The bellmouth is not rigidly coupled to the shock tube but rather a rubber transition piece attached to the shock tube fills the gap of approximately 1.9×10^{-2} meters (3/4-in.) between the tube and bellmouth. In this way, any impulse loading on the shock tube that may be created when the shock wave is initiated is isolated from the engine.

The experimental configuration sketched in Fig. 4 raises the question of possible reduced pressure at the bellmouth as a result of the inlet air flowing through the long pipe (of diameter D) upstream of the inlet. The engine used in these experiments has previously been used at Calspan in the development of a rotating-stall control system. Therefore, there exists a large body of performance data obtained with the engine operating under ideal conditions. The engine performance while installed in the Ludwieg-tube configuration was checked against some of these previous results which are given in [4]. The results presented in this paper were all obtained at corrected engine speeds in the range of 70 to 95 percent. The measured static pressure increase across the compressor and the stall-control system sensitivities indicated that the Ludwieg tube installation had associated with it a slightly lower inlet pressure and a relatively small amount of inlet distortion when compared to the previous measurements obtained for undistorted inlet flow. For the purposes of the blast-wave experiments of interest to this program, both of these influences are sufficiently small that they will not compromise the results.

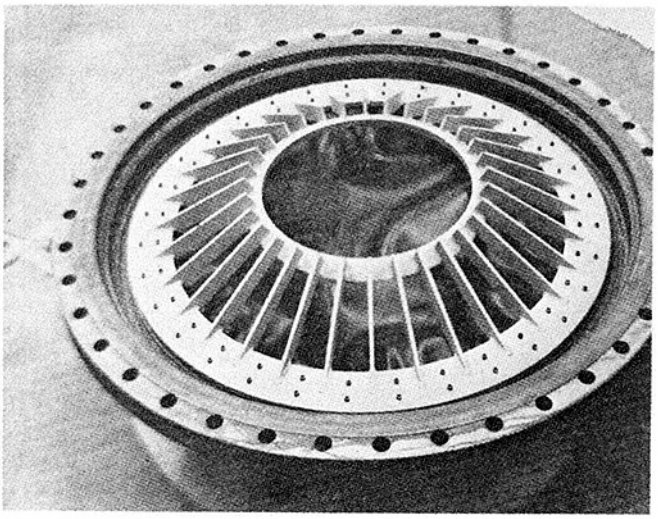

(a) Neoprene diaphragm

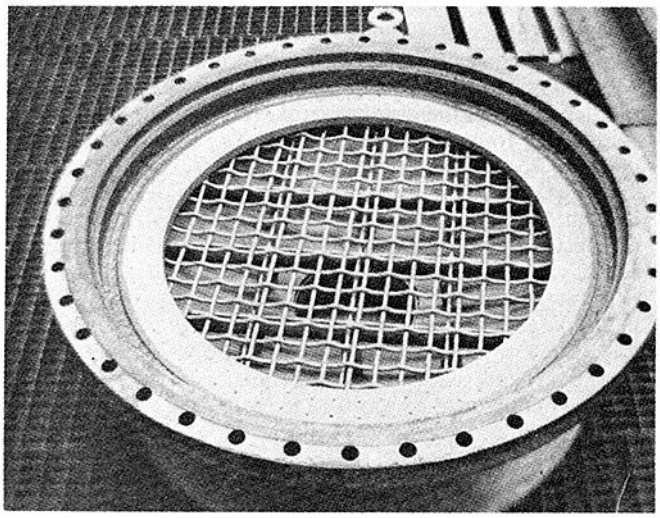

(b) Back-up grid for diaphragm

Fig. 3 Photograph of actuating chamber

Figure 5 is a photograph taken inside the receiver tank of the large diameter shock tube and the engine illustrating the manner in which the shock wave is directed into the engine and the rubber fairing which isolates the shock tube from the engine. This photograph demonstrates that a portion of the bellmouth is not in use which could account for the minor steady-state distortion discussed above. Several of the static pressure taps in the large diameter pipe can also be seen on this photograph. A description of transducer locations in both

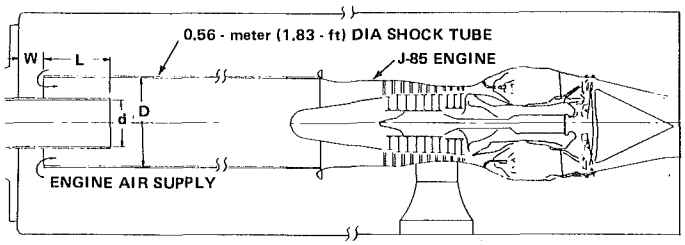

Fig. 4 Sketch of engine in test section

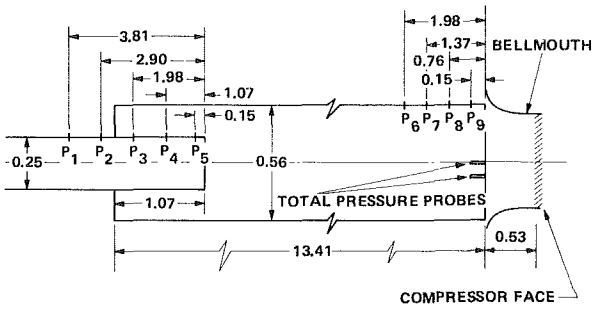

NOTE: ALL DIMENSIONS ARE METERS

Fig. 6 Sketch of shock-tube instrumentation

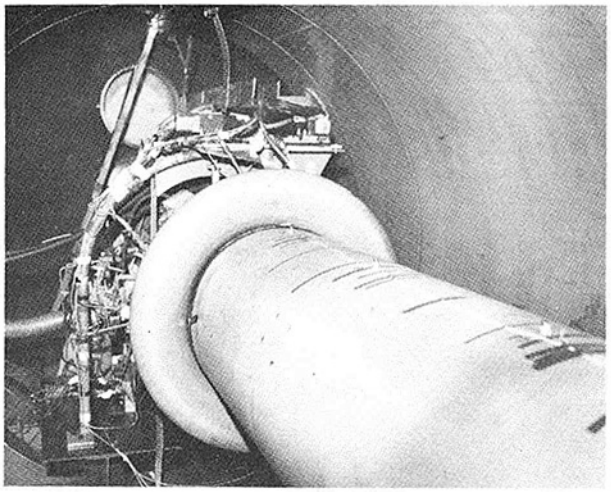

Fig. 5 Photograph of large diameter shock tube and bellmouth junction

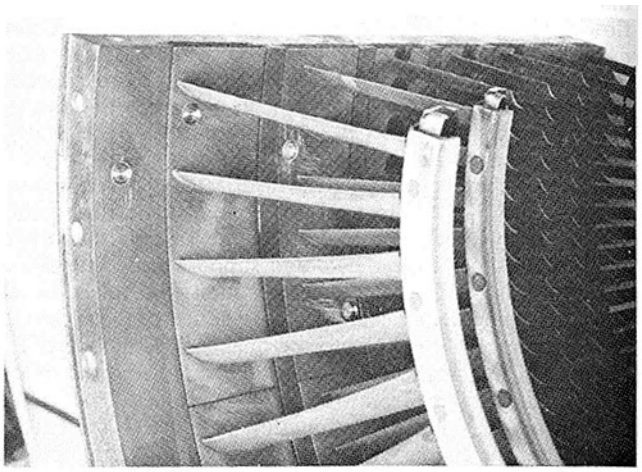

Left side

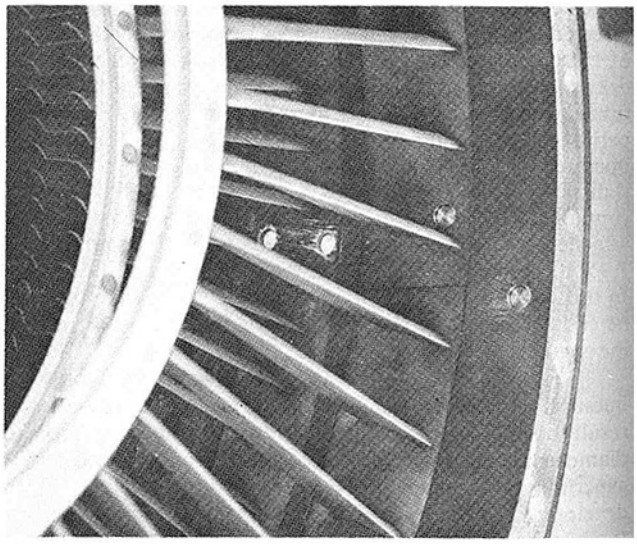

Right side

Fig. 7 Pressure transducer locations in forward portion of J-85 compressor

the small and large diameter shock-tubes is given in the next section.

Shock-Tube and Engine Instrumentation. Figure 6 is a sketch of the instrumentation locations in the shock tubes. In addition, the overlap of the large diameter tube relative to the smaller tube and the distance from the tube exit plane to the compressor force are also illustrated. The ratio of shock-tube diameter to entrance tube diameter, d/D, and the overlap length were sized on the basis of calculations [5] performed by Kaman AviDyne. A significantly more detailed discussion of this instrumentation and further details of the experimental results can be found in [6].

Total-pressure time histories were obtained at two locations in the large-diameter tube just upstream of the compressor face. These transducers were not installed while the transient engine-response data were being obtained, but were rather used to obtain detailed shock-tube performance data at times when engine data were not being taken.

The front portion of the compressor of the GE J-85-5 engine used for these experiments is instrumented [7] with eight Piezotronic pressure transducers (20 to 40 KHz response) as the photograph presented in Fig. 7 illustrates. The eight transducers are located at four axial locations with two at each of the following locations:

(*a*) near the first stage rotor midchord; (1RMCT, 1RMCL)
(*b*) near the quarter-chord of the first stage stator, as close to the stator suction surface as possible; (1SQCT, 1SQCL)
(*c*) between the second stage stator trailing edge and the third stage rotor leading edge; (2STET, 2STEL).

Two additional pressure transducers are located near the rear of the compressor as illustrated in the photograph of Fig. 8 between the seventh stage stator blades at approximately midchord (7SMCL). However, because of engine geometry, these transducers could not be flush mounted and thus the frequency response is less than that of the forward transducers.

In addition to the pressure measurements noted above, one other pressure transducer is installed on the engine. This transducer is used in conunction with those noted above to measure the static pressure rise across the compressor, and is located at the throat of the bellmouth upstream of the compressor face.

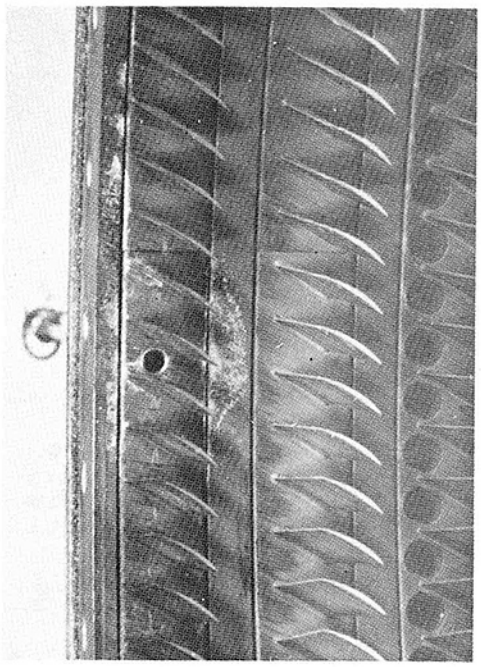

Left side installation

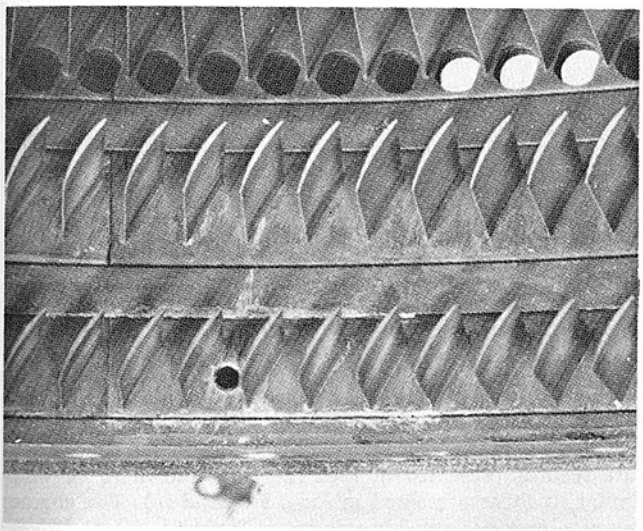

Upper installation

Fig. 8 Pressure transducer locations in rear of J-85 compressor

An accelerometer is mounted on the compressor casing from which the peak-to-peak displacement history can be deduced using a suitable electonics package. Time histories of compressor casing displacement were recorded along with the engine pressure histories and are discussed next.

Discussion of Experimental Results

This section of the paper has been divided into two separate discussions: (1) basic shock-tube and engine measurements performed with the compressor at rest, and (2) shock-tube and engine measurements performed with the engine operating and the bellmouth attached to the engine as sketched in Fig. 4. The J-85 is equippped with bleed doors located just aft of the first stage of the compressor. These bleed doors are normally open or partially open until the corrected engine speed has exceeded approximately 93 percent. It was previously noted that the engine used in this work was equipped with a Calspan-developed stall control system. However, this stall control system was not intended for use when the corrected

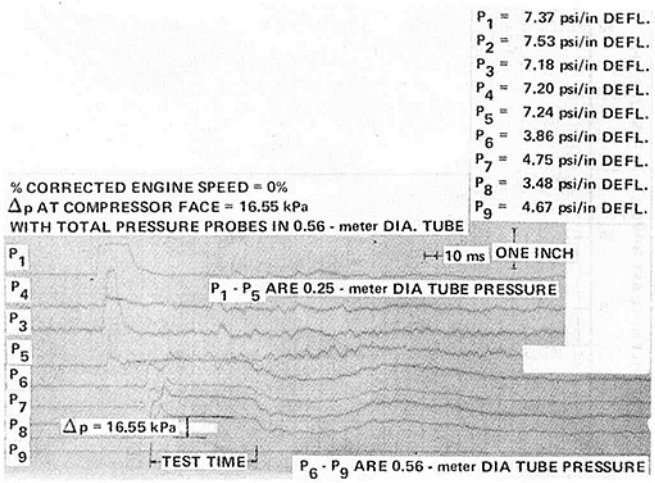

Fig. 9(*a*) Shock-tube pressure histories for Δp = 16.55 kPa with engine at rest

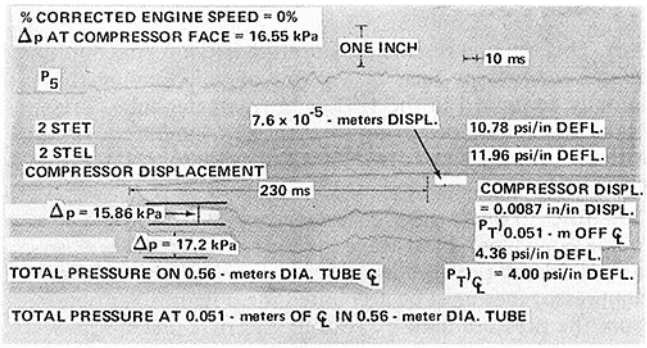

Fig. 9(*b*) Total pressure measurements in shock tube with engine at rest

engine speed was in excess of 90 percent. The blast-wave experiments discussed herein were all performed with the stall control system inactive and thus the bleed door position was under control of the normal engine schedule.

Basic Shock-Tube Data and Engine Measurements Performed With Compressor at Rest. A sketch of the locations of all of the shocktube instrumentation is given in Fig.6 and photographs of the engine instrumentation are given in Figs. 7 and 8.

Figures 9(*a*) and 9(*b*) are representative of the shock-tube data obtained. Pressure transducers P_1-P_5 are in the sidewall of the 0.25-meter (0.83-ft) diameter tube, transducers P_6-P_9 are in the sidewall of the 0.56-meter (1.83-ft) diameter tube, and the total pressure probes were located on the center line and 0.05-meters (0.17-ft) off the center line of the 0.56-meter (1.83-ft) diameter tube. Pressure transducer P_5 is located at approximately 0.15-meters (0.5-ft) from the open end of the 0.25-meter (0.83-ft) diameter tube. The upstream moving expansion fan as a result of the shock wave existing from the open end of the shock tube can be observed at this location and it can be traced back upstream to location P_1. The characteristic of the pressure pulse at location P_5 makes it attractive for time sequencing the three data recorders.

Throughout this paper we refer to a value "at the compressor face." This value is obtained from the P_9 data record as illustrated on Fig. 9(*a*). The peak pressure occurring at early time on the P_9 data record is a result of the reflection of the incident shock wave from the compressor face. This reflected wave can also be traced back up the 0.56-meter (1.83-ft) diameter tube and into the 0.25-meter (0.83-ft) diameter tube.

The duration of the useful shock-tube time is noted as Fig.

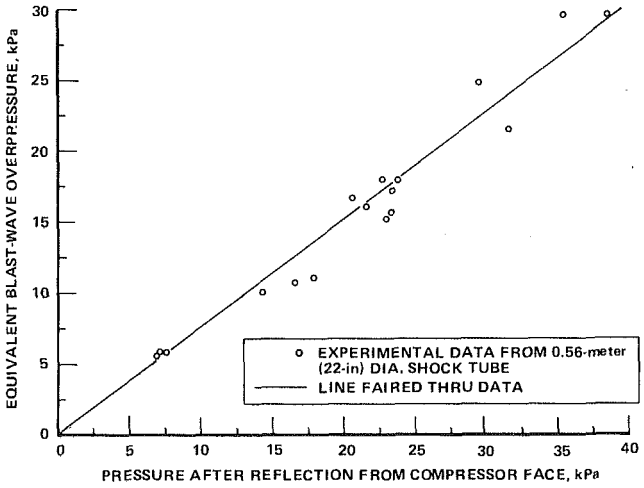

Fig. 10 Equivalent blast-wave overpressure

9(*a*). This time represents the duration of uniform conditions at the compressor face as a result of compressing the gas initially contained in the 1.83-meter diameter tube. Pressure peaks and valleys occurring after the test time are associated with the driver gas and are thus not relevant to the experiment being performed.

In order to relate the pressure increase measured at P_9 (ΔP) to an equivalent blast-wave overpressure, the increase in incident shock pressure as a result of the reflection from the compressor face must be accounted for. Figure 10 as obtained from the pressure data by reading the first plateau pressure occurring in the P_6, P_7, and P_8 pressure records and comparing that reading to the (ΔP) marked on the P_9 trace. As can be seen from Fig. 10, a 13.8 kPa (2 psi) blast-wave overpressure results in a pressure increase at the compressor face corresponding to approximately 17.2 kPa (2.5 psi).

Figure 9(*b*) includes a comparison between the compressor casing displacement history and two total-pressure histories taken in the 1.83-meter diameter tube. The characteristics of the total pressure pressure records and the corresponding pressure levels are in good agreement with the P_9 data presented in Fig. 9(*a*). Note that the maximum total pressure is associated with that period of time called shock-tube test time. It is illustrated in Fig. 9(*b*), and will be shown several times later in this paper, that the peak in the compressor vibration occurs much later in time than the peak total pressure. Figure 11 is a summary of the casing vibration data. This figure demonstrates that the magnitude of the casing displacement increases rapidly with overpressure but it is a relatively weak function of engine speed. Results are presented both with the compressor operating and with the compressor at rest to demonstrate this point.

Since the purpose of this experimental program was to investigate the tansient response of the engine to a shock wave incident on the compressor face, it was necessary to obtain a baseline measurement with the bleed doors closed and the engine at rest. Recall that this engine is equipped with bleed doors and that at corrected speeds in excess of approximately 93 percent these doors are closed. Most of the data will be taken at these higher corrected speeds so that the bleed doors will remain closed, thus the reason for obtaining the baseline data with the bleed doors closed.

Figures 12(*a*) and (*b*) are a second set of shock-tube pressure histories, engine pressure histories and a compressor-displacement time history obtained for a ΔP of 26.9 kPa. The conditions for these experiments are different from those shown in Fig. 9 in that the total pressure probes have been removed from the large diameter tube and the imposed

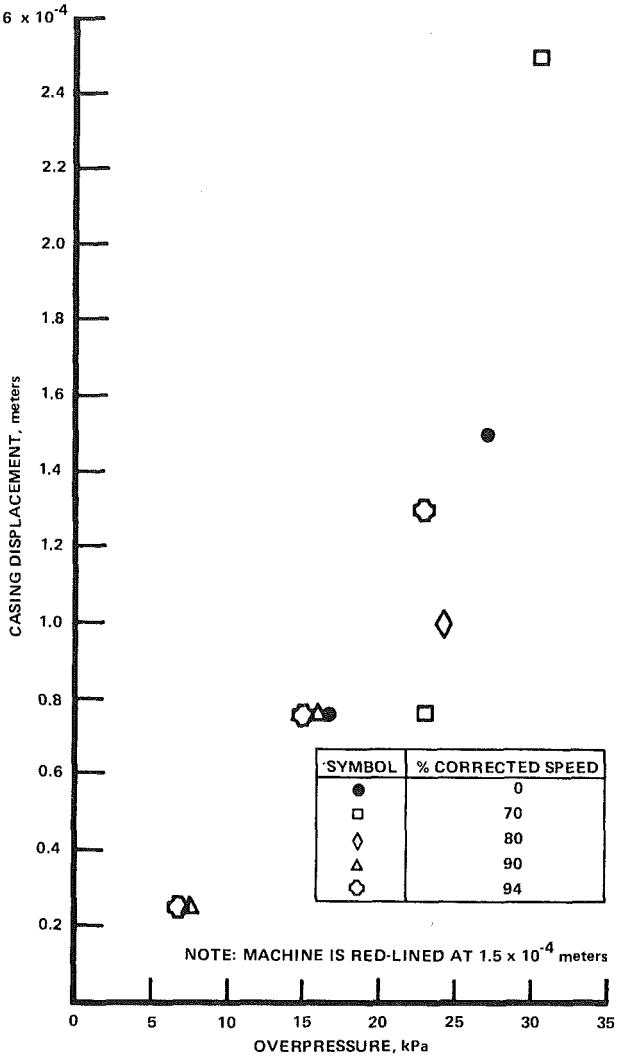

Fig. 11 Measured compressor casing peak to peak displacement

pressure pulse is larger. The characteristics of the shock-tube data records presented in Fig. 12(*a*) are shown to be very similar to those presented in Figs. 9(*a*) and (*b*). The engine pressure histories illustrate that the incident shock moves through the machine at a propagation velocity approximately equal to its velocity in the 1.83-meter diameter tube. The early time peak-pressure pulse is followed by an uniform pressure pulse the shape of which is consistent with the P_9 pressure record. These characteristics of the engine pressure records change significantly when the compressor is operating as will be demonstrated later. Figure 12(*b*) illustrates two of these engine pressure histories, 2STET and 2STEL, the compressor casing displacement history, and the P_9 record. From Fig. 12(*b*) it can be seen that the peak compressor-casing displacement occurs at approximately 230 ms after shock arrival at the compressor face. This displacement and time history is essentially the same as that measured when the machine was operating at high corrected speed as will be shown in the next subsection.

Shock-Tube and Engine Measurements Performed with Compressor Operating. With the ASME bellmouth attached to the engine and the experimental configuration shown in Figs. 5 and 6, a series of experiments were performed to investigate the performance of the J-85-5 turbojet engine under simulated nuclear-blast environments. Measurements were performed with the engine operating at corrected speeds in the

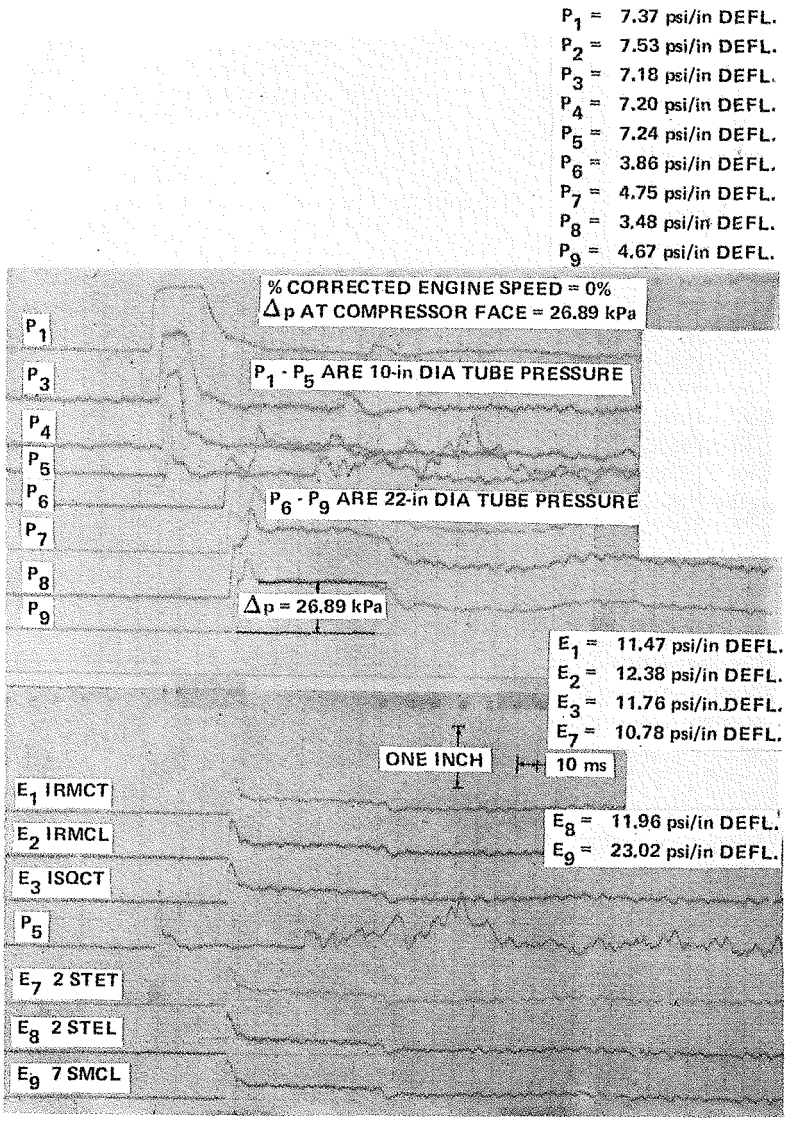

Fig. 12(*a*) Shock-tube and engine pressure histories for Δp = 26.89 kPa shock wave with engine at rest

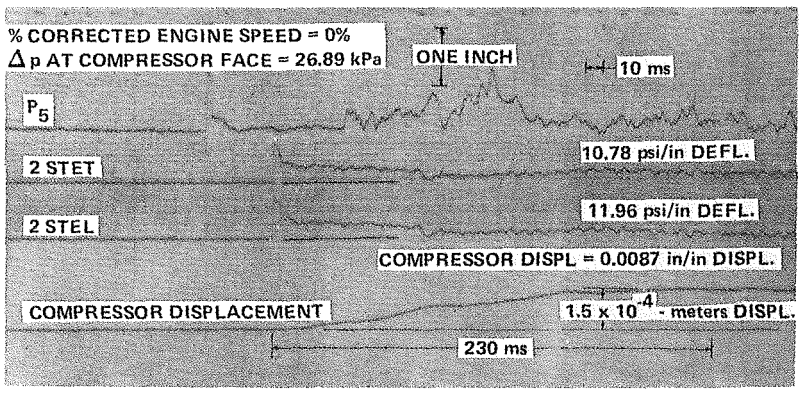

Fig. 12(*b*) Engine pressure and compressor casing displacement histories for Δp = 26.89 kPa shock wave with engine at rest

range of approximately 93 to 95% for equivalent blast-wave overpressures in the range of 5.5 kPa (0.8 psi) to 17.2 kPa (2.5 psi). Data records obtained from those experiments are presented in detail in [6], but only representative results will be shown here.

In addition to the shock-tube and engine pressure histories described above, two brush recorders were used to record time histories of engine rpm, bleed-door position, static-pressure increase across the compressor, and pitot pressure in the bellmouth from which engine weight flow rate was calculated.

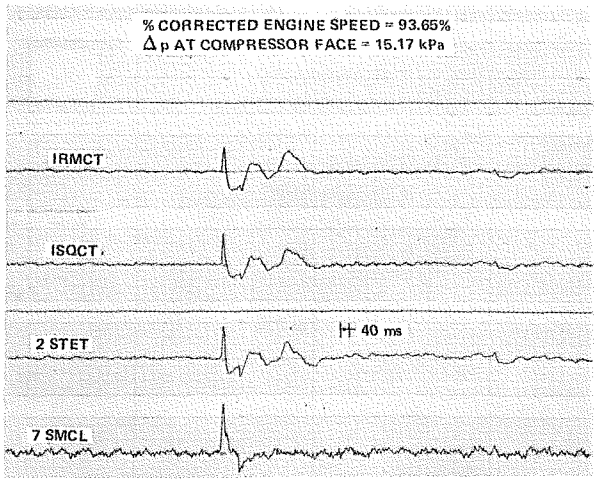

Fig. 13(*a*) Selected engine pressure histories for Δp = 15.17 kPa shock wave

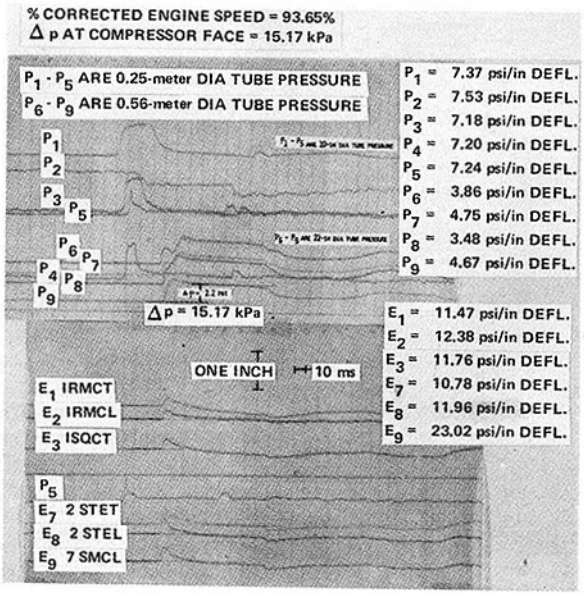

Fig. 13(*b*) Shock-tube and engine pressure histories for Δp = 15.17 kPa shock wave

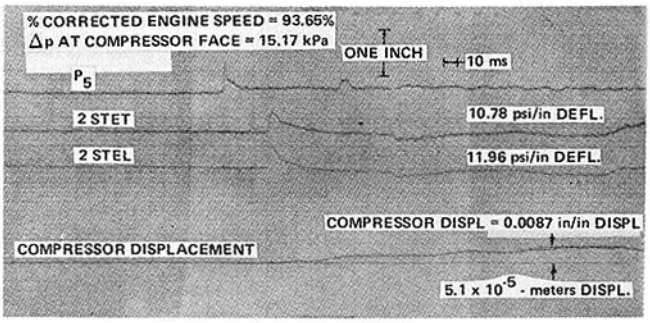

Fig. 13(*c*) Selected engine pressure histories for Δp = 15.17 kPa shock wave

The second of these brush recorders was used to record four engine pressure-transducer histories on a much slower sweep rate than that used on the CEC recorders. As noted above, the raw data from many of these experiments are presented in [6].

Figures 13(*a*), (*b*), and (*c*) present typical data for an engine operating point of 93 percent corrected speed, with a ΔP = 15.2 kPa (2.2 psi). The engine speed record indicated a small (0.6 percent) speed increase as a result of the shock-wave.

A second brush recorder was used to record four engine pressure histories on a slower sweep rate than was used for Figs. 13(*b*) and (*c*). The same engine pressures are included in Figs. 13(*b*) and (*c*), along with the shock-tube data, for a sweep speed four times faster than that used on Fig. 13(*a*). Engine pressures 1RMCT, 1SQCT, 2STET and 7SMCL were selected for the larger sweep rate display. These pressure histories indicate that events occur essentially simultaneously through the machine, compared with one engine revolution (~4 milliseconds). It can be seen from the records presented in Fig. 13(*a*) that the peak engine pressure is associated with the passage of the initial wave system through the machine. It can also be noted that the compressor regains its initial operating pressure level at approximately 1200 milliseconds after arrival of the shock. The post test-time pressure dip shown on Fig. 13(*b*) is associated with the shock-tube gas (as shown on Fig. 9(*b*)) and is not indicative of the compressor performance.

Figure 13(*b*) presents the shock-tube and engine pressure histories on a sweep rate of four times faster than the sweep rate used on Fig. 13(*a*). The four engine pressures presented on Fig. 13(*a*) are also included on Fig. 13(*b*). The general shape of these engine pressure histories should be compared with those shown in Figs. 11(*a*) and (*b*) for the engine at rest. The first 10 ms or so of these data records are similar but then the engine pressures shown on Fig. 13(*b*) return to their pre-shock values suggesting that possibly the turbine stage was operating very nearly choked and could not accommodate the increased weight flow associated with the shock-processed gas. As the shock overpressure is increased at the higher corrected speeds, this general character of the engine pressure records will become more pronounced. Figure 13(*c*) isolates two engine pressure records, 2STET and 2STEL so that their histories can be observed more closely. The bottom trace on Fig. 13(*c*) is the compressor casing displacement history. It can be seen from this record that the peak displacement occurs at approximately the same time after shock reflection as it did for the compressor at rest.

The results shown in Fig. 13(*c*) include the compressor casing displacement history in addition to the engine pressure histories. The casing displacement reached a maximum value at a time consistent with that shown in Fig. 12(*b*).

These pressure measurements can be used to demonstrate that the transient overpressure imposed at the compressor face is not magnified by the compression ratio in moving through the compressor. Comparison of seventh stage compressor records given on Fig. 12(*a*) for 0 percent speed with the corresponding record given on Fig. 13(*b*) for 93.65 percent speed and on Fig. 14(*b*) for 94.3 percent speed illustrates comparable magnitudes of an initial pressure spike independent of speed but the pressure history following this initial pulse is entirely different. Figures 12(*a*) and 14(*a*) illustrate that the pressure pulse is not magnified by the compression ratio. In fact, the imposed pressure pulse decays very rapidly after the initial step rise.

The highest overpressure for which engine measurements were obtained was 22.8 kPa (3.3 psi) and typical results for this experiment are given in Fig. 14. The selected engine pressure histories shown in Fig. 14(*a*) illustrate a characteristic similar to that obtained at lower overpressures but with larger amplitudes as would be expected. Comparison of Fig. 13(*a*) with Fig. 14(*a*), as well as the engine pressure histories presented in Figs. 13(*b*) and 14(*b*), does not suggest any evidence of rotating stall or surge as we are accustomed to seeing it on a transient basis. In addition, the engine did not flame out or suffer any damage during the course of these experiments. The comparison cited above indicates that with increasing overpressure, the compressor pressures return to their pre-shock level at an earlier time after shock arrival. For the ΔP = 22.8 kPa (3.3 psi) case, the local pressures fall

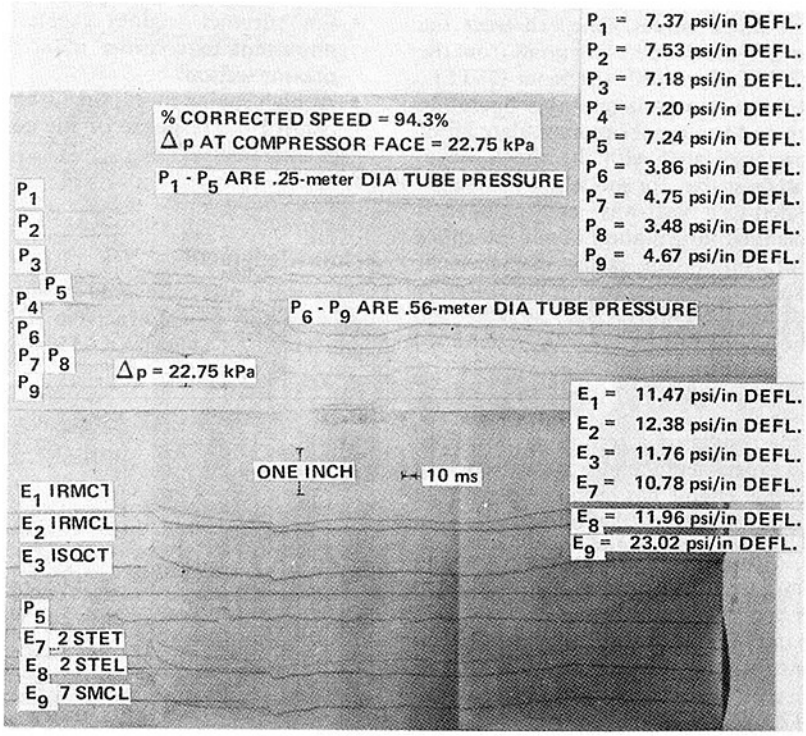

Fig. 14(*a*) Selected engine pressure histories for Δp = 22.75 kPa shock wave

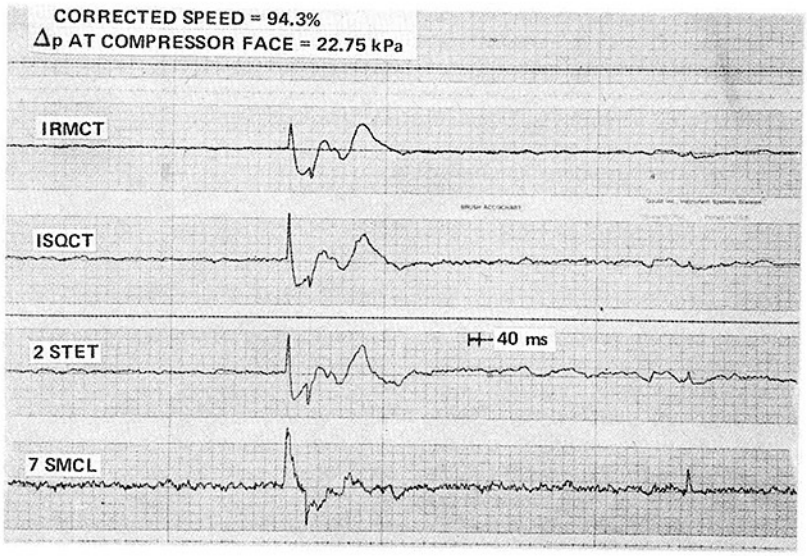

Fig. 14(*b*) Shock-tube and engine pressure histories for Δp = 22.75 kPa

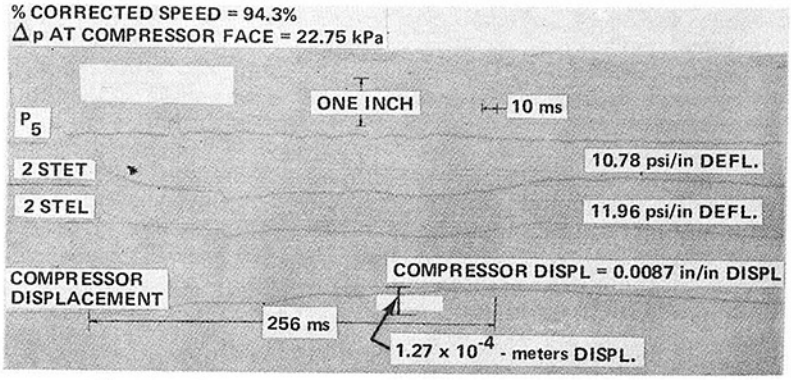

Fig. 14(c) Selected engine pressure histories for Δp = 22.75 kPa

somewhat below their pre-shock values. One can trace the movement of the return to pre-shock operating point from the rear of the compressor (7SMCL) towards the front (2STEL, 1RMCL) suggesting that the turbine was probably operating near the choked condition and could not accommodate all of the increased weight flow associated with the shock wave. This observation would suggest that for modeling the engine performance when subjected to a blast-wave environment, it is important to include detailed information about the entire machine. The increase of compressor casing displacement with increasing overpressure can be observed on Fig. 14(*c*). A displacement of 1.5×10^{-4} m (0.006 in.) is near the recommended limit for the engine.

Conclusions

This paper describes the results of a technology development program. The initial experimental phase of this program utilizing a GE J-85-5 turbojet engine has been completed. At the present time it is possible to conclude the following:

- A facility has been developed that can be used to obtain controlled laboratory data for the study of the influence of blast waves on air breathing propulsion systems.
- The turbojet engine used in this technology development program did not appear to stall or surge for overpressures up to
  $\Delta P)_{\text{Blast Equivalent}} = 17.2$ kPa (2.5 psi)
- The shock-wave overpressure imposed on the compressor front face is not amplified as it passes through the compressor.
- For turbojet engines encountering blast waves, it is important to consider induced vibrations in the compressor section.
- At high engine speed, the turbine gas dynamics appear to control the response of the compressor to the imposed pressure pulse.

Acknowledgment

This work was sponsored by the Defense Nuclear Agency under support of Contract No. DNA001-79-C-0155, RMSS Code B3420 7964 N99QAXAJ50405 H2590D.

References

1 Muirhead, J.C., Naylor, R. and Felt, G.D., "The Transmission of Blast Waves Through an Orenda 8 Engine", Suffield TN No. 219, 1969.

2 Muirhead, J.C., "A Review of DRES Studies on the Effect of Blast on Gas Turbine Engines", Suffield Rept. No. 267.

3 Muirhead, J.C., Naylor, R. and Felt, G.D., "The Transmission of Blast Waves Through an Orenda 8 Engine from Exhaust to Inlet", Suffield Memo. 89/69, Dec. 1969.

4 Ludwig, G.R., "Tests of an Improved Rotating Stall Control System on a J-85 Turbojet Engine", AFAPL TR-79, May 1979.

5 Private Communication, R. Smiley and J.R. Ruetenik, Kaman AviDyne Corp., to M. Dunn, Calspan Corp., 2-3 Nov. 1978.

6 Dunn, M.G., "Nuclear Blast Vulnerability of Airbreathing Propulsion Systems: Laboratory Measurements with an Operational J-85-5 Turbojet Engine", Calspan Rept. No. 6484-A-1, 31 March 1980.

7 Ludwig, G.R. and Arendt, R.H., "Investigation of Rotating Stall Phenomena in Axial Flow Compressors," Vol. III Development of a Rotating Stall Control System, AFAPL-TR-76-48, Vol. III, June 1976.

The Influence of Blade Number Ratio and Blade Row Spacing on Axial-Flow Compressor Stator Blade Dynamic Load and Stage Sound Pressure Level

H. E. Gallus
Prof. Dr.-Ing.
Mem. ASME

H. Grollius
Dipl.-Ing.

J. Lambertz
Dr.-Ing.

Institute for Jet Propulsion
and Turbomachines,
Technical University Aachen,
West Germany

In axial-flow turbomachines considerable dynamic blade loads and noise production occur as a result of the unsteady blade row interaction between rotor and stator blades. This paper presents results of midspan measurements of the dynamic pressure distribution on the stator blade surface (fixed number of blades) for various rotor-blade numbers and various axial clearances between rotor and stator. For this purpose, one stator blade had been provided with eleven semiconductor pressure transducers in the midspan section. Simultaneously, the sound pressure level was measured at two axial distances downstream of the stator by four condensator microphones distributed along the circumference in each of the two sections and mounted flush with the wall surface. The wake-flow distribution downstream of the rotor could be obtained by a rotating three-hole pressure probe. The results of the corresponding dynamic pressure-measurements and noise measurements are discussed and compared with results from theory.

Introduction

The prediction of the unsteady flow effects is of great importance for axial-flow turbomachines with respect to the process of energy conversion, to the excitation of blade vibrations, to sound generation, to unsteady profile and wall boundary layers, to flow separation, to rotating stall, to compressor surge, and to the influence on the various loss sources in turbomachines.

The unsteady flow components are caused by disturbances from inside and outside the machine. Fluctuations of the required mass flow and nonuniformities of the flow properties in the inlet and outlet cross sections may be listed in the category of disturbances from outside. Disturbances of the rotational symmetry of pressure and temperature distributions can propagate from the inlet to the outlet and are the subject of research on "flow distortion." If we consider the front section of the first blade row as the inlet section for the bladed part of the machine, the wakes from struts upstream of this first blade row may be regarded as disturbances from outside. If these wakes are still present when passing the first rotating blade rows, considerable dynamic forces may be produced on the blade surfaces.

Even in the case of a steady inlet flow and ideal uniform inlet conditions in front of the first blade row, the flow field in the bladed part of the machine must become unsteady because of several internal disturbances. The first one results from the fact that the blades are moving relative to each other. At any time during one blade-passing period, the relative positions of the adjacent blades change and thus modify the circulation and static pressure distribution around the upsteam and downstream blades. According to Thomson's law, the overall circulation around the blade and its wake is kept constant at any time by vortex elements of corresponding intensity separating from the airfoil and moving downstream. When the effects of fluid viscosity are not taken into account, the above blade-row interaction can be described by means of potential-theoretic prediction methods. The authors compared the results of several unsteady flow prediction theories according to this potential-theoretic interaction model with their experimental values. Some results of this comparison are presented in this paper; others were published in previous contributions to this problem [1-6]. Among the potential-theoretic prediction methods investigated by the authors, the calculation according to Lienhart [7] turned out to be very precise and most comprehensive with respect to all effects involved in the potential-theoretic interaction model.

Another interaction model considers only the downstream wake influence on the following blade row due to fluid viscosity, causing boundary layer buildup along the airfoil surfaces. The slower flow within these profile boundary layers

Contributed by the Gas Turbine Division and presented at the International Gas Turbine Conference and Products Show, Houston, Texas, March 9-12, 1981, of THE AMERICAN SOCIETY OF MECHANICAL ENGINEERS. Manuscript received at ASME Headquarters December 10, 1980. Paper No. 81-GT-165.

produces wakes within the velocity distribution behind the trailing edges. The shape of these wakes is narrow and deep immediately behind the trailing edges and gradually becomes broader and less deep by energy exchange with the neighboring jet zones of the flow. This downstream development of the wakes is influenced by stage geometry, aerodynamic blade loading, fluid viscosity, axial distance between the blade rows, and inlet turbulence level. The downstream decay rate of wakes is different for rotors and stators. The flanks of the wakes are asymmetric, i.e., steeper behind the pressure side of the blade than behind the suction side. Increasing blade loading by reduced flow coefficients deforms the wake shape in such a way that the gradient of the suction-side wake flank decreases and becomes very broad in the case of separated flow [8]. Such wakes cause large pressure fluctuations within the downstream blade rows. The wakes decay very slowly on their way downstream and are shown to exist still some blade rows downstream. This explains some remarkable results presented in this paper, namely, that wake interaction dominates for large axial distances of the blade rows whereas the potential-theoretic interaction is very strong only in case of very small axial gaps. As was verified by the authors, not only the depth and width of the wakes but also their asymmetric shape influence the dynamic blade forces and noise generation in the downstream blade row. Therefore, the wake shape, size, and frequency are necessary input quantities for all theoretical methods using the wake interaction model. Among other calculation methods involving this model, the authors programmed that of Henderson [9] and developed another one [10]. These methods were applied to the blade rows under consideration in this paper.

The complex behavior of all blade-row interactions and the resulting total dynamic blade forces have not yet been described by any theory because of the very difficult nonlinear physical conditions involved in the unsteady complete flow. Besides, up to now, all theoretical approaches known to the authors were devised for two-dimensional unsteady flows. Most of the calculation methods are valid for only incompressible unsteady flows.

The different unsteady flow calculations involving the abovementioned blade-row interaction models are therefore approximations. It is possible to proceed this way as far as the validity range of each of the two models has been estimated before. The main criterion for that is the axial distance between the blade rows, as is shown in this paper. Eventually, the influence of this parameter should be checked by using both models.

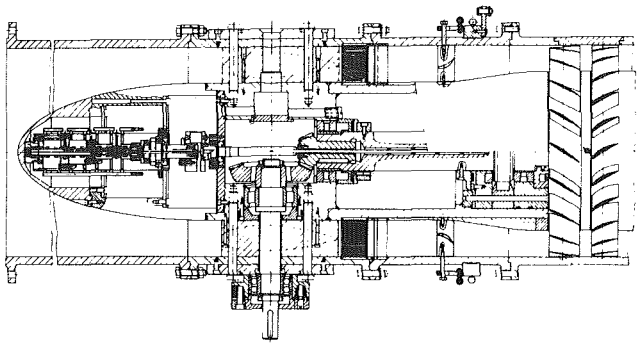

Fig. 1 Upstream part of the test-rig (meridional section)

The knowledge of the dynamic loads on the whole blade surface is necessary for a stage design that is vibration proof and moderate in noise generation. As a matter of fact, the flow field over the blade height is three-dimensional with radial components and, often, varying airfoil geometry. In a compressible flow the propagation of disturbances in every direction, including the radial direction, has to be considered. Thus it is necessary to carry out three-dimensional calculations of the fluctuating flow field and of the dynamic blade loads. To the authors' knowledge, this has not been realized up to now. In case of axial-flow compressor blades with low camber, it is possible to obtain some satisfactory approximations by means of two-dimensional simplified calculation methods [11].

The research reported here concentrated on the experimental and theoretical results regarding the influence of some main parameters of the stage geometry, like axial distance between blade rows and their blade number ratio, on both the intensity of dynamic blade forces and the noise generation.

Experimental Investigations

Construction and Data of the Test Rig. The experiments were performed in a test rig as shown in Fig. 1. It consists of an annular inlet, 48 turnable inlet guide vanes, a wake

Nomenclature

b_D' = width of the wake
b_p = width of the profile
c = absolute flow velocity
c_A = lift coefficient
c_p = pressure characteristic
d = diameter
f = frequency of oscillation, Hz
F_a' = unsteady axial force = $\tilde{F}_a/(\rho b_p \cdot c_2^2/2)$
F_u' = unsteady tangential force = $\tilde{F}_u/(\rho b_p \cdot c_2^2/2)$
h_D' = velocity difference in the wake = $(w - w_{min})/\bar{w}$
k = harmonic components
l = integer number $-\infty < l < +\infty$
L_p = sound pressure level [dB]
m = number of circumferential wavelengths of the mode
M_t' = unsteady aerodynamic moment of forces = $\tilde{M}/(\rho_2 b_p^2 c_2^2/2)$
M = Mach number
n = number of revolutions
p = pressure
$\tilde{p}$ = unsteady pressure = $p(t) - \bar{p}$
r = radius
s = chord length
S = stimulus = $\tilde{F}/\bar{F}$
Sr = Strouhal number
t = time
t = spacing
T_p = period of $p(t)$
u = blade speed
w = relative flow velocity
x = axial coordinate
y = circumferential coordinate
z = number of blades
α = angle of absolute flow
β = angle of relative flow
Δx = axial clearance between the blade rows
ρ = fluid density
λ = stagger angle

Subscripts

1 = upstream of the rotor
2 = downstream of the rotor
3 = downstream of the stator
H = trailing edge
IGV = inlet guide vanes
m = averaged
min = minimum
M = measured cascade
N = number of measurements
rel = relative
R = rotor
S = center of gravity

Superscripts

$(\bar{\ })$ = time-averaged
$(\tilde{\ })$ = unsteady

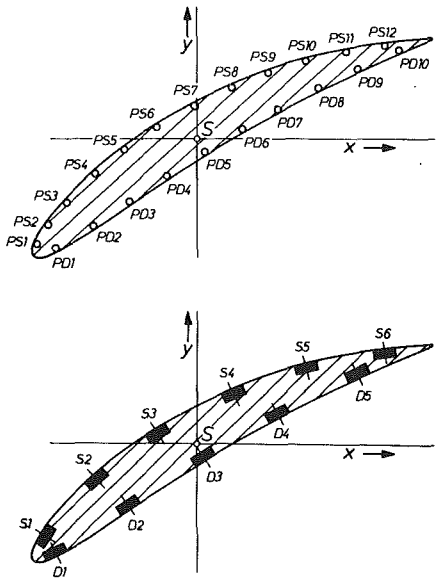

Fig. 2 Measuring blades of compressor blade row

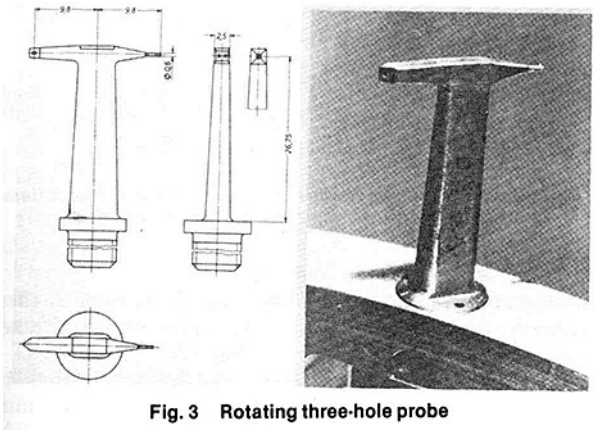

Fig. 3 Rotating three-hole probe

producing rotor with various blade numbers (24, 19, 12, 4, 3, 2), and a subsequent stationary axial-flow compressor or turbine blade row whose axial distance behind the rotor blade trailing edge was altered in steps (3.5; 8; 20; 48 mm). The static pressure fluctuation induced by the rotor and its wakes on the blade surface of the stator blade row was determined by midspan measurements on one blade provided with six semi-conductor pressure transducers along the suction side of the airfoil and further five transducers along the pressure side as shown in Fig. 2. This figure also indicates the measurement section of another blade with static pressure holes distributed around the airfoil just in the same positions where the semiconductor pressure transducers along the suction side of the airfoil and further five transducers along the pressure side between them. Due to the moderate static pressure fluctuations at the holes, the pneumatically measured static pressure can be considered as the time-averaged mean value of the local unsteady static pressure. A rotating pneumatically measuring three-hole miniature probe behind the rotor can be shifted circumferentially and permits the determination of the wake shape in various axial distances from the trailing edge of the rotor blade. The wake shape as it enters the stator blade row is the main input data for theoretical methods predicting the unsteady static pressure distribution on the airfoils as a result of the downstream wake influence. Figure 3 shows this rotating three-hole probe and its small dimensions with respect to the measurement in the wake fields with steep gradients.

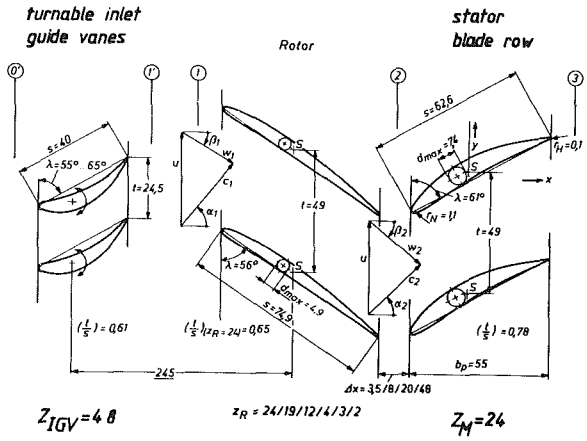

Fig. 4 Survey of the cascade data of rotor and stator

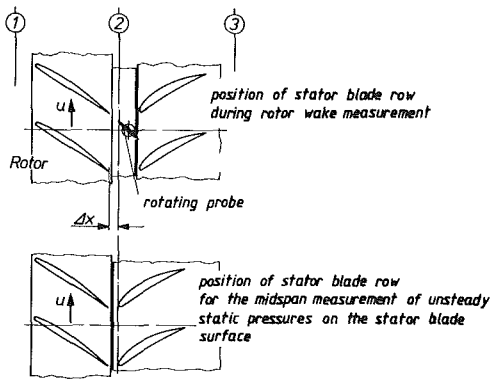

Fig. 5 Principle of the rotor wake and unsteady static pressure measurements

Figure 4 permits a survey of the cascade data of rotor and stator. A turbocompressor set provides the continuous airflow for the test rig. The latter was used for the investigation of both turbine and compressor stators under the influence of an upstream rotor that was acting as a weak turbine, and whose main task was to produce the wakes entering the downstream stator blading. In the case of the compressor stator reported on in this paper, the airflow gets its moment of momentum in front of the rotor by 48 turnable inlet guide vanes whose wakes have almost disappeared when reaching the leading edge of the rotor blades. The latter have the task to produce deep and narrow wakes comparable to wake shapes behind compressor rotors. The rotor blades therefore have small thickness and camber. The small turning of the flow by the rotor blades is just sufficient for achieving the desired rotor speeds.

Figure 5 demonstrates the principle of the rotor-wake measurement by use of the rotating probe. In the upper part of the figure this probe can be seen as it is positioned for the measurements between the blade rows. The lower part shows the probe removed for the measurements of the unsteady static pressures and their time-averaged mean values on the stator blade. The probe has to be removed for these measurements not only to allow the various small axial cascade distances but also to avoid the disturbances of the steady and unsteady flow by the presence of the probe. The figure indicates also that the probe head position is identical with the position of the stator-blade leading edge during blade pressure measurements. By the way, for the wake measurements the stator blade row was shifted as much downstream as necessary but, nevertheless, was kept present in order to maintain at least approximately its upstream effects.

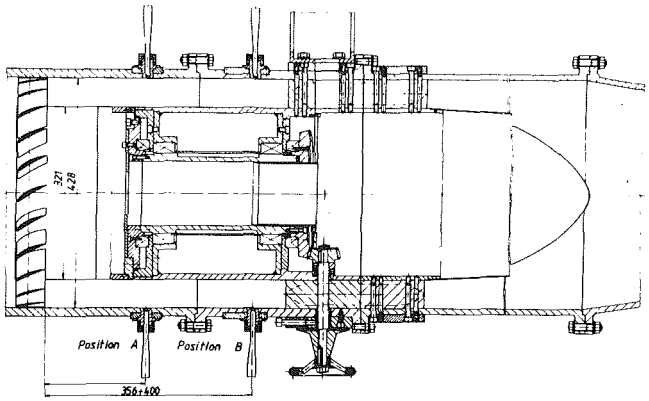

Fig. 6 Downstream part of the test rig (meridional section)

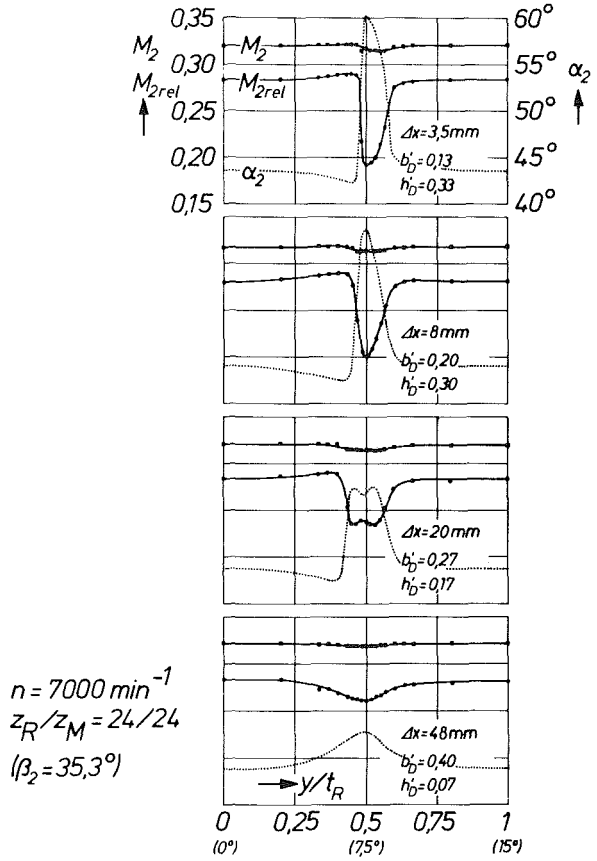

Fig. 7 Measured wakes in the flow behind the rotor at four different axial distances between the blade rows (24-rotor blades)

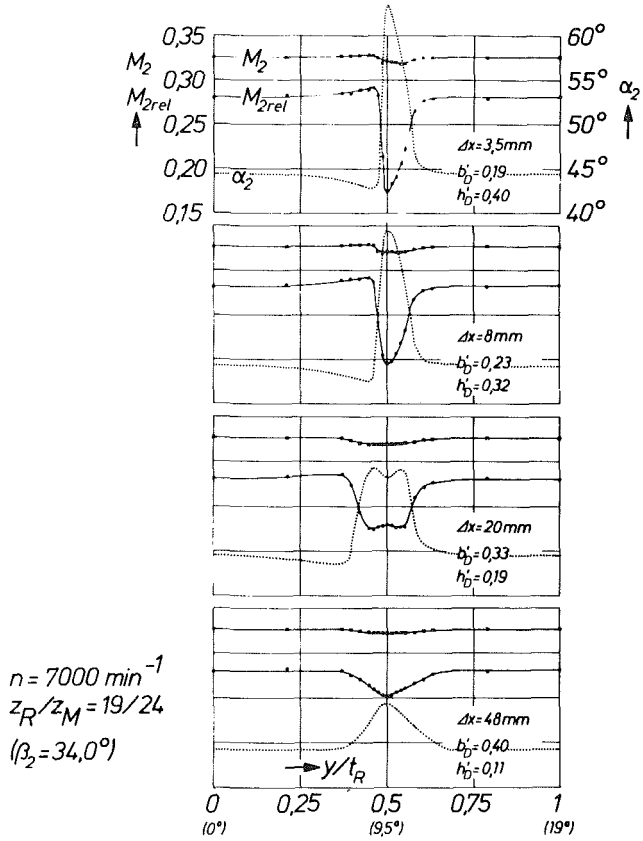

Fig. 8 Measured wakes in the flow behind the rotor at four different axial distances between the blade rows (19-rotor blades)

As to the abovementioned miniature design of the rotating probe (see Fig. 3), the three holes were distributed to both ends of the probe head, two holes to one end for detecting the flow angle and one hole to the other for total pressure measurement. Both measurements could be performed in switching the probe by exactly 180 deg. By this construction, the probe head could be miniaturized to an outer diameter of only 0.6 mm to allow for the strong gradients in the wake flow.

Figure 6 shows the meridian of cross section of the downstream part of the test rig. At a distance A, i.e., 227 to 271 mm downstream the trailing edge of the stator blades, four condenser microphones were distributed along the circumference of the casing flush with the inner wall surface in order to measure the sound pressure level in the near-field parallel with the unsteady static pressure distributions on the stator blade surface for all the variations of rotor/stator blade ratio and axial distance of the blade rows. At each of these microphone positions the body sound intensity was checked by acceleration transducers.

The acoustic downstream behavior was measured by another four microphones at a distance B (356 to 400 mm) farther downstream of the stator blade trailing edge. The measured microphone signals were evaluated by the aid of a two-channel frequency-analyzer. In addition to the representation of the frequency spectrum the correlation analysis between unsteady static pressure distribution on the blades and sound pressure level could be performed.

Program of Experiments. The experiments under consideration in this paper aimed at the measurement of the unsteady static pressure midspan distribution around the airfoil of an axial-flow compressor stator blade row and subsequently the resulting axial and circumferential dynamic blade forces. Parallel to this, measurements of the downstream sound pressure level were performed and correlated. These investigations were conducted to various values of the following essential parameters of the airflow and stage geometry, having strong influence on the dynamic forces:

- Variation of inlet flow angle
- Variation of the axial distance between rotor and stator blade row ($\Delta x = 3.5$; 8; 20; and 48 mm)
- Variation of the rotor/stator blade ratio (z_R/z_M = 24/24; 19/24; 12/24; 4/24; 3/24; 2/24)

The last-mentioned small blade ratios have been investigated in order to check the intensity of the dynamic forces as a result of widely spaced wakes as they correspondingly occur behind a small number of struts in the intake of an axial-flow turbomachine.

For each of the abovementioned variations, the authors measured:

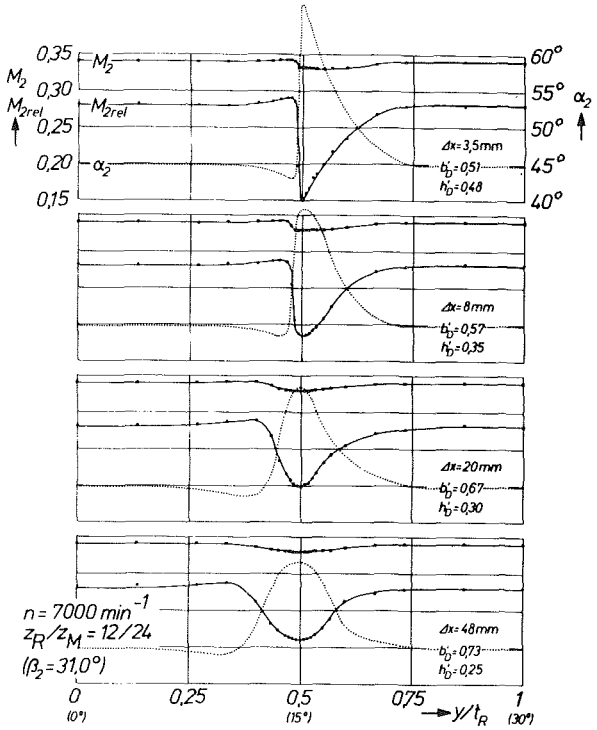

Fig. 9 Measured wakes in the flow behind the rotor at four different axial distances between the blade rows (12-rotor blades)

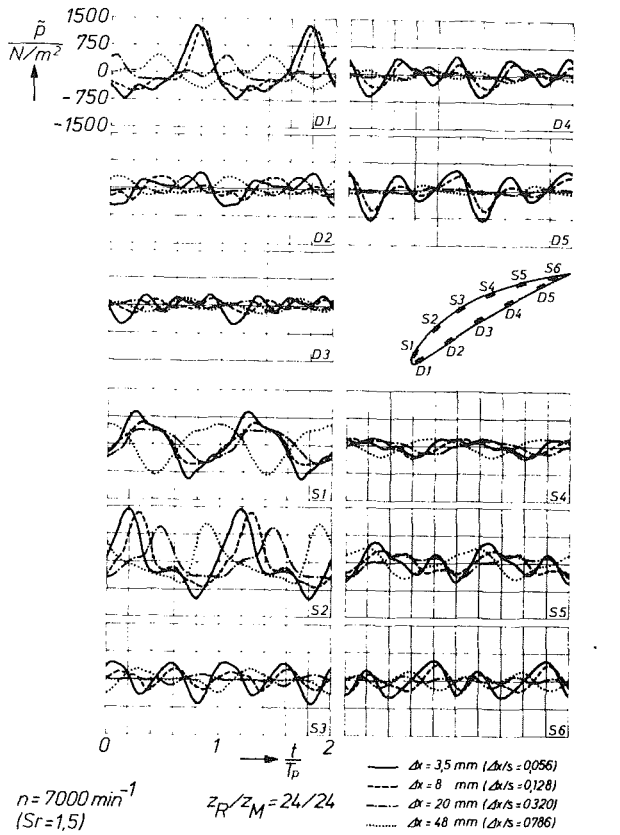

Fig. 10 Local dynamic midspan pressure differences at four different axial distances between the blade rows

- The local time-averaged static pressure at 22 midspan positions around the airfoil (pneumatical measurements)
- The local unsteady static pressure at 11 midspan positions around the airfoil (by semiconductor pressure transducers of the type "Kulite LQL-080-25S")
- The midspan rotor wake shape at the axial position of the stator-blade leading edge (by rotating probe)
- The sound pressure level downstream along the inner casing wall (by condenser microphones)

Experimental Results

The results of the rotor wake measurements are represented in Figs. 7, 8, and 9 for various rotor blade numbers. The wakes were measured at four different axial distances from the trailing edge of the rotor blade. In the diagrams, the different wake shapes correspond to different aerodynamic rotor blade loads in the various test cases. The wakes differ from each other not only by width and depth but also by asymmetry. This becomes especially evident for the variations with twelve rotor blades (Fig. 9). In the topmost part of the diagram, i.e., for the axial distance of $\Delta x = 3.5$ mm, the suction side course of the wake indicates separation.

Figures 7 to 9 demonstrate both the course of relative and absolute Mach numbers along one rotor spacing. Whereas the absolute Mach number does not alter so much within the wake, one can state strong changes of the absolute flow angle α_2 in front of the stator. For small axial distances these changes amount up to about 20 deg. The results also clearly demonstrate the wake decay with increasing axial distance from the rotor-blade trailing edge. Nevertheless, this decay is retarded with increasing axial distance since wakes keep existing far downstream as shown in the diagrams for $\Delta x = 48$ mm.

The consequences of various axial distances between the blade rows for the local dynamic midspan pressure differences can be taken from Fig. 10. There are heavy fluctuations of the local static pressure at the positions D1, S1, and S2 near the leading edge in case of short axial distances ($\Delta x = 3.5$ and 8 mm). Figure 11 represents the influence of the blade number ratio on the midspan blade pressure fluctuation. The strongest fluctuations occur near the leading edge at the positions D1 and S1. They progressively increase with decreasing blade number ratio z_R/z_M. Figure 12 shows the fluctuation of the local pressure coefficients c_p compared with the local mean values. Obviously, the intensity of the fluctuation increases with smaller axial gaps and even stronger with smaller number of rotor blades.

Evaluation of the Experimental Results and Comparison with Results from Theories

The influence of the axial distance between the blade rows essentially results from:

(*a*) the wakes from the upstream blade row,

(*b*) the potential-theoretic interaction of the blade rows moving relative to each other which results in time-dependent changes of the circulation round the airfoils and, consequently, vortex sheets leaving the trailing edges and propagating downstream.

As had been shown by previous investigations of the authors, the abovementioned influences under (*b*) become negligibly small compared with the influence according to (*a*), if the axial distance grows over more than 10 to 20 per cent of the blade row width, according to the circumstances of blade geometry, aerodynamic load, etc. In stationary compressors, the axial gaps normally are of the order of 10 to 15 percent of the cascade width. In compressors of modern jet engines one finds values of about 25 percent for low-pressure stages and about 45 percent for high-pressure stages. Therefore, the wake influence is dominating in many practical designs. For smaller axial directions, the potential-theoretic influences according to (*b*) must not be neglected.

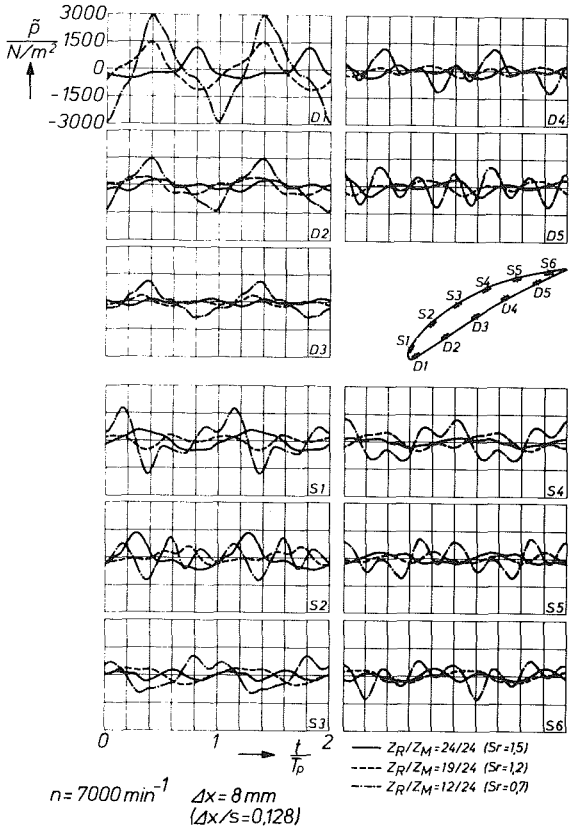

Fig. 11 Influence of the blade number ratio on the midspan blade pressure fluctuation

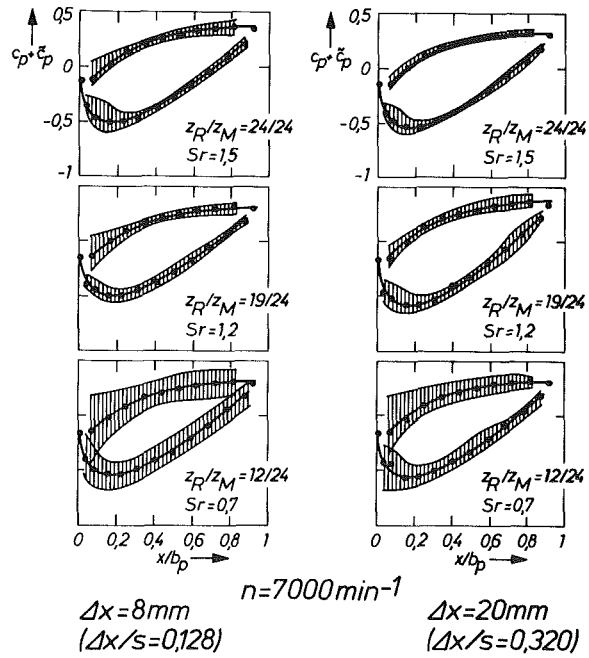

Fig. 12 Fluctuation of the local pressure coefficients c_p compared with the local mean values

The "stimuli" S_x and S_y which are characteristics for the excitation intensity of blade vibration, are plotted along the axial distance Δx in Fig. 13. The measured stimuli are marked by square, circular, and triangular symbols for the first, second, and third harmonic. They had been measured only in the stator blade row. Figure 13 also contains results from

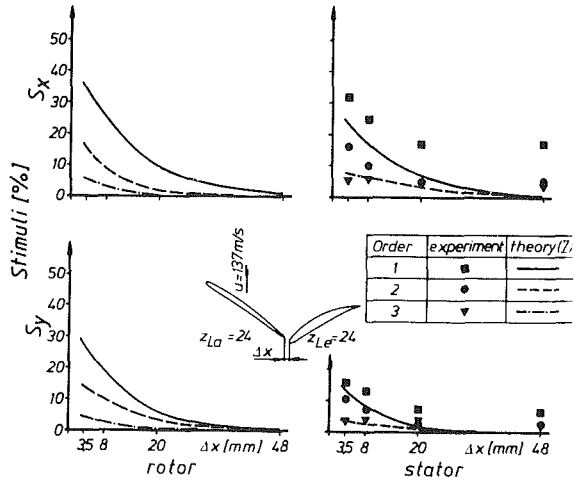

Fig. 13 Computed and measured "stimuli" as a function of the axial distance between the blade rows

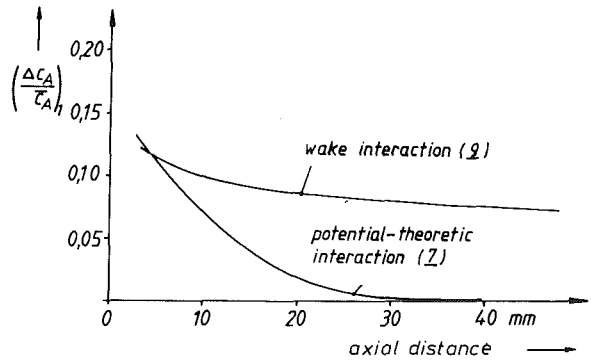

Fig. 14 Comparison of the potential-theoretic and wake interactions as a function of the axial distances between the blade rows

theories for the purpose of comparison. The stimuli calculated after [7] are plotted as full lines for the first harmonic and as dashed lines for the second harmonic. This prediction method takes into account only potential-theoretic blade row interaction and does not consider the wake influence. On the left of Fig. 13, there are plotted the stimuli due to the potential-theoretic upstream actions from stator to rotor which were also calculated according to [7] for the considered blade rows with 24 blades each. The calculations result in stronger potential-theoretic dynamic blade forces upstream from stator to rotor than downstream from rotor to stator. The comparison of the measured stimuli on the stator blades with the values from the prediction method [7] indicates that the potential-theoretic interaction contributes considerably to the actually measured forces if the axial distance is small, whereas for larger axial gaps (20 to 48 mm) this contribution becomes negligible. Obviously, the wake interaction is dominating in the latter region. This becomes evident as one examines the theoretical results of reference [9] that takes into account the wake influence. The results of both theories ([7] and [9]) are compared in Fig. 14, where the first harmonics of the relative fluctuating lift coefficient were plotted. The amplitudes of the predicted individual dynamic forces cannot simply be added because of the nonlinear connection of the physical effects. The effects by the wakes from the upstream cascade are superposed on those from the potential-theoretic interaction with a phase lag depending on the axial distance between the blade rows.

Summing up, it can further be stated that within the region of small axial gaps a small increase of the latter leads to a

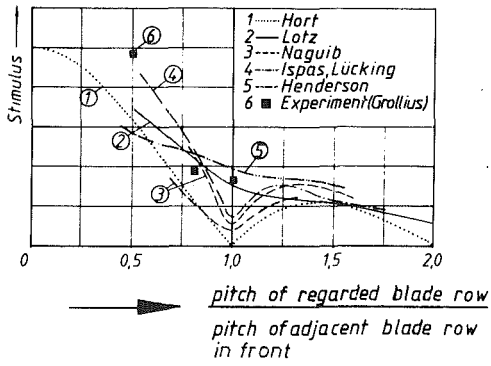

Fig. 15 Influence of the blade number ratio on the dynamic blade force

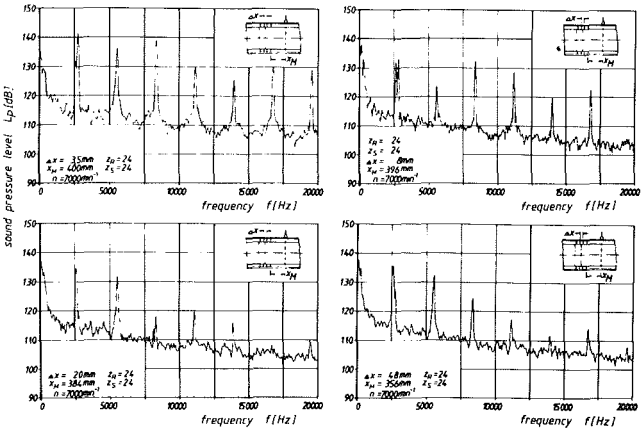

Fig. 16 Measured sound pressure level for 24 rotor blades as a function of the axial distances between the blade rows

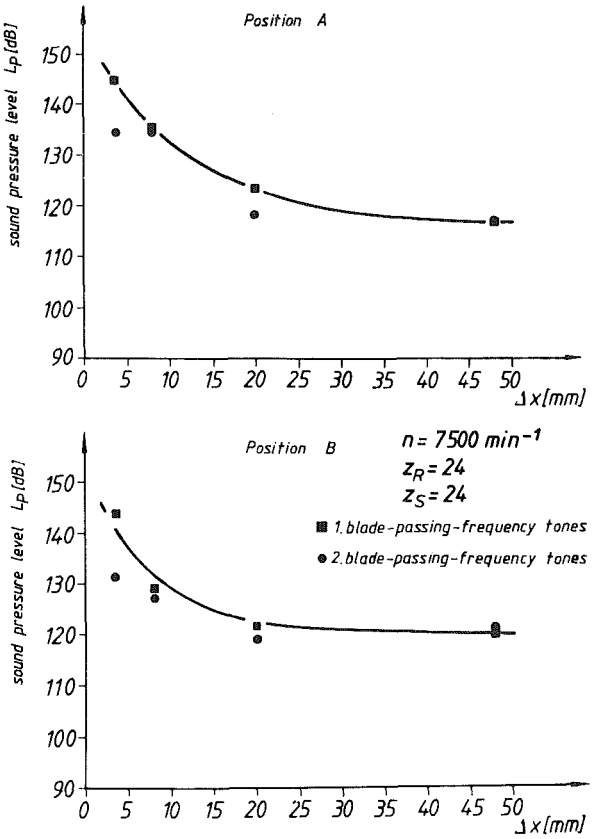

Fig. 17 Measured sound pressure level of the first and the second blade-passing-frequency tones as a function of the axial distances between the blade rows

steep decrease of the first harmonic of dynamic forces. Nevertheless, within narrow sections of variation of the axial distance this tendency can be changed by a phase-lag between the abovementioned interactions.

At the end of this section it should be pointed out that there is still an urgent need of experimental results in the field of unsteady flow measurements in real turbomachines. Among other recent publications to this topic there should be mentioned [13] and [14].

The influence of the blade-number ratio on the dynamic blade forces was discussed by Hort [12] as early as 1926. The course of the stimulus which he predicted as a function of the blade number ratio under simplifying assumptions is plotted in Fig. 15. Investigations by the authors affirm the predicted tendency as shown in Fig. 15 by experimental results and the results calculated after various theories. The absolute values of the stimuli do not agree as well as those shown in Fig. 15. The curves were shifted because of an easier comparison of their pattern. The stimulus drops with increasing blade number in the upstream blade row. There is no hint at increasing dynamic forces for the blade number ratio 1. Nevertheless, a blade number ratio of exactly 1.0 is practically not used because of other unfavorable aspects, as is well known. For example, there is no damping of blade vibration by the blade fixing in this case, as all the blades move with the same phase-lag. With that, blade-packages become inefficient with equal blade numbers in adjacent blade rows. Besides, with the same number of blades in adjacent rows the acoustics shows that all modes are propagating as plane waves. The cut-off frequency of a plane wave is zero, i.e., all modes can propagate without damping. The most intensive dynamic forces result from adjacent blade rows with only few blades, e.g., from struts. At any rate, for a conclusive decision on a favorable blade number ratio there must additionally be considered the vibration characteristics and the damping behavior of the integral system consisting of the blades, the disks, and the shaft. Besides, the blade number ratio influences the noise generation. In special cases, this influence turns out to be different from the tendency of the generation of dynamic blade forces.

Comparison of Dynamic Blade Forces and Sound Pressure Level

The axial distance between the blade rows has great influence on the blade-passing-frequency tones.

Figure 16 represents the measured sound pressure level up to a frequency of 20,000 Hz for 24 rotor blades and a speed of 7000 rpm. The axial distance was varied from 3.5 to 48 mm. Obviously, the decrease of the sound pressure level with increasing axial distance is much stronger in the range of smaller distances. This behavior is similar to that of the dynamic blade forces. The decrease of the sound pressure level with increasing axial distance between the blade rows depends on the wake shape, the blade number ratio, the flow velocity, and the geometry of the flow channel and the connected pipes.

The results of measurements with 24 rotor blades are shown in Fig. 17. The values measured by condenser microphones at the downstream positions A and B (see Fig. 6) have been averaged along the wall circumference according to the formula

$$P_m^2 = \frac{1}{N} \sum_{i=1}^{N} P_i^2 \qquad (1)$$

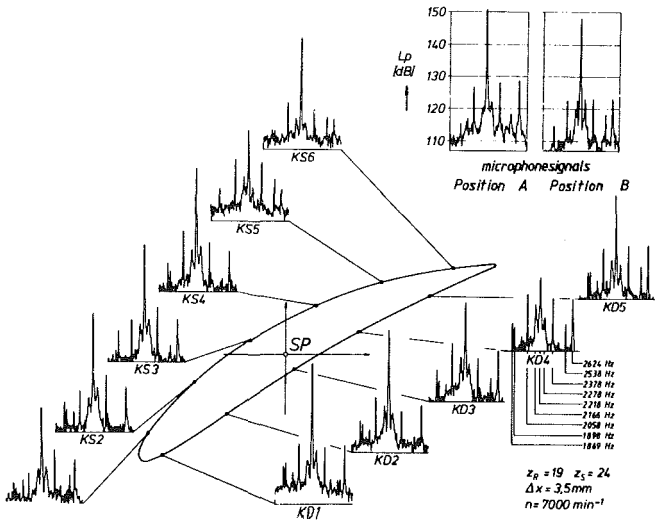

Fig. 18 Sound pressure spectrum within the range of the first blade-passing-frequency tones

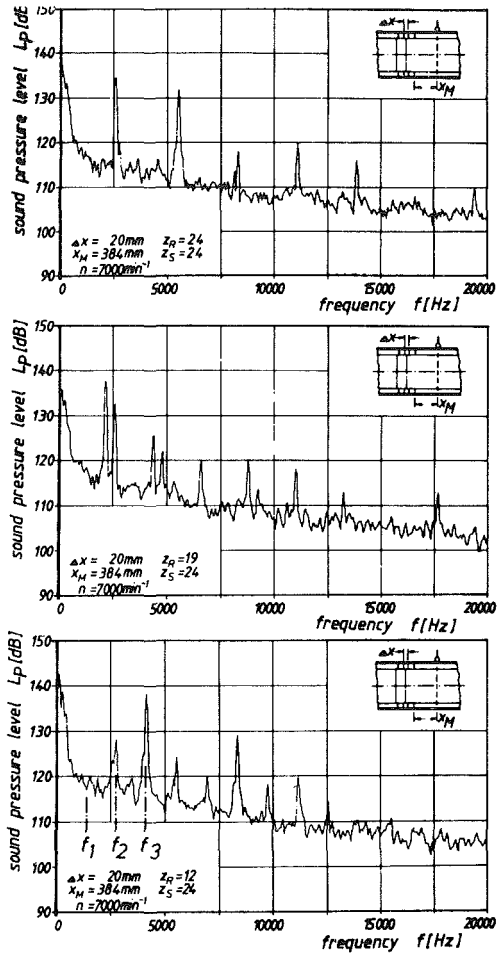

Fig. 19 Measured sound pressure level for three different rotor blade numbers

As could be expected the level decreases downstream from A to B. It should be mentioned that the distance between the source of the noise and the microphone slightly changed because of the axial shifting of the stator blade row due to the different axial distances between the blade rows. Figure 17 affirms the tendency of a progressive increase of the sound pressure level with decreasing axial distance in the range of small Δx-values.

Thus, taking into account the behavior of both unsteady blade forces and sound pressure level and also considering the need of a short stage length in multi-stage machines, a compromising solution of all problems seems achievable by avoiding only too narrow axial distances between the blade rows.

From the measurements cited above, the following correlations between noise generation and axial distance between the blade rows can be explained: As the velocity profile of the rotor downstream flow has strong gradients close to the trailing edge, the Fourier analysis shows many high-frequency components. With increasing axial distance, the wake shape flattens until only the first harmonic component is still of importance. From this it can be concluded that in particular the high-frequency blade passing tones will diminish with increasing axial distance.

The blade-passing-frequency tones do not consist of pure tones. The exact control of the sound spectrum within the range of the first harmonic of blade-passing tones is demonstrated in Fig. 18, which shows that the single top values of compressor noise occur within a certain frequency range and, consequently, are not discrete tones. This effect is caused by the cyclic change in the rotor downstream flow due to deviations of the rotor blade geometry and rotor channel flow. By inaccurate fabrication, e.g., errors in constant blade spacings, the sound spectrum is enhanced by quite a number of corresponding effects both in the local measurements of the unsteady pressure on the blade surface and in the results of microphone measurements at the downstream positions A and B.

According to equation

$$m = k \cdot z_R - 1 \cdot z_M \tag{2}$$

the occurring modes are determined by the rotor and stator blade numbers z_R and z_M. Their influence is also valid for the intensity and the damping. Figure 19 represents the frequency analysis of sound pressure for three different rotor blade numbers (z_R = 24; 19; 12) at an axial distance of Δx = 20 mm between the blade rows. For the same case, Fig. 20 compares the various sound pressure levels with the correspondent harmonics of the axial and circumferential dynamic blade forces F_a' and F_u'. Whereas the first and second harmonics of these forces progressively increase with decreasing rotor blade number, the theoretically well known cut-off effect was affirmed by the measurement with rotor blade number z_R = 12. The first harmonics of the blade passing tones (1400 Hz) do not generate any mode that is able to propagate, i.e. all modes existing in the near-field are exponentially damped so that they cannot propagate in the axial direction. From Fig. 20 it becomes evident that the first harmonics of the unsteady forces (1400 Hz) have grown enormously whereas the corresponding sound pressure level almost completely disappears in the broad band noise (see also Fig. 19). In order to obtain a rather large frequency range in which the propagation of sound pressure is being damped, the difference of the blade numbers of rotor and stator should be large.

This statement is in contradiction to the development of the unsteady blade forces described before. As a matter of fact, the sound pressure level generated by the unsteady forces close to the source is much higher for the blade number ratio z_R/z_M = 12/24 than for the ratios 19/24 and 24/24, but due to the cut-off effect is is so intensively damped that it is no longer existent at an axial distance of 396 mm downstream of the trailing edge of the stator blades.

Conclusions

The dynamic blade forces due to potential-theoretic blade-

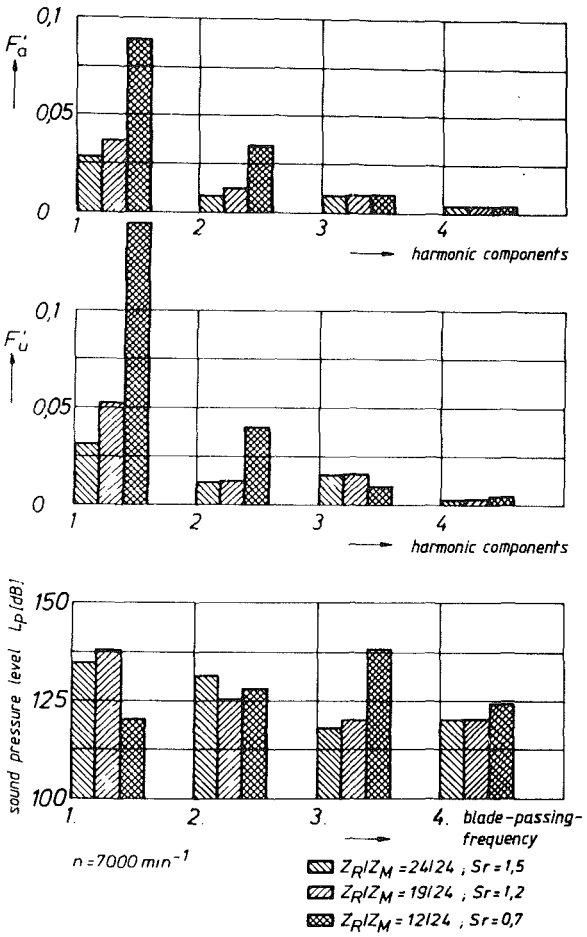

Fig. 20 Comparison of the dynamic blade forces F_a' and F_u' with the amplitude of the sound pressure for three different rotor blade numbers

row interaction are of the same order of magnitude as the forces due to wake-flow interaction if the axial distance between the blade rows is very small. But, the pressure fluctuations as a result of potential-theoretic interactions decrease much faster as the distance Δx increases than those due to wake-flow. For axial distances of about half the width of the following blade row both theoretical and experimental investigations resulted in the statement that the ratio of dynamic blade forces due to the two effects is of the order of 10:1 or more, i.e., prediction methods considering only the wake influence obtain results close to experimental values. Within the range of very small axial distances where both influences are of the same order, in all cases under consideration the measured values of the forces were larger than the calculated partial values for each of the two influences. A mere addition of the partial values would lead to the prediction of too large forces and would not be correct because of the nonlinear conditions.

Among the numerous causes of noise generation in axial-flow turbomachines the influence of both axial distance between the blade rows and blade number ratio has been investigated by variation of these parameters. It became evident that the discrete tones level can be reduced considerably by only slight increases of the axial gap within the range of small axial distances of the blade rows. As a matter of fact, the wake shape influences the intensity of the various harmonics.

The theoretical prediction of the cut-off effect could be proved experimentally. By choosing suitable blade number ratios, this effect can be used for the reduction of certain discrete blade-passing-frequency tones.

The sound generation by unsteady flow effects and the propagation of sound inside and outside the compressor can be predicted from solutions of the unhomogeneous wave equation. With that the influence of the compressor-channel geometry on the sound propagation must not be neglected.

References

1 Gallus, H.E., "Results of Measurements of the Unsteady Flow in Axial Subsonic and Supersonic Compressor Stages," *AGARD Conference Proceedings*, No. 177, Monterey, Calif., 1975.

2 Gallus, H.E., Lambertz, J., and Wallmann, Th., "Blade-Row Interaction in an Axial-Flow Subsonic Compressor Stage," *ASME Gas Turbine Conference*, San Diego, ASME Paper 79-GT-92, 1979.

3 Gallus, H.E., Lambertz, J., and Wallmann, Th., *"Experimentelle Untersuchung der Relativströmung im Laufrad einer Axialverdichterstufe,"* Forschungsbericht des Landes NRW No. 2711, 1978, Westdeutscher Verlag GmbH., Leverkusen-Opladen.

4 Gallus, H.E., Lambertz, J., and Wallmann, Th., "Untersuchungen der instationären Vorgänge in einer subsonischen Axialverdichterstufe infolge Laufrad-Leitrad-Interferenz," Mitteilungen Nr. 78-01 des Instituts für Strahlantriebe und Turboarbeitsmaschinen der RWTH Aachen, July 1978.

5 Gallus, H.E., Kummel, W., Lambertz, J., and Wallmann, Th., "Measurement of the Rotor-Stator-Interaction in a Subsonic Axial-Flow Compressor Stage," R.F.M., Symposium I.U.T.A.M. sur l'aeroelasticité dans les turbomachines, Paris, Oct. 1976.

6 Lambertz, J., Wallmann, Th., and Gallus, H.E., "Vergleich der Meßergebnisse dynamischer Schaufelkräfte in axialen Turbomaschinen mit Berechnungsverfahren verschiedener Autoren," VDI-Berichte No. 361, 1980.

7 Lienhart, W., "Berechnung der instationaren Stromung durch gegeneinander bewegte Schaufelgitter und der instationären Schaufelkrafte," VDI-Berichte No. 193, 1973.

8 Wallmann, Th., "Experimentelle Untersuchungen zur Wechselwirkung zwischen stehenden und umlaufenden Schaufelreihen einer Unterschall-Axialverdichterstufe," Dissertation thesis Aachen, 1980.

9 Henderson, R.W., "The Unsteady Response of an Axial Flow Turbomachine to an Upstream Disturbance," Ph.D. Dissertation, University of Cambridge, 1972.

10 Ispas, I., Grollius, H., and Gallus, H.E., "Über den Einfluß von Nachlaufdellen auf die instationäre Druckverteilung an den nachfolgenden Schaufelreihen in Axialverdichtern und Axialturbinen," VDI-Berichte No. 361, 1980.

11 Lambertz, J., "Instationäre Schaufelkräfte axialer Turbomaschinen und ihre Auswirkungen auf dynamische Belastung und Lärmentwicklung," Dissertation thesis Aachen, 1980.

12 Hort, W., "Schwingungen der Räder and Schaufeln in Dampfturbinen," VDI-Zeitung 70, No. 43, 1926.

13 Fleeter, S., Jay, R.L., and Bennett, W.A., "Wake Induced Time-Variant Aerodynamics Including Rotor-Stator Axial Spacing Effects," *Proceedings of the ASME Symposium on Nonsteady Fluid Dynamics*, 1978.

14 Franke, G.F., and Henderson, R.E., "Unsteady Stator Reponse to Upstream Rotor Wakes," *AIAA Journal of Aircraft*, Vol. 17, July 1980, pp. 500–509.

Application of Lifting Line Theory to Streamsurface Theory in Subsonic Flow

P. T. Chang
Research Associate,
Institute of Engineering Thermophysics,
Academia Sinica,
Republic of China

The paper shows that the streamsurface theory does not take account of the effect of the trailing vorticity on the performance of a subsonic rotor. Based on the S_2-streamsurface, an equation for the perturbations in velocity induced by the trailing vorticity is derived. Numerical examples for the change in the total pressure behind an annular rotating cascade in a circumferentially sinusoidal inlet flow are given in the assumptions of lifting line theory. The results agree quite well with Henderson's data. Also, the calculated results are given for the conditions of nonuniform circulation along the span. Compared with existing results, the results of the present paper are reasonable. The conclusion is that the perturbation equation presented can be applied as an additional consideration when the design is based on the streamsurface theory.

Introduction

The flow in axial turbomachinery is complicated because of unsteady flow, with rotation due to the fluid viscosity and twisted passage. Many analyses have been carried out in order to meet the demands of design and testing. Streamsurface theory [1] is one of the better and earlier analyses, which can describe the three-dimensional ideal flow in turbomachinery with great accuracy. Of course, there still are some problems left to be solved, for example, the variation of vortex strength trailing along the mean streamsurface, the trailing vorticity shed from the trailing edges of blades, wake flow passing through the blade row, and so on. These kinds of physical phenomena, like the sources of disturbance in the field, frequently make the flow field depart from one calculated by stream-surface theory. Such a disturbance field is usually called a secondary flow field.

The theory of shear flow which can describe secondary flow in turbomachinery has been reviewed in reference [2]. Reference [3] has reviewed the achievements of theory, experiment and application of secondary flow in turbomachinery aerodynamics. Recently, references [15, 16, and 17] make good steps to describe the behaviour of secondary flow in highly loaded axial turbomachines. Reference [18] works out the approach with inlet shear flow. These papers present the methods which describe the behavior of secondary flow. The purpose of the present paper is to explore a way to deal with the secondary flow problems of large shear and large disturbance by applying the methods presented in the theory of shear flow to streamsurface theory. Following the approach used in secondary flow theory, the flow field in the present analysis will be divided into two parts: primary flow and disturbance flow. Flow calculated by the S_2-mean streamsurface will be selected as primary flow. Since streamsurface theory describes a three-dimensional rotational flow field, no restrictions of flow behavior, such as blade loading (disturbance level) and flow swirl, are imposed. On the other hand, it will be shown that streamsurface theory does not account for the effect of secondary flow induced by secondary vorticity. Hence, a disturbance flow will be added to modify the primary flow. The modified flow will finally be regarded as a real physical flow.

Selection and Standardization of Primary Flow

Streamsurface theory presents a method which divides a three dimensional flow problem into two two-dimensional flow problems, i.e., using the iterative approach with two kinds of streamsurfaces, S_1 and S_2, to obtain a three dimensional flow field. Each streamsurface is mathematically a two-dimensional space, and is rather convenient for calculation. The S_2-mean streamsurface has a shape given approximately by the camber surface of the blade. The flow lying in the S_2-mean streamsurface is naturally selected as the primary flow. The primary flow is assigned to have an irrotational character for convenience. Obviously, the physical flow mentioned in the foregoing does not meet this requirement. To do so, a new flow field which has the main characteristics of the physical flow calculated by the S_2-stream surface theory is introduced.

First, we introduce nonorthogonal curvilinear coordinates on the S_2-mean streamsurface (Fig. 1). The definitions and relationships between various vectors are put in the Appendix. Then the new flow field (i.e., the transformed flow field) $\vec{W}_o$ is related to the physical one by the definition

$$\vec{W}_o = B\vec{W} = W_{ro}\vec{r} + W_{zo}\vec{z} + W_{\theta o}\theta = W_{ro}\vec{R} + W_{zo}\vec{Z} \quad (1)$$

Contributed by the Gas Turbine Division and presented at the International Gas Turbine Conference and Products Show, Houston, Texas, March 9-12, 1981, of THE AMERICAN SOCIETY OF MECHANICAL ENGINEERS. Manuscript received at ASME Headquarters, December 18, 1980. Paper No. 81-GT-166.

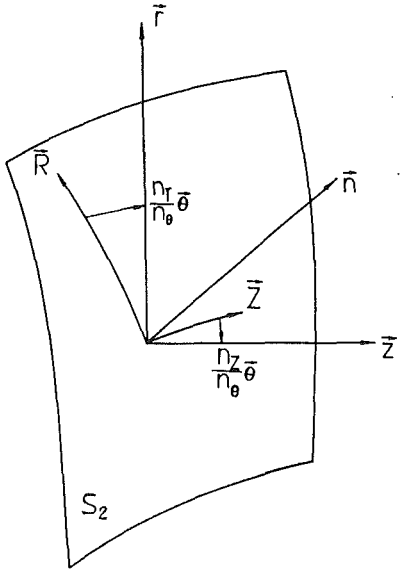

Fig. 1 Vectors on S_2-streamsurface

where $\vec{W}$ is the physical flow field in the S_2-mean streamsurface, the quantities $W_{ro} = BW_r$, $W_{\theta o} = BW_\theta$, $W_{zo} = BW_z$ are the velocity components in the cylindrical coordinates (r, θ, z) respectively, the quantity rb is the thickness of the S_2-mean stream-surface sheet, the sets of vectors $\vec{R}$, $\vec{Z}$, $\vec{\mathrm{H}}$ and **r, z, n** are reciprocal vectors (see the Appendix).

According to (35) in the Appendix, the transformed flow field $\vec{W}_o$ satisfies the continuity equation under steady conditions:

$$\nabla \cdot \rho \vec{W}_o = n_\theta \rho_{-\infty}^{-1} \left(\frac{\partial \bar{r} b \rho W_r}{\partial r} + \frac{\partial \bar{r} b \rho W_z}{\partial z} \right) = 0 \tag{2}$$

Because $\nabla \cdot \rho \vec{W}_o = B \nabla \cdot \rho \vec{W} + \rho \vec{W} \cdot \nabla B = 0$ and $\nabla \cdot \rho \vec{W} = 0$, it follows that

$$\vec{W} \cdot \nabla B = 0 \tag{3}$$

i.e., B is constant along a streamline. The significance of the factor B is that the flow field can become an "axisymmetric" flow field in the nonorthogonal coordinates $(\vec{R}, \vec{Z}, \vec{\mathrm{H}})$. Meanwhile, the ratio of streamsurface sheet thickness of the field $\vec{W}$, b/b_d is equal to that of the field $\vec{W}_o$ and $\mathbf{n} \cdot \vec{W} = \mathbf{n} \cdot \vec{W}_o = 0$.

Defining a transformed density $\rho' = B^{-2}\rho$, the continuity equation (2) can be rewritten in the following form

$$\nabla \cdot \rho' \vec{W}_o = 0 \tag{4}$$

The steady momentum equation for $\vec{W}_o$ is

$$-\vec{W}_o \times (\nabla \times \vec{W}_o + 2\vec{\omega}_o) = \frac{-1}{\rho'} \nabla P - \frac{1}{2} \nabla W_o^2 + \omega_0^2 \bar{r} \tag{5}$$

where $\vec{\omega}_o = B\vec{\omega}$. Comparing (5) with the momentum equation for $\vec{W}$, it can be concluded that the two flow fields have the same streamline patterns and same pressure distribution, according to Munk and Prim's principle [13].

We now only consider the flow in the S_2-mean streamsurface. Using (36) in the Appendix, the curl of $\vec{W}_o$ can be expressed by

$$\nabla \times \vec{W}_o = \frac{-1}{n_\theta} \left(\frac{\partial W_{zo}}{\partial r} - \frac{\partial W_{ro}}{\partial z} \right) \mathbf{n} \tag{6}$$

The expression (6) indicates that the curl of $\vec{W}_o$ on the S_2-mean streamsurface has only one component in the normal direction to the streamsurface, **n**. This is because the field $\vec{W}_o$ is of the "axisymmetric" character in the coordinates $(\vec{R}, \vec{Z}, \vec{\mathrm{H}})$, and $\vec{W}_o$ has no velocity component in the $\vec{n}$ direction.

We now check if the expression (6) can remain constant along a streamline on the S_2-mean streamsurface. Because we are interested in the effects of shearing and disturbance of flow we will temporarily neglect the effects of the angular velocity $\vec{\omega}$ and compressibility, i.e., we will assume that $\vec{W}_o \cdot \nabla \rho = 0$. Taking the curl of both sides of the equation (5) under the conditions that the density ρ is a function of pressure P only and $\vec{\omega} = 0$, and allowing for the $\nabla \cdot \rho \vec{W}_o = 0$ and $(\vec{n} \cdot \nabla)\vec{W}_o = 0$ on the S_2-mean stream surface, we obtain

$$(\vec{W}_o \cdot \nabla)(\nabla \times \vec{W}_o) = 0 \tag{7}$$

Nomenclature

$\vec{A}$ = velocity singularity
B = $n_\theta b r \rho_{-\infty}^{-1}$
b = angular thickness of S_2-stream sheet
C = vector
F = vector having the unit of force per unit mass of fluid
$\Delta\mathbf{F}$ = perturbation of the **F**
$\mathbf{F}$ = $\mathbf{F} + \Delta\mathbf{F}$
h = r_h/r_t
I = stagnation rothalpy
i = unit vector in x direction
i = $\sqrt{-1}$
J = unit vector in Y direction
k = unit vector normal to the (x,y) plane
M = Mach number
m = $\sqrt{\left(\frac{\partial S}{\partial r}\right)^2 + \left(\frac{\partial S}{r\partial\theta}\right)^2 + \left(\frac{\partial S}{\partial z}\right)^2}$
N = number of blades
n = integer $(\pm)$
n = unit vector normal to the S_2-streamsurface
P_o = stagnation pressure
P = static pressure
p = unperturbed static pressure
Δp = perturbation of the p
q = quantity on the S_2-streamsurface
$\vec{R}$ = $\mathbf{r} - (n_r/n_\theta)\theta$
r = unit vector in the radial direction
r = radial distance
$\bar{r}$ = r/r_t
S = variable in the non-orthogonal coordinates
S_1 = relative stream surface passing through fluid particles lying on a circular arc upstream of or somewhere inside blade row
S_2 = relative stream surface passing through fluid particles lying on a radial line upstream of or somewhere inside blade row
s = entropy per unit mass
T = static temperature
t = blade spacing
$\vec{U}$ = velocity of blade
$\vec{V}$ = absolute velocity of fluid
v' = absolute perturbation velocity
v'' = induced velocity on the blades
$\vec{W}$ = unperturbed relative velocity
$\vec{w}$ = relative perturbation velocity
$\vec{\mathcal{W}}$ = $\vec{W} + \vec{w}$

which indicates that the strength of the relative vorticity $\nabla \times \vec{W}_o$ is constant along a streamline on the S_2-mean streamsurface. For convenience, we will assume that the $\nabla \times \vec{W}_o = 0$ in the following analysis. Then

$$\nabla \times \vec{W} = \vec{W} \times \nabla \ \ln \ B \neq 0 \tag{8}$$

The expression (8) indicates that the physical flow is rotational.

The expression of secondary vorticity of the steady flow field $\vec{W}_o$ can be found in reference. [2]:

$$\rho \vec{W}_o \cdot \nabla \frac{\vec{\Omega} \cdot \vec{W}_o}{\rho W_o} = \vec{W}_o \times \nabla I_o \cdot \nabla \frac{1}{W_o^2} - \vec{W}_o \times \nabla s \cdot \nabla \frac{T}{W_o^2} - \vec{W}_o \times (\nabla \times \vec{W}_o) \cdot \frac{2\vec{\omega}_o}{W_o^2} \tag{9}$$

As in previous treatments, when all parametes, $\vec{W}_o$, I_o, T, s, in the field $\vec{W}_o$ are taken from the S_2-mean streamsurface, the scalar triple products $W_o \times \nabla I_o \cdot \nabla(1/W_o^2)$ and $\vec{W}_o \times \nabla s \cdot \nabla (T/W_o^2)$ become zero. Now only the third term, containing the angular velocity $\vec{\omega}$, is left. As pointed out previously, $\nabla \times \vec{W}_o$ = constant along a S_2-stream filament (or along a streamline on the S_2-streamsurface), therefore the term $\vec{W}_o \times (\nabla \times \vec{W}_o) \cdot (2\vec{\omega}_o / W_o^2)$ is constant along the streamline. The fact that the rate of change of secondary vorticity along the streamline is constant indicates that there is no secondary vorticity caused directly by $\vec{W}_o$. When $\vec{\omega} = 0$ or $\nabla \times \vec{W}_o = 0$, this is particularly true. It leads to the conclusion that the S_2-streamsurface itself does not contain secondary vorticity. In other words, neither the velocity field $\vec{W}_o$ nor $\vec{W}$, calculated by streamsurface theory, takes account of the existence of secondary vorticity.

The streamsurface theory, as stated previously in (8), is able to describe a physical velocity field $\vec{W}$ with rotation, but it can not allow for the effects of existing secondary vorticity.

Because the transformed field $\vec{W}_o$ is the type $\nabla \times \vec{W}_o$ = constant or zero along a streamline in the S_2-mean streamsurface, it displays a two-dimensional flow pattern on that streamsurface. Thus, the flow $\vec{W}_o$ in the S_2-mean streamsurface will be selected as a primary flow on which to base the modification of secondary flow.

Generalized Perturbation Equations

We consider an adiabatic and reversible, i.e., isentropic, flow ($Ds/D\tau = 0$. This also implies that density ρ is a function of pressure P only, that the circulation along a streamline is constant, $(D\Gamma/D\tau) = 0$, and that the blade force $\mathbf{F}$ acting on the fluid is perpendicular to the streamline, $\mathbf{F} \cdot \vec{W} = 0$. In order to make the equations linearized, further assumptions are needed besides those mentioned in the foregoing, namely, (*i*) the primary flow is steady, is of unit order of magnitude, $o(1)$, and the secondary flow or perturbation is allowed to be unsteady, and of small order of magnitude, $o(\epsilon)$, where $\epsilon << 1$. From the linearized point of view, all terms of order ϵ^2 and greater would be omitted in deriving the final equation and (*ii*) if the inlet flow is nonuniform in the normal direction to the streamsurface, $\mathbf{n}$, it will be assumed that the amplitude of nonuniformity is small compared with the mean value, i.e., of order ϵ. The exit flow from a blade row upstream can be regarded as a nonuniform flow due to the viscous wakes, which is an example of circumferential nonuniformity with periodicity.

Based on assumption (1), we can define a new velocity field $\underline{\vec{W}}_o$

$$\underline{\vec{W}}_o = (W_{ro} + w_{ro})\vec{R} + (W_{zo} + w_{zo})\vec{Z} + A_o \vec{\mathrm{H}} \tag{10}$$

Applying expression (10) to the continuity equation, after some simplification, we obtain

$$\frac{\bar{\partial} rb\rho w_r}{\partial r} + \frac{\bar{\partial} rb\rho w_z}{\partial z} = \frac{-1}{n_\theta}\left[\frac{\partial \rho}{\partial \tau} + \rho \frac{\partial A_o}{\partial S/m}\right] \tag{11}$$

where $w_{ro} = Bw_r$, $w_{zo} = Bw_z$ are perturbation velocity components. The quantity A_o represents a singularity of order ϵ introduced to allow for the effects of perturbation lift, designated by ΔF_n. It will be seen that w_{ro} and w_{zo} involve discontinuities related to the singularity A_o.

To solve the perturbation field, as an approximate approach, we define a mass flow potential of $\rho \vec{w}_o$ (12), ϕ,

$$\frac{\partial \phi}{\partial r} = \rho b w_r, \qquad \frac{\partial \phi}{\partial z} = \rho b w_z \tag{12}$$

Nomenclature (cont.)

X, Y = cartesian coordinates relative to moving blade system (see Fig. 3)
x, y = cartesian coordinates (see Fig. 3)
$\vec{Z}$ = $\mathbf{z} - (n_z/n_\theta)\vec{\theta}$
z = axial distance
$\mathbf{z}$ = unit vector in the axial direction
α = $\beta + \gamma$, angle γ angle between $\vec{V}$ and $\vec{W}$
$\bar{\beta}$ = stagger angle
β = air inlet angle
$\vec{\Gamma}$ = circulation
$\Delta\vec{\Gamma}$ = perturbation of the $\vec{\Gamma}$
$\underline{\vec{\Gamma}}$ = $\vec{\Gamma} + \Delta\vec{\Gamma}$
δ = Dirac's delta function
ϵ = small quantity
$\vec{\mathrm{H}}$ = $(1/n_\theta)\theta$
θ = unit vector in the circumferential direction
$\vec{\Lambda}$ = instantaneous angular velocity
λ^2 = $1 - M_z^2$
μ = frequency
ξ = distance along a streamline on S_2-streamsurface
π = Pi
ρ = fluid density
ρ' = transformed density
τ = time coordinate
ϕ = mass flow potential of the $\rho\vec{w}_o$
$\vec{\omega}$ = angular velocity of blade
$\vec{\Omega}$ = $\nabla \times \vec{W}_o + 2\vec{\omega}_o$, absolute vorticity
$\bar{\delta}$ = partial derivative following stream surface
K = $\mu U \cos \alpha / W_{om}$

Subscripts

d = reference
h = hub
i = image part of the function
m = mean
n = normal to the S_2-streamsurface
o = transformed flow
q = quasi-state
r = radial component, or real part of the function
t = tip
X = component in the X direction
x = component in the x direction
z = axial component
θ = circumferential component
$-\infty$ = far upstream
∞ = far downstream

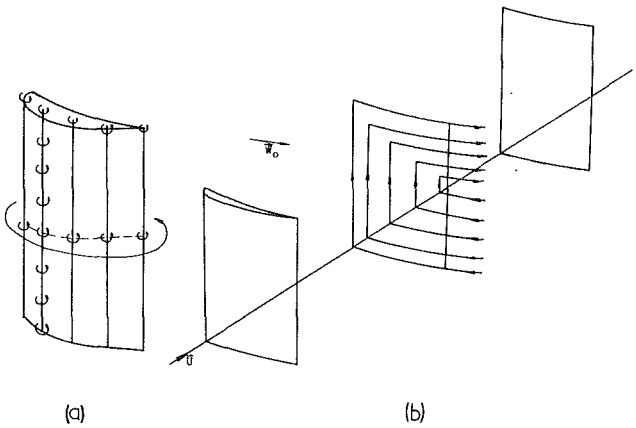

Fig. 2 Bound vortices and trailing vortices

Substituting (12) into (11), the continuity equation becomes

$$\frac{1}{r}\frac{\partial}{\partial r}\left(r\frac{\partial r}{\partial \phi}\right)+\frac{\partial}{\partial z}\left(\frac{\partial \phi}{\partial z}\right)=\frac{-1}{n_\theta r}\left[\frac{\partial \rho}{\partial \tau}+\rho\frac{\partial A_o}{\partial S/m}\right] \quad (13)$$

The next step is to study Euler's momentum equation. Before proceeding to it, it is useful to establish a physical picture. We regard a blade as an S_2-mean streamsurface. The blade will be replaced by a vorticity distribution, composed of an infinite number of discrete bound vortices in the spanwise direction. Every bound vortex in the distribution represents an elemental blade made up from the continuous distribution of vorticity along the chord. The profile of the elemental blade is constructed by the intersection of the S_2-mean streamsurface with the S_1-streamsurface. Every bound vortex will produce a perturbation potential when it moves in space. Assume that an instantaneous motion of the bound vortex persists forever. Such a motion is called a quasi-steady motion. Hence, it can be said that every profile of the blade section, like an airfoil section, moves forward in the uniform flow field at a given instant. On the other hand, the rotating blade encounters fluctuations when the flow in the azimuthal direction is nonuniform. It means that the motion should be the resultant of an infinite number of different quasi-steady situations, caused by a so-called "impulse force." Finally, the behaviour of a real flow can be regarded as the motion found by adding up the infinite numbers of quasi-steady motions performed by the infinite numbers of discrete bound vortices accompanying the trailing vortices that are shed from the blades over an infinite number of instants. Figure 2 demonstrates the main aspects of the physical model at a given instant.

Based on the model mentioned above, and taking the origin of coordinates on the section of the elemental blade, Euler's momentum equation becomes

$$\frac{D\vec{\underline{W}}_o}{D\tau}=\frac{-1}{\rho'}\nabla P-\vec{\omega}_o\times\vec{W}_o-\vec{\underline{F}}_o \quad (14)$$

where $\mathbf{F}_o$ is the blade force acting on a unit mass of fluid in the $\vec{\underline{W}}_o$ field, $\mathbf{F}_o = \mathbf{F}_o + \Delta\mathbf{F}$. The quantity $\mathbf{F}_o$ is the blade force in the $\vec{W}_o$ field, which is proportional to the undisturbed strength of the vorticity [7] [8], $\vec{\Gamma}_{qo}$, $\mathbf{F}_o = \vec{\Gamma}_{qo}\times\vec{W}_o$. The quantity $\vec{\Gamma}_{qo}$ has the dimensions of circulation per unit area of the vortex. The quantity $\Delta\mathbf{F}$ is the perturbation of the blade force. Since the disturbance field $\vec{W}_o$ cannot cause a net change in the blade force [6], $\Delta\mathbf{F} = (\Delta\vec{\Gamma}_{qo} + \vec{\Lambda})\times\vec{W}_o$. The quantity $\Delta\vec{\Gamma}_{qo} = \vec{\underline{\Gamma}}_{qo} - \vec{\Gamma}_{qo}$ is the perturbation of $\vec{\Gamma}_{qo}$ and $\vec{\Lambda}$ is the instantaneous angular velocity caused by the circumferential nonuniform flow through which the blade passes. It has the dimensions of circulation per area, and is a source of fluctuations on the blade. If $\vec{\Lambda} = 0$, the blade row will move in a circumferentially uniform flow, and the fluctuating blade force will disappear. The quantity $\vec{\underline{\Gamma}}_{qo}$ is the circulation per area in the $\vec{\underline{W}}_o$ field. The static pressure P can also be divided into two parts: unperturbed p and perturbation Δp. Concerning the density ρ, assume that the perturbation of density is of order ϵ^2 due to using the definition of the mass flow potential, ϕ, which has allowed for the effects of compressibility on the primary flow. It will be omitted in the following analysis. Then applying the approach adopted in reference [4], we obtain

$$\left(\frac{\partial}{\partial \tau}+\vec{W}_o\cdot\nabla\right)\vec{w}_o=\frac{-1}{\rho'}\nabla(\Delta p)-(\vec{w}_o\cdot\nabla)\vec{W}_o \quad (15)$$

which applies throughout the flow except where there are singularities. The equation

$$\left(\frac{\partial}{\partial \tau}+\vec{W}_o\cdot\nabla\right)\vec{A}_o=-\Delta\mathbf{F}-(\vec{A}_o\cdot\nabla)\vec{W}_o \quad (16)$$

represents the effects of the singularities $\vec{A}_o$.

The quantity $(\vec{A}_o\cdot\nabla)\vec{W}_o = 0$ when $\vec{A}_o = A_o n$ and the values of $\vec{W}_o$ are taken from the S_2-streamsurface. The component of the equation (16) in the $\mathbf{n}$ direction is

$$\left(\frac{\partial}{\partial \tau}+\vec{W}_o\cdot\nabla\right)A_o=-\Delta F_n \quad (17)$$

$$\left(\frac{\partial}{\partial \tau}+\vec{W}_o\cdot\nabla\right)\frac{\partial A_o}{\partial S/m}=-\frac{\partial \Delta F_n}{\partial S/M} \quad (18)$$

where the latter equation (18) is obtained by differentiation of equation (17) with respect to the variable S. Integrating equations (17) and (18) along a streamline ξ of $\vec{W}_o$ under steady condition, we obtain

$$A_o=-\int_{\xi_d}^{\xi}\frac{1}{W_o}\Delta F_n d\xi \quad (19)$$

$$\frac{\partial A_o}{\partial S/m}=-\int_{\xi_d}^{\xi}\frac{1}{W_o}\frac{\partial \Delta F_n}{\partial S/m}d\xi \quad (20)$$

Substituting expression (20) into (13) and translating it into cylindrical coordinates, we obtain

$$\nabla^2\phi=\frac{+\rho}{n_\theta r}\int_{\xi_d}^{\xi}\frac{1}{W_o}\frac{\partial \Delta F_n}{\partial S/m}d\xi \quad (21)$$

The expression (13) is a generalized perturbation equation with the equations (17) and (18) based on the S_2-mean streamsurface, which describes the distribution of secondary flow. Obviously, there are no restrictions on quantities, such as the loading on the blades and the rotation of the inlet flow. The effects of blade loading and the rotation of the inlet flow on the distribution of secondary flow are reflected in the thickness of the streamsurface sheet, b. The effects of compressibility of the flow could also be accounted for by the local distribution of density ρ which is submerged in the definition of the potential ϕ.

Small Circumferential Shear Flow

As an application of the equations mentioned in the preceding section, an interesting example is to study the behavior of the wake flow exiting from a blade row upstream and passing through a blade row downstream. This is an unsteady flow. To simplify the problem, attention will be restricted to two-dimensional incompressible flow. Assuming that the incoming flow is circumferentially of sinusoidal shape, that the amplitude of the sinusoidal flow, v', is of order ϵ, and that the blade load is slight, then, the trailing vorticity shed from the blades may be considered to lie in the chordwise direction and to be transported at a speed equal to the mean velocity between inlet and exit of the blade. Ac-

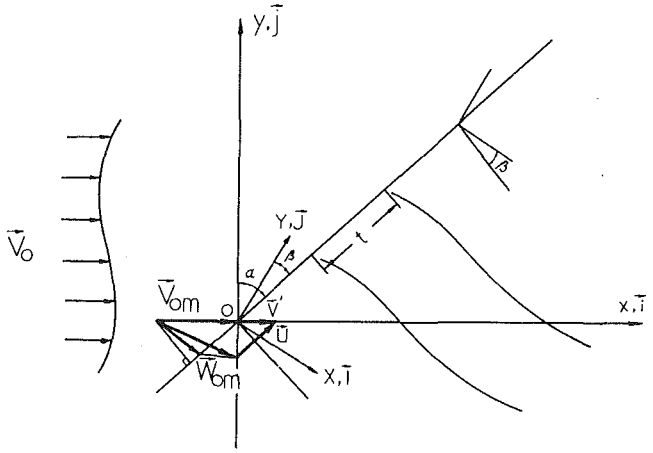

Fig. 3 Coordinate systems of flow field with fluctuation

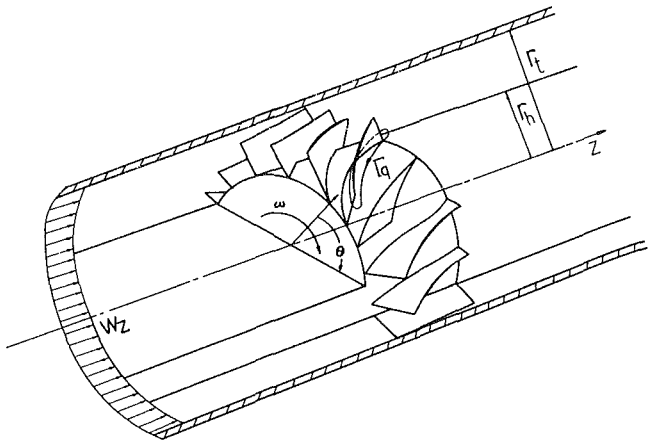

Fig. 4 Blade row and duct

cording to the assumptions, the blades are regarded as lifting lines. The relative position between the lifting lines and incoming flow is shown in Fig. 3. The equations in the previous section can be written as follows:

$$\frac{\partial \phi}{\partial X} = w_X, \qquad \frac{\partial \phi}{\partial Y} = w_Y$$

$$\nabla^2 \phi = -\nabla \cdot \vec{A}_o$$

$$\left(\frac{\partial}{\partial \tau} + W_{Xo}\frac{\partial}{\partial X}\right)\nabla\phi = \left(\frac{\partial}{\partial \tau} + W_{Xo}\frac{\partial}{\partial X}\right)\vec{A}_o = \frac{-1}{\rho}\nabla(\Delta p)$$

$$\left(\frac{\partial}{\partial \tau} + W_{Xo}\frac{\partial}{\partial X}\right)\nabla^2\phi = \left(\frac{\partial}{\partial \tau} + W_{Xo}\frac{\partial}{\partial X}\right)\nabla\cdot\vec{A}_o = -\nabla\cdot(\Delta \mathbf{F}) \tag{22}$$

which are similar to the equations from reference [4]. Hence, the expression for the stagnation pressure P_o is

$$P_o = p + \frac{1}{2}\rho V_{xo} + \rho V_{xo}\frac{\partial \phi}{\partial x} + \rho V_{xo}\mathbf{i}\cdot\vec{A}_o$$

after assuming that all disturbances vanish far upstream, i.e., $\phi_{-\infty} = 0$ at $x = -\infty$. Integrating (22) along a streamline, the change in stagnation pressure P_o across the rotor is obtained as:

$$\Delta\frac{P_o - P_{o,-\infty}}{\rho} = V_{xo}\mathbf{i}\cdot\vec{A}_o - \frac{\partial \phi}{\partial \tau} \tag{23}$$

The source of impulse inducing the fluctuating lift is of the form $\vec{\Lambda} = v'\mu \sin^2(\alpha - \beta)e^{i\mu y}\mathbf{k}$ in this case, where $\mathbf{k}$ is a unit vector perpendicular to the plane (x,y). The incidence angle varies due to nonuniform flow in the circumferential direction. This leads to the production of trailing vorticity. Reference [5] shows the expression of singularities A_o at $x = \infty$:

$$\vec{A}_{o,\infty} = -\mathbf{J}v'\sin(\alpha-\beta)Q(K,t,\bar{\beta})\sum_{n=-\infty}^{\infty} e^{-i\mu}$$

$$[y + nt\ \sin\ \beta\ \sin(\alpha-\beta)] \times \delta[Y - nt\ \cos\ \beta]$$

$$Q(K,t,\bar{\beta}) = \frac{\pi}{2}K\left[(J_1 s_r + N_1 s_i) + (J_1 s_i - N_1 s_r)\frac{2Rt}{R^2+1}\frac{\cos\ \bar{\theta}_{st}}{\cos\ \bar{\beta}}\right]$$

$$-i\left\{\frac{Kt(R^2-1)}{4R}\sin\ \bar{\beta} + \frac{\pi K}{2}\left[(J_1 s_r + N_1 s_i)\frac{2Rt}{R^2+1}\frac{\cos\ \bar{\theta}_{st}}{\cos\ \bar{\beta}} + N_1 s_r - J_1 s_i\right]\right\} \tag{24}$$

where $\bar{\beta}$ is the stagger angle, $K = \mu U \cos\ \alpha / W_{om}$, $s(K) = s_r(K) + is_i(K)$ relates to the Theodorsen function [14]. It has been plotted in Fig. 6. The parameters R and $\bar{\theta}_{st}$ are the expressions in Weinig's cascade theory (see reference [12]), and $J_1(K)$ and $N_1(K)$ are the usual Bessel functions.

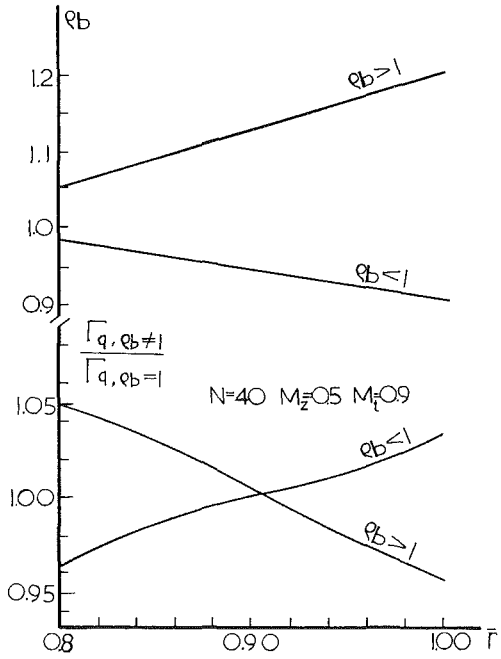

Fig. 5 Distributions of Γ_q with $\rho b \neq 1$

Applying (24) to (23), and noting that the potential ϕ_∞ is a periodic function with period (t/U), the time-mean stagnation pressure change across such a rotor is

$$\frac{\Delta P_{o,\infty}}{\rho} = \frac{U}{t}v'\sin(\alpha-\beta)Q(K,t,\bar{\beta}) \times \sum_{n=-\infty}^{\infty} e^{-i\mu[y + nt\ \sin\ \beta\ \sin(\alpha-\beta)]} \tag{25}$$

We are interested in the amplitude of the time-mean stagnation pressure changes. Calculations have been done under the conditions of the stagger angle $\bar{\beta}$ = air inlet angle β = 45 deg, $V_o = U$, and $t = 0.676, 1.353$. The results of the calculations are given in Table 1. Also, Henderson's results [9] are quoted in Table 1 for comparison.

Taking account of uncertainty in the unsteady motion, the present results are rather satisfactory.

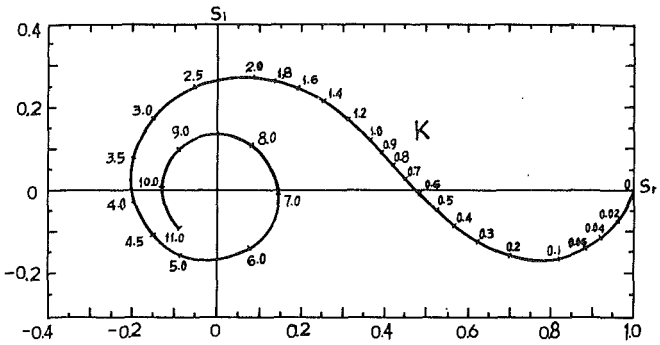

Fig. 6 Function $s(K) = s_r(K) + is_i(K)$

Table 1 Comparison of time-mean stagnation pressure changes

t	K	v' (m/s)	V_o (m/s)	$\frac{\Delta P_{o,\infty}}{\frac{1}{2}\rho U^2}$	$\frac{\Delta P_{o,\infty}}{\frac{1}{2}\rho U^2}$ in [9]
0.676	0.272	1.48	21.66	0.1409	0.0965
0.676	0.542	1.40	22.77	0.1372	0.0860
0.676	0.804	1.48	21.47	0.1117	0.1075
0.676	0.817	1.37	21.45	0.1041	0.1140
0.676	1.082	1.37	22.58	0.0954	0.1055
0.676	1.365	1.26	22.81	0.0847	0.0820
0.676	1.642	1.44	22.21	0.0978	0.1030
1.353	0.275	1.45	21.70	0.0853	0.0720
1.353	0.542	1.33	22.77	0.0620	0.0623
1.353	0.822	1.37	21.49	0.0617	0.0755
1.353	1.368	1.24	22.81	0.0493	0.0583
1.353	1.655	1.42	22.19	0.0557	0.0555

Nonuniform Circulation Along the Span

Another application of equation (13) or (21) is to calculate the effects of nonuniform circulation along the span. The assumptions of lifting line theory are still adopted. We consider the flow in an annular duct (Fig. 4), and assume that the incoming flow is uniform both in the radial and azimuthal directions. The perturbation of lift is only caused by the trailing vortices originating from the nonuniform circulation along the span

$$\Delta F_n = \Delta\Gamma_{qo} W_o \delta(\xi) \sum_{n=-\infty}^{\infty} \delta\left(\frac{S}{m} - \frac{2\pi n_\theta r}{N} n\right) \tag{26}$$

where δ is Dirac's delta function. Using the following boundary conditions: (*i*) the normal perturbation velocities are equal to zero at the tip r_t and hub r_h of the duct; (*ii*) there are periodic changes in the parameters in the circumferential direction; (*iii*) all disturbances of the axial velocities w_z vanish far upstream, i.e., at $z = -\infty$; (*iv*) there are no sources and sinks of mass flow at any section perpendicular to the z axis; (*v*) both the potential and the axial velocity w_z are continuous at $z = 0$, i.e., at the location of the blade row, then equation (21) with the expression (26) gives the solution of the induced velocity on the blades [11], v'':

$$\frac{v''}{W} = \frac{1}{2W_z t}\left[\Delta\Gamma_q - \frac{\sin^2\beta}{\lambda^2}\frac{2}{1-h^2}\frac{1}{\rho b}\int_h^1 \rho b\bar{r}\Delta\Gamma_q d\bar{r} - \frac{2}{N\rho b}\sum_{n=1}^{\infty}\kappa_n\right] \tag{27}$$

Adding the induced velocity of the primary flow, the expression (27) becomes

$$\frac{v''}{W} = \frac{2W_z t}{1}\left[\Gamma_q - \frac{\sin^2\beta}{\lambda^2}\frac{2}{1-h^2}\frac{1}{\rho b}\int_h^1 \rho b\bar{r}\,\Gamma_q d\bar{r} - \frac{2}{N\rho b}\sum_{n=1}^{\infty}\kappa_n\right] \tag{28}$$

where

$$\kappa_n \equiv \kappa_{nN}(nN\bar{r}) = \frac{K'(\bar{r}_t)I'(\bar{r}_h)K(\bar{r}) - K'(\bar{r}_t)K'(\bar{r}_h)I(\bar{r})}{K'(\bar{r}_t)I'(\bar{r}_h) - K'(\bar{r}_h)I'(\bar{r}_t)}$$

$$\int_{\bar{r}_h}^{\bar{r}_t} \bar{r}I'(\bar{r})\frac{df}{d\bar{r}}d\bar{r}$$

$$+ \frac{I'(\bar{r}_t)K'(\bar{r}_h)I(\bar{r}) - I'(\bar{r}_t)I'(\bar{r}_h)K(\bar{r})}{K'(\bar{r}_t)I'(\bar{r}_h) - K'(\bar{r}_h)I'(\bar{r}_t)}$$

$$\int_{\bar{r}_h}^{\bar{r}_t} \bar{r}K'(\bar{r})\frac{df}{dr}d\bar{r} + I(\bar{r})\int_{\bar{r}_h}^{\bar{r}} \bar{r}K'(\bar{r})\frac{df}{d\bar{r}}d\bar{r} - K(\bar{r})\int_{\bar{r}_h}^{\bar{r}} \bar{r}I'(\bar{r})\frac{df}{d\bar{r}}d\bar{r}$$

where $I(\bar{r}) = I_{nN}(nN\bar{r})$, $K(\bar{r}) = K_{nN}(nN\bar{r})$ are the modified Bessel functions of the first and second kind, and we have used the notion $I'(\bar{r}) = (d/d\bar{r})I_{nN}(nN\bar{r})$, $K'(\bar{r}) = (d/d\bar{r})K_{nN}(nN\bar{r})$. Each $\kappa_n(\bar{r})$ depends on the blade number N through its appearance both in the order and the argument of the Bessel functions. The quantity $f = N\rho b\Delta\Gamma_q$. Formula (28) has the same form as formula (13) in reference [10]. In particular, they are exactly the same for $\rho b = 1$ and $\Delta\Gamma_q = \Gamma_q$ in (28). The third term in (28) represents the effects of the trailing vorticity. As stated in reference [10], its effects are small and mainly appear at the outer and inner regions of the duct. The case $\rho b \neq 1$ represents the effects of the blade load and rotation in flow. Figure 5 plots the distribution of Γ_q, $\rho b \neq 1$ for $N = 40$, $M_z = 0.5$ and $M_t = 0.9$. In order to make the value for $\kappa_n(nN\bar{r})$ finite at the hub and tip, we set up $df/d\bar{r} = 0$ at the hub and tip by using the approach in reference [10]. Obviously, $\rho b \neq 1$ plays a role of redistributing the circulation along the span. The effects of $\rho b > 1$ are opposite to the effects of $\rho b < 1$. This example indicates numerically that the streamsurface theory does not account for the effects of the existing secondary flow.

Summary and Conclusions

The fact that streamsurface theory for adiabatic and isentropic flow does not account for the effects of secondary flow has been demonstrated by applying the theory of shear flow to the streamsurface theory. A set of generalized perturbation equations describing the secondary flow field in an axial turbomachine has been developed, based on the S_2-mean streamsurface. The equations include the effects of compressibility by variations in the local density. This treatment is different from some existing linearized theories which account for the effects of compressibility by the Mach number far upstream, for example, in reference [10]. Reference [19] suggests using a given mean Mach number between the inlet and exit of the blade. The equations do not differentiate whether the flow is rotational or irrotational, or which shape of blade is used, since they introduce the streamsurface sheet thickness b.

Two numerical examples have been completed. It is worthwhile to note that the set of generalized perturbation equations of the present paper can not only describe the existing perturbation phenomena relative to secondary vorticity, but can also describe more complex flows.

References

1 Wu, C. H., "A General Theory of Three-Dimensional Flow in Subsonic and Supersonic Turbomachines of Axial, Radial and Mixed-Flow Types," ASME Paper No. 50-A-79, Trans. ASME, Nov. 1952, or NACA TN 2604, 1952.

2 Hawthorne, W. R., "On the Theory of Shear Flow," M.I.T., G.T.L. Report No. 88, 1966.

3 Horlock, J. H., and Lakshminarayana, B., "Secondary Flow: Theory, Experiment, and Application in Turbomachinery Aerodynamics," *Annual Review of Fluid Mechanics*, Vol. 5, 1973, pp. 247-280.

4 Hawthorne, W. R., "Flow Through Moving Cascades of Lifting Lines with Fluctuating Lift," *Journal of Mechanical Engineering Science*, Vol. 15, No. 1, 1973, pp. 1-10.

5 Chang, P. T., "Small Shear Flow Through Moving Cascades of Lifting Lines with Fluctuating Lift," Academia Sinica, Institute of Mechanics Report, 1976.

6 Batchelor, G. K., *An Introduction to Fluid Dynamics*, Cambridge, England, 1970, pp. 517-520.

7 Durand, W. F., Editor-in-Chief, *Aerodynamic Theory*, Vol. 2, Berlin, 1935, pp. 15-17.

8 Robinson, R., and Laurmann, J. A., *Wing Theory*, Cambridge University Press, 1956, pp. 176-186.

9 Henderson, R. E., "The Unsteady Response of An Axial Flow Turbomachine to An Upstream Disturbance," thesis, Cambridge, England, 1972.

10 McCune, J. E., and Dharwadkar, S. P., "Lifting Line Theory for Subsonic Axial Compressor Rotors," M.I.T., GLT Report, No. 110, July 1972.

11 Chang, P. T., "The Effects of Trailing Vortices Behind Rotor in Subsonic Flow," Academia Sinica, Institute of Mechanics, Report, 1980.

12 *Aerodynamics of Turbines and Compressors*, ed., W. R. Hawthorne, Oxford, 1964, pp. 21-31.

13 Munk, M., and Prim, R. C., "On the Multiplicity of Steady Gas Flows Having the Same Streamline Pattern," *Proceedings of the National Academy of Science of the U.S.*, Vol. 33, No. 5, 1947, pp. 137-141.

14 Kemp, N. H., "On the Lift and Circulation of Airfoils in Some Unsteady Flow Problems," *Journal of Aeronautical Sciences*, Vol. 19, No. 10, 1952, pp. 713-714.

15 McCune, J. E., and Hawthorne, W. R., "The Effects of Trailing Vorticity on the Flow Through Highly Loaded Cascades," *Journal of Fluid Mechanics*, Vol. 74, Part 4, pp. 721-740.

16 McCune, J. E., "Three-Dimensional Inviscid Flow Through a Highly Loaded Transonic Compressor Rotor," *Transonic Flow Problems in Turbomachinery*, eds., T. C. Adamson, Jr. and M. F. Platzer, Hemisphere Publishing Corporation, Washington, 1977, pp. 20-59.

17 McCune, J. E., "Three-Dimensional Flow in Highly Loaded Axial Turbomachines," *Zeitschrift fur Angewandte Matematik and Physik*, Vol. 28, 1977, pp. 865-878.

18 Hawthorne, W. R., et al., "Nonaxisymmetric Flow Through Annular Actuator Disks: Inlet Distortion Problem," ASME JOURNAL OF ENGINEERING FOR POWER, 100, 1978, pp. 604-617.

19 Chauvin, J., Sieverding, C., and Griepentrog, H., "Flow in Cascades with a Transonic Regime," *Flow Research on Blading*, ed., L. S. Dzung, Elsevier Publishing Company, London, 1970, pp. 151-189.

APPENDIX

Some relationships given in reference. [1] are quoted as follows:

$$
\left.
\begin{aligned}
&S[r,z,\theta(r,z)]=0\\
&\frac{\partial S}{\partial r}dr+\frac{\partial S}{\partial z}dz+\frac{\partial S}{r\partial\theta}d\theta=0\\
&\mathbf{n}=n_r\mathbf{r}+n_\theta\vec{\theta}+n_z\mathbf{z}\\
&\frac{n_r}{\dfrac{\partial S}{\partial r}}=\frac{n_\theta}{\dfrac{n_\theta}{r\partial\theta}}=\frac{n_z}{\dfrac{\partial S}{\partial z}}=\frac{1}{m}\\
&m=\sqrt{\left(\frac{\partial S}{\partial r}\right)^2+\left(\frac{\partial S}{r\partial\theta}\right)^2+\left(\frac{\partial S}{\partial z}\right)^2}\\
&\mathbf{n}\cdot\vec{W}_o=0\quad\text{or}\quad \mathrm{n_r W_{ro}+n_z W_{zo}+n_\theta W_{\theta o}}=0\\
&n_r dr+n_\theta r d\theta+n_z dz=0\\
&\frac{\bar\partial q}{\partial r}=\frac{\partial q}{\partial r}-\frac{n_r}{n_\theta}\frac{\partial q}{r\partial\theta}\\
&\frac{\bar\partial q}{\partial z}=\frac{\partial q}{\partial z}-\frac{n_z}{n_\theta}\frac{\partial q}{r\partial\theta}
\end{aligned}
\right\}\qquad (29)
$$

where the quantity q is considered on the S_2-streamsurface as a function of r and z. Using (29), the operator ∇ can be written as

$$
\left.
\begin{aligned}
\nabla&=\mathbf{r}\frac{\partial}{\partial r}+\vec{\theta}\frac{\partial}{r\partial\theta}+\vec{z}\frac{\partial}{\partial z}\\
&=\mathbf{r}\frac{\bar\partial}{\partial r}+\mathbf{z}\frac{\bar\partial}{\partial z}+\mathbf{n}\frac{\partial}{\partial S/m}\\
&=\vec{R}\frac{\partial}{\partial r}+\vec{Z}\frac{\partial}{\partial z}+\vec{\mathrm{H}}(n\cdot\nabla)
\end{aligned}
\right\}\qquad (30)
$$

where $\mathbf{r}$, $\vec{\theta}$, $\mathbf{z}$ are unit vectors in cylindrical coordinates (r, θ, z) respectively, and $\partial/\partial r$ and $\bar\partial/\partial z$, as stated in reference [1], are derivatives with respect to r and z on S_2-streamsurface, respectively. The quantity $\partial/\partial S/m$ is a derivative with respect to S in the $\mathbf{n}$ direction. Since

$$
\left.
\begin{aligned}
&\frac{\bar\partial S}{\partial r}=\frac{\partial S}{\partial r}-\frac{n_r}{n_\theta}\frac{\partial S}{r\partial\theta}=0\\
&\frac{\bar\partial S}{\partial z}=\frac{\partial S}{\partial z}-\frac{n_z}{n_\theta}\frac{\partial S}{r\partial\theta}=0
\end{aligned}
\right\}\qquad (31)
$$

then r, z, S/m are three independent variables in non-orthogonal curvilinear coordinates built on the S_2-streamsurface. Define the sets of vectors $\vec{R}$, $\vec{Z}$, $\vec{\mathrm{H}}$ and $\mathbf{r}$, $\mathbf{z}$, $\mathbf{n}$, which are called reciprocal vectors

$$
\left.
\begin{aligned}
&\vec{R}=\mathbf{r}-\frac{n_r}{n_\theta}\vec{\theta}\\
&\vec{Z}=\mathbf{z}-\frac{n_z}{n_\theta}\vec{\theta}\\
&\vec{\mathrm{H}}=\frac{1}{n_\theta}\vec{\theta}
\end{aligned}
\right\}\qquad (32)
$$

The sets of reciprocal vectors have the following properties:

$$
\left.
\begin{aligned}
&\mathbf{r}\cdot\vec{R}=\mathbf{z}\cdot\vec{Z}=\vec{\mathrm{H}}\cdot\mathbf{n}=1\\
&\vec{R}\cdot\mathbf{z}=\vec{R}\cdot\mathbf{n}=\vec{Z}\cdot\mathbf{r}=\vec{Z}\cdot\mathbf{n}=\vec{\mathrm{H}}\cdot\mathbf{r}=\vec{\mathrm{H}}\cdot\mathbf{z}=0\\
&\vec{R}=\frac{\mathbf{z}\times\mathbf{n}}{\mathbf{r}\cdot\mathbf{z}\times\mathbf{n}};\vec{Z}=\frac{\mathbf{n}\times\mathbf{r}}{\mathbf{r}\cdot\mathbf{z}\times\mathbf{n}};\vec{\mathrm{H}}=\frac{\mathbf{r}\times\mathbf{z}}{\mathbf{r}\cdot\mathbf{z}\times\mathbf{n}}\\
&\mathbf{r}=\frac{\vec{Z}\times\vec{\mathrm{H}}}{\vec{R}\cdot\vec{Z}\times\vec{\mathrm{H}}};z=\frac{\vec{\mathrm{H}}\times\vec{R}}{\vec{R}\cdot\vec{Z}\times\vec{\mathrm{H}}};n=\frac{\vec{R}\times\vec{Z}}{\vec{R}\cdot\vec{Z}\times\vec{\mathrm{H}}}\\
&\mathbf{r}\cdot\mathbf{z}\times\mathbf{n}=-n_\theta;\ \vec{R}\cdot\vec{Z}\times\vec{\mathrm{H}}=\frac{-1}{n_\theta}
\end{aligned}
\right\}\qquad (33)
$$

We can find from (33) that vectors $\mathbf{R}$ and $\mathbf{Z}$ lie on the S_2-stream surface. Define a vector field $\vec{C}$ which is expressed in terms of reciprocal vectors as

$$
\left.
\begin{aligned}
\mathbf{C}&=C_r\mathbf{R}+C_z\mathbf{Z}+C_n\vec{\mathrm{H}}\\
&=C^r\vec{r}+C^z\vec{z}+C^n\vec{n}
\end{aligned}
\right\}\qquad (34)
$$

The divergence of $\mathbf{C}$ can be expressed in nonorthogonal curvilinear coordinates as

$$\nabla \cdot \mathbf{C} = n_\theta \left[\frac{\partial \bar{C}_r / n_\theta}{\partial r} + \frac{\partial \bar{C}_z / n_\theta}{\partial z} + \frac{\partial C_n / n_\theta}{\partial S/m} \right] \tag{35}$$

The curl of $\mathbf{C}$ can be expressed in nonorthogonal curvilinear coordinates as

$$\left.\begin{aligned} \nabla \times \mathbf{C} = \frac{-1}{n_\theta} \left[\left(\frac{\partial C_n}{\partial z} - \mathbf{n} \cdot \nabla C_z \right) \bar{r} + \left(\mathbf{n} \cdot \nabla C_r - \frac{\partial C_n}{\partial r} \right) \mathbf{z} \right. \\ \left. + \left(\frac{\partial C_z}{\partial r} - \frac{\partial C_r}{\partial z} \right) \mathbf{n} \right] = n_\theta \left[\left(\frac{\partial \bar{C}^n}{\partial z} - \frac{\partial C^z}{\partial S/m} \right) \mathbf{R} \right. \\ \left. + \left(\frac{\partial C^r}{\partial S/m} - \frac{\partial \bar{C}^n}{\partial r} \right) \mathbf{Z} + \left(\frac{\partial \bar{C}^z}{\partial r} - \frac{\partial \bar{C}^r}{\partial z} \right) \vec{\mathrm{H}} \right] \end{aligned}\right\} \tag{36}$$

It can be seen that $\mathbf{n} \cdot \nabla q = 0$ if only the flow in the S_2-streamsurface is considered and $\mathbf{n} \cdot \mathbf{W} = 0$ is applied.

An Inverse Time Marching Method for the Definition of Cascade Geometry

G. Meauzé
Office National d'Etudes et de Recherches Aerospatiales (ONERA), Chatillon, France

The article describes a so-called "inverse mode" calculation method, providing the geometry of a cascade corresponding to a given velocity distribution, and gives some examples of application. The velocity distribution may be assigned over the whole of the suction and pressure sides or over only a part of them, the remaining parts being already known. The closure condition of the profile is ensured by an iterative process on the solidity of the cascade. A second version allows the definition of the geometry of a profile with a given thickness evolution law and as assigned velocity distribution on the suction side. The method makes use of a pseudo-unsteady calculation, enabling one to treat the case of flows with shock waves in a two-dimensional stream with possible variations of cross section. This flexibility of use confers to the method a wide field of application, covering all possible configurations of flow in turbine and compressor cascades.

1 Introduction

1.1 Purpose of the Study. Improvement of the aerodynamic performance of turbomachines involves the mastering of the velocity distributions over the blading walls.

It is well known that it is the importance of the viscous zones and the intensity of the shock waves that condition the efficiency of a stage of compressor or turbine: the boundary layers developing along a wall have a strong tendency to thicken, even to separate, as soon as the flow is slowed down, particularly under the effect of a shock wave. If then we want to improve the blading performance, it is necessary to look for the wall geometric shape implying a velocity distribution minimizing shock wave intensities and viscous effects.

Such a research can be carried out iteratively by modification of the wall and successive direct calculations; but this process is long and does not always lead to the expected result, although the problem still remains of the existence of a better profile.

It is, on the other hand, much more fruitful to use an inverse method in which we start from a pressure distribution, given on both the suction and pressure sides so as to minimize the importance of the boundary layers, the blade geometry resulting from the calculations. It should however be noted that this geometry may not correspond to a realistic configuration: too thin profile, or even negative thicknesses or not meeting the technological requirements as regards size; but in this case it will be proved that the expected velocity distribution is impossible to obtain.

We shall then use a semi-inverse solution, which determines the geometry of a blading with a given thickness evolution law and a pressure distribution assigned only on the suction side.

It is for these various reasons that ONERA developed an inverse calculation method as general as possible, taking account in particular of the presence of shock waves.

The principle of this method, and a few examples of application, are the object of this paper.

1.2 Previous Studies. Various types of inverse methods have been published by several authors. These methods, valid in insentropic flow, have resulted in very tangible progress, especially in the design of compressor and turbine blades. The main ones are very briefly described in the forthcoming.

- Hodographic methods [1], where the evolution of the velocity module V is assigned as a function of the direction θ of the velocity vector, are perfectly convenient for the cases where viscous effects do not a priori constitute a problem (as for instance for turbine blades); on the other hand, they apply less well when we try to avoid separation problems, as in compressors and air intakes, as, in this case, it is the evolution of the velocity V along the curvilinear abscissa s that determines the boundary layer.
- Inverse methods where $V(s)$ is assigned [2–7], very often used for the design of turbomachine blade profiles, are only applicable to subsonic or just transonic flows, remaining isentropic and strictly two dimensional.
- Using the method of characteristics does not raise any basic problem for the determination of a streamline corresponding to a given pressure evolution, but it naturally only applies to supersonic flows.

2 Principle of the Method

To avoid this limitation to either entirely subsonic or en-

Contributed by the Gas Turbine Division and presented at the International Gas Turbine Conference and Products Show, Houston, Texas, March 9-12, 1981, of THE AMERICAN SOCIETY OF MECHANICAL ENGINEERS. Manuscript received at ASME Headquarters, September 19, 1980; revised manuscript received December 18, 1980. Paper No. 81-GT-167.

tirely supersonic flows, and above all to take into account the entropy variation through shocks, it is mandatory to call upon a method solving the Euler equations.

To this day, in view of the mixed-elliptic and hyperbolic character of the Euler equation in steady state regime, the problem has only been solved in practice through the use of methods of unsteady type. The introduction of some time derivatives [8, 9, 10] into the system of equations constitutes an expedient for solving it numerically without difficulties of a fundamental nature; the calculation is carried out iteratively, and the solution of the steady-state flow looked for is considered as being the asymptotic state of an unsteady motion.

Thus, it is not necessary for the intermediate states to have a physical meaning, which makes it possible to retain only part of the unsteady terms to reach the final solution as fast as possible.

Viviand and Veuillot [11] applied themselves for several years to developing and perfecting these methods at ONERA. Reference [11] constitutes a detailed review of these works; the principle of the calculation presented here is directly derived from it and constitutes only one of its applications; before describing its peculiarities, let us recall the broad lines of the method.

The study of the mathematical properties of the system of unsteady equations used leads to the determination of the characteristics cone and to the establishment of a stability criterion for the explicit numerical schemes.

From the predictor-corrector scheme of MacCormack, various discretization techniques of the equations in arbitrary curvilinear mesh pattern may be used. A new technique of direct discretization in the phsycial plane into an arbitrary mesh pattern makes it possible to do away with a coordinate transformation. A general method for treating the boundary conditions, based on the use of compatibility relation, improves the precision of the calculation.

Essentially there are two calculation methods: the first one, which involves the assumption of a uniform total enthalpy, allows the calculation of rotational, nonisentropic flows that may include strong shocks; the second, which assumes as well that entropy is uniform, applies only to potential flows but allows, within the validity domain of this approximation, the treatment of weak shocks.

Only the first method, where the stagnation enthalpy is considered as constant, will be retained here because of the existence of strong shocks in most of the applications presented.

The principle of the inverse method is briefly outlined in the last section of reference [11], which describes the calculation of a jet issued from a supersonic nozzle exhauting into an isobaric enclosure. The streamline is obtained by integration of the slopes at the boundary.

The originality of the work presented here consists in the extension to the general case where an evolving pressure law is given, and its application to the determination of the walls of a duct or to the profile of a blade cascade.

Let us recall that, for a fixed observer in the physical plane, the Euler equations may be written in the form:

$$\frac{\partial f}{\partial t}+\frac{\partial F}{\partial x}+\frac{\partial G}{\partial y}+f\cdot\frac{u}{h}\frac{dh}{dx}=0$$

where f, F, G are single-column, three-component matrixes:

$$f=\begin{pmatrix}\rho\\ \rho u\\ \rho\vartheta\end{pmatrix}\quad F=\begin{pmatrix}\rho u\\ p+\rho u^2\\ \rho u\vartheta\end{pmatrix}\quad G=\begin{pmatrix}\rho\vartheta\\ \rho u\vartheta\\ p+\rho\vartheta^2\end{pmatrix}$$

ρ being the density and p the pressure; u and ϑ are the velocity components along x and y; h is the transverse thickness, depending weakly on x only and assumed known. For a strictly two-dimensional flow, h is constant.

If the mesh points are mobile and if w represents the displacement rate field of these points, these equations become:

$$\frac{\partial f}{\partial \tau}-(w\ \text{grad})f+\frac{\partial F}{\partial x}+\frac{\partial G}{\partial y}+f\frac{u}{h}\frac{dh}{dx}=0$$

where $\partial f/\partial\tau=0$ means that the quantity f is steady for an observer linked to the point of the mobile mesh pattern.

Before starting the calculation, it is necessary to define an initial mesh pattern and to properly initialize the flow field. Then the calculation runs as follows:

Before each iteration, we determine the pressure at every point at the pattern boundary where we intend to assign the pressure law chosen as a function of an abscissa x or of a curvilinear abscissa. We then apply the numerical scheme, and then again the boundary conditions defined later.

On the boundaries where pressure is assigned, the streamline is determined by integration of the local slopes of the velocity. It is then necessary to define a new mesh pattern whose boundaries are the new streamlines. This process is iteratively pursued until convergence, i.e., in practice, until the displacements of the mesh points between two successive iterations become negligible.

The number of necessary iterations varies according to the shape of the duct, but is usually between 600 and 1000.

Let us note that the relations used in the treatment of the boundary conditions are strictly valid only in the case of a fixed mesh pattern. The use made of them here is thus not rigorous; however, when the asymptotic state is reached and, consequently, the mesh pattern is frozen, this incoherence disappears.

In the same way, experience shows that it is quite possible to neglect the displacement rate of the mesh pattern.

3 General Scheme – Boundary Conditions

Before approaching the case of a blade cascade, let us consider that of a duct.

3.1 Case of a Duct. In a general way, we try to define the geometry of a duct displaying on its walls a given pressure distribution.

Figure 1 presents the general sketch of such a configuration. The upper, AC, and lower, BD, walls of this duct might include a first part, AE and BF, whose geometry is known, the given pressure distribution being only applied downstream of E and F. The lines EC and FD being a priori undetermined, their initial position may be arbitrarily chosen, as will be seen later on examples.

On the upstream boundary AB, two cases should be considered:

(*i*) If, on AB, the velocity component normal to AB is supersonic, it is necessary to assign, at every point:

– the entropy or, in practice, the stagnation pressure P_t as the stagnation enthalpy H_t is constant;

– the Mach number or, in practice, the density;

– the flow direction θ.

(*ii*) If, on the contrary, the velocity, component is subsonic, we only have to assign the entropy (or P_t) and either the Mach number (or ρ), or the direction θ.

On the downstream boundary CD, no data is assigned if the velocity component is supersonic. But if it is subsonic, a static pressure distribution, possibly constant, compatible with pressure data in C and D, is assigned, and the direction $\theta_2(y)$ will result.

On the AE and BF elements we apply a slip condition, i.e. we treat the direct problem as the geometry is known. On the

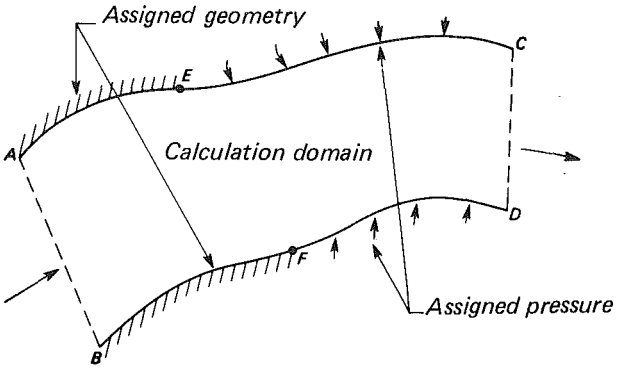

Fig. 1 General scheme of the calculated duct

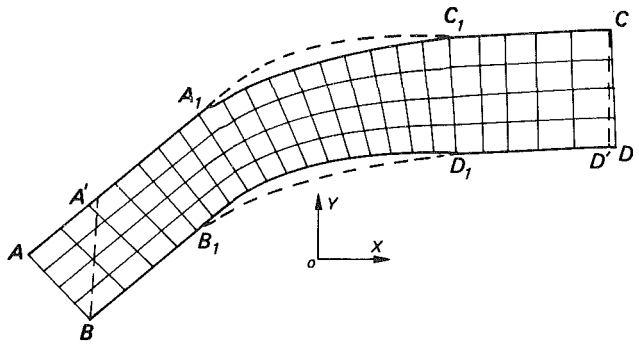

Fig. 2 Quasi-orthogonal mesh pattern

EC and FD elements, we treat the inverse problem by assigning the pressure distribution.

Remarks

1 Point E may be the same as A or C, and F the same as B or D, which means that the upper and lower walls can be integrally treated either in the direct or in the inverse mode.

2 Obviously, it is necessary that the assigned pressure distributions correspond to a physical reality. In particular, several cases may occur at the joining points E or F:

If the local flow is supersonic, the assigned pressure downstream of the point may present a discontinuity relative to that which would result from the calculation upstream of this point; the wall will then present a slope discontinuity corresponding either to the shock or to the expansion;

On the other hand, if the local flow is subsonic a too great variation will entail a divergence in the calculation; to avoid this drawback, it is possible to modify locally the assigned pressure distribution so that it takes the value calculated just upstream of the joining point.

Several examples of application of inverse calculation for determining the shape of a duct with assigned pressure distributions along its walls are given in reference 12.

3.2 Case of a Cascade. Before approaching the case of a cascade in inverse mode, we should first recall the general scheme and the boundary conditions assigned in direct mode.

Let us consider the sketch of Fig. 2, which represents a quasi orthogonal mesh pattern. This type of pattern is mandatory if we want to limit computing times, as it is well known that the value of the time steps between each iteration depends on the mesh pattern shape, this value being maximum when the mesh is rectangular. On the other hand, the adoption of quasi orthogonal patterns presents some difficulties and requires some precautions when compared to patterns whose columns are parallel to the cascade front.

The upstream and downstream boundaries AB and CD are chosen so as to represent practically the upstream and downstream infinities. On the upstream boundary, if the absolute velocity of the flow is subsonic, we preferably fix the flow direction; it is the case of cascades of transonic compressor or of turbine, whether the flow is chocked or not. But if the upstream velocity is supersonic with a subsonic component normal to the cascade front, it is the Mach number that is assigned, the flow incidence resulting from the application of the unique incidence [13].

Practically, in the particular case of cascades where the downstream boundary is subsonic, we fix a uniform pressure p.

The slip condition is assigned on the internal walls A_1C_1 and B_1D_1 of the blade-to-blade channel. If the flow in the trailing edge region is subsonic, a complementary condition expressing the Kutta-Jukowski condition is necessary: we

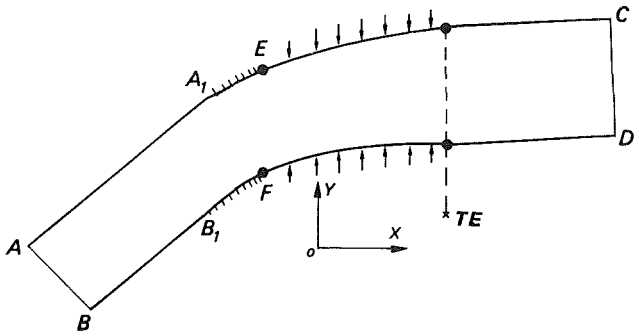

Fig. 3 Inverse mode calculation of a cascade – calculation domain

shall for instance assign the flow direction at the points of the mesh pattern just behind the trailing edge.

On the $A'A_1$, BB_1 boundaries upstream of the cascade, and C_1C, D_1D' downstream of it (which are geometrically identical and spaced by one cascade pitch), we assign a condition of periodicity, i.e., of equality of aerodynamic parameters parallel to the cascade front.

But, as the mesh points are not homologous, an appropriate interpolation process is necessary; moreover, the upstream and downstream boundaries comprise two elements AB, AA′ and CD, DD′. On each portion, it is necessary to apply boundary conditions according to the subsonic or supersonic value of the velocity component normal to the boundary element considered.

We shall now study the determination of a cascade in inverse mode.

Let us consider the case of Fig. 3, where we define the points A_1B_1 on the cascade front, distant by the cascade pitch s, assumed known. Upstream, we define the boundaries AA_1 and BB_1, where the boundary conditions to be assigned have already been examined in the case of direct mode calculation.

We assume known the geometry of a part A_1E (possibly nil) of the pressure side, and B_1F of the suction side. We then define the pressure distributions on the suction and pressure sides known to an abscissa X_{TE} of the supposed trailing edge, the two pressures being identical just behind this point.

It is then necessary to apply the periodicity condition downstream of X_{TE}, as well as a boundary condition on the downstream boundaries CD and D′D, but there usually appear the two following difficulties:

(i) The downstream pressure p_2 should be such that, account being taken of the pressure distribution chosen on the pressure and suction sides of the profile, the flow satisfies the periodicity condition of a cascade. But, as has been shown in [12], this pressure p_2, which should respect the general theorems of flowrate and momentum conservation along the

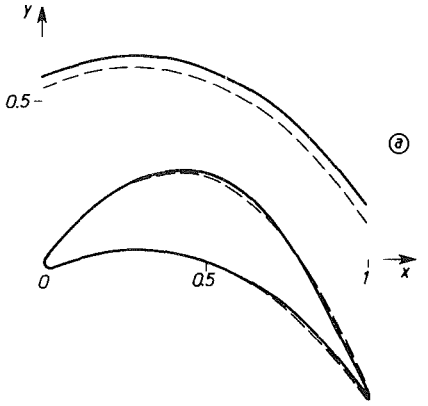

Fig. 4(a) Cascade geometry — — — initial blade
——— final blade

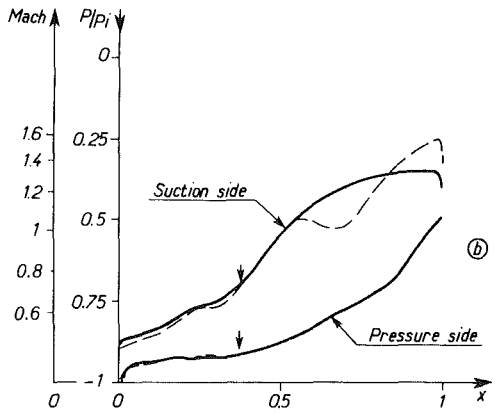

Fig. 4(b) Pressure distribution — — — initial blade (direction calculation)
——— assigned for inverse calculation

Fig. 4 Definition of a turbine blade and the cascade pitch, for pressure distributions assigned on the pressure and suction sides

cascade front, cannot be determined a priori in the case of a nonisentropic flow.

It is then necessary to replace the pressure condition on the downstream boundary by a particular condition, called "nonreflexion" condition according to Veuillot. This condition consists in the extension to the two-dimensional case of the method where, in the one-dimensional case, one assigns a value for the Riemann invariant associated with the unsteady characteristic included in the range of calculation.

(*ii*) There is a priori no reason for the streamlines issued from E and F to be distant by the cascade pitch at abscissa X_{TE} or, in other words, for the profile to be closed at the trailing edge. Indeed, there exists a single value of the solidity corresponding to a closed profile. And this value cannot be predetermined in the case of non-isentropic flow.

Thus, obtaining a closed profile requires the use of a particular procedure. This will be determined, according to the case, from one of the following principles:

(*a*) In case the cascade pitch is not assigned, the pitch variation can be made during the iterations of the pseudo-unsteady calculation, provided some precautions, so as to end up in the calculation with a blade having a given trailing edge thickness.

(*b*) If the solidity is assigned, it will be necessary to perform several calculations with successive alterations of the assigned pressure distributions, until a satisfactory solution is reached. But this process, which requires several calculations, could with advantage be replaced by the following original solution:

(*c*) Whatever the process used for ensuring the profile closure at the trailing edge, either by pitch variation or by alteration of assigned pressure distributions when the pitch is predetermined, the shape obtained may not be realizable, the thickness being either too large or too small, or even negative.

Obtaining realistic profiles requires in that case several calculations, with successive alterations of assigned pressure distributions. This reduces the advantage of the inverse method relative to the process used when we have only direct methods at our disposal, viz., a large number of calculations of profiles whose geometry is successively modified to obtain a given pressure distribution.

But it appears that in most applications one is mainly interested in the pressure distribution over the suction side, which is the most critical as regards the boundary layer, for compressors as well as turbine. This distribution is usually determined so as to minimize the losses due to viscous effects. It is particularly endeavored to reduce overvelocities and avoid separation.

As regards velocity distributions over the pressure side, they usually present no particular risk.

For these various reasons, a new solution is proposed: input data on the thickness evolution law of the profile looked for replace the input data on the velocity distribution chosen for the pressure side, which will then result from the calculation. We thus directly obtain a profile corresponding to a given velocity distribution over the suction side and having the mechanical characteristics wished.

We shall note that, the profile being automatically closed, the cascade solidity may be chosen in advance.

On the other hand, if it is desired to assign a complementary condition, such as downstream angle, or if the pressure distribution obtained on the pressure side has such a shape as presenting risks of flow separation, it will be necessary to adjust the solidity by an iterative process.

4 Examples of Application

4.1 – Determination of a turbine blading with given pressure distributions on the pressure and suction sides, the solidity not being fixed.

The following example shows how it is possible to modify the geometry of the section of a turbine with high expansion ratio, with a view to improve the flow though the cascade.

Let us consider the cascade whose profile is represented by the broken line in Fig. 4(*a*); the pressure side of the upper blade is traced so as to show the blade-to-blade channel. The flow through this cascade is not satisfactory, as shown by the results of a direct calculation previously performed. The pressure distributions calculated for the pressure and suction sides are presented as broken lines on Fig. 4(*b*). It will be noted that, on the suction side, the pressure evolution presents a "bump" soon after the middle of the blade; also, the overvelocity before the trailing edge is rather high.

It was decided to look for a profile shape and a cascade pitch corresponding to the solid line traced on figure 4b, where the bump has been eliminated and the overvelocity reduced, while retaining the same pressure distribution on the pressure side. The arrows indicate the points from which the pressures are assigned; upstream of these arrows, the initial geometry of the blade has been retained. The blade shape obtained after convergence of the calculation is traced as a

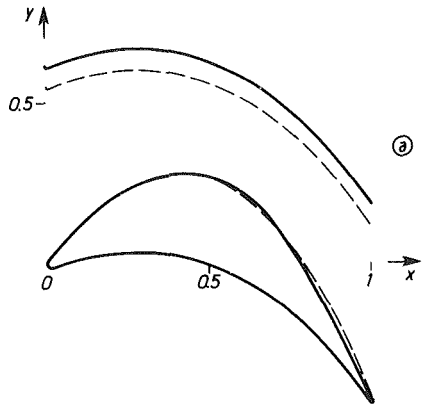

Fig. 5(a) Cascade geometry — — — initial blade
——— final blade

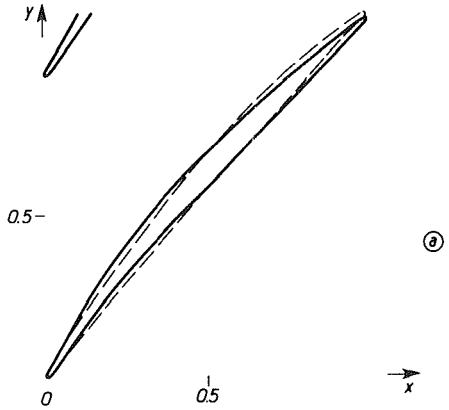

Fig. 6(a) Cascade geometry — — — initial blade
——— final blade

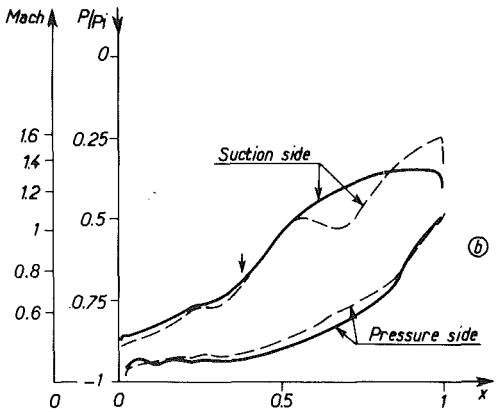

Fig. 5(b) Pressure distribution — — — initial blade (direct calculation)
——— assigned for inverse calculation

Fig. 5 Definition of a turbine blade and the cascade pitch, for a given pressure side and an assigned pressure distribution on the suction side

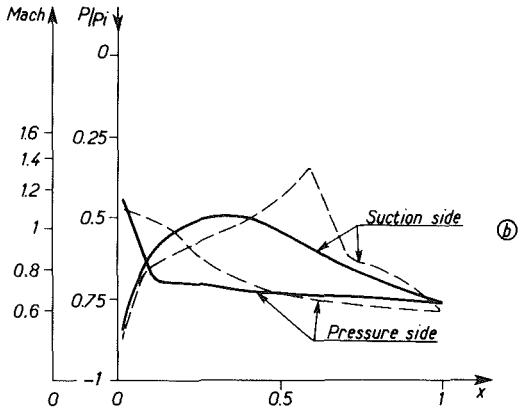

Fig. 6(b) Pressure distribution — — — initial blade (direct calculation)
——— assigned for inverse calculation

Fig. 6 Definition of a transonic compressor blade having a given thickness evolution law, with pressure distribution assigned on the suction side

solid line on Fig. 4(*a*); the tracing of the pressure side of the upper blade shows the new pitch obtained.

Figure 5 shows a second example, from the same initial cascade. But in this case we look for the shape of a cascade where the pressure distribution on the suction side is the same as that assigned in the first case, while retaining the geometry of the initial blade pressure side, instead of the pressure distribution on it.

The result obtained is presented as a solid line on Fig. 5. It will be noted that the pressure distribution, a priori unknown, on the pressure side of the new blade is naturally different from the initial one, and also that the pitch of the new cascade is slightly wider.

4.2 Determination of a Compressor Cascade with a Given Pressure Distribution on the Suction Side and a Given Thickness Evolution Law. The third example concerns a section of mobile transonic row in chocked regime.

Let us consider a blade of conventional shape, whose pressure and suction side are arcs of circle connected by rounded parts at the leading and trailing edges. The profile of that blade is represented by broken lines on Fig. 6(*a*).

The direct calculation of the flow over this profile has been performed in two-dimensional conditions, for an upstream flow angle $\theta = 52.5$ deg and such a downstream pressure that the flow is choked, but with a moderate supersonic zone. The resulting upstream Mach number is 0.73. The pressure distributions resulting from this calculation are traced on Fig. 6(*b*) (broken lines). It will be noted that the pressure evolution on the suction side is irregular, and even reveals the presence of a shock, while its shape on the pressure side is monotonous.

We then looked for the shape of a blade having the same thickness as the original blade, but providing on the suction side the pressure distribution traced as a solid line on Fig. 6(*b*). The profile obtained after convergence of the calculation is traced as a solid line on Fig. 6(*a*). The pressure distribution on the pressure side, a priori unknown, is a calculation result (Fig. 6(*b*)), as well as the pressure and angle of the downstream flow.

The fourth example concerns a section of supersonic mobile row, with an upstream Mach number of 1.2. The initial blade (in broken line, Fig. 7(*a*)) is here again made of arcs of circle. The pressure distribution on the suction side shows that the flow is constantly accelerated, and the final straight shock occurs at a Mach number of 1.6.

We looked for the shape of a blade having the same thickness evolution law, but presenting on the suction side a

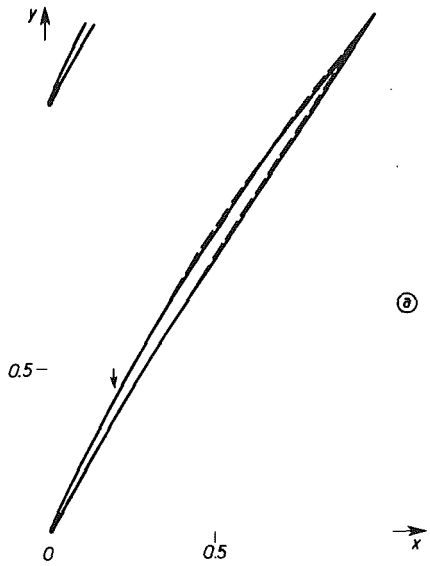

Fig. 7(*a*) Cascade geometry — — — initial blade
——— final blade

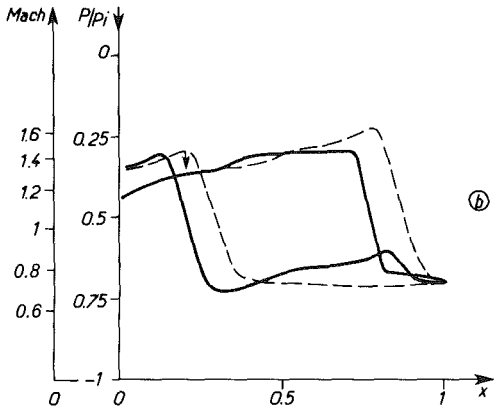

Fig. 7(*b*) Pressure distribution — — — initial blade (direction calculation)
——— assigned for inverse calculation

Fig. 7 Definition of a section of supersonic compressor

flat part at Mach 1.45, as shown by the solid line on Fig. 7(*b*). The result after convergence is traced on figure 7a, as a solid line. We shall remark the very slight difference between the final and initial blades.

The pressure distribution on the pressure side of the new blade (Fig. 7(*b*)) presents an irregular shape, especially in the trailing edge region; this is due to the evolutions of the pressure side curvature in this rear part of the blade, which necessarily follow those of the suction side as the thicknesses are assigned.

This defect may however be easily corrected by a local alteration of the pressure side geometry; but this obviously entails modification of the thickness law. This modification, which concerns only the rear part of the pressure side, has however only a small effect on the flow through the duct; this makes it possible to obtain a satisfactory solution without iterations.

As an example, figure 8 shows the result obtained by a direct calculation on the blade obtained previously, with a

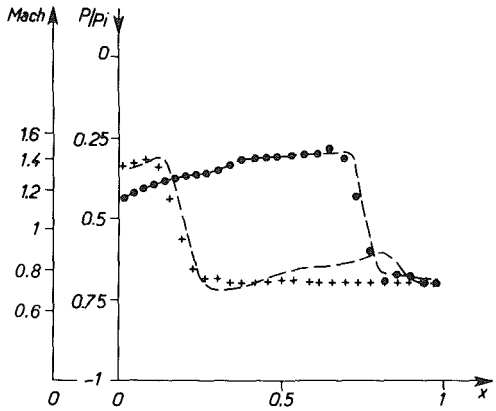

Fig. 8 Direct calculation performed, after smoothing of the pressure side, on the blade obtained by an inverse method
Pressure distribution — — — inverse calculation
• suction side
+ pressure side Direct calculation

simple smoothing of the profile on the pressure side. The pressure distribution on the pressure side is now regular, and on the suction side it perfectly fits the given pressure distribution.

It is useful to mention that the pitch variation during iterations leads to an important increase of the number of iterations necessary to obtain a satisfactory convergence.

As an example, the first two cases presented above required about 2500 iterations each, while for the two other cases, where there is no pitch variation, convergence was reached after 800 iterations. Let us remark that the direct calculation requires 1200 iterations.

In a general way, the pursuit of iterations after a seemingly satisfactory convergence brings to light an oscillation in time of the residuals, whose effect remains negligible on the geometry obtained.

Lastly, it should be noted that if the initial configuration is too far from the final solution the calculation might diverge; but in this case divergence appears rather soon, and never after more than 400 iterations.

5 Conclusions

We presented several cases of application for the definition of transonic and supersonic cascades by the semi-inverse, pseudo-unsteady calculation method developed at ONERA. There exist two versions of the calculation:

- The first provides the definition of a blade profile with pressure distributions, along a straight or curvilinear abscissa, assigned in part or in full on the suction and pressure sides of the profile, the solidity being a calculation result as well as the downstream angle
- The second provides the definition of a blade profile with a given thickness evolution law and a pressure distribution assigned only on the suction side, the solidity being then given, while downstream pressure and angle result from the calculation

References

1 Legendre, R., "Calcul d'un profil pour ailette de turbine à partir d'un hodographe," *Rech. Aéron.*, No. 84, 1961.

2 Stanitz, J.D., "Design of Two-Dimensional Channels with Prescribed Velocity Distributions Along the Channel Walls," NACA Tech. Notes 2593/2595.

3 Stanitz, J.D., and Sheldrake, L.J., "Application of a Channel Design Method to High—Solidity Cascades and Tests of an Impulse Cascade with 90 deg of Turning," NACA Tech. Note 2652.

4 Karadimas, G.,, "Definition des profils d'aubages de turbomachine par une methode analytique"—3ème Symposium Franco-Soviétique, Paris, December, 1-4, 1969.

5 Legendre, R., "Calcul d'un profil ou d'une grille de profils pour une distribution de vitesse donnée en fonction du potentiel," *Rech. Aérosp.*, No. 1972-4, pp. 231-232.

6 Lecomte, C., "Calculation of cascade profiles from the velocity distribution," ASME Paper No. 74-GT-70.

7 Le Foll, J., "Inverse Method for Optimized Blading Calculations—Transonic Flows in Axial Turbomachinery," VKI Lecture Series 84, February 2-6, 1976.

8 Magnus, R., and Yoshihara, H., "Steady Inviscid Transonic Flow Over Planar Airfoils—A Search for Simplified Procedure," NASA CR 2 186, 1972.

9 Magnus, R., and Yoshihara, H., "Inviscid Transonic Flow Over Airfoils," *AIAA Journal*, Vol. 8, No. 2, 1970, pp. 2157-2162.

10 Gopalakrishnam, S., "Fundamentals of Time Marching Methods," VKI L.S. 59, 1973.

11 Viviand, H., and Veuillot, J.P., "Méthodes Pseudo-instationnaires pour le calcul d'écoulements transsoniques," Publication ONERA No. 1978-4, English transl., ESA TT 549.

12 Meauzé, G., "Méthode de calcul aérodynamique inverse pseudo-instationnaire," *La Rech. Aerosp.* No. 1980-1, English translation, ESA TT 651, pp. 23-30.

13 Aerodynamics of cascades—AGARDograph No. 220.

A. Comte

Engineer,
Etudes et Recherches,
Electricité de France

G. Ohayon

Engineer,
Sté Metraflu, France

K. D. Papailiou

Professor,
Chair of Thermal Turbomachines,
National Technical University
of Athens, Greece

A Method for the Calculation of the Wall Layers Inside the Passage of a Compressor Cascade With and Without Tip Clearance

A method is presented for calculating the wall shear layers of a compressor cascade. The integrated across the blade spacing Navier-Stokes equations are used. Closure is obtained using an integral equation of the boundary layer type and the secondary vorticity generation equation. The calculation is performed inside the passage and a dialogue is established between the longitudinal velocity profile, associated with the primary vorticity (generated and diffused) and the transverse profile, associated with the secondary vorticity, which is generated by the primary one. A unique feature of the method is that it takes into account the velocities induced by the secondary vorticity in the "free stream" flow (the problem is elliptic in the transverse direction). The influence of the tip clearance vortex is included in the method and comparisons with experimental results for two heavily loaded cascades with and without tip clearance show good agreement.

Introduction

The lateral cascade wall shear layer calculation problem has traditionally followed two approaches. The first one, which attempts to predict the losses, emphasizes viscous effects, while the second, treating the flow as inviscid, aims at the prediction of the velocity field associated with the secondary vorticity and thus the cascade exit flow angle variation. Excluding early attempts as well as correlations, we can cite Railly's [1] work as the first important effort in the direction of the first approach. He developed the integral equations corresponding to the circumferentially averaged turbulent Navier-Stokes equations. Here, we shall be concerned only with methods that have followed this general approach.

Concerning the second approach, the work of Squire and Winter [2], has been followed by numerous publications. We shall limit ourselves by citing Hawthorne, Smith, Horlock, Lakshminarayana and Marsh (references [3-10]).

These two approaches have gradually evolved, and towards the end of the sixties, one may find theories treating the two aspects simultaneously (references [12, 13, 21]). We shall write down first the basic equations underlying this work.

The Basic Equations

The basic equations used in the present work are the following:

1 The Integral Momentum Equations. They are derived from the circumferentially averaged turbulent Navier-Stokes equations. The derivation can be found in the work of Railly [1], Horlock (for example, reference [12]) or Mellor and Wood [13]. In the case of a plane cascade, they take the form:

$$\frac{1}{s(x)}\frac{d}{dx}[s(x)\,\tilde{u}_e{}^2(\delta_x^* + \vartheta_{xx})] = DX_1 - DX_2 - DX_3 - \tilde{u}_e\frac{d}{dx}(\tilde{u}_e\delta_x^*) + \frac{\tau_{wx}}{\rho} \tag{1}$$

$$\frac{1}{s(x)}\frac{d}{dx}[s(x)\,\tilde{u}_e{}^2(\tan\beta_e\delta_x^* + \vartheta_{zx})] = DZ_1 - DZ_2 + \frac{\tau_{wx}}{\rho} \tag{2}$$

The definition of the various quantities is given in the list of symbols. These equations differ from the usual integral boundary layer equations in the terms DX_1, DX_2, DZ_1, DZ_2 which are additional unknowns. We shall call them the additional terms, their appearence being related directly to the loss of information which occurred during the circumferentially performed integration. They are defined as follows:

(*a*) *Defect Force Terms*

$$s(x)\,DX_1 = \int_o^h \frac{s(x)}{\rho}(f_{x_e} - f_x)\,dy \tag{3}$$

$$s/x \times DZ_1 = \int_o^h \frac{s(x)}{\rho}(f_{z_e} - f_z)\,dy \tag{4}$$

They express the variation of the blade force inside the

Contributed by the Gas Turbine Division and presented at the International Gas Turbine Conference and Products Show, Houston, Texas, March 9-12, 1981, of The American Society of Mechanical Engineers. Manuscript received at ASME Headquarters, December 18, 1980. Paper No. 81-GT-168.

viscous layer in the direction normal to the lateral walls of the cascade.

In the foregoing equations the blade forces are given by the expressions:

$$f_z = p_p - p_s \tag{4a}$$

$$f_x = -(p_p - p_s)\tan\bar{\beta}'$$

(*b*) *Fluctuation Terms*

$$s(x)DX_2 = \int_o^h \frac{\partial}{\partial x}[s(x)(\overline{u_e'^2} - \overline{u'^2})]dy \tag{5}$$

$$s(x)DZ_2 = \int_o^h \frac{\partial}{\partial x}[s(x)(\overline{u_e' w_e'} - \overline{u' w'})]dy \tag{6}$$

They express the change inside the wall viscous layer of the variations of each velocity component in the circumferential direction.

(*c*) *Pressure Term*

$$s(x)DX_3 = \int_o^h \frac{\partial}{\partial x}\left[\frac{s(x)}{\rho}(\bar{p}_e - \bar{p})\right]dy \tag{7}$$

It expresses the change inside the viscous layer of the axial static pressure gradient.

The wall shear stress terms τ_{w_x} and τ_{w_z} are defined by the equations:

$$s(x)\tau_{w_x} = -\frac{d}{dx}\left[\int_o^h s(x)\bar{\tau}_{xx}dy\right] + s(x)\bar{\tau}_{yx_w} \tag{8}$$

$$s(x)\tau_{w_z} = -\frac{d}{dx}\left[\int_o^h s(x)\bar{\tau}_{xz}dy\right] + s(x)\bar{\tau}_{yz_w} \tag{9}$$

2 The Entrainment Equation of Head (12). It is a mass conservation equation for the flow inside the boundary layer. Here it is used in its circumferentially averaged form, which reads

$$\frac{1}{s(x)}\frac{d}{dx}[s(x)\bar{V}_{s_e}(H_e\vartheta_{ss} + \tan\bar{\beta}_e\delta_n^*)] = \frac{\bar{V}_{s_e}}{\cos\bar{\beta}_e}E + \frac{\bar{V}_{s_e}\delta_n^*}{\cos^2\bar{\beta}_e} \tag{10}$$

with the entrainment function E defined as

$$E = \frac{1}{\bar{V}_{s_e}}\left(\bar{V}_{s_\delta}\frac{\partial\delta}{\partial s} + \bar{V}_{n_\delta}\frac{\partial\delta}{\partial n} - \bar{V}_{y_\delta}\right) = \frac{1}{\bar{V}_{s_e}}\left(\bar{u}_\delta\frac{\partial\delta}{\partial x} - \bar{V}_\delta\right) \tag{11}$$

This form was derived by following a similar approach as in deriving equations (1) and (2). All fluctuation terms have been neglected.

3 The Secondary Vorticity Equation. The expression used here is the one developed by Squire and Winter (2). It is taken to be valid for the circumferentially averaged flow

$$d\left(\frac{\bar{\xi}_s}{\bar{V}_{s_e}}\right) = -2\frac{\bar{\xi}_n}{\bar{V}_{s_e}}d\bar{\beta}_e \tag{12}$$

Preliminary Discussion

Our experience with integral methods (14), (15) indicates that one auxiliary equation is sufficient for the prediction of the velocity profile form factor variation. Head's equation is used for that purpose, as, for reasons analysed in reference (13), the energy equation cannot be used. Head's equation

Nomenclature

a = radius of the vortex core
c = blade chord
DX_1, DZ_1 = defect force terms (equations (3), (4))
DX_2, DZ_2 = fluctuation terms (equations (5), (6))
DX_3 = pressure term (equation (7))
E = entrainment function (equation (11))
f = blade force (equation (4a))
G = Clauser's form factor (equation (18))
$H_{12_s} = \delta_s^*/\vartheta_{ss}$ = momentum thickness form factor
$H_e = (\delta - \delta_s^*)/\vartheta_{ss}$ = entrainment form factor
h = half span
j = dimension of the tip-clearance
p = static pressure
p_p, p_s = static pressure at the pressure and suction sides of blade
p_t = total pressure
$s(x)$ = passage width, in tangential direction; its value for zero blade tangential thickness specified simply by s
s,n = distances in longitudinal and transverse directions (see Fig. 1)
u_τ = friction velocity
u,w = velocity components in axial and tangential directions
u',v',w' = differences of corresponding velocity component at given circumferential position and its mean circumferential value
V = velocity module
V_s, V_n, V_y = velocity components in longitudinal, transverse and normal to lateral wall directions
x,y,z = distances in the axial, normal to the lateral wall and tangential directions (see Fig. (1))
β = flow angle
β' = blade angle
Γ = circulation associated with tip-clearance vortex
$\delta_x^* = \int_o^h \frac{(\bar{u}_e - \bar{u})}{\bar{u}_e}dy$ = axial displacement thickness
$\delta_s^* = \int_o^h \left(1 - \frac{\bar{V}_s}{\bar{V}_{s_e}}\right)dy$ = longitudinal displacement thickness

presents the additional advantage of not containing the force deficit terms.

To achieve closure, we shall be using a large amount of semi-empirical information established for two or three-dimensional classical turbulent boundary layers. This is not quite evident in our case, as we are dealing with circumferentially mean quantities. This has been discussed in references [16, 17 and 18]. We intend to use the relations established in these references and we are summarizing the conclusions in the forthcoming.

While two-dimensional semi-empirical turbulent boundary layer information can be used to predict the longitudinal velocity profile, this is not valid for the transverse profile. More specifically, it was established [16, 17, 18] that the inner part of the transverse profile could be described by the law of the wall for three-dimensional turbulent boundary layers. However, simple representations, as the triangular one proposed by Johnston [19], cannot be used to describe the outer part. The reasons, which can also be deduced indirectly from references [2–10] and be found in references [12, 17 and 20] will be discussed later. Consequently, closure of the problem needs the establishment of expressions for the transverse velocity profile as well as for the additional terms appearing in equations (1) and (2).

In fact, the different methods of calculation can be distinguished by examining the assumptions underlying the calculation of the additional terms. While all methods agree in dropping the pressure and the fluctuation terms DX_3, DX_2 and DZ_2, they differ in the expressions used to predict the defect force terms. Railly [1] drops them altogether. Mellor and Wood [13], recognizing their importance, take them into account. Unable, though, to cope with the difficulties related with a detailed description of the flow they perform an additional integration in the axial direction. Their formulation predicts downstream quantities in terms of upstream ones and closure is obtained on the basis of secondary flow considerations. Horlock and his collaborators (see, for instance, reference [12]), proceed in calculating the flow inside the passage. Secondary flow considerations guide them to the following expression in our notation,

$$DX_1 - DX_2 - DX_3 = 0 \tag{13}$$

which permits the uncoupling of equations (1) and (2). Finally, De Ruyck, Hirsch and Kool [21], Horlock's expression having proved invalid [17], develop a method of calculation inside the passage, using an experimental correlation for the defect force terms and Johnston's model for the outer part of the transverse velocity profile.

This small historic review is by no means complete. It leaves out many important contributions, like, for instance, Smith's [28], who has pointed out earlier the importance of the defect force terms. It is, however, very useful for our purposes, because it builts up a frame of reference, which contributes to the understanding of the development of the present method.

The Development of the Present Calculation Method

We shall consider that the flow inside the passage can be split into two parts. One, which can be described by Euler's equations when the displacement effect of the wall layers is taken into account ("inviscid", primary or free stream flow). Another one, which results as a difference of the first one and the real flow. This second part is called here wall viscous layer or secondary flow part. Of course, circumferentially mean quantities for both parts are considered. We shall use two coordinate systems. One following the primary flow (s,n,y) and another related to the cascade geometry (x,y,z), as

Nomenclature (cont.)

$\delta_n^* = \int_o^h \frac{\bar{V}_n}{\bar{V}_{s_e}} dy$ = transverse displacement thickness

δ = boundary layer thickness associated with longitudinal velocity profile

ϵ_w = angle between axial direction and flow at wall

$\vartheta_{xx} = \int_o^h \frac{(\bar{u}_e - \bar{u})}{\bar{u}_e} \frac{\bar{u}}{\bar{u}_e} dy$ = axial momentum thickness

$\vartheta_{zx} = \int_o^h \frac{(\bar{w}_e - \bar{w})\bar{u}}{\bar{u}_e^2} dy$ = mixed momentum thickness

$\vartheta_{ss} = \int_o^h \left(1 - \frac{\bar{V}_s}{\bar{V}_{s_e}}\right) \frac{\bar{V}_s}{\bar{V}_{s_e}} dy$ = longitudinal momentum thickness

$\vartheta_{sn} = \int_o^h \left(1 - \frac{\bar{V}_s}{\bar{V}_{s_e}}\right) \frac{\bar{V}_n}{\bar{V}_{s_e}} dy$ = mixed momentum thickness

$\vartheta_{ns} = \int_o^h \frac{\bar{V}_s \bar{V}_n}{\bar{V}_{s_e}^2} dy$ = mixed momentum thickness

$\vartheta_{nn} = \int_o^h \left(\frac{\bar{V}_n}{\bar{V}_{s_e}}\right) dy$ = transverse momentum thickness

λ = cascade stagger angle

ξ_s, ξ_n = vorticity components in the longitudinal and transverse directions

ξ_j = vorticity associated to the tip-vortex

$\tilde{\pi}$ = Coles' velocity profile free parameter

ρ = density

τ = total shear stress

ψ_j = stream function associated with the tip-clearance vortex flow field

Subscripts

x,y,z,s,n = components in the corresponding direction (note that p_s will denote static pressure on suction side)

w = value at wall

e = value corresponding to primary flow

δ = value corresponding at distance δ from lateral wall

Superscripts

$(\bar{})$ = circumferentially mean value

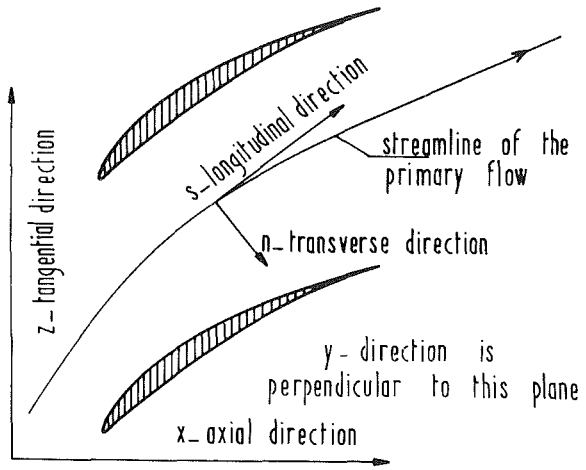

Fig. 1 Description of the coordinate systems used in the present work

presented in Fig. 1. To avoid misunderstanding, our discussion will be limited to the case of uniform incoming primary flow along the span at the cascade inlet.

(a) Semiempirical Information at our Disposal. As we already stated, we shall be using the semi-empirical information established in references [16, 17 and 18]. In these references, it was established that the longitudinal velocity profile (direction of the primary flow) could be described with adequate accuracy for engineering purposes, by the velocity profile family of Coles [22] or (better for our purpose) the analytical expression developed by Kuhn and Nielsen [23], given in the forthcoming.

$$\frac{\bar{V}_s}{\bar{u}_\tau} = 2.51\ln(y^*+1) + 5.1 - (3.39y^*+5.1)e^{-0.37y^*} + \\ + \bar{\pi}\left(1-\cos\left(\frac{\bar{\pi}y}{\delta}\right)\right) \tag{14}$$

where

$$y^* = \frac{y\bar{u}_\tau}{\nu} \tag{15}$$

and the corresponding skin friction law (for $y=\delta$)

$$2\pi = \frac{\bar{V}_e}{\bar{u}_\tau} - 2.51\ln\left(1+\frac{\delta\bar{u}_\tau}{\nu}\right) - 5.1 + \left(3.39\frac{\delta\bar{u}_\tau}{\nu} + \\ + 5.1\right)e^{-0.37\frac{\delta\bar{u}_\tau}{\nu}} \tag{16}$$

Better agreement with experimental results were obtained by the semi-empirical relations concerning the integral quantities. The following relations will be used:

$$H_{12_s} = \frac{\delta_s^*}{\vartheta_{ss}} \tag{17}$$

$$G = \frac{1-\dfrac{1}{H_{12_s}}}{\bar{u}_\tau/\bar{V}_{s_e}} \tag{18}$$

$$= \frac{2+3.2\bar{\pi}+1.522\bar{\pi}^2}{0.41(1+\bar{\pi})} \tag{19}$$

$$\delta = \frac{\delta_s^*\bar{V}_{s_e}}{\bar{u}_\tau}\frac{0.41}{1+\bar{\pi}} \tag{20}$$

The system of equations (15), (16), (17) (18) and (19) has seven unknowns. It suffices to know two of them in order to determine the rest. Additionally, form factors like Head's can be determined as follows,

$$H_e = \frac{\delta-\delta_s^*}{\vartheta_{ss}} \tag{21}$$

or from empirical relations, as the following one

$$H_e = 1.535(H_{12_s}-0.7)^{-2.715}+3.3 \tag{22}$$

The entrainement function E can be also determined by using the relation

$$E = 0.0306(H_e-3.)^{-0.633} \tag{23}$$

Accordingly, two independent variables are needed for the description of the longitudinal profile, the longitudinal component of the wall shear stress and the entrainement function.

The inner part of the transverse velocity profile can be described by the empirical law

$$\bar{V}_n = \bar{V}_s\tan(\bar{\beta}_e - \bar{\epsilon}_w) \tag{24}$$

where $\bar{\epsilon}_w$ is the angle formed at the wall by the flow and the axial direction. The total shear stress is given by the following expression

$$\tau_w = \frac{\rho\bar{u}_\tau^2}{\cos(\bar{\beta}_e-\bar{\epsilon}_w)} \tag{25}$$

Besides the semi-empirical laws, which concern the longitudinal velocity profile, it was established in the above mentioned references that the defect force components obeyed the following relation which stems from our definitions (equation (4a)).

$$DX_1 + \tan\bar{\beta}'DZ_1 = 0 \tag{26}$$

The pressure term DX_3 was found negligeable and so were the fluctuation terms. We shall comment on them later.

(b) The Present Calculation Method [27]. The development of the present calculation method is based on the secondary vorticity concept. References [2-10] show that it has been used to predict the angle variation at the cascade exit and that the results show qualitative but not quantitative agreement with experiment. One must add that the exit angle calculation has been performed using the *inlet* longitudinal velocity profile to calculate the outlet transverse one as well as the flow angle. It may be argued, then, that the generation and diffusion of the primary vorticity as well as the shape of the longitudinal velocity profile at the outlet may be at the origin of the difference between theoretical and experimental results.

In order to test this argument we proceed in the following way. We have considered Flot's [16] data (case B), which are taken inside the passage of a compressor cascade. Using equation (12), we have calculated the increase of the secondary vorticity from station to station, using each time the measured longitudinal velocity profile. More precisely, the measured integral quantities of the longitudinal velocity profile were used and a velocity profile generated through equation (14). The corresponding transverse velocity profile was calculated then by using the theoretical development of reference [20]. The theoretical results thus obtained, are compared with experiment in Fig. 2. The agreement is satisfactory. In order to complete the picture, some more calculations were performed, using Hawthorne's [14] method, for the same secondary vorticity distribution and for different values of s/δ. The results are presented in Fig. 3. They demonstrate along with the equations used, the elliptic character of the flow and the strong influence of the boundary conditions. Although the secondary vorticity is always found

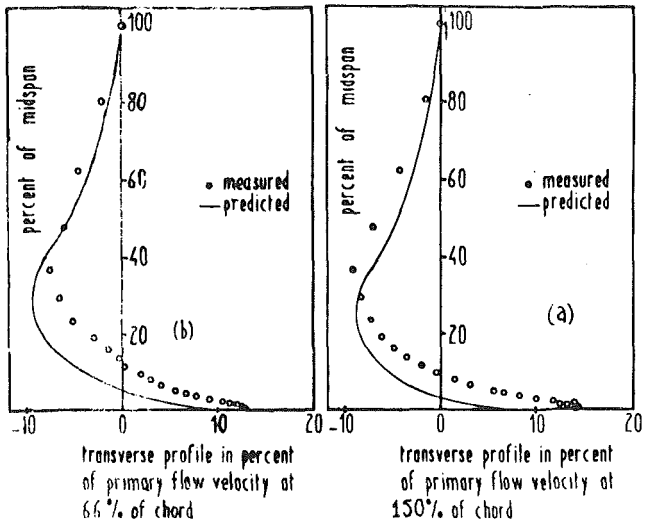

Fig. 2 Comparison between theory and experiment for the transverse velocity profile using the secondary vorticity concept. The experimental results were used for the longitudinal velocity profile.

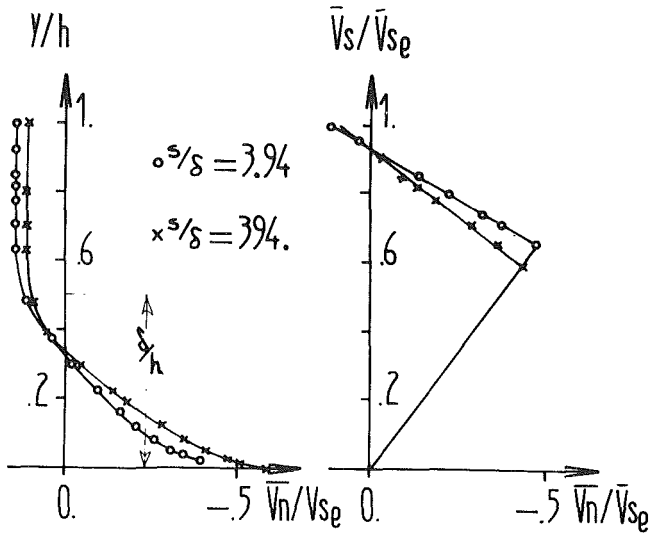

Fig. 3 The variation of the transverse velocity profile shape with changing boundary conditions

inside a distance δ from the wall, the associated transverse velocity profile may assume nonzero values at all points inside the passage. Additional calculations were performed for increasing values of h/s. These calculations show, as expected, that the induced velocity at midspan decreases with increasing h/s. Consequently, the triangular transverse velocity profile form of Johnston [19] is reached (and correspondingly the transverse velocity profile is confirmed inside a distance δ from the wall) only when s and h tend to infinity.

The above discussions and calculation show clearly that, for the present case, methods, using triangular or similar representations, assuming generally the existence of a velocity profile family for the transverse profile, must be in error. They also indicate that a differential approach must be used to predict the flow characteristics in a transverse plane. For these reasons we have decided to adopt equation (12) for the calculation of the circumferentially mean value of the secondary vorticity and the method of reference [4] for the calculation of the corresponding transverse velocity profile. This choice makes it possible to avoid the use of the second momentum integral equation, which contains one defect force term. In addition, instead of using equation (1), we decided to take advantage of equation (26) and, combining equations (1) and (2), produce the following equation (where the fluctuation terms and the pressure term have been neglected)

$$\frac{1}{s(x)}\frac{d}{dx}\left(s(x)\bar{u}_e^{*}\vartheta_{xx}\right)+\frac{\tan\bar{\beta}'}{s(x)}\frac{d}{dx}\left(s(x)\bar{u}_e^{2}\vartheta_{zx}\right)=$$

$$=-\delta_x^{*}\bar{u}_e\left(\frac{d\bar{u}_e}{dx}+\tan\bar{\beta}'\frac{d\bar{w}_e}{dx}\right)+\frac{1}{\rho}\left(\tau_{w_x}+\tan\bar{\beta}'\tau_{w_z}\right) \quad (27)$$

This equation does not contain any force deficit terms.

It is possible now to formulate the new calculation method in the following way. Considering two successive stations inside the passage of the cascade blades, one may calculate the transverse velocity profile at the second station, knowing all the properties at the first one and using equation (12) along with the method of reference [4]. Then, equations (10) and (27) may be used to calculate the integral quantities of the longitudinal velocity profile at the second station. From them, the complete longitudinal velocity profile is known by using equations (14) to (20). This procedure may be repeated from station to station until the end of the calculation.

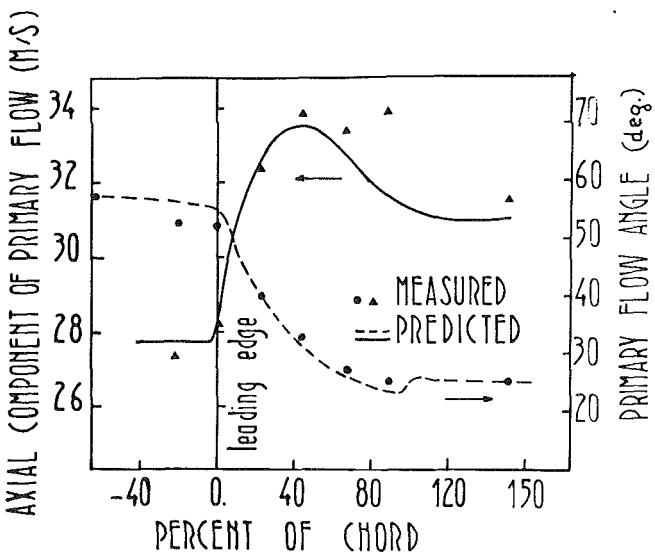

Fig. 4 Comparison between theoretically predicted and measured primary flow axial velocity and angle distribution at mid-span (Case B of Flot [16])

The present calculation method is integral in the longitudinal and differential in the transverse direction. As it is set up, it permits the dialogue of the longitudinal and transverse velocity profiles. The generation and diffusion of vorticity in the longitudinal direction is thus taken into account.

Equation (27) contains integral quantities expressed in the (x,z) coordinate system, while all shear layer information is expressed in the (s,n) coordinate system. We have (see reference [12,24]) four more equations relating the integral quantities in the two systems, which are the following:

$$\vartheta_{xx}=\vartheta_{ss}+\tan^2\bar{\beta}_e\vartheta_{nn}+\tan\bar{\beta}_e\left(\vartheta_{sn}-\vartheta_{ns}\right) \quad (28)$$

$$\vartheta_{zx}=\tan\bar{\beta}_e\left(\vartheta_{ss}+\vartheta_{nn}\right)+\vartheta_{ns}+\tan^2\bar{\beta}_e\vartheta_{sn} \quad (29)$$

$$\delta_x^{*}=\delta_s^{*}-\tan\bar{\beta}_e\delta_n^{*} \quad (30)$$

$$\delta_n^{*}=\vartheta_{sn}+\vartheta_{ns} \quad (31)$$

These equations are used to obtain closure.

Comparison of Theoretical and Experimental Results

The method described in the previous chapter was applied

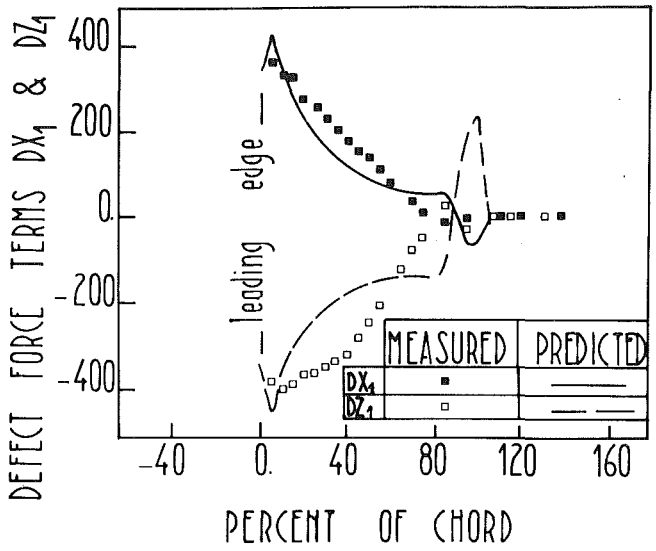

Fig. 5 Comparison between theoretically predicted and measured defect force terms (Case B of Flot [16])

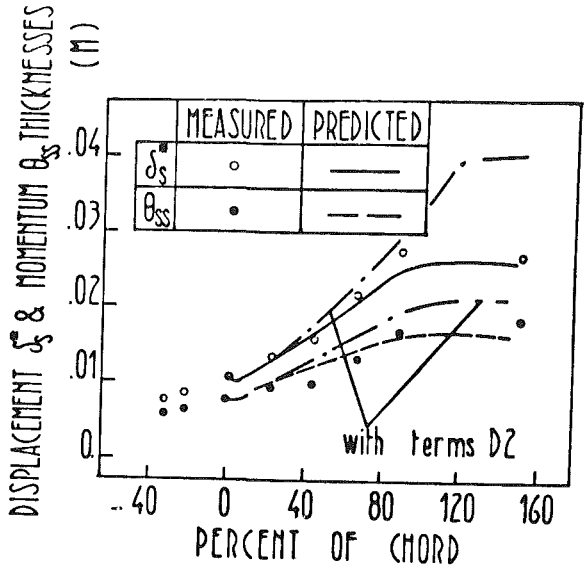

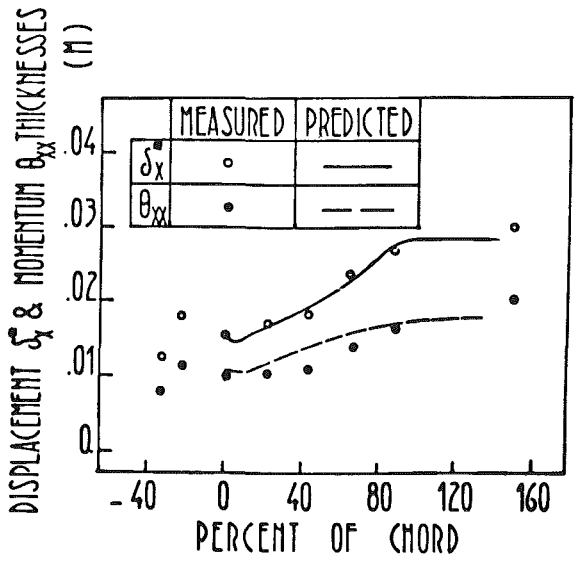

Fig. 6 Comparison between theoretically predicted and measured $\delta_s^*, \delta_x^*, \vartheta_{xx}, \vartheta_{ss}$ distributions (Case B of Flot [16])

to the experimental results of Flot [16] (Case B). Flot's experiment was performed with a highly loaded compressor cascade turning the flow from approximately 55 deg to 25 deg. A theoretical inviscid calculation method was used to predict the circumferentially mean primary flow angle $\bar{\beta}_e$—distribution inside the blade passage. This distribution was supplied as data and the system of the above developed equations was solved in the described way. The variation of the axial component of the primary flow velocity was calculated using the following overall continuity equation.

$$\frac{1}{s(x)}\frac{d}{dx}[s(x)\bar{u}_e(h-\delta_x^*)]=0 \tag{32}$$

The comparison between theoretical and experimental results is presented in Figs. 4 to 9. Figure 4 shows the comparison between the theoretical primary flow angle distribution and the corresponding experimental data results. The observed differences correspond to the calculated transverse velocity profile value at midspan. While in our case it induces angle differences of approximately 1.5 deg, for high turning low aspect ratio blades important differences may be expected. Figure 4 shows the comparison between the calculated x-velocity component variation and the experimental results. Figure 5 compares the calculated defect force terms (equation (2)) and the experimental results. The agreement is satisfactory. Figures 6, 7 and 8 present the comparison between theory and experiment of the integral quantities and the corresponding longitudinal and transverse velocity profiles. The agreement can be considered satisfactory.

An additional calculation was realized taking into account the experimental values of the fluctuation terms. The results are also reported in Fig. 6. From this comparison we can see that the fluctuation terms are not important in a first approximation of the problem.

The Inclusion of the Tip Clearance Effects in the Presents Calculation Method [28]

In this section we shall explain how it is possible to include the tip-clearance effects in the present calculation method.

Our approach does not consider the formation of the tip clearance vortex. We accept its existence and therefore we are obliged to use semi-empirical information to locate its position and establish its strength. Before describing the appropriate semi-empirical information, we shall consider how it is possible to introduce the velocity field associated with the tip clearance vortex in our calculation method.

We postulate that the tip-clearance vortex along with the velocity field associated with it can be considered as a disturbance which is superimposed on the primary flow. More precisely, the tip clearance velocity field is considered in our method in the same way the secondary vorticity velocity field is.

This way of treating the tip-clearance effects implies that additional losses due to the presence of the tip clearance vortex, besides the kinetic energy of the tip clearance flow itself considered lost, must be exclusively the result of its interaction with the wall viscous layer. No direct proof exists to support this statement. We may simply say that, if the secondary vorticity velocity profile may be treated as "inviscid", it seems reasonable to assume that the tip-clearance velocity profile may be considered in the same way, the two effects being of the same order of magnitude.

We now turn our attention to the already established method of calculation. To use equation (27) when tip clearance effects are present, we have to make sure that equation (26), is verified. Figure 9(a) presents experimental

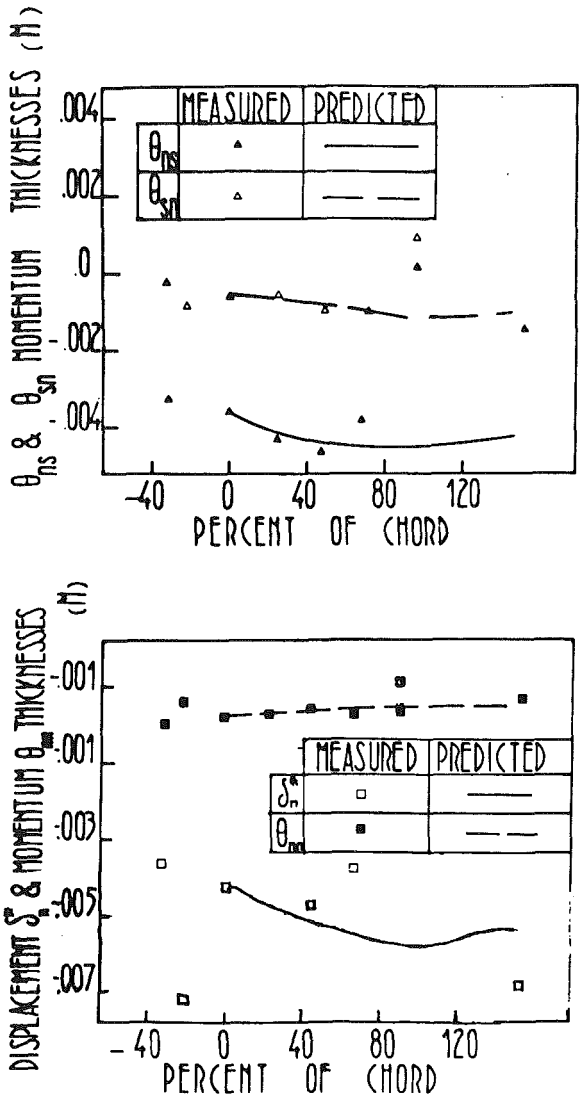

Fig. 7 Comparison between theoretically predicted and measured $\delta_n^*, \vartheta_{nn}, \vartheta_{ns}, \vartheta_{sn}$ distributions (Case B of Flot [16])

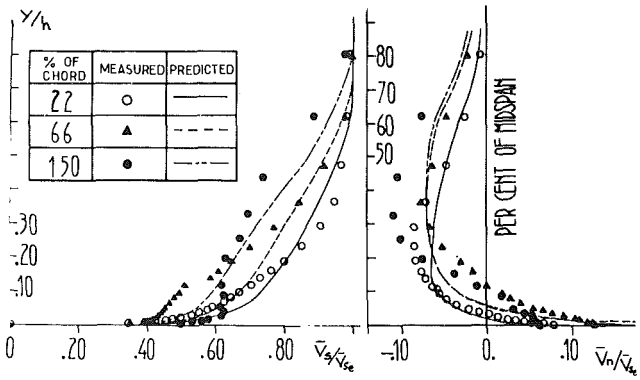

Fig. 8 Comparison between theoretically predicted and measured longitudinal and transverse velocity profiles at different axial distances (Case B of Flot [16])

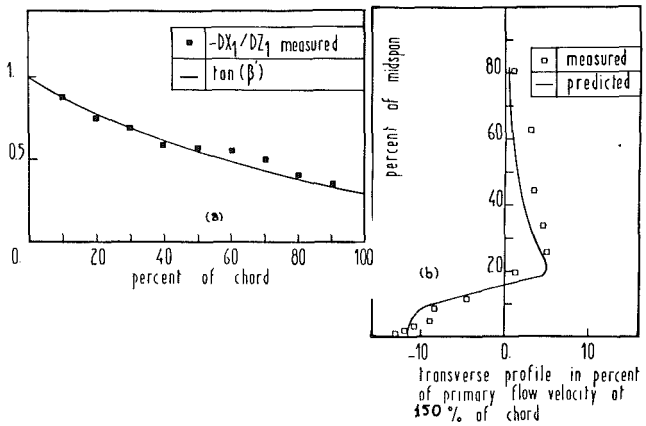

Fig. 9(*a*) Equation 16 applied on experimental results with tip clearance present. (*b*) Comparison between experiment and theory for the induced transverse velocity profile by the tip clearance vortex. Experimental results of Flot [16], Case C.

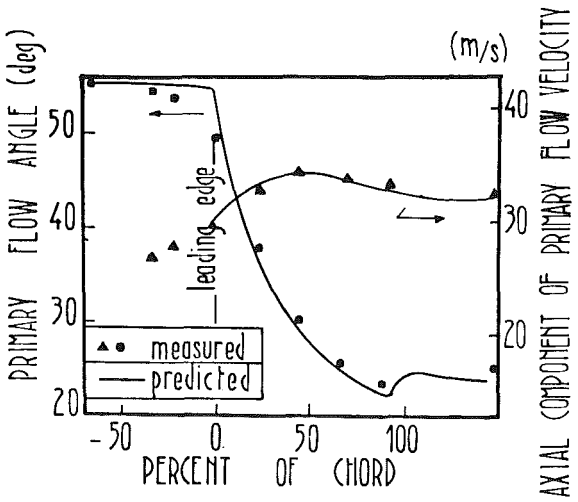

Fig. 10 Comparison between theoretically predicted and measured primary flow axial velocity and angle distribution at mid-span (Case C of Flot [16])

results from Flot's (16) work (experimental C with tip clearance). It can be seen that, at least for this set of test results, equation (26) is verified with remarkable accuracy. This means that the set of equations established in the previous sections, can be used when tip-clearance effects are present. On the other hand, as no restrictions are imposed upon the shape of the transverse velocity profile, the present calculation method can be modified in the following way, in order to accomodate the tip-clearance effects: knowing the flow properties at a station, we may calculate the transverse velocity profile due to the secondary component due to the tip clearance vorticity and then calculate the longitudinal velocity profile using the resultant transverse velocity profile in the same way as before. Of course the longitudinal component of the tip-clearance induced velocity must be added to the longitudinal velocity profile.

The description of the necessary procedure to obtain the circumferentially mean velocity profile associated with the tip clearance vortex is presented in the appendix. More details may be found in reference [26].

Comparison of Theoretical and Experimental Results When Tip-Clearance Effects are Present

We have already mentioned experiment C of Flot [16] discussing Fig. 9(*a*). In fact, experiment C differs from the already described experiment B only in that a tip clearance gap exists at one end of each blade. The free stream flow and the inlet conditions are practically identical for both experiments. Consequently, if the approximations underlying the present calculation method are valid, the velocity induced by the tip-clearance vortex may be deduced by comparing the

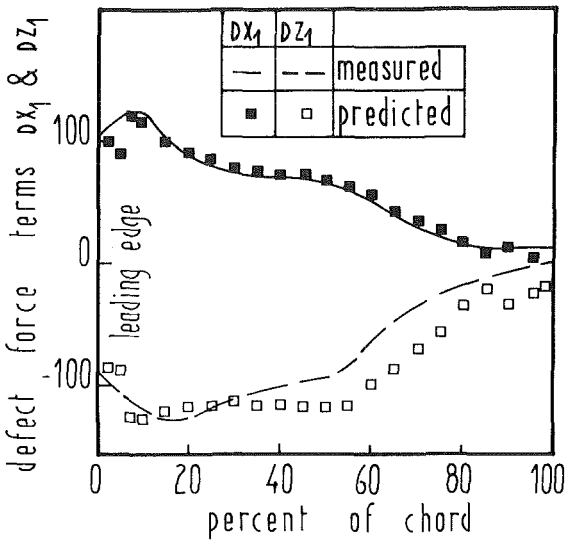

Fig. 11 Comparison between theoretically predicted and measured *defect force terms (Case C of Flot [16])*

two flows. This was done and the comparison between theory, as described in the previous paragraph and the appendix, and experiment is presented in Fig. 9(*b*). The agreement is good.

Figures 10 to 14 present comparisons between theory and experiment for case C, in the same way that was done for case B in the previous section. Figure 10 shows the comparison between the theoretical primary flow angle and the measured one. The same remarks apply in this case. Figure 10 shows also the comparison between the x-primary flow velocity component variation calculated through equation (31) and experiment. The agreement is good.

Figure 11 compares the calculated through equation (2) defect force terms with the experimental results. Figures 12, 13 and 14 give the comparison between theory and experiment of the integral quantities and the corresponding longitudinal and transverse velocity profiles. The agreement is good as far as the integral quantities are concerned and fair as far as the details of the flow are concerned. The additional calculation which was realised taking into account the experimental values of the fluctuation terms shows the relatively small influence of these terms on the theoretical results, as was already remarked for the previous case.

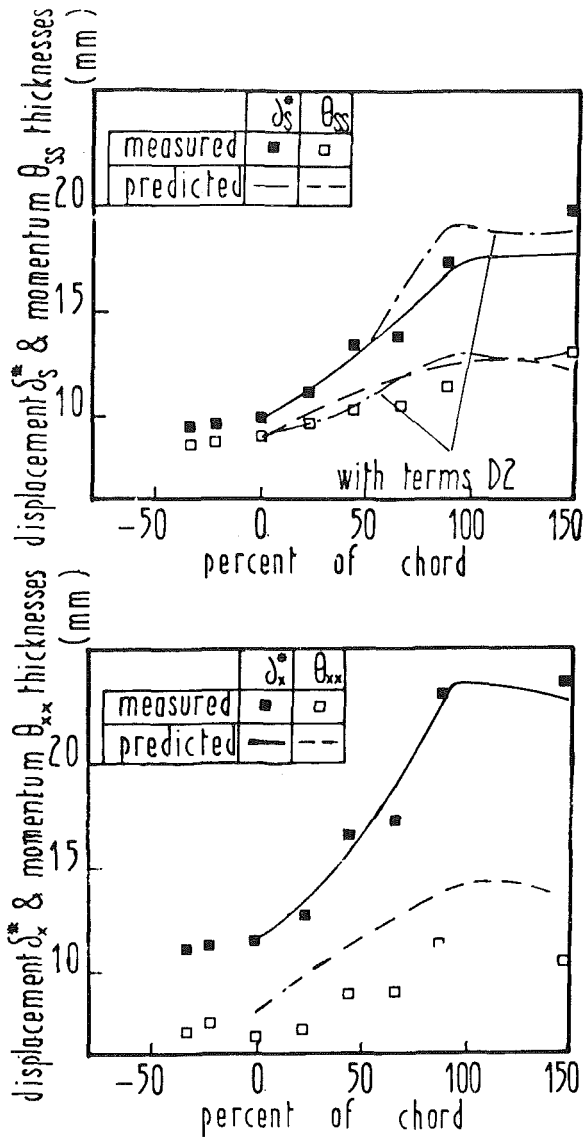

Fig. 12 Comparison between theoretically predicted and measured $\delta_s^*, \delta_x^*, \vartheta_{xx}\ \vartheta_{ss}$ distributions (Case C of Flot [16])

Additional Remarks and Conclusions

In the previous paragraphs we have presented a theoretical method of calculation of the wall shear layers developing along the lateral walls of a compressor cascade.

The particular future of this method is that it makes use of the secondary vorticity concept in order to arrive at a formulation with the least possible assumptions concerning the force deficit terms. We have used this approach for this particular formulation, which considers the circumferentially mean averaged flow, for convenience reasons. We feel, however, that our presentation made clear enough the fact that, in internal aerodynamics problems, where the duct dimenisons are comparable with the boundary layer thickness, the flow is elliptic in the transverse plane. This combined with the fact that the secondary vorticity induced velocities are not negligible at every position inside the passage, suggests that approaches, which are either integral in the transverse direction, or make use of a velocity profile family in that direction must be in error.

A differential approach could be possible in the longitudinal direction. We feel that in our case this is not advisible. It would imply the application of detailed information from turbulent boundary layers to circumferentially averaged quantities. This could be more appropriate in the case of a fully three dimensional method based on the same principles. In this latter case the secondary vorticity concept could be more efficient as, in the present case it is used with the circumferentially mean value of the vorticity. It was not quite evident from the beginning that the two secondary vorticity distributions (three dimensional and circumferentially mean average) would give the same circumferentially mean transverse velocity profiles.

Implications of the secondary vorticity velocity field can be found also in the analysis of experimental results. In fact, when such flows are analysed experimentally, it is essential, according to our model, to differentiate between the viscous part (longitudinal and transverse velocity profiles) from the "inviscid" part of the flow. The "inviscid" part, however, can be deduced only when the secondary flow vorticity is known, which, in turn, cannot be singled out if the "inviscid" part itself is not known. An iterative procedure is necessary but in practice one or two iterations are sufficient. The quantity which must be known with adequate precision is the "inviscid" flow angle, in order to deduce correctly the transverse velocity profile.

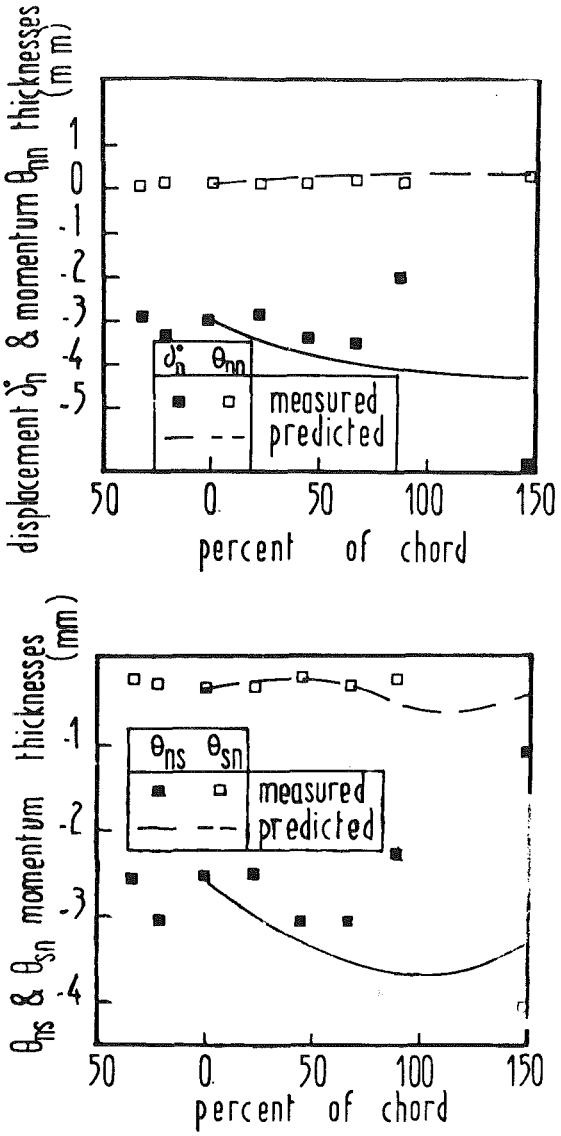

Fig. 13 Comparison between theoretically predicted and measured $\delta_n^*, \vartheta_{nn}, \vartheta_{ns}\, \vartheta_{sn}$ distributions (Case C of Flot [16])

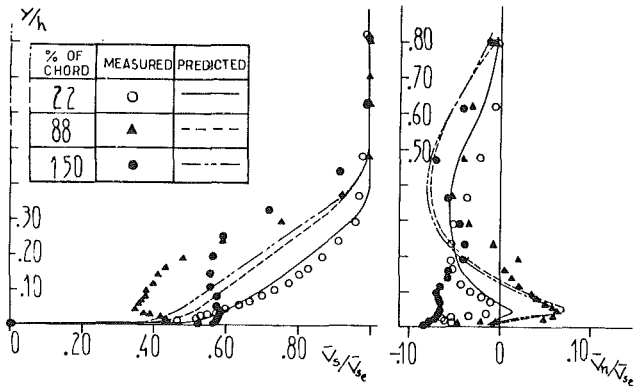

Fig. 14 Comparison between theoretically predicted and measured longitudinal and transverse velocity profiles at different axial distances (Case C of Flot [16])

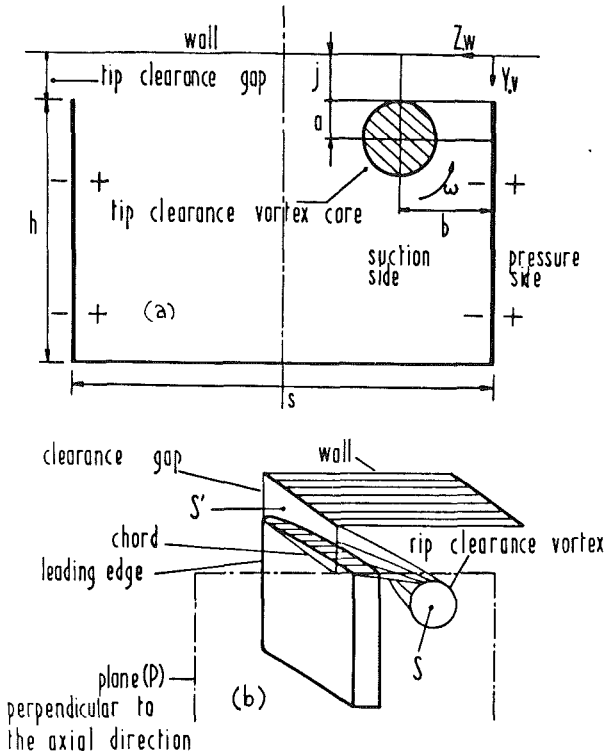

Fig. 15(*a*) Schematic representation of the model used for the calculation of the tip clearance effects. The plane presented is perpendicular to the axial direction and found at a distance x_0 from the leading edge. (*b*) Schematic representation of the tip clearance vortex formation. The mass injected through the tip clearance into the vortex is conserved inside the vortex core.

Coming back to the comparison between theory and experiment, we must point out that the transfer of the secondary vorticity was done on planes parallel to the lateral walls of the cascade. The wall shear layer displacement effect was in this respect neglected. The influence of the trailing vorticity was equally well neglected in the calculation of the flow properties downstream of the trailing edge.

Finally, the fluctuation terms in this analysis were not taken into account except on the basis of the experimental results. Note, however, that the secondary vorticity concept provides us not only with a velocity field but also with a field of velocity gradient. This information could be used in order to make a first estimation of the fluctuation terms.

We can conclude by saying that:

(*a*) We have presented a method of calculation of the secondary flows developing along the lateral walls of a compressor cascade. This method is based on the secondary vorticity concept and concerns circumferentially mean averaged quantities.

(*b*) Discussing the secondary vorticity concept we have pointed out certain aspects of the internal flow viscous layers. In our opinion, these aspects must form integral part of any attempt to analyse them theoretically and experimentally.

(*c*) We have described how the tip clearance effects could be introduced into the present calculation method. A tip clearance vortex model was introduced to this effect.

(*d*) We have compared the present calculation method with available experimental results for both cases with and without tip clearance. The agreement between theory and experiment was found to be sufficient for engineering purposes.

Acknowledgment

The authors wish to express their thanks to S.N.E.C.M.A. (Societe Nationale d'Etudes et de Constuctions de Motéurs d'Avions) and to D.R.E.T. (Direction des Recherches, Etudes et Techniques) for their encouragment and financial support, which both contributed to the acccomplishment of the present work.

References

1 Railly, J.W., and Howard, J.H.G., "Velocity Profile Development in Axial Flow Compressors," *Journal of Mechanical Engineering Science,* Vol. 4, 1962.

2 Squire, H.B., and Winter, K.G., "The Secondary Flow in a Cascade of Aerofoils in a Nonuniform Stream," *Journal of Aeronautical Sciences,* Vol. 18, 1951.

3 Hawthorne, W.R., " Secondary Circulation in Fluid Flow," *Proceedings of the Royal Society,* Vol. A206, 1951, pp. 374-387.

4 Hawthorne, W.R., "Rotational Flow Through Cascades: The Components of Vorticity," *Quarterly Journal of Mechanical and Applied Mathematics,* Vol. VIII-3, 1955.

5 Hawthorne, W.R., and Armstrong, W.D., "Rotatonal Flow Through Cascades. Part II: The Circulation About the Cascade," *Quarterly Journal of Mechanical and Applied Mathematics,* Vol. 8, 1955, pp. 280-292.

6 Hawthorne, W.R., "The Applicability of Secondary Flow Analyses to the Solution of Internal Flow Problems," *Fluid Mechanics of Internal Flow,* ed., G. Sovran, Elsevier, 1967, pp. 238-269.

7 Smith, L.H., Jr., "Secondary Flow in Axial Flow Turbomachinery," TRANS. ASME, Oct. 1955, Vol. 77, pp-1065-I076.

8 Lakshminarayana, B., and Horlock, J.H., "Generalised Expressions for Secondary Vorticity Using Intrinsic Coordinates". *Journal of Fluid Mechanics,* Vol. 59-1, 1973, pp. 97-115.

9 Lakshminarayana, B., and Horlock, J.H., "Effects of Shear Flows on the Outlet Angle in Axial Compressor Cascades, Methods of Prediction and Correlation with Experiments," *Journal of Basic Engineering,* Vol. 89, pp. 191-200.

10 Marsh, H., "Secondary Flow in Cascades. The Effect of Compressibility," A.R.C.,R and M No. 3778.

11 Head, M.R., "Entrainment Approach," VKI, Short Course on Turbulent Boundary Layers, March 4/5, 1968.

12 Horlock, J.H., and Perkins, H.J., "Annulus Wall Boundary Layers in Turbomachines," AGARDograph AG 185, 1974.

13 Mellor, G.L., and Wood, G.M., "An Axial Compressor End-Wall Boundary Layer Theory," *Journal of Basic Engineering,* Vol. 93, June 1971, pp-300-316.

14 Papailiou, K.D., "Boundary Layer Optimisation for the Design of High Turning Axial Flow Compressor Blades," ASME JOURNAL OF ENGINEERING FOR POWER, Vol. 93, Jan. 1971, pp. 147- 155.

15 Assassa, G., and Papailiou, K.D., "An Integral Method for Calculating Turbulent Boundary Layer With Separation," *Journal of Fluids Engineering,* Vol. 101, No. 1, Mar. 1979, pp. 110-116.

16 Flot, R., "Contribution à l'étude des ecoulements secondaires dans les compresseurs axiaux," Thèse de Docteur-Ingenieur, Universite de Lyon 1, 1975.

17 Papailiou, K.D., Flot, R., and Mathieu, J., "Secondary Flows in Compressor Bladings," ASME JOURNAL OF ENGINEERING FOR POWER, Vol. 99, April 1977, pp. 211-224.

18 Papailiou, K.D., "Secondary Flows in Axial Compressors," VKI short course on secondary flows in turbomachines (VKI LS72), 1972.

19 Johnston, J.P., "On the Three-Dimensional Turbulent Boundary Layers Generated by Secondary Flows," *Journal of Basic Engineering,* No. 82-1, 1960.

20 Horlock, J.H., "Cross-Flows in Bounded Three-Dimensional Turbulent Boundary Layers," Cambridge University, CUED/A-Turbo/TR 28.

21 De Ruyck,, J., Hirsch, C., and Kool, P. "An Axial Compressor End Wall Boundary Layer Calculation Method," ASME Paper No. 78-GT-81, 1978.

22 Coles, D.E., "The Law of the Wake in the Turbulent Boundary Layers," *Journal of Fluid Mechanics,* Vol. 12, 1956.

23 Kuhn, G.D., and Nielsen, J.N., "Prediction of Turbulent Separated Boundary Layers," *AIAA Journal,* Vol. 12, No. 7, July 1974, pp. 881-882.

24 Comte, A., "Calcul des écoulements secondaires à l'interieur du canal d une grille d'aube," These de Docteur, Ingénieur, Université de Lyon I, Juillet 1978.

25 Ohayon, G., "Contribution a l etude des ecoulements secondaires dans les compresseurs axiaux avec effects du jeu raidal," These de Doctorat de 3eme Cycle. Universite de Lyon I, July 1979.

26 Lakshminarayana, B., "Methods of Predicting the Tip Clearance Effects in Axial Flow Turbomachinery," *Journal of Basic Engineering,* Sept. 1970, pp. 467-482.

27 Lakshminarayana, B., and Horlock, J.H., "Tip Clearance Flows and Losses for an Isolated Compressor Blade," ARC,R and M No. 3316, June 1962.

28 Smith, L.H., "Casing Boundary Layers in Multistage Axial-Flow Compressors," Brown Boveri Symposium, Flow Research in Blading, Elsevier, Amsterdam, 1969.

APPENDIX

The Semi-Empirical Information Concerning the Tip-Clearance Vortex

The model describing the position and the strength of the tip-clearance vortex used in the present work is basically the one proposed by Lakshminarayana [26]. Details concerning the reasons which led us to adopt it well as pertinent bebliography concerning the tip clearance effects and their importance may be found in reference [25].

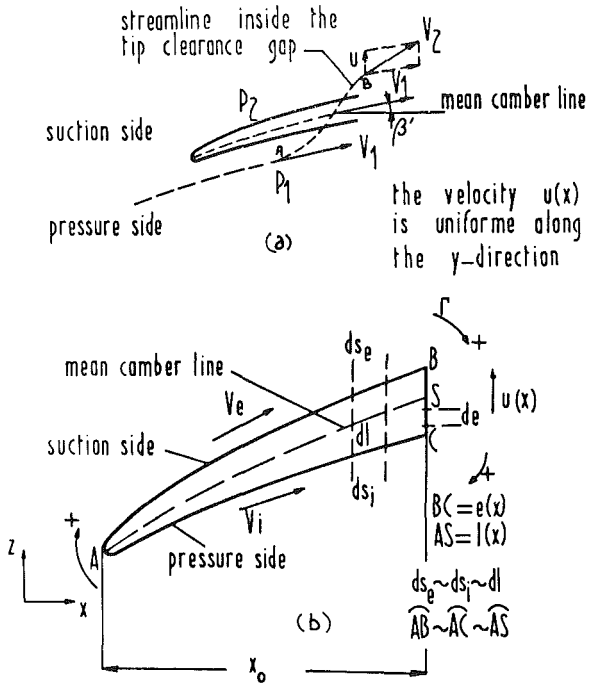

Fig. 16(a) Schematic representation of the flow inside the tip-clearance gap. The tip clearance flow is coming out of the suction side of the tip clearance gap with y-wise uniform velocity *u(X)*. (*b*) Schematic representation of part of the blade tip region which helps in understanding the development of the expression giving the vortex intensity Γ (equation (43)).

Lakshminarayana, on the basis of experimental evidence, assumes that the tip clearance vortex core radius a has a finite value. This situation is schematically presented in Fig. 15(*a*), which gives the trace of the tip clearance vortex on a plane perpendicular to the axial direction at a distance x_o from the cascade leading edge.

The visualizations realised by Flot [16] show that the flow inside the tip clearance seems to be roughly parallel to the cascade front. This explains why we have considered the trace of the tip-clearance vortex on such a plane.

The Induced Velocity. Considering the plane presented in Fig. 15(*a*) and assuming that the vorticity inside the vortex core is constant and outside of it zero, we have

$$\xi_j(y,z) = \text{const inside the vortex core}$$
$$\xi_j(y,z) = 0 \text{ outside of the vortex core} \tag{33}$$

Let $\psi_j(y,z)$ be the stream function associated with the velocity field induced by the tip clearance vortex. The two velocity components v and w along the y and z directions, respectively, are expressed as follows

$$v(y,z) = -\frac{\partial \psi_j}{\partial z}(y,z) \tag{34}$$

$$w(y,z) = \frac{\partial \psi_j}{\partial y}(y,z)$$

The boundary conditions demand that ψ_j be zero on all four sides of the rectangle formed by the pressure and suction sides and the upper and lower cascade walls of Fig. 15(*a*).

Then ψ_j is given as the solution of the following Poisson's

equation

$$\Delta\psi_j = \frac{\partial^2\psi_j}{\partial y^2} + \frac{\partial^2\psi_j}{\partial z^2} = \xi_j(y) \tag{35}$$

Equation (35) was solved and the circumferentially mean tip clearance velocity profile was obtained using the method described in reference [26] for a number of cases. Additional calculations of the circumferentially mean velocity profile were performed, using the circumferentially mean vorticity distribution $\bar{\xi}_j(y)$ and the method of reference [4]. The results of the two calculations were practically the same. For simplicity, we decided to adopt the second calculation procedure and obtain the circumferentially mean tip clearance velocity profile, using $\bar{\xi}_j(y)$.

If the center of the vortex core is found at a distance $(a+j)$ from the upper cascade and wall [26], the circumferentially mean value of the tip clearance vorticity is given as

$$\bar{\xi}_j(y) = \frac{2\Gamma}{s\pi a^2} \cdot \sqrt{a^2 - (y-a-j)^2} \tag{36}$$

In this way the knowledge of the distance b (see Fig. 15) is not necessary. On the contrary, in order to define the mean vorticity $\bar{\xi}_j(y)$ it is necessary to know the core radius a and the vortex intensity Γ.

The Radius of the Vortex Core. Following Horlock and Lakshminarayana [26, 27], we can assume on the basis of experimental evidence, that the mass flowing through the tip clearance into the tip clearance vortex is conserved inside the tip clearance vortex core (see Fig. 15).

Consequently, assuming uniform flow through the tip-clearance gap and considering the flow up to a distance x_o from the leading edge we can write for the mass flow rate $[m_{s_j}]_{x_o}$ through the tip clearance from the leading edge up to the point $x = x_o$

$$[m_{s_j}]_{x_o} = \int_o^{x_o} \rho \cdot j \cdot u(x) \cdot dx \tag{37}$$

where $u(x)$ is the y-phase uniform velocity through the tip clearance gap.

Assuming isentropic flow through the tip clearance gap along a streamline AB (see Fig. 16) and a pressure difference Δp between the two sides of the blade at tip, Bernoulli's equation gives the following expression (26) for the tip-clearance velocity

$$u(x) = V_1 \cdot \sin\bar{\beta}' \left\{ \sqrt{1 + \frac{2 \cdot \Delta p}{\rho \cdot V_1{}^2 \cdot \sin^2\bar{\beta}'}} - 1 \right\} \tag{38}$$

where $\bar{\beta}'$ is the mean blade camber angle and V_1 is a characteristic flow velocity at the vicinity of x_o.

In the present work, Δp is calculated taking into account the value of the defect force terms at $y=j$ and the characteristic velocity V_1 is taken equal to the value of the longitudinal velocity at $y=j$.

The mass flow rate $[m_{s_j}]_{x_o}$ may be equally expressed in the following way

$$[m_{s_j}]_{x_o} = \pi\rho \cdot_{1x_o} \cdot a^2 \tag{39}$$

where V_{1x_o} is the axial component of the velocity V_1 at $x = x_o$. Consequently, combining equations (37) and (39), we have

$$a(x_o) = \sqrt{\frac{j\left\{\int_o^{x_o} u(x) \cdot dx\right\}}{\pi \cdot V_{1x_o}}} \tag{40}$$

W can see that the knowledge of a(x_o) does not introduce any additional unknowns to our problem.

The Intensity of the Vortex Core. The vortex lines coming out of the blade tip (tip plane, see Fig. 15) are carried away by the flow and assume more or less its direction. Assuming that the circulation is conserved, we can calculate the tip-clearance vortex intensity, considering the tip plane (see Fig. 16).

The vortex intensity Γ is given by the following expression

$$\Gamma = \int_{AB} \mathbf{V} \cdot \mathbf{ds} + \int_{BC} \mathbf{V} \cdot \mathbf{ds} + \int_{CA} \mathbf{V} \cdot \mathbf{ds} \tag{41}$$

In reference [25], introducing the simplifications presented in Fig. 16, the following expression is derived for the intensity Γ

$$\Gamma = \int_{AB} (V_e - V_i)\, dl - ue \tag{42}$$

where e is the tangential blade thickness.

This expression, assuming that the kinetic energy $1/2 \cdot \rho u^2$ is lost, becomes

$$\Gamma = \int_o^{x_o} \left(\frac{2 \cdot \Delta p}{\rho} - \frac{\tilde{s}}{\tilde{L}} \right) \frac{\sqrt{1 + \tan^2\bar{\beta}'}}{2V_1} \cdot dx - u_e \tag{43}$$

where

$$\tilde{s} = \int_0^{x_o} u^2 \cdot \sqrt{1 + \tan^2\bar{\beta}'} \cdot dx \tag{44}$$

$$\tilde{L} = \int_o^{x_o} \sqrt{1 + \tan^2\bar{\beta}'} \cdot dx$$

Solution of Plane Cascade Flow Using Improved Surface Singularity Methods

E. R. McFarland
NASA Lewis Research Center,
Cleveland, Ohio

A solution method has been developed for calculating compressible inviscid flow through a linear cascade of arbitrary blade shapes. The method uses advanced surface singularity formulations which were adapted from those found in current external flow analyses. The resulting solution technique provides a fast flexible calculation for flows through turbomachinery blade rows. The solution method and some examples of the method's capabilities are presented.

Introduction

Current design of turbomachinery blade rows relies on the use of computer codes to model the flow on blade-to-blade surfaces. Most of the codes currently used for blade designs model the flow as inviscid, irrotational, and compressible. The flow field is solved using finite difference or finite element numerical techniques. The solutions given by these codes can be quite accurate. However, it has been the experience of the author that use of the field techniques can require an experienced user to manipulate input data and control parameters, and that these codes may also limit a designer in the types of blade geometries, cascade configurations, and flow conditions that can be considered. The designer can therefore spend a considerable portion of his effort in making a preliminary design conform to the requirements and eccentricities of a particular flow analysis code. In order to accelerate the blade design process and give the designer more freedom in developing blade shapes, a simple blade-to-blade flow code has been developed. The objective of the code is to provide a versatile, stable, and efficient calculation which has sufficient accuracy to determine the basic merits of a particular blade row design. The simple code provides a means of rapidly screening blade designs for analysis by more complex codes which have better accuracy.

The panel or integral equation solution technique was selected as a basis for the simple design code. This technique meets the requirements of being a versatile, stable, and efficient calculation scheme. It is however an incompressible solution and requires the use of a compressibility correciton to account for compressible flow effects.

Panel solutions have been used for several years by external aerodynamicists who have developed and refined them into one of the primary design tools of the aircraft industry. In the past, internal flow aerodynamicists such as Martensen [1], Geising [2], and Hess and Stockman [3] have made use of integral solutions, but the basic technique has not been pursued extensively for internal flow problems.

In this paper, a panel solution is described for inviscid compressible flow through a plane cascade. An incompressible solution is developed using advanced integral equation formulations. Compressibility effects and stream channel variations are included by adapting the Lieblein-Stockman correction technique [4] from engine inlet calculations to the cascade problem. Several example solutions are given to demonstrate the capabilities of the method.

Analysis

The general cascade problem is shown in Fig. 1. The governing equations and boundary conditions for an inviscid incompressible cascade flow are the following:

$$\nabla \cdot \mathbf{V} = 0 \tag{1}$$

$$P + \frac{1}{2}\rho V^2 = \text{constant} = P_t \tag{2}$$

$$\mathbf{V} \cdot \mathbf{n}_{\substack{\text{body} \\ \text{surface}}} = \mathbf{V}_{N_{\substack{\text{body} \\ \text{surface}}}} \tag{3}$$

$$\mathbf{V} \to \mathbf{V}_I \text{ as } x \to -\infty \tag{4}$$

$$\mathbf{V} \to \mathbf{V}_E \text{ as } x \to +\infty \tag{5}$$

The solution is developed using a velocity potential which is the sum of a constant velocity potential plus a disturbance. The constant velocity potential is determined from the mean of the upstream and downstream velocities. The distrubance quantities are unknown.

$$\Phi = \phi_{\text{onset}} + \phi$$

$$\mathbf{V} = -\nabla\Phi = \mathbf{V}_{\text{onset}} + \mathbf{v} \tag{6}$$

The constant or onset velocity and potential satisfy continuity (equation (1)) exactly. The disturbance potential and velocity are to be determined so that continuity is satisfied.

$$\nabla \cdot \mathbf{v} = \nabla^2\phi = 0 \tag{7}$$

$$\mathbf{V}_{\text{onset}} = \text{constant} \tag{8}$$

Contributed by the Gas Turbine Division of THE AMERICAN SOCIETY OF MECHANICAL ENGINEERS and presented at the Gas Turbine Conference and Products Show, March 9-12, 1981, Houston, Texas. Manuscript received at ASME Headquarters December 18, 1980. Paper No. 81-GT-169.

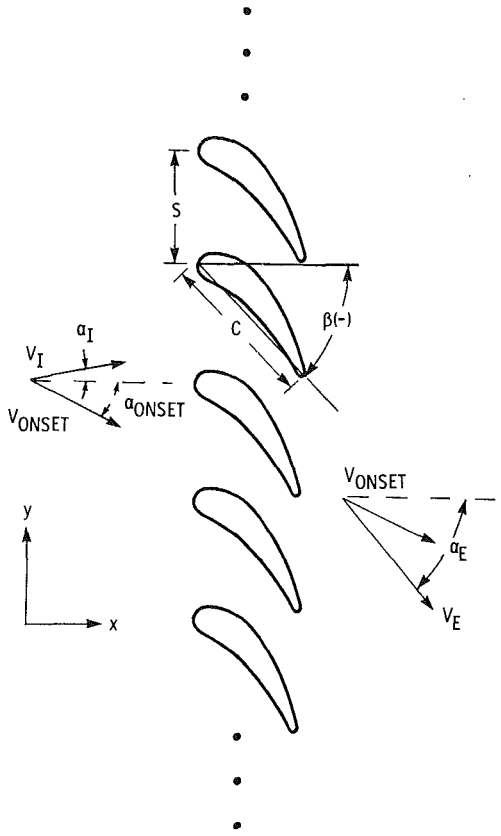

Fig. 1 Cascade problem

The flow field is determined by solving equations (6), (7), and (8) subject to boundary conditions (3, 4), and (5). The momentum equation (2) does not enter into the calculation except to relate the pressure to the velocity field.

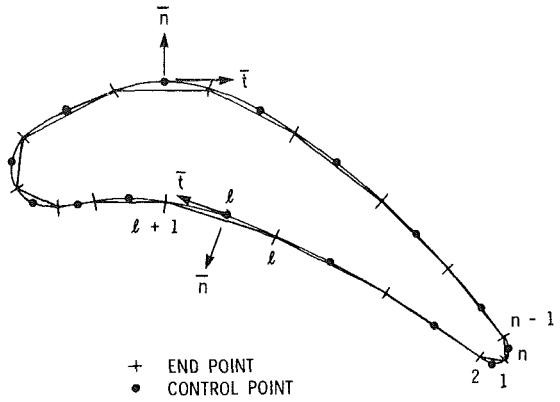

Fig. 2 Panel representation of turbomachinery blade

The equation for the disturbance potential (equation (7)) is Laplace's equation. Since it is a linear equation, superposition of known simple solutions of Laplace's equation may be used to develop more complex solutions. A general solution to flow over a body or cascade of bodies may be developed by using basic incompressible potential flow solutions for source and vortex flows distributed along the body surfaces, and varying the strength of the source and vortex singularities so that the problem's boundary conditions are satisfied. This is the basis of the panel method as described by Hess and Smith [5].

In practice, the surface of the body is represented by inscribing a polygon as shown in Fig. 2. The simple source and vortex singularity solutions are described over each element, and a control point is selected on each element where the normal velocity boundary condition is to be applied. There will be n element end points and $n - 1$ control points. The first and nth element end points are coincident.

The simplest form of the solution would be to use flat

Nomenclature

$As,Bs,Av,Bv,$
Ad,Bd = source, vortex, and vortex jump influence coefficients
C = blade chord
c = curvature parameter
$\mathbf{i},\mathbf{j}$ = unit vectors
ℓ = a control point on the cascade surface
$\mathbf{n},\mathbf{t}$ = surface unit normal and tangential vectors
P = arbitrary point in space
S = cascade pitch or gap
s = surface distance from center of panel
V = velocity relative to the blade
v = disturbance velocity
X,Y = $\pi(x-\xi)/S$, $\pi(y-\eta)/S$
x,y = coordinate system associated with the point where the velocity is to be calculated
α = flow angle relative to axial direction
β = cascade stagger or blade setting angle
Δ = element or panel chord length
ξ,η = coordinate system associated with cascade elements
σ,γ,δ = source, vortex, and vortex jump singularity strengths
Φ = total velocity potential
ϕ = component of total velocity potential
θ = orientation angle of panel or velocity point coordinate system with respect to reference coordinate system
ρ = fluid density
∇ = gradient vector operator

Subscripts

i,c = incompressible and compressible
E,I = exit and inlet conditions
i,j,k = panel indices for source, vortex, and vortex jump singularity strengths
N,T = normal and tangential component on blade surfaces
TE = trailing edge quantity
t = stagnation or total condition
U,L = upper and lower surfaces
onset = mean undisturbed flow

Superscript

$(\bar{\ })$ = averaged quantity

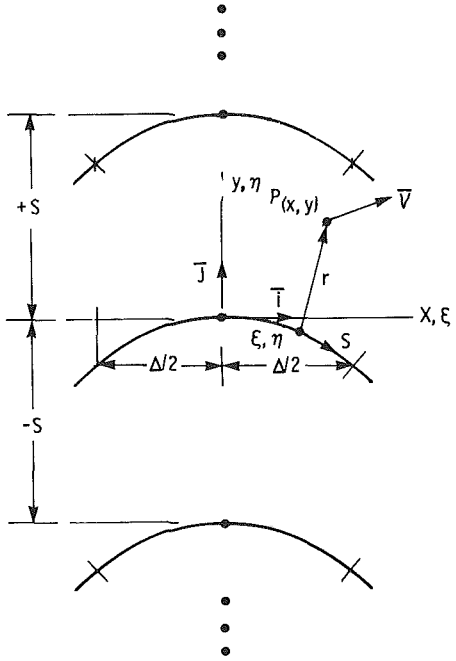

Fig. 3 Cascade panel elements

elements with constant source and vortex singularity strengths over each element and the control points located at the center of the flat element. However, Hess [6] demonstrated a means of developing higher order accurate panel solutions by using curved elements with varying singularity strengths and locating the control points closer to the true body surface. Building on Hess's work, a higher order accurate panel solution is developed for linear cascades.

Cascade Panel Formulation. A single cascade panel is shown in Fig. 3. The panel has associated with it a Cartesian coordinate system with unit vectors **i,j**. The coordinate system is centered on the panel. Its origin is located at the panel control point and the x or ξ axis is aligned with the panel chord. The velocity at any point P due to the singularity distribution along each cascade panel is to be determined. The coordinates for point P are denoted as x, y and those for points on the panel as ξ, η.

Hess showed that the velocity at any point P due to a single panel with a source strength distribution, $\sigma(s)$, is given by

$$\mathbf{V}=2\int_{-\Delta/2}^{\Delta/2}\left[\frac{x-\xi}{r^2}\mathbf{i}+\frac{y-\eta}{r^2}\mathbf{j}\right]\sigma(s)\,\frac{ds}{d\xi}\,d\xi \tag{9}$$

where

$$r=\sqrt{(x-\xi)^2+(y-\eta)^2}$$

For a cascade problem, a series of these integrals is needed.

$$\mathbf{V}=2\int_{-\Delta/2}^{\Delta/2}\left[\frac{(x-\xi)\mathbf{i}+(y-\eta)\mathbf{j}}{r^2}+\sum_{k=1}^{\infty}\left\{\frac{(x-\xi)\mathbf{i}+(y-(\eta-kS))\mathbf{j}}{(x-\xi)^2+(y-(\eta-kS))^2}+\frac{(x-\xi)\mathbf{i}+(y-(\eta+kS))\mathbf{j}}{(x-\xi)^2+(y-(\eta+kS))^2}\right\}\right]\sigma(s)\,\frac{ds}{d\xi}\,d\xi \tag{10}$$

where k is the summation index for cascade bodies. This series is the cascade potential velocity which was shown in reference [2] to be

$$\mathbf{V}=\frac{2\pi}{S}\int_{-\Delta/2}^{\Delta/2}\left[\frac{\sinh(X)\cosh(X)\mathbf{i}+\sin(Y)\cos(Y)\mathbf{j}}{\sinh^2(X)+\sin^2(Y)}\right]\sigma(s)\,\frac{ds}{d\xi}\,d\xi \tag{11}$$

where

$$X=\frac{\pi}{S}(x-\xi);\quad Y=\frac{\pi}{S}(y-\eta)$$

Hess [6] developed the higher order panel formulas by integrating equation (9) using series expansions for the different terms in the integrand. These expansions for a second order accurate panel solution are

$$\eta=c\xi^2+0(\xi^3)$$
$$\sigma=\sigma_0+\sigma_1 s+0(s^2)$$
$$s=\xi+\frac{2}{3}c^2\xi^2+0(\xi^4)$$
$$\frac{1}{r^2}=\frac{1}{r_f^2}+\frac{2cy\xi^2}{r_f^4}+0(\xi^4) \tag{12}$$

where

$$r_f=\sqrt{(x-\xi)^2+y^2}$$

The factor c appearing in the series expansion is related to the panel curvature and is determined by a three point curve fit using the averaged element slopes at the end points of the panel. The expansion of $1/r^2$ is needed for numerical stability. As point P approaches the path of integration, the integrand becomes very large and the resulting expresion for velocity becomes divergent. The expansion in terms of r_f alleviates this problem.

In the present study, equation (11) was integrated numerically. The series expansions for η, s, σ in terms of ξ were substituted into the integrand. The resulting expression was evaluated using a three point ($\xi = -\Delta/2, 0, \Delta/2$) Simpson's rule. Again, numerical difficulties were encountered in calculating the integrands as the velocity point approached the path of integration. However, from equation (10), it can be seen that only the first term in the series is causing the difficulty and that this term is identical to the velocity equation for an isolated body (equation (9)). Therefore, the numerical problem may be avoided by subtracting the first term of the series from the integrand, integrating, and adding Hess's analytical expression to the integral. Equation (11) becomes

$$\mathbf{V}=\frac{2\pi}{S}\int_{-\Delta/2}^{\Delta/2}\left[\frac{\sinh(X)\cosh(X)\mathbf{i}+\sin(Y)\cos(Y)\mathbf{j}}{\sinh^2(X)+\sin^2(Y)}-\left\{\frac{X\mathbf{i}+Y\mathbf{j}}{X^2+Y^2}\right\}\right](\sigma_0+\sigma_1\xi)(1)d\xi+\mathbf{V}_{\substack{\text{isolated}\\\text{body}}} \tag{13a}$$

Equation (13a) has been developed for a source singularity distribution. It can also be used for the vortex singularity distribution since from incompressible potential flow theory, the source and vortex singularities are related. The vortex equation would be similar to equation (13a) except σ would be replaced by γ, the velocity components change. the resulting equation is

$$\mathbf{V}=\frac{2\pi}{S}\int_{-\Delta/2}^{\Delta/2}\left]\frac{\sin(Y)\cos(Y)\mathbf{i}-\sinh(X)\cosh(X)\mathbf{j}}{\sinh^2(X)+\sin^2(Y)}-\left\{\frac{Y\mathbf{i}-X\mathbf{j}}{X^2+Y^2}\right\}\right](\gamma_0-\gamma_1\xi)(1)d\xi$$

$$+2\int_{-\Delta/2}^{\Delta/2}\left[\frac{(y-\eta)\mathbf{i}-(x-\xi)\mathbf{j}}{r^2}\right]\gamma(s)\,\frac{ds}{d\xi}\,d\xi \qquad (13b)$$

Integral Equation Formulation. The integral equation formulation of Bristow [7] was used in the present cascade panel solution. The primary feature of this formulation is the use of Green's third identity [8]. Bristow demonstrated that by using this identity for two dimensional flow, a direct relationship can be developed between the onset flow and the source and vortex singularity distributions. Along the body surface, the tangential and normal velocity will be given by

$$V_T = V_{\text{onset}}\mathbf{t} + \gamma \qquad (14a)$$

$$V_N = V_{\text{onset}}\mathbf{n} + \sigma \qquad (14b)$$

These relationships mean that the singularity strengths will remain bounded regardless of the flow boundary conditions or geometry. Bristow [7] showed that the mild singularity strength distribution generated by using Green's third identity will result in panel solutions which are less sensitive to coordinate smoothness and thin airfoil geometries.

Before making use of Green's third identity, an approximation of equation (6) is needed. This can be written in scalar components as

$$V_{x_p} = V_{\text{onset}}\cos(\theta_p-\alpha) + \sum_{i=1}^{n-1} As_{pi}\sigma_i + \sum_{j=1}^{n} Av_{pj}\gamma_j + \sum_{k=1}^{m} Ad_{pk}\delta_k \qquad (15a)$$

$$V_{y_p} = -V_{\text{onset}}\sin(\theta_p-\alpha) + \sum_{i=1}^{n-1} Bs_{pi}\sigma_i + \sum_{j-1}^{n} Bv_{pj}\gamma_j + \sum_{k=1}^{m} Bd_{pk}\delta_k \qquad (15b)$$

The first terms in the equations (15) are the contribution of the constant or onset velocity to the total velocity vector in equation (6). The angles θ and α are the orientations of the coordinate system associated with point P and the onset velocity vector with respect to a reference direction. The summation terms represent the disturbance velocity v in equation (6). Each term in the summation is an integration of equations (13*a*) or (13*b*) over one of the elements which make up the cascade body. The A's and B's in the summation are coefficients of the singularity strength values from the element integrations. These influence coefficients depend on the geometry of the problem and must be recalculated for each point where a velocity calculation is to be made. The source strengths σ which are assumed to vary linearly over the element surface are defined in terms of the element control points using a three point curve fit. The vortex strengths γ also are assumed to vary linearly, but they are defined in terms of the element end points using four point divided differences. the additional singularity strengths δ are part of the vortex singularity distribution. They represent a jump in the vortex strength which Green's identity, equation (14*a*), indicates will occur at discontinuities in surface slopes. Such discontinuities are encountered, for example, at sharp leading and trailing edges of blades. When a surface slope discontinuity is encountered in the calculation, one sided curves fits and differences are used for the source, vortex, and geometry terms on each side of the discontinuity.

Normalizing equations (14) and (15) by the onset velocity magnitude, applying equation (15) to a control point ℓ on the body surface, and resolving the calculated velocity into tangential and normal velocity components, expressions for the surface velocity may be written which relate Green's third identity to the integral equation approximation.

$$V_{T_\ell} = \cos(\theta_\ell-\alpha) + \gamma_\ell^* \qquad (16a)$$

$$V_{N_\ell} = -\sin(\theta_\ell-\alpha) + \sigma_\ell \qquad (16b)$$

$$V_{T_\ell} = \cos(\theta_\ell-\alpha) + \sum_{i=1}^{n-1} As_{\ell i}\sigma_i + \sum_{j=1}^{n} Av_{\ell j}\gamma_j + \sum_{k=1}^{m} Ad_{\ell k}\delta_\ell \qquad (16c)$$

$$V_{N_\ell} = -\sin(\theta_\ell-\alpha) + \sum_{i=1}^{n} Bs_{\ell i}\sigma_i + \sum_{j=1}^{n-1} Bv_{\ell j}\gamma_j + \sum_{k=1}^{m} Bd_{\ell k}\delta_\ell \qquad (16d)$$

where γ with an * denotes that the vortex strength is evaluated at a panel control point, while γ without an * is evaluated at the panel end point.

A system of linear algebraic equations to calculate the singularity strengths may now be constructed. This system of equations is similar to those developed by Bristow [7] for isolated bodies. These equations are generated by using the normal velocity surface boundary condition, farstream boundary conditions, and a tangential velocity error minimization equation. The normal velocity boundary condition is first used with equation (16*b*) to solve for the source strengths, and then with equation (16*d*) to give n - 1 equations. The farstream boundary conditions, the given inlet and exit flow angles, are used to calculate the circulation of the cascade. This is used with equation (16*c*) to provide one equation. The tangential velocity error minimization equations are needed if there are surface slope discontinuities, and vortex jump strengths are to be calculated. One minimization equation will be added to the system for each surface slope discontinuity. The tangential velocity error function is the sum of the squares of the difference between equations (16*a*) and (16*c*) multiplied by the local panel chord length.

This system of equations satisfies all the problem boundary conditions and includes all the unknown singularity strengths. However, there is one more equation than unknowns. This occurs because the first and last element end points are coincident for a closed body and therefore γ_1 and γ_n are equal. The additional unknown used to complete the system is an assumed uniform error in the normal velocity boundary conditions. The uniform error variable is denoted as ϵ and is included in the normal velocity equations.

In final form, the equations to be solved for the singularity strengths and uniform error are:

1 Normal Velocity Surface Boundary Condition

$$\sigma_i = \sin(\theta_i-\alpha) + V_{N_i} \qquad (17a)$$

$$\sum_{j=1}^{n} Bv_{\ell j}\gamma_j + \epsilon + \sum_{k=1}^{m} Bd_{\ell k}\delta_k = V_{N_\ell} + \sin(\theta_\ell-\alpha) - \sum_{i=1}^{n-1} Bs_{\ell i}\sigma_i \qquad (17b)$$

2 Circulation

$$\Gamma = S\cos(\alpha)[\tan(\alpha_I)-\tan(\alpha_E)] = \oint_{\text{body}} V_T\,ds \qquad (17c)$$

$$\sum_{\ell=1}^{n-1}\left(\sum_{j=1}^{n} Av_{\ell j}\gamma_j + \sum_{k=1}^{m} Ad_{\ell k}\delta_k\right)\Delta_\ell = \Gamma - \sum_{\ell=1}^{n-1}\left(\cos(\theta_\ell-\alpha) + \sum_{i=1}^{n-1} As_{\ell i}\sigma_i\right)\Delta_\ell \qquad (17d)$$

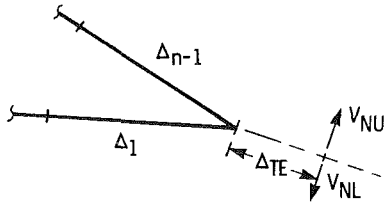

$$\Delta_{TE} = 0.001\,(\Delta_1 + \Delta_{n-1})$$

$$\bar{V}_{NL} = -\bar{V}_{NU} = 0$$

a. Sharp trailing edge.

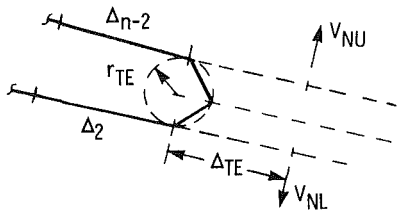

$$\Delta_{TE} = 0.001\,(\Delta_2 + \Delta_{n-2}) + 2r_{TE}$$

$$\bar{V}_{NL} = -\bar{V}_{NU}$$

b. Round trailing edge.

Fig. 4 Kutta condition configurations

3 Tangential Error Minimization

$$\frac{\partial}{\partial \delta_\ell}\left\{\sum_{i=1}^{n-1}\left(V_{T_{16c}} - V_{T_{16a}}\right)_i^2 \Delta_i\right\} = 0$$

$$\sum_{j=1}^{n}\left[\sum_{i=1}^{n-1}\left(\Delta_i A d_{i\ell} A v_{ij}\right) - \left(\Delta_j A d_{j\ell} + \Delta_{j-1} A d_{j-1\ell}\right)/2\right]\gamma_j$$

$$+ \sum_{k=1}^{m}\left[\sum_{i=1}^{n-1}\Delta_i A d_{i\ell} A d_{ik}\right]\delta_k = -\sum_{j=1}^{n-1}\left[\sum_{i=1}^{n-1}\Delta_i A d_{i\ell} A s_{ij}\right]\sigma_j \tag{17e}$$

If only the upstream flow conditions are given, the circulation cannot be calculated directly and equation (17*d*) is replaced by a Kutta condition. An iteration procedure is then used to find the proper onset flow direction and circulation. The Kutta condition for sharp trailing edges is the same as Bristow [7] used, that is, flow normal to the trailing edge bisector is zero. For the round trailing edge found in turbomachinery, this condition is modified. Two-line segments are constructed parallel to the trailing edge bisector from the trailing edge circle tangency points of the upper and lower blade surfaces. At a point on each line just downstream of the trailing edge, the normal flows to these lines are required to be equal and opposite. The two types of Kutta conditions are illustrated in Fig. 4. The Kutta condition equation is written as

$$\sum_{j=1}^{n}\left(Bv_{TE,U} + Bv_{TE,L}\right)_j \gamma_j + 2\epsilon = 2\sin(\theta_{TE} - \alpha) - \sum_{i=1}^{n-1}\left(Bs_{TE,U} + Bs_{TE,L}\right)_i \sigma_i \tag{18}$$

In the iteration procedure equations (17*a*, 17*b*, 18), and (17*e*) are solved using a guessed value for α. The resulting singularity strengths are used in equation (17*d*) to determine the circulation. The calculated circulation and onset flow angle α are then used in the following relation to determine the upstream flow condition

$$\alpha_f = \tan^{-1}\left[\frac{\sin(\alpha) + \Gamma/(2S)}{\cos(\alpha)}\right] \tag{19}$$

If the calculated value of α_f differs from the specified inlet value, the onset flow angle α is updated and the procedure is repeated.

This system of equations is solved using a direct method. The technique used is known as Cholesky's method. It resolves the coefficient matrix into upper and lower triangular matrices so that additional solutions for variations in surface normal velocities and farstream boundary conditions require only a back substitution. This property is used in the iteration procedure for the Kutta condition and in the calculation of multiple inlet and exit flow angle cases.

Table 1 Sample calculations

Case	Inlet		Exit		Gap / Chord	Number of panels	CPU s IBM TSS/370
	V/V_{cr}	α_I	V/V_{cr}	α_E			
Gostelow	-----	53.5	-----	30.025	1.239	49	2.42
Katsanis	0.231	0	0.727	-67.00	0.747	32/98	1.54/7.30
Hobson	0.610	46.123	0.610	-46.123	0.526	61	3.43
Sanz	0.826	44.61	0.529	3.91	0.863	51	2.61

Compressibility Correction. The internal flow compressiblity correction of Lieblein and Stockman [4] is used in this study. This correction has been used successfully for a number of years to calculate engine inlet flows. The correction is expressed in the following form

$$V_c = V_i\,(\rho_i/\tilde{\rho}_c)^{V_i/\tilde{V}_i} \tag{20}$$

where V_c is the corrected compressible velocity, V_i is the local incompressible velocity from the panel solution, ρ_i is the incompressible density taken to be the stagnation density ρ_t, $\tilde{\rho}_c$ is the average compressible density, and $\tilde{V}_i$ is the average incompressible velocity across the flow passage. The average compressible density is found by solving the following expression derived from the one-dimensional continuity equation and the isentropic relations.

$$\left(\frac{\tilde{\rho}_c}{\rho_t}\right)\left\{\frac{\gamma+1}{\gamma-1}\left[1 - \left(\frac{\tilde{\rho}_c}{\rho_t}\right)^{\gamma-1}\right]\right\}^{1/2} = \frac{\tilde{V}_i}{V_{cr}}$$

where γ is the ratio of specific heats and V_{cr} is the critical velocity. The average incompressible velocity is calculated on planes which are normal to the mean flow and which contain the local velocity to be corrected.

For inlets with little streamwise turning of the flow, the application of the compressibility correction is straightforward. The mean flow direction can be assumed to be approximately normal to axial stations and the average incompressible velocities are calculated using the axial station flow areas. However, for cascade flows with significant amounts of flow turning, the mean flow direction cannot be assumed and must be calculated. In this study, the components of the mean velocities are first calculated at axial stations by using continuity and circulation equations. Next, the mean flow direction through the blade passage is determined from the axial station velocity components. Planes normal to the mean flow are then constructed for each surface velocity to be corrected. Finally, the average incompressible velocity on the normal planes is found by interpolation of the axial station values.

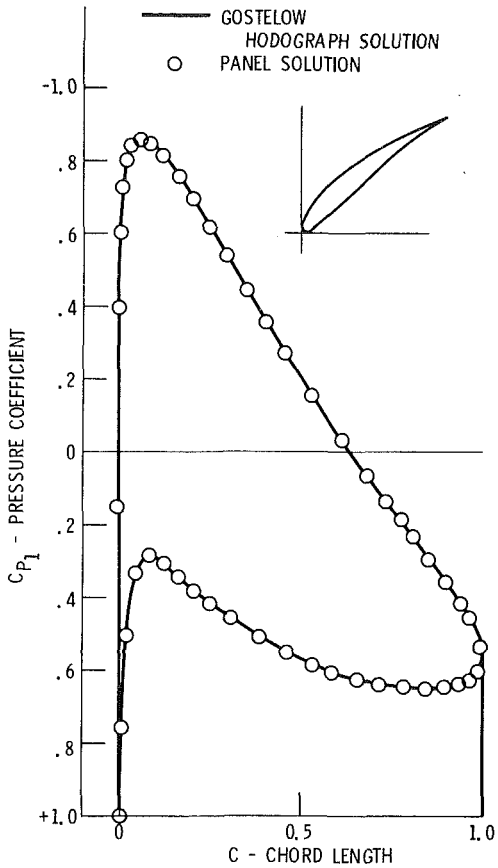

Fig. 5 Incompressible cascade flow

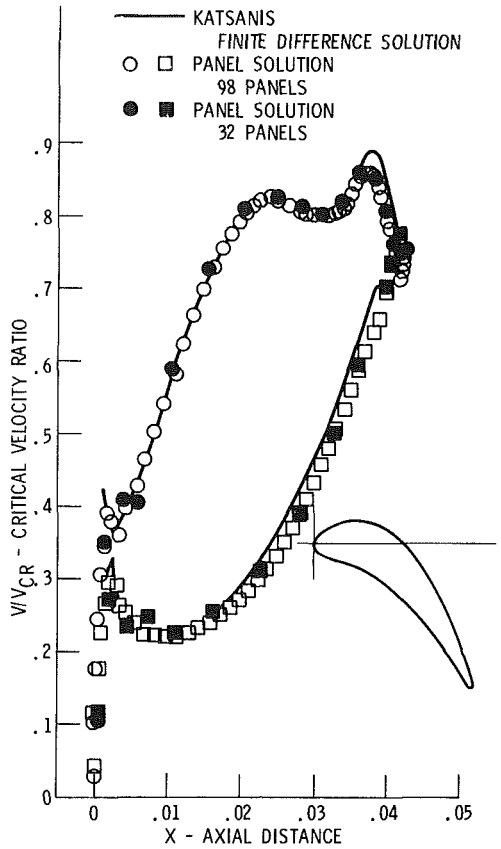

Fig. 6 Compressible cascade flow

Stream Channel Variation Corrections. A simple correction for the stream channel variations was made during the compressibility correction calculation. The incompressible surface velocities and mean flow are calculated assuming a uniform stream channel height using the inlet flow conditions as a reference. These velocities are then scaled by the ratio of the inlet to local specified stream channel height. The resulting scaled velocities are used in the compressible corrections of equation (20).

Sample Calculations and Discussion

Four sample calculations are presented to demonstrate the solution method. Table 1 shows the general flow and solution conditions for each calculation. All examples were calculated using the IBM 3033 computer at Lewis Research Center. A FORTRAN computer code of the solution method was developed for the calculations. Most blade shapes were approximated by using 40–60 elements and the solution required less than 4 s of computer time. While this computation time is very rapid, it should be noted that compressible field methods have been reported which have run times on the same order [9]. In the Gostelow and Sanz cases, the cascade airfoil shapes were described directly using discrete points. However, in the Katsanis and Hobson cases, the cascade body shapes were generated by using spline fits for the upper and lower surfaces, and circles or ellipses for the rounded leading and trailing edges.

Incompressible Cascade Flow. The exact incompressible solution of Gostelow [10] is compared with the present solution in Fig. 5. The large velocity gradients in the leading edge region and the flow past the thin trailing edge are well modeled by the panel solution. The overall agreement between the two solutions is very good.

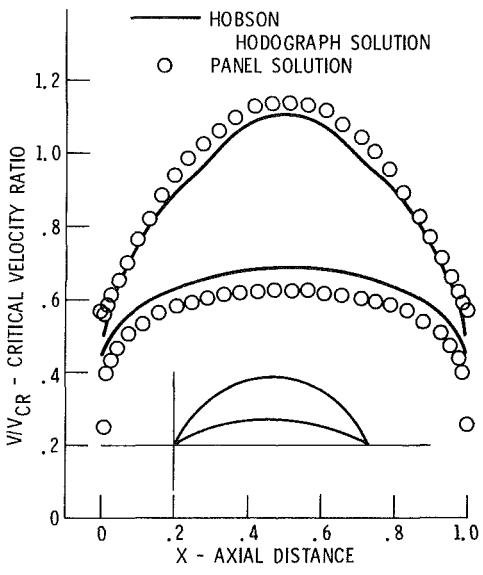

Fig. 7 Transonic cascade flow

Compressible Cascade Flow. In Fig. 6, a comparison is shown between the panel solution and the finite difference solution of Katsanis [11] for a turbine stator. Blade surface velocities are in the high subsonic range. The overall solution agreement is good, but differences do occur along the pressure surface and near the suction surface trailing edge. These differences are attributable to the compressibility

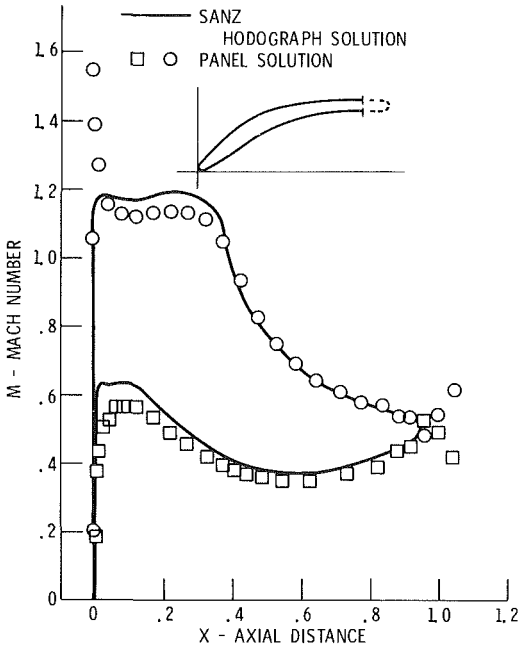

Fig. 8 Supercritical compressor stator

correction, since the two solutions were found to be identical for incompressible flow through the same cascade.

The general accuracy of the panel method is also shown in Fig. 6. Two panel solutions are shown with a different number of panels used in each case. The less accurate solution with fewer panels differs slightly from the more accurate solution. Most of this difference occurs in the leading edge region where large variations in surface curvature occur. The coarser paneling is unable to resolve the rapid change in curvature and as a result the curvature effect on the flow is smeared over a larger surface area. By considering the terms used in developing the cascade panel solution, the accuracy of the solution should be on the order of the panel size squared; although this accuracy has not been verified.

Transonic Cascade Flow. Comparison with transonic hodograph solutions are shown in Figs. 7 and 8. In Fig. 7, the comparison is with Hobson solution [12], and in Fig. 8, the comparison is with a Sanz cascade blade design using the hodograph solution technique of Bauer, et al. [13]. The panel solution compares well with the hodograph solutions for the sophistication of the computation involved.

Discrepancies in the solutions are caused primarily by the compressiblity correction which cannot be expected to exactly predict the flow at such a high level of compressibility. The large velocity spike at the leading edge of the compressor stator is due to the lack of blade geometry information given in the region, and the extraneous velocities downstream of the blade trialing edge are caused by an extension of the blade downstream to account for the blade wake.

Kutta Condition and Stream Channel Variation

In the sample calculations just presented, the downstream flow angle was given. These calculations have also been made using the inlet condition and a Kutta condition to determine the downstream flow condition. The calculated downstream flow angles were 31.19 deg (Gostelow), −67.88 deg (Katsanis, 32), −67.23 deg (Katsanis, 98), −44.16 deg (Hobson), and −31.0 deg (Sanz). In the first two cases, Gostelow and Katsanis, the flow leaves the blade surface smoothly with little deviation from the trailing edge blade angle and the Kutta condition works well. However, in the Hobson and Sanz cases, there is significant flow deviation at the blade trailing edge and the Kutta condition results are poor. Some improvements in these results could be made by including a deviation model in the Kutta condition formulation.

The effect of stream channel variation on the flow has not been studied extensively. Some comparisons have been made with the finite difference code of Katsanis [11] for subsonic flows and the agreement was good.

Conclusion

Current external aerodynamic integral equation techniques may be adopted for use in internal flow calculations. The inherent computational speed and flexibility of integral equation solution can make them very useful for design calculations. The present cascade method is a versatile design tool that will allow a designer to explore many preliminary blade designs in a short period of time. Although the method does not give exact solutions for compressible flows, example calculations do demonstrate that it is sufficiently accurate to provide a means of selecting blade designs for further analysis.

References

1 Martensen, E., "The Calculation of Pressure Distribution on a Cascade of Thick Airfoils by Means of Fredholm Integral Equations of the Second Kind," NASA TT F-702, 1971.

2 Giesing, J. P., "Extension of the Douglas Neuman Program to Problems of Lifting Infinite Cascades," LB-31653, Douglas Aircraft Co., Inc., Long Beach, Calif., AD-605207, 1964.

3 Hess, J. L., and Stockman, N. O., "An Efficient User-Oriented Method for Calculating Compressible Flow about Three-Dimensional Inlets," AIAA Paper No. 79-0081, Jan. 1979.

4 Lieblein, S., and Stockman, N. O., "Compressibility Correction for Internal Flow Solutions," *Journal of Aircraft*, Vol. 9, No. 4, Apr. 1972, pp. 312-313.

5 Hess, J. L., and Smith, A. M. O., "Calculation of Potential Flow about Arbitrary Bodies," *Progress in Aeronautical Sciences*. Vol. 8, Kuchemann, K., ed., Pergamon Press, Oxford, 1967, pp. 1-138.

6 Hess, J. L., "Higher Order Numerical Solution of the Integral Equation for the Two-Dimensional Neumann Problem," *Computer Methods in Applied Mechanics and Engineering*. Vol. 2, Feb. 1973.

7 Bristow, D. R., "Recent Improvements in Surface Singularity Methods for Flow Field Analysis about Two-Dimensional Airfoils," AIAA paper 77-641, in *Computational Fluid Dynamics Conference*, 3rd, American Institute of Aeronautics and Astronautics, Inc., New York, 1977, Paper No. 77-641, pp. 95-105.

8 Karamcheti, K., *Principles of Ideal-Fluid Aerodynamics*, Wiley, New York, 1966, pp. 344-350.

9 Caspar, J. R., Hobbs, D. E., and Davis, R. L., "Calculation of Two-Dimensional Potential Cascade Flow Using Finite Area Methods," *AIAA Journal*, Vol. 18, No. 1, Jan. 1980, pp. 103-109.

10 Gostelow, J. P., "Potential Flow Through Cascades - A Comparison Between Exact and Approximate Solutions," CP No. 807, Aeronautical Research Council, 1963.

11 Katsanis, T., "Fortran Program for Calculating Transonic Velocities on a Blade to Blade Stream Surface of a Turbomachine," NASA TN D-5427, 1969.

12 Hobson, D. G., "Shock-Free Transonic Flow in Turbomachinery Cascades," CUED/A Turbo/TR65, University of Cambridge, Dept. of Eng., 1974.

13 Bauer, F., Garabedian, P., and Korn, D., "*Supercritical Wing Sections III*," *Lecture Notes in Economics and Mathematical Systems*, Vol. 150, Springer-Verlag, New York, 1977.

Supersonic Stall Flutter of High-Speed Fans

J. J. Adamczyk

W. Stevans

National Aeronautics and Space Administration, Lewis Research Center, Cleveland, Ohio 44135

R. Jutras

General Electric Company, Evendale, Ohio 45215

An analytical model is developed for predicting the onset of supersonic stall bending flutter in axial-flow compressors. The analysis is based on a modified two-dimensional, compressible, unsteady actuator disk theory. It is applied to a rotor blade row by considering a cascade of airfoils whose geometry and dynamic response coincide with those of a rotor blade element at 85 percent of the span height (measured from the hub). The rotor blades are assumed to be unshrouded (i.e., free standing) and to vibrate in their first flexural mode. The effects of shock waves and flow separation are included in the model through quasisteady, empirical, rotor total-pressure-loss and deviation-angle correlations. The actuator disk model predicts the unsteady aerodynamic force acting on the cascade blading as a function of the steady flow field entering the cascade and the geometry and dynamic response of the cascade. Calculations show that the present model predicts the existence of a bending flutter mode at supersonic inlet Mach numbers. This flutter mode is suppressed by increasing the reduced frequency of the system or by reducing the steady-state aerodynamic loading on the cascade. The validity of the model for predicting flutter is demonstrated by correlating the measured flutter boundary of a high-speed fan stage with its predicted boundary. This correlation uses a level of damping for the blade row (i.e., the log decrement of the rotor system) that is estimated from the experimental flutter data. The predicted flutter boundary is shown to be in good agreement with the measured boundary. These results show that the model can be used to estimate the relative stability between operating points of a given rotor system. If, in addition, a measure of the mechanical damping of the rotor system is available, the model can also be used to estimate the absolute stability at an operating point.

Introduction

Flutter can result in costly (both in time and money) overruns in turbofan-engine development programs. Solving the problem of flutter (at the engine development stage) may well mean major engine redesign and retesting. For this reason, engine manufacturers and government agencies are currently supporting numerous research programs in an attempt to develop flutter prediction systems that can be used to design flutter-free engines. To date, these research programs have identified five regions of the compressor performance map where flutter is generally encountered (Fig. 1).

Of the five regions shown in Fig. 1, the supersonic low back-pressure flutter region has been the most thoroughly investigated analytically [1 - 3]. In general, these analyses have considered the flow field through a cascade of two-dimensional airfoils undergoing simple harmonic pitching or plunging. The gas stream was assumed to be an inviscid, nonconducting, perfect gas. Shock waves that originated in the flow field were assumed to be weak so that supersonic small-disturbance theory could be used. Although these assumptions appear to oversimplify the flow conditions encountered by a rotor at the onset of flutter, the flutter boundaries predicted by these analyses correlate well with experimental data.

A recent analysis [4] has attempted to apply the supersonic, linearized, small-disturbance theory to higher backpressure operating conditions (i.e., region IV of Fig. 1) by including a finite-strength shock wave within the cascade passage. Results from this analysis show that the unsteady motion of the shock wave tends to induce bending flutter. The existence of this flutter mode is documented in reference [5].

The remaining operating region where supersonic flutter occurs (region V of Fig. 1) lies close to the stall line of a stage. Analyses of this region have not appeared in the open literature. Literature on this subject (e.g., [5 - 7]) generally presents experimental data to document the extent of the flutter region. These data provide a very limited base from which an empirical correlation can be derived for predicting the onset of this flutter mode.

The objective of the present analysis is to develop a model for predicting the onset of supersonic stall flutter encountered by rotors that do not have part-span dampers or tip shrouds.

Contributed by the Gas Turbine Division and presented at the International Gas Turbine Conference and Products Show, Houston, Texas, March 9-12, 1981, of THE AMERICAN SOCIETY OF MECHANICAL ENGINEERS. Manuscript received at ASME Headquarters, September 25, 1980. Revised manuscript received December 23, 1980. Paper No. 81-GT-184.

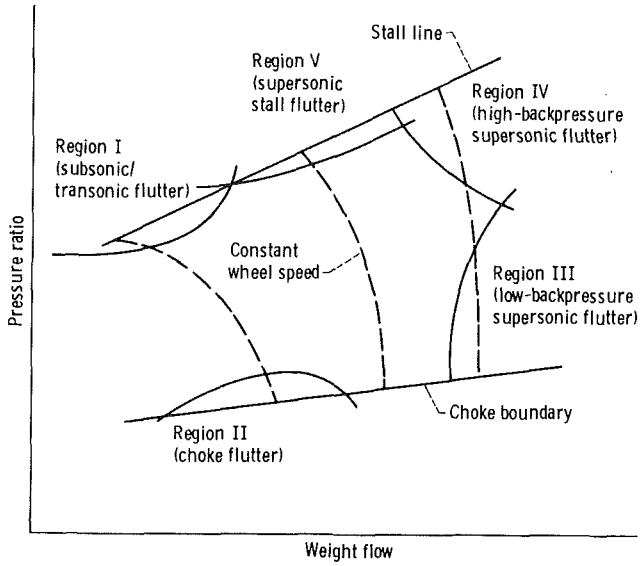

Fig. 1 Compressor performance and stability map

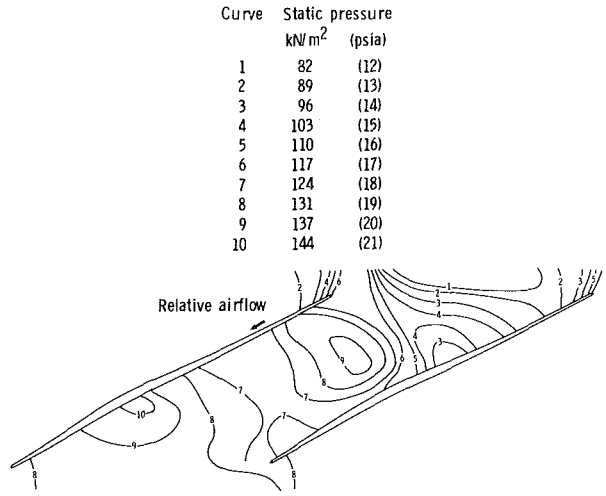

Fig. 2 Typical tip rotor static-pressure distribution near supersonic stall flutter boundary

Experimental data reveal that the flutter mode is generally the first flexural mode at a reduced frequency (based on tip relative velocity and tip semi-chord) of about 0.2. The vibratory pattern around the rotor tends to be very regular: All blades vibrate at the same frequency but are shifted in phase by a positive interblade phase angle of about 20 deg to 50 deg [7]. This positive phase shift implies that the vibratory pattern is traveling around the wheel in the direction of rotation (i.e., a forward-traveling wave).

A further characteristic of the flow regime associated with stall flutter is shown by the steady-state pressure distribution in Fig. 2. This pressure distribution was produced from measurements taken across a rotor tip while the rotor was operating near the flutter boundary. This figure clearly indicates a detached, leading-edge bow shock wave impinging on the suction surface of the adjacent blade. The large extent of the compression region at the base of the shock wave seems to suggest a separated flow region that would increase in size as the fan operating point moved toward the supersonic stall bending flutter boundary.

The present analysis develops a flutter model for the highly complicated flow field illustrated in Fig. 2 by using two-dimensional actuator disk theory. The effects of flow separation are included in the model through rotor-loss and

Nomenclature

b = airfoil semichord
c = average blade chord and damping coefficient
d = circumferential distance around wheel
F_i = aerodynamic force
h_1 = axial displacement of an airfoil
h_2 = tangential displacement of an airfoil
i = $\sqrt{-1}$
K = constant
k = reduced frequency based on circumferential distance, $\omega d/q_{-\infty}$
k_b = reduced frequency based on semichord, $\omega b/q_{-\infty}$
k_2 = wave number of disturbance along cascade plane
M = Mach number
M_b = mass of a rotor blade per unit length
N = number of blades in rotor
n = integer
n_i = unit vector
P = total pressure
p = static pressure
q = magnitude of velocity field
R = radial distance
s = entropy
T = temperature
t = time
U_i = velocity components
U_n = relative velocity component normal to disk
U^R = rotational velocity
W_{Aero} = aerodynamic work per cycle of motion
W_D = energy dissipated per cycle of motion by mechanical damping
w = mass flow rate
X_i = spacial coordinates
α = incidence angle
β = flow angle
γ = ratio of specific heat axial wave number
δ = log decrement; deviation angle, equation (13), (15)
δ_{m_1} = metal angle at leading edge
δ_{m_2} = metal angle at trailing edge
θ = stagger angle
μ = solidity
ξ = amplitude of blade motion
ρ = density
σ = interblade phase angle
τ = cascade pitch or average thickness of a rotor blade
Φ = velocity potential
χ = total-pressure-loss coefficient
ω = frequency of oscillation

Subscripts

$-\infty$ = upstream variable
$+\infty$ = downstream variable

Superscripts

$\bar{(\ )}$ = steady-state variable
$\tilde{(\ )}$ = time-dependent variable
$*$ = complex conjugate
Rel = relative component

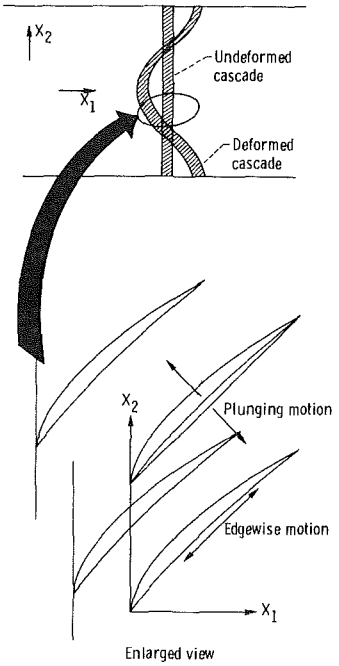

Fig. 3 Cascade plane deformation

deviation-angle correlations. For low-speed flows, actuator disk flutter models have been able to predict the onset of a single-degree-of-freedom bending flutter mode (e.g., [8 and 9]). The success of the models at low speeds suggests that a compressible actuator disk model might be capable of predicting the onset of bending flutter at supersonic speeds. This hypothesis has been confirmed by a number of calculations. These calculations, however, did require as input the interblade phase angle at the onset of flutter. So that this requirement could be avoided, the actuator disk model was modified to allow for moderate values of interblade phase angle. This modification results in a flutter model that can be developed into a flutter prediction system. The validity of this flutter prediction system is demonstrated by comparing the predicted flutter boundary of a high-speed fan stage with its measured boundary.

Formulation

The present analysis for stall bending flutter of an isolated rotor models the rotor as a two-dimensional cascade of airfoils. The cascade is defined by the blade-element geometry on a cylindrical surface at a distance R from the axis of rotation. The flow field in the cascade plane is assumed to be two dimensional, compressible, and time dependent. Viscous forces are considered only within the blade channel. The unsteady flow variables associated with the rotor vibratory motion are assumed to be smaller than their steady-state counterparts. These variables at an instant in time are required to be periodic around the wheel at a period equal to a fractional part of the circumferential distance $d = 2\pi R$.

The motion of the airfoils in the cascade plane is restricted to simple harmonic plunging and edgewise motion at a cyclic frequency ω (Fig. 3). In addition the motion of each airfoil at an instant in time is assumed to be shifted from that of its neighbor by an interblade phase angle of $\sigma = 2\pi n/N$, where n is an integer and N is the number of blades in the rotor. In the present analysis the reduced-frequency parameter k_b and the interblade phase angle are assumed to be small. (Reduced frequency $k_b = \omega b/\bar{q}_{-\infty}$, where b is the semi-chord of an airfoil and $\bar{q}_{-\infty}$ is the magnitude of the relative inlet velocity in the cascade plane.)

Field Equations. The governing linearized equations for the flow field upstream and downstream of the cascade are written with respect to the relative coordinate system. The variables in these equations are nondimensionalized by the steady inlet speed $\bar{q}_{-\infty}$, the circumferential distance around the wheel d, the inlet steady-state fluid density $\bar{\rho}_{-\infty}$, and the inlet steady-state fluid temperature $\bar{T}_{-\infty}$. In addition the subscripts $(\infty, -\infty)$ signify downstream and upstream flow variables.

The linearized continuity equation for the upstream and downstream flow fields is

$$\frac{\partial \tilde{\rho}_{\pm\infty}}{\partial t} + \bar{U}_{i,\pm\infty}\frac{\partial \tilde{\rho}_{\pm\infty}}{\partial X_i} + \bar{\rho}_{\pm\infty}\frac{\partial \tilde{U}_{i,\pm\infty}}{\partial X_i} = 0 \tag{1}$$

where the tilde denotes a time-dependent variable and the bar signifies a steady-state variable. The variables ρ, U_i, t, and X_i are the density, velocity components, time, and spacial coordinates, respectively. (See Fig. 3 for definition of coordinate system.) In addition the use of repeated indices denotes summation with respect to the repeated index. The linearized momentum equations for the flow fields are

$$\frac{\partial \tilde{U}_{i,\pm\infty}}{\partial t} + \bar{U}_{j,\pm\infty}\frac{\partial \tilde{U}_{i,\pm\infty}}{\partial X_j} = -\frac{1}{\bar{\rho}_{\pm\infty}}\frac{\partial \tilde{P}_{\pm\infty}}{\partial X_i} \quad i = 1, 2 \tag{2}$$

where $\tilde{P}_{\pm\infty}$ is the nondimensional pressure. The remaining field equations are the energy equation for an inviscid, nonconducting gas

$$\frac{\partial \tilde{s}_{\pm\infty}}{\partial t} + \bar{U}_{i,\pm\infty}\frac{\partial \tilde{s}_{\pm\infty}}{\partial X_i} = 0 \tag{3}$$

and the equation of state

$$\tilde{s}_{\pm\infty} = \frac{1}{\bar{M}^2_{-\infty}\gamma}\frac{1}{\gamma - 1}\frac{\tilde{P}_{\pm\infty}}{\bar{P}_{\pm\infty}} + \frac{1}{\gamma - 1}\frac{1}{\bar{M}^2_{-\infty}}\frac{\tilde{\rho}_{\pm\infty}}{\bar{\rho}_{\pm\infty}} \tag{4}$$

The variables appearing in equations (3) and (4) are the entropy s; the ratio of specific heats γ; and the inlet steady-state relative Mach number $\bar{M}_{-\infty}$. (The entropy was nondimensionalized with respect to $\bar{T}_{-\infty}/\bar{q}^2_{-\infty}$.)

The present analysis assumes that there are no sources of entropy or vorticity upstream of the cascade. The upstream, unsteady velocity field must therefore be irrotational and hence is equal to the gradient of a potential function $\tilde{\Phi}_{-\infty}$, where

$$\tilde{U}_{i,-\infty} = \frac{\partial \tilde{\Phi}_{-\infty}}{\partial X_i} \quad i = 1, 2 \tag{5}$$

The unsteady velocity field downstream of the cascade is expressed as

$$\tilde{U}_{i,\infty} = \frac{\partial \tilde{\Phi}_{\infty}}{\partial X_i} + \tilde{U}^R_{i,\infty} \quad i = 1, 2 \tag{6}$$

where $\partial\tilde{\Phi}_{\infty}/\partial X_i$ represents the irrotational component of the field and $\tilde{U}^R_{i,\infty}$ its rotational component. The source of the rotation field is the vorticity shed by the oscillating airfoils.

The solution to the field equations is obtained by assuming a simple harmonic spacial and temporial dependency for the potential, the rotational velocity fields and the downstream entropy field. The details of the solution procedure can be found in reference 10.

Boundary Conditions. It is shown in reference 10 that four boundary conditions must be specified at the actuator disk to relate the unsteady flow field to the cascade deformation and the steady inlet flow conditions.

The first of these boundary conditions requires the flow to be continuous across the deforming disk. The analytical form of this boundary condition is

$$(1 + \bar{\rho}_{-\infty})\, U^{\mathrm{Rel}}_{n,-\infty} = (\bar{\rho}_{\infty} + \tilde{\rho}_{\infty})\, U^{\mathrm{Rel}}_{n,\infty} \quad \text{at } X_1 = 0 \tag{7}$$

where $U^{\mathrm{Rel}}_{n,\pm\infty}$ represents the normal velocity components relative to the deforming disk. These velocity components to first order (i.e., small cascade-plane deflection) are equal to

$$U^{\mathrm{Rel}}_{n,-\infty} = \bar{U}_{1,-\infty} + \frac{\partial \tilde{\Phi}_{-\infty}}{\partial X_1} - \frac{\partial \tilde{h}_1}{\partial t} - \bar{U}_{2,-\infty}\frac{\partial \tilde{h}_1}{\partial X_2} \tag{8}$$

$$U^{\mathrm{Rel}}_{n,\infty} = \bar{U}_{1,\infty} + \frac{\partial \tilde{\Phi}_{\infty}}{\partial X_1} - \frac{\partial \tilde{h}_1}{\partial t} - \bar{U}_{2,\infty}\frac{\partial \tilde{h}_1}{\partial X_2} + \tilde{U}^{R}_{1,\infty} \tag{9}$$

where $\tilde{h}_1$ is the displacement of the disk from its mean position in the axial (X_1) direction (Fig. 4).

The next boundary condition requires the total enthalpy with respect to the deforming actuator disk to be locally conserved across the disk. The equivalent mathematical statement is

$$\frac{1}{\gamma-1}\frac{1}{\bar{M}^2_{-\infty}}T_{-\infty} + \frac{1}{2}q^{2,\mathrm{Rel}}_{-\infty} = \frac{1}{\gamma-1}\frac{1}{\bar{M}^2_{-\infty}}T_{\infty} + \frac{1}{2}q^{2,\mathrm{Rel}}_{\infty} \quad \text{at } X_1 = 0 \tag{10}$$

where $T_{\pm\infty}$ is the upstream and downstream gas temperature and $q^{\mathrm{Rel}}_{\pm\infty}$ is the magnitude of the relative velocity approaching and leaving the disk. The expressions for $q^{\mathrm{Rel}}_{\pm\infty}$ are

$$q^{\mathrm{Rel}}_{-\infty} = \left[\left(\bar{U}_{1,-\infty} + \frac{\partial \tilde{\Phi}_{-\infty}}{\partial X_1} - \frac{\partial \tilde{h}_1}{\partial t}\right)^2 + \left(\bar{U}_{2,\infty} + \frac{\partial \tilde{\Phi}_{-\infty}}{\partial X_2} - \frac{\partial \tilde{h}_2}{\partial t}\right)^2\right]^{1/2} \tag{11}$$

$$q^{\mathrm{Rel}}_{\infty} = \left[\left(\bar{U}_{1,-\infty} + \frac{\partial \tilde{\Phi}_{-\infty}}{\partial X_1} + \tilde{U}^{R}_{1,\infty} - \frac{\partial \tilde{h}_1}{\partial t}\right)^2 + \left(\bar{U}_{2,\infty} + \frac{\partial \tilde{\Phi}_{\infty}}{\partial X_2} + \tilde{U}^{R}_{2,\infty} - \frac{\partial \tilde{h}_2}{\partial t}\right)^2\right]^{1/2} \tag{12}$$

where $\tilde{h}_2$ is the local displacement of the cascade in the tangential (X_2) direction (Fig. 4).

The third boundary condition requires that the local inlet and exit flow angles relative to the deforming disk satisfy a deviation angle correlation of the form

$$\delta = g(\alpha, \mathrm{M}_{-\infty}, \mu, \theta') \tag{13}$$

where α is the local, relative incidence angle, $M_{-\infty}$ is the local, relative inlet Mach number, μ is the local solidity of the deformed cascade, and θ' is the local stagger angle measured from the normal to the leading-edge plane (Fig. 4). The local, relative incidence angle is related to the local, relative inlet flow angle $\beta_{-\infty}$ measured from the normal to the leading-edge plane by the equation

$$\alpha = \beta'_{-\infty} - \theta' - \delta_{m_1} \tag{14}$$

The variable δ_{m_1} in this equation is the angle between the chord line and the tangent to the camber line at the leading edge. The corresponding relation for the local deviation angle is

$$\delta = \beta'_{\infty} - \theta' - \delta_{m_2} \tag{15}$$

where β'_{∞} is the local, relative exit flow angle measured from the normal to the trailing-edge plane and δ_{m_2} is the angle between the chord line and the tangent to the camber line at the trailing edge.

Relationships for the angles, inlet Mach number and cascade solidity in the above equations are derived by expanding these variables along with equations (13), (14) and (15) to first order. The details of this expansion can be found in reference [10].

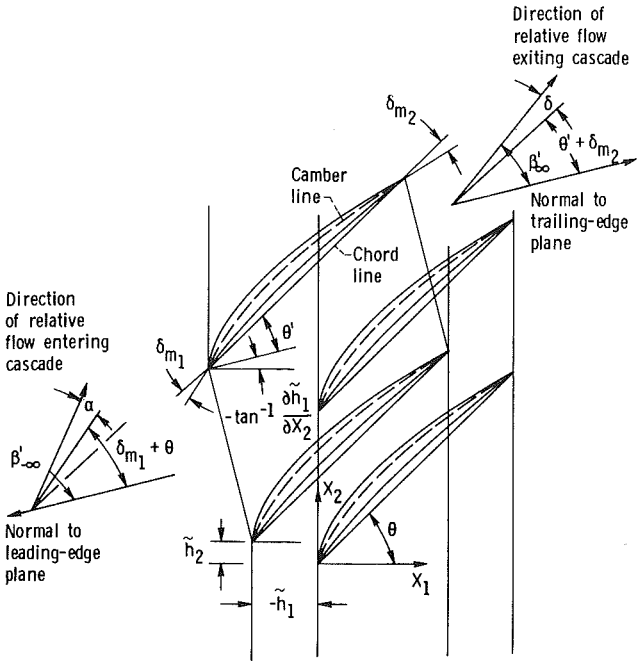

Fig. 4 Geometry of deformed cascade

The last boundary condition specifies the local entropy that is generated as the fluid passes through the cascade. The loss associated with the local entropy rise is defined in terms of a loss coefficient defined as

$$\chi = \frac{P^{\mathrm{Rel}}_{0,-\infty} - P^{\mathrm{Rel}}_{0,\infty}}{\frac{1}{2}\rho_{-\infty}q^{2,\mathrm{Rel}}_{-\infty}} \tag{16}$$

The variable $P^{\mathrm{Rel}}_{0,-\infty} - P^{\mathrm{Rel}}_{0,\infty}$ in this equation represents the local total-pressure loss measured relative to the deforming actuator disk. The entropy rise across the disk is related to this quantity by the equation of state

$$P^{\mathrm{Rel}}_{0,-\infty} - P^{\mathrm{Rel}}_{0,\infty} = P^{\mathrm{Rel}}_{0,-\infty}\left(1 - e^{-\gamma \bar{M}^2_{-\infty} s_{\infty}}\right)$$

Thus s_{∞} must be equal to

$$s_{\infty} = -\frac{1}{\gamma \bar{M}^2_{-\infty}}\ln\left(1 - \frac{1}{2}\frac{\rho_{-\infty}q^{2,\mathrm{Rel}}_{-\infty}\chi}{P_{0,-\infty}}\right) \tag{17}$$

The analysis assumes that the local loss coefficient χ is related to the local inlet flow field, as observed with respect to the deforming disk, by a relationship of the form

$$\chi = \chi(\alpha, \mathrm{M}_{-\infty}, \mu, \theta') \tag{18}$$

As in equation (13) the parameters appearing in this equation can be related to the unsteady flow field approaching the cascade and the cascade deformation. Upon combining equation (17) with equation (18) the entropy rise across the cascade can be evaluated in terms of these perturbed quantities.

Aerodynamic Force. Having described the procedure for determining the flow field surrounding the cascade, the unsteady forces acting on the cascade and hence its stability can be assessed. The aerodynamic force acting on the cascade is obtained by considering the flow field through a control

volume that is fixed to a cascade passage (Fig. 3). The present analysis assumes that the relative motion between neighboring airfoils, a measure of which is the interblade phase angle, is small and that the reduced frequency of this motion is also small. The first assumption implies that the spatial variations of the flow variables across a cascade passage are small and thus can be neglected. The low-frequency assumption suggests that the rate of change of mass and momentum within the control volume is smaller than the net mass and momentum flux across the control volume surface and thus will also be neglected. Based on these considerations the linearized momentum equation for the control volume illustrated in Fig. 3 can be written as

$$F_1 = (\tilde{p}_\infty - \tilde{p}_{-\infty})\,\tau + (\bar{p}_\infty - \bar{p}_{-\infty})\,\tilde{\tau} + \tilde{W}^{\mathrm{Rel}}(\bar{U}_{1,\infty} - \bar{U}_{1,-\infty}) + \bar{W}(\tilde{U}_{1,\infty} - \tilde{U}_{1,-\infty}) \tag{19}$$

$$\tilde{F}_2 = (\tilde{p}_\infty - \tilde{p}_{-\infty})\,\tau \tilde{n}_2 + \tilde{W}^{\mathrm{Rel}}(\bar{U}_{2,\infty} - \bar{U}_{2,-\infty}) + \bar{W}(\tilde{U}_{2,\infty} - \tilde{\mathrm{H}}_{2,-\infty}) \tag{20}$$

where $\tilde{F}_i$ is the force exerted by the airfoils on the control volume, τ is the pitch of the cascade, W^{Rel} is the mass flow exiting the control volume, and n_i is the unit vector normal to the exit plane of the control volume. (This equation can be derived by expanding the quasi-steady momentum equations for the control volume shown in Fig. 3 to first order in perturbed variables. The details can be found in reference [10].)

The work done by the aerodynamic force on an airfoil over a cycle of motion is equal to

$$W_{\mathrm{Aero}} = -\frac{1}{2}\,\Re e\left[\int_0^{2\pi/k}\left(\tilde{F}_1\frac{\partial \tilde{h}_1^*}{\partial t} + \tilde{F}_2\frac{\partial \tilde{h}_2^*}{\partial t}\right)dt\right] \tag{21}$$

where $\Re e\,[\ ]$ denotes the real part of the expression and the asterisk superscript signifies the complex conjugate of the variable. The airfoil's motion can be described by

$$\tilde{h}_1 = h_1 e^{ik_2X_2}e^{ikt}$$

$$\tilde{h}_2 = h_2 e^{ik_2X_2}e^{ikt}$$

where k_2, the wave number in the X_2 direction, is equal to $k_2 = 2\pi n$. Equation (21) can be integrated to yield

$$W_{\mathrm{Aero}} = -\ell m(\tilde{F}_i\tilde{h}_i^*) \tag{22}$$

where $\ell m\,[\ ]$ represents the imaginary part of the expression within the brackets. At the onset of flutter the aerodynamic work per cycle is equal to the mechanical energy dissipated over a cycle. If the mechanical dissipative force is proportional to the velocity of the airfoil, the mechanical energy dissipated over a cycle of motion is

$$W_D = \frac{C}{2\bar{\rho}_{-\infty}q_{-\infty}d}\,\Re e\left[\int_0^{2\pi/k}\left(\frac{\partial \tilde{h}_1}{\partial t}\frac{\partial \tilde{h}_1^*}{\partial t} + \frac{\partial \tilde{h}_2}{\partial t}\frac{\partial \tilde{h}_2^*}{\partial t}\right)dt\right] \tag{23}$$

where the damping coefficient C is defined as

$$C = \frac{\delta M_b}{2\pi}k\frac{\bar{q}_{-\infty}}{d} \tag{24}$$

The variable δ in this equation is the log decrement of the mechanical damping, and M_b is the mass per unit length of a rotor blade. This variable is defined as

$$M_b = K\rho_b\tau c \tag{25}$$

where K is a constant of proportionality, ρ_b is the blade density, τ is the average thickness of the blade, and c is its average chord length. Introducing this equation along with equation (24) into the integrated form of equation (23) yields

$$W_D = 2\delta k\left(\frac{\rho_b}{\bar{\rho}_{-\infty}}\right)\frac{\tau}{c}k_b^2(\tilde{h}_1\tilde{h}_1^* + \tilde{h}_2\tilde{h}_2^*) \tag{26}$$

Equating equation (26) with equation (22) and solving for δ establishes the minimum level of mechanical damping required for stability at an operating point as

$$\delta_{\mathrm{Onset}} = -\frac{\pi}{2K}\left(\frac{\rho_{-\infty}}{\rho_b}\right)\frac{1}{\frac{\tau}{c}}\,\frac{1}{k_b^2(h_1h_1^* + h_2h_2^*)}\,\mathrm{Min}_{k_2}\,[\ell m(\tilde{F}_2\tilde{h}_2^*)] \tag{27}$$

The symbol Min_{k_2} denotes the minimum value of the function with respect to k_2. If the available mechanical damping of a rotor blade exceeds this critical level, any small bending motion imparted to the blade will decay in time. Hence the system is stable and flutter will not occur. However, if δ_{Onset} is greater than the available mechanical damping of a rotor blade, any small bending motion imparted to the blade will cause the blade to flutter.

Results

For the flutter mode under study the amplitude of the motion increases monotonically along the blade span from the node line. For blades that are rigidly fixed at their root (i.e., mechanically constrained), the node line can be assumed to lie outboard of the blade platform (i.e., outboard of the aerodynamic hub of the blade). The node line of the first flexural mode of the rotor to be investigated later in this section is approximately 20 percent of span height outboard of the platform. Thus, the vibratory motion of the blade in the rotor at any spanwise section is

$$h_1 = -\xi\sin\bar{\theta}'(20\%) \tag{28}$$

$$h_2 = \xi\cos\bar{\theta}'(20\%) \tag{29}$$

where ξ is the amplitude of the motion at the section and $\theta'(20\%)$ is the stagger angle at 20 percent of span.

The aerodynamic work per unit of span at a given radial location depends on the amplitude of the motion of the section and the relative dynamic pressure of the incoming streamline to the section. Thus because both increase with distance from the hub, the total work done by the airstream on a blade is strongly influenced by the unsteady flow field surrounding the tip region. A simple calculation shows that this influence is concentrated in the outer 25 percent of the span. If the outer-casing boundary layer is assumed to influence the flow field over 5 percent of the tip region of a blade, a direct correlation might exist between the flutter boundary of a rotor and a two-dimensional cascade whose geometry and dynamic response coincide with that of the rotor at 85 percent of span (i.e., algebraic mean of 75 and 95 percent of span). The results presented in the remainder of this section are based on this premise.

The objective of the first series of calculations is to establish the influence of reduced frequency k_b and interblade phase angle on the aeroelastic stability of a cascade of airfoils. For this study a normalized damping parameter defined as

$$\delta_N = -\frac{1}{2}\,\frac{\bar{\rho}_{-\infty}}{\bar{\rho}_{0,\mathrm{Amb}}}\,\frac{1}{k_b^2}\,\frac{\pi}{\bar{\xi}}\left[-\sin\bar{\theta}'(20\%)\ell m(\tilde{F}_1e^{-ik_2X_2}e^{-ikt}) + \cos\bar{\theta}'(20\%)\ell m(\tilde{F}_2e^{-ik_2X_2}e^{-ikt})\right] \tag{30}$$

is calculated as a function of k_b and the interblade phase angle. The parameter $\bar{\rho}_{0,\mathrm{Amb}}$ in this equation is the inlet

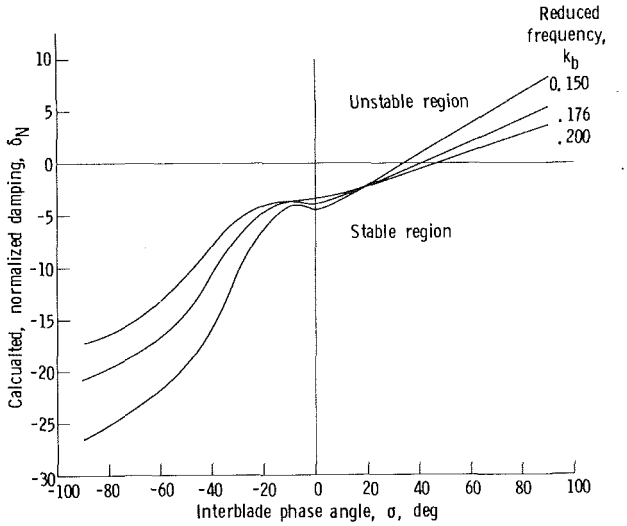

Fig. 5 Calculated, normalized damping as a function of interblade phase angle and reduced frequency for NASA two-stage fan.

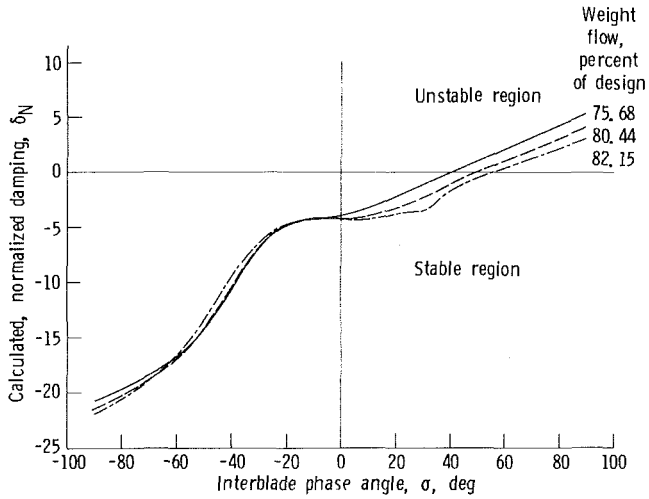

Fig. 6 Calculated, normalized damping as a function of interblade phase angle and weight flow for NASA two-stage fan at 85 percent of design wheel speed

stagnation density measured in the absolute coordinate system. For δ_N greater than zero the airstream is supplying energy to the cascade. If the mechanical damping of the cascade system is zero, the operating condition would be unstable. For values of δ_N less than zero the cascade is doing work on the airstream, and hence the system is stable.

Solving equation (30) requires as input information the steady-state inlet flow properties, the geometry of the cascade, and the frequency of oscillation. A set of loss and deviation-angle correlations must also be specified. The present analysis makes use of the correlations derived in reference [10]. The steady-state inlet flow conditions are derived from the blade-element data, measured at 85 percent of design speed, of the second stage of the NASA 1450-ft/sec-tip-speed two-stage fan. This blade-element data set is reported in reference [5]. The cascade geometry represents the geometry of the second-stage rotor element at 85 percent of span height from the hub.

Figure 5 shows a plot of δ_N as a function of interblade phase angle and reduced frequency k_b for the second stage rotor operating at the flutter-boundary at 85 percent of design speed. This figure shows that the bending flutter mode is

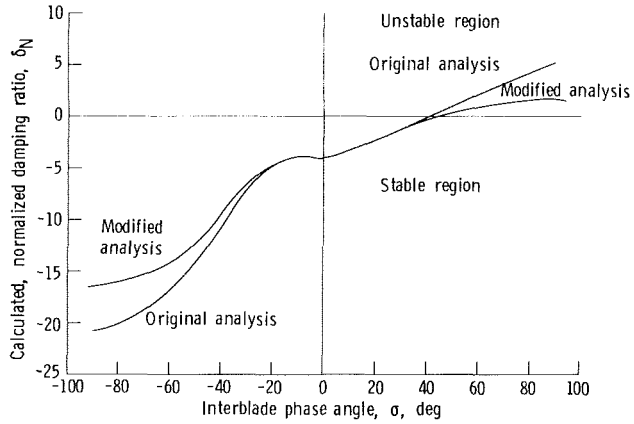

Fig. 7 Original and modified analyses for NASA two-stage fan at 85 *percent of design wheel speed and 75.68 percent of design weight flow*

associated with a positive interblade phase angle (i.e., implies that the vibration pattern is traveling around the rotor in the direction of rotation). The figure also shows that increasing the reduced frequency stabilizes the motion at a constant interblade phase angle.

Figure 6 shows a plot of δ_N as a function of interblade phase angle and percentage of design weight flow along the 85-percent-speed line. For a given interblade phase angle, decreasing the weight flow at constant wheel speed (i.e., increasing the steady-state aerodynamic loading) tends to destabilize the rotor.

The results presented in Figs. 5 and 6 are also consistent with the observed characteristics of supersonic bending flutter reported in reference [7].

A deficiency of the present theory, as shown by the results in Figs. 5 and 6, is that it predicts the damping, δ_N to increase monotonically with interblade phase angle. This trend is physically unrealistic, and is a consequence of the small interblade phase angle assumption inherent in actuator disk theory. To overcome this deficiency an additional assumption was incorporated into the theory which limited the value of the aerodynamic damping. The assumption is made to replace σ by sin σ everywhere in the analysis. This assumption is mathematically constant with the actuator disk model. Figure 7 shows the results obtained with this assumption incorporated into the analysis. For $|\sigma| \leq 45$ deg, the modified analysis yields results that are comparable to those obtained from the original formulation. In addition the modified analysis predicts a finite maximum value for δ_N for $\sigma = 90$ deg. This maximum value for damping is equal to the value computed at $\sigma = 1$ radian using the original formulation. Experimental results of reference [7] show that this value for σ (i.e., $\sigma = 1$ radian) corresponds rather closely to the measured interblade phase angle of the least stable flutter mode.

An additional validation of the modified analysis as a flutter prediction system for supersonic stall bending flutter can be established by showing that, for a given rotor, flutter will be observed whenever the predicted maximum value of δ_N exceeds the normalized structural damping of a rotor assembly. For this demonstration the measured flutter boundary of a scaled model of Fan C of the NASA Quiet Engine Program [6] is correlated with the predicted boundary. The performance map for the scale model (Fig. 8) shows two flutter instability zones. The first zone is torsional flutter that occurs at part speed and lies close to the stall line. Just above this zone lies a zone of bending flutter that appears to extend past 95 percent of design speed. Only the bending flutter mode of this rotor is analyzed in this paper.

Figure 9 shows a plot of the phase shift between the amplitude time history of a rotor blade and the reference blade

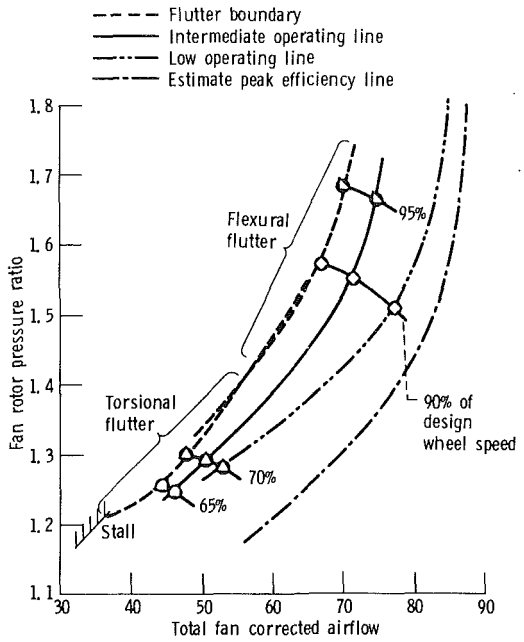

Fig. 8 NASA rotating rig, fan C model

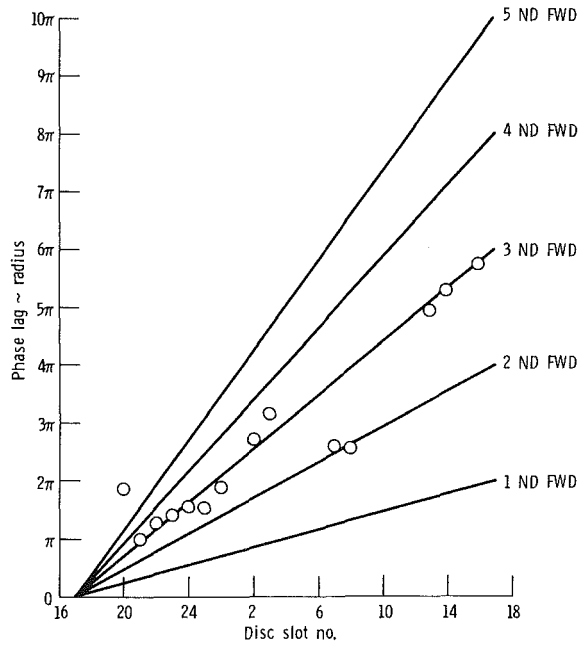

Fig. 9 Rotating rig blade phase data 95 percent speed, flexural flutter

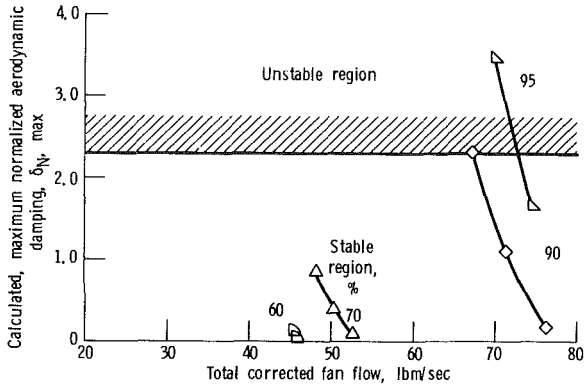

Fig. 10 Maximum normalized damping as a function of weight flow and wheel speed for fan C model

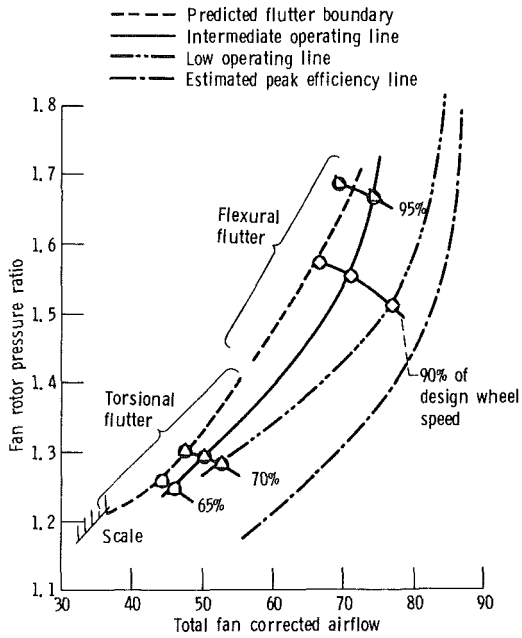

Fig. 11 NASA rotating rig, fan C model

No. 17 at the 95 percent of the design speed flutter point. The data implies the flutter mode is predominately a 3 nodal diameter forward traveling wave which corresponds to an interblade phase angle of approximately 41 deg. This value for the interblade phase angle of the flutter mode correlates well with the data of reference [7] and lies within the unstable range predicted by the analysis. Figure 10 shows the calculated maximum normalized aerodynamic damping for this rotor as a function of weight flow and wheel speed. The results presented on this curve were calculated using the blade element data recorded at the five operating condition shown on Fig. 8. The shaded region on Fig. 10 represents the unstable flutter region. The boundary of this region was estimated by assuming a log decrement of 0.025 for the mechanical damping of the assembly [3]. Hence, all operating conditions which have an aerodynamic damping level in excess of this value are assumed to be within the flutter region, while those that have an aerodynamic damping level less than 0.025 are stable.

The results on Fig. 10 clearly show the significant influence of wheel speed and aerodynamic loading on the aerodynamic damping. The calculated aerodynamic damping at 60 and 70 percent wheel speed lie significantly below the instability boundary. No bending flutter was observed at these operating conditions. At 90 percent of design speed bending flutter was observed near the stall region. The calculated aerodynamic damping for the near stall operating point is seen to lie just inside the unstable region. Bending flutter was also observed at 95 percent of design speed near the stall boundary. The calculated aerodynamic damping for this operating point lies well within the unstable region of Fig. 10. At the intermediate operating point on the 95 percent speed line the calculated aerodynamic damping falls below the instability boundary. Therefore the predicted flutter boundary at this wheel speed lies between the measured flutter boundary and the intermediate operating point. Transcribing the stability boundary of Fig. 10 onto the Fan C performance map yields at theoretical flutter boundary, which is shown as a dashed

line on Fig. 11. The measured operating conditions at which bending flutter occurred are shown on this figure as solid symbols. The overall agreement between theory and measurement is very good, with the analysis slightly over predicting the extent of the flutter boundary at 95 percent of wheel speed. Below 90 percent of wheel speed the analysis predicts the flutter boundary will bend back into the stall region. This result is confirmed by the experimental measurements.

The results presented in this section clearly show that the current analysis can be used to predict the onset of supersonic bending flutter in unshrouded fans. The input variables to the analysis can all be derived from fan structural and aerodynamic design variables. The governing equations are simple algebraic equations, and hence are easily programmed. These features provide the designer with a simple and reliable model for analyzing the susceptibility of a fan design to supersonic stall bending flutter. In addition it provides him with a tool that can also be used to evaluate proposed fixes to an existing flutter problem.

The engineering approximation introduced to extended the range of validity of actuator disk theory appears reasonable. To develop a correct first principles extension of actuator disk theory to finite interblade phase angle for the flow conditions as they exist at the tip of a rotor at the onset of supersonic stall flutter would require a viscous transonic cascade analysis for finite interblade phase angle. No such analysis appears to be forthcoming in the near future. Any extension which is derived from inviscid aerodynamic theory would be an approximation, the result perhaps being no more accurate than the simple extension developed in this analysis.

Concluding Remarks

In the present investigation an analytical model was developed to predict the onset of supersonic stall bending flutter in high-speed rotors. The stability boundary predicted by the analysis was shown to be in good agreement with the measured boundary of a high speed fan. The analysis also predicted that the flutter mode would be a forward traveling wave, be sensitive to wheel speed and aerodynamic loading. This was confirmed by the experimental measurements. In addition the analysis showed that reduced frequency and dynamic head also play a significant role in establishing the supersonic stall bending flutter boundary of an unshrouded fan.

This analysis provides the designer with a simple and efficient prediction tool which he can use to analyze the susceptibility of a fan design to supersonic stall bending flutter.

References

1 Kurosaka, M., "On the Unsteady Supersonic Cascade with a Subsonic Leading Edge—An Exact First Order Theory: Parts 1 and 2," ASME JOURNAL OF ENGINEERING FOR POWER, Vol. 96, No. 1, Jan. 1974, pp. 13-31.

2 Verdon, J. M., and McCune, J. E., "Unsteady Supersonic Cascade in Subsonic Axial Flow," *American Institute of Aeronautics and Astronautics Journal,* Vol. 13, No. 2, Feb. 1975, pp. 193-201.

3 Snyder, L. E., and Commerford, G. L., "Supersonic Unstalled Flutter in Fan Rotors; Analytical and Experimental Results," ASME JOURNAL OF ENGINEERING FOR POWER, Vol. 96, No. 4, Oct. 1974, pp. 379-386.

4 Goldstein, M. E., Braun, W., and Adamczyk, J. J., "Unsteady Flow in a Supersonic Cascade with Strong In-Passage Shocks," *Journal of Fluid Mechanics,* Vol. 83, Pt. 3, Dec. 5, 1977, pp. 569-604.

5 Ruggeri, R. S., and Benser, W. A., "Performance of a Highly Loaded Two-Stage Axial-Flow Fan," NASA TM X-3076, 1974.

6 Griffin, R. G., Parker, D. E., and Dunbar, L. W., "Experimental Quiet Engine Program Aerodynamic Performance of Fan C," General Electric Co., NASA CR-120981, Cincinnati, Ohio, Aug. 1972.

7 Loiseau, H., and Maquennehan, B., "Aeroelastic Instabilities in Compressors and Tests in a Rectilinear Blade Cascade Wind Tunnel," *Revue Francaise de Mecanique,* Special Issue, 1976, pp. 157-167.

8 Whitehead, D. S., "Bending Flutter of Unstalled Cascade Blades at Finite Deflection," *R&M-3386, British Aeronautical Research Council, 1965.*

9 Whitehead, D. S., "The Vibration of Cascade Blades Treated by Actuator Disc Methods," *Institution of Mechanical Engineers (London), Proceedings,* Vol. 173, No. 20, 1959, pp. 555-563.

10 Adamczyk, J. J., "Analysis of Supersonic Stall Bending Flutter in Axial-Flow Compressor by Actuator Disk Theory," NASA TP-1345, 1978.

11 I. A. Johnsen, and R. O. Bullock, "Aerodynamic Design of Axial-Flow Compressors," eds., NASA SP-36, 1965.

The Influence of Unsteady Rotor Response on a Distorted Flow Field

R. E. Henderson
Associate Director,
Garfield Thomas Water Tunnel, and
Professor of Mechanical Engineering,
Mem. ASME

I. C. Shen
Graduate Assistant.

Applied Research Laboratory,
The Pennsylvania State University,
State College, Pa. 16801

The influence of the unsteady rotor response on the shape of stagnation pressure and axial velocity distortions passing through an axial flow rotor are investigated. Experimental data obtained with an isolated rotor in an incompressible, distorted inflow demonstrate that the magnitude of the distortion downstream of the rotor is a strong function of the ratio of the blade spacing s to the distortion wavelength l_n. An existing actuator disk analysis based on a quasi-steady model of the rotor response and used extensively to predict the downstream distortion, has been extended to include the unsteady response of the rotor. By examining a series of sinusoidal distortions of varying wavelength, a semi-actuator disk analysis, which includes the unsteady rotor response, is shown to predict the same trend with s/l_n as exhibited by the experimental data.

Introduction

In the design of a turbomachine, the pressure, velocity, and temperature at the inlet are assumed to be steady and axisymmetric. In some cases this is a very valid assumption at the design operating point. In many other cases and under certain operating conditions, the inlet flow will exhibit either, or both, circumferential and radial nonuniformities or distortions. Time-independent radial distortions, such as those caused by wall boundary layers, can be accounted for in the design. However, the existence of wall separation in the flow delivery system, armament firings, and wakes from upstream blades or supports means that the flow is circumferentially nonuniform. Hence, the flow through a rotor or impeller is unsteady.

The significance of both circumferential and radial distorted inlet flows in turbomachines has been the subject of many publications. Recent publications by Stenning [1] and Greitzer [2] summarize the influence of circumferential inlet distortions on the performance of axial-flow compressors. The consequences of a compressor operating in a circumferentially distorted inflow are performance degradation and blade vibration. It is therefore important for the turbomachinery designers to be able to predict both the influence of the distorted inflow on the turbomachine blades, i.e., the unsteady forces and pressures and the occurrence of stall, and the influence of the blades on the distortion, i.e., is the distortion amplified or attenuated as it passes through the blades? This latter capability is especially important for multistage machines.

As summarized in references [1 and 2], the literature describes several methods for predicting the consequences of the interaction of a circumferentially distorted inflow with an axial-flow compressor. These methods are based on either a parallel-compressor model [3-5], or an actuator disk model [3, 6, 8]. Both of these models require a knowledge of the compressor operating characteristic, pressure rise ψ versus flow coefficient ϕ, when operated in a circumferentially uniform inflow. In these models the influence of the unsteady response of the blades is included as an instantaneous or quasi-steady change in flow coefficient ϕ' from the circumferential uniform value $\bar{\phi}$. The influence of ϕ' is determined from the uniform-flow operating characteristic by determining the resultant value of $\psi = \bar{\psi} + \psi'$ at $\phi = \bar{\phi} + \phi'$. In some cases the effect of fluid acceleration through the blades is also included [5]. This results in a model that ignores the unsteady blade-to-blade interaction and the vorticity shed in the wakes of the blades. Thus, the unsteady affect is approximated only when the wavelength of the distortion in the direction of blade motion l is much larger than the blade spacing s.

The restriction that $l >> s$ has been demonstrated to be inconsequential for square-wave distortions that cover more than 60 degrees of the compressor circumference [1, 3, 8]. For a typical aircraft compressor this would correspond to values of $l > 5\ s$, making the distorted inflow essentially uniform over five successive blade channels. With the inclusion of the effects of fluid axial acceleration, Mazzawy [5] estimates that square-wave distortions, where $l > 2\ s$, can be predicted using the multiple-segment, parallel-compressor model.

However, if the distortion is not a square-wave form but, rather, a sinusoidal form like that from the wakes of upstream struts or stator blades, the unsteady response of the rotor is not quasi-steady and must be predicted using an unsteady cascade model such as described in references [9 through 11].

Contributed by the Gas Turbine Division and presented at the International Gas Turbine Conference and Products Show, Houston, Texas, March 9-12, 1981, of THE AMERICAN SOCIETY OF MECHANICAL ENGINEERS. Manuscript received at ASME Headquarters, December 22, 1980. Paper No. 81-GT-185.

This is demonstrated in Reference 12 where it is shown that the quasi-steady actuator disk model over predicts by approximately 40 percent the amplitude of a sinusoidal total pressure distortion down-stream of an isolated rotor when $s/l_n = 0.33$. Further reference [12] shows that the measured amplitude of the distortion downstream of the rotor is also a function of the rotor stagger angle and solidity, and its attenuation approaches a maximum at $s/l_n = 0.5$.

The method presented in this paper is an extension of the quasi-steady actuator disk model described by Mokelke [3] which includes the unsteady response of a cascade. This work employs the analysis of Horlock and Daneshyar [13], which describes the changes in time-mean stagnation pressure downstream of a cascade with unsteady lift, plus the unsteady cascade model described in references [10, 14, and 15]. The analysis of reference [13] shows that these changes in stagnation pressure are a function of the unsteady blade circulation at the cascade trailing edge. In reference [16], this approach has been used to derive the unsteady circulation from measurements of the change in time-mean stagnation pressure.

Unsteady Semi-Actuator Disk Model

The assumptions employed in the quasi-steady actuator disk model described in reference [3] are:

1 The flow is two-dimensional, incompressible, and inviscid.
2 The flow field can be broken into regions upstream and downstream of the blade rows with each blade row represented by an actuator disk of infinitesimal axial length, i.e., zero chord length.
3 The amplitude of the time-mean pressure and velocity variations are small compared to the circumferential mean values, i.e., $p = \bar{p} + p'$ and $v = \bar{v} + v'$.
4 The blade rows respond quasi-steadily to the distorted inflow.

The present analysis also employs assumptions 1 and 3. However, assumption 2 has been altered by considering the actuator disk to be located at the mid-chord of the blade row, thus maintaining the finite chord length of the blades. Horlock [17] describes this semi-actuator disk model as more representative of the actual case. Further, the response of the blade row to the distorted inflow is modeled as an unsteady rather than a quasi-steady response.

Flow-Field Equations. Assumption 1 allows the equations describing the flow field upstream and downstream of the blade row to be written in a simplified form. Assumption 3 linearizes these equations by considering the pressure and velocities of these flow regions to be a circumferential mean plus a perturbation contribution. If the linearized representation of the pressure and velocity are nondimensionalized by circumferential mean axial velocity $\bar{v}_x$ and substituted into the equations describing the flow field, the following perturbation equations are obtained [3]:

Conservation of Mass:

$$\frac{\partial V_\theta'}{\partial \theta} + \frac{\partial V_x'}{\partial X} = 0 \tag{1a}$$

X-Momentum:

$$2a\left(\frac{\partial V'_x}{\partial \theta} - \frac{\partial V_\theta'}{\partial X}\right) = -\frac{\partial P_T'}{\partial X} \tag{1b}$$

θ-Momentum:

$$2\left(\frac{\partial V_x'}{\partial \theta} - \frac{\partial V_\theta'}{\partial X}\right) = \frac{\partial P_T'}{\partial \theta}. \tag{1c}$$

As discussed by Mokelke [3], the solution of these equations can be expressed in term of an infinite series summed on an index n that represents the Fourier harmonics of P_T', V_x', V_θ'. For each Fourier harmonic, three coefficients must be determined from the boundary conditions and the "matching" conditions across the blade row. As will be described below, these matching conditions link the flow regions upstream and downstream of the blade row and will be used to introduce the unsteady response of the blade row to the distortion. Assuming a quasi-steady response, Mokelke is able to obtain a solution for the compressor with circumferentially distorted flow. In a latter publication [8], this solution is extended to include compressible flows.

The present method will continue to employ the assumption that the flow is incompressible and will also be restricted to a situation for a single or isolated rotor. There appears to be no reason why this method could not be extended to consider multistage machines, however. The matter of compressibility is different, however, since the unsteady cascade analyses to be employed are derived for only an incompressible flow.

For an incompressible flow through an isolated rotor, the solutions obtained for equations (1*a*), (1*b*), and (1*c*) are:

Nomenclature

a = circumferential mean swirl factor ($= \bar{v}_\theta/\bar{v}_x$)
c = blade chord length
h = axial blade length/radius
l_n = wavelength of nth harmonic of distortion inflow in circumferential direction
n = harmonic number
p_s = pressure
p_T = stagnation pressure
P_s = nondimensional pressure ($= p_s/\frac{1}{2}\rho\bar{v}_x^2$)
P_T = nondimensional stagnation pressure ($= p_T/\frac{1}{2}\rho\bar{v}_x^2$)
δP_T = stagnation pressure loss
ΔP_T = nondimensional stagnation pressure rise
r = radius
s = blade spacing
U = blade speed ($= \Omega r$)
v = velocity
w_{d_n} = velocity distortion amplitude of nth harmonic from mean value
V = nondimensional velocity ($= v/\bar{v}_x$)
x = axial direction
X = nondimensional axial position ($= x/r$)
β = time-mean relative fluid angle
Γ = blade circulation
η = streamline coordinate/radius
θ = circumferential coordinate
ξ = stagger angle
ρ = fluid density
τ_n = intrablade frequency, nth harmonic ($= -2\pi s/l_n$)
ϕ = flow coefficient ($= \bar{v}_x/U$)
ψ_n = circulation influence factor (defined equation 14)
ω_n = reduced frequency, nth harmonic $\left(= \frac{\pi c}{l_n}\sin\xi\right)$
Ω = angular velocity

Subscripts

x = axial
θ = circumferential
u = upstream of rotor
d = downstream of rotor
n = harmonic number
l = leading edge
t = trailing edge

Superscripts

$\bar{}$ = circumferential mean
$'$ = perturbation
$\tilde{}$ = unsteady
$\hat{}$ = amplitude

Upstream of Rotor (u):

$$P'_{T_u}(X,\theta) = 2(1+a_u^2)\sum_{n=1}^{\infty} A_{3_{n_u}} e^{ina_u X} e^{in\theta}$$

$$V'_{x_u}(X,\theta) = \sum_{n=1}^{\infty}\left\{A_{1_{n_u}} e^{nX} + A_{3_{n_u}} e^{-ina_u X}\right\} e^{in\theta} \tag{2}$$

$$V'_{\theta_u}(X,\theta) = \sum_{n=1}^{\infty}\left\{iA_{1_{n_u}} e^{nX} + a_u A_{3_{n_u}} e^{-ina_u X}\right\} e^{in\theta}$$

Downstream of Rotor (d):

$$P'_{T_d}(X,\theta) = 2(1+a_d^2)\sum_{n=1}^{\infty} A_{3_{n_d}} e^{-ina_d X} e^{in\theta}$$

$$V'_{x_d}(X,\theta) = \sum_{n=1}^{\infty}\left\{-A_{2_{n_d}} e^{-nX} + A_{3_{n_d}} e^{-ina_d X}\right\} e^{in\theta} \tag{3}$$

$$V'_{\theta_d}(X,\theta) = \sum_{n=1}^{\infty}\left\{iA_{2_{n_d}} e^{-nX} + a_d A_{3_{n_d}} e^{-ina_d X}\right\} e^{in\theta}.$$

As input to the problem, the circumferential variation of $P'_T(X, \theta)$ far upstream of the rotor ($X = -\infty$) is specified. This determines the coefficient $A_{3_{n_u}}$. The remaining coefficients are determined by satisfying the matching conditions across the rotor.

Matching Conditions. To determine the coefficients $A_{1_{n_u}}$, $A_{2_{n_d}}$, and $A_{3_{n_d}}$, it is necessary to relate P'_{T_u}, V'_{x_u}, and V'_{θ_u} and P'_{T_d}, V'_{x_d}, and V'_{θ_d} at the leading edge (l) and trailing edge (t) of the rotor. For the quasi-steady actuator disk method, this is done by using the law of conservation of mass to relate V'_{x_u} and V'_{x_d}, the laws of conservation of energy and angular momentum to relate P'_{T_u} and P'_{T_d}, and the inlet and exit relative fluid angles (β_l and β_t) measured in a uniform flow to relate V'_{θ_u} and V'_{θ_d}. For the unsteady, semiactuator disk method, a similar approach is followed to relate V'_x and P'_T, except that an additional term derived by Horlock and Daneshyar [13] is included to account for the time-mean stagnation pressure contributed by the unsteady response of the blades. The velocity components in the circumferential direction V'_θ are related to the unsteady circulation on the blades. Thus, the only dependence upon available experimental data is for the inclusion of the stagnation pressure loss through the blades.

Relation of V'_{x_u} and V'_{x_d}. By applying the law of conservation of mass between the leading and trailing edges of the cascade shown in Fig. 1, the assumption that the flow field is linear results in two conditions that relate the circumferential-mean and perturbation components of V_x,

$$\begin{aligned} \bar{V}_{x_l} &= \bar{V}_{x_t} \\ V'_{x_l} &= V'_{x_t}. \end{aligned} \tag{4}$$

Relation of P'_{T_u} and P'_{T_d}. Between the leading and trailing edges of the cascade in Fig. 1, the law of conservation of energy can be expressed as

$$P_{T_l} + \Delta P_T = P_{T_t} + \delta P_T, \tag{5}$$

where ΔP_T is the ideal stagnation pressure rise across the moving cascade, and δP_T is the stagnation pressure loss.

The term ΔP_T represents the energy addition to the fluid per unit mass and can be expressed as

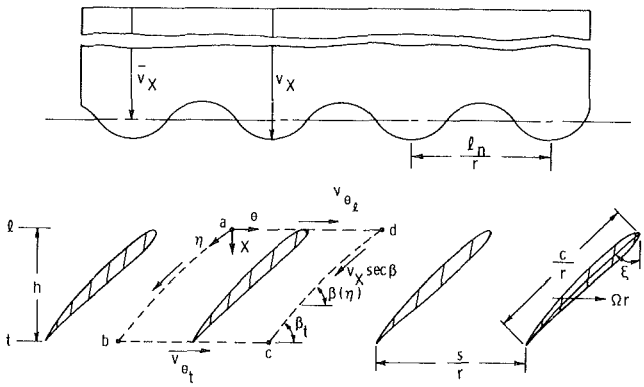

Fig. 1 Development of rotor blade on a surface of radius r

$$\Delta P_T = \overline{\Delta P}_T + \Delta P'_T.$$

The $\overline{\Delta P}_T$ contribution can be expressed by the law of conservation of angular momentum (Euler's pump equation) as

$$\overline{\Delta P}_T = \frac{U}{\bar{v}_x}(\bar{V}_{\theta_l} - \bar{V}_{\theta_t}) = \frac{1}{\bar{\phi}}(\bar{V}_{\theta_l} - \bar{V}_{\theta_t})$$

The term $\Delta P'_T$ is the contribution of the unsteady forces (circulation) on the blades to the time-mean stagnation pressure rise through the cascade. From reference [13],

$$\Delta P'_T = \frac{U}{s\bar{v}_x{}^2}\tilde{\Gamma}_t, \tag{6}$$

where $\tilde{\Gamma}_t$, the unsteady circulation of the cascade blades, is referenced to the blade trailing edge.

By writing $\delta P_T = \overline{\delta P}_T + \delta P'_T$ and substituting the foregoing expressions for $\overline{\Delta P}_T$ and $\Delta P'_T$ into equation (5), the following mean and perturbation matching conditions are obtained, respectively,

$$\bar{P}_{T_l} + \frac{1}{\bar{\phi}}(\bar{V}_{\theta_t} - \bar{V}_{\theta_l}) = \bar{P}_{T_t} + \overline{\delta P}_T \tag{7}$$

$$P'_{T_l} + \frac{\tilde{\Gamma}_t}{s\bar{v}_x\bar{\phi}} = P'_{T_t} + \delta P'_T \tag{8}$$

These expressions are identical to those employed by Mokelke [3] when the axial length of the actuator disk h is $0(\epsilon)$ or if $l >> s$. In reference [3], the second term on the right-hand side of equation (8) is given as $1/\bar{\phi}\ [V'_{\theta_t} - V'_{\theta_l}]$ (see the Appendix).

Relation of V'_{θ_u} and V'_{θ_d}. The third required matching condition relates V'_{θ_u} to V'_{θ_d}. In the quasi-steady actuator disk model this is accomplished by conducting an experimental evaluation of the rotor, or stage, in an undistorted, uniform, inlet flow to determine the variation of the exit fluid angle β_t as a function of the inlet fluid angle β_l. From these data and the construction of the velocity diagrams, V'_{θ_l} and V'_{θ_t} can be related. This step, plus the assumption of an actuator disk of infinitesimal axial length, makes the analysis of reference [3] quasi-steady.

The approach taken in the present analysis is to assume a semi-actuator disk model in which blades have a finite chord length c, and the energy addition is accomplished by a discontinuity (actuator disk) located at the blade mid-chord. The third matching condition is then obtained by relating the total circulation on the cascade blades—mean plus unsteady ($\Gamma = \bar{\Gamma} + \tilde{\Gamma}$)—to the velocities of the flow field at the leading and trailing edges of the blades. This relationship is derived in the Appendix,

$$\frac{\Gamma}{s\bar{v}_x\bar{\phi}} = \frac{1}{\bar{\phi}}[\bar{V}_{\theta_t} - \bar{V}_{\theta_l}] + \frac{1}{\bar{\phi}}[V'_{\theta_t} - V'_{\theta_l}] + \frac{rV'_x}{s\bar{\phi}}\psi_n \quad (9)$$

where ψ_n is defined by equation (14). The resulting mean and perturbation matching conditions are

$$\frac{\bar{\Gamma}}{s\bar{v}_x} = \bar{V}_{\theta_t} - \bar{V}_{\theta_l} \quad (10)$$

$$\frac{\tilde{\Gamma}_{n_t} e^{-i2\omega_n}}{s\bar{v}_x} = [V'_{\theta_t} - V'_{\theta_l}] + \frac{rV'_x}{s}\psi_n. \quad (11)$$

The employment of equation (11) requires a knowledge of the unsteady circulation on the blades.

Prediction of Unsteady Circulation in a Cascade. The unsteady circulation in a cascade required in the matching condition described by equation (11) can be predicted by the analysis of the unsteady cascade response described in references [10, 14, or 15]. This analysis considers the two-dimensional, incompressible, inviscid flow through a cascade of thin airfoils with small camber; therefore, it is a linearized, small-perturbation analysis. The cascade is modeled by continuous distribution of vorticity on the primary blade and in the wakes of all the blades. The bound vorticity on the neighboring blades is modeled by a single vortex located at the quarter-chord of each blade. The strength of each vortex is variable and a function of the intrablade frequency, i.e., a function of s/l_n.

The cascade interacts with an inlet flow whose perturbation velocity relative to the cascade is harmonic in time and is transported through the cascade with the mean relative velocity between the leading and trailing edges of the cascade. By satisfying the boundary conditions on the primary blade, an expression for its unsteady circulation can be determined. In reference [14] it is shown that $\tilde{\Gamma}_n$ is a function of the geometry of the cascade (camber, stagger angle ξ, and solidity c/s and the characteristics of the disturbance inflow (reduced frequency ω_n, intrablade frequency τ_n, and disturbance amplitude w_{d_n})).

The resulting expression for $\tilde{\Gamma}_n$ will not be presented here; it is presented in detail in references [10, 14, and 15] for $\tilde{\Gamma}_n$ referenced to the cascade mid-chord. Similar expressions can be obtained from other analyses, such as reported in references [9 and 11], although these references do not give an explicit formulation for $\tilde{\Gamma}_n$. In any case, the expression for $\tilde{\Gamma}_n$ must be that referenced to the trailing edge of the blades for use in equations (8) and (11). The transformation required to change the reference position is described in detail in references [10, 14, and 15].

Determination of Distortion Flow Field. A detailed discussion of the procedure required to obtain the coefficients $A_{1_{n_u}}$, $A_{2_{n_d}}$ and $A_{3_{n_d}}$ (the latter is specified by the known distortion of the upstream stagnation pressure), will not be presented here as it follows the procedure described in reference [3]. Basically it involves the simultaneous solution of the matching conditions given in equations (4), (8), and (11) and equations (2) and (3) which describe the flow field upstream and downstream of the rotor.

Comparison of Analysis and Experiment

To demonstrate the validity of the unsteady, semiactuator disk model described in the foregoing, it has been employed to predict the distorted flow field upstream and downstream of several isolated axial-flow rotors. In all cases, it was assumed that the loss term δP_T was zero. The four rotor configurations described in Table 1 were used in the comparisons. Measurements were made [18, 19] of the time-mean, incompressible flow field at the mean radius r_m upstream and downstream of rotors no. 1, 2, and 3 when operating in a variety of inlet distortions. These measurements, made with United Sensor 5-hole pressure probes, determined the circumferential distribution of velocity (axial and circumferential) and pressure.

Table 1 Characteristics at mean radius for four rotor configurations

Rotor configuration	No. rotor blades	c/s	ξ (deg)	$[\bar{C}_L$	Reference
1	12	1.48	45.0	0	[18]
2	9	1.11	45.0	0	[19]
3	9	1.11	50.3	0.5	[19]
4	26	1.00	50.0	>0	[20]

The distorted inflows were generated by inserting screens of varying mesh size upstream of the rotor. The porosity was arranged to produce a 90-degree square-wave distortion and a series of nearly sinusoidal distortions having between 1 and 15 cycles around the circumference of the test facility. This produced a series of distortions with various wavelengths and, hence, varying reduced frequencies, which alters the unsteady response of the rotor. In all cases, the distortions produced a maximum velocity deficit of approximately 20 percent of the circumferential-mean axial velocity far upstream of the rotors.

Comparisons of the analysis based on an unsteady, semi-actuator disk model and the data were made by considering: 1) the circumferential variation of the velocity and pressure 0.137 rotor chord lengths (c) upstream of rotor leading edge and 0.82 c downstream of the rotor trailing edge; 2) the ratio of the amplitude of the axial velocity and stagnation pressure distortion downstream of the rotor to that upstream of the rotor. This latter comparison is presented as a function of s/l_n. This presentation is similar to that of reference [12] and shows the attenuation or amplification of the distortion. In all cases, the input to the analysis was the measured stagnation pressure distortion far upstream of the rotors.

Figure 2 compares the measured circumferential variation of P_T and V_x upstream and downstream of Rotor Configuration No. 1 operated in a 90-deg square-wave distortion with both the methods based on the present unsteady model and the quasi-steady model of reference [3]. In general, both analytical methods predict the measured variation quite well. While the predictions which include the unsteady rotor response are somewhat closer to the measured data, significant differences between the analytical methods are not expected, since the ratio of s/l is small (0.33) and perhaps more importantly, the distortion velocity is uniform over 3 blade spacings.

Figure 3 compares data similar to that of Fig. 2 except for a 4-cycle sinusoidal distortion. In this case s/l_n ($n = 4$) equals 0.33, but the distortion velocity is not uniform over a single-blade spacing. The influence of the unsteady response of the blades is evident downstream of the rotor. The measured variation of both P_T and V_x with θ show a considerably greater attenuation of the distortion downstream of the rotor than do predictions by the quasi-steady model. The unsteady model predicts a maximum amplitude approximately halfway between those by the quasi-steady model and the measured data. However, the unsteady model does not include the effect of losses and neither model includes the effect of the turbulent mixing that occurs in the measured case.

A third comparison of the unsteady, semi-actuator disk model and experimental data is shown in Fig. 4. The data presented here were obtained by Ashby [20] with Rotor Configuration No. 4 operated downstream of a single 1/4-india cylindrical rod. Figure 4 shows the distribution of stagnation pressure coefficient measured by Ashby upstream and downstream of the rotor together with predictions of the downstream distribution by the present unsteady model and

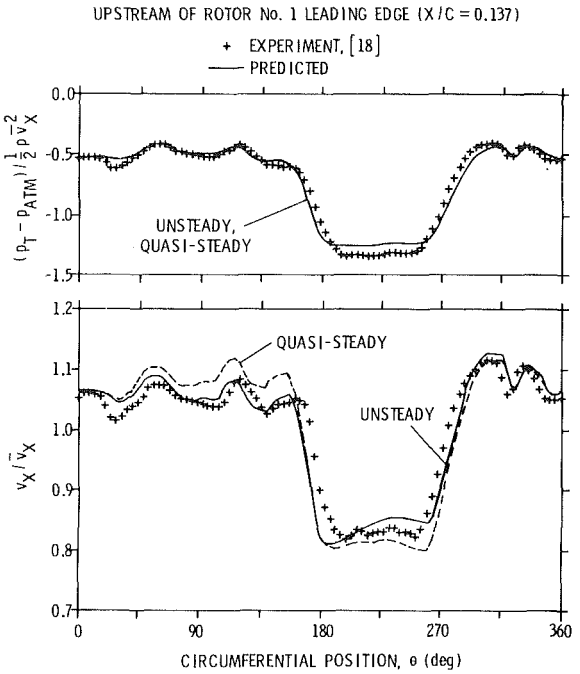

Fig. 2(*a*) 90-deg square-wave flow field upstream of rotor

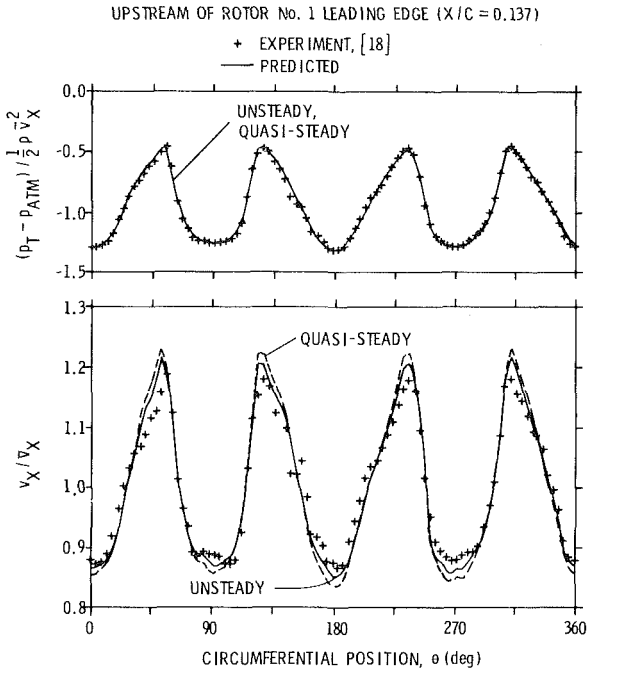

Fig. 3(*a*) Four-cycle sinusoidal distortion flow field upstream of rotor

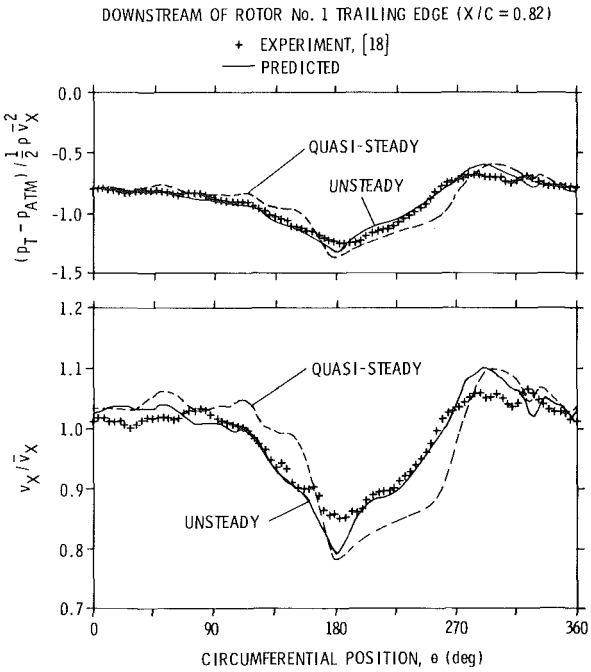

Fig. 2(*b*) 90-deg square-wave distortion flow field downstream of rotor

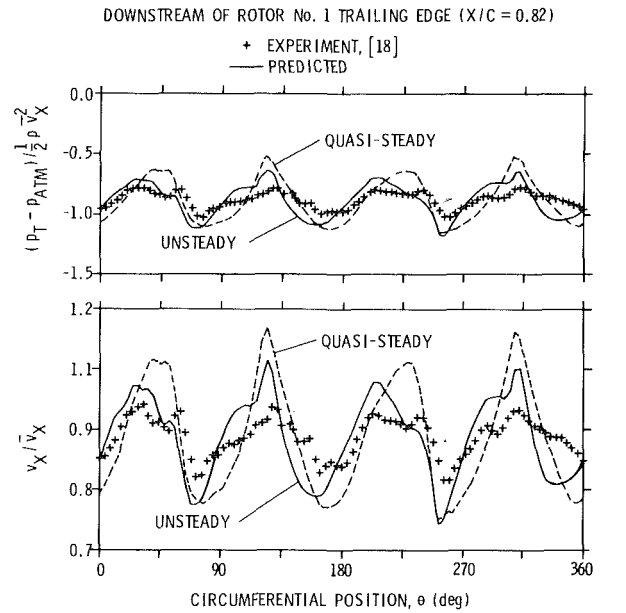

Fig. 3(*b*) Four-cycle sinusoidal distortion flow field downstream of rotor

the semi-actuator disk model of Savell and Wells [21]. Because of the shape of the inlet wake, 40 Fourier harmonics were required to provide a good representation, thereby introducing a significant unsteady influence. As in Fig. 3, the shape of the predicted variation of stagnation pressure by the unsteady model is quite good, but the predicted maximum and minimum levels are too high. Again, the predictions assume the flow to have no losses through the rotor.

A better representation of the attenuation of the distortion as it passes through the rotor and the effect of the unsteady response is obtained by examining the ratio of the distortion amplitude downstream of the rotor to its amplitude upstream of the rotor. Such a comparison is conducted by examining the primary harmonic of the experimental data, i.e., for a 4-cycle inlet distortion the fourth harmonic of the Fourier representation of the data. This ratio, for both P_T and V_x, is then plotted as a function of s/l_n, where l_n is the wavelength of the primary harmonic. This type of representation, reported in reference [12], showed an increasing attenuation as a s/l_n value of 0.5 was approached. Increasing values of s/l_n correspond to increasing values of intrablade frequency which, for a nonvibrating blade row, corresponds to increasing values of reduced frequency.

Figures 5 and 6 show the variation of these amplitude ratios

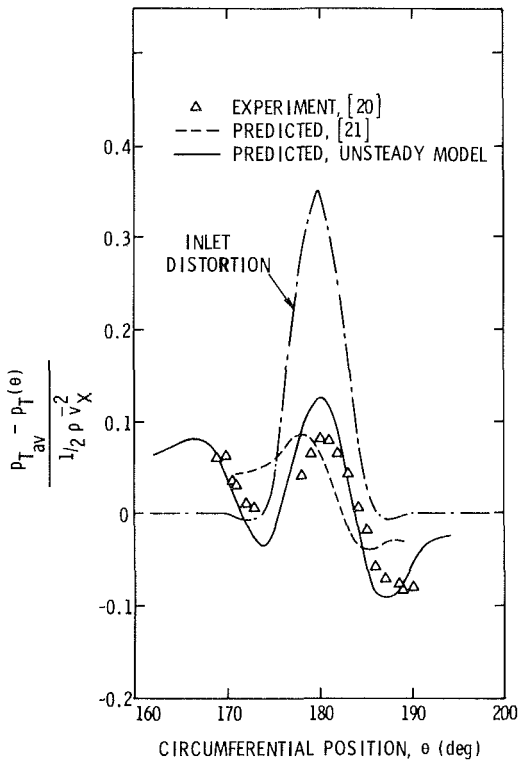

Fig. 4 Stagnation pressure coefficient downstream of rotor no. 4 operated with a circular cylinder upstream of the rotor

with s/l_n for Rotor Configuration Nos. 2 and 3. The data measured with these rotors show an increasing attenuation of the distortion downstream of the rotors as s/l_n is increased toward a value of 0.5. This is identical to the data reported in reference [12] for Rotor Configuration No. 1. However, as s/l_n is increased beyond 0.5, the attenuation of the downstream distortion is decreased until, at a value of $s/l_n \simeq 1.0$, it starts to increase again. The unsteady model predicts a similar trend for both rotor configurations up to a value of $s/l_n = 1.0$. For $s/l_n > 1.0$, the unsteady model predicts a continuing decrease in attenuation of the downstream distortion, but at a greatly reduced rate compared to the range of $0.5 < s/l_n \leq 1.0$.

In all cases the measured attenuation is greater than or nearly equal to the predicted attenuation. Again, this is understandable since the analysis does not include the effects of losses and turbulent mixing, both of which contribute to the attenuation of the distortion. On the other hand, the quasi-steady model predicts a constant value of the stagnation pressure amplitude ratio and a slight attenuation of the axial velocity ratio with increasing values of s/l_n.

Discussion of Results

Comparisons have been presented (Figs. 2 through 6) of measured data and predictions of the passage of a distorted inflow through an isolated rotor by an unsteady, semi-actuator disk model and a quasi-steady actuator disk model. The comparisons indicate that for a 90-deg square-wave distortion, both methods give a good prediction of the magnitude of the axial velocity and stagnation pressure distortion downstream of the rotor. This agreement of the measured data and the quasi-steady model supports the findings of many other authors [1, 3, 4, 5, and 8] who have shown that for square-wave distortions that cover several blade channels at an instant of time, a quasi-steady model is adequate to predict the distortion magnitude. Such a situation means that while the blades of the rotor experience unsteady forces as they enter and leave the distortion, these forces are minimal within the distorted inflow. In such cases the maximum variation between the predictions by the quasi-steady model and the measured data occurs at the extremities of the distortion, where the maximum unsteady blade forces occur.

Figure 2 shows that by including the unsteady response of the rotor, the detailed shape of the 90-deg square-wave distortion downstream of the rotor is more accurately predicted. The details of this shape are determined by the higher harmonics of the Fourier series representation of the distortion, increasing the necessity to include the unsteady response of the rotor. However, both the unsteady and quasi-steady models predict the magnitude of the square-wave distortion equally well, as it is predominately controlled by the lower harmonics. In this region of lower harmonics or reduced frequency, the results of the two analyses are similar. This region also corresponds to low values of the ratio of the blade spacing s to the circumferential wavelength l_n of the nth harmonic of the distortion.

Figure 3 demonstrates, however, that for a sinusoidal distortion having the same predominate s/l_n as the 90-deg square-wave distortion of Fig. 2, the unsteady model gives a much better prediction of both the magnitude and shape of the distortion downstream of the rotor. In this case the inflow to the rotor is continuously changing and is never uniform over successive blade channels. Therefore, the blades are continuously experiencing an unsteady force that influences the downstream distortion.

The inlet stagnation pressure distortion shown in Fig. 4 represents the practical situation of a distortion created by the wake of an upstream strut, in this case a circular cylinder. In this case the amplitude of the first 22 Fourier harmonics have an amplitude within 8.5 percent of each other. For this particular rotor, this covers a s/l_n range up to 0.85. The unsteady semi-actuator disk model provides a very good prediction of this distortion after it has passed through the rotor. This prediction is closer to the measured stagnation pressure variation than that predicted by the semi-actuator disk model of reference [21].

The presentation of measured data and predictions as the ratio of the amplitude of the downstream distortion to the amplitude of the upstream distortion versus s/l_n (Figs. 5 and 6) further demonstrated the influence of the blade unsteady response. These data, all obtained with sinusoidal distortions with varying predominate harmonics, show that for $0 < s/l_n \leq 0.5$ the attenuation increased as s/l_n increased. For the idealized case of a cascade of infinitesimally thin, uncambered airfoils operating in a perfectly sinusoidal inlet distortion, this can be reasoned as follows. At the condition of $s/l_n = 0.5$, the instantaneous response of adjacent blades in such a cascade is 180 degrees out-of-phase, i.e., when one blade experiences a perturbation velocity w_{d_n}, its neighboring blades experience $-w_{d_n}$. The unsteady contribution from the entire cascade is therefore a minimum due to the cancellation of unsteady induced velocities and work input to the fluid by the out-of-phase response of adjacent blades.

Contrasting the condition at $s/l_n = 0.5$ to that at $s/l_n = 1.0$ (or at $s/l_n = 0$, a uniform inflow), all of the blades in the ideal cascade experience the same value of w_{d_n} at an instant in time. At this condition the unsteady response of adjacent blades is in-phase and act to reinforce rather than cancel the induced velocities and work input to the fluid. At $s/l_n = 0$ and 1.0, the quasi-steady analysis should give its best prediction of the amplitude ratio (also at $s/l_n = 2, 3, 4 \ldots$), while, at $s/l_n = 0.5$ it should show the maximum difference with measured data. This is demonstrated in Figs. 5 and 6 for a case in which the inlet distortion is predominately, but not perfectly, sinusoidal with wave-length l_n. As a result, there is

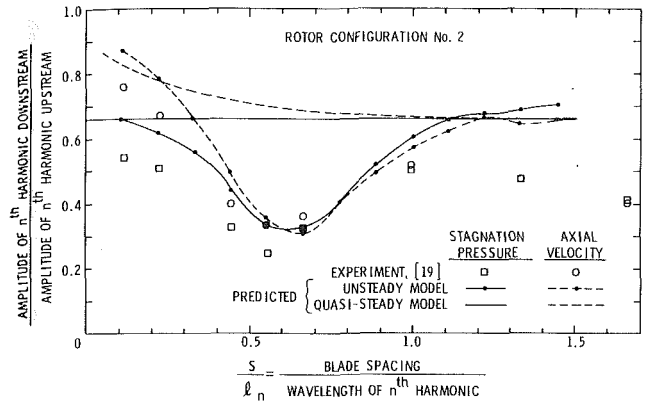

Fig. 5 Distortion amplitude ratio versus s/l_n

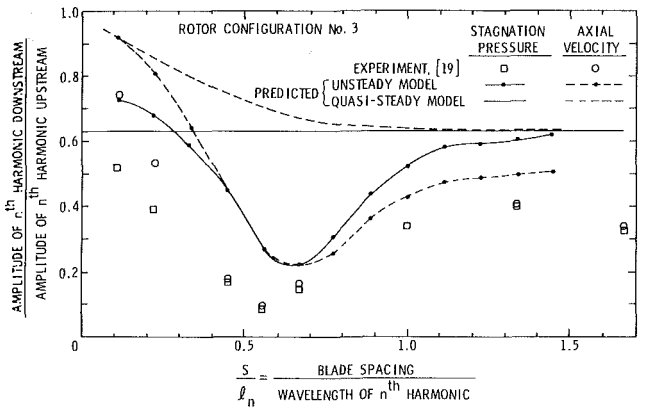

Fig. 6 Distortion amplitude ratio versus s/l_n

a shift of the maximum attenuation point to a value of s/l_n slightly greater than 0.5 due to the response to the harmonics other than n.

On the other hand, the inclusion of the unsteady response of the cascade results in the prediction of the same trend with s/l_n as exhibited by the measured data. The differences between the measured data and that predicted by the unsteady model are attributed to the assumption that the losses, δP_T, were assumed to be zero in the analysis. These losses are composed of both a steady, or circumferential-mean, contribution as determined in a uniform flow, plus an unsteady contribution, $\delta P_T'$. Both of these, and particularly $\delta P_T'$ as it is a function of s/l_n, contribute to the attenuation of the distortion.

The data and predictions presented in Figs. 5 and 6 are simplifications of a distortion experienced in an operating turbomachine, since only sinusoidal distortions with different predominate harmonics are considered. In reality, a distortion will contain a large number of harmonics with varying amplitudes. The necessity for including the influence of the unsteady blade response on the distortion amplitude will depend upon the ratio of the blade spacing s to the wavelength l_n of the harmonics present plus the magnitude of these harmonics. While this influence of the higher harmonics is small for square-wave distortions, it is of significance for the wakes of upstream struts and stator blades. The simplified data of Figs. 5 and 6 serve to demonstrate this significance and the influence of the unsteady blade response. Further, the influence of all of the harmonics of the distortion inflow should be considered rather than only the very low harmonics considered by a quasi-steady model.

There are several limitations of the present unsteady, semi-actuator disk model with respect to its application to axial-flow fans and compressors. These are:

1 The unsteady cascade model employed is limited to lightly loaded airfoils. Therefore, it is not applicable to operating conditions approaching the stall point of the blades and cannot be used to predict the effect of unsteady rotor response on the occurrence of rotating stall or surge. The quasi-steady model of reference [3] can predict stall effects based on the performance of the rotor in a uniform flow.

2 The unsteady model employed is also limited to incompressible flows. However, several compressible flow analyses have been developed that could be used to include the unsteady cascade response instead of the present model. The effects of compressibility must also be included in the equations of motion and matching conditions.

3 The influence of unsteady losses have been ignored due to the lack of data describing this contribution. While Mazzawy [5] shows that this effect can be significant compared to the steady losses, the open literature contains no systematic data. Such data should particularly show the influence of reduced frequency. If available, these data should be included in the matching condition given by equation (8).

4 The present analysis has been developed only for an isolated rotor. As described in reference [3], the solution for an isolated rotor can be extended to obtain the solution for a single or multi-stage configuration. Since a downstream stator is stationary with respect to the flow downstream of the preceding upstream rotor (except for the rotor blade wakes), its effect can be modeled as a quasi-steady actuator disk. However, the predicted velocity field downstream of the stator serves as the input to predict the unsteady circulation on the next rotor.

Summary and Conclusions

The quasi-steady actuator disk model employed by many authors to predict the passage of a circumferential inlet distortion through an axial-flow compressor or fan has been extended to include the unsteady response of a rotor. While the unsteady semi-actuator disk model presented is limited to a single, isolated rotor operating in a incompressible, inviscid flow, it demonstrates several important conclusions regarding such flows. These are:

1 If the distortion is not a square-wave type that provides a uniform distortion velocity over at least several blade spacings, the unsteady response of the rotor has a significant influence on the amplitude of the downstream distortion.

2 The inclusion of the influence of the unsteady rotor response to the higher harmonics of the distorted inflow provides a better description of the details of the response to both a square-wave and sinusoidal inlet distortion.

3 Existing experimental data show that the attenuation of the inlet distortion is increased as it passes through the rotor as the ratio of the blade spacing s to the distortion wavelength l_n approaches 0.5. For $0.5 < s/l_n < 1.0$, the attenuation decreases and then increases for $s/l_n > 1.0$. The unsteady, semi-actuator disk method predicts a similar trend for $s/l_n < 1.0$. The quasi-steady actuator disk method does not predict a maximum attenuation; in fact, it predicts a constant value of stagnation pressure for all values of s/l_n.

4 The unsteady response of the rotor and its influence on the attenuation of the distortion is also a function of the blade stagger angle, as shown in reference [12]. Combined with the demonstrated influence of s/l_n, which is the combined effect of solidity and reduced frequency, the proper choice of rotor-blade geometry can attenuate the magnitude of certain distortion harmonics downstream of the rotor. This approach

may be of value in the control of the forced vibration of downstream blade rows.

Acknowledgments

This research was supported by the Naval Sea Systems Command, Code 063R and the Exploratory and Foundation Program of the Applied Research Laboratory. The authors wish to thank Mr. A. M. Yocum and Dr. E. P. Bruce for making their experimental data available for purposes of comparison.

References

1 Stenning, A. H., "Inlet Distortion Effects in Axial Compressors," ASME *Journal of Fluids Engineering*, Vol. 102, Mar. 1980, pp. 7–13.

2 Greitzer, E. M., "REVIEW—Axial Compressor Stall Phenomena," ASME *Journal of Fluids Engineering*, Vol. 102, June 1980, pp. 134–150.

3 *Distortion Induced Engine Instabilities*, AGARD Lecture Series, AGARD-LS-72, 1974.

4 Plourde, G., and Stenning, A., "Attenuation of Circumferential Inlet Distortions in Multistage Axial Compressors," *AIAA Journal of Aircraft*, Vol. 5, No. 3, 1968, pp. 236–242.

5 Mazzawy, R. S., "Multiple Segment Parallel Compressor Model," ASME JOURNAL OF ENGINEERING FOR POWER, Vol. 99, Apr. 1977, pp. 288–296.

6 Ehrich, F., "Circumferential Inlet Distortions in Axial-Flow Compressors," *Journal of Aeronautical Sciences*, Vol. 24, No. 6, 1957, pp. 413–417.

7 Dunham, J., "Non-Axisymmetric Flows in Axial Compressors," Mechanical Engineering Science Monograph, No. 3, Institution of Mechanical Engineers, 1965.

8 Mokelke, H., "The Prediction of Steady, Circumferential Pressure and Temperature Distortions in Multistage Axial Flow Compressors," ASME JOURNAL OF ENGINEERING FOR POWER, Vol. 102, No. 2, Apr. 1980, pp. 448–458.

9 Whitehead, D. S., "Force and Moment Coefficients for Vibrating Airfoils in Cascade," Aeronautical Research Council (U.K.), ARC R and M 3254, Feb. 1960.

10 Henderson, R. E., and Daneshyar, H., "Theoretical Analysis of Fluctuating Lift on the Rotor of an Axial Turbomachine," Aeronautical Research Countil (U.K.), ARC R and M 3684, Sept. 1970.

11 Attasi, H., and Akai, T. J., "Aerodynamic and Aeroelastic Characteristic of Oscillating Loaded Cascades at Low Mach Number, Part I: Pressure Distribution, Forces and Moments," ASME JOURNAL OF ENGINEERING FOR POWER, Vol. 102, No. 2, Apr. 1980, pp. 344–351.

12 Yocum, A. M., and Henderson, R. E., "The Effects of Some Design Parameters of an Isolated Rotor on Inlet Distortions," *ASME Journal of Engineering for Power*, Vol. 102, No. 1, Jan. 1980, pp. 178–186.

13 Horlock, J. H., and Daneshyar, H., "Stagnation Pressure Changes in Unsteady Flow," *Aeronautical Quarterly*, Vol. XXII, Part III, Aug. 1971.

14 Henderson, R. E., "The Unsteady Response of an Axial Flow Turbomachine to an Upstream Disturbance," PhD dissertation, Churchill College, Cambridge University, 1973.

15 Bruce, E.P., "Axial Flow Rotor Unsteady Performance," PhD thesis, Aerospace Engineering Department, The Pennsylvania State University, Nov. 1979.

16 Henderson, R. E., "The Unsteady Response of a Blade Row from Measurements of the Time-Mean Total Pressure," ASME Paper 73-GT-94, Gas Turbine Conference, Washington, DC, April 1973.

17 Horlock, J. H., *Actuator Disc Theory*, McGraw-Hill Publishing Co., New York, 1980.

18 Yocum, A. M., "The Effects of Design and Operating Variables on the Response of an Axial Flow Fan to Inlet Flow Distortions," MS thesis, Mechanical Engineering Department, The Pennsylvania State University, Aug. 1978.

19 Bruce, E. P., private communications, May 1980.

20 Ashby, G. C., "Investigation of the Effect of Velocity Diagram of Inlet Total Pressure Distortion Through Single-Stage Subsonic Axial-Flow Compressor," NACA RM L57A03, Apr. 1957.

21 Savell, C. T., and W. R. Wells, "Rotor Design to Attenuate Flow Distortion, Part I: A Semiactuator Disc Analysis," ASME JOURNAL OF ENGINEERING FOR POWER, Vol. 97, Jan. 1975, pp. 11–20.

APPENDIX

Relation of Unsteady Circulation, v_x', and v_θ' for a Cascade

It is necessary to determine a relationship between the unsteady circulation $\tilde{\Gamma}$ of the cascade blades and the perturbation velocities v_x' and v_θ'. This is done by determining the circulation in an area abcd, Fig. 1. The total circulation, $\bar{\Gamma} + \tilde{\Gamma}$, calculated in this manner will include the upstream free vorticity associated with the distortion. Since a linearized flow model is assumed the free vorticity remains unchanged through the cascade. The cascade contributes a perturbation due to the unsteady circulation on the blades. After determining the total circulation, in abcd, only the perturbation component $\tilde{\Gamma}$ is used. This is equated to the expression for unsteady blade circulation determined from a linearized model of unsteady flow in a cascade.

From Fig. 1 the total circulation in abcd can be written as

$$\Gamma = r\int_a^b v_{X_{ab}} \sec\beta(\eta)\,d\eta + r\int_b^c v_{\theta_{bc}}(\theta)\,d\theta + r\int_c^d v_{X_{cd}} \sec\beta(\eta)\,d\eta + r\int_d^a v_{\theta_{da}}(\theta)\,d\theta. \tag{12}$$

Assuming the velocity variations in the η and θ directions to be harmonic in θ, the velocities on abcd for the nth harmonic can be written as

$$v_{X_{ab}} = \bar{v}_X + \hat{v}_X e^{in\theta} e^{-iX\tan\beta} = \bar{v}_X + v'_{X_{ab}}$$

$$v_{X_{dc}} = \bar{v}_X + \hat{v}_X e^{in\theta} e^{i\left(\frac{2\pi s}{l_n} - X\tan\beta\right)} = \bar{v}_X + v'_{X_{dc}} \tag{13}$$

$$v_{\theta_{ad}} = \bar{v}_{\theta_l} + \hat{v}_{\theta_l} e^{in\theta} = \bar{v}_{\theta_l} + v'_{\theta_l}$$

$$v_{\theta_{bc}} = \bar{v}_{\theta_t} + \hat{v}_{\theta_t} e^{in\theta} e^{-iX\tan\beta} t = \bar{v}_{\theta_t} + v'_{\theta_t}$$

noting that by equation (4) $\bar{v}_{X_l} = \bar{v}_{X_t} = \bar{v}_X$.

If the boundaries ab and cd are approximated as being coincident with a line parallel to the chord line, $\beta(\eta) = \xi$. Then,

$$\eta = X\sec\beta \doteq X\sec\xi,$$

and the first and third integrals, I_1 and I_3, of equation (12) become, after substitution of equation (13) into equation (12),

$$I_1 + I_3 = r\hat{v}_X e^{in\theta}\left(1 - e^{i\frac{2\pi s}{l_n}}\right)\sec^2\xi\int_o^h e^{-iX\tan\xi}\,dX.$$

$$= \frac{-ir\hat{v}_X e^{in\theta}\left(1 - e^{i\frac{2\pi s}{l_n}}\right)\left(1 - e^{-ih\tan\xi}\right)}{\sin\xi\cos\xi} \tag{14}$$

$$= r\hat{v}_X e^{in\theta}\psi_n$$

Similarly, the second and fourth integrals become

$$I_2 + I_4 = r\int_o^{\frac{2\pi}{N}} [\bar{v}_{\theta_t} - \bar{v}_{\theta_l}]\,d\theta + r\int_o^{\frac{2\pi}{N}} [\hat{v}_{\theta_t} e^{-iX\tan\xi} - \hat{v}_{\theta_l}]e^{in\theta}\,d\theta$$

$$= [\bar{v}_{\theta_t} - \bar{v}_{\theta_l}]s + [v'_{\theta_t} - v'_{\theta_l}]s, \tag{15}$$

where v'_{θ_t} and v'_{θ_l} are the average perturbation velocities in the θ direction at the trailing and leading edges, respectively, over the distance $\theta = 2\pi/N = s/r$.

The substitution of Equations (14) and (15) into equation (12) gives the following expression for the unsteady circulation in terms of the fluid velocities at the leading edge (l) and trailing edge (t)

$$\tilde{\Gamma} = [v'_{\theta_t} - v'_{\theta_l}]s$$

$$- \frac{ir\hat{v}_x e^{in\theta}\left(1 - e^{i\frac{2\pi s}{l_n}}\right)\left(1 - e^{-ih\tan\xi}\right)}{\sin\xi\cos\xi}. \quad (16)$$

Since the model employs the leading edge of the cascade as the origin of its coordinate axis, $\tilde{\Gamma}$ is referenced to the cascade leading edge. Transformation of this reference point to the blade trailing edge is accomplished by the transformation

$$\tilde{\Gamma}_t = \tilde{\Gamma}_l e^{i2\omega n},$$

where ω_n is the reduced frequency defined by the disturbance wavelength and the cascade chord length ($\omega_n \propto c/l_n$).

Note that when $l_n >> s$ or $l_n = ns$, the last term of equation (16) is very small or zero. This term accounts for the blade-to-blade variation of the instantaneous distortion velocity through the cascade. Also note that when the axial length of the cascade approaches zero, as in the actuator disk representation of reference [3], the last term of equation (16) again approaches zero.

B. L. Lewis

Currently at Teledyne CAE,
Toledo, Ohio 43612

A. Jay

Assoc. Mem. ASME
United Technologies Corporation,
Pratt & Whitney Aircraft Group,
Commercial Products Division,
East Hartford, Conn. 06108

E. G. Stakolich

National Aeronautics
and Space Administration,
Lewis Research Center,
Cleveland, Ohio 44135

Effect of Time-Dependent Flight Loads on Turbofan Engine Performance Deterioration

A jet engine's efficiency is strongly dependent upon clearances between rotating blades and the corresponding stationary gas-path seals. Analytical studies to examine the effects of various flight cycle loads on powerplant clearances suggest that rotor/seal interferences may contribute to the short-term performance deterioration exhibited by all high bypass jet propulsion systems. In prior analytical studies, flight cycle loads were treated in a quasi-steady, static manner, even though some flight cycle loadings are decidedly dynamic in nature. Gust encounters and aircraft landings are classical examples of dynamic flight loads found in typical airline service. An analytical technique for predicting the effects of aircraft dynamic flight loads on engine performance was developed and is described herein.

Introduction

The deterioration of a jet engine's fuel efficiency can be generally attributed to erosion, contamination of airfoils, thermal distortion of hot section parts, and increases in clearances between rotating blades and the corresponding outer air seals. The high bypass propulsion systems powering today's wide body aircraft fleet suffer a short-term deterioration process with losses in thrust specific fuel consumption (TSFC) during the first few flights that is undesirable in light of current fuel costs. To combat high bypass engine deterioration, a study to understand the deterioration mechanisms has been conducted at Pratt / Whitney Aircraft under the Engine Diagnostics (ED) part of the Engine Component Improvement (ECI) program. The ECI program is an element of the NASA sponsored Aircraft Energy Efficiency (ACEE) program which is directed toward reducing fuel consumption of commercial air transports. One task of this study was the utilization of an analytical model of the JT9D-7 to examine the potential effects of flight induced loads on performance deterioration.

Previous analytical studies [1] treating flight induced propulsion system loads in a quasi-steady manner suggest the primary cause of short-term deterioration to be the increase in operating clearances resulting from flight load induced rotor/seal interference. These results are in good agreement with engine performance data in the low-cycle (1–300-flights) regime.

Although the quasi-steady approach to the flight loads spectrum appears to provide an adequate simulation of the clearance induced deterioration process, some flight loads are inherently time dependent in nature, raising the possibility of significant dynamic effects in the rotor/seal interference process. A transient dynamic analysis of the JT9D-7/747 propulsion system was conducted to provide insight into the dynamic structural behavior of the engine and relate this knowledge to seal rub patterns and performance characteristics exhibited by testing and inspection of engines from typical revenue service.

Analytical Model

The NASTRAN (NASA STRUCTURAL ANALYSIS) finite element model of the JT9D/nacelle structure utilized in these studies was identical to that employed in the steady loads analysis [1]. Engine cases were modeled primarily with quadrilateral plate elements with enhanced membrane capabilities. Triangular plate elements were used in areas of mesh transitioning or irregular geometry. The high/low-pressure rotor spools were beam-lumped mass model duplicates of those employed in standard critical speed design analyses of the JT9D.

The model was substructured by component regions consisting of the fan/low-pressure compressor, high-pressure compressor, diffuser/turbine cases, and high/low-pressure rotors, as well as the inlet cowl, tailcone, and wing pylon structures. Figure 1 shows a side view of the engine model.

Modal Analysis Consideration. The modal tansient approach was selected as the analysis procedure due to its economic advantages over other available techniques for this problem. It also provided physical insight into the analysis regarding the frequency spectrum, participation of the various modes in the response, and led to the convenient use of modal damping.

In general the standard NASTRAN transient analysis package was utilized. Some modifications were required to

Contributed by the Gas Turbine Division and presented at the International Gas Turbine Conference and Products Show, Houston, Texas, March 9–12, 1981, of THE AMERICAN SOCIETY OF MECHANICAL ENGINEERS. Manuscript received at ASME Headquarters, September 23, 1980. Revised manuscript received December 23, 1980. Paper No. 81-GT-203.

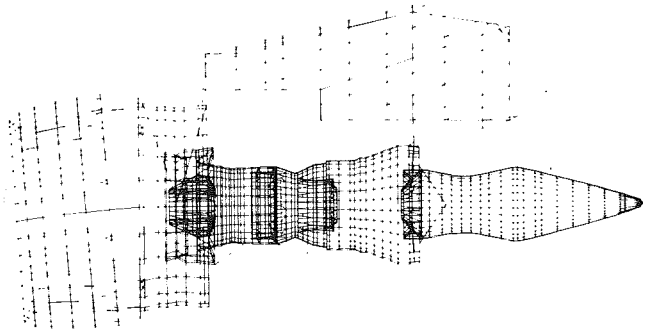

Fig. 1 JT9D-7 finite element model

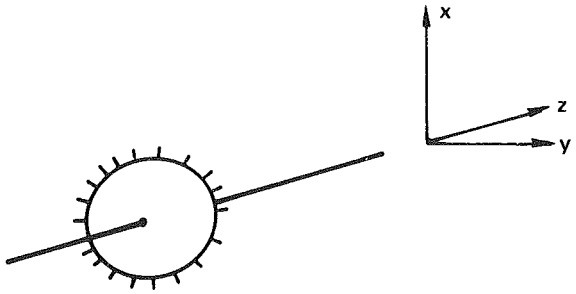

Fig. 2 Orientation of a typical rotor stage in the analysis coordinate system

the basic NASTRAN computational procedures, however, due to the following considerations:

- desired utilization of structural symmetry,
- modal damping,
- time-dependent enforced displacements,
- nonstandard NASTRAN dynamic reduction procedure, and
- gyroscopic effects.

An overview of the impact of these considerations on the NASTRAN transient response procedure follows.

Modal Transient Formulation. The modal transient formulation is available in many references, [2] and [3], and will only be outlined. The equation to be solved is:

$$[M]\{\ddot{x}\} + [C]\{\dot{x}\} + [G]\{\dot{x}\} + [K]\{x\} = (F(t)\} \tag{1}$$

where $[M]$ = structure mass matrix
$[G]$ = structure viscous damping matrix
$[C]$ = rotor gyroscopic matrix
$[K]$ = structure stiffness matrix

Since the model is substructured, the matrices of equation (1) represent the assembled contributions from the various substructures. The zero speed, undamped modal matrix of equation (1) (ϕ_N) is then formed.

$$[M]\{\ddot{x}\} + [K]\{x\} = \{0\} \tag{2}$$

$$\{x\} = \{x_0\}e^{i\omega t} \tag{3}$$

$$\{[M]\omega^2 + [K]\}[\phi_N] = \{0\} \tag{4}$$

The modal matrix $[\phi_N]$ is mass normalized and the standard modal transformation applied to equation (1).

$$\{x\} = [\phi_N]\{\eta\} \tag{5a}$$

$$[\phi_N]^T[M][\phi_N]\{\ddot{\eta}\} + [\phi_N]^T[C][\phi_N]\{\dot{\eta}\} + [\phi_N]^T[G][\phi_N]\{\dot{\eta}\} + [\phi_N]^T[K][\phi_N]\{\eta\} = [\phi_N]^T\{F(t)\} \tag{5b}$$

$$\underbrace{[M]}\{\ddot{\eta}\} + [\phi_N]^T[C][\phi_N]\{\dot{\eta}\} + [\phi_N]^T[G][\phi_N]\{\dot{\eta}\} + \underbrace{[K]}\{\eta\} = [\phi_N]^T\{F(t)\} \tag{6}$$

where: $\underbrace{[M]}$ = generalized mass $= [I]$
$\underbrace{[K]}$ = generalized stiffness $= [\omega^2]$

Damping in the propulsion system is developed in numerous ways. Bolted flanges, case/strut attachments, mount points, mechanical dampers, and inherent structural damping are some examples. In a structure with the complexity of the JT9D, an accurate representation of the discrete damping matrix $[C]$ is impractical if not impossible. Consequently, as in many engineering applications, modal damping was employed. The matrix product $[\phi_N]^T[C][\phi_N]$ thereby is reduced to diagonal form with each entry proportional to the critical damping factor for the respective mode. Modal damping factors are typically obtained from test data or assigned values consistent with prior experience.

Gyroscopic Considerations. With the incorporation of modal damping, the equations of motion are generally uncoupled, leading to substantial computational savings. The gyroscopic behavior of the rotors, characterized by the matrix $[G]$, couples the equations of motion. The physical significance of this behavior is that the symmetric and antisymmetric components of motion became coupled, and the half model used in the quasi-steady loads analysis can no longer directly describe the powerplant structural response.

A typical stage of the rotor system and the associated analysis coordinate system is shown in Fig. 2. Each stage of the rotor behaves as a gyroscope, tending to resist rotation in any direction other than the axis of rotation. Mathematically, the gyroscopic behavior of each stage is defined by equation (7).

$$\begin{Bmatrix} F_x \\ F_y \\ F_z \\ M_x \\ M_y \\ M_z \end{Bmatrix} = \begin{bmatrix} 0 & 0 & 0 & 0 & 0 & 0 \\ 0 & 0 & 0 & 0 & 0 & 0 \\ 0 & 0 & 0 & 0 & 0 & 0 \\ 0 & 0 & 0 & 0 & -I_p\Omega & 0 \\ 0 & 0 & 0 & I_p\Omega & 0 & 0 \\ 0 & 0 & 0 & 0 & 0 & 0 \end{bmatrix} \begin{Bmatrix} \dot{x} \\ \dot{y} \\ \dot{z} \\ \dot{\theta}_x \\ \dot{\theta}_y \\ \dot{\theta}_z \end{Bmatrix} \tag{7}$$

where I_p = polar mass moment of inertia of stage
Ω = rotor rotational velocity

To aid in the physical interpretation of the large amounts of displacement data, it was desirable to maintain the symmetric/antisymmetric displacement representation of the structure. This representation was preserved by using symmetric and antisymmetric half models of the structure and coupling the two representations through the gyroscopic matrix. This technique could be conveniently employed because the coupling occurs along the plane of structural symmetry.

Dynamic Reduction Considerations. The half model of the JT9D powerplant contained approximately 11,000 degrees of freedom. In preserving the symmetric/antisymmetric displacement representation, the problem size was doubled. For such a problem size, it is economically impractical to extract the modes required for the modal analysis, consequently some form of dynamic reduction was necessary. It is well known that the type and level of reduction performed can have an adverse effect upon frequency and modal data. Since the quality of any modal transient analysis is governed

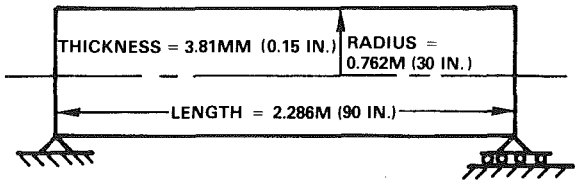

Fig. 3 Simply supported cylindrical shell used in evaluation of dynamic reduction procedures

by the frequency and modal data used, the dynamic reduction performed must be done judiciously.

Several reduction schemes are commonly used, and four types were examined for use in this analysis. The types examined were:

- mass lumping followed by static condensation,
- Guyan reduction,
- distributed parameter systems, and
- fixed boundary modal synthesis techniques.

Both mass lumping and Guyan reduction have been extensively used. Studies with these techniques on shell structures have indicated that substantial modal errors may be induced even for the low modes of the structure when heavy levels of reduction are utilized. Distributed parameter systems include the FEER eigenvalue technique [4] and the generalized dynamic reduction procedure of MacNeal [5]. Both of these techniques are relatively new and the latter has shown promising performance for some engine hardware applications. At the initiation of this analysis, however, no evaluation has been made using these techniques for shell structures. Consequently both techniques were ruled out, although subsequent studies have indicated these to be promising techniques for future analyses.

A procedure developed by Craig and Bampton [6] was found to produce excellent results for shell structures and to be readily adaptable to the NASTRAN program. In this procedure, both physical and modal degrees of freedom are used to describe the structure. The modal variables are generated by fixing each substructure at its interfaces with other substructures and extracting the "fixed boundary modes" of the substructure. Displacement compatibility is then required at the various substructure boundaries to form the system description. A brief mathematical overview of the Craig and Bampton technique follows.

Each substructure is partitioned into internal and boundary degrees of freedom per equation (8). The boundary set must include, at a minimum, all freedoms which are common with other substructures.

$$\begin{bmatrix} M_{BB} & 0 \\ 0 & M_{II} \end{bmatrix} \begin{Bmatrix} \ddot{x}_B \\ \ddot{x}_I \end{Bmatrix} + \begin{bmatrix} K_{BB} & K_{BI} \\ K^T{}_{BI} & K_{II} \end{bmatrix} \begin{Bmatrix} x_B \\ x_I \end{Bmatrix} = \begin{Bmatrix} 0 \\ 0 \end{Bmatrix} \quad (8)$$

The fixed boundary frequencies and mode shapes ($\{\phi_I\}$) of each substructure are then extracted from equation (9).

$$\omega^2 [M_{II}]\{\phi_I\} = [K_{II}]\{\phi_I\} \quad (9)$$

The final displacements of each substructure are then expressed as a linear combination of the boundary induced displacements and the participation of the various fixed boundary modes.

$$\begin{Bmatrix} x_B \\ x_I \end{Bmatrix} = \left[\begin{array}{c|c} I & 0 \\ \hline \phi^c & \phi_I \end{array}\right] \begin{Bmatrix} P_b \\ P_I \end{Bmatrix} \quad (10)$$

where P_b = substructure boundary displacements

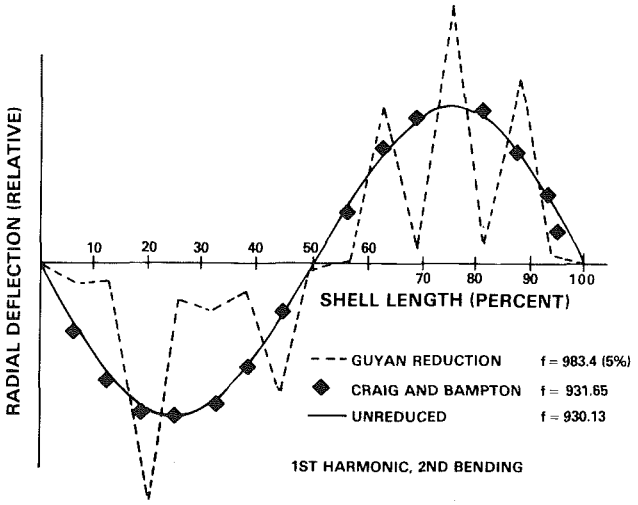

Fig. 4 Mode shape comparisons for simply supported cylindrical shell

P_I = participation factors for various substructure fixed boundary modes

$\{\phi^c\}$ = displacement of internal degree of freedom due to boundary displacement, i.e.,

$\{\phi^c\} = -[K_{II}]^{-1} \cdot [K_{IB}]$

Since each modal degree of freedom (P_I) represents a physically meaningful displacement pattern for the substructure, this technique is generally more efficient than Guyan reduction where one freedom may represent a rather arbitrary displacement pattern. Computationally, the Craig and Bampton technique compares favorably with Guyan reduction.

In addition to the effectiveness and simplicity of the Craig and Bampton technique, the procedure also provides the following intermediate checks on the structural model and analysis.

- By extracting the fixed boundary modes of the substructures, the analyst is given a means of checking the structural model early in the assembly phase.
- The frequency spectrum of the fixed boundary modes provides insight into the likely participation of the various modes, particularly if the harmonic content of the transient loads is known.
- The fixed boundary mode procedure provides a means for further reducing the dynamic problem size. If the fixed boundary frequencies are considerably higher than the component's transient forcing functions, the fixed boundary modes may simply be restrained from participating.

The need for carefully managing the dynamic reduction procedure is illustrated by the simply supported shell of Fig. 3. The results of the first harmonic, second bending mode, frequency for this structure are shown in Fig. 4, comparing the Craig and Bampton procedure with a Guyan reduction scheme similar to the one employed in the original normal modes analysis [7]. As can be seen, the approach utilized leads to a substantial improvement in the modal data for this case.

Enforced Dynamic Displacements. In the quasi-steady analysis of the JT9D/747, the wing pylon was attached to a

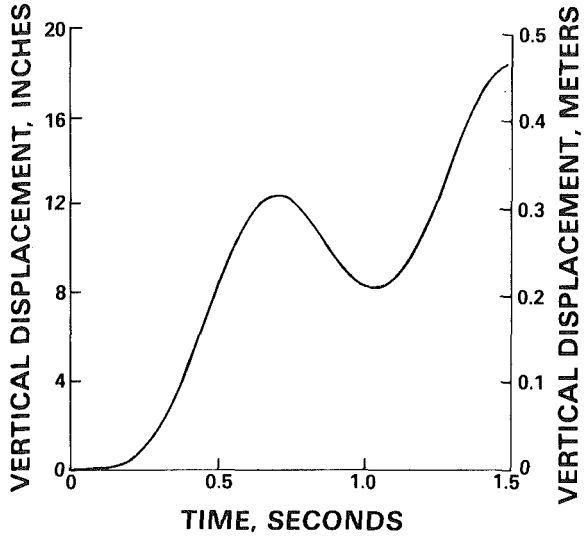

Fig. 5 Wing vertical displacement history for once-per-flight vertical gust

rigid mount. In dynamic analyses, the powerplant displacements are due primarily to the elastic response of the aircraft wing. Consequently, a procedure must be available whereby time dependent displacement histories may be enforced on the model. These displacement histories are products of the airframe aeroelastic analysis and are defined for all six motions of the wing elastic axis at its intersection with the pylon centerplane. A typical wing vertical displacement history for the once-per-flight vertical gust is shown in Fig. 5.

In NASTRAN, enforced dynamic displacements are applied through a "large mass" or "acceleration generator." A mass several orders of magnitude larger than the structure is assigned to each degree of freedom where time dependent displacements are to be applied. The large masses result in essentially zero frequency, rigid body modes of the structure. These rigid-body modes may then be excited by forces producing accelerations that integrate to the desired displacement histories.

Analysis Conditions. The computational costs involved and limited availability of airframe aerolastic data permitted evaluation of only two flight load conditions in the mission profile analyzed in the quasi-steady analysis. The two points from the steady loads spectrum which generate the most interesting dynamic load conditions are gust encounters and landing touchdowns. Both are inherently dynamic in nature and are described in a relatively short time period. For these flight conditions, the Boeing Commercial Airplane Company (BCAC) generated aeroelastic data for a vertical gust and four different landing sequences. The aeroelastic data employed reflects the behavior of the wing at the outboard engine location. The four landing sequences represent variations in aircraft gross weights, fuel loads, and sink rates. The vertical gust encounter analyzed was a Federal Aviation Administration FAR 25.341 "1-cosine" gust of 0.76-s duration with a once-per-flight value of 10 ft/s (3.05 m/s) at the following flight condition:

- Altitude 22,100 ft (6736m)
- Gross weight 730,400 lb (331,303 Kg)
- Mach number 0.875
- True airspeed 897.8 ft/sec (273.6 m/s)

Although wing displacement data were available for 1.5 s, only the first 0.76 s was judged to be valid by the airframe manufacturer. For the gust conditions, cowl aerodynamic load histories were also generated by Boeing Commercial Airplane Company and imposed upon the NASTRAN model.

Of the four landings described by Boeing Commercial Airplane Company, the following was chosen for analysis.

- Gross weight 490,000 lb (222,260 Kg)
- Fuel weight 43,000 lb (1950 Kg)
- Sink rate 3 ft/sec (0.91 m/s)

This case represents a typical revenue service profile landing.

For the landing event analyzed, the inlet aerodynamic forces were estimated by Boeing Commercial Airplane Company to be negligible and were neglected. Consequently, the dynamic loads for the landing simulation consisted only of the enforced wing displacements.

Damping and Transient Time Step Considerations. To extract modal damping factors for the propulsion system, accelerometer data from Pratt & Whitney Aircraft's flight testing was reviewed. Although the flight test aircraft was a B-52, the pylon and engine structures were similar to the JT9D/747 system modeled in this analysis. The particular test sequence utilized concerned verification of the aircraft flight envelope by recording the aircraft response to various control surface inputs. Accelerometer data from various points on the powerplant were also recorded.

A high-speed transient analysis of the power-plant accelerometer data was conducted and the following frequencies identified:

2.2 Hz	25.0 Hz
5.2 Hz	31.0 Hz
10.2 Hz	58.0 Hz
14.6 Hz	60.4 Hz

This frequency spectrum is similar to that extracted from the current analysis as shown in Table 1. The trace of the higher modes was of insufficient strength or duration for constructing accurate amplitude versus time histories. Consequently a 12-Hz band filter was utilized and an amplitude versus time history was created for the first mode of the system (2.2 Hz). Using equation (11) in conjunction with the accelerometer data, several calculations of damping factors were made, resulting in an average damping factor of 6.06 percent.

$$\delta = \frac{\log A_o/A_n}{[1.862N^2 + (\log A_o/A_n)^2[^{1/2}} \tag{11}$$

where

δ = damping ratio
A_o = amplitude of wave at time t_1
A_n = amplitude of wave after nth cycle
N = number of cycles

Because of the many sources of damping in the propulsion system and pylon structures, the value of 6 percent critical damping was felt to be reasonable for the lower modes of the system. Additionally, the dynamic response of the propulsion system to the loads being analyzed was anticipated to be dominated by the lower modes of the system. Consequently, an accurate assessment of a typical lower mode damping factor was felt to be more important than for higher modes.

In selecting the transient step size there were three governing considerations:

- In a modal transient analysis, the step size selected directly affects the numerical results through the stability of higher mode contributions.
- The time step must be small enough to track the orbit of each rotor in order to provide accurate circumferential clearance/interference information.

Table 1 Integrated propulsion system frequencies

Mode	S or A [a]	Frequency (Hz)	Ground test results (Hz)	Description
1	A	2.5199	2.4	First pylon lateral
2	S	4.4986	4.6	First pylon vertical
3	A	6.8272	6.5	Strut torsion
4	S	11.115		Thrust frame, engine axial
5	A	12.836		Engine roll
6	A	14.497		Fan case rocking side
7	S	14.816		Fan case rocking—vertical
8	A	19.123		
9	S	20.089		Fan thrust reversers
10	S	24.510		Higher pylon bending with low rotor motion
11	A	27.489		Case Torsion, low rotor bending
12	S	29.024		
13	S	31.809		
14	A	32.499		
15	S	35.126		
16	A	37.833		Core engine bending
17	S	45.539		
18	A	45.556		
19	S	46.648		
20	A	51.473		
21	S	53.115		
22	A	54.059		
23	S	56.636	56.	Tailcone wagging, low-rotor bending
24	S	62.207		
25	A	63.216		
26	S	70.002		
27	S	70.896		
28	A	72.600		
29	S	74.723		
30	A	75.101		
31	A	75.865		
32	A	76.513		
33	S	77.930		
34	A	83.489		
35	S	86.212		
36	S	87.184		
37	A	87.775		
38	A	88.225		
39	S	89.475		
40	A	90.955		

[a] S = symmetric mode
A = antisymmetric mode

- Economic factors and computing resources.

The relationship between a given time step (Δt) and the error induced for a participating mode of frequency ω can be expressed by equation (12) [3].

$$\frac{A_f}{A_e} = 1 + \frac{1}{8}\omega^2 \Delta t^2 \tag{12}$$

where A_f = computed amplitude of modal contribution from mode with frequency ω
A_e = amplitude of modal contribution from exact solution
ω = circular frequency
Δt = time step size

For the dynamic analysis, it was anticipated that the propulsion system response would be governed by the wing displacements. These displacements are primarily of relatively low-frequency content when compared to the computed integrated propulsion system frequency spectrum. Consequently, the modes in the 0–20-Hz range were expected to have the highest participation factors. If, in the modal analysis, modes to the 100-Hz level were retained (48 modes have system frequencies less than 100 Hz), this would provide a 5 to 1 frequency margin over the anticipated primary participation range and would also provide adequate coverage for higher modes which might be excited in the hard landing, or whose static contributions were required.

It was required that there be less than 5 percent error in a mode with a frequency of 100 Hz, and equation (12) was used to yield a time step of 0.001 second. The 0.001 second transient time step provides approximately 8 examinations per revolution of the high-pressure rotor and 17 of the low-pressure rotor at cruise conditions.

JT9D/747 Transient Dynamic Results

To assess the effects of aircraft dynamic flight loads on engine performance deterioration the following steps were performed in the analysis of the dynamic flight conditions.

- The symmetric and antisymmetric fixed boundary modes of each substructure were computed, and the dynamic mass and stiffness properties of the various substructures were formed. The rotor substructure was reduced using Guyan reduction.
- Substructure matrices were assembled and the zero speed modes of the integrated propulsion system were extracted.
- A modal transient response of the Boeing Commercial Airplane Company supplied dynamic loads with a transient step size of 0.001 s was conducted.
- The rotor and case displacements of the individual engine substructures were computed at the various times during the transient and the data used to construct a performance evaluation via a performance deterioration post-processor computer program.

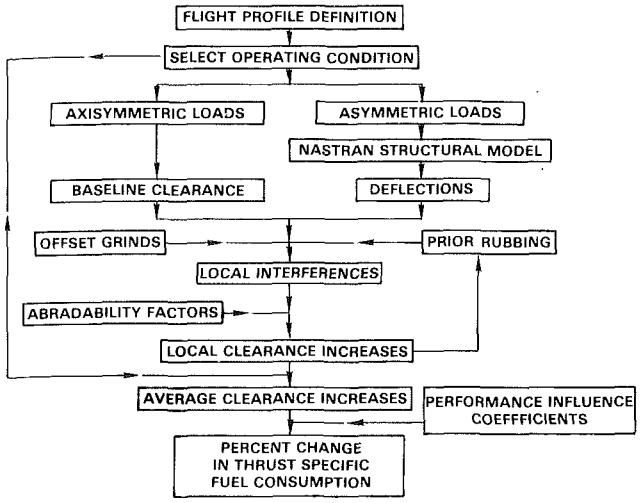

Fig. 6 Flow chart for the deterioration post-processor program

- An evaluation of the results obtained was conducted, and an assessment of their accuracy was made.

An assessment of the validity of the calculations can be made through an engineering evaluation of various intermediate results of the analysis. For the JT9D-7 study, the computed frequency spectrum and the modal participation data provides check points for examining the analysis.

Empirical data for verification of the computed frequency spectrum is somewhat limited. The frequencies obtained, however, were in good agreement with the available ground test data and calculations made using the standard Pratt & Whitney Aircraft design analysis tools. Table 2 summarizes the available calibration data.

In addition to these sources of verification, various other computed frequencies and mode shapes were found to be in good agreement with design studies employing body of revolution, shell of revolution, or beam modeling of miscellaneous engine components. On the basis of the available means of correlation, the computed propulsion system frequencies were believed accurate, providing confidence in the basic elastic and mass modeling of the structures.

One problem associated with large scale dynamic analysis is the generation of a large quantity of data which does not readily yield to a comprehensive evaluation. For this analysis, approximately 99 million pieces of data were generated in the process of characterizing the performance deterioration for the gust and landing simulations.

Table 2 Correlation of computed frequency spectrum

	NASTRAN Analysis (Hertz)	Test (T) or Analysis (A) (Hertz)
Strut lateral bending	2.52	2.40 (T)
Strut vertical bending	4.50	4.60 (T)
Strut torsion	6.50	6.80 (T)
Tailcone vertical wagging	56.60	56.00 (T)
Fan case rocking/low rotor	24.51	22.83 (A)
LPC case bending/low rotor	29.02	30.17 (A)

A performance deterioration post-processor was developed to eliminate the large amount of hand work that would be required to perform these calculations. The program computes clearance increases for each stage in the engine and performance deterioration resulting from blade-tip/rub-strip interferences. The program accepts NASTRAN deflection data as input. Three NASTRAN internal data blocks are used to define case and rotor geometry, and these must also be obtained from the NASTRAN run for each stage in the engine. The flow of the program is depicted in Fig. 6. The time dependent engine case and rotor displacement data were processed at various times during the load transients, and the resulting blade-tip/rub-strip interferences were related to engine performance deterioration. For the gust and landing simulations considered, it was determined that the effect of these dynamic loads on engine performance deterioration is negligibly small.

In light of service experience, the once-per-flight vertical gust and the revenue service landing was expected to result in negligible performance loss and the analysis supports this experience. The primary response of the engine is the gyroscopic behavior of the fan induced by the wing pitching motions. Inertia forces during the gust encounter are not sufficient to induce seal wear at the top or botton of the outer air seals, supporting the results of the quasi-steady analysis.

Conclusions

An analytical evaluation of the dynamic effects of two flight conditions of the JT9D-7/747 propulsion system was conducted. Predicted performance changes associated with a once-per-flight vertical gust, and a typical revenue service landing were calculated. The predicted dynamic load effects on thrust specific fuel consumption were found to be negligibly small. The results indicate that the quasi-steady state approach to flight loads modeling is adequate to investigate the factors important to the deterioration process.

Acknowledgments

The authors wish to express appreciation to Dr. Edward S. Todd, Dr. Steve R. Lionberger, and G. Phillip Sallee of Pratt & Whitney Aircraft, Commercial Products Division for their many valuable suggestions during the course of this investigation. Loading and forcing function data were provided by John White and Paul Kafka of The Boeing Company. This work was funded as a part of NASA contract NAS3-20632, Joseph A. Ziemianski, Project Manager, NASA Lewis Research Center. The results of this work are reported on in detail in NASA CR-159681 [8].

References

1 Jay, A., and Todd, E. S., "Effect of Steady Flight Loads on JT9D-7 Performance Deterioration," NASA CR-135407, June 1978.

2 Meirovitch, L., *Analytical Methods in Vibrations,* The MacMillan Company, Chapter 9, 1967.

3 NASTRAN Theoretical Manual, ed., R. H. MacNeal, Apr. 1972.

4 Newman, M. and Pipano, A. "Fast Modal Extraction in NASTRAN via the FEER Computer Program," NASA TM-X-2893, Sept. 1973.

5 MSC/NASTRAN Application Manual, Vol. 1, Section 2.4, The MacNeal-Schwendler Corporation.

6 Craig, R. R., Jr., and Bampton, M. C., "Coupling of Substructures for Dynamic Analysis," *AIAA Journal,* Vol. 6, No. 7, July 1968, pp. 1313-1319.

7 White, J. L., and Todd, E. S., "Normal Modes Vibration Analysis of the JT9D/B747 Propulsion System," *Journal of Aircraft,* Vol. 15, No. 1, Jan. 1978, pp. 28-32.

8 Jay, A., and Lewis, B. L., "Effect of Time-Dependent Flight Loads on JT9D-7 Performance Deterioration," NASA CR-159681, Aug. 1979.

O. P. Sharma

R. A. Wells

Pratt & Whitney Aircraft Group,
Commercial Products Division,
East Hartford, Conn.

R. H. Schlinker

D. A. Bailey

United Technologies Research Center,
East Hartford, Conn.

Boundary Layer Development on Turbine Airfoil Suction Surfaces

This paper presents results of a study, supported by NASA Contract NAS3-20646 under the Energy Efficient Engine Program, conducted to investigate the development of boundary layers under the influence of velocity distributions simulating the suction sides of two state-of-the-art turbine airfoils. One velocity distribution represented a forward loaded airfoil ("squared-off" design) while the other represented an aft loaded airfoil ("aft loaded" design). These velocity distributions were simulated in a low-speed high aspect ratio wind tunnel specifically designed for boundary layer investigations. It is intended that the detailed data presented in this paper be used to develop an improved turbulence model suitable for application to turbine airfoil design.

Introduction

The depletion of fuel resources and continued increases in fuel costs make it imperative that future aircraft gas turbines have the highest possible efficiencies. Optimization of airfoil surface static pressure (velocity) distribution holds a promise for improving efficiency through the reduction of airfoil profile loss. This profile loss is generated by the boundary layers which develop on the airfoil surfaces. For a typical turbine airfoil, 75–80 percent of the total profile loss can be attributed to the suction surface boundary layers. Presently, the most efficient method of estimating this loss for a new design is to predict the boundary layer development through the use of a boundary layer calculation procedure.

A number of calculation procedures are available in literature for estimating the laminar and turbulent boundary layer development. However, boundary layers on turbine airfoils have large regions of transitional flows [1, 2]. Relatively few of the calculation procedures [3–7] are capable of estimating the development of the resulting boundary layers. In most of the existing calculation procedures, concepts of turbulent boundary layers have been extrapolated in transitional regimes to facilitate computation. McDonald and Fish [3] used the turbulent kinetic energy transport equation with several assumptions about the structure of turbulence in transitional flows. In this way, they were able to predict heat transfer data on turbine cascades. Their assumptions about the structure of turbulence were, however, based on intuitive agruments instead of an analytical formulation or experimental data. Arnal and Michel [4] and Wilcox [5] used a two equation turbulence model and Donaldson [6] used a five equation turbulence model for calculating transitional boundary layers. However, several constants in the higher order turbulence models were selected to optimize computer calculations instead of modeling the physics of the transitional flow process. Finally, none of these models have been assessed experimentally due to the lack of transitional boundary layer data on turbine airfoils.

Only one investigator attempted to introduce physical concepts describing transitional flows in his calculation for boundary layer flow development. Forest [7] utilized intermittency factor data when he developed a generalized procedure for calculating boundary layers on turbine airfoils. Such information has been demonstrated to be one of the most reliable features describing wall transitional flows. This is because the intermittency factor distribution has a universal shape in the transitional region in zero pressure gradient boundary layer flows. Unfortunately, Forest's approach required some intuitive arguments and empirical constants to predict heat transfer data on turbine airfoils. Currently, there are no experimental data available in the open literature to substantiate his assumptions.

Based on the foregoing discussion, current calculation methods for turbulent boundary layers in transitional flows employ numerous assumptions about the turbulence structure which cannot be verified due to a lack of detailed experimental data. The objective of the present study was, therefore, to experimentally assess the mean and turbulent velocity profiles developing under the influence of pressure gradients typical of state-of-the-art turbine airfoils. The resulting boundary layer data would provide unique insight into the processes governing the onset of transition for developing boundary layers.

Detailed measurements were obtained for a constant inlet turbulence level (Tu = 2.4 percent) and an approximately constant Reynolds number based on exit velocity and test section length ($Re_S = 8 \times 10^5$).

Two velocity distributions were selected representing candidate designs of the fourth blade mean section of a low pressure turbine. Figure 1 gives the two airfoil shapes and predicted pressure distributions associated with each geometry.

The resulting data describing the laminar, transitional, and turbulent regimes of each boundary layer are compared to theoretical predictions obtained from the turbulence model of McDonald and Fish [3]. The experimental results also provide

Contributed by the Gas Turbine Division of THE AMERICAN SOCIETY OF MECHANICAL ENGINEERS and presented at the Gas Turbine Conference and Products Show, March 9–12, 1981, Houston, Texas. Manuscript received at ASME Headquarters December 23, 1980. Paper No. 81-GT-204.

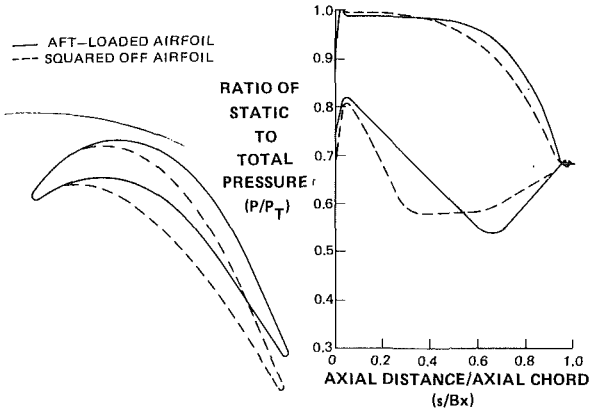

Fig. 1 Two state-of-the-art airfoil profiles and the associated surface static pressure distributions

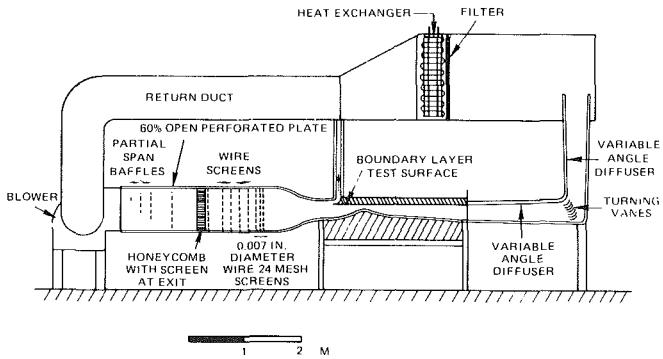

Fig. 2 Schematic of the boundary layer wind tunnel

a unique data base for other investigators to compare existing turbulence models or develop new models.

Experimental Apparatus

Wind Tunnel. The experiment was conducted in a low speed wind tunnel specifically designed for conducting fundamental studies of two-dimensional, incompressible boundary layers. The tunnel operates at a constant air temperature and over a wide range of flow speeds and turbulence levels. Details of the wind tunnel, schematically shown in Fig. 2, and turbulence generating grids are given in a paper by Blair, et al. [8]. Also given in the paper of Blair are the results of a flat plate two-dimensional laminar, transitional, and turbulent boundary layer study that substantiates the application of this wind tunnel for acquiring quality boundary layer data.

Test Section. As shown in Fig. 2, the test section (0.86 m × 2.44 m) of the boundary layer tunnel is situated between the nozzle and the diffuser. It consists of a flat aluminum test plate, a contoured wall, and two transparent side walls. The inlet boundary layer was removed through a bleed scoop at the leading edge of the test plate. The contoured wall opposite the test plate was designed to generate the required pressure distribution. Two differently contoured walls were used in the present investigation, one for the squared-off pressure distribution, another for the aft-loaded pressure distribution. These pressure distribution shapes reflect two approaches toward designing turbine airfoil suction surfaces and represent the static pressure coefficient distributions on the two airfoils shown in Fig. 1. The potential flow analysis of Casper, et al. [9], was used to design the contoured wall shapes needed to produce the desired pressure distributions. Schematics of these test sections and static pressure coefficient distributions for each test section are given in Fig. 3.

A number of holes were drilled in the contoured walls to insert hot-film/wire probes for boundary layer velocity profile measurements. The side walls of the test section were constructed from clear plexiglass to facilitate flow visualization and positioning of the probes.

Nomenclature

B = constant for the law-of-the-wall
Bx = axial chord of the airfoil
C = correlation coefficient = $\overline{-uv}/\sqrt{\overline{u^2}}\sqrt{\overline{v^2}}$
C_p = pressure coefficient
C_f = skin friction = $\dfrac{2\tau_w}{\rho U_\infty^2}$
H = shape factor = $\dfrac{\delta^*}{\theta}$
k = von Karman's constant
P = static pressure
P_T = total pressure
$\overline{q^2}$ = turbulence intensity = $\overline{u^2} + \overline{v^2} + \overline{w^2}$
Re_S = Reynolds number = $\dfrac{U_{\text{exit}} S}{\nu}$
Re_θ = Reynolds number = $\dfrac{U_\infty \theta}{\nu}$
S = test section length
s = axial distance
Tu = inlet turbulence level = $\dfrac{\sqrt{\bar{u}^2}}{U_{\text{inlet}}}$
U = streamwise component of mean velocity
U^+ = dimensionless velocity = U/v^*
U_∞ = velocity at the edge of the boundary layer
$\overline{u^2}$ = streamwise component of turbulence intensity
u^+ = dimensionless turbulence intensity = $\sqrt{\bar{u}^2}/v^*$
$\overline{-uv}$ = Reynolds shear stress
v^* = friction velocity = $\sqrt{\tau_w/\rho}$
$\overline{v^2}$ = normal component of turbulence intensity
$\overline{w^2}$ = traverse component of turbulence intensity
y = normal distance from the wall
y^+ = dimensionless distance from the wall = $\dfrac{yv^*}{\nu}$
γ = intermittency factor
δ = boundary layer thickness
δ^* = boundary layer displacement thickness = $\int_0^\delta \left(1 - \dfrac{U}{U_\infty}\right) dy$
θ = boundary layer momentum loss thickness = $\int_0^\delta \dfrac{U}{U_\infty}\left(1 - \dfrac{U}{U_\infty}\right) dy$
ν = kinematic viscosity
ρ = density
τ_w = wall shear stress

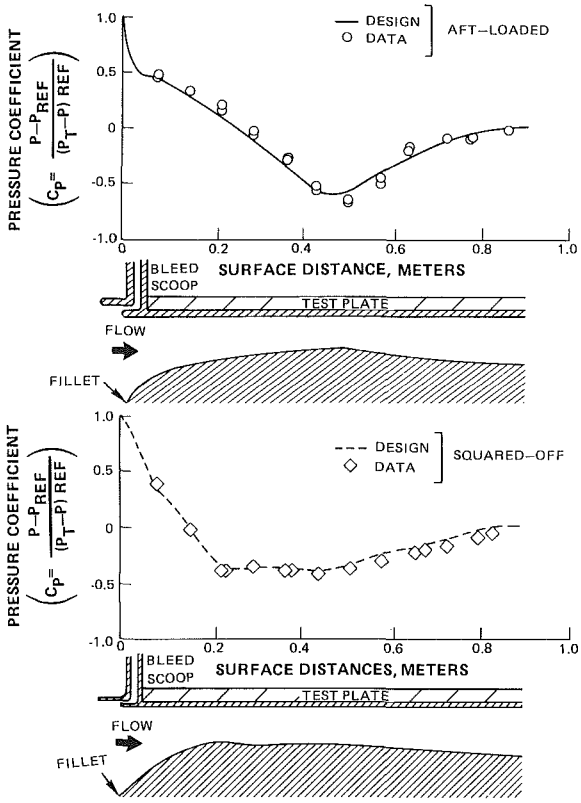

Fig. 3 Test section geometries and pressure distributions simulating the different airfoil configurations

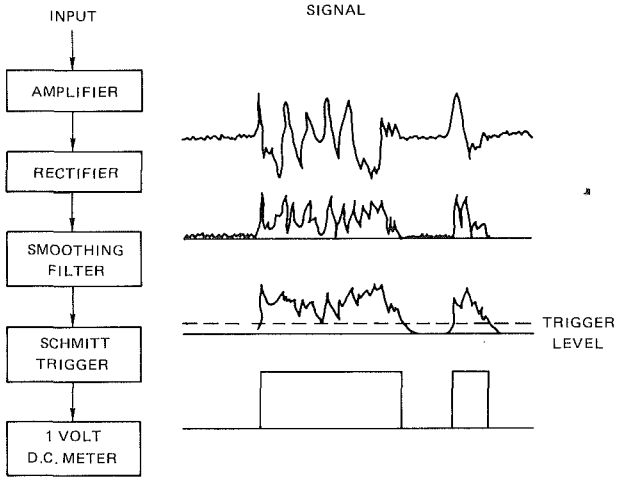

Fig. 4 Schematic of intermittency meter with typical signal outputs

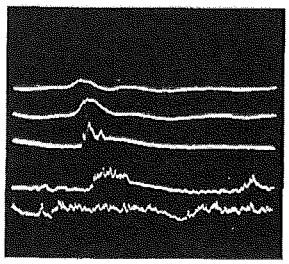

STREAMWISE LOCATION (s)	INTERMITTENCY FACTOR (γ)
0.4668	0.0
0.4922	0.04
0.5429	0.10
0.5938	0.45
0.6954	0.92

Fig. 5 Oscilloscope traces from flush mounted hot-film probes for the "squared-off" test section

Instrumentation and Data Acquisition

Wall Static Pressure. The distribution of wall static pressure on the test plate was measured at a number of streamwise and cross-stream locations. Variation of the static pressure coefficient in the cross-stream direction was found to be within ± 1.0 percent of the mean value at all streamwise locations. The pressure coefficient is plotted along the length of the test section in Fig. 3 for both the squared-off and the aft-loaded test sections. Also plotted in that figure are the calculated pressure distributions of the two airfoils from Fig. 1. Experimental data show good agreement with the calculated airfoil pressure coefficient distribution, verifying that the desired velocity distributions were obtained in the present investigation.

Wall Intermittency Factor. Flush mounted hot-film probes were used to identify the regions of laminar, transitional, and turbulent boundary layer flow. An intermittency meter, shown schematically in Fig. 4, was used to measure intermittency factor distribution in the transitional regime. For laminar flows, the intermittency factor is zero whereas, for turbulent flows, it is one. The intermittency factor by definition [10] is the fraction of time during which the flow is turbulent.

Figure 5 is a photograph showing oscilloscope traces of the output signals from a series of hot-film probes spanning the laminar to fully turbulent boundary layer region. Each trace corresponds to a sensor at the streamwise location listed. Distinct regions of laminar instability, generation of turbulent fluctuations, and subsequent growth to a fully turbulent flow are evident for the squared-off test condition presented in the figure. Similar observations were made for the aft-loaded test condition.

Mean Velocity and Streamwise Component of Turbulence

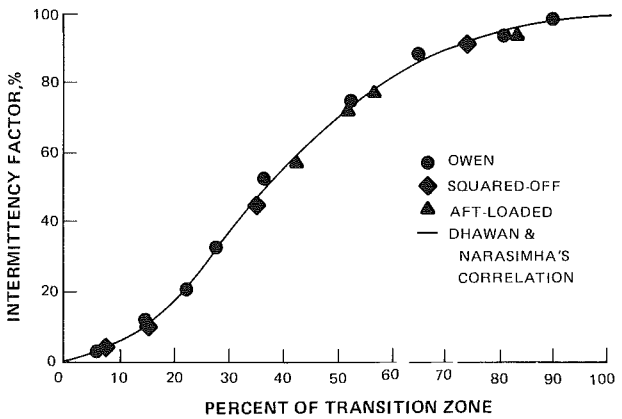

Fig. 6 Distribution of wall intermittency factors data in the transition zone compared with previous investigations

Intensity Profiles. The reference speed of the wind tunnel was set with a pneumatic probe whereas all other velocities were measured with single element cylindrical hot-film sensors. Goose-necked boundary layer sensors, with a sensing area of 0.051 mm in dia and 1 mm in length, were used to measure the streamwise velocity, the streamwise turbulence intensity, and the transverse turbulence intensity profiles. The streamwise mean and turbulence velocity profiles were measured at ten stations for each test configuration. Nine of these stations were located on the duct centerline while the tenth station was displaced 15 cm in the transverse direction from the centerline at the end of each test section. This latter station was selected to check the two-dimensionality of the flow field. Five of the ten profiles were located in the diffusing part of each test section to insure comprehensive coverage of the turbulent boundary layer regimes.

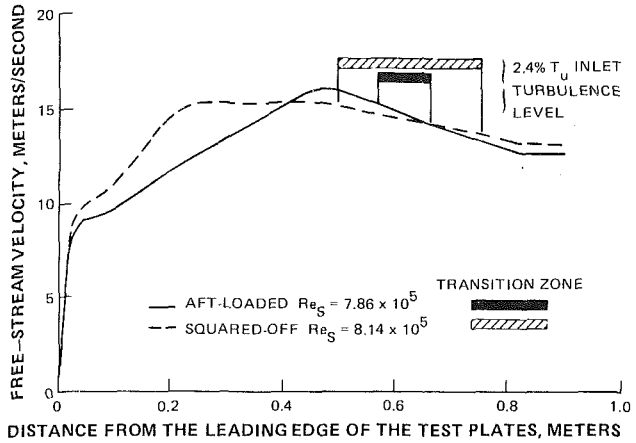

Fig. 7 Free-stream velocity distributions and transition zones for the two test configurations

Boundary layer integral parameters, defined by the momentum loss thickness Reynolds number (Re_θ), shape factor (H), and skin-friction (C_f), were calculated from the mean velocity profile data.

Turbulence Intensity Profiles. The normal component of turbulence intensity was measured with a cross-wire geometry hot-film boundary layer probe. Measurement of the streamwise ($\overline{u^2}$), normal ($\overline{v^2}$), and transverse components ($\overline{w^2}$) of turbulent intensity in the boundary layer were obtained at two streamwise locations for each test geometry. One measurement station was situated in the transition region and the second station was located in the fully turbulent regime. The resulting measurements provided complete information about the boundary layer in both the transitional and fully turbulent flow regimes. A discussion of the results and a comparison of experimental data with theoretical predictions are presented in the following section.

Results and Discussion

Boundary layers for both test configurations were laminar near the leading edge of the test plate and became fully turbulent after passing through the transitional regime. Detailed discussions of the measured data for each boundary layer regime, in addition to theoretical predictions, are given in this section. Theoretical predictions were obtained from the STAN-5 [12] version of Patankar-Spalding [11] boundary layer calculation method. The turbulence model of McDonald-Fish was used in the foregoing calculation method to facilitate the boundary layer predictions through the transition regimes.

Intermittency Factor Data. Measurements of intermittency factor distribution in the transitional region of the two test boudnary layers were obtained from the flush mounted hot-film probes and the intermittency meter described previously. These data are plotted in Fig. 6 along with the flat plate data of Owen [13] and the empirical correlation of Dhawan and Narasimha [10]. As shown in this figure, present data are in good agreement with the data of Owen and the correlation of Dhawan and Narasimha. This correlation was developed on the basis of data from transitional boundary layers developing under the influence of a zero free-stream pressure gradient. Transition regions for the present test conditions were found to be located in the adverse pressure gradient region, as shown in Fig. 7. Good agreement of the present data with Dhawan and Narasimha's correlation indicates that the distribution of intermittency factor in transitional flows is independent of the free-stream pressure gradient.

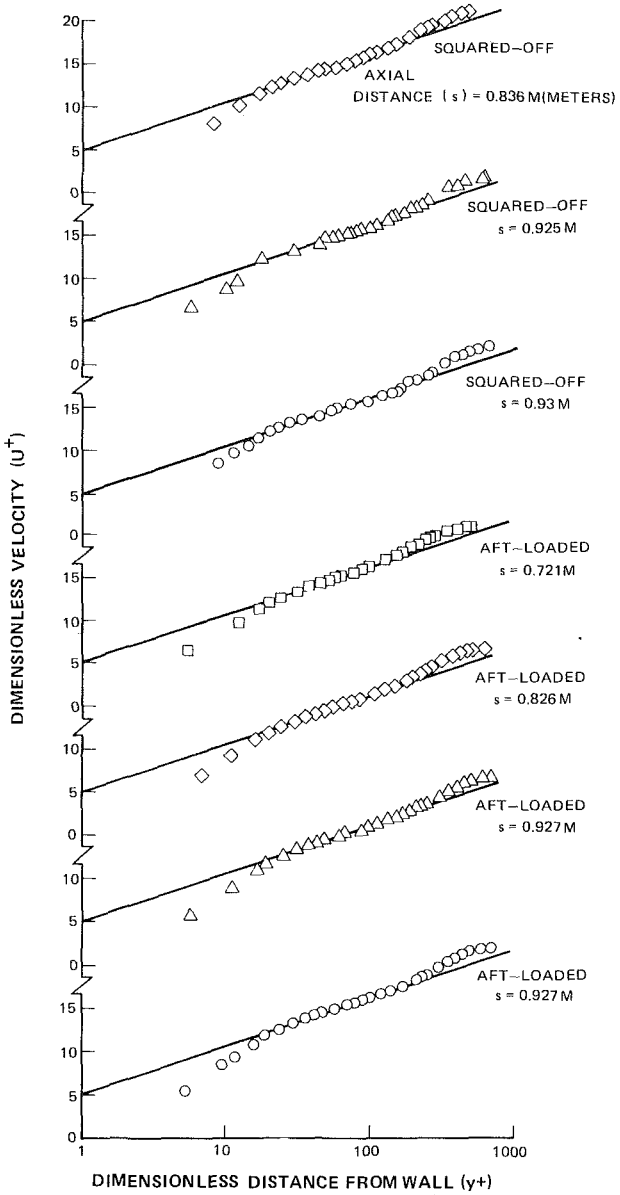

Fig. 8 Turbulent boundary layer velocity profiles using law-of-the-wall dimensionless parameters

Mean Velocity Profile Data and Theoretical Predictions. Ten mean velocity profiles were measured for each test geometry. Nine of the combined twenty velocity profiles obtained from both test sections were located in the laminar flow region, four were in the transitional flow region, and the remaining seven were in the fully turbulent flow region. A comparison of the mean velocity profile data in the transitional and turbulent boundary layer regimes with well established semi-empirical formulations is presented hereafter.

Historically, turbulent velocity profile data are presented in terms of a semi-log plot of dimensionless velocity (U^+) versus dimensionless distance from the wall (y^+). It was shown by Ludweig and Tillmann [14] and substantiated by a number of other investigators (see Coles [15] for further references), that all turbulent boundary layer data show a universal region where the following equation is valid:

$$U^+ = \frac{1}{k} \ln y^+ + B \tag{1}$$

where: U^+ = dimensionless velocity; k = von Karman's

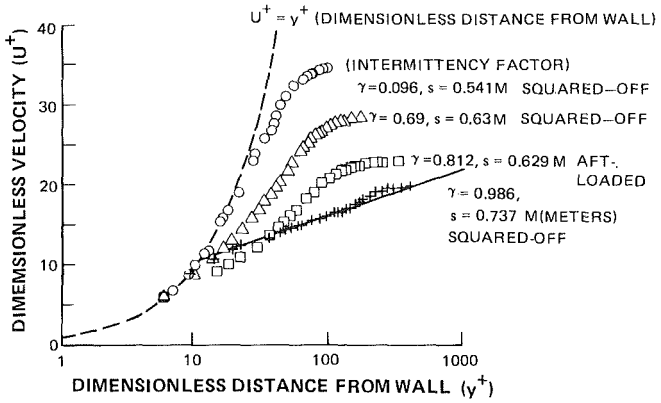

Fig. 9 Transitional boundary layer velocity profile using law-of-the-wall dimensionless parameters

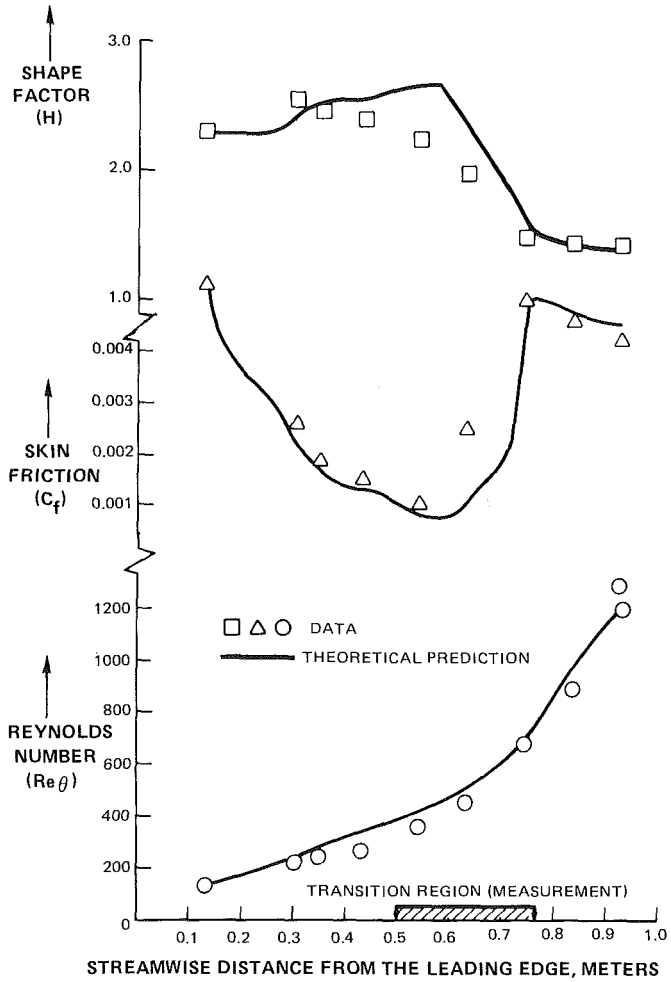

Fig. 10 Comparison of measured integral parameters for the squared-off test section with theoretical predictions using McDonald-Fish turbulence model

constant; y^+ = dimensionless distance from the wall; and B = constant for the law-of-the-wall.

Equation (1) is often referred to as the "law-of-the-wall." Turbulent boundary layer mean velocity profile data from the two test configurations are plotted in Fig. 8 using the dimensionless parameters of equation (1). Large regions exist where the law-of-the-wall is valid. Constants k and B were found to be 0.41 and 5.0, respectively, which are consistent with constants obtained by Coles from the data base presented at the Stanford Conference.

Unlike fully turbulent flows, there is no available published mean velocity profile data comprehensive enough to represent transitional boundary layer development. As a result, the transitional boundary layer data from the present tests are plotted in Fig. 9 in the same coordinate system as used for the turbulent boundary layer data in Fig. 8. Also shown in Fig. 9 are the wall intermittency factor data associated with each profile and velocity profiles expected in the viscous sublayer and in the fully turbulent flows. This figure shows that as the intermittency factor increases, the velocity profiles change from a viscous sublayer shape to a fully turbulent shape. The velocity profile for the boundary layer, where the intermittency factor is 0.982, exhibits a turbulent profile shape similar to the velocity profiles in Fig. 8.

Integral parameters defined by the momentum loss thickness Reynolds number (Re_θ), shape factor (H), and skin-friction (C_f) were calculated from the mean velocity profile data. The data are compared to theoretical predictions in the following two sub-sections for the two test boundary layers. Free-stream velocity distributions, shown in Fig. 7, and measured inlet turbulence level (Tu = 2.4 percent) were parameters input for the boundary layer calculation method STAN-5. Theoretical calculations started with the velocity profile measured at the station nearest the leading edge of the test plate.

Comparison of Squared-Off Test Data with Theoretical Predictions. Experimental data for the integral parameters obtained from the squared-off test configurations are plotted in Fig. 10 along with the theoretical predictions. In general, theoretical predictions show good agreement with the data.

Detailed mean velocity profile data are compared to the theoretical predictions in Fig. 11. Theoretical predictions show good agreement with laminar and turbulent velocity profiles. However, the predictions are in poor agreement with the transitional velocity profile data.

Comparison of Aft-Loaded Test Data with Theoretical Predictions. A comparison of the experimental and theoretical integral parameters for the aft-loaded test is shown in Fig. 12. Theoretical predictions are in good agreement with the data for the laminar region of the flow field, but show separation of the flow in the diffusing part of the boundary layer. Calculations were repeated and the boundary layer was artificially made transitional, at a distance of two boundary layer thicknesses upstream of the expected separation point, to obtain theoretical predictions. It is difficult to say, on the basis of the present data, whether the boundary layer had really separated at the predicted location. However, it should be pointed out that the calculated separation location is slightly upstream of the transition region identified with the hot-film probes. Even if separation had occurred, it did not influence the behavior of the intermittency factor in the transitional region as shown previously.

Figure 13 shows detailed velocity profile data along with the theoretical predictions. Again, measured mean velocity profiles for the laminar and turbulent regions are found to be in good agreement with predictions.

Comparisons of theoretical predictions with the experimental data for the two test configurations indicate that, overall, the McDonald-Fish turbulence model provides good estimates for the mean integral parameters for attached transitional boundary layers.

Turbulence Intensity Profiles in the Turbulent Boundary Layer Regions. Three components of turbulence intensity measured at the test section exit plane for the two test boundary layers were used to obtain total turbulence intensity profiles. The data obtained from the present test are plotted in Fig. 14 along with the flat plate boundary layer data of

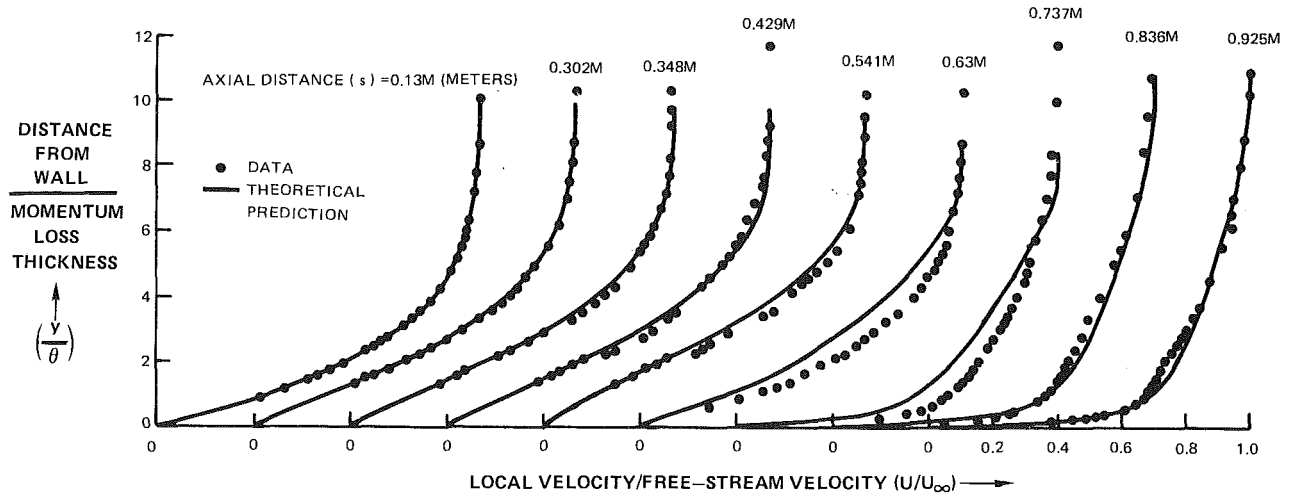

Fig. 11 Comparison of the mean velocity profile data (squared-off) with the theoretical predictions using McDonald-Fish turbulence model

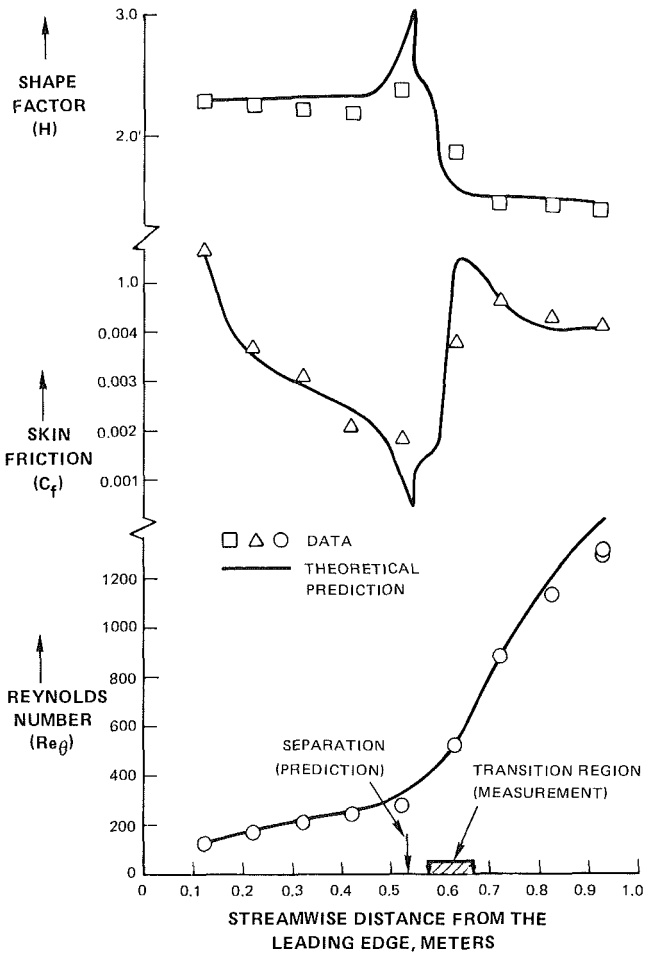

Fig. 12 Comparison of measured integral parameters for the aft-loaded test with theoretical predictions using McDonald-Fish turbulence model

Klebanoff [20]. The present data are found to be in good agreement with Klebanoff's data. Relative magnitudes of various components of turbulence intensity for the squared-off test configuration are plotted in Fig. 15. The data indicate that the streamwise ($\overline{u^2}$), the normal ($\overline{v^2}$), and the transverse ($\overline{w^2}$) components of turbulence intensity contain about 50, 20 and 30 percent of the total turbulence intensity, respectively, which is consistent with the data of Klebanoff. Lines drawn at 50, 30 and 20 percent represent the values used in the McDonald-Fish turbulence model and the present data support their assumptions, at least in the fully turbulent region.

Turbulence Intensity Profiles in the Transitional Boundary Layer Regions. Relative magnitudes of turbulence intensity components for the transitional region of the squared-off test boundary layer are plotted in Fig. 16. The present data show that the streamwise and normal components of turbulence intensity contain about 80 and 10 percent of the total turbulence intensity, respectively. This data also show that turbulence in transitional boundary layers is more nonisotropic than in fully turbulent flows.[1] Further comments on the nonisotropic nature of turbulence on the behavior of transitional boundary layers are made in the following subsection.

Turbulence Intensity in the Laminar Boundary Layer Regions. Systematic growth of the streamwise component of turbulence intensity was observed in the laminar region of both test boundary layers. The present data, along with similar observations from previous data, are subsequently discussed.

Dimensionless turbulence intensity (u^+) data in the laminar boundary region are plotted as a function of dimensionless distance from the wall (y^+) in Fig. 17 for both test boundary layers. This figure shows the following two important features of the turbulence profiles:

1 Turbulence intensity profiles in the laminar boundary layer region have a maximum value in the neighborhood of 25.
2 Maximum turbulence intensity (u^+ at $y^+ = 25$) increases in the downstream direction as the onset of transition is approached.

Similar observations can be deduced from the measurements of Leipmann [17] and Schubauer and Klebanoff [19]. The data from the latter work are plotted in Fig. 18 and show the same trend as observed in the present investigation. Both Leipmann and Schubauer and Klebanoff concluded that these high turbulence intensities were due to the presence of strongly amplified oscillations. These disturbances do not significantly influence the shape of the

[1] Where the streamwise and normal components of turbulence intensity contain about 50 and 20 percent of the total turbulence intensity, respectively.

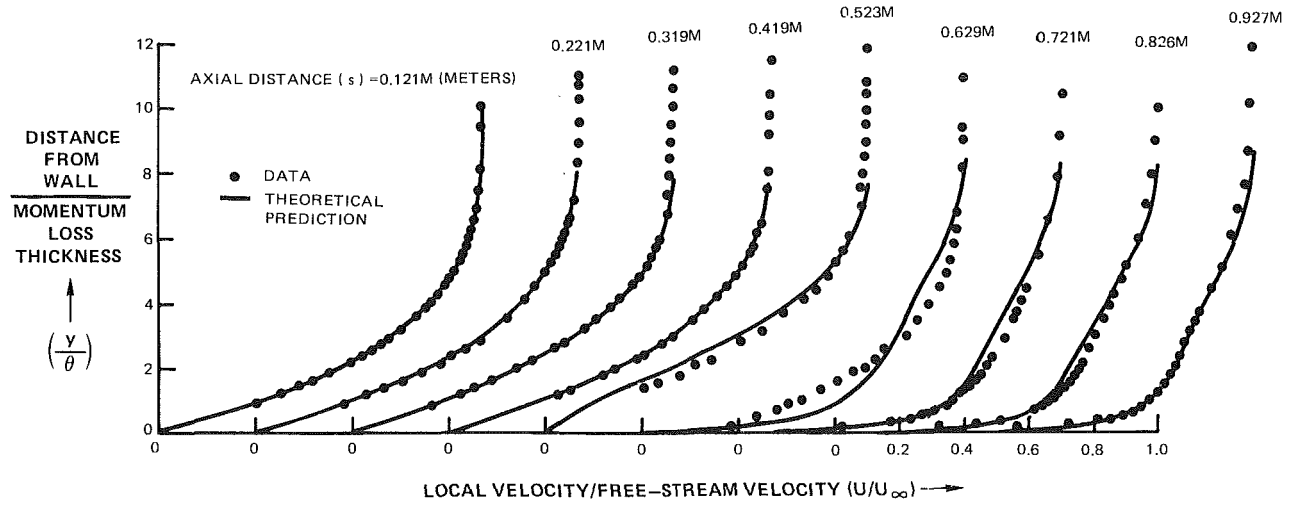

Fig. 13 Comparison of the measured mean velocity profile data (aft-loaded) with the theoretical predicitons using the McDonald-Fish turbulence model

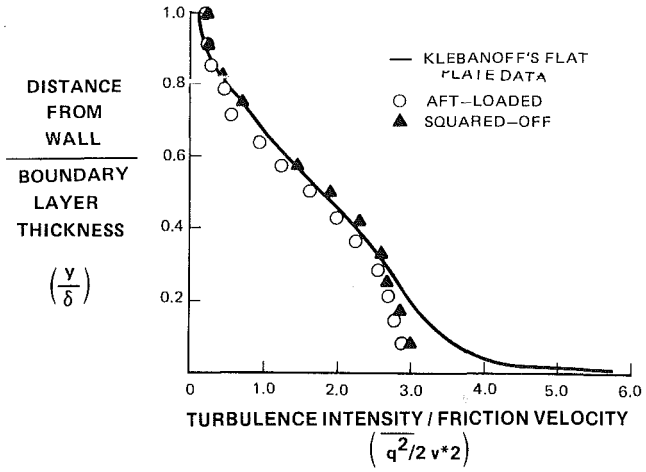

Fig. 14 Comparison of measured total turbulence intensity profiles with the flat plate data of Klebanoff

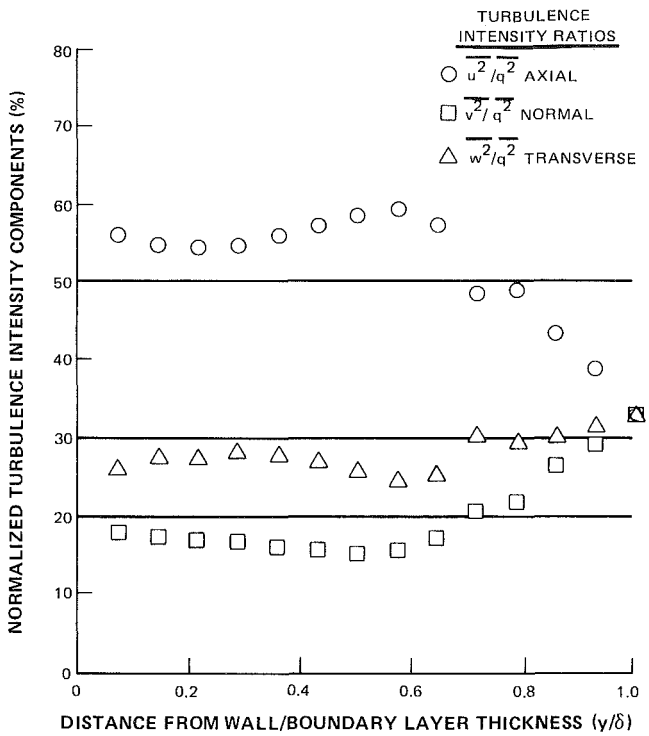

Fig. 15 Distribution of normalized turbulence intensity components in the fully turbulent region of the squared-off test configuration

mean velocity profiles as shown by the aforesaid two investigations in which the mean velocity profile data matched the Blasius solution for laminar regions.

The results of the present study and the conclusions reported in references [17] and [19] form the basis of a hypothesis for the onset of transition in boundary layer flows. Conceptually, disturbances grow in laminar boundary layers in the streamwise direction until they reach a threshold value where the process of transition is initiated. If the onset of transition is assumed to occur when the intermittency factor reaches a value of about 0.1, then, on the basis of the present data, the threshold disturbance value corresponds to maximum dimensionless turbulence intensity equal to 3.

The present hypothesis for the onset of transition may be written as:

$$\overline{u^2} = 9\ v^{*2} \tag{2}$$

where: $\overline{u^2}$ = streamwise component of turbulence intensity; and v^* = friction velocity.

Leipmann obtained detailed measurements of various components of turbulence intensity in laminar boundary layers which indicate that streamwise and normal components of turbulence intensity contain about 90 and 4 percent of the total turbulence intensity, respectively. In addition, Leipmann also proposed a hypothesis for the onset of transition according to which the flow becomes transitional when the maximum value of Reynolds shear stress in the laminar flow equals the wall shear stress. Leipmann's hypothesis for the onset of transition may be written as:

$$-\overline{uv} = v^{*2} \tag{3}$$

where: $-\overline{uv}$ = Reynolds shear stress and v^* = friction velocity.

If it is assumed that Leipmann's hypothesis is consistent with the present hypothesis for the onset of transition, then equations (2) and (3) and turbulence intensity data of Leipmann may be used to obtain the following relationship between the Reynolds shear stress and total turbulence intensity.

$$-\overline{uv} = 0.1\ \overline{q^2} \tag{4}$$

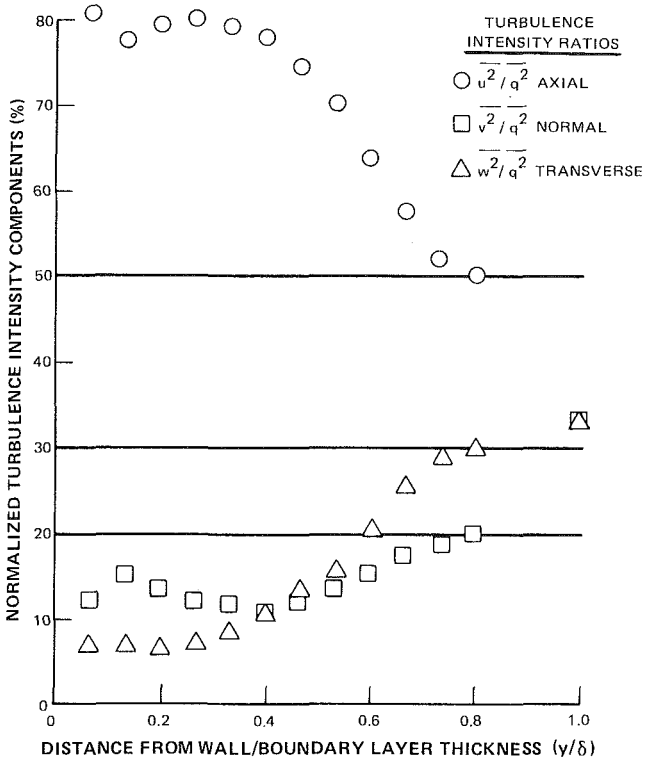

Fig. 16 Distribution of normalized turbulence intensity components in the transitional region of the squared-off test configuration

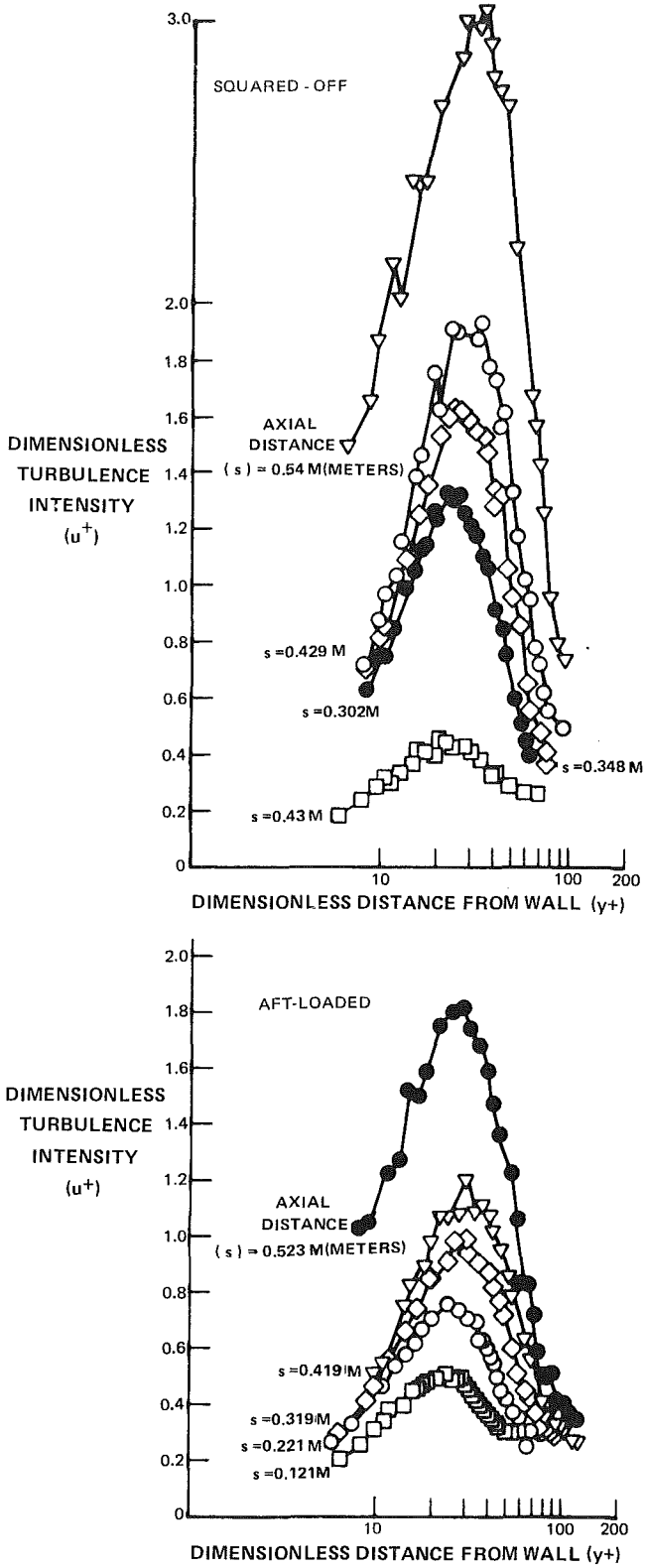

Fig. 17 Growth of turbulence intensity in the laminar region of each boundary layer

where: $-\overline{uv}$ = Reynolds shear stress and $\overline{q^2}$ = turbulence intensity.

It is interesting to find that $-\overline{uv}/\overline{q^2}$ in the laminar boundary layer (equation (4)) is of the same order as obtained in fully turbulent flows where $-\overline{uv}/\overline{q^2}$ is typically 0.12.

Equations (2) and (3) and Leipmann's data may also be used to obtain typical values of the correlation coefficient between the streamwise and normal components of turbulence intensity. The correlation coefficient (C) may be written in terms of Reynolds shear stress and the two components of turbulence intensity as follows:

$$C = \frac{-\overline{uv}}{\sqrt{\overline{u^2}}\sqrt{\overline{v^2}}} \tag{5}$$

where: C = correlation coefficient; $-\overline{uv}$ = Reynolds shear stress; $\overline{u^2}$ = streamwise component of turbulence intensity; and $\overline{v^2}$ = normal component of turbulence intensity

Substituting v^{*2} for $-\overline{uv}$ from equation (3), $\overline{v^2} = \overline{u^2}/22.5$ from Leipmann's data and $\overline{u^2} = 9\,v^{*2}$ from equation (2), into equation (5) leads to:

$$C = 0.527 \tag{6}$$

Since the correlation coefficient is typically 0.45 in fully turbulent flows, the value in equation (6) is in close agreement, implying that the magnitude of the correlation coefficient may be independent of the state of the boundary layer.

A number of turbulence models [3-5] implicitly assume that either the variation in correlation coefficient (C) or a variation in $-\overline{uv}/\overline{q^2}$ is responsible for low magnitudes of Reynolds shear stress in laminar or transitional boundary layers. However, equations (4) and (6) show that both C and $-\overline{uv}/\overline{q^2}$ may be independent of the state of the boundary layer. Lower magnitudes of Reynolds shear stress in laminar and transitional boundary layers, as opposed to fully turbulent boundary layers, are possible due to lower magnitudes of the normal component of turbulence intensity in these flows. This statement implies that the nonisotropic nature of turbulence in laminar and transitional boundary layers may be a dominating mechanism governing the process of transition in boundary layers. None of the available turbulence models recognizes this nonisotropic behavior of turbulence for predicting transitional boundary layer growth.

On the basis of the present data for transitional and tur-

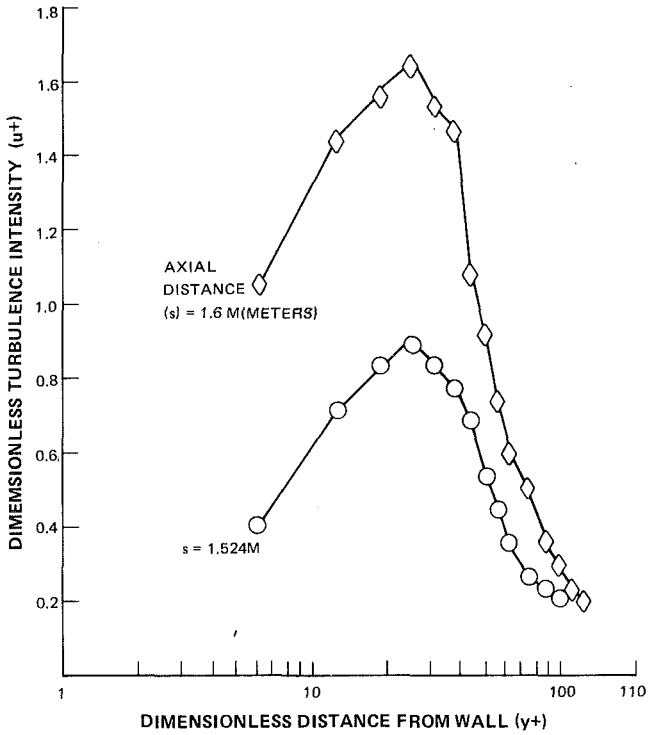

Fig. 18 Growth of turbulence intensity in the flat plate laminar boundary layer region of Schubauer and Klebanoff

bulent boundary layers, and Leipmann's data for laminar boundary layers, the process of transition in boundary layers may be visualized to occur in the following manner. Disturbances, due to the presence of instabilities in the viscous flow, grow in the laminar boundary layer where most of the disturbance energy is contained in the streamwise component of turbulent intensity. Initially, the normal component of turbulent intensity has a low value in the laminar boundary layer, but it increases in the downstream direction by obtaining energy from the streamwise component of the turbulence intensity. Simultaneously, the Reynolds shear stress is generated due to the presence of the normal component of the turbulence intensity. When the maximum value of the Reynolds shear stress in the laminar boundary layer is equivalent to the wall shear stress, the flow ceases to be laminar and the process of transition is initiated. Both streamwise and normal components of turbulent intensity grow in the transitional region with the latter component growing at a faster rate than the former, resulting in an overall increase of the Reynolds shear stress. Transition is terminated when the streamwise and the normal components of turbulence intensity and the Reynolds shear stress reach their respective equilibrium magnitudes.

Conclusions

Reliable turbulence models are vital for predicting the profile loss on the suction side of turbine airfoils having different free-stream velocity distributions. An experimental and analytical investigation was, therefore, conducted to assess the influence of free-stream velocity distribution on the development of two dimensional transitional boundary layers. The study provided a unique data base for evaluating existing and future turbulence models for transitional boundary layers. The following conclusions result from the present investigation:

- Wall intermittency factor data, in adverse pressure gradient boundary layers, agree with the zero pressure gradient correlation of Dhawan and Narasimha. Thus, the present data indicate the intermittency factor distribution in transitional boundary layers is independent of the free-stream pressure gradients typical of turbine airfoils.
- Turbulence intensity profiles have a maximum value at y^+ equal to 25 in laminar boundary layers. This maximum intensity increases in the streamwise direction and the onset of transition occurs when the streamwise turbulence intensity ($\sqrt{\overline{u^2}}$) reaches a threshold value of three times the friction velocity (v^*).
- Deductions, based on the present data and the work of Leipmann, indicate that the ratio of Reynolds shear stress to turbulence intensity ($-\overline{uv}/\overline{q^2}$) is approximately the same in the laminar and the turbulent flow. The correlation coefficient ($-\overline{uv}/\sqrt{\overline{u^2}}\sqrt{\overline{v^2}}$) is also similar in these two flow regimes.
- The McDonald-Fish turbulence model gives reasonable predictions for mean integral parameters in attached transitional boundary layers.

Acknowledgments

This work was funded by the NASA, Lewis Research Center, under the Energy Efficient Engine Component Development and Integration Program, Contract NAS3-20646, Carl C. Ciepluch, Project Manager.

References

1 Turner, A. B., "Local Heat Transfer Measurements on a Gas Turbine Blade," *Journal of Mechanical Engineering Science*, Vol. 13, 1971.

2 Graziani, R. A., et al., "An Experimental Study of Endwall and Airfoil Surface Heat Transfer in a Large Scale Turbine Blade Cascade," ASME JOURNAL OF ENGINEERING FOR POWER, Vol. 102, 1980.

3 McDonald, H., and Fish, R. W., "Practical Calculations of Transitional Boundary Layers," *International Journal of Heat and Mass Transfer*, Vol. 16, No. 9, 1972.

4 Arnal, D., and Michel, R., "Effect of Free Stream Turbulence on Turbulent Boundary Layers and on Boundary Layer Transition," ERUOMECH 72, Boundary Layers and Turbulence in Internal Flows, University of Salford, Salford, U.K., Mar. 30–Apr. 1, 1976.

5 Wilcox, D. C., "A Model for Transitional Flows," AIAA Paper No. 77-126, 1977.

6 Donaldson, C. du P., "A Computer Study of an Analytical Model of Boundary Layer Transition," AIAA Paper No. 68-38, 1968.

7 Forest, A. E., "Engineering Predictions of Transitional Boundary Layers," Laminar-Turbulent Transition, AGARD-CP-224, Paper 22, 1977.

8 Blair, M. F., Bailey, D. A., and Schlinker, R. H., "Development of Large-Scale Wind Tunnel for the Simulation of Turbomachinery Airfoil Boundary Layers," presented at the ASME Gas Turbine Conference, Houston, Tex., 1981.

9 Casper, J. C., Hobbs, D. E., and Davis, R. L., "The Calculation of Two-Dimensional Compressible Potential Flow in Cascades Using Finite Area Techniques," AIAA Paper 79-0007, Jan. 1979.

10 Dhawan, S., and Narasimha, R., "Some Properties of Boundary Layer Flows during Transition from Laminar to Turbulent Motion," *Journal of Fluid Mechanics*, Vol. 3, pp. 418–836, 1958.

11 Patankar, S. V., and Spalding, D. B., *Heat and Mass Transfer in Boundary Layers*, Intertext Books, London, 1970.

12 Crawford, M. E., and Kays, W. M., "STAN-5 - A Program for Numerical Computation of Two-Dimensional Internal and External Boundary Layer Flows," NASA CR-2742, 1976.

13 Owen, F. K., "Transition Experiments on a Flat Plate at Subsonic and Supersonic Speeds," *AIAA Journal*, Vol. 8, No. 3, 1970, pp. 518–523.

14 Ludweig, H., and Tillmann, W., "Investigation of the Wall Shearing Stress in Turbulent Boundary Layers," NACA Report TM 1285, 1949.

15 Coles, D., "The Law of the Wake in Turbulent Boundary Layer," *Journal of Fluid Mechanics*, Vol. 1, 1956.

16 Coles, D., "The Young Person's Guide to the Data," A Survey Lecture prepared for the 1968 AFOSR-ISP-Stanford Conference on Computation of Turbulent Boundary Layers.

17 Liepmann, H. W., "Investigations of Laminar Boundary Layer Stability and Transition on Curved Boundaries," NACA ACR No. 3H30, 1943.

18 Liepmann, H. W., "Investigation of Boundary Layer Transition on Concave Walls," NACA ACR No. 4J28, 1945.

19 Schubauer, G. B., and Klebanoff, P. S., "Contributions on the Mechanics of Boundary Layer Transition," NACA TR 1289, 1956.

20 Klebanoff, P. S., "Characteristics of Turbulence in a Boundary Layer with Zero Pressure Gradient," NACA Report 1247, 1955.

J. P. Van Buijtenen
Supervising Development Engineer,
Thomassen, Holland B. V.

W. M. Farrell
Chief Engineer,
Fern Engineering,
Bourne, Mass.

Mechanical Design of a High-Efficiency 7.5-MW (10,000-hp) Gas Turbine

This paper describes the mechanical design features on TF-10 gas turbine. The TF-10 gas turbine features an intercooled centrifugal compressor and an annular combustor. A regenerator is added as a standard item. The ISO rating is 7.5 MW (10,000 hp) with a rotor inlet temperature (RIT) of 1116°C (2042°F) and a thermal efficiency of approximately 44 percent. Description of the combustion, rotors, stators, bearings, and shafting is presented.

Introduction

In 1976, Thomassen Holland and Fern Engineering began the development of a high efficiency 7.5 MW gas turbine. The objective was to design a gas turbine with the highest possible thermal efficiency using proven state of the art mechanical design practice in order to achieve maximal reliability with minimal development.

Many studies were made to determine the cycle parameters such as pressure ratio and RIT, along with the basic turbomachinery flow path, number of stages, etc., which would optimize thermal efficiency. These were made in conjunction with mechanical design analysis to determine cooling air required, leakages, and bearing losses.

The final cycle selected was an intercooled, regenerative gas turbine with rotor inlet temperature of 1116°C and overall pressure ratio of 9:1.

The cycle optimization study was presented at the 1980 ASME conference [1].

The unit is a two-shaft design with an annular combustor, single stage axial high pressure turbine driving a double ended LP centrifugal compressor and a single hp centrifugal compressor, followed by a two stage load turbine.

Basic Machine Arrangement

The basic mechanical design approach was to combine the advantages of both the heavy duty industrial type design and aircraft derivatives. Features taken from aircraft design include:

- full annular combustion liner
- modular construction
- nickel base alloy turbine wheel material
- wheel space bucket cooling air boarding
- multiple fuel nozzles
- nonsplit combustor casing and exhaust frame for structural integrity

Similarly, features taken from heavy duty industrial gas turbine design include:

- hydrodynamic bearings
- low alloy steels as casing materials
- low cost construction
- simple maintenance, no special tools
- fewer stages of turbo machinery
- split turbine shell for hot gas path inspections and service
- rugged, long life design

The basic aerodynamic approach was to make full use of the parameters that make the regenerative intercooled cycle [RIC] one of the highest in thermal efficiency.

The 9:1 pressure ratio was selected by optimizing on a firing temperature [RIT], which in turn was optimized by including the effect of mechanical design in terms of cooling and sealing. For example, without realistic evaluation of the required hot gas path cooling and leakage air, the indicated optimum pressure ratio would be near 11:1. The number of stages was also selected by considering the effect of bucket cooling air, wheel space cooling air, shroud, nozzle, and stage seal leakage. The exhaust diffuser is optimized also in mechanical requirements such as strut cooling air introduction and gas path overlaps.

One of the most important aspects of a gas turbine machine arrangement is the construction and location of the rotors and bearings. In the early stage of the TF-10 design, both two shaft and single shaft versions were considered. Also, combined and separate compressor and turbine casings and simply supported and overhung wheels were studied. Twenty different shaft and bearing arrangements were considered as depicted in Fig. 2.

The single shaft versions were eliminated and the final choice was No. 17, i.e., six bearings with over hung turbine rotors and separate turbine and compressor casings.
The advantages of this choice are:

1 Each of the three pieces of turbomachinery has its own rotor with two bearings of known reactions and is vibrationally isolated from the other rotors via flexible couplings.

Contributed by the Gas Turbine Division of THE AMERICAN SOCIETY OF MECHANICAL ENGINEERS and presented at the Gas Turbine Conference and Products Show, March 9-12, 1981, Houston, Texas. Manuscript received at ASME Headquarters December 30, 1980. Paper No. 81-GT-210.

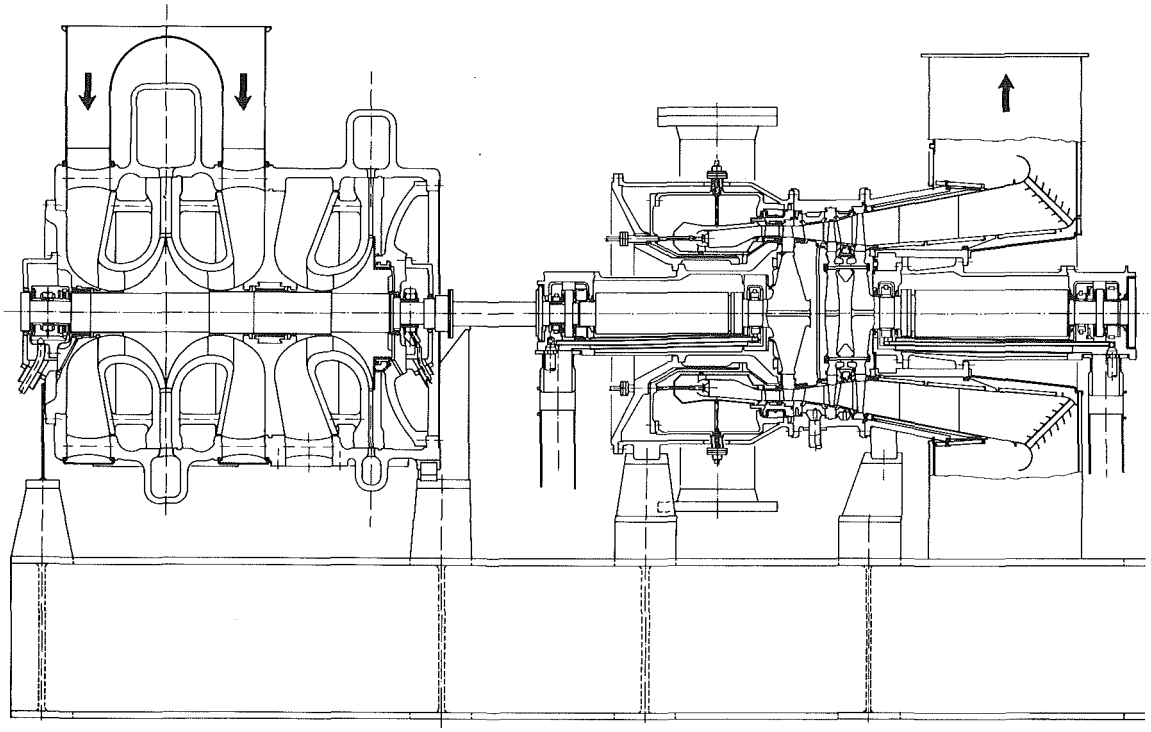

Fig. 1 TF-10 cross section

2 Problems of alignment are minimized and no shaft stresses are introduced through misalignment.
3 Better control is possible of critical speeds, rotor response, loss of bucket capability, and subsynchronous whirl.
4 Each section of turbomachinery can be designed and optimized in a modular fashion independent of each other.
5 Changes in design and application (such as a low Btu gas combustor or a different load turbine) can be accomplished without major redesign.
6 Maintenance and/or replacement of each section is independent of the other.

The arrangement then consists of a compressor with LP and hp centrifugal impellers straddle mounted on a two bearing shaft in its own independently supported casing. The compressor is connected to the turbine with a flexible coupling.

The turbine consists of two modules, hp and L.P. Six flanges break these into five major assemblies: hp casing, hp rotor cartridge, LP casing, exhaust frame, and LP rotor cartridge.

The turbine casing is also independently centerline supported and gibbed. The exhaust has an isolated hood that is sealed and supported from the exhaust frame.

Air is piped from the LP compressor outlet to the intercooler, from the intercooler to the hp compressor inlet and from the hp compressor outlet to the regenerator. Pipes return heated air from the regenerator to four inlet ports in the combustor casing.

Compressor Design

Rotor. Both impellers of the two stage centrifugal compressor are located on one shaft supported by bearings at each end. The shaft is driven from the hp end, while at the LP end, a coupling drives the accessory gear. The dimensions, shape and speed of the impellers are set by aerodynamic optimization, taking into account optimum running conditions of the HP turbine stage. So the double entry LP stage configuration was established as being necessary to approach optimum specific speed for all three turbomachinery components running at the same physical speed [2].

Wheel stress calculations were performed by finite element methods to assure mechanical and aerodynamic optimization. The results of these stress calculations indicated that a number of materials were possible, such as high alloy steels, nickel base alloys, and Titanium alloys. Other considerations, such as corrosion and erosion resistance, manufacturing and weight (critical speed), were taken into account in making the final selection: German grade 1.4405A 16/5 chromium nickel stainless steel.

An early analysis of the LP wheel showed an advantage of the LP double flow concept: the symmetric shape gives a more uniform stress distribution at the bore. Giving the backside of the hp hub a shape either inwards or outwards resulted in an improvement in the hp bore stress. (Figs. 4(*a–c*)). Integration of a balancing piston with hp impeller hub gave a shape which is very close to the shape of the LP hub. The result of the analysis showed a considerable decrease in bore stress. However, an unacceptable stress peak occurred in the corner between balance piston and hub (Fig. 4(*d*)). Different designs were investigated to solve this problem. The best solution was the shape of Fig. 4(*c*) [3, 4].

Aerodynamic design of the inlet channels of the radial impellers gave a lower limit to the amount of axial spacing between the impellers and/or other components. A number of different shaft configurations were considered and analyzed for critical speed with the influences of bearing span, overhang weight, and location of masses between the bearings (see Fig. 5).

Figure 5(*a*) was eliminated in an early stage. Apart from not fulfilling the critical speed demands. In this case, it is not possible to take full advantage of the overhung impeller concept because both shaft ends bear a coupling to another machine part.

A major remaining consideration was the thrust bearing location. Putting the thrust collar between the radial bearings increased the bearing span, while putting it outside increased the overhung weight.

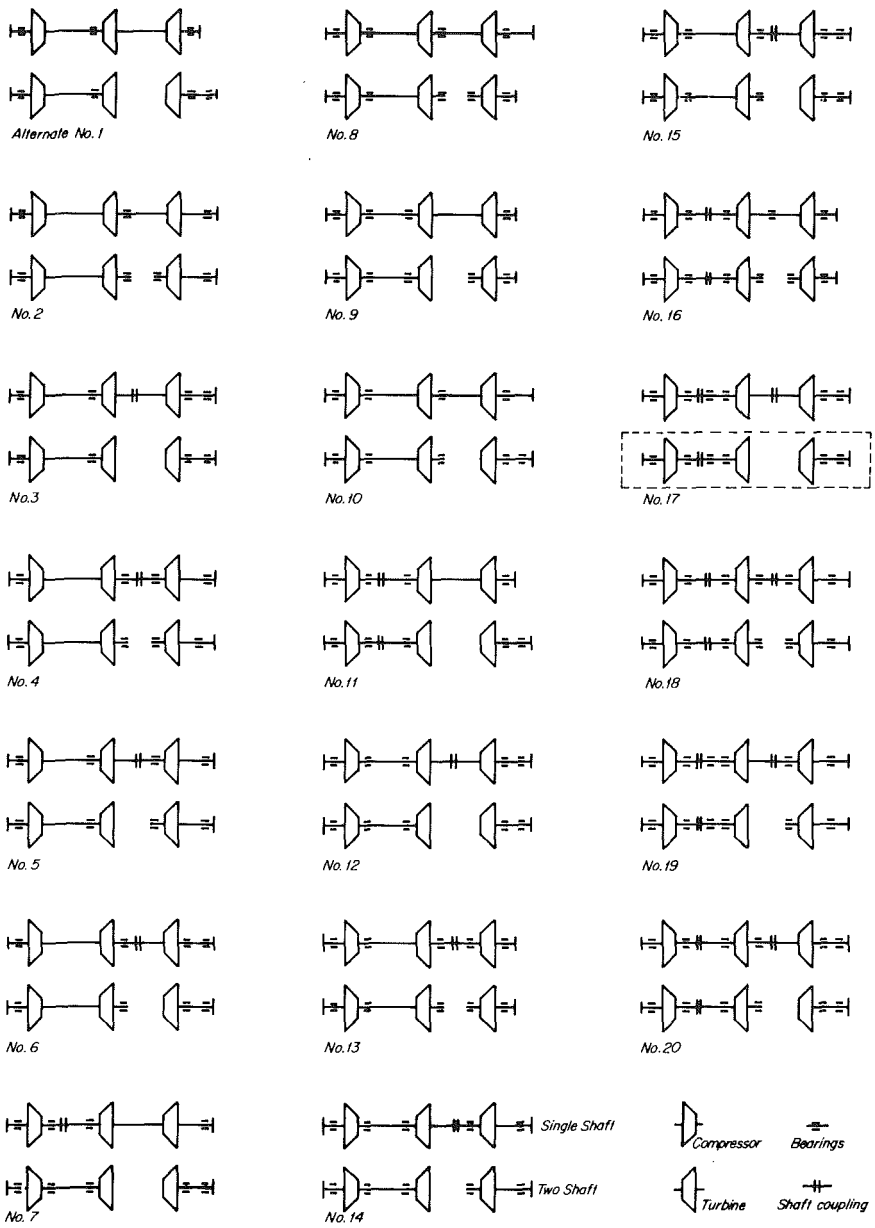

Fig. 2 Rotor arrangements

None of these locations gave a satisfactory fulfillment of critical speed demands (Figs. 5(*b*) and (*c*)).

The solution was found by separating the active and inactive thrust bearing and locating them at either side of the radial bearing (see Figs. 5(*e*) and (*f*)).

As thrust faces the shaft material itself is used, being the remaining surface between radial bearing diameter and overall shaft diameter (see Fig. 6.) Because this surface is too small to carry the full thrust as calculated for hp impeller, the latter is equipped with a thrust balancing device (see Fig. 7).

The diameter of this balancing piston is chosen in a way that under all operating conditions there will be a force present in a constant direction.

The balancing piston will be made integral with the hp impeller, which is favorable for the maximum bore stress in the wheel (see Fig. 4). Comparing Figs. 5(*c*) and (*d*) proved that the location of the hp wheel mass as close as possible to the bearing was favorable.

The use of the balancing piston gave the opportunity to level off the hp wheel exhaust pressure to atmospheric pressure in different stages, thus minimizing the amount of air leaking to atmosphere.

A scheme for the hp sealing is also shown in Fig. 7. The backface of the hp impeller is subjected to the static pressure of the wheel outlet at the outer part, while the inner part is subjected to the pressue maintained next to the bearing housing, which pressure is approximately 1.3 bar. The seal of the balance piston is split into two portions: The first seal seals from hp wheel discharge pressure to hp inlet pressure and the second seals the hp stage inlet pressure from the pressure next to the bearing housing.

Casing

The compressor module of the TF-10 has been designed fulfilling the following demands:

- horizontally split casing
- all piping connections in bottom half
- inlet hood to be mounted in any clock position

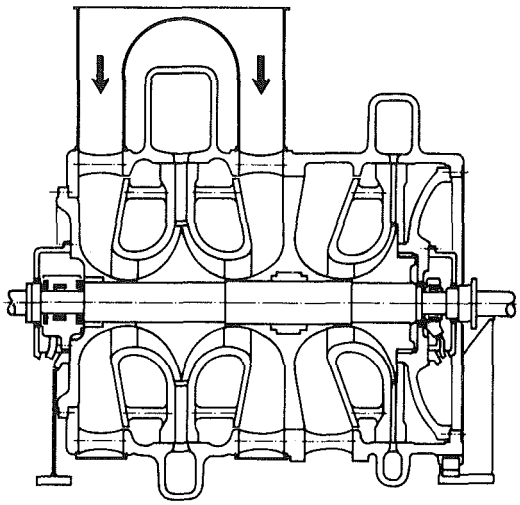

Fig. 3 Compressor cross section

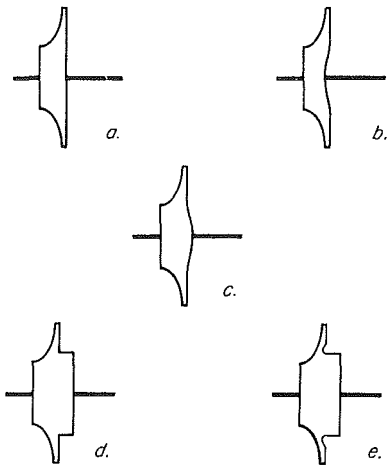

Fig. 4 Impeller designs

- no bolting in flow path
- bearing inspection possible without lifting upper half

The main element of the casing is a cylinder (see Fig. 3). To allow the inlet air to flow in, openings are cast in circumferentially. The lower half has openings for the hp inlet.

Outside the cylinder, the scrolls are located for collecting the discharge air of both stages.

The piping connections of the scrolls are in the bottom half. The bearing housings are located in the end walls of the cylinder. Within the cylinder, there are three diaphragms:

- shrouds and diffusor of the LP stage
- shroud and diffusor of the hp stage
- interstage diaphragm

Pressure loading on structural parts is avoided as much as possible. The LP end-wall is only subjected to the load equal to the pressure drop across the inlet. The interstage is loaded by the pressure difference between hp and LP inlet. The hp end-wall is only subjected to hp inlet pressure at the outside. This is another advantage of the split seal on the balancing piston. Moreover, the hp diaphragm is subjected to the same pressure at both sides. The hp discharge pressure is contained between both walls of the diffusor. The only part that has to withstand full compressor discharge pressure is the hp scroll. Thrust load is taken by the LP endwall, which is shaped to do that with minimal deflection.

The LP part and hp part of the casing were analyzed by finite element methods. The pressure load and thrust load can be taken easily by the proposed design. To decrease temperature stresses, material has been removed at places where no pressure or mechanical load is of high value. Therefore, LP inlet struts were made smaller, although their number increased. Wall thickness of the main cylinder was adapted to flatten out stress peaks.

Combustion Design

The combustor liner (shown in Fig. 9) is one of the components in the TF-10 that is contributing to industrial gas turbine "state of the art" design. It is an annular design, employing aero-combustor technology. The combustor inlet temperature, due to regeneration, is high for industrial combustors, yet due to the TF-10's low pressure ratio, the air mass flow is relatively low. This, along with a relatively high firing temperature 1116°C (2042°F) RIT, provided a challenging heat transfer design objective.

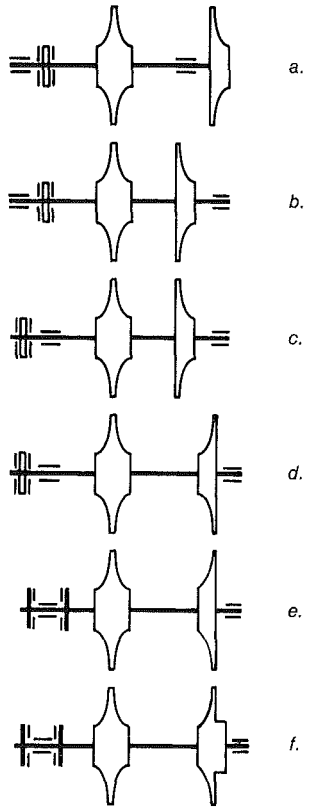

Fig. 5 Thrust bearing locations

To accomplish this high temperature combustor liner design and still maintain simplicity, mechanical integrity, and high degree of reliability, the liner will be made out of Hastalloy-x and will use 560°C (1040°F) inlet air to cool the liner walls.

Air is supplied to the combustor via four radial regenerator feed pipes, where it then impinges on an annular flow distributor and then turns 180 deg to approach the combustor in an axial direction.

The liner walls will be cooled using a combination of splash-impingement and film cooling. In order to keep the cooling film effectiveness high, the cooling air is introduced at 16 different axial locations (eight inner and eight outer).

This construction offers a short stiff liner that has a high

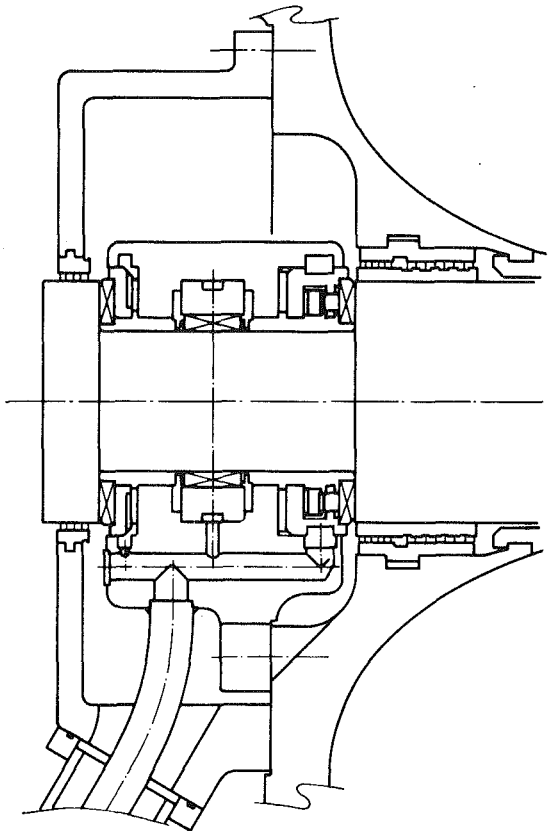

Fig. 6 Thrust bearing

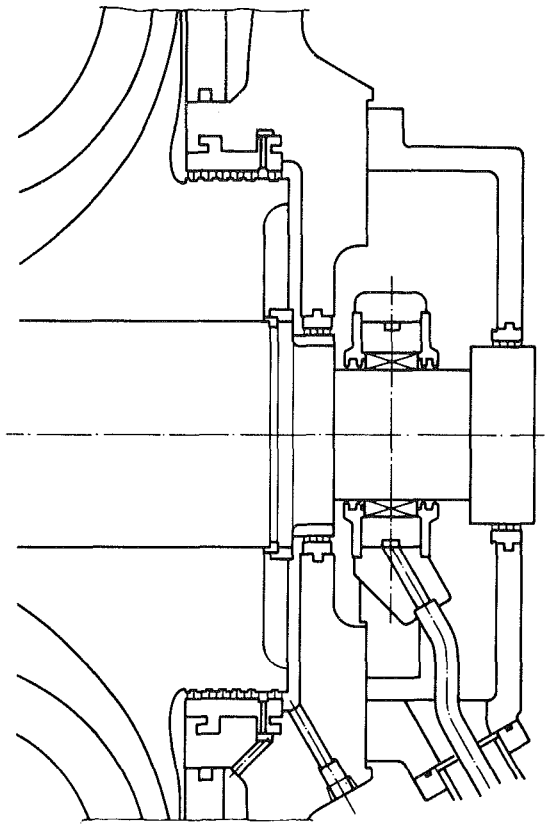

Fig. 7 Balance piston with hp sealing arrangement

plate stiffness, producing high resistance to vibration problems and creep buckling.

The annular flow distributor has also been kept short and rigid and is supported in such a manner that its thermal growth is independent from both the combustor liner and combustor casing, hence avoiding high thermal stresses.

The fuel injection system consists of 24 axial injector tubes fed from one annular manifold. The tubes are mounted for easy removal and maintenance. The ignition system consists of two radially located retractible igniters (180 deg apart). Flame detection will be provided by two radially located (again 180 deg apart) uv detectors. The detectors are mounted outside of the hp casing. Tubes, located on the flow distributor, provide sight into the primary combustion zone via a primary air injection hole.

The combustor liner, combustor casing, flow distributor, and all peripherals have been designed to allow adaption (by resizing) to a wide variety of fuels. By virtue of the TF-10 modular concept, the turbine can easily adapt even a very low Btu gas, via change in only the turbine and combustor liner, casing, and flow distributor.

Turbine Gas Path Design

The turbine stator vanes (nozzles) are cast and machined cobalt base material because of its high melting temperature for resistance to hot streaks and for its repairability (welding). The A0 nozzle is made of FSX 414 for its superior oxidation and corrosion resistance and the A1 and A2 nozzles are made from X40 for the high strength. In this section, the hp turbine is referred to as A0 stage and the power turbine is referred to as A1 and A2 stage.

The A0 nozzle and A0 shroud are hook mounted on a pin supported complete ring of Greek Ascoloy (12 percent Cr) material. This ring of low temperature expansion coefficient is used to better maintain seal and bucket tip clearances. The A0 nozzle is integrally cast in a two-vane segment; 12 segments to an assembly with seal strip and groove type sealing between segments at the inner and outer side walls. A Hastalloy X T-shaped seal is used to seal regenerator air discharge pressure at the inner wall.

A0 nozzle is cooled utilizing a combination of impingement and film cooling techniques. The outer sidewall and the airfoil body are impingement cooled with Inconel 60 plate and insert. The inner sidewall and trailing edge of the airfoil is film cooled via drilled holes. The trailing edge uses two rows of pressure side bleed holes and one row of slots.

The A1 nozzle is made of 12 two-vane segments that are hook mounted to the forward Hastalloy X support segments and to 321 S.S. A1 stator shrouds. It is also sealed by strip-and-groove seals at the sidewalls. The A1 nozzle supports a diaphragm disc of 302 stainless steel. A body impingement insert and one row of pressure side drilled cooling holes is used to cool the A1 nozzle.

The uncooled A2 nozzle is made of 12 three-vane segments that are hook mounted on the A1 stator shroud segments and on the 304 S.S. A2 stator shroud segments. It supports the segments of 304 S.S. A1/A2 interstage seal.

The turbine rotor blades (buckets) are all of the long shank integral cover type design with one horizontal platform pin and one radial side cover pin for damping and sealing. The buckets are mounted in their wheels via a high efficiency, low stress, three tang dovetail using a loose fit. The buckets are locked axially, using a single segment locking wire hoop of Inconel X750 laced through the hookover groove that alternates between wheel and bucket dovetail ends. All three stages are cast and machined from IN 738 LC material and carry two wheel seal wings on both sides for better wheel space cooling control. The A0 bucket is cooled using ten ECM drilled holes which run from the bottom of the dovetail to a

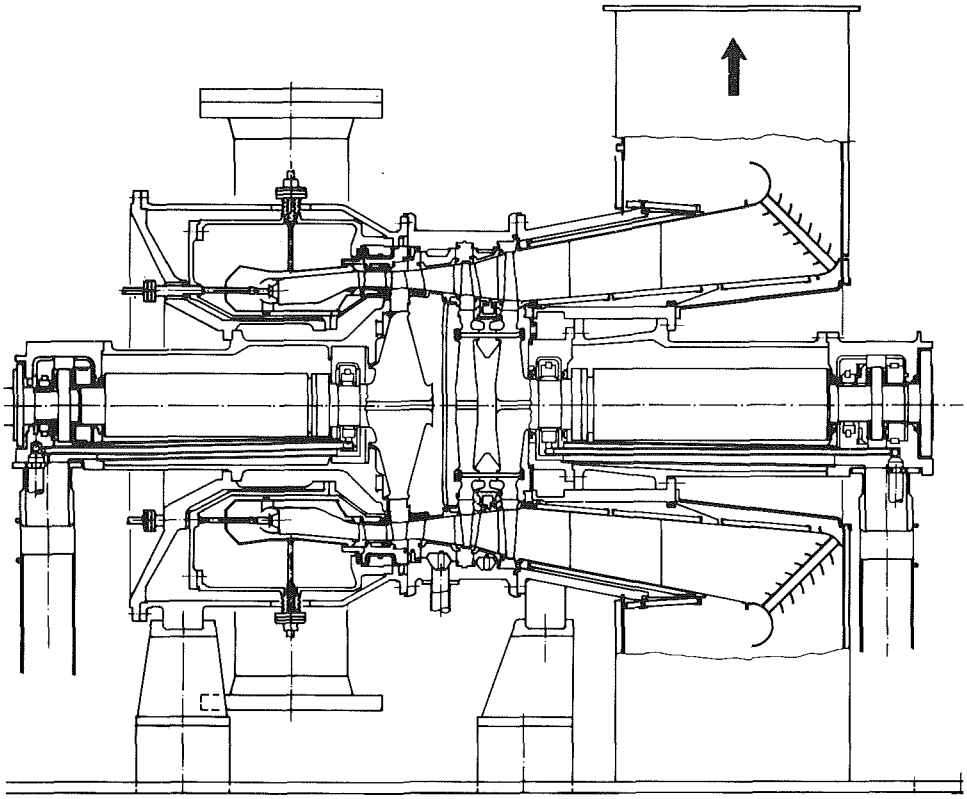

Fig. 8 Turbine cross section

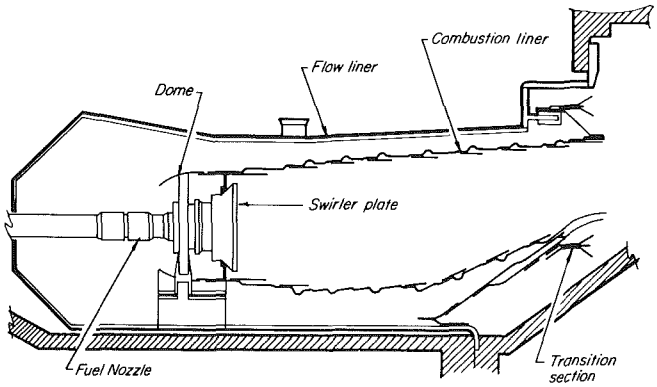

Fig. 9 Combustor cross section

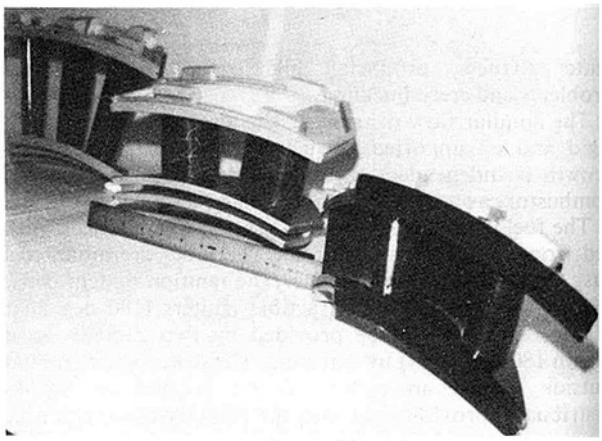

Fig. 10 A0 - A-1 - A2 nozzle

hollow cavity in the bucket tip. The cooling air is supplied from compressor discharge air and accelerated to wheel speed into the A0 forward wheel space. From there it boards and flows through holes in the wheel, one per dovetail, to a cavity at the bottom of the dovetail. There are 60 A0 buckets and 72 buckets each for the A1 and A2 stage. The A0 bucket has a free tip, whereas the A1 and A2 buckets have a Z-shaped interlocking shroud with a single rotor seal and two stator seals.

The buckets have been designed for standard and conservative static and dynamic stress levels with metal temperatures supporting long industrial parts life.

The design of the A2 bucket has been taken to the full capacity of present state of the art. It is believed to be the highest aerodynamic loading of any gas turbine in terms of annulus area carrying capacity. The parameter for this is annulus area speed squared.

Each stage of the buckets, especially the A2, will be submitted to a series of vibration tests, including a full production rotor wheel-box test for determination of the acceptability of their vibration characteristics. This will be further verified in actual prototype gas turbine operation.

The exhaust diffuser is an important part of the gas path design and its aerodynamic performance is critical to the overall gas turbine performance. The resulting diffuser as shown in Fig. 8 is an optimization of aerodynamic performance (with a recovery factor of approximately 0.6) and the mechanical design in terms of length, diameter, weight, and cost. It is fabricated of 321 S.S. with insulation jackets to help exhaust frame cooling and includes turning vanes and airfoil shaped enclosures of the exhaust frame struts.

Turbine Rotor Design

An example of the turbine rotor construction is shown with the example of the high pressure rotor in Fig. 12.

The problem of attaching a highly stressed large growth

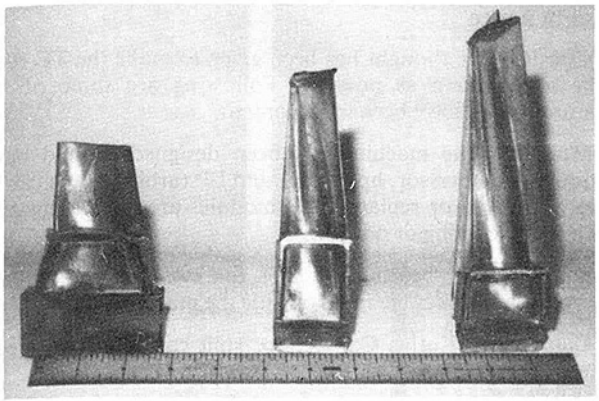

Fig. 11 A0 - A-1 - A2 bucket

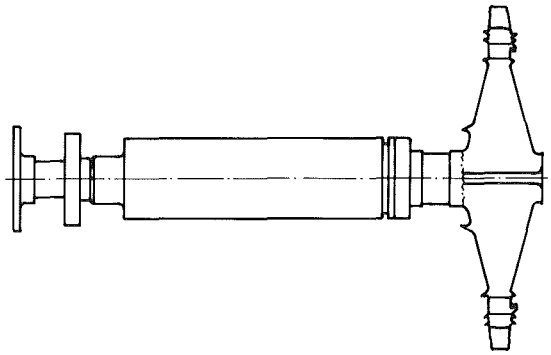

Fig. 12 High pressure rotor

component such as a turbine wheel to a cold, low stress shaft is solved for these rotors through the use of an integral stub. This allows the turbine wheel to be made of an excellent Nickel based material, IN718. Moreover, the wheels can be made more or less symmetrically shaped with a small bore providing excellent stress distribution. It is then bolted to a steel AMS 6304 material shaft. Therefore, the bolting flange is in an area of minimum strength requirement. The hp rotor is then a simple construction of only three components: buckets, wheel, and shaft, thereby minimizing stacking and assembly tolerances.

Both rotors are designed to have their free-free bending critical at over 150 percent speed. The two basic oil film modes, rock and bounce exhibit nearly straight-line mode shapes with little or no shaft bending and split the speed range so as to have highly damped and minimum vibration response.

All four journal bearings are highly stable, five pad, low L/D, tilt pad designs. These bearings have been designed with good industrial conservative practice in terms of clearance and oil temperature rise. The thrust bearings are also of the tilt pad design and have been sized for a specific loading considerably less than the thrust bearing capacity.

The couplings are designed to be of the dry flexible type marine flange connection for use between the rotors and the load and gas turbine compressor. These couplings are basically the only connections between the turbine section or module and the load compressor and gas turbine compressor module and allow for thermal growth mismatches exceeding those expected.

Turbine Stator Design

The turbine stator consists of five easily separated assemblies: hp rotor cartridge, LP rotor cartridge, hp casing, LP casing and exhaust frame.

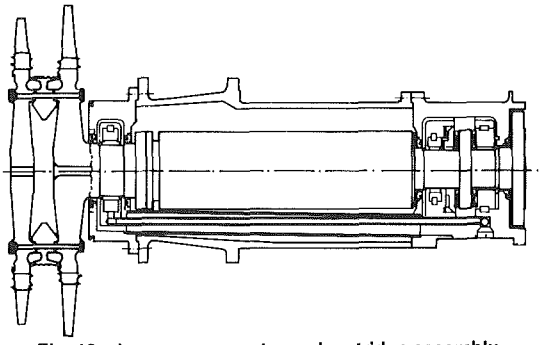

Fig. 13 Low pressure rotor and cartridge assembly

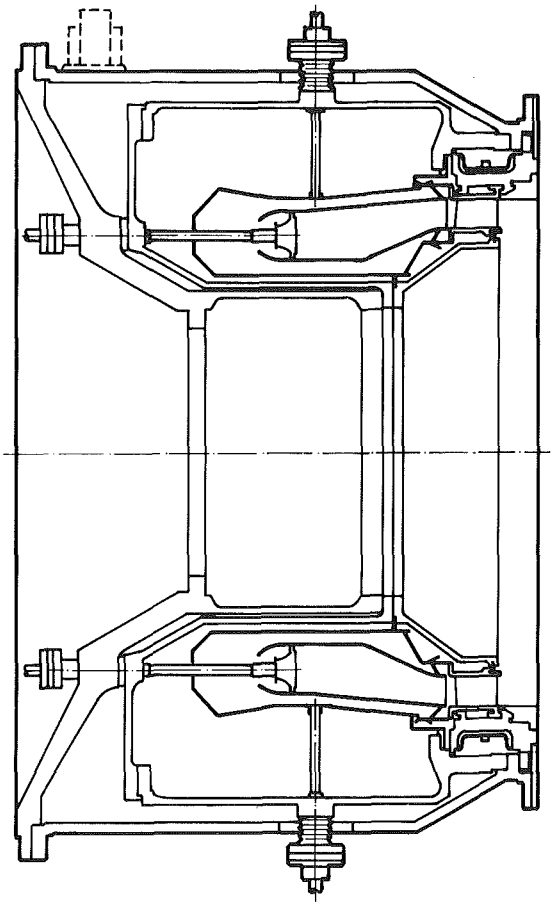

Fig. 14 High pressure casing assembly

Each cartridge assembly consists of two low alloy steel bearing housings, two tilting pad journal bearings, a tilting pad thrust bearing, an inactive thrust bearing, a nodular cast iron supporting cylindrical cartridge, oil feed and drain lines and seals. Tilting pad journal bearings were selected for their dynamic stability and vibration damping characteristics. The oil sump operates at a 0.5 psi vacuum to prevent oil leaks. Air ducts are cast into the hp cartridge to supply cooling air to the A0 buckets through the forward wheel space.

The hp casing assembly consists of a two piece outer cast iron support structure and a two piece inner 2¼ ′CR-Mo pressure vessel. The vessel contains the combustor assembly and the outer structure supports the hp cartridge and A0 nozzle assemblies. The casings are not split.

The LP casing assembly consists of a split nodular cast iron

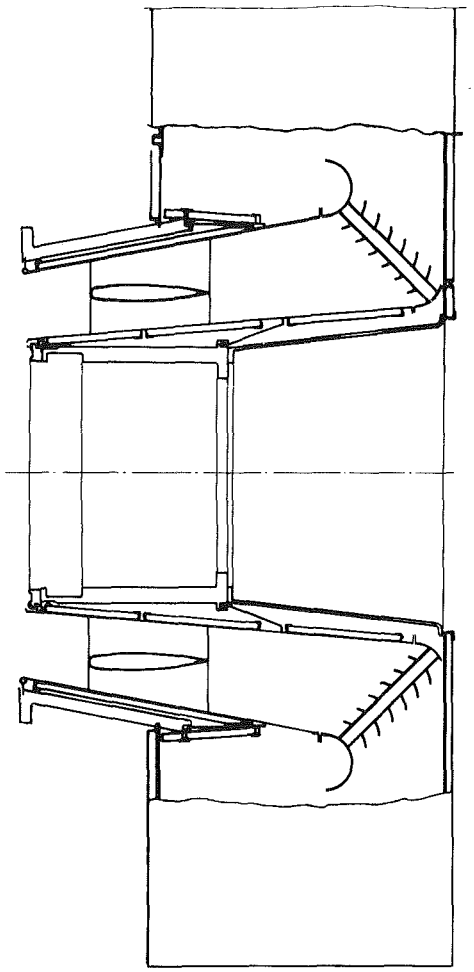

Fig. 15 Exhaust frame assembly

casing, nozzle support blocks, A1 and A2 blade shroud blocks, A1 and A2 nozzles, and interstage diaphragms.

The exhaust assembly consists of a low alloy fabricated steel frame, a CRES 321 diffuser, turning vanes, and an exhaust hood. The frame has six struts and supports the LP cartridge. It is completely protected from the exhaust gas by the diffuser and is cooled by compressor leakage air. It also supports the exhaust collector hood which may be bolted to the frame so to exhaust in any direction.

Maintenance

Considerable thought has been given to make the TF-10 as easy to maintain as possible. Following are some of the features which have been incorporated.

Modules. The machine has been designed around basic modules: compressor, hp turbine and LP turbine. Each can be easily removed or replaced. All modules are interchangeable without machining or dowling.

Bearings. All bearings, except the two turbine inboard journals, are accessible from outside the machine.

Compressor Rotor. Compressor split casing allows access to compressor rotor.

Turbine Blades. All blades can be inspected from outside the machine through boroscope access ports. All blades can be replaced through boroscope access ports. All blades can be replaced by removing the split LP casing.

Turbine Nozzles. A0 nozzles can be inspected through fuel nozzle tube mounting pads. A1 and A2 nozzles can be inspected through boroscope ports in the LP casing. A1 and A2 nozzles can be replaced by removing LP casing halves.

Combustor. Fuel nozzles, igniters, and flame monitors can be easily inspected and replaced from outside the engine. Combustor may be inspected through the 24 fuel nozzle mounting pads.

Conclusions

The TF-10 is designed using conservative proven design concepts. The relatively low pressure ratio and the free standing modular compressor and turbine designs provide greater flexibility for the designer and flexible maintenance options for the user.

Acknowledgments

Both authors wish to thank their colleagues at Thomassen, Holland B.V., and Fern Engineering who have been of great help in preparing this paper.

References

1 Hendriks, R., and Levine, P., "Cycle Optimization of a 10,000 SHP High Efficiency Gas Turbine System," ASME Paper 80-GT-157.

2 Balje, O. E., "A Study of Design Criteria and Matching of Turbomachines," ASME JOURNAL OF ENGINEERING FOR POWER, 1962.

3 Peterson, R. E., *Stress Concentration Factors,* Wiley, New York.

4 Thum, A., and Bautz, W., "Der Entlastungsubergang-Günstige Ausbildung des Uberganges an abgesetzen Wellen u. dgl.," *Forschung im Ingenieurwesen,* Vol. 6, 1934, p. 269.

Theoretical Study of Flow Instabilities and Inlet Distortions in Axial Compressors

P. Ferrand
Research Engineer.

J. Chauvin
Professor.
Mem. ASME

Institut de Mécanique
des Fluides de Marseille,
13003 Marseille, France

This paper describes a method of evaluation of the single and multistage compressors response to steady and unsteady inlet distortions. It allows also the evaluation of the appearance of unstable regimes and their characterization (rotating stall and surge). It is based on a linearized approach using mean line calculations. The compressor is considered as a series of vaned and vaneless spaces, and the corresponding equations are solved by use of Fourier series for time independent variables and by Laplace's transform for time-dependent variables. An analogy between the compressor's response and a servo-mechanism is developed, using Nyquist's diagram. Results are compared with experimental data which prove the validity of the approach. A parametric study indicates which parameters can be modified to improve the flow stability.

Introduction

The safe field of operation of a compressor on the pressure-mass flow map is limited towards the high-pressure range by a line above which flow instabilities can appear. Those instabilities can result in an unsteady periodical regime (rotating stall, surge) or in random fluctuations (turbulence). Additionally, the inlet flow conditions can depart from the normally assumed axisymmetric conditions, and present circumferential asymmetries of total pressure, for instance. They can modify the region of safe operation.

A computation method is developed below, which attempts to predict the onset and to characterize the various unstable flow regimes.

Background

The first approach on steady circumferential distortions used the concept of parallel compressors [1]; this was later improved to take into account the unsteady effect due to the relative motion of the blade rows with respect to the distortion [2]. Unsteady distortions have been approached through actuator disk theories for a simple rotor, with a two-dimensional incompressible flow hypothesis [3]. Reference [4] extends this approach to the case of compact (i.e., with zero blade row spacing) multistage compressors. Reference [5] considers the case of multistage compressors, assuming compressible flow and a steady distortion. In reference [6], there appeared for the first time a nonlinear approach for a basic two-dimensional incompressible flow, using the actuator disk approach. This theory has finally been extended to a quasi three-dimensional model. Our approach has been influenced by these developments.

Hypothesis

In what follows, we propose a linear theory applicable to multistage compressors with blade row spacing presenting a small change in radius. The aim is to study the response of the compressor to steady and unsteady distortions, to evaluate the limit of stable operation, and, finally, for the case where rotating stall appears, the number of cells and their velocity of propagation.

The vaned and vaneless spaces are treated distinctly. For each category, the space, a transfer function presented in matrix form, allows the calculation of the flow characteristics at the space outlet in terms of those at the inlet.

The hypotheses are:

- For the vaneless spaces:

(*a*) inviscid incompressible two-dimensional steady flow, linearised equations

- For vaned spaces:

(*a*) actuator disk approach
(*b*) two-dimensional unsteady flow
(*c*) viscosity taken into account through a steady flow loss coefficient
(*d*) linearised equations

The aerodynamic quantities are expressed under the form of a mean flow and perturbations:

$$x=\bar{x}+x'(z,\theta,t) \quad x' << \bar{x}$$

Transfer Equations for the Vaneless Spaces

We repeat and extend here the approach presented in [4] considering the Euler equations in axial and circumferential directions for the perturbed flow:

Contributed by the Gas Turbine Division of THE AMERICAN SOCIETY OF MECHANICAL ENGINEERS and presented at the Gas Turbine Conference and Products Show, March 9-12, 1981, Houston, Texas. Manuscript received at ASME Headquarters December 30, 1980. Paper No. 81-GT-211.

$$\frac{\partial v_\theta'}{\partial t} - \frac{\bar{V}_z}{r}\cdot\frac{\partial V_z'}{\partial \theta} + \bar{V}_z\cdot\frac{\partial V_\theta'}{\partial z} + \frac{1}{\rho}\cdot\frac{\partial p_0'}{r\partial\theta} = 0 \quad (1)$$

$$\frac{\partial V_z'}{\partial t} + \frac{\bar{V}_\theta}{r}\cdot\frac{\partial V_z'}{\partial \theta} - \bar{v}_\theta\cdot\frac{\partial V_\theta'}{\partial z} + \frac{1}{\rho}\cdot\frac{\partial P_0'}{\partial z} = 0 \quad (2)$$

and the continuity equation,

$$\frac{\partial V_\theta'}{r\partial\theta} + \frac{\partial V_z'}{\partial z} = 0 \quad (3)$$

The linear character of the equations allows a Fourier series development in the circumferential direction:

$$X'(s,\theta,t) = \sum_{n=1}^{\infty} (X_n'^{c}(z,t)\cos n\theta + X_n'^{s}(z,t)\sin n\theta) \quad (4)$$

The solution of the system can be achieved through the use of Laplace's transforms:

$$\tilde{X}_n(z,S) = \int_0^\infty e^{-st}\cdot X_n'(z,t)\,dt \quad (5)$$

The perturbation quantities are assumed to be zero up to the initial time.

Using the following reduced variable:

$$v_{z,n} = \frac{\tilde{V}_{z,n}}{\bar{v}_z} \quad (6)$$

$$v_{\theta,n} = \frac{\tilde{V}_{\theta,n}}{\rho\bar{v}_z} \quad (7)$$

$$p_{0,n} = \frac{\tilde{P}_{0,n}}{\rho\bar{v}^2} \quad (8)$$

The solutions can be written as:

$$[D] = [E]\cdot[C] \quad (9)$$

where:

$$\begin{bmatrix} v_{z,n}^c \\ v_{z,n}^s \\ v_{\theta,n}^c \\ v_{\theta,n}^s \\ p_{0,n}^c \\ p_{0,n}^s \end{bmatrix} = \begin{bmatrix} E_{11} & -E_{21} & E_{13} & 0 & E_{15} & 0 \\ E_{21} & E_{11} & 0 & E_{13} & 0 & E_{15} \\ E_{31} & -E_{41} & 0 & E_{13} & 0 & -E_{15} \\ E_{41} & E_{31} & -E_{13} & 0 & E_{15} & 0 \\ E_{31} & -E_{61} & E_{53} & 0 & E_{55} & 0 \\ E_{61} & E_{51} & 0 & E_{53} & 0 & E_{55} \end{bmatrix} \begin{bmatrix} a_n^c \\ a_n^s \\ b_n^c \\ b_n^s \\ c_n^c \\ c_n^s \end{bmatrix} \quad (10)$$

with

$E_{11} = \cos\xi\cdot e^{\lambda_1 z}$ $\qquad A = p^2 + q^2$

$E_{21} = \sin\xi\cdot e^{\lambda_1 z}$ $\qquad p = \frac{n}{r}\bar{v}_z$

$E_{31} = \left(\frac{q}{p}\cos\xi - \frac{S}{p}\sin\xi\right)e^{\lambda_1 z}$ $\qquad q = \frac{n}{r}\bar{v}_\theta$

$E_{41} = \left(\frac{q}{p}\sin\xi - \frac{S}{p}\cos\xi\right)e^{\lambda_1 z}$ $\qquad \xi = \frac{n}{r}\frac{q}{p}z$

$E_{51} = \left(\cos\xi - \frac{Sq}{A}\sin\xi\right)e^{\lambda_1 z}$ $\qquad \lambda_1 = -\frac{S + i\frac{n}{r}\bar{V}_\theta}{\bar{V}_z}$

$E_{61} = e^{\lambda_2 z}$

$E_{53} = \frac{Sp}{A}e^{\lambda_2 z}$

$E_{55} = \frac{Sp}{A}e^{-\lambda_2 z}$ $\qquad \lambda_2 = \frac{n}{r}$

$E_{15} = e^{-\lambda_2 z}$

Coefficients a_n, b_n and c_n, are arbitrarily integration constants.

At $z = 0$, these coefficients can be expressed in matrix form as functions of the perturbations:

$$[C] = [P]\cdot[D]$$

where

$$\begin{bmatrix} a_n^c \\ a_n^s \\ b_n^c \\ b_n^s \\ c_n^c \\ c_n^s \end{bmatrix} = \frac{2}{P_1}\begin{bmatrix} 0 & 0 & p_{31} & -p_{32} & p_{51} & -p_{52} \\ 0 & 0 & p_{32} & p_{31} & p_{52} & p_{51} \\ p_1 & 0 & p_{33} & -p_{34} & p_{53} & -p_{54} \\ 0 & p_1 & p_{34} & p_{33} & p_{54} & p_{53} \\ p_1 & 0 & p_{35} & -p_{36} & p_{55} & -p_{56} \\ 0 & p_1 & p_{36} & p_{35} & p_{57} & p_{56} \end{bmatrix} \begin{bmatrix} v_{z,n}^c \\ v_{z,n}^s \\ v_{\theta,n}^c \\ v_{\theta,n}^s \\ p_{0,n}^c \\ p_{0,n}^s \end{bmatrix} \quad (11)$$

with

$$p_1 = \frac{1}{2}(\delta^2 + 2q^2S^2)$$

$$p_{31} = 2qpS^2$$

$$p_{32} = -pS\delta$$

$$p_{33} = \frac{qS}{2}(\eta - 2qS)$$

$$p_{34} = \frac{1}{2}(\delta(Sp - A) + 2q^2S^2)$$

Nomenclature

A = sound speed
c = chord length
G_n = transfer function of the compressor
i = incidence
i = $\sqrt{-1}$
K = number of stage
M = Mach number
n = harmonic number
p = static pressure
p_0 = total pressure
r = mean radius
s = Laplace operator
t = time
u = wheel speed at the mean radius
V = velocity
W = relative velocity
z = blade row spacing
α = damping factor
β = relative air angle
δp_0 = pressure distortion
Δ_n = denominator of G_n
ν = number of blades
ω = pulsation frequency
$\bar{\omega}$ = pressure loss
π = total pressure ratio
Ω = wheel angular velocity
ρ = density
θ = circumferential coordinate

Subscripts

e = inlet
n = Fourier coefficient
s = exit
z = axial direction
θ = circumferential direction

Superscripts

$(-)$ = mean value
$(\,)'$ = perturbation
v = Laplace transform
c = Fourier coefficient in cosinus
s = Fourier coefficient in sinus

$$p_{35} = -\frac{qS}{2}(\eta + 2qS)$$

$$p_{36} = \frac{1}{2}(\delta(Sp+A) - 2q^2S^2)$$

$$p_{51} = A\delta$$

$$p_{52} = 2qAS$$

$$p_{53} = \frac{A}{2p}(\delta(S-p) + 2q^2S)$$

$$p_{54} = \frac{qA}{2p}(\eta - 2pS)$$

$$p_{55} = \frac{A}{2p}(\delta(S+p) + 2q^2S)$$

$$p_{56} = \frac{qA}{2q}(\eta + 2pS)$$

and

$$\delta = S^2 - A$$

$$\eta = S^2 + A$$

These perturbations can be expressed in z_2 in terms of those in z_1:

$$[D(z_2)] = [E(z_2)] \cdot [P(z_1)] \cdot [D(z_1)] \tag{12}$$

If points z_1 and z_2 represent, respectively, the inlet and outlet of the vaneless space, it is always possible to choose the coordinate origin in z_1; matrix $[EP(z_2)] = [E(z_2)][P(D)]$ characterises the considered interblade row space.

Transfer Equations for the Blade Rows (Vaned Spaces)

Mass flow continuity through one blade channel is expressed,

$$\rho_e V_{z_e} S_e = \rho_s V_{z_s} S_s$$

global mass flow continuity is,

$$\rho_e \bar{V}_{z_e} \cdot \nu \cdot S_e = \rho_s \cdot \bar{V}_{z_s} \cdot \nu \cdot S_s$$

(ν = number of blades).

Dividing the first by the second leads to the conservation of the perturbed reduced axial velocity,

$$\frac{V'_{z_e}}{\bar{V}_{z_e}} = \frac{V'_{z_s}}{\bar{V}_{z_s}} \tag{13}$$

As to the relation in circumferential direction, it is generally accepted that the outlet relative angle is only a function of the inlet angle, $tg\beta_s = f(t_g\beta_e)$.

With a series development limited to the first order and taking turning (13) into account, it follows that,

$$v_{\theta_{s,n}} = \left[\frac{\bar{V}_{\theta_s} - U_s}{\bar{V}_{z_s}} \cdot \bar{v}_{\theta_e} - U_e \cdot \frac{\bar{W}_s^2 \cdot \bar{V}_{z_e}}{\bar{V}_e^2 \cdot \bar{V}_{z_s}^2} \cdot \frac{\partial \beta_s}{\partial \beta_e}\right] \cdot v_{z_{e,n}} + \frac{\bar{W}_s^2 \cdot \bar{V}_{z_e}^2}{\bar{W}_e^2 \cdot \bar{V}_{z_s}^2} \cdot \frac{\partial \beta_s}{\partial \beta_e} \cdot v_{\theta_{e,n}} \tag{14}$$

axial transfer.

The relative total pressure loss

$$\bar{\omega} = \frac{\Delta \mathrm{Pr}}{\frac{1}{2}\rho_e W_e^2}$$

is considered to be function of inlet incidence and relative inlet Mach number, i.e., of the axial and tangential inlet velocities.

By linearising the relative total pressure variations and working in an absolute frame of reference, one obtains:

$$p_{0_{s,n}} = \frac{\rho_e \bar{V}_e^2}{\rho_s \bar{V}_s^2} \cdot p_{0_{e,n}} - \frac{\rho_e r_e \Omega \bar{V}_{z_e}}{\rho_s \bar{V}_s^2} \cdot v_{\theta_{e,n}} + \frac{r_s \Omega V_{z_s}}{\bar{V}_s^2} \cdot v_{\theta_{s,n}} - \frac{\bar{V}_{z_e}}{\rho_s \bar{V}_s^2} \cdot \frac{\partial \Delta \mathrm{Pr}}{\partial V_{\theta_e}} \cdot v_{\theta_{e,n}} - \frac{\bar{V}_{z_e}}{\rho_s \bar{V}_s^2} \cdot \frac{\partial \Delta \mathrm{Pr}}{\partial V_{z_e}} \cdot v_{z_{e,n}} \tag{15}$$

with

$$\frac{\partial \Delta \mathrm{Pr}}{\partial V_{z_e}} = \frac{1}{2}\rho_e W_e^2 \left(\frac{\partial \bar{\omega}}{\partial \beta_e} \cdot \frac{\partial \beta_e}{\partial V_{z_e}} + \frac{\partial \bar{\omega}}{\partial M_{r_e}} \cdot \frac{\partial M_{r_e}}{\partial V_{z_e}}\right) + \rho_e \bar{\omega} v_{z_e} \tag{16}$$

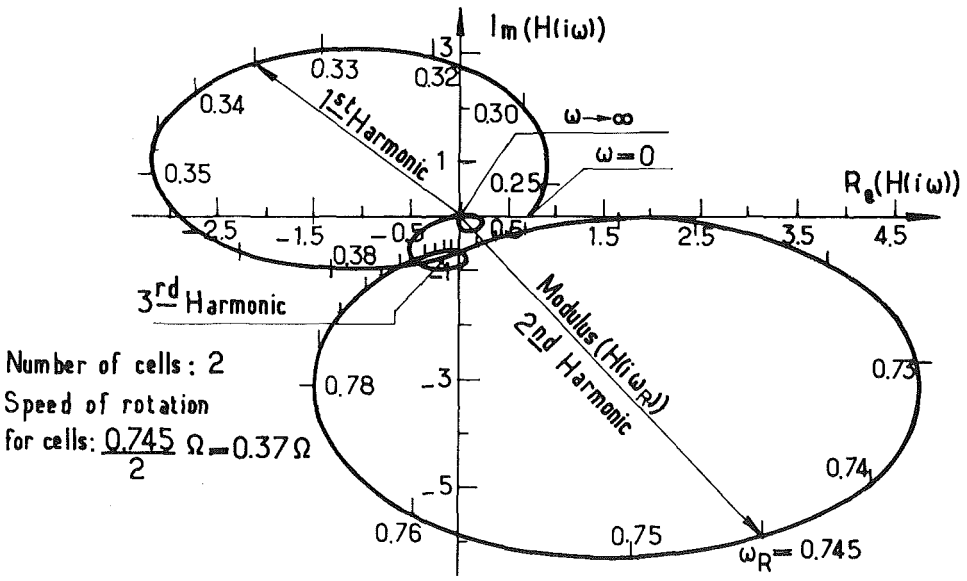

Fig. 1 Frequency response – NACA compressor ($\phi = 0.766$ – rotating stall point)

$$\frac{\partial \Delta \mathrm{Pr}}{\partial V_{\theta_e}} = \frac{1}{2}\rho_e W_e^2\left(\frac{\partial \bar{\omega}}{\partial \beta_e}\cdot\frac{\partial \beta_e}{\partial V_{\theta_e}} + \frac{\partial \bar{\omega}}{\partial M_{r_e}}\cdot\frac{\partial M_{r_e}}{\partial V_{\theta_e}}\right) + $$

$$+\rho_e \bar{\omega}(V_{\theta_e} - U_e) \qquad (17)$$

The coefficients $\partial\beta_s/\partial\beta_e$, $\partial\bar{\omega}/\partial i$, $\partial\bar{\omega}/\partial M_{r_e}$, $\bar{\omega}$ can be obtained either experimentally, or through a mean flow calculation program.

The linearity hypothesis allows superposition of the unsteady effect in the rotors through a blade channel, the latter being assumed similar to a diffuser.

In the relative system of coordinates:

$$\frac{\partial w}{\partial t} + \frac{1}{\rho}\cdot\frac{\partial P_{0_r}}{\partial z} = O \qquad (18)$$

with the continuity equation: $w(z)\cdot S(z) = w_e \cdot S_e$.

Assuming a linear variation of section, (18) can be integrated using the reduced Laplace transform and the Fourier series development so that the total pressure change that occurs in the blade passage can be written for any harmonic, n, as:

$$p^c_{0_{s,n}} = P^c_{0_{e,n}} - \frac{\rho_m c}{\bar{w}_e - \bar{w}_s} Ln\left(\frac{\bar{w}_e}{\bar{w}_s}\right)\cdot[S(V^c_{z_{e,n}} + $$

$$+ tg\bar{\beta}_e V^c_{\theta_{e,n}}) + n\Omega(V^s_{z_{e,n}} + tg\bar{\beta}_e \cdot V^s_{\theta_{n,e}})] \qquad (19)$$

$$P^s_{0_{s,n}} = P^s_{0_{e,n}} - \frac{\rho_m c}{\bar{w}_e - \bar{w}_s} Ln\frac{\bar{w}_e}{\bar{w}_s}\cdot[-n\Omega(V^c_{z_{e,n}} +$$

$$tg\bar{\beta}_e V^c_{\theta_{e,n}}) + \mathrm{S}\cdot(V^s_{z_{e,n}} + tg\bar{\beta}_e \cdot V^s_{\theta_{n,e}})] \qquad (20)$$

with $\rho_m = \dfrac{\rho_1 + \rho_2}{2}$.

The total pressure perturbation through a blade row is obtained by use of equations (15), (19), and (20). Finally, the outlet perturbations can be expressed in function of the inlet one:

$$[\mathrm{D}]_s = [\mathrm{A}]\cdot[\mathrm{D}]_\mathrm{E} \qquad (21)$$

where:

$$\begin{bmatrix} V^c_{z,n} \\ V^s_{z,n} \\ V^c_{\theta,n} \\ V^s_{\theta,n} \\ P^c_{0,n} \\ P^s_{0,n} \end{bmatrix}_s \begin{bmatrix} 1 & 0 & \mathrm{L} & 0 & 0 & 0 \\ 0 & 1 & 0 & 0 & 0 & 0 \\ \mathrm{VCA} & 0 & \mathrm{VCC} & 0 & 0 & 0 \\ 0 & \mathrm{VCA} & 0 & 0 & 0 & 0 \\ \mathrm{PA\text{-}S.STA} & \mathrm{n\ .STA} & \mathrm{PC\text{-}S.STC} & -\mathrm{n.\ STC} & \mathrm{PP} & 0 \\ -\mathrm{n\ \ .STA} & \mathrm{PA-S.STA} & \mathrm{n\ .STC} & \mathrm{PC\text{-}S.STC} & 0 & \mathrm{PP} \end{bmatrix} \begin{bmatrix} V^c_{z,n} \\ V^s_{z,n} \\ V^c_{\theta,n} \\ V^s_{\theta,n} \\ P^c_{0,n} \\ P^s_{0,n} \end{bmatrix} \qquad (22)$$

with:

$$\mathrm{VCA} = \frac{\bar{V}_{\theta_s} - U_s}{\bar{V}_{z_s}} - \frac{\partial tg\beta_s}{\partial tg\beta_e}\cdot\frac{\bar{V}_{\theta_e} - U_e}{\bar{V}_{z_e}}$$

$$\mathrm{V_{CC}} = \frac{\partial tg\beta_s}{\partial tg\beta_e}$$

$$\mathrm{STA} = \frac{\rho_e + \rho_s}{2}\cdot\frac{\bar{W}_s}{\bar{W}_e}\cdot\frac{c}{\bar{W}_e - W_s} Ln\left(\frac{\bar{W}_e}{\bar{W}_s}\right)\cdot\frac{\bar{V}^2_{z_e}}{\bar{V}^2_s}$$

$$\mathrm{STC} = \frac{\bar{V}_{\theta_e} - U_c}{V_{z_e}}\cdot\mathrm{STA}$$

$$\mathrm{PA} = \frac{1}{\bar{V}^2_s}\left[U_s\cdot(\bar{V}_{\theta_s} - U_s) - \frac{\bar{V}_{z_s}}{\bar{V}_{z_e}}\cdot U_s(\bar{v}_{\theta_e} - U_e)\cdot\frac{\partial tg\beta_s}{\partial tg\beta_e} - \right.$$

$$\left. - \frac{\bar{V}_{z_e}}{\rho_s}\cdot\frac{\partial \Delta \mathrm{Pr}}{\partial V_{z_e}}\right]$$

$$\mathrm{PC} = \frac{1}{\bar{V}^2_s}\left[-\frac{\rho_s}{\rho_e}\cdot U_e\cdot\bar{V}_{z_e} + U_s\cdot\bar{V}_{z_s}\cdot\frac{\partial tg\beta_s}{\partial tg\beta_e} - \frac{\bar{V}_{z_e}}{\rho_s}\cdot\frac{\partial \Delta \mathrm{Pr}}{\partial V_{\theta_e}}\right]$$

$$\mathrm{PP} = \frac{\rho_e \bar{V}^2_e}{\rho_s \bar{V}^2_s}$$

$\partial \mathrm{Pr}/\partial V_{z_e}$ and $\partial \mathrm{Pr}/\partial \bar{V}_\theta$ being defined through equations (16) and (17), these relations have been established for rotors; the stator case is obtained for $u = 0$.

Method of Solution

A total pressure distortion, which can rotate with an angular velocity ω, is imposed at a distance z_G from the compressor inlet:

$$\delta P_0 = \sum_{n=1}^{\infty}\left[(\mathrm{S}.\delta \mathrm{P}^c_n + n\omega.\delta \mathrm{P}^s_n)\frac{\cos \mathrm{n}\theta}{\mathrm{S}^2 + n^2\omega^2} + (n\omega.\delta \mathrm{P}^c_n + \right.$$

$$\left. + \mathrm{S}\cdot\delta \mathrm{P}^s_n)\frac{\sin n\theta}{\mathrm{S}^2 + n^2\omega^2}\right] \qquad (23)$$

To simplify the writing, we will suppose from now on that the distortion is symmetrical in $\theta(\partial \mathrm{P}^s_n = 0)$ and is a step function in time.

Equations (9), (12) and (21) allow matrix C to be expressed as a function of the integration coefficients of any plane k in function of the conditions in the upstream infinity plane (subscript 0):

$$[\mathrm{C}_K] = \prod_{j=1}^{K}\{[\mathrm{P}]\cdot[\mathrm{A}]\cdot[\mathrm{E}]\}_{K+1-j}\cdot[\mathrm{C}_\infty] \qquad (24)$$

On the other hand, as boundary conditions, it is imposed that the perturbations be zero at upstream and downstream infinity. These conditions define the matrix $[\mathrm{C}]_{-\infty}$ and $[\mathrm{C}]_{+\infty}$

$$[\mathrm{C}]_{-\infty} = \begin{bmatrix} 0 \\ 0 \\ b^c_n \\ b^s_n \\ 0 \\ 0 \end{bmatrix} \qquad (25) \qquad [\mathrm{C}]_{+\infty} = \begin{bmatrix} a^c_n \\ q^s_n \\ 0 \\ 0 \\ C^c_n \\ C^s_n \end{bmatrix} \qquad (26)$$

Taking (23–26), into account it is possible to evaluate matrix $[\mathrm{C}]_{-\infty}$, i.e., $b^c_{n-\infty}$ and $b^s_{n-\infty}$, i.e.:

$$b^{c-\infty}_n = G^c_n(\mathrm{S})\cdot\frac{\delta P^c_n}{\mathrm{S}} \qquad (27)$$

$$b^{s-\infty}_n = G^s_n(\mathrm{S})\cdot\frac{\delta P^c_n}{\mathrm{S}} \qquad (28)$$

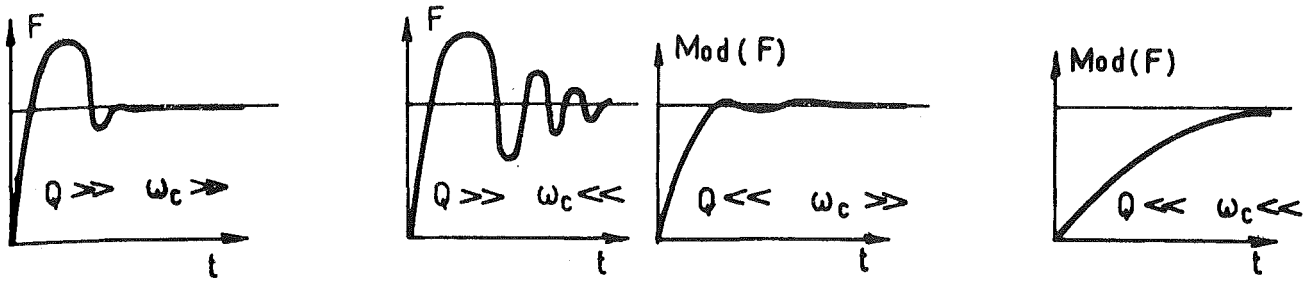

Fig. 2 Different transitory regimes in function of Q and ω_c

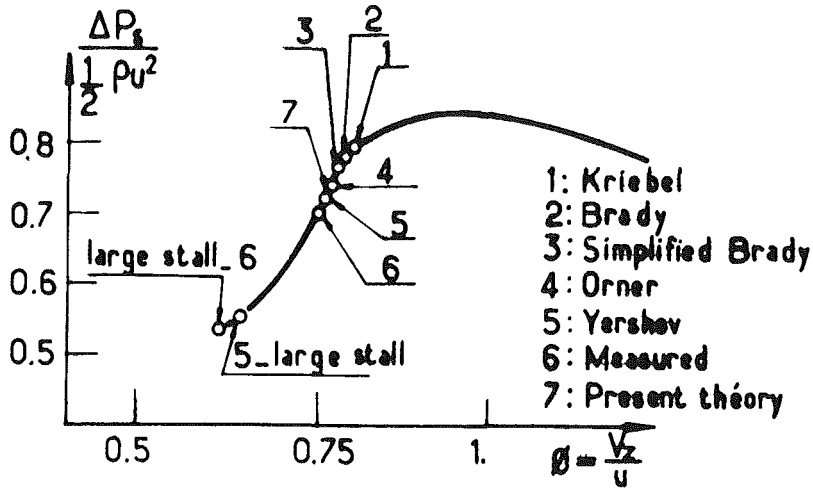

Fig. 3 Rotating stall onset – NACA compressor

with:

$$G_n^c(S) = \frac{M_{35} \cdot LS - M_{45} \cdot KS}{\Delta n} \tag{29}$$

$$G_n^s(S) = \frac{M_{45} \cdot KC - M_{35} \cdot LC}{\Delta n} \tag{30}$$

$$\Delta n = LC \cdot KS \; KC \cdot LS \tag{31}$$

$$KC = M_{31} - M_{34} - \frac{Sr\bar{V}_z^{-\infty}}{n\bar{V}_{-\infty}^2} M_{35} \quad KS = M_{32} + M_{33} - \frac{Sr\bar{V}_z^{-\infty}}{n\bar{V}_{-\infty}^2} M_{36}$$

$$LC = M_{41} - M_{44} - \frac{Sr V_z^{-\infty}}{n\bar{V}_{-\infty}^2} M_{45} \quad LS = M_{42} + M_{43} - \frac{Sr\bar{V}_z^2}{n\bar{V}_{-\infty}^2} M_{46}$$

$$M = [P_{+\infty}] \cdot [A_{2K}] \cdot [EP_{2K}] \; \ldots \; [EP_G]$$

From function $b_n^{c-\infty}$ and $b_n^{s-\infty}$, it is possible to calculate the characteristics of the perturbed flow in the whole machine. However, the expressions obtained are not explicit in S. It is thus impossible to obtain analytical expressions in function of time. The unsteady flow study will thus be carried directly from the images of the Laplace transform of the time function. Criterion is based upon complex variable theory at the theorem of Cauchy usually terms the "principle of the argument" [9]. Consider an arbitrary function H(S); replace Laplace operator S by imaginary $i\omega$ (where ω is a frequency); H(S) function is then complex, and it is possible to draw its real part in function of its imaginary part in so-called Nyquist plane (Fig. 1). The curve is graduated in ω. To each point corresponds a frequency, ω, the modulus and the phase of H ($i\omega$). From those curves it is possible to define a series of criteria which allow the analysis of the unsteady response of the compressor.

Stability criterion. The analytic form of the time function is exponential of the type $e^{(\alpha+i\omega)t}$. According to the sign of α, the function will decay or not with increasing time. The system will be stable if $\alpha<0$. Physically, the limit $\alpha=0$ will determine the point where the equilibrium of an axisymmetric steady mean flow is broken, and from which a rotating stall or surge regime (according to the value of ω) or of turbulence can be established.

One can establish [9] a relation between the sign of α and the phase of the corresponding Laplace transform. Applied to the global transfer function of the compressor $G_n^c(S)$, equation (29), and $G_n^s(S)$, equation (30), the criterion can be expressed as follows:

The number of unstable terms in the solution is equal to the number of turns made around the origin by the curve representing the denominator Δ_n, equation (31), of the functions $G_{n_n}^c$ and G_n^s, in Nyquist's plane when $s=i\omega$ varies between $-i^\infty$ and $+i^\infty$.

Frequency response. The study in the evaluation of frequencies permits, on the one hand, the possibility of appearance of rotating stall, and, on the other hand, the system's response to unsteady inlet distortions.

The resonant pulsation frequency ω_R is defined as the pulsation corresponding to the maximum value of the function considered.

It is to be noted that the value of the modulus corresponding to the resonant frequency is as important as the resonant frequency itself. A modulus of unity means that the system transmits the initial perturbation without amplification and defines the limit between spatial damping or amplification.

On the other hand, an overload coefficient is defined: it is the ratio of the modulus of the function at resonant frequency to the one at zero frequency (steady case) $Q = H(i\omega_R)/H(0)$.

The cut-off pulsation ω_c is defined by the value 0.5 of the ratio of the modulus for $\omega \neq 0$ to that at zero frequency.

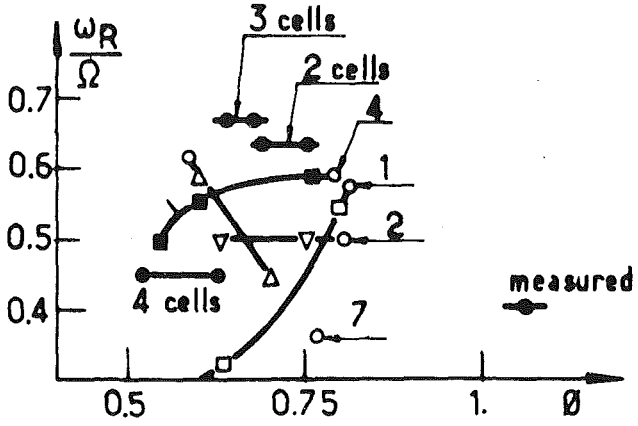

Fig. 4 Number and speed of rotation of the cells

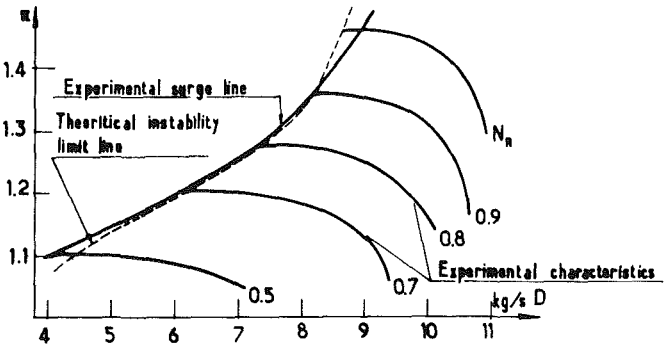

Fig. 5 Single-stage compressor C_1

This cut off frequency fixes the bandwidth $[0,\omega_c]$ which determines the domain of sensitivity of the compressor.

The study of rotating stall is made at the points where instabilities appear ($\alpha>0$). The preceding criteria are applied to the curves representing functions G_n^c and G_n^s (and this independently of the introduced distortion δP_0) at compressor inlet and of the equivalent function ahead of each stage.

The conditions for rotating stall appearance are:

- ω_R exists as a resonant pulsation in the domain $[0.1\Omega; 0.8\Omega]$ as this is the bracket of cell rotating speed;
- large Q (>3)
- the function modulus is large (>2) for ω_R; and
- n = harmonic n, presenting the largest modulus at resonant frequency fixes the number of stalled cells.

The study of the compressor's response to unsteady distortions is made from consideration of functions b_n^c, equation (27), and b_n^s, equation (28), and of the equivalent function obtained in each plane by equations (12), (21), and (24). It is supposed, in this case, that the introduced distortion δP_0 is governed by equation (23).

The study of the Laplace transform allows the evaluation of the initial (convergence or divergence as a function of time) and final (response in frequency for the established regime) phases. A priori, the transitory state cannot be studied. However, experience, particularly in servo-systems, shows that there exist correlations between the frequency response and the transitory regime. Thus, following the values of Q and ω_c, four typical responses can be obtained (Fig. 2).

The overload coefficients define the influence of the unsteady distortions in comparison with that of the steady ones; the bandwidth fixes the frequency range to which the compressor is sensitive, the distortions at a frequency larger than ω_c having no effect.

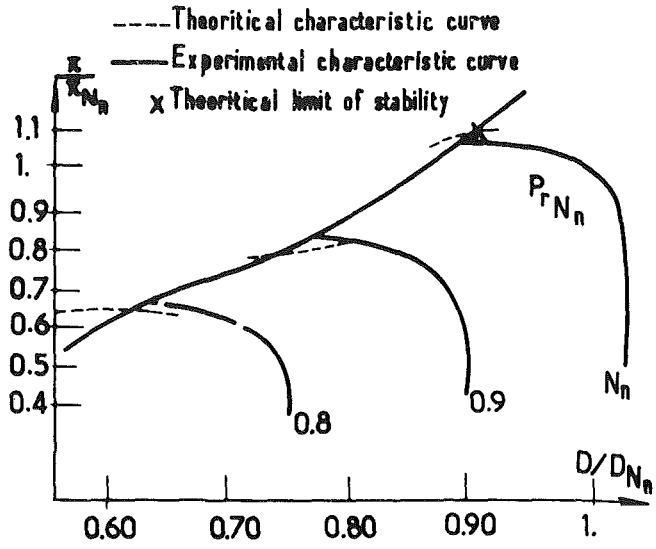

Fig. 6 Five-stage compressor CM-5

Analysis of Data

Comparison with experiments. A NACA compressor (TN 3518) made of a single wheel rotating at 8000 rpm [8], a single stage compressor C-1 with an axial Mach number of 0.46 at the nominal rpm of 10,800, a single stage compressor C-2 (low speed, axial M = 0.13, rpm 3000), and, finally, a high-pressure five-stage compressor CM-5 (axial Mach number 0.485, rpm 13,300) have been studied. More details are presented in [10].

Figure 3 shows the NACA compressor characteristics and compares the present method with the ones already existing. The rotating stall onset is predicted within 5 percent of mean flow and 10 percent in pressure ratio. The speed of rotation of the cells (Fig. 4) is poorly predicted. Only Orner's method gives it within 25 percent. On the other hand, our method is the only one giving the right cell number (2).

The error on the speed of propagation can be explained by the fact that the single wheel configuration is singular for the theoretical method (see [6] and [7]) as the effect of the neighbouring volume cannot be simulated.

The comparison between the experimental "surge line" and the stability limit for the C-1 compressor gives an error of less than 5 percent in flow (Fig. 5).

As the C-2 compressor was at design stage, no comparison with experimental data could be made; this example has allowed, however, to show the possibilities of the method to evaluate the limits of the operating range from the design stage and was the base for a parametric study.

The study of the CM-5 compressor met with a problem of mean flow definition. The base characteristics on which the stability study is carried out are obtained theoretically. Moreover, the experimental and theoretical slopes are very different near the surge line. The matching of these curves can be made through empirical coefficients which are selected to straddle the experimental constant speed line at ±1 percent in mass flow near surge. To this difference of 2 percent corresponds a change of 5 percent on the corrective coefficients which, among other things, produce a change of 30 percent on the mean value of all stages of the terms $\partial\omega/\partial i$, with some of those terms doubling or trebling. It is thus difficult to consider that the internal cohesion of the flow is respected. As the stability of the system strongly depends of $\partial\bar{\omega}/\partial i$, the fact that the stability limit could not be predicted correctly at part speed is not surprising; on the contrary, at nominal speed the theoretical limit exactly matches the experimental one (Fig. 6).

Synoptic Table

Parameter / Effect on	C	Z	$\frac{\partial\bar{\omega}}{\partial i}$	$\frac{\partial\bar{\omega}}{\partial M_R}$	$\frac{\partial\beta_s}{\partial\beta_e}$	$\bar{\omega}$
Unstability	$-B$	$-B$	$+A$	$-C$	$\pm D$	$-E$
Overload coefficient	$+\bar{B}$	$+B$	$+\hat{B}$	$+\hat{C}$	$+\hat{C}$	$-\hat{C}$
Resonant pulsation frequency	$+D$	$-B$	$-D$	$-C$	$-B$	0
Number of stalled cells	$-C$	$-C$	$+A$	$-B$	$-C$	$-E$
Unsteady distortions modules	$+\hat{B}$	$\pm\hat{B}$	$+\hat{B}$	$+B$	$-B$	$+C$
Steady distortions modulus	$-C$	$\pm B$	$+B$	$+D$	$+A$	$-E$

The letters A to E represent proportionality coefficients that indicate the importance of variation. For example: $\omega_R \rightarrow -D$. $\partial\bar{\omega}/\partial i$ (through the curve are not straight line). The letter A indicates a very large value, the letter E a very small value. The $\hat{}$ means that it exists a preference value that gives the magnification or the maximum extenuation.

Parametric study. A parametric study has been developed on the basis of the different compressors, and has pointed out the essential elements which influence on the one had, the stability and the probable flow configuration, and on the other hand, the amplificaiton of the distortions.

It is difficult to generalize the results which are necessarily limitative; this is why, instead of giving detailed figures, we prefer to present a synoptic table which shows the observed general tendancies.

It is to be noted that the appearance of a phenomenon (for instance transition from a stable to an unstable regime) depends on the conjunction of limit values of several parameters and not of one only.

The stable limit of operation is strongly influenced by the value of the $\partial\omega/\partial i$ coefficient (which characterises roughly boundary layer separation) to a lesser degree by $\partial\omega/\partial_{M_R}$, the effect of $\partial\beta/\partial\beta_e$ being secondary.

One can notice the influence of the geometrical parameters and the interest to increase chord and interrow axial spacing to set back the instability point.

The appearance of rotating stall depends on the overload coefficient, Q, and one can see that for a parameter $\partial\omega/\partial i$, $\partial\omega/\partial_{M_R}$, and $\partial\beta_s/\partial\beta_e$, there exists a particular value which enhances its appearance. This shows that rotating stall does not occur necessarily through boundary layer separation but that a conjunction of conditions in losses and deviation must be present for it to happen.

The cell speed is mainly influenced by the change in outlet angle ($\partial\beta_s/\partial\beta_e$), while the number of cells is governed by $\partial\omega/\partial i$ and $\partial\omega/\partial_{M_{Re}}$. The geometrical characteristics play also an important role in the case.

The amplitude of the unsteady distortions will be maximum for privileged values of $\partial\omega/\partial i$, $\partial\omega/\partial_{M_{Re}}$ and of chord; on the contrary, it will be smaller when $\partial\beta_s/\partial\infty_e$ is small. Further, the influence of the distance between blade rows can change depending on the operation point. The steady distortion will be less filtered when $\partial\beta_s/\partial\beta_e$ will be small (opposite to the case of unsteady distortions), while small values of $\partial\omega/\partial i$ will be favourable.

Conclusion

1 The nature of oscillatory phenomena in an axial compressor depends on phenomena of linear nature.

2 The appearance of an oscillatory regime or of a high level of turbulence depends mainly on the coefficient $\partial\omega/\partial i$. This suggests the use preferably of profiles which present a progressive increase in losses (or B. L. thickness with incidence) even if this leads to some efficiency reduction at nominal point.

oscillatory regime depends on geometry (chord, axial blade spacing). The internal organization of rotating stall (number of cells, velocity of propagation) depends on the rate of outlet angle change.

4 The amplification in space of distortion depends not only on the loss gradients and of the change in outlet angle but also on the geometrical dimensions of the compressor.

Reference

1 Pearson and McKenzie, "Wakes in Axial Compressors," *Journal of the R.A.S.*, Vol. 63, 1959.

2 Colpin, J., "Influence des distorsions d'entrée sur les performances et le comportement aérodynamique d'un compresseur axial," these de Doctorat, IVK, 1977.

3 Adamizyk, J. J., "Unsteady Fluid Dynamic Response of an Isolated Rotor With Distorted in Flow," *AIAA Journal*, 1974, p. 74–79.

4 Fabri, J., "Growth of a Perturbation in an Axial Flow Compressor," ASME, Paper No. 78-GT-80, 1978.

5 Mokelke, H., "The Prediction of Steady Circumferential Pressure and Temperature Distortions in Multistage Axial Flow Compressor," ASME Paper No. 79-GT-184, 1979.

6 Takata, H., and Nagano, S., "Nonlinear Analysis of Rotating Stall," ASME, Paper No. 72-GT-3, 1972.

7 Orner, N., "Prédiction du decrochage tournant dans les compresseurs axiaux," thèse de Doctorat, Faculte de Mons, IV 1976.

8 Costilow, E. L., and Hupper, M. C., "Rotating Stall Characteristics of a Rotor With High Hub Tip Radius Ratio," NACA TN.3518, 1955.

9 Wylie, C. R., *Advances in Engineering Mathematics*, McGraw-Hill, New York, 1975.

10 Ferrand, P., "Etude théorique des instabilités de l'écoulement dans les compresseurs axiaux," these de 3e Cycle, I.M.F.M., 1980.

ERRATA

Figure 18 of "Rotor Wake Mixing Effects Downstream of a Compressor Rotor," A. Ravindranath and B. Takshminarayana, published in the January 1982 issue of the ASME JOURNAL OF ENGINEERING FOR POWER, pp. 202–210, is in error. The revised figure is given below:

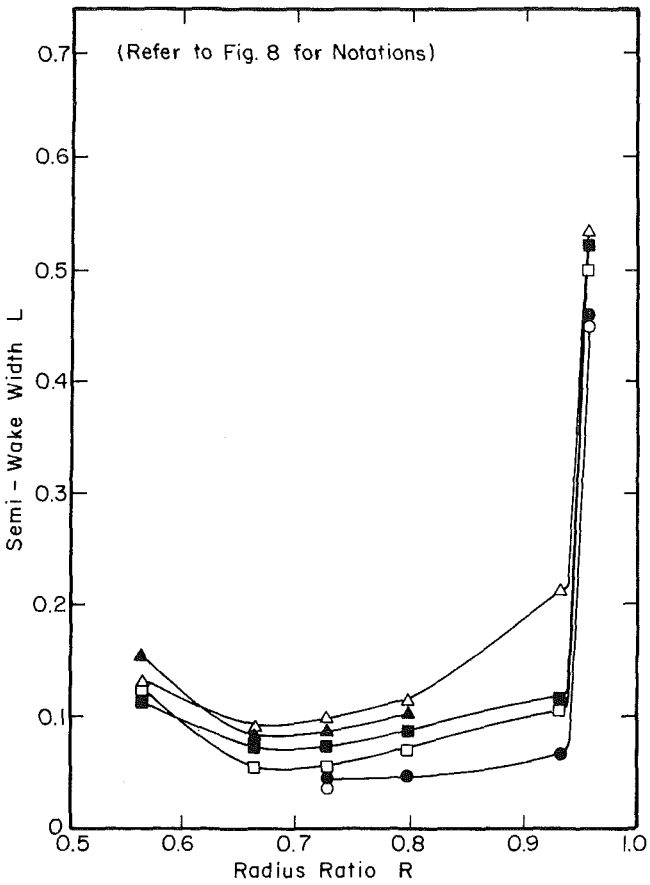

Fig. 18 Radial variation of semiwake width at various axial locations